



HAL
open science

Storage of solar energy by absorption: process experimentation and modeling

Fredy Huaylla

► **To cite this version:**

Fredy Huaylla. Storage of solar energy by absorption: process experimentation and modeling. Chemical and Process Engineering. Université Grenoble Alpes, 2017. English. NNT : . tel-02050102

HAL Id: tel-02050102

<https://theses.hal.science/tel-02050102>

Submitted on 26 Feb 2019

HAL is a multi-disciplinary open access archive for the deposit and dissemination of scientific research documents, whether they are published or not. The documents may come from teaching and research institutions in France or abroad, or from public or private research centers.

L'archive ouverte pluridisciplinaire **HAL**, est destinée au dépôt et à la diffusion de documents scientifiques de niveau recherche, publiés ou non, émanant des établissements d'enseignement et de recherche français ou étrangers, des laboratoires publics ou privés.

THÈSE

Pour obtenir le grade de

DOCTEUR DE LA COMMUNAUTÉ UNIVERSITÉ GRENOBLE ALPES

Spécialité : Doctorat Sciences Pour l'Ingénieur

Arrêté ministériel : 25 mai 2016

Présentée par

Fredy HUAYLLA ROQUE

Thèse dirigée par **Benoît STUTZ**, , USMB, et

codirigée par **Nolwenn LE PIERRES** USMB

préparée au sein du **Laboratoire Laboratoire d'Optimisation de la Conception et Ingénierie de l'Environnement**
dans l'**École Doctorale SISEO - Sciences et Ingénierie des Systèmes de l'Environnement et des Organisations**

Stockage d'énergie solaire par absorption: expérimentation et modélisation du procédé

Storage of solar energy by absorption: process experimentation and modeling

Thèse soutenue publiquement le **25 septembre 2017**,
devant le jury composé de :

Madame Nathalie MAZET

Professeur des Universités, PROMES-CNRS, Rapporteur

Monsieur Jean-Pierre BEDECARRATS

Professeur des Universités, Université de Pau et des pays de l'Adour,
Rapporteur

Monsieur Marc CLAUSSE

Professeur des Universités, INSA Lyon, Examineur

Monsieur Michel GRADECK

Professeur des Universités, Université de Lorraine, Président

Monsieur Benoit STUTZ

Professeur des Universités, Université Savoie Mont Blanc, Directeur de
thèse

Madame Nolwenn LE PIERRÈS

Maître de Conférences, Université Savoie Mont Blanc, Co-directeur de
thèse



À ma sœur Ruth Marlene

Remerciements

« La différence de base entre un homme ordinaire et un guerrier est qu'un guerrier prend tout comme un défi, alors qu'un homme ordinaire prend tout comme une bénédiction ou une malédiction ».

Différentes personnes m'ont aidé à pouvoir achever ce travail. J'aimerais transmettre ma profonde gratitude aux personnes suivantes :

Nolwenn LE PIERRES et Benoit STUTZ, mes directeurs de thèse qui ont dirigé ce travail et qui ont fait preuve de beaucoup de disponibilité, patience et d'humanité. Les questions scientifiques ont toujours eu une réponse et quelques fois, comme est naturel en recherche, des nouvelles questions.

Thierry GOLDIN et Cédric POINARD, personnel technique du LOCIE qui m'ont guidé dans toutes les étapes de construction du prototype et, hors des heures de travail, m'ont accompagné avec son amitié.

Les partenaires du projet PROSSIS 2 : Philippe LANCEREAU, Guillaume MONTZIEUX, Aline AUROUX, Denis MANGIN, Emilie GAGNIER, Simona BENICCI, Franck LIAUDET, Lingai LUO, pour leur apports et éléments de réflexion.

Tous les membres permanents ou doctorants du LOCIE qui m'ont aidé de différentes manières à travers des échanges d'idées, démarches administratives et activités diverses. Entre autres je pense à Martine VILLARD, Isabelle D'ERRICO, Elizabeth DESBOS, Jonathan OUTIN, Michel ONDARTS, ainsi que à Carolina FLORES, Carlos MORENO, Marie SWIATEK, José SILVA.

Je suis également très reconnaissant envers Monika WOLOSZYN, Catherine BUHE, Lamia BERRAH, Vincent CLIVILLE, qui m'ont soutenu afin de commencer une formation doctorale.

Aux amis et, avec beaucoup de gratitude et estime, à toute ma famille.

Résumé

Les préoccupations environnementales liées à la consommation d'énergie et aux émissions de gaz à effet de serre ne cessent d'augmenter. Leur impact devrait conduire à une augmentation de 3.1°C de la température terrestre d'ici 2100 par rapport aux niveaux préindustriels. Les systèmes mettant en œuvre les énergies renouvelables ont attiré l'intérêt de la société, du fait de leur très faible impact sur l'effet de serre et l'utilisation du soleil comme source inépuisable d'énergie. La difficulté de faire coïncider la disponibilité de l'énergie solaire avec la consommation de chaleur a conduit la communauté scientifique à porter une attention particulière aux technologies de stockage de chaleur au cours des dernières années, en particulier en ce qui concerne les technologies capables de stocker la chaleur pendant de longues périodes. Dans cette thèse, un système capable de stockage intersaisonnier de l'énergie solaire thermique appliqué au chauffage des bâtiments et mettant en œuvre un procédé par absorption est proposé. Son mode de fonctionnement est basé, respectivement, sur le stockage de la chaleur pendant l'été et sa restitution en hiver à l'aide d'une solution aqueuse absorbante. Un état de l'art des systèmes à absorption similaires développés et expérimentés durant ces 5 dernières années a été réalisé. L'importance d'une bonne conception du réacteur constitue un point clef. Un modèle original simulant le comportement des composants du système de stockage intersaisonnier a été développé. Il a permis de dimensionner un prototype mettant en œuvre le couple LiBr-H₂O. Une validation du modèle a été faite sur la base des résultats expérimentaux obtenus ainsi qu'avec des comparaisons à d'autres résultats de la littérature. Une étude paramétrique de l'influence des conditions de fonctionnement sur la performance du système a été menée avec des conditions opératoires correspondant aux besoins de chauffage d'une maison individuelle. Les expérimentations en phase de charge et de décharge ont été menées et des puissances comprises respectivement entre 1 et 2 kW et entre 0.6 et 1.5 kW ont été obtenues. Une densité énergétique de stockage de chaleur comprise entre 109 et 120 kWh/m³ a été obtenue. Une simulation du fonctionnement d'un système de stockage de chaleur intersaisonnier couplé à une maison individuelle pendant une période de 2 ans a été réalisée et discutée.

Mots clés: sorption, absorption, stockage de chaleur intersaisonnier, énergie solaire, transfert de chaleur et de masse, échangeurs de chaleur et de masse, bromure de lithium/eau, cristallisation, modélisation, simulation dynamique, prototype, expérimentation, chauffage de bâtiments.

Abstract

Environmental concerns related to energy consumption and greenhouse gas emissions have grown in recent years due to the impact they have on the global earth temperature, estimated to increase in 3.1°C by the year 2100 with respect to pre-industrial temperatures. Renewable energy systems have gained the society interest since they can produce thermal heat and electricity without generation of greenhouse gases and can use the sun as an inexhaustible energy source. Due to the inner difficulty to match the solar energy production with the energy demands, a scientific effort to develop heat storage technologies has been carried out during the last years; in particular, technologies capable of storing the heat for long periods. In this thesis a system capable of inter-seasonal solar heat storage, dedicated to building space heating applications and based on the sorption process is proposed. Its working principle is based, respectively, in the storage or restitution of heat during summer or winter trough the desorption or absorption of an aqueous solution. A review of the state of the art of similar experimental systems constructed during the last 5 years and based on the sorption phenomenon on four aqueous solutions was developed. The importance of a good design of the reactor was highlighted. A detailed and original simulation model of the components of the interseasonal heat storage system, particularly of the heat and mass exchangers inside the reactor (absorber, desorber, evaporator and condenser), was developed and proposed. The LiBr-H₂O working couple was selected for this research, since its physical properties are widely characterized in the literature. A validation of the model against experimental results from other studies was performed, with good agreements obtained. Furthermore, a parametrical study of the working conditions influence on the system performance was carried out. Based on this study, a system experimental prototype was constructed and tested in operating conditions compatible with the space heating needs of a dwelling. Charging and discharging processes were proven to be successful with measured powers between 1 and 2 kW and between 0.6 and 1.5 kW, respectively. The system heat storage capacity measured was between 109 and 120 kWh/m³. A comparison of the model against the prototype experimental results, as well as the study of the simulated behavior of the interseasonal heat storage system when coupled to a dwelling for a two years' period were performed and discussed.

Keywords: sorption, absorption, interseasonal heat storage, solar energy, heat and mass transfer, heat and mass exchangers, lithium bromide/water, crystallization, modeling, dynamic simulation, prototype, experiments, building heating.

Table of contents

REMERCIEMENTS	II
RESUME	III
ABSTRACT.....	IV
TABLE OF CONTENTS.....	V
LIST OF THE FIGURES	X
LIST OF THE TABLES	XVI
NOMENCLATURE	XVIII
RÉSUMÉ	XXI
R1.Systèmes intersaisonnier de stockage de chaleur – État de l’art	xxi
<i>R1.1. Systèmes de stockage de chaleur solaire à basse température</i>	xxi
<i>R1.2. Systèmes intersaisonniers de stockage de chaleur basés en procédés de sorption gaz/liquide: Révision des cas expérimentaux</i>	xxi
R2. Modélisation et simulation du système intersaisonnier de stockage de chaleur	xxii
<i>R2.1. Réacteur</i>	xxii
<i>R2.2. Réservoirs</i>	xxiii
<i>R2.3. Tubes</i>	xxiv
<i>R2.4. Système de stockage global</i>	xxiv
R3. Prototype expérimental du système de stockage de chaleur intersaisonnier	xxiv
<i>R3.1. Conception et construction du prototype</i>	xxiv
<i>R3.2. Tests expérimentaux</i>	xxiv
<i>R3.3. Comparaison des résultats expérimentaux avec le modèle de simulation</i>	xxv
R4. Performance annuelle du système intersaisonnier de stockage de chaleur	xxv
<i>R4.1. Modèle de simulation du système de stockage intersaisonnier de chaleur/maison</i>	xxv
<i>R4.2. Simulation de la configuration de référence</i>	xxv
<i>R4.3. Étude paramétrique et configuration optimisée</i>	xxvi
<i>R4.4. Performance annuelle du système de stockage intersaisonnier de chaleur avec une solution de KCOOH-H₂O</i>	xxvi
Références	xxvi
INTRODUCTION	XXVIII

CHAPTER 1. INTERSEASONAL HEAT STORAGE SYSTEMS – STATE OF THE ART . 1

1.1. Low temperature solar heat storage system	2
1.2. Interseasonal heat storage systems based on gas/liquid sorption process: Experimental cases review	6
1.2.1. Lithium chloride (LiCl-H ₂ O) systems	6
1.2.1.1. ClimateWell - Sweden	6
1.2.1.2. Shanghai Jiao Tong university - China	8
1.2.2. Calcium chloride (CaCl ₂ -H ₂ O) systems	11
1.2.2.1. LOCIE – University Savoie Mont Blanc - France	11
1.2.2.2. University of Minnesota -USA	14
1.2.3. Sodium hydroxide (NaOH-H ₂ O) – EMPA - Switzerland	15
1.2.4. Lithium Bromide (LiBr-H ₂ O) systems	18
1.2.4.1. LOCIE – University Savoie Mont Blanc - France	18
1.2.4.2. Tsinghua university - China	21
1.2.5. Comparison summary of the study cases	23
1.3. Conclusions	24
Bibliography	24

CHAPTER 2. MODELLING AND SIMULATION OF THE INTERSEASONAL HEAT STORAGE SYSTEM27

2.1. Reactor	28
2.1.1. Reactor components simulation models	30
2.1.1.1. Modelling of an absorption/desorption heat exchanger	30
2.1.1.1.1. <i>Falling film boundary conditions</i>	30
2.1.1.1.2. <i>Mass and heat transfer convective coefficients of the falling film</i>	32
2.1.1.1.3. <i>Nodal discretization and control volume balance</i>	34
2.1.1.1.4. <i>Solving procedure</i>	36
2.1.1.2. Modelling of the evaporator	37
2.1.1.3. Modelling of the condenser	38
2.1.1.4. Coupling model for the absorption/desorption and evaporation/condensation heat exchangers	40
2.1.1.5. Modelling of a wetting effect on the metallic plates	41
2.1.2. Model validation	42
2.1.2.1. Comparison against a numerical case of water absorption on a LiBr solution film falling along a vertical plate	42
2.1.2.2. Comparison against an experimental case of water absorption on a LiBr solution film falling along a vertical tube	43
2.1.2.3. Interpretation of simulation results against an experimental case of desorption/condensation and absorption/evaporation in the reactor of an interseasonal heat storage prototype	45
2.1.2.3.1. <i>Experimental setup</i>	45
2.1.2.3.2. <i>Model's comparison against an experimental case in desorption/condensation operating mode</i>	46
2.1.2.3.3. <i>Model's comparison against an experimental case in absorption/evaporation operating mode</i>	48
2.1.2.3.4. <i>Wettability tests on brass and stainless steel plates</i>	50
2.1.3. Parametrical study and optimal working conditions for a grooved vertical flat plate heat exchanger configuration	53
2.1.3.1. Reference simulation case and inlet working conditions parametrical study	54
2.1.3.1.1. Simulated desorption/condensation process performance	55

2.1.3.1.2. Simulated absorption/evaporation process performance	60
2.1.3.2. Optimized working conditions	66
2.1.3.2.1. Simulated desorption/condensation process	66
2.1.3.2.2. Simulated absorption/evaporation process	68
2.1.4. Mesh number and fluids movement direction influence	71
2.2. Tanks	75
2.2.1. LiBr solution tank model	75
2.2.1.1. Liquid solution tank discretization and nodal approach	75
2.2.1.1.1. Simulation stability indicators	81
2.2.1.2. LiBr solution crystallization approach	82
2.2.1.3. Case studies	84
2.2.1.3.1. Liquid solution case	84
2.2.1.3.2. Crystal/liquid solution case	87
2.2.2. Water tank model	90
2.3. Pipes	93
2.4. Overall storage system	95
2.5. Conclusions	97
Bibliography	98

CHAPTER 3. EXPERIMENTAL PROTOTYPE OF THE INTERSEASONAL HEAT STORAGE SYSTEM

3.1. Prototype conception and construction	100
3.1.1. Prototype conception	100
3.1.1.1. Reactor container and heat exchangers	100
3.1.1.2. LiBr solution tank	103
3.1.1.3. Water tank	104
3.1.1.4. Connection pipes	104
3.1.1.5. Thermal modules and pumps	104
3.1.1.6. Flowmeters	105
3.1.1.7. Temperature, pressure and level sensors	106
3.1.2. Prototype construction	106
3.2. Experimental tests	109
3.2.1. Gas leakage rate	109
3.2.2. General experimental plan	110
3.2.3. Tests	112
3.2.3.1. Desorption/condensation: typical results	112
3.2.3.2. Desorption/condensation: summary of the results	120
3.2.3.3. Absorption/evaporation: typical results	122
3.2.3.4. Absorption/evaporation: summary of the results	129
3.2.4. Crystallization	131
3.2.4.1. Desorption/condensation functioning	131
3.2.4.2. Absorption/evaporation functioning	132
3.2.5. Energy storage density	134
3.3. Comparison of the experimental results against simulation	135

3.3.1. Desorption/condensation	136
3.3.2. Absorption/evaporation	139
3.4. Conclusions	144
Bibliography	145
CHAPTER 4. INTERSEASONAL HEAT STORAGE SYSTEM ANNUAL PERFORMANCE	147
4.1. Interseasonal heat storage system/dwelling simulation model	149
4.1.1. Solar thermal collector	149
4.1.2. Heat source/sink	150
4.1.3. Mixing tank	151
4.1.4. Global compilation	152
4.2. Simulation reference configuration	154
4.2.1. Technical characteristics	154
4.2.1.1. Dwelling.....	154
4.2.1.2. Heat storage system	155
4.2.1.3. Mixing tank	157
4.2.1.4. Solar collector	157
4.2.1.5 Heat source/sink.....	158
4.2.2. Simulated annual performance	159
4.3. Parametrical study and improved configuration	165
4.3.1. Solution tank insulation thickness	165
4.3.2. Initial solution tank mass.....	169
4.3.3. Solar collector surface and solar collector HTF outlet temperature	174
4.4. Heat storage system annual performance with a KCOOH- H ₂ O solution	182
4.5. Conclusions and outlooks	185
Bibliography	187
GENERAL CONCLUSIONS AND OUTLOOKS.....	188
General conclusions	189
Outlooks	191
ANNEX A	192
Annex A1	193
<i>A1.1. Closed heat storage system based on water absorption/desorption in aqueous lithium chloride (LiCl-H₂O) – Shanghai Jiao Tong university - China</i>	<i>193</i>
<i>A1.3. Closed heat storage system based on water absorption/desorption in aqueous lithium bromide (LiBr-H₂O) – Tsinghua university - China</i>	<i>194</i>
ANNEX B	196
Annex B1	197
B1.1. Physical numbers.....	197

B1.2. Physical correlations for the LiBr solution.....	197
B1.3. Simulation model adaptation to a heat exchanger configuration.....	203
<i>B1.3.1. Flat plate configuration</i>	203
<i>B1.3.2. Shell and tube configuration</i>	203
B1.4. Modelling of a wetting effect on the metallic plates	204
B1.5. Modelling of recirculation.....	205
B1.6. Comparison against an experimental case of desorption/condensation and absorption/evaporation in the reactor of an interseasonal heat storage prototype: additional cases	208
<i>B1.6.1. Simulation model validation for a desorption/condensation operating mode</i>	208
<i>B1.6.2. Simulation model validation for an absorption/evaporation operating mode</i>	208
B1.7. Simulated desorption/condensation and absorption/evaporation process performance.....	211
Annex B2	214
B2.1. Liquid solution tank simulation model stability indicators	214
B2.2. Heat transfer across the solution tank wall in crystals presence.....	214
 ANNEX C	 216
Annex C1	217
C1.1. Prototype components technical description	217
C1.2. Temperature sensors calibration.....	222
C1.3. System gas leakage rate calculation method	223
Annex C2	225
C2.1. Experimental tests in desorption/condensation and absorption/evaporation operating mode	225
<i>C2.1.1. Desorption/Condensation experimental tests</i>	226
<i>C2.1.2. Absorption/Evaporation experimental tests</i>	234
C2.2. Solution LiBr mass concentration correlation	238
C2.3. LiBr mass balance in the reactor	238
C2.4. Dühring diagram associated to the system components	239
Annex C3	239
C3.1. Comparison against simulation	239
<i>C3.1.1. Desorption/condensation</i>	240
<i>C3.1.2. Absorption/evaporation</i>	242
 ANNEX D	 244
Annex D1	245
<i>D1.1. Physical properties correlations for the KCOOH-H₂O solution</i>	245
<i>D1.1.1. Density</i>	245
<i>D1.1.2. Specific heat</i>	245
<i>D1.1.3. Thermal conductivity</i>	246
<i>D1.1.4. Absolute viscosity</i>	246
<i>D1.1.5. Solubility crystallization curve</i>	247
<i>D1.1.6. Vapor pressure of the KCOOH-H₂O solution</i>	248

List of the figures

Figure 1.1. Energy density of high energy storage methods.....	3
Figure 1.2. Schematic of a single unit thermos-chemical accumulator	7
Figure 1.3. CW10 TCA machine. a) Schema of the CW10 prototype (Single barrel); b) Schematic of the commercial version of the CW10 machine (Two barrels)	8
Figure 1.4. Experimental system of the sorption thermal energy storage system.....	9
Figure 1.5. Structure details of the experimental prototype. a) Experimental prototype; b) Sorption reactor; c) Sorption unit; d) Copper mesh; e) Condenser/Evaporator	9
Figure 1.6. Operating principle and thermodynamic working conditions for a three-phase sorption cycle in winter seasons involving LiCl-H ₂ O working pair.....	10
Figure 1.7. a) Heat storage capacity vs. charging temperature; b) Heat storage capacity vs. discharging temperature	11
Figure 1.8. Scheme of the prototype.....	12
Figure 1.9. a) Design of the heat exchanger with helical fins b) Experimental setup of the absorption storage system	13
Figure 1.10. Schematic of a closed –cycle absorption heating system with a single tank for storage of water, diluted and concentrated calcium chloride solution	14
Figure 1.11. Prototype absorption/sensible storage tank. a) Illustration of immersed heat exchanger and stratification manifold; b) convective flow patterns expected during charging period; c) Photograph of prototype liquid CaCl ₂ tank including laser sheet and PIV/PLIF imaging cameras.....	15
Figure 1.12. a) Picture of the complete prototype from the outside (solar collectors placed on top and side of the ship container); b) Picture of the complete prototype from the inside; c) Scheme of the hydraulic concept around the heat and mass exchangers in the sorption system	16
Figure 1.13. Falling film bundle heat and mass exchanger considered in the sorption reaction zone	17
Figure 1.14. a) Power development (Φ) as a function of the temperature difference (ΔT) between absorber and evaporator chamber during discharging process; b) Illustration of the absorber and evaporator heat and mass exchangers results with approximately 10 mbar pressure resulting from non-condensing gases	17
Figure 1.15. Interseasonal absorption storage system principle. Charging mode (top) and discharging mode (bottom).	18
Figure 1.16. a) Schematic of the interseasonal absorption storage system; b) Constructed prototype	19
Figure 1.17. Reactor design and operation principle of the heat exchangers. a) Reactor; b) Fluids circulation in the heat exchanger (principle); c) Liquid distribution chamber (principle).	19
Figure 1.18. Schematic diagram and operational processes of the ATES a) Charging process; b) Discharging process	21
Figure 1.19. Constructed apparatus of the experiment system	22
Figure 2.1. Interseasonal sorption heat storage system.....	28
Figure 2.2. Schematic description of the exchanger chosen for the model in the case of the LiBr solution falling film.....	29
Figure 2.3. Schematic description of the mass and energy fluxes crossing the falling film interfaces. a) Mass fluxes. b) Energy fluxes.	31
Figure 2.4. Inlet concentration effect on the downstream variation of the local Sherwood and Nusselt number for an isothermal plate	33
Figure 2.5. Modified Nu correlation	34
Figure 2.6. Heat exchanger nodal division used for the volume control energy and mass balance in the absorber/desorber.....	35
Figure 2.7. Heat exchanger nodal division used for the volume control energy and mass balance in the evaporator	37
Figure 2.8. Coupling of the evaporator/absorber (desorber/condenser) in the reactor at saturated conditions	40

Figure 2.9. Desorber/Absorber boundary conditions in the nodal approach when counter-current movement is considered (bleu: know values, red: unknown values)	41
Figure 2.10. Heat transfer across a metallic surface not completely wetted by a falling film. a) Liquid film on stainless steel plate b) Optimistic case transfer mode (1F); c) Pessimistic case transfer mode (2F).....	41
Figure 2.11. Comparison of our simulation model against simulated results obtained by Karami. a) Scheme of the simulated case. b) Comparison of temperature and mass fraction at the film interface.	42
Figure 2.12. Comparison of our simulation model against experimental results obtained by Miller and Keyhani (2001) and Medrano et al. (2002). a) Scheme of the simulated case. b) Comparison of the absorbed mass flux per unit surface for different inlet solution Reynolds numbers.	43
Figure 2.13. a) Constructed prototype of the heat storage system based on sorption process. b) Distribution head for the LiBr solution or water. c) Detail of the shell and tube heat exchangers constructed in the reactor ..	45
Figure 2.14. Comparison between experimental and simulated results for the desorption/condensation operation mode tests (N'Tsoukpoe et al., 2013). a) LiBr solution temperature; b) LiBr solution mass fraction; c) HTF temperature in the desorber; d) HTF temperature in the condenser.	47
Figure 2.15. Comparison between experimental and simulated results for the absorption/evaporation operation mode. a) LiBr solution temperature; b) LiBr mass fraction in the solution; c) HTF temperature in the absorber; d) HTF temperature in the evaporator.	50
Figure 2.16. Scheme of the experimental setup to test the surface wettability of metallic plates.	51
Figure 2.17. Wetted surface at the maximum flow rate. a) Detail of the software treatment for the Brass plate/LiBr solution image; b) LiBr solution wetting the stainless steel surface; c) Distilled water wetting the brass surface before homogenization; d) Distilled water wetting the stainless steel surface before homogenization.....	52
Figure 2.18. Wettability tests made on stainless steel and brass plates at atmospheric pressure. a) With an aqueous LiBr solution (52.5% LiBr concentration). b) With distilled water.	52
Figure 2.19. Grooved vertical flat plate sandwich configuration. a) front view of the grooved plate; b) Grooves associated to the falling films; c) Flat serpentine network associated to the HTF.	54
Figure 2.20. Exchangers performance in the desorption/condensation coupled process. a) LiBr solution temperature; b) Solution LiBr mass fraction; c) HTF temperature at the desorber; d) HTF temperature at the condenser.	56
Figure 2.21. Exchangers performance in the desorption/condensation coupled process. a) Water mass flow desorbed from the LiBr solution falling film; b) Pressure of the vapor system; c) Thermal output of the HTF in the desorber; d) Thermal output of the HTF in the condenser.....	57
Figure 2.22. Evaluation of the desorbed water mass flow indicator as a function of the inlet LiBr mass concentration for different inlet parameters. a) LiBr solution inlet mass flow; b) Desorber HTF inlet mass flow; c) Condenser HTF inlet mass flow; d) Desorber HTF inlet temperature; e) Condenser HTF inlet temperature.	59
Figure 2.23. Synthesis of the evolution of the average desorbed water mass flow indicator for the different simulated cases.	60
Figure 2.24. Exchangers performance in the absorption/evaporation process. a) LiBr solution temperature; b) LiBr mass fraction in the solution; c) HTF temperature in the absorber; d) HTF temperature in the evaporator.	61
Figure 2.25. Exchangers performance in the absorption/evaporation process. a) Water mass flow absorbed by the LiBr solution; b) Pressure of the vapor; c) Thermal output from the HTF in the absorber; d) Thermal output from the HTF in the evaporator.	62
Figure 2.26. Evaluation of the absorber HTF temperature indicator as a function of the inlet LiBr mass fraction for different inlet parameters. a) LiBr solution inlet mass flow; b) Water film inlet mass flow; c) Absorber HTF inlet mass flow; d) Evaporator HTF inlet mass flow; e) Absorber HTF inlet temperature; f) Water film and Evaporator HTF inlet temperatures.	64
Figure 2.27. Synthesis of the evolution of the average absorber HTF temperature indicator for the different simulated cases.	65
Figure 2.28. Desorption/condensation performance as a function of the inlet LiBr mass fraction for the optimized and reference simulation cases. a) Desorbed water mass flow; b) Desorbed water mass flow	

indicator; c) Condenser HTF thermal output; d) Desorber HTF temperature; e) Desorber HTF thermal input	67
Figure 2.29. Absorption/evaporation performance as a function of the inlet LiBr mass concentration for the optimized and reference simulation cases. a) Absorber HTF temperature; b) Absorber HTF temperature indicator; c) HTF thermal output at the absorber; d) Absorbed water mass flow; e) HTF thermal input at the evaporator	70
Figure 2.30. Graphical description of the different mesh types considered for the sensibility study.	72
Figure 2.31. Average mesh indicators values for simulation cases with different mesh numbers and fluids movement type; a) Desorption/condensation operating mode; b) Absorption/evaporation operating mode	73
Figure 2.32. Computing time needed for simulation cases with different mesh numbers and fluids direction type; a) Desorption/condensation operating mode; b) Absorption/evaporation operating mode	75
Figure 2.33. Scheme and nodal discretization of the cylindrical LiBr solution tank	76
Figure 2.34. Nodal discretization of the LiBr solution tank at the time “1-1” and “1”	77
Figure 2.35. LiBr solution crystallization curve.	82
Figure 2.36. Liquid LiBr solution tank. Simulation response of the temperature, LiBr mass fraction and mass parameters for the “charge” mode; a) b) c) Case 1; d) e) f) Case 2; g) h) i) Case 3; j) k) l) Case 4.	86
Figure 2.37. Liquid LiBr solution tank. Simulation response of the temperature, LiBr mass fraction and mass parameters for the “discharge” mode; a) b) c) Case 5; d) e) f) Case 6; g) h) i) Case 7.	87
Figure 2.38. Crystal/liquid LiBr solution tank. Simulation response of the temperature, LiBr mass fraction and mass parameters for the charge, standby and discharge modes.	88
Figure 2.39. Average GrstRest2 and Rast numbers associated to the solution tank. a) Case 1; b) Case 2; c) Case 5.....	89
Figure 2.40. Nodal discretization of the water tank at the time “1-1” and “1”	90
Figure 2.41. Nodal discretization of the LiBr solution cylindrical pipe	94
Figure 2.42. Schema of the compilation of the interseasonal heat storage components models	96
Figure 3.1. Interseasonal heat storage system prototype schema.....	101
Figure 3.2. a) Reactor container design; b) sandwich grooved vertical flat plate heat exchangers design; c) Container and heat exchangers assembling.....	102
Figure 3.3. LiBr solution tank design	103
Figure 3.4. Water tank design.....	104
Figure 3.5. Flowmeters positioning associated to the solution and water leaving the reactor.	105
Figure 3.6. Constructed interseasonal heat storage prototype. a) b) Views of the global assembled system; c) Detail of the Coriolis flowmeters and the connecting tubes at the reactors outlet; d) Grooved flat plate heat exchangers; e) Detail of the heat exchangers positioning in the reactor container	108
Figure 3.7. Experimental results obtained in desorption/condensation operating mode for the Test 1. a) LiBr solution temperature (desorber); b) LiBr mass concentration (desorber); c) LiBr solution mass flow (desorber); d) Water film temperature (condenser); e) Desorbed/condensed water (reactor)	113
Figure 3.8. Experimental results obtained in desorption/condensation operating mode for the Test 1. a) HTF temperature (desorber); b) HTF temperature (condenser); c) Power given from the HTF to the system (desorber); d) Power given from the HTF to the system (condenser)	114
Figure 3.9. Experimental results obtained in desorption/condensation operating mode for the Test 1. a) Vapor pressure; b) LiBr solution temperature (solution tank); c) Water temperature (water tank)	115
Figure 3.10. Inlet, outlet and thermocouples positioning at the solution tank	115
Figure 3.11. Experimental results obtained in desorption/condensation operating mode for the Test 2. a) LiBr solution temperature (desorber); b) LiBr mass concentration (desorber); c) LiBr solution mass flow (desorber); d)) Desorbed/condensed water (reactor); e) Vapor pressure of the system main components	118
Figure 3.12. Experimental results obtained in desorption/condensation operating mode for the Test 2. a) HTF temperature (desorber); b) HTF temperature (condenser); c) Power given from the HTF to the system (desorber); d) Power given from the HTF to the system (condenser)	119
Figure 3.13. Experimental limitations in the desorption/condensation tests due to low wettability in the heat exchangers grooved surfaces. a) Libr solution falling film flowing along the desorber; b) Condensed water along the condenser.....	122

Figure 3.14. Experimental results obtained in absorption/evaporation operating mode for Test 7. a) LiBr solution temperature (absorber); b) LiBr fraction (absorber); c) LiBr solution mass flow (absorber); d) Water film temperature (evaporator); e) Water film mass flow (evaporator); f) Absorbed/evaporated water (reactor)	124
Figure 3.15. Experimental results obtained in absorption/evaporation operating mode for the Test 7. a) HTF temperature (absorber); b) HTF temperature (evaporator); c) Power given from the HTF to the system (absorber); d) Power given from the HTF to the system (evaporator)	125
Figure 3.16. Experimental results obtained in desorption/condensation operating mode for the Test 7. a) Vapor pressure; b) LiBr solution temperature (solution tank); c) Water temperature (water tank)	126
Figure 3.17. Experimental results obtained in absorption/evaporation operating mode for the Test 8. a) LiBr solution temperature (absorber); b) LiBr mass concentration (absorber); c) LiBr solution mass flow (absorber); d) Absorbed water (reactor); e) Vapor pressure of the system main components	128
Figure 3.18. Experimental results obtained in absorption/evaporation operating mode for the Test 8. a) HTF temperature (absorber); b) HTF temperature (evaporator); c) Power given from the HTF to the system (absorber); d) Power given from the HTF to the system (evaporator)	129
Figure 3.19. LiBr solution crystals formation during the desorption/condensation tests. a) End of day 1; b) End of day 3; c) During the day 4; d) End of day 4	131
Figure 3.20. LiBr solution along the crystals formation in “day 4” test (desorption/condensation). a) LiBr solution temperature (solution tank); b) LiBr mass fraction (desorber)	132
Figure 3.21. LiBr solution crystals formed in the solution tank during the “day 5” absorption/evaporation test.	133
Figure 3.22. LiBr solution conditions along the crystals dilution “day 5” test (absorption/evaporation). a) LiBr solution temperature (solution tank); b) LiBr mass concentration (absorber)	133
Figure 3.23. Comparison between experimental and simulated results obtained in desorption/condensation operating mode for the Test 1. a) Pressure in the reactor b) LiBr solution temperature (desorber); c) LiBr mass concentration (desorber); d) Desorbed/condensed water mass flow (reactor); e) Water film temperature (condenser)	137
Figure 3.24. Comparison between experimental and simulated results obtained in desorption/condensation operating mode for the Test 1. a) HTF temperature (desorber); b) HTF temperature (condenser); c) Power given from the HTF to the system (desorber); d) Power given from the HTF to the system (condenser) .	138
Figure 3.25. Comparison between experimental and simulated results obtained in absorption/evaporation operating mode for the Test 7 - (with $\Delta P = 4$ mbar). a) Pressure in the reactor; b) LiBr solution temperature (absorber); c) LiBr mass concentration (absorber); d) Absorbed/evaporated water mass flow (reactor); e) Water film temperature (evaporator)	140
Figure 3.26. Comparison between experimental and simulated results obtained in absorption/evaporation operating mode for the Test 7 - (with $\Delta P = 4$ mbar). a) HTF temperature (absorber); b) HTF temperature (evaporator); c) Power given from the HTF to the system (absorber); d) Power given from the HTF to the system (evaporator)	141
Figure 3.27. Non-condensable gas presence during the absorption/evaporation process. a) Pressure gradient in the absorbing film; b) Scheme of the evaporator/absorber pressure gap considered in the model	142
Figure 4.1. Scheme of the components of the interseasonal heat storage system by absorption. a) In charging period (summer); b) In discharging period (winter)	148
Figure 4.2. Scheme of the solar thermal collector	149
Figure 4.3. Scheme of the heat sink	150
Figure 4.4. Scheme of the mixing tank and its associated components	151
Figure 4.5. Scheme of the coupling of the components of the interseasonal heat storage system when it is associated to a dwelling. Charging operating mode	152
Figure 4.6. Scheme of the coupling of the components of the interseasonal heat storage system when it is associated to a dwelling.	153
Figure 4.7. Annual heating power required by the passive dwelling	154

Figure 4.8. System reactor annual physical behavior (second year). a) HTF desorber/absorber temperature; b) HTF condenser/evaporator temperature; c) HTF desorber/absorber power; d) HTF condenser/evaporator power; e) Desorbed (-)/Absorbed (+) water mass flow; f) System components pressure.....	160
Figure 4.9. LiBr solution tank annual physical behavior (second year). a) Temperature; b) LiBr mass fraction; c) Masses; d) Heights.....	162
Figure 4.10. Water tank annual physical behavior. a) Temperature; b) Mass	162
Figure 4.11. System annual performance (second year). a) Heating power provided by the reactor and the solar collector; b) Heating power provided by the electrical source; c) Reactor working period in discharge mode; d) Solar collector working period in discharge mode); e) Dwelling heating needs coverage provided by different sources.....	163
Figure 4.12. Solution tank temperature (a, b, c, d)) and LiBr mass concentration (e, f, g, h)) annual physical behavior for cases in Table 4.10 (second year). a) e) No insulation (reference case); b) f) 10 cm wall thickness insulation; c) g) 20 cm wall thickness insulation; d) h) 30 cm wall thickness insulation.....	166
Figure 4.13. Solution tank mass physical behavior (a, b, c, d)) and solar collector and system reactor generated heating power (e, f, g, h)) for cases in Table 4.10. a) e) No insulation (reference case); b) f) 10 cm wall thickness insulation; c) g) 20 cm wall thickness insulation; d) h) 30 cm wall thickness insulation	167
Figure 4.14. System annual performance: dwelling heating needs coverage provided by different sources for cases in Table 4.10. a) No insulation (reference case); b) 10 cm wall thickness insulation; c) 20 cm wall thickness insulation; d) 30 cm wall thickness insulation.	169
Figure 4.15. Solution tank temperature (a, b, c, d)) and LiBr mass concentration (e, f, g, h)) annual physical behavior for cases in Table 4.11 (second year). a) e) 14132 kg initial solution tank mass (reference case B); b) f) 12000 kg initial solution tank mass; c) g) 10000 kg initial solution tank mass; d) h) 8000 kg initial solution tank mass.....	171
Figure 4.16. Solution tank mass physical behavior (a, b, c, d)) and solar collector and system reactor generated heating power (e, f, g, h)) for cases in Table 4.11 (second year). a) e) 14132 kg initial solution tank mass (reference case B); b) f) 12000 kg initial solution tank mass; c) g) 10000 kg initial solution tank mass; d) h) 8000 kg initial solution tank mass	173
Figure 4.17. System energy annual performance: dwelling heating needs coverage provided by different sources for cases in Table 4.11 (second year). a) 14132 kg initial solution tank mass (reference case B); b) 12000 kg initial solution tank mass; c) 10000 kg initial solution tank mass; d) 8000 kg initial solution tank mass.	174
Figure 4.18. Solution tank temperature (a, b, c, d)) and LiBr mass fraction (e, f, g, h)) annual physical behavior for cases in Tables 4.12 and 4.13 (second year). a) e) 12 m ² solar collector surface (reference case “C”); b) f) 10 m ² solar collector surface; c) g) 8 m ² solar collector surface (reference case “D”); d) h) 70 °C solar collector HTF minimal threshold outlet temperature (charging mode).....	176
Figure 4.19. Solution tank mass physical behavior (a, b, c, d)) and solar collector and system reactor generated heating power (e, f, g, h)) for cases in Tables 4.12 and 4.13 (second year). a) e) 12 m ² solar collector surface (reference case “C”); b) f) 10 m ² solar collector surface; c) g) 8 m ² solar collector surface (reference case “D”); d) h) 70 °C solar collector HTF minimal threshold outlet temperature (charging mode)	177
Figure 4.20. System energy annual performance: dwelling heating needs coverage provided by different sources for cases in Tables 4.12 and 4.13 (second year). a) 12 m ² solar collector surface (reference case “C”); b) 10 m ² solar collector surface; c) 8 m ² solar collector surface (reference case “D”); d) 70 °C solar collector HTF minimal threshold outlet temperature (charge mode).....	178
Figure 4.21. Annual desorbed (-)/absorbed (+) water mass flow in the reactor (second year). a) “Reference case D” (THTF/sc/ch. op. modelmin. treshold = 50°C); b) Case 10 (THTF/sc/ch. op. modelmin. treshold = 70°C).....	180
Figure 4.22. System annual physical behavior (second year). a) Solution tank temperature; b) Solution tank KCOOH mass fraction; c) Solution tank mass; d) Heating power provided by the solar collector and the reactor; e) Dwelling annual heating needs coverage provided by different sources	183

Figure 4.23. System annual physical behavior (second year). Dwelling heating needs and heating power provided by the reactor in “case 11” (KCOOH) and in “reference case” (LiBr) 184

List of the tables

Table 1.1. Comparison of the three available technologies for seasonal thermal energy storage	5
Table 1.2. Test results of a single unit of a CW10 TCA prototype. Tests carried out at ClimateWell AB in November 2005.....	7
Table 1.3. Technical characteristics of the prototype components	12
Table 1.4. Working conditions and system performance of experimental tests in desorption/condensation and absorption/evaporation operating mode	13
Table 1.5. Main features of each heat exchanger.....	19
Table 1.6. Charging and discharging test results	20
Table 1.7. Corrosion data of three solution couples for stainless steel 304	21
Table 1.8. Main features of the study cases prototypes	23
Table 2.1. Experimental inlet conditions considered for the LiBr solution falling film and HTF on the desorber and condenser (charge mode)	46
Table 2.2. Experimental inlet conditions considered for the LiBr solution falling film, water film and HTFs on the absorber and evaporator (discharge mode)	49
Table 2.3. Grooved vertical flat plate heat exchangers characteristics considered for the reference simulation case	54
Table 2.4. Reference case inlet conditions considered for the LiBr solution falling film and HTF on the desorber and condenser (charge mode)	55
Table 2.5. Inlet conditions considered for the study of desorption/condensation process performance.	58
Table 2.6. Reference case inlet conditions considered for the LiBr solution falling film, water falling film and HTF (discharge mode)	61
Table 2.7. Inlet conditions considered for the study of the absorption/evaporation process	63
Table 2.8. System inlet working conditions considered for the reference and optimized cases in the desorption/condensation operating mode.....	66
Table 2.9. System inlet working conditions considered for the reference and optimized cases in the absorption/evaporation operating mode.....	69
Table 2.10. Simulation cases considered for the mesh number and movement direction sensibility study in desorption/condensation and absorption/evaporation operating modes.....	71
Table 2.11. Characteristics and initial conditions of the liquid solution tank	84
Table 2.12. Liquid solution tank boundary conditions for different cases in charge operating mode	85
Table 2.13. Liquid solution tank boundary conditions for different cases in discharge operating mode.....	85
Table 2.14. Crystal/liquid solution tank boundary conditions in charge and discharge operating modes	88
Table 3.1. System elements technical characteristics	106
Table 3.2. System sensors technical characteristics.....	107
Table 3.3. Gas leakage rate associated to the prototype main components	109
Table 3.4. Experimental plan for desorption/condensation operating mode tests; components working conditions	110
Table 3.5. Experimental plan for absorption/evaporation operating mode tests; components working conditions	111
Table 3.6. Working conditions for the experimental tests in desorption/condensation operating mode	112
Table 3.7. Components working conditions and system performance of all the experimental tests in desorption/condensation operating mode.....	120
Table 3.8. Working conditions for two tests in absorption/evaporation operating mode	123
Table 3.9. Working conditions and system performance of all the experimental tests in absorption/evaporation operating mode	130
Table 3.10. Prototype ESD during Tests 7 and 8 (discharge operating mode) – ($x_{LiBr} \approx [0.59 - 0.54]$).....	134

Table 3.11. Comparison between experimental and simulation results associated to Test 1 and Test 2 in the prototype desorption/condensation operating mode	136
Table 3.12. Comparison between experimental and simulation results associated to Test 7 and Test 8 in the prototype absorption/evaporation operating mode.....	139
Table 3.13. Extrapolated prototype ESD for Tests 7 and 8 (discharge operating mode) –.....	143
Table 4.1. Dwelling technical characteristics	154
Table 4.2. Reactor and heat exchangers characteristics	155
Table 4.3. LiBr solution tank characteristics	156
Table 4.4. Water tank characteristics	156
Table 4.5. Pipes characteristics	156
Table 4.6. Simulation time step associated to each system component	157
Table 4.7. Mixing tank characteristics	157
Table 4.8. Solar thermal collector characteristics	158
Table 4.9. Heat sink characteristics	158
Table 4.10. Simulation cases considered to study the solution tank insulation thickness influence on the system capability to cover the dwelling heating needs	165
Table 4.11. Simulation cases considered to study the solution mass influence on the system capability to cover the dwelling heating needs	169
Table 4.12. Simulation cases considered to study the solar collector surface influence on the system capability to cover the dwelling heating needs	174
Table 4.13. Simulation cases to study the solar collector HTF minimal threshold outlet temperature (charging mode) influence on the system capability to cover the dwelling heating needs.	179
Table 4.14. System ESD for Case 9 during the second year simulation (discharging period)	181
Table 4.15. System annual efficiency coefficient for Case 9 during the second year simulation	181
Table 4.16. Simulation case characteristics considered to study the system capability to cover the dwelling heating need when a KCOOH-H ₂ O solution is used.	182

Nomenclature

<i>General</i>		
a_0	solar collector optical efficiency	(J/(kg.K))
a_1	solar collector thermal loss coefficient	(-)
a_2	solar collector thermal loss coefficient	(W/(m ² .K))
A	Area	(m ²)
$ATES$	absorption thermal energy storage	
c_p	specific heat	(J/(kg.K))
C	molar density	(mol/ m ³)
Co	Courant number	(-)
COP	coefficient of performance	
$Con./Eva.$	condenser/evaporator or condensed/evaporated	
D_h	hydraulic diameter	(m)
D	mass diffusivity	(m ² /s)
$Des./Abs.$	desorber/absorber or desorbed/absorbed	
DHN	dwelling heating needs	
dx	differential length	(m)
e	Thickness	(m)
f	function of variables	
Fo	Fourier number	(-)
g	gravitational acceleration	(m/s ²)
G	solar global irradiance	(W/m ²)
h	Enthalpy	(J/kg)
h_p	partial enthalpy	(J/kg)
h_m	convection mass transfer coefficient	(m/s)
h_T	heat transfer coefficient	(W/(m ² .K))
H	Height	(m)
HTF	heat transfer fluid	
$"l"$	discretization time indicator	
L	height level / Plate width	(m)
LEC	low energy consumption	
M, m	Mass	(kg)
\dot{m}	mass flow rate	(kg/s)
\dot{m}''	mass flux per unit surface	(kg/(s.m ²))
n	number of grids	(-)
NCG	non condensable gas	
Nu	Nusselt number	(-)
P	Pressure	(Pa)
$Param$	Parameter	
Pe	Peclet number	(-)
Per	Perimeter	(m)
PIV	particle image velocimetry	
$PLIF$	planar laser induced fluorescence	
Pr	Prandtl number	(-)
\dot{q}	heat flux	(W/m ²)
RC	recirculation percentage	
Re	Reynolds number	(-)
S	wetted surface percentage	
Sh	Sherwood number	(-)
t	Time	(s)
T	Temperature	(K)
u	velocity - component x	(m/s)
U	thermal transmittance	(W/(m ² .K))
v	velocity - component y	(m/s)
V	Valve	
wt	weight mass fraction	(kg/kg)

W	Power	(W)
x	mass fraction / x axis	(kg/kg)
X	molar fraction	(mol/mol)
y	y axis	
z	z axis	

Greek symbols

ξ	down stream distance	
Δ	uncertainty	
Δt	time interval	(s)
Δx	height of the grid (reactor) /length of the grid (pipe)	(m)
Δy	height of the grid (tank)	(m)
μ	viscosity	(kg/(m.s))
λ	thermal conductivity	(W/(m.K))
ρ	density	(kg/m ³)
δ	film thickness	(m)
α	thermal diffusivity	(m ² /s)
ν	kinematic viscosity	(m ² /s)

Subscripts

<i>amb</i>	ambiance
<i>avg</i>	bulk film average
<i>abs/des</i>	absorbed or desorbed water ; absorption/desorption
<i>ad</i>	absorber/desorber
<i>ch. op.mode</i>	charge operating mode
<i>cry</i>	crystal/crystallization
<i>DHN</i>	dwelling heating needs
<i>disch. op.mode</i>	discharge operating mode
<i>ec</i>	evaporator/condenser
<i>envp</i>	envelope
<i>equ</i>	equilibrium
<i>eva/con</i>	evaporated or condensed water ; evaporation/condensation
<i>exp</i>	experimental
<i>ext</i>	external
<i>f_water</i>	water film
<i>hs</i>	heat sink
<i>htf</i>	heat transfer fluid
<i>H₂O</i>	water
<i>i</i>	inlet
<i>int</i>	film interface
<i>k</i>	node <i>k</i>
<i>KCOOH</i>	potassium formate
<i>LiBr</i>	lithium bromide
<i>min</i>	minutes
<i>mt</i>	mixing tank
<i>o</i>	outlet
<i>opt</i>	optimal
<i>pp</i>	partial pressure
<i>rc</i>	recirculation
<i>ref</i>	reference
<i>sat</i>	saturated conditions
<i>sim</i>	simulation
<i>sc</i>	thermal solar collector
<i>st</i>	LiBr solution film
<i>tr</i>	transversal
<i>vap</i>	water vapor in the reactor
<i>var</i>	Variable
<i>w</i>	metallic plate wall
<i>wt/f_water</i>	water film

l

Superscripts
Time

Résumé

Au cours des dernières années, les préoccupations environnementales liées à la consommation d'énergie aux émissions de gaz à effet de serre ont augmenté et ont conduit à l'établissement de différents accords internationaux. Différentes études indiquent que le principal problème relié aux émissions de gaz à effet de serre est leur impact sur la température terrestre, estimée entre 2.6 et 3.1 °C pour l'année 2100, par rapport aux niveaux préindustriels (Vandyck et al., 2016). D'un autre côté, les combustibles fossiles, qui en ce moment sont responsables de fournir 81% de l'énergie primaire totale mondiale (IEA, 2016), seront épuisés. Les systèmes basés sur les énergies renouvelables apportent des réponses durables aux ces deux problèmes, du fait qu'ils ne génèrent pas ou peu de gaz à effet de serre pendant leur fonctionnement et que leur source d'énergie est inépuisable.

R1. Systèmes intersaisonnier de stockage de chaleur – État de l'art

Pendant les 10 dernières années différentes études sur le stockage d'énergie solaire pour le chauffage du bâtiment ont été faites ; certains systèmes appelés 'stockage intersaisonnier de chaleur' stockent la chaleur pendant l'été pour son usage pendant l'hiver (Xu et al., 2014).

R1.1. Systèmes de stockage de chaleur solaire à basse température

L'intérêt en développer des systèmes capables de stocker la chaleur a augmenté du fait de l'utilisation croissante de l'énergie solaire et la difficulté naturelle à faire coïncider temporellement la génération d'énergie avec la demande (Xu et al., 2014). Les technologies de stockage de chaleur reliées aux bâtiments peuvent être classifiées selon leur durée, niveau de température, capacité et phénomène physique. Concernant les matériaux, le stockage de chaleur peut être réalisé en utilisant les mécanismes de chaleur sensible, de chaleur latente et thermochimique (N'Tsoukpoe et al., 2009). Le stockage de chaleur par chaleur sensible consiste à stocker l'énergie disponible en augmentant la température des matériaux. Le stockage de chaleur par chaleur latente utilise la grande quantité de chaleur libérée ou absorbée par certains matériaux lorsqu'ils sont soumis à un changement de phase (solidification et fusion respectivement). Le stockage de chaleur thermochimique utilise les liaisons chimiques et/ou physiques entre deux matériaux. Ces systèmes sont classés selon le processus mis en œuvre : sorption chimique, adsorption physique et absorption (voir Tableau 1.1).

Par rapport à la capacité de stocker la chaleur solaire, deux types de systèmes peuvent être trouvés : les petits systèmes de stockage de chaleur solaire reliés aux maisons résidentielles et dédiés principalement aux applications d'eau chaude sanitaire et chauffage, et les grands systèmes de stockage de chaleur solaire reliés au chauffage urbain. Les systèmes à sorption sont beaucoup plus complexes que les systèmes sensibles ou latents, mais ils sont peu sensibles aux pertes de chaleur. Cette propriété les rend intéressants pour les petits systèmes de stockage de chaleur pour lesquels les pertes de chaleur sont importantes en présence de système de stockage par chaleur sensible ou latente. Parmi les autres propriétés intéressantes concernant les systèmes thermochimiques on compte leur haute densité énergétique (Figure 1.1) et leur modularité (capacité à refroidir ou chauffer un bâtiment en utilisant le même système).

R1.2. Systèmes intersaisonniers de stockage de chaleur basés en procédés de sorption gaz/liquide: Révision des cas expérimentaux

Pendant les 5 dernières années, différents systèmes de stockage de chaleur intersaisonnier ont été étudiés pour des applications de chauffage des bâtiments utilisant des procédés à absorption. Différents prototypes démonstratifs ont été construits et testés. Sept prototypes trouvés dans la littérature sont présentés. Dans tous ces systèmes, l'eau est utilisée comme sorbat. Quatre différents sorbants ont été étudiés : le LiCl, le CaCl₂, le NaOH et le LiBr; leurs principales caractéristiques sont décrites dans le mémoire de thèse.

Climate Well en Suède (Bales and Nordlander, 2005) apparaît comme le pionnier des systèmes de stockage de chaleur par absorption. Un système de stockage de chaleur basée sur un "procédé à trois phases" (Yu et al.,

2014) et mettant en œuvre le Chlorure de Lithium ($\text{LiCl-H}_2\text{O}$) a été développé par le laboratoire Solar Energy Research Center (SERC) et l'entreprise ClimateWell. Le système, appelé "Accumulateur thermo-chimique (TCA)", n'a pas besoin de quatre dispositifs d'échange le stockage intersaisonnier fonctionnant de manière non continue (charge en été et décharge en hiver). Les quatre échangeurs de chaleur traditionnels des machines à absorption (absorbeur, désorbeur, condenseur et évaporateur) sont combinés en deux échangeurs dont les fonctions changent durant les périodes de charge et de décharge : Un absorbeur/désorbeur et un évaporateur/condenseur. Le système Climate Well utilise deux réservoirs de stockage, un pour la solution de LiCl (sorbant) et l'autre pour l'eau. Pour une opération potentielle de chauffage de bâtiments, la version commerciale du TCA (unité CW10) serait capable de produire une puissance de chaleur autour de 4 kW (Figure 1.3). La plupart des prototypes présentés ci-dessous ont considéré le même principe de fonctionnement que celui du système ClimateWell. Un second prototype de stockage thermique par absorption utilisant le couple LiCl- H_2O a été construit par Zhao (Zhao et al., 2016) à l'université Shanghai Jiao Tong. Le prototype a été dessiné pour présenter une capacité de stockage de 10 kWh et a été testé sous conditions représentatives d'hiver (Figure 1.5).

Le couple Chlorure de Calcium / eau ($\text{CaCl}_2\text{-H}_2\text{O}$) par Liu (Liu, 2011) au laboratoire LOCIE en France (Figure 1.9). Des puissances en désorption entre 1.8 et 4 kW ont été obtenues ; néanmoins, les puissances mesurées en absorption ont été très faibles (Table 1.5). Un second système à absorption Chlorure de Calcium / eau a été proposé par Quinnell et Davidson (Quinnell et Davidson, 2012) à l'Université de Minnesota aux Etats Unis. La caractéristique principale du système proposé est l'usage d'un seul réservoir de stockage pour la solution concentrée, la solution diluée et l'eau, dans le but d'augmenter la densité énergétique du système et de réduire les coûts, par rapport aux systèmes qui utilisent deux réservoirs séparés pour la solution et l'eau. (Figure 1.10).

Fumey (Fumey et al., 2015) ont étudié un troisième couple l'Hydroxyde de Sodium /eau ($\text{NaOH-H}_2\text{O}$) dans le cadre du projet COMTES financé par l'Union Européenne. Les échangeurs de masse et chaleur sont à de type tube-calandre horizontaux et films ruisselants. Ils ont été conçus pour produire une puissance thermique de 8 kW.

N'Tsoukpoe (N'Tsoukpoe et al., 2013) a construit un prototype démonstratif mettant en œuvre le couple Bromure de Lithium / eau ($\text{LiBr-H}_2\text{O}$) à l'Université de Savoie en France pour évaluer le potentiel d'un système de stockage à long terme (Figure 1.16). Le prototype a été dessiné pour présenter une capacité de stockage de chaleur de 8 kWh et une puissance de décharge de 1 kW (N'Tsoukpoe et al., 2012). Les tests en mode de charge ont été satisfaisants avec une génération moyenne autour de 2 kW; néanmoins, les résultats obtenus pendant les tests en décharge ont montré que les transferts de chaleur entre les films tombants et les fluides caloporteurs ont été très faibles. Zhang (Zhang et al., 2014) a également développé un prototype de stockage thermique intersaisonnier mettant en œuvre le couple ($\text{LiBr-H}_2\text{O}$) pour des applications de chauffage de bâtiments à l'Université de Tsinghua en Chine (Figure 1.19). Les résultats expérimentaux associés au mode de charge présentent des puissances de génération autour de 8 kW. Le mode de décharge est caractérisé par des puissances de autour de 7 kW, associés à la chaleur d'absorption de vapeur, la température de la solution étant à une température plus haute que celle du fluide caloporteur au démarrage des tests.

R2. Modélisation et simulation du système intersaisonnier de stockage de chaleur

Un modèle numérique du système intersaisonnier de stockage de chaleur est proposé. Les principaux composants du système sont : le réacteur incluant les échangeurs absorbeur/désorbeur et évaporateur/condenseur, le réservoir de solution de LiBr, le réservoir d'eau, ainsi que les tuyaux de solution et d'eau (Figure 2.1).

R2.1. Réacteur

Pendant la période de charge, les échangeurs du réacteur se comportent comme un désorbeur et un condenseur, tandis que pendant la période de décharge les échangeurs du réacteur se comportent comme un absorbeur et un évaporateur. Lors du fonctionnement du procédé, les deux échangeurs interagissent par le biais de la vapeur. Un modèle décrivant le comportement de chaque échangeur de chaleur au sein du réacteur est présenté.

Des échangeurs de chaleur considérés pour le modèle sont de type échangeurs à plaques et films ruisselants. Chaque échangeur est composé de deux plaques planes. Le fluide caloporteur s'écoule entre les plaques tandis que le film ruisselant (solution de LiBr ou eau) s'écoule sur la face externe des plaques (Figure 2.2).

Différentes hypothèses pour les transferts de chaleur et de masse au sein des films tombants ont été considérées (Grossman, 1983), (Killion and Garimella, 2001); notamment : des gaz incondensables ne sont pas présents dans la vapeur, le film est en équilibre avec la vapeur à l'interface liquide/vapeur, des vaguelettes ne se développent pas au long du film, etc.

Les corrélations adaptées décrivant les transferts de chaleur et de masse au sein des films ruisselants sont tirés des travaux de Brauner (Brauner, 1991)

Les échangeurs à plaques et films ruisselant sont discrétisés en tranche horizontales. Des bilans de masse et d'énergie sont établis sur des volumes de contrôle. Les transferts de masse et de chaleur sont couplés à l'interface du film ruisselant via une loi d'état décrivant les conditions de saturation à l'interface.

Une procédure de couplage a été mise en œuvre pour décrire le procédé d'évaporation/absorption et le procédé de condensation/désorption. Cette approche considère que la vapeur générée par l'évaporateur (désorbeur) est entièrement absorbée (condensée) par l'absorbeur (condenseur), l'évaporateur/absorbeur (désorbeur/condenseur) étant à la même pression. Les conditions d'entrée variant très lentement en comparaison au temps requis aux films tombants pour atteindre des régimes stationnaires, les échangeurs sont supposés fonctionner dans un mode d'opération quasi-stationnaire.

Les résultats de simulations obtenus avec le modèle sont comparés à des résultats numérique et expérimentaux de la littérature réalisés par des autres auteurs (sections 2.1.2.1, 2.1.2.1 and 2.1.2.3): un cas numérique d'absorption de vapeur d'eau sur un film de solution de LiBr tombant le long d'une plaque verticale (Karami and Farhanieh (2009)), un cas expérimental d'absorption de vapeur d'eau sur un film de solution de LiBr tombant le long d'un tube vertical (Miller and Keyhani (2001) and Medrano et al. (2002)) et un cas expérimental de désorption/condensation et absorption/évaporation au sein du réacteur d'un prototype de stockage de chaleur intersaisonnier (N'Tsoukpoe (2013)). Une relativement bonne concordance globale est obtenue entre notre modèle et les résultats de la littérature (Figures 2.14 and 2.15). Pour le dernier cas, la comparaison aux résultats expérimentaux a nécessité l'introduction d'un taux de mouillage dans le modèle. De bonnes concordances sont obtenues dans les modes de charge et de décharge lorsqu'un taux de mouillage autour de 20% est considéré. L'influence critique du taux de mouillage des films sur les surfaces d'échange est mise en évidence du fait qu'il peut réduire considérablement la quantité d'eau ab/désorbée ou la quantité de chaleur échangée avec le fluide caloporteur.

Une configuration d'échangeur de chaleur à plaque verticale rainurée est proposée afin d'assurer un haut taux de mouillage. Afin d'étudier le comportement physique de cette nouvelle configuration, un cas de simulation de référence a été défini (section 2.1.3.1). Une étude paramétrique de l'influence de la variation des conditions à l'entrée des échangeurs de chaleur sur la performance du système est aussi réalisée. Un cas avec des conditions d'entrée optimales permettant d'obtenir une haute performance du système est aussi présenté (section 2.1.3.2).

Finalement, une étude sur l'influence du mode de fonctionnement co-courant ou contre-courant des échangeurs, ainsi que du nombre de mailles (discrétisation du modèle) sur la réponse du système (réduction du 'temps-machine') est réalisée.

R2.2. Réservoirs

Un modèle 1D axisymétrique instationnaire du réservoir de solution de LiBr est développé (section 2.2.1). L'entrée et sortie de la solution de LiBr sont placées respectivement en bas et en haut du réservoir. Le réservoir en acier inoxydable est isolé thermiquement et plongé dans un milieu environnant à température constante (Figure 2.33). Des transferts diffusifs de masse et de chaleur sont considérés au sein de la solution, ainsi que les déperditions latérales. La phase gazeuse est supposée composée de vapeur pur. L'écoulement de solution dans le réservoir est supposé laminaire et complètement développé (Killion and Garimella, 2001) (Incropera et al., 2011). Le réservoir est discrétisé en 10 mailles adaptatives permettant de prendre en compte le niveau de solution variable dans le réservoir. Le modèle incorpore également une loi d'état permettant de décrire la quantité de LiBr cristallisé au sein de la solution de LiBr est présenté (section 2.2.1.2). Quelques cas d'étude sont proposés pour montrer la réponse et cohérence du modèle (section 2.2.1.3).

Une approche similaire est considérée pour le modèle du réservoir d'eau (section 2.2.2).

R2.3. Tubes

Le modèle décrivant les conduites cylindriques de solution de LiBr et d'eau est 1D. Les conduites sont en acier inoxydable recouvertes d'isolant. Leur surface externe est considérée à une température uniforme (Figure 2.41). Le modèle décrit les échanges de chaleur entre la solution et l'extérieur. Les conduites sont discrétisées en 4 tronçons. L'écoulement est supposé complètement développé et laminaire.

R2.4. Système de stockage global

Afin de modéliser la totalité du système de stockage de chaleur, une procédure de compilation de tous les composants du système a été développée (Figure 2.42). En fonction de la taille du réservoir (hauteur), le pas de temps de simulation doit être adapté pour garder une cohérence avec la longueur des mailles de discrétisation. Enfin, l'approche du système global présentée dans cette section sera utilisée dans le Chapitre 4 afin d'étudier la performance annuelle du système de stockage de chaleur intersaisonnier appliqué au chauffage de maisons.

R3. Prototype expérimental du système de stockage de chaleur intersaisonnier

Basé sur les résultats obtenus et analysés dans les chapitres précédents, un prototype de système de stockage intersaisonnier a été construit. Dans ce chapitre, la conception et les performances du prototype sont présentées.

R3.1. Conception et construction du prototype

Au cours des dernières années Liu (Liu, 2011) et N'Tsoukpoe (N'Tsoukpoe, 2013) ont construit des prototypes de stockage de chaleur intersaisonnier (Chapitre 1). Dans cette thèse, un nouveau prototype a été construit en considérant une configuration similaire (Figure 3.1); néanmoins, des modifications majeures ont été apportées pour pallier aux problèmes rencontrés dans les études antérieures, telles qu'un arrangement à 2 étages des éléments, avec un positionnement du réacteur placé au-dessus des réservoirs. Les échangeurs de masse et de chaleur composant le réacteur développés pour les besoins du prototype sont de type échangeurs à plaques verticales rainurées et films ruisselants. Les deux échangeurs de chaleur travaillent respectivement comme désorbeur/condenseur et absorbeur/évaporateur pendant les modes de charge et décharge. Les caractéristiques techniques proposées pour le réacteur (chambre) et les échangeurs de chaleur sont aussi décrites (Figures 3.2 and 3.6, sections 3.1.1.1 to 3.1.1.7).

R3.2. Tests expérimentaux

La caractérisation des performances du prototype de stockage intersaisonnier de chaleur sont montrés dans cette section.

La capacité du réacteur, du réservoir de solution et du réservoir d'eau à maintenir des conditions de vide a été testée. Des taux de fuite très faibles sont obtenus dans les composants du système (Table 3.1) (Umrath et al., 2007) (Medrano et al., 2002); la valeur maximale étant $4.3E-4$ (mbar.l)/s au réservoir de solution. À partir des résultats de simulation obtenus au Chapitre 2 une série d'expériences en désorption/condensation et absorption/évaporation est proposée (Tables 3.3 et 3.4). Pour le mode d'opération en désorption/condensation l'influence de 3 paramètres est étudiée : le débit massique de solution dans le réacteur, la température du fluide caloporteur au désorbeur et les débits massiques des fluides caloporteurs au désorbeur et condenseur, chacun de ces paramètres ayant un impact important sur le débit massique d'eau désorbée. De façon similaire, pour le mode d'opération en absorption/évaporation, l'influence de 4 paramètres est étudiée : le débit massique de solution dans le réacteur, la température du fluide caloporteur à l'absorbeur et les débits massiques des fluides caloporteurs à l'absorbeur et l'évaporateur.

Six tests expérimentaux en mode opératoire de désorption/condensation et quatre tests expérimentaux en absorption/évaporation ont été réalisés. Les conditions des tests ainsi que la performance du système sont présentés (charge : Tableaux 3.6 et, 3.7, Figures 3.7 to 3.12, décharge : Tableaux 3.8 et, 3.9, Figures 3.14 to 3.18). Les principaux résultats obtenus pour les tests en désorption/condensation sont les suivants : un débit massique d'eau désorbée/condensée entre 0.5 et 2 kg/h, des puissances cotés fluides caloporteurs entre 1 et 2 kW au désorbeur et entre -0.5 et -1.5 kW au condenseur, et des pressions de vapeur entre 21 et 24 mbar. Pour les

tests en absorption/évaporation : débit massique d'eau absorbée/évaporée entre 1 et 2 kg/h, puissances coté fluide caloporteur -0.6 et -1.5 kW à l'absorbeur et entre 0.3 et 1 kW à l'évaporateur, et des pressions de vapeur entre 12 et 15 mbar. Un taux de mouillage bas dans les échangeurs de chaleur a été observé dans certains tests, ainsi que quelques projections de gouttelettes dans certains tests de charge (Figure 3.1). Des tests additionnels ont été faits afin d'étudier la performance du système lorsque des conditions de cristallisation sont atteintes dans le réservoir de solution (section 3.2.4 et Figures 3.19 to 3.22). Il a été observé que le système peut travailler normalement même si des cristaux sont présents dans le réservoir de solution ; néanmoins, une mauvaise gestion de la position de formation de ces cristaux peut conduire à une cristallisation de LiBr dans les tuyaux, empêchant alors la solution liquide de circuler. La densité de stockage énergétique établie sur la base des tests expérimentaux d'absorption/évaporation oscille entre 29.6 et 33.7 kWh/m³ sur la gamme de concentration restreinte parcourue, et des valeurs extrapolées sur l'ensemble de la gamme entre 109 et 120 kWh/m³.

R3.3. Comparaison des résultats expérimentaux avec le modèle de simulation

Le modèle décrit au Chapitre 2 (section 2.1) a été utilisé pour simuler le fonctionnement du prototype pour des conditions d'entrée identiques à deux tests expérimentaux en modes de désorption/condensation et d'absorption/évaporation. Les simulations ont considéré le taux de mouillage des plaques estimé lors des expérimentations. Les conditions de sorties modélisées sont comparées avec les résultats expérimentaux (Tableaux 3.11 and 3.12). En général, une bonne concordance a été obtenue entre les résultats de simulation et expérimentaux (Figures 3.23 to 3.26). Cette comparaison, néanmoins, suggère la présence de gaz incondensables dans le réacteur pendant les expérimentations, avec un impact importante en mode absorption/évaporation. L'effet des incondensables est pris en compte dans le modèle à l'aide d'une différence de pression partielle de vapeur d'eau entre l'évaporateur et l'absorbeur de 4 à 5 mbar (Figure 3.27).

R4. Performance annuelle du système intersaisonnier de stockage de chaleur

Dans ce Chapitre, un modèle global du système de stockage de chaleur intersaisonnier couplé à une maison est développé afin d'étudier la performance annuelle du système lorsque des besoins de chauffage de la maison doivent être partiellement ou complétement couverts. Un schéma descriptif du modèle global pendant chaque mode opératoire du système (charge en été et décharge en hiver), est proposé (Figure 4.1).

Le principe du couplage du système de stockage de chaleur à la maison est décrit. Pendant la période de charge (été) un capteur solaire thermique est utilisé pour chauffer un fluide caloporteur associé au désorbeur, permettant la désorption de vapeur de la solution de LiBr. Dans un même temps, un dissipateur thermique est utilisé pour refroidir le condenseur, permettant la condensation de la vapeur produite dans le réacteur. Pendant la période de décharge (hiver) une bouteille de mélange couple la maison, au capteur solaire thermique et au système de stockage par absorption. Lorsque la température du fluide caloporteur issu des capteurs est assez haute pour contribuer à la couverture des besoins de chauffage de la maison, il est injecté dans la bouteille de mélange. Lorsque les besoins de chauffage de la maison ne peuvent être couverts uniquement par le capteur solaire, le système de chauffage intersaisonnier est mis en marche. Le fluide caloporteur quittant l'absorbeur est alors injecté dans la bouteille de mélange et utilisé pour contribuer partiellement ou totalement à la couverture des besoins de chauffage de la maison. Parallèlement à cela, une source de chaleur géothermique basse température est utilisée pour chauffer le fluide caloporteur associé à l'évaporateur.

R4.1. Modèle de simulation du système de stockage intersaisonnier de chaleur/maison

Dans cette section, le modèle de simulation global permettant de coupler le modèle du système de stockage intersaisonnier de chaleur, développé au Chapitre 2, avec un système de chauffage d'une maison basse consommation est présenté (Figure 4.1). Des modèles d'un capteur solaire thermique, de l'échangeur géothermique basse température et de la bouteille de mélange sont ajoutés au modèle de stockage intersaisonnier. Les modèles des nouveaux composants et leurs conditions de couplage sont présentés.

R4.2. Simulation de la configuration de référence

Un cas de configuration de référence du système de stockage intersaisonnier de chaleur couplé à la maison est proposé afin de simuler la performance annuelle du système. Les caractéristiques techniques considérées pour la

maison, le capteur solaire, source/dissipateur de chaleur, réservoir de mélange et système de stockage de chaleur sont présentées (section 4.2.1, Figure 4.7, Tableaux 4.1 à 4.9), ainsi que les résultats de la performance annuelle simulée (section 4.2.2, Figures 4.8 à 4.11). Le système de stockage intersaisonnier est capable de couvrir partiellement les besoins annuels de chauffage d'une maison basse consommation de 120 m², avec une énergie fournie par le réacteur du système de 1698 kWh (équivalent à une couverture de 78%).

R4.3. Étude paramétrique et configuration optimisée

Une étude paramétrique sur la performance du système est aussi mise en œuvre. Quatre paramètres sont considérés : l'épaisseur d'isolation du réservoir de solution, la masse initiale du réservoir de solution, la surface du capteur solaire et le seuil minimale de température de sortie du fluide caloporteur associé au capteur solaire pendant la période de charge. Les caractéristiques restantes du système sont les mêmes que celles auparavant décrites pour la configuration de référence. Les résultats de simulation annuelle ont été analysés (section 4.2.3, Figures 4.12 au 4.21). Certains des résultats obtenus dans cette étude sont:

- Lorsque l'épaisseur d'isolation du réservoir de solution est augmentée, la température moyenne et la fraction massique moyenne de LiBr dans le réservoir de solution augmentent, ainsi que le taux de cristallisation et la puissance de chauffage générée par le réacteur.
- Lorsque la masse de solution est réduite, la température moyenne et la fraction massique moyenne de LiBr dans le réservoir de solution ainsi que la puissance de chauffage générée par le réacteur sont légèrement influencées ; néanmoins, le taux de cristallisation augmente fortement.

En outre, la densité de stockage d'énergie du système et le coefficient de performance du système ont été calculés pour un des cas modélisés, donnant des valeurs de 157 kWh/m³ et 2.2, respectivement ; ce sont des valeurs très intéressantes en comparaison aux valeurs d'autres cas expérimentaux (voir section 1.2).

R4.4. Performance annuelle du système de stockage intersaisonnier de chaleur avec une solution de KCOOH-H₂O

La performance thermo-physique de différentes solutions aqueuses, couples sel + eau, a été évaluée en remplacement du couple standard LiBr-H₂O (Lefebvre, 2015). Comme résultat de cette étude, une solution aqueuse de KCOOH-H₂O a été proposée comme une option alternative capable de couvrir les besoins énergétiques du système et, en même temps, réduire les coûts du matériau. Une étude de simulation de la performance du système de stockage intersaisonnier lorsqu'une solution aqueuse de KCOOH-H₂O est utilisée a été faite. Une modification du modèle de simulation développé au Chapitre 2 a été mise en œuvre afin de considérer les propriétés thermo-physiques de la solution KCOOH-H₂O, trouvés dans la littérature (Balarew et al., 2001), (Lefebvre, 2015), (Longo et Gasparella, 2015), (Longo et Gasparella, 2016). Les caractéristiques techniques du système considérées pour ce cas de simulation ont été les mêmes que celles utilisées dans le cas de référence avec une solution de LiBr (section 4.2.1), à l'exception de 2 paramètres: la masse initiale de solution et la fraction massique initiale du sel, qui ont été modifiées (voir Table 4.16). Les résultats simulés pour ce cas ont montré la présence de cristaux pendant une période de 7 mois, ainsi que la capacité du système de couvrir les besoins de chauffage annuels de la maison avec un usage négligeable de sources électriques (Figures 4.22 et 4.23).

Références

- Balarew C.; Dirkse T. P.; Golubchikov O. A.; Salomon M.; Trendafilova S.; Ageyeva T.; Baldini P.; D'Andrea G.; *IUPAC-NIST Solubility Data Series 73. Metal and Ammonium Formate Systems*. J. Phys. Chem. Ref. Data 30 (2001); p. 1-163.
- Bales C., Nordlander S.; *TCA Evaluation – Lab measurements, modelling and system simulation*. Report of the Solar Research Energy Center (SERC), Sweden (2005); p. 2–22.
- Brauner N.; *Non isothermal vapour absorption into falling film*. Int. J. Heat Mass Tran. Vol. 34, N° 3 (1991); p.767–784.

Fumey B., Weber R., Gantenbein P., Daguene-Frick X., Stoller S., Fricker R., Dorer V.; *Operation results of a closed sorption heat storage prototype*. Energy Procedia 73 (2015); p. 324-330.

Grossman G.; *Simultaneous heat and mass transfer in film absorption under laminar flow*. International Journal Heat Mass Transfer Vol. 26, N° 3 (1983); p.357–371.

IEA (International Energy Agency); *Key world energy statistics*. <https://www.iea.org/publications/freepublications/publication/KeyWorld2016.pdf>. Last accessed November 2016; p. 6-7.

Incropera F., Dewitt D., Bergman T., Lavine A.; *Fundamentals of heat and mass transfer*. Seventh edition; John Wiley & sons (2011); USA; p.675–679.

Karami S., Farhanieh B.; *A numerical study on the absorption of water vapor into a film of aqueous LiBr falling along a vertical plate*. Heat Mass Transfer 46 (2009); p.197–207.

Killion J., Garimella S.; *A critical review of models of coupled heat and mass transfer in falling film absorption*. International Journal of Refrigeration 24 (2001); p.755–797.

Lefebvre E.; *Procédé par absorption avec stockage d'énergie solaire intersaisonnier intensifié par la cristallisation de l'absorbant: Recherche & caractérisation thermodynamique de nouveaux couples; Conception de la cuve de stockage*. Doctoral thesis defended in October 2015. University of Lyon 1-Claude Bernard; Lyon, France.

Liu H.; *Inter-seasonal solar energy storage for buildings by absorption*. PhD thesis at the University of Grenoble, France (2011).

Longo A. G., Gasparella A.; *Three years experimental comparative analysis of a desiccant based air conditioning system for a flower greenhouse: Assessment of different desiccants*. Appl. Therm. Eng. 78 (2015); p. 584-590.

Longo A. G., Gasparella A.; *Experimental measurement of thermophysical properties of H₂O/KCOOH (potassium formate) desiccant*. Int. J. Refrig. 62 (2016); p. 106-113.

Medrano M., Bourouis M., Coronas A.; *Absorption of water vapour in the falling film of water-lithium bromide inside a vertical tube at air-cooling thermal conditions*. International Journal of Thermal Sciences 41 (2002); p. 891–898.

Miller W.A., Keyhani M.; *The correlation of simultaneous heat and mass transfer experimental data for aqueous lithium bromide vertical falling film absorption*. J. Solar Energy Engrg. Trans. ASME 123 (1) (2001); p. 30–42.

N'Tsoukpoe K.E., Liu H., Le Pierrès N., Luo L.; *A review on long-term sorption solar energy storage*. Renew. Sust. Energ. Rev. 13 (2009); p. 2385-2396.

N'Tsoukpoe K. E., Le Pierrès N., Luo L.; *Numerical dynamic simulation and analysis of a lithium bromide/water long-term solar heat storage system*. Energy 37 (2012); p.346-358.

N'Tsoukpoe K. E., Le Pierrès N., Luo L.; *Experimentation of a LiBr-H₂O absorption process for long-term solar thermal storage: Prototype design and first results*. Energy 53 (2013); p.179-198.

Quinnell J. A., Davidson J. H.; *Long-term solar thermal energy storage using aqueous calcium chloride*. In: Proceedings of the American Solar Energy Society, Washington D.C. (May 2012); p. 13–18.

Umrath W., Adam H., Bolz A., Boy H., Dohmen H., Gogol K., Jorisch W., Mönning W., Mundinger H., Otten H., Scheer W., Seiger H., Schwarz W., Stepputat K., Urban D., Wirtzfeld H., Zenker H.; *Fundamentals of Vacuum Technology*. (Erlikon Leybold Vacuum (2007); p.14, 110.

Vandyck T.; Keramidis K.; Saveyin B.; Kitous A.; Vrontisi Z.; *A global stocktake of the Paris pledges: Implications for energy systems and economy*. Global Environmental Change 41 (2016); p. 46-63.

Xu J., Wang R. Z., Li Y.; *A review of available technologies for seasonal thermal energy storage*. Sol. Energy 103 (2014); p. 610-638.

Yu N., Wang R. Z., Lu Z. S., Wang L. W., Ishugah T.F.; *Evaluation of a three-phase sorption cycle for thermal energy storage*. Energy 67 (2014); p. 468-478.

Zhang X., Li M., Shi W., Wang B., Li X.; *Experimental investigation on charging and discharging performance of absorption thermal energy storage system*. Energ Convers Manage 85 (2014); p. 425–434.

Zhao Y. J., Wang R. Z., Li T. X., Nomura Y.; *Investigation of a 10 kWh sorption heat storage device for effective utilization of low-grade thermal energy*. Energy 113 (2016); p. 739–747.

Introduction

In recent years, environmental concerns related to the energy consumption and the greenhouse gas emissions have increased and lead to different international agreements; being one of the most important the one reached at the 21st edition of the annual United Nations-led conference on climate change (COP21) held in Paris (December 2015). According to different studies, the main problem about greenhouse gas emissions is their impact on the increase of the global earth temperature estimated to up to 3.1°C in 2100 with respect to pre-industrial levels. Furthermore, fossil fuels, which are responsible of 81% of the world total primary energy supply, will be largely exhausted. In this context, renewable energies systems are naturally studied and applied as a potential solution for both problems indicated before, since they do not produce greenhouse gases during their functioning and the energy source is inexhaustible.

Sorption heat storage systems have raised the interest of the scientific community during the last years due to their high energy density, low thermal losses and their potential use for solar energy storage during seasonal periods. Furthermore, considering the operation temperature of conventional flat solar collectors, these systems can be used for solar building space heating applications.

Sorption heat storage systems are based on the working principle of a classic sorption machine (Figure i1a). Traditionally used for cooling purposes, an absorption machine is a closed system based in the use of an aqueous solution and the phase changes (liquid/vapor) produced due to the supply or removal of heat. Composed of a desorption chamber, an absorption chamber, a condensation chamber and an evaporation chamber functioning in a continuous mode, an absorption machine works as follows (Figure i1a): weak solution (typically LiBr-H₂O) is pumped from the absorber to the desorber, in this latter heat is supplied (from a hot source) permitting to desorb water vapor from the solution and to obtain an strong solution which flows towards the absorber; once in the absorption chamber, the strong solution releases heat (towards a cold source) and due to the interaction with vapor present in the chamber it starts to absorb the vapor producing again a weak solution. Regarding the water vapor produced in the desorption chamber, it flows towards the condensation chamber where it releases heat (towards a cold source) and is condensed, the produced liquid water flowing towards the evaporation chamber afterwards; once in the evaporation chamber, the liquid water receives heat from a hot source (typically a room that is being air-conditioned) and is evaporated, the produced vapor flowing at the same time towards the absorption chamber.

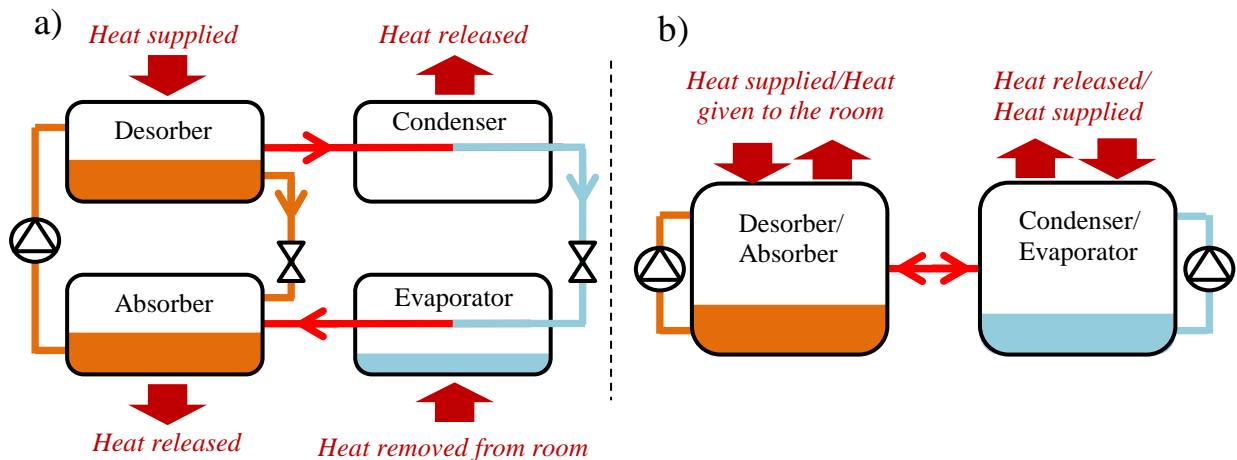


Figure i1. Scheme of a sorption machine. a) Refrigeration purposes, b) Building space heating purposes

The working principle of a sorption heat storage system is similar to the conventional sorption refrigeration machine (previously described), with the difference that the further works in a discontinuous mode since the desorber and condenser are also used as absorber and evaporator during the charge (desorption) and discharge (absorption) periods, respectively (Figure 11b). Furthermore, the heat released in the absorption process (discharge) can be used for space heating purposes. Complementarily, the system can be composed of a storage solution tank and water tank separated from the reactor.

The present doctoral thesis is defined in the research axe of *thermal solar systems and storage* based in sorption processes that has been developed in the LOCIE laboratory for more than ten years; this thesis being consistent with the contributions produced in two previous doctoral works carried out in this laboratory by Liu (2010) and N'Tsoukpoe (2013), who constructed and tested interseasonal heat storage experimental prototypes based on $\text{CaCl}_2\text{-H}_2\text{O}$ and $\text{LiBr-H}_2\text{O}$ couples, respectively.

This thesis is also defined in the research project Inter-Seasonal Solar Storage Process 2 (PROSSIS 2), belonging to the Non-carbon and Energy Efficient Systems (SEED) program supported by the French National Research Agency (ANR). Furthermore, this project counted as collaborators with laboratories from Lyon (IRCELYON, LAGEP), Grenoble (CEA-LITEN), Nantes (LTN) and Chambéry (LOCIE, CIAT).

In this doctoral work an initial review of different heat storage prototypes based on sorption processes and developed during the last 5 years is carried out in chapter 1. Four solution working couples are analyzed: $\text{LiCl-H}_2\text{O}$, $\text{CaCl}_2\text{-H}_2\text{O}$, $\text{NaOH-H}_2\text{O}$ and $\text{LiBr-H}_2\text{O}$.

In order to have a better understanding of the physical processes happening inside the reactor, in chapter 2 a detailed and original model for the system heat and mass exchangers (absorber, desorber, evaporator and condenser) is proposed, as well as a coupling model for cases in which the absorber and evaporator or the desorber and condenser work together. This model is compared to experimental results from the literature, considering LiBr solution as the system sorbent. Other components of the storage system such as the solution tank, water tank and pipes are also modeled; furthermore, a crystallization model associated to the solution tank is also proposed. Additionally, with the objective to improve the system charge and discharge powers, the simulated performance of a grooved plate heat exchanger configuration is studied.

In chapter 3 the construction of an interseasonal sorption heat storage prototype is described. The prototype performance in charging and discharging tests is studied. The working couple used is $\text{LiBr-H}_2\text{O}$. The constructed heat and mass exchangers are based on a grooved vertical plate configuration. This prototype is tested and a comparison of the prototype experimental results against the model results is carried out.

In chapter 4 an overall model is developed to study the performance of the heat storage system to cover the annual heating needs of a low energy consumption dwelling. A reference case is defined and the influence of the parameters, such as the solution tank insulation, solution tank mass and solar collector surface on the whole system behavior is studied. Finally, with purposes of evaluating a new working couple in future research, system annual simulations are carried out considering a $\text{KCOOH-H}_2\text{O}$ solution.

Chapter 1. Interseasonal heat storage systems – State of the art

In the European Union, an important actor of the energy consumption is the building sector, which represents 40% of the total final energy consumption in Europe (EUROPEAN COMMISSION, 2016), (COP21, 2016), (Vandyck et al., 2016), (IEA, 2016). Furthermore, from the total EU heating and cooling demand in 2012 (546 Mtoe⁽¹⁾ of 1102 Mtoe total final energy consumption), space heating represented 52% of this demand⁽²⁾ (EUROPEAN COMMISSION², 2016).

In France, by the year 2012, the energy consumption of buildings in the residential and the tertiary sectors represented 44% of the total energy consumption (EDF, 2016), (L'énergie en questions, 2016); additionally, the energy consumption for space heating purposes in each of these sectors represented respectively 61.3% and 66.1% of their total energy consumption (ADEME, 2016).

During the last 10 years several studies on solar energy storage for building heating have been carried out; some of these systems called interseasonal heat storage store the heat during summer for winter use (Xu et al., 2014). In this chapter, a review of different interseasonal heat storage systems is made. A focus is done on sorption processes that are weakly sensitive to heat losses and correspond to the present study

In section 1.1, a description of the main characteristics of the different heat storage technologies is presented. In section 1.2, a review of several interseasonal heat storage prototypes constructed during the last 5 years and based on liquid/gas absorption processes is shown. Finally, in section 1.3 the conclusions of this chapter are presented.

1.1. Low temperature solar heat storage system

The first significant scientific works to develop heat storage technologies start from the 1970s during the energy shortage crisis. In recent years the interest in developing systems able to store heat have grown again in interest mainly because of the extensive use of solar energy applications and their inner difficulty to match the energy production with the energy demands (Xu et al., 2014).

Heat storage technologies devoted to building can be classified by duration, temperature level, heat capacity and physical process.

Heat storage can be performed using sensible heat mechanism, latent heat mechanism and thermo-chemical mechanism (N'Tsoukpoe et al., 2009). The heat storage by sensible mechanism consists in storing the available energy by increasing the temperature of a material. The amount of stored heat is in relation with the material specific heat, the density and the temperature increase. Heat flux during heat charging and heat release depends also on the conductivity of the material; in general, this kind of technology is simple, low-cost and well developed (Li, 2016). When the heat is stored using liquids, attention must be paid to the thermal stratification (ie. the quality of the thermocline). When the heat is stored through solid materials, attention must be paid to the heat exchange system, most of solids used for heat storage applications being characterized by low heat conductivity.

The heat storage by latent mechanism takes advantage of the large amount of heat released or absorbed by phase change materials (PCM) during respectively their solidification and their fusion. Phase change of pure PCM occurs at constant temperature, whereas phase change of mixture occurs on a temperature range. In general, this kind of heat storage has a higher energy density than sensible storage mechanisms. Attention must be paid to the supercooling phenomenon and the thermal conductivity during the choice of the PCM and the design of the heat storage system. (Ali Memon, 2014) (Dutil et al., 2014) (Tittlein et al., 2015).

The thermochemical heat storage takes advantage of chemical bond or/and physical attraction between a pair of materials.

- Chemical sorption storage involves the reversible reaction between two substances to form a third one and vice-versa ($C + \text{heat} \leftrightarrow A + B$). It is characterized by endothermic decomposition and exothermic synthesis processes (the storage is made through chemical bounds). In several cases, each of these

⁽¹⁾ Million tonnes of oil equivalent.

⁽²⁾ The EU heating and cooling demand can be also classified by sectors consumption; with the residential, industry and tertiary sectors representing a 45%, 37% and 18% of the demand, respectively.

substances (A, B) can be separately stored during the decomposition stage and, afterwards, be gathered during the synthesis stage (Neveu et al., 2013), (Fopah Lele, 2016), (N'Tsoukpoe et al., 2016).

- Physical adsorption and absorption involves respectively Van der Waals attraction and hydrogen bonds (intermediate between Van der Waal attraction and covalent bonds). Considering a heat storage application criteria, absorption is related to the process in which a gas is absorbed by a liquid (absorbent); while adsorption is related to the process in which a physical binding is produced between a gas and the surface of a solid.

Additionally, sorption processes can be classified as open or closed systems (Fopah Lele, 2016). Open systems use the vapor contained in air to react with the sorbent, whereas closed systems take and release the sorbate contained in a reservoir during the discharge and charge phases.

Unlike sensible and latent heat storage systems, sorption process store energy as physical or chemical potential at ambient temperature, and is therefore weakly sensitive to thermal heat losses (Scapino et al., 2017). Another feature related to chemical storage systems is their higher energy density compared to sensible and latent systems, as it is shown in Figure 1.1 (N'Tsoukpoe et al., 2009).

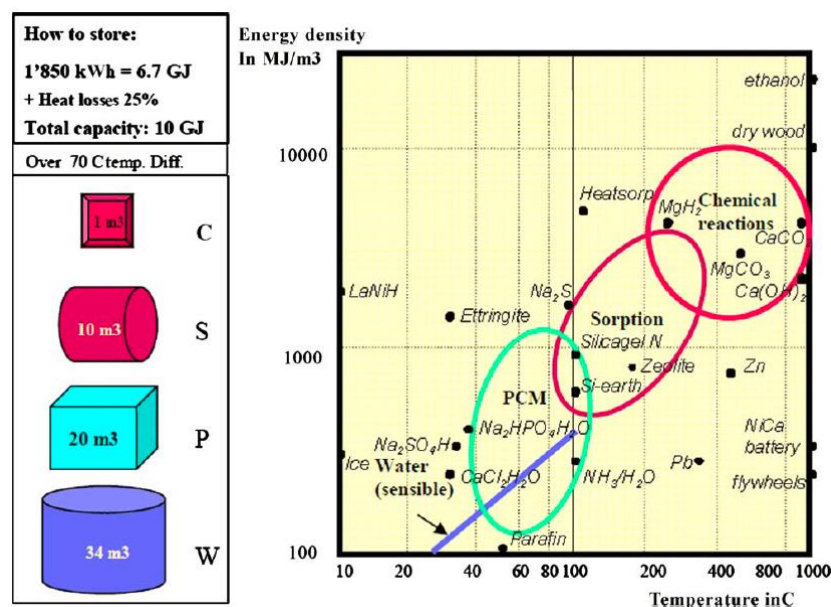


Figure 1.1. Energy density of high energy storage methods (Hadorn, 2005; Bales, 2006; N'Tsoukpoe et al., 2009)

Regarding the solar heat storage capacity, two types of systems can be encountered: minuscule solar heat storage systems devoted to family homes, concerning mainly domestic hot water and space heating applications, and large solar heat storage systems concerning mainly district heating. (Fisch et al., 1998) studied 27 large-scale solar heating systems based on short term and long-term storage; the results revealed that the short-term systems had a lower capacity (10-20%) to satisfy the annual heating demand than the long-term systems (50-70%). However, although the long-term storage systems are more capable to store the energy, they are more technologically challenging than short-term systems due to the larger storage volume, heat losses and material selection; with this latter requiring to be economical, reliable and ecological (Yu et al., 2017).

Two main duration are mostly encountered in solar heat storage systems devoted to building: the short-term storage related to the daily periods and long-term storage such as the seasonal periods. The former are largely used for domestic hot water and heating of buildings. The latter are mostly at the research stage. Some real-scale interseasonal applications using sensible heat storage exist. Interseasonal solar energy storage prototypes based on latent heat and sorption heat storage have been constructed and tested during recent years. The technologies or main materials used for each of these long-term systems are described below.

Interseasonal heat storage systems based on sensible heat (Li, 2016), (Zhang et al., 2015):

- *Water based storage*; which uses water as the storage medium and the heat transfer fluid. This technology can be further classified as water tank systems and aquifer systems: the former based on artificial constructions in stainless steel or reinforced concrete surrounded by thick insulation (usually placed underground) and the latter based on natural water aquifer located in underground layers.
- *Rock bed storage*; which is based on heat storage in materials such as pebble, gravel and bricks. In these systems the heat is provided in summer and taken off in winter by the use of heat transfer fluids (HTFs), such as water or air, circulating inside heat exchanger tubes placed all along the bed.
- *Ground heat storage*; which directly use the ground itself as the storage medium. The heat exchange is performed using borehole heat exchangers inside (vertical/ U-type horizontal tubes implanted in the ground)

The materials used for seasonal latent heat storage systems, can be classified as follows (Ali Memon, 2014):

- *Organic materials*; such as paraffins and non-paraffins (fatty acids). Examples: Propyl palmitate, Glycerin, Paraffin C₁₇, Paraffin C₁₃₋₂₄, Lactic acid, Capric acid, etc.
- *Inorganic materials*; such as hydrated salts and metallics. Examples: CaCl₂.6H₂O, Na₂SO₄.10H₂O, KF.4H₂O, etc.
- *Eutectics*, which are a melting compound of two or more components: organic-organic, inorganic-inorganic or organic-inorganic mixtures. Examples: 50%CaCl₂ + 50%MgCl₂.6H₂O, Octadecane + docosane, 47%Ca(NO₃)₂.4H₂O + 53%Mg(NO₃)₂.6H₂O, etc.

Pairs of materials used for seasonal sorption heat storage systems are presented hereafter (Fopah Lele, 2016), (Yu et al., 2017):

- Absorption pairs (liquid/gas); LiCl/H₂O, NaOH/H₂O, CaCl₂/H₂O, LiBr/H₂O, NH₃/H₂O, etc.
- Adsorption pairs (solid/gas); MgSO₄.7/H₂O, Al₂(SO₄)₃.18/H₂O, MgCl₂.6/H₂O, CaCl₂.2/H₂O, MgSO₄-zeolite/H₂O, etc.

A summary of all the described technologies, their advantages, disadvantages, present status and future work is presented in Table 1.1 (Xu et al., 2014).

Sensible long-term heat storage systems are performing well when heat losses become small compared to the heat stored. That is the case when the size of the heat storage system becomes very large. Therefore, such systems are particularly interesting for district heating. Sorption systems are much more complex, but are weakly sensitive to heat losses. This property is interesting for small heat storage systems for which heat losses can be significant when using sensible or latent heat. Another property that can be interesting considering sorption systems is its ability to refresh or heat building using the same system, heating being delivered at the absorber/adsorber, cooling being generated at the evaporator.

Compared to adsorption systems, absorption systems present the advantage to dissociate the exchangers where heating or cooling is generated from the tanks where the liquids are stored. This can be particularly interesting for the compactness of the system.

In general, desirable attributes of long-term storage systems for solar space heating are: high energy density, charge temperatures achievable with flat-plate or vacuumed tube collectors, discharge temperatures suitable for the load, adequate charge/discharge power, stable materials over many cycles; non-toxic and environmentally friendly materials, low cost and abundant materials.

The following part is devoted to a brief description of absorption heat storage systems already experimented.

Table 1.1. Comparison of the three available technologies for seasonal thermal energy storage (Xu et al., 2014)

	Sensible	Latent	Chemical
Storage medium	Water, gravel, pebble, soil..	Organics, inorganics	Metal chlorides, metal hydrides, metal oxides..
Advantage	Environmentally friendly cheap material Relative simple system, easy to control Reliable	Higher energy density than sensible heat storage Provide thermal energy at constant temperature	Highest energy density, compact system Negligible heat losses
Disadvantage	Low energy density, huge volumes required Self-discharge and heat losses problem High cost of site construction Geological requirements	Lack of thermal stability Crystallization Corrosion High cost of storage material	Poor heat and mass transfer property under high density condition Uncertain cyclability High cost of storage material Corrosion
Present status	Large-scale demonstration plants	Material characterization, laboratory-scale prototypes Screening for better suited PCM materials with higher heat of fusion Optimal study on store process and concept	Material characterization, laboratory-scale prototypes
Future work	Optimization of control policy to advance the solar fraction and reduce the power consumption Optimization of storage temperature to reduce heat losses Simulation of ground/soil based system with the consideration of affecting factors (e.g. Underground water flow)	Further thermodynamic and kinetic study, noble reaction cycle	Optimization of the particle size and reaction bed structure to get constant heat output Optimization of temperature level during charging/discharging process Screening for more suitable and economical materials Further thermodynamic and kinetic study, noble reaction cycle

1.2. Interseasonal heat storage systems based on gas/liquid sorption process: Experimental cases review

During the last 5 years, different interseasonal solar heat storage systems for heating purposes using gas/liquid sorption processes have been studied. Demonstrative prototypes have been constructed and tested. In this section, a review of 7 of these prototypes is presented. All of them use water as sorbate. Four different sorbents have been studied: LiCl, CaCl₂, NaOH and LiBr. Their main characteristics (sorbent solution, design, performance, limitations) are described.

1.2.1. Lithium chloride (LiCl-H₂O) systems

1.2.1.1. ClimateWell - Sweden

ClimateWell in Sweden (Bales and Nordlander, 2005) appears to be the pioneers of absorption heat storage systems. A sorption heat storage system based on a “three-phase process” (Yu et al., 2014) was developed in 2005 by the laboratory Solar Energy Research Center (SERC) and the company ClimateWell.

The system, called “Thermo-Chemical Accumulator (TCA)”, uses a LiCl-H₂O working pair. The working principle of the long-term heat storage system is similar to an absorption heat pump cycle, although evaporation/absorption and desorption/condensation do not occur at the same time. The system does not require four exchange units (absorber, desorber, condenser and evaporator) since the interseasonal heat storage functions in a discontinuous way (charging in summer and discharging in winter). Consequently, the four heat exchangers can be combined into two reversible exchangers: one heat exchanger operates as a desorber and the other as a condenser in the charging period, and as an absorber and an evaporator in the discharging period, respectively.

The ClimateWell system uses two storage tanks, one for the LiCl solution (sorbent) and the other for the water. Crystallization of the solution allowing a higher energy storage density is allowed in the sorbent tank. Several prototypes of this system (patented in 2000) have been constructed. The first prototypes were not reliable because of corrosion problems leading to non-condensable gases emission, and unwanted crystallization problems in tubes and exchangers leading to blockages and poor wetting. In 2005 the machine has been redesigned and a new prototype called ClimateWell 10 (CW10) was constructed and tested. The data collected showed that the machine worked consistently with no noticeable vacuum problems. Figure 1.2 shows the schematic of a TCA unit.

Each tank includes an exchanger located on the upper part. During the charging period the solution is pumped at the base of the sorbent tank and spread over the heat exchanger working as desorber. Vapor generated condenses on the exchanger located in the water tank and working as a condenser. As water is desorbed from the solution, its concentration increases. Once it reaches the saturation point, crystallization can occur. The solid crystals formed in the solution fall under gravity into a vessel, forming a slurry at the vessel’s bottom. A sieve located around the tank wall prevents the crystals to flow into the solution circuit.

During the discharging period the process is reversed. Water is pumped at the base of the water reservoir and spread over the exchanger working as evaporator. The vapor is absorbed by the concentrated solution pumped at the base of the solution tank and spread over the heat exchanger working as an absorber. Depending on the operation mode, the heat required for the vaporization is provided by the environment (heating mode operation) or the building (cooling mode operation). The diluted solution falling from the absorber returns into the vessel where it passes through the slurry of crystals and dissolves them progressively, as long as there are some crystals in the vessel.

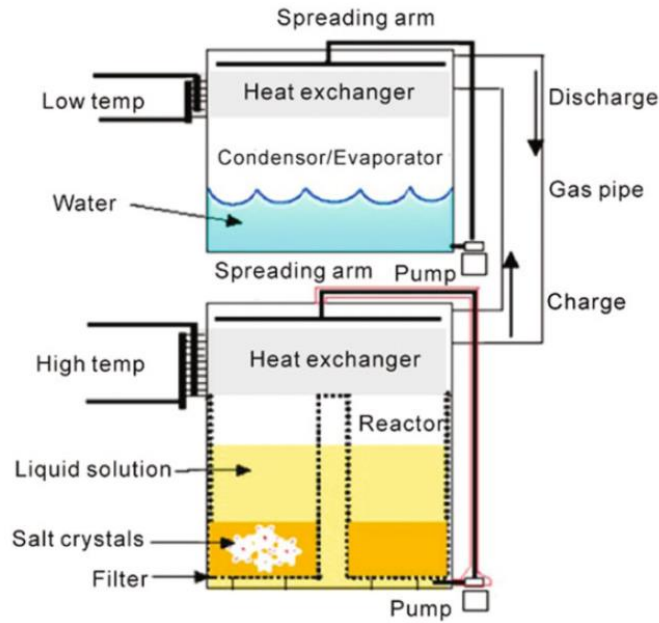


Figure 1.2. Schematic of a single unit thermos-chemical accumulator (Bales and Nordlander, 2005)

A scheme of the TCA prototype CW10 is shown in Figure 1.3a. Some characteristics of this model are that: the heat exchangers and pipes are in standard carbon steel, the internal surfaces were enameled to prevent corrosion, the number of external components was reduced, the pipes were rerouted to prevent unnecessary bends and pressure drops (a central “chimney” simplifies the flow routing) and the wetting method for the heat exchanger surfaces was improved. Table 1.2 shows the results of some experimental tests made on a single unit of a CW10 TCA (Bales, 2008).

Table 1.2. Test results of a single unit of a CW10 TCA prototype. Tests carried out at ClimateWell AB in November 2005 (Bales, 2008)

Parameter	Values	Boundary conditions
LiCl salt weight [kg]	54	
Water weight [kg]	117	
Storage capacity for heat [kWh]	35	At charging/discharging rates (shown below)
Energy density of prototype – heating mode [kWh/m ³] / (ratio respect to heat stored in water, temperature gap : 25-85°C)	85 / (1.2)	Based on short term storage
Energy density of prototype – cooling mode [kWh/m ³] / (ratio respect to heat stored in water, temperature gap : 7-17°C)	54 / (4.7)	Based on cooling energy that can be extracted and comparison to cold water storage
Charging rate [kW]	15	Condenser inlet/outlet: 13/25°C Reactor inlet: 46-87°C
Discharging rate [kW]	8	Evaporator inlet/outlet: 21/12°C Reactor inlet/outlet: 25/30°C

Figure 1.3b shows an image of a commercial version of the CW10 TCA. This model is composed of two identical units called barrels, which work together. Each barrel is composed of four vessels (see Figure 1.3a): the reactor (absorber/ generator), the condenser/evaporator (these two vessels connected by a vapor channel), the solution vessel and the water vessel. Since the system is composed of two units, a switching device is required to change the external circuits associated to the heat exchangers, this latter is possible through the use of eight three-way valves placed at the top of the unit (see Figure 1.3b). A control algorithm permits the CW10 TCA to be operated in seven different modes: manual, normal, full cycles, double, timer, turbo and test (Rosato and Sibilio, 2013). In “normal mode” for example, both barrels alternate in charging and discharging, permitting the machine to be able to provide cooling power or building heating power (evaporation/absorption) and to use the supplied heat (desorption/condensation) at the same time. Conversely, in “double mode” both barrels are charged and discharged at the same time, resulting in a higher cooling/heating power (discharge) and higher charging power (charge).

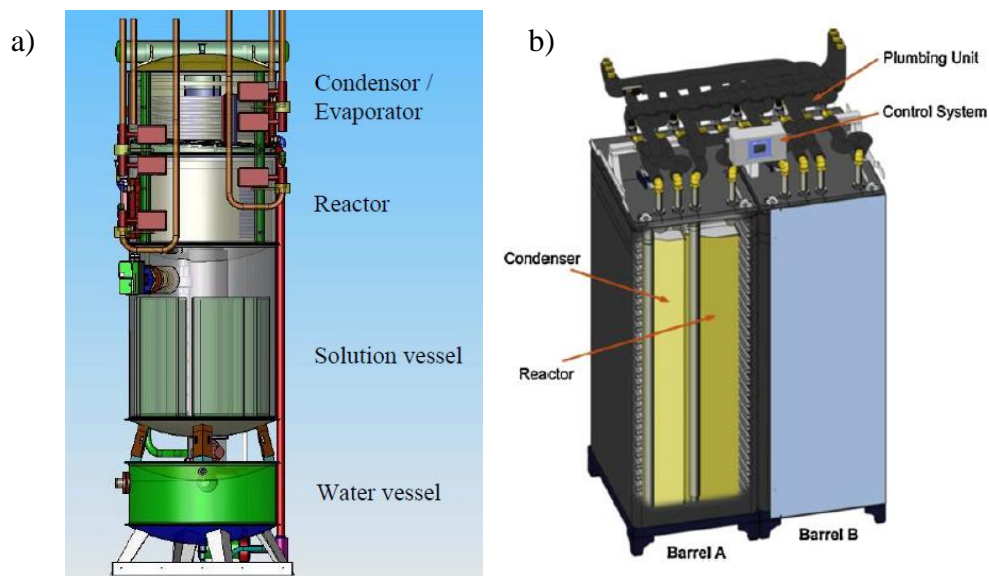


Figure 1.3. CW10 TCA machine. a) Schema of the CW10 prototype (Single barrel); b) Schematic of the commercial version of the CW10 machine (Two barrels) (Bales, 2008), (Rosato and Sibilio, 2013)

Finally, recent experimental evaluations of the CW10 TCA machines were done by (Rosato and Sibilio, 2013) at the Second University of Naples in Italy. These tests were carried out in “normal mode” and “double mode”; however, these tests were aimed to evaluate the cooling capacity of the system, so the heat storage performances were not assessed.

1.2.1.2. Shanghai Jiao Tong university - China

An energy storage system prototype based on a sorption process using LiCl-H₂O pair was constructed by Zhao (Zhao et al., 2016) at the Shanghai Jiao Tong University. The prototype was designed to have a heat storage capacity of 10 kWh and was tested under conditions representative of transition or winter conditions. Although the system was designed for short-term heat storage applications, the working principle could be adapted for long-term purposes.

The heat storage experimental system is shown in Figures 1.4 and 1.5. The system is composed of a sorption reactor, an evaporator/condenser and a connection valve. A hot water tank, a cooling tower and a thermostatic bath are associated to the system. The hot water tank (power capacity up to 20 kW) aims to control the absorber/desorber HTF temperatures (reactor). The cooling tower controls the evaporator/condenser HTF temperatures. The thermostatic bath associated to the evaporator HTF is used to improve the system performance by simulating heat recovery from the domestic hot water in order to increase the system evaporation temperature.

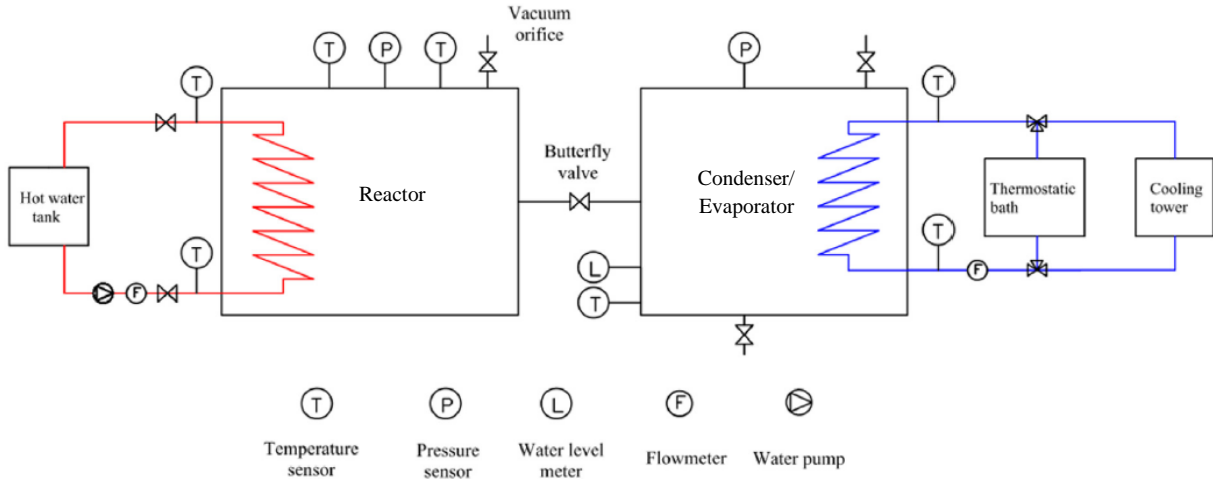


Figure 1.4. Experimental system of the sorption thermal energy storage system (Zhao et al., 2016)

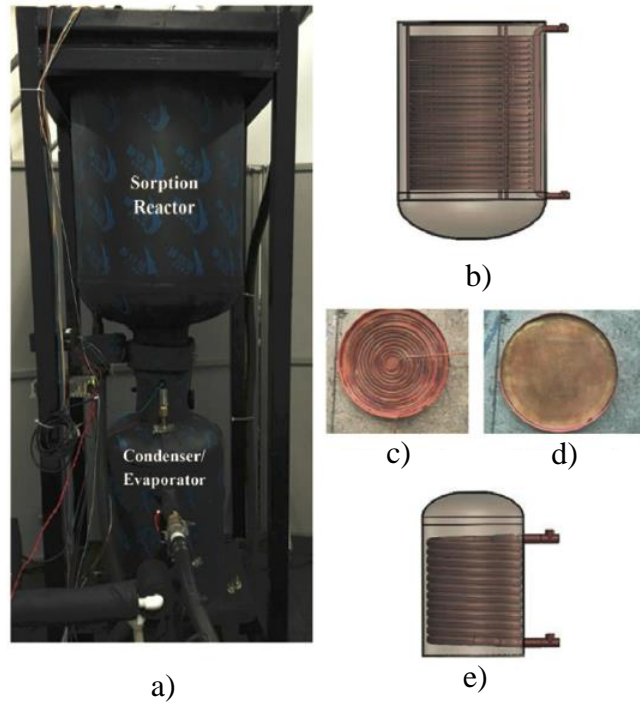
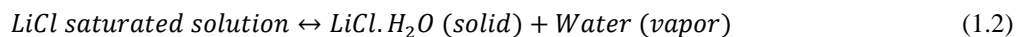
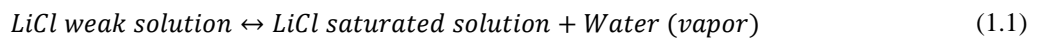
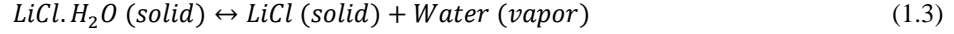


Figure 1.5. Structure details of the experimental prototype. a) Experimental prototype; b) Sorption reactor; c) Sorption unit; d) Copper mesh; e) Condenser/Evaporator (Zhao et al., 2016)

In order to improve the heat and mass transfer properties, a composite sorbent formed with lithium chloride (LiCl) and expanded graphite (EG) is used. The reactor design is based on a modular concept involving a stack of 25 sorption bed units. Each unit includes a high efficient copper-coil tray holding the composite sorbent (technical characteristics of the heat exchanger are shown in Annex A1.1). The condenser and evaporator are combined into one vessel to simplify the prototype.

The system working principle is based on the alternation of charging and discharging periods, respectively associated to desorption/condensation and absorption/evaporation processes. In order to increase the system performance a variation of these processes was considered and is shown in the equations below.





The system desorption process is described from equations (1.1) to (1.3), while the absorption process can be described in the opposite direction. This process, first presented by (Lourdudoss and Stymme, 1987), was named “the super solution field system”, but is also known as the “three-phase process” (Yu et al., 2014) since water vapor, liquid solution and solid crystal coexist in the same reactor.

The system operating principle is presented in a pressure-temperature-concentration (P-T-x) diagram in Figure 1.6. Typical conditions are considered in the diagram for the charging and discharging periods, with temperatures associated to the HTFs in the desorber, condenser, absorber and evaporator of 75 °C, 15 °C, 35 °C and 5 °C, respectively. For both processes, the absorber/desorber and the evaporator/condenser are separated by a valve.

During the charging process the solution starts from point c_1 , corresponding to a weak solution at ambient temperature (10°C). The solution is heated up to point c_2 at a constant concentration (no vapor desorption produced). In c_2 the reactor and condenser are connected (valve opened) and the solution is heated up to the crystallization point c_3 and further, up to point c_4 and c_5 corresponding to crystalline hydrate state ($\text{LiCl} \cdot \text{H}_2\text{O}$) and anhydrous state (LiCl), respectively.

During the discharging process (Figure 1.6), the process starts connecting the absorber and evaporator (valve opened), the anhydrous LiCl goes from point d_1 (at 10°C ambient temperature) to point d_3 , becoming a weak solution and releasing an important amount of heat.

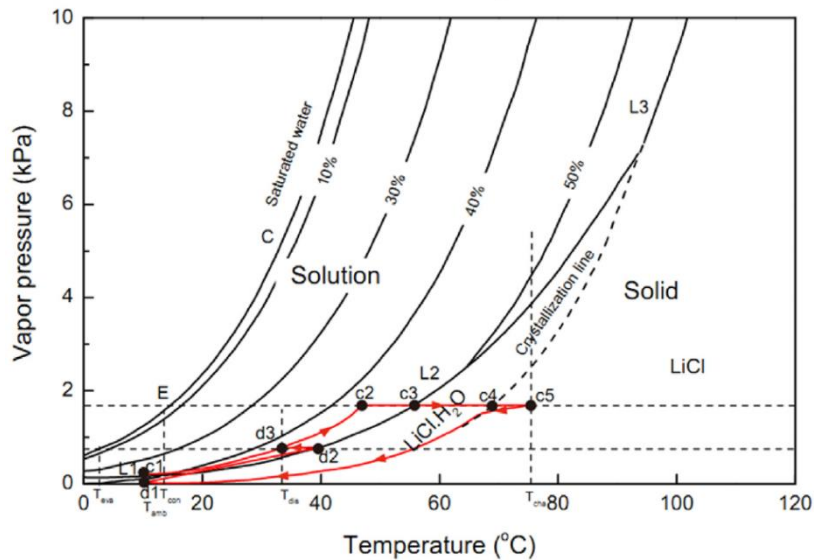


Figure 1.6. Operating principle and thermodynamic working conditions for a three-phase sorption cycle in winter seasons involving $\text{LiCl}-\text{H}_2\text{O}$ working pair (Zhao et al., 2016)

Experimental tests in charging and discharging operating modes were carried out on the prototype shown in Figures 1.4 and 1.5. Tests in charging mode were divided in two periods: The sensible heat period and the sorption period. The sensible heat period corresponds to heating of the system thermal mass (tubes, shells, solution, water, etc.) with the HTF (between points c_1 and c_2). The sorption period corresponds to the water desorption. Furthermore, a similar period division was considered for the experimental discharging tests.

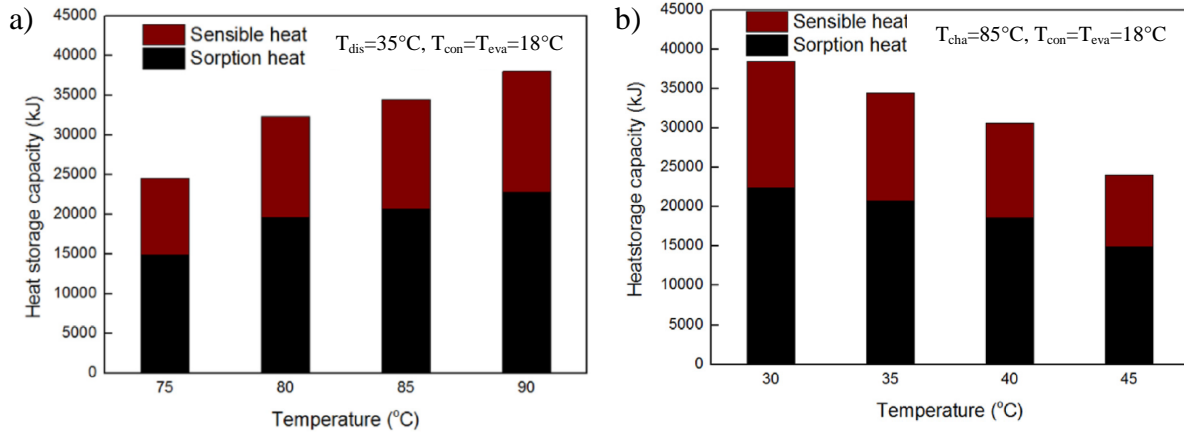


Figure 1.7. a) Heat storage capacity vs. charging temperature; b) Heat storage capacity vs. discharging temperature (Zhao et al., 2016)

Figures 1.7a and 1.7b show the influence of different working conditions on the prototype heat storage capacity (energy available for space heating purposes) when the charging (desorber HTF) and discharging (absorber HTF) temperatures are modified, respectively. As shown in Figure 1.7a, the heat storage capacity increases when the charging temperature is increased, with a sharper growth when moving from 75°C to 80°C possibly due to the formation of crystals. Conversely, Figure 1.7b indicates that the heat storage capacity is reduced when the discharging temperature is increased. For both cases, the sorption contribution to the storage capacity is in the range of 58 % to 62 %.

For working conditions of $T_{\text{charging}} = 85 \text{ }^{\circ}\text{C}$ and $T_{\text{discharging}} = 40 \text{ }^{\circ}\text{C}$, the stored energy is around 8.52 kWh. Considering a 157 liters prototype volume, the system energy storage density is 54 kWh/m^3 (this value can be increased by 20% by rising the evaporation temperature using a heat recovery technology). Finally, it must be highlighted that the system energy storage density is about two times higher than that of a conventional heat storage water tank (for a volume of 300 liters and a temperature rise of 30 °C).

1.2.2. Calcium chloride ($\text{CaCl}_2\text{-H}_2\text{O}$) systems

CaCl_2 is a very hygroscopic salt that can fix up to 6 molecules of water with an energy density of 380 kWh.m^{-3} . Moreover calcium chloride is mass produced at very low cost (0.3 - 2 USD/kg). It is characterized by high thermal conductivity (compared to other material of the same type), good thermal and chemical stability, less corrosiveness than other salt hydrates, high latent heat of fusion, non-toxicity, etc. Nevertheless, there are also some undesirable properties associated to CaCl_2 such as disintegration/decomposition/deterioration after several operating cycles when no special measures are taken (depending on the application), corrosion to certain metals in the presence of oxygen, etc. (N'Tsoukpoe et al., 2015).

1.2.2.1. LOCIE – University Savoie Mont Blanc - France

A study to evaluate the potential use of sorption processes in interseasonal heat storage applications was carried out by (Liu, 2011) at the LOCIE laboratory in the University Savoie Mont Blanc in France. The main components of this system are: a reactor (composed of two heat exchangers working as generator/absorber and condenser/evaporator), a solution tank, a sorbate tank, a solar collector and a heat source/sink.

During summer the poor solution (low mass fraction of sorbent) in the solution tank is pumped to the generator where it is heated by the solar energy (provided by the solar collector). The sorbate inside the solution is vaporized and transferred to the condenser where its latent heat is given to the heat sink. The condensed sorbate is stored in the sorbate tank. The rich solution (high mass fraction of sorbent) leaving the generator is stored in the solution tank.

During winter the sorbate is transferred from the sorbate tank to the evaporator where it is evaporated due to the heat given by the heat source (for example a geothermal source). The vaporized sorbate is absorbed by the rich solution (high mass fraction of sorbent) in the absorber; the thermal energy liberated in this process being used

to cover the heating needs of a building. The poor solution (low mass fraction of sorbent) leaving the absorber is stored in the solution tank.

Seven sorbate/sorbent couples were analyzed through a static model in order to determine their performance in the system, these couples were: $\text{CaCl}_2\text{-H}_2\text{O}$, Glycerine- H_2O , $\text{KOH-H}_2\text{O}$, $\text{LiBr-H}_2\text{O}$, $\text{LiCl-H}_2\text{O}$, $\text{NaOH-H}_2\text{O}$ and $\text{H}_2\text{O-NH}_3$. Several criteria were considered in the analysis: storage capacity (absorption heat divided by the sorbent mass), storage efficiency (absorption heat divided by the desorption heat), solar collector temperature required in desorption, absorption temperature required for building heating applications, easy handling and non-toxicity, and material low cost. Following this analysis, the couple $\text{CaCl}_2\text{-H}_2\text{O}$ was chosen for the experimentation due to its acceptable storage capacity with respect to its price and its higher safety compared to the $\text{KOH-H}_2\text{O}$, $\text{NaOH-H}_2\text{O}$ and $\text{H}_2\text{O-NH}_3$ couples.

A scheme of the constructed prototype is shown in Figure 1.8. Similarly as the heat storage system, the prototype is mainly composed of a solution tank ($\text{CaCl}_2\text{-H}_2\text{O}$), a water tank (sorbate), a reactor and two thermostats (which simulate the solar collector and the heat source/sink).

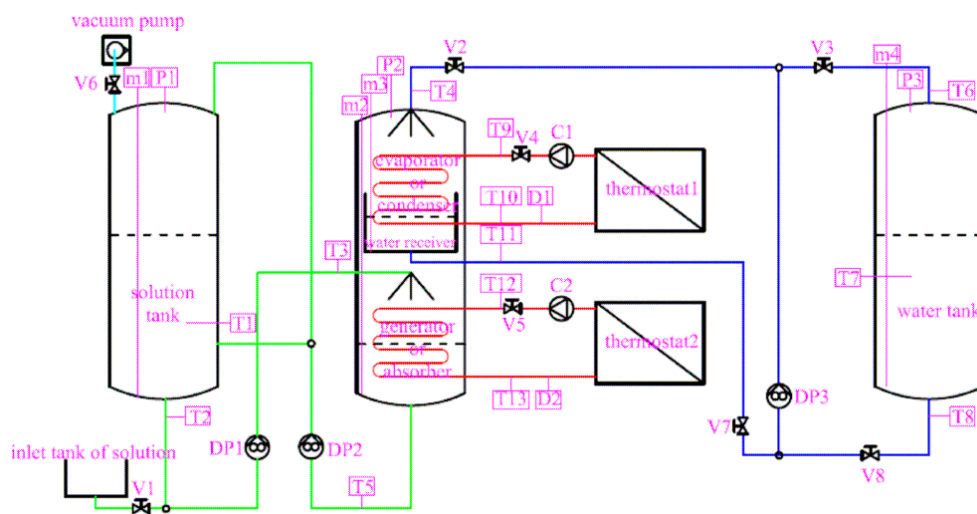


Figure 1.8. Scheme of the prototype (Liu, 2011)

Table 1.3 shows a description of the technical characteristics of some of the main components of the constructed prototype.

Table 1.3. Technical characteristics of the prototype components

	Type	Volume (m^3)	Material
Solution tank	Cylindrical	0.15	Stainless steel 316L
Water tank	Cylindrical	0.05	Stainless steel 304L
Reactor container	Cylindrical	0.13	Stainless steel 316L
Heat and mass exchanger	16 vertical tubes arrangement with external helical fins	-	Stainless steel 316L

As indicated in Table 1.3, the heat exchanger configuration used in the reactor for the condenser/evaporator and desorber/absorber is based on 16 vertical tubes arrangement with helical fins outside, as it is shown in Figure 1.9a. The HTFs flow inside the tubes. The solution (distilled water), coming from the solution tank (water tank), is distributed above every helical fin on the heat exchanger, flows along the helical fins outside of the tubes and is collected by a solution (water) receiver placed at the bottom of the exchanger (respectively), (see Figure 1.8). According to its design, this type of heat exchanger should be capable to produce powers in the generator, condenser, absorber and evaporator of 4.4 kW, 2.2 kW, 0.25 kW and 0.28 kW for a HTF flow rate of 500 kg/h, 200 kg/h, 150 kg/h and 200 kg/h, respectively.

The initial conditions in the solution tank considered a 207 kg mass and a 0.369 mass fraction. Figure 1.9b shows the constructed prototype. Several tests in desorption and absorption were launched in order to test the prototype performance. Working conditions and obtained powers in some of these tests are described in Table 1.4.

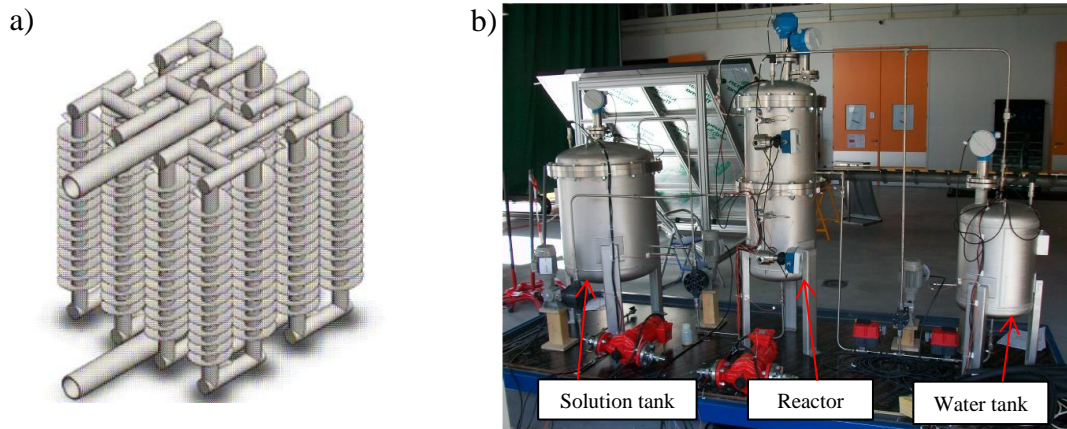


Figure 1.9. a) Design of the heat exchanger with helical fins b) Experimental setup of the absorption storage system (Liu, 2011)

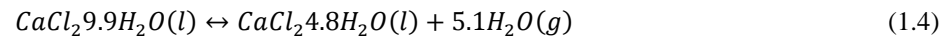
Table 1.4. Working conditions and system performance of experimental tests in desorption/condensation and absorption/evaporation operating mode (Liu, 2011)

Components	Parameters	DESORPTION/ CONDENSATION	ABSORPTION/ EVAPORATION
		Test 1	Test 2
Generator/Absorber	Duration [min]	461	404
	Inlet solution mass flow [kg/h]	115	115
	Mass fraction range [m_CaCl ₂ /m_st]	[0.345 - 0.381]	[0.417 - 0.41]
	HTF mass flow [kg/h]	500	150
	HTF inlet temperature [°C]	80	20
Condenser/Evaporator	Inlet water film mass flow [kg/h]	0	24
	HTF mass flow [kg/h]	200	200
	HTF inlet temperature [°C]	30	15
System	Generator/Absorber power	1.81 to 4 kW	0.02 to 0.11 kW
	Condenser/Evaporator power	0.25 to 3 kW	-0.04 to 0.06 kW

As observed in Table 1.4, although some interesting generation powers were obtained in the charging tests, the absorber powers measured during the discharging tests were near to zero. The reason to this latter behavior was, according to the authors, due to a presence on non-condensable gases (NCG) in the system as well as a low wettability of the helical fins exchange surfaces where the solution and water film flows. An improvement of the absorber power (0.08 to 0.56 kW) was obtained by increasing the evaporator HTF inlet temperature and mass flow to 40 °C and 1000 kg/h, respectively. This latter proved that the absorption process really happened during the tests. Hence, a possible use of the system for building space heating applications is possible, if technical improvements are made on the prototype (for example, to avoid the presence of NCG).

1.2.2.2. University of Minnesota -USA

A closed absorption system involving water and calcium chloride (CaCl_2) has been proposed by (Quinnell and Davidson, 2012¹) at the University of Minnesota in USA. The CaCl_2 desorption and absorption processes used are described by equation (1.4):



The heat storage system principle proposed by Quinnell and Davidson is shown in Figure 1.10.

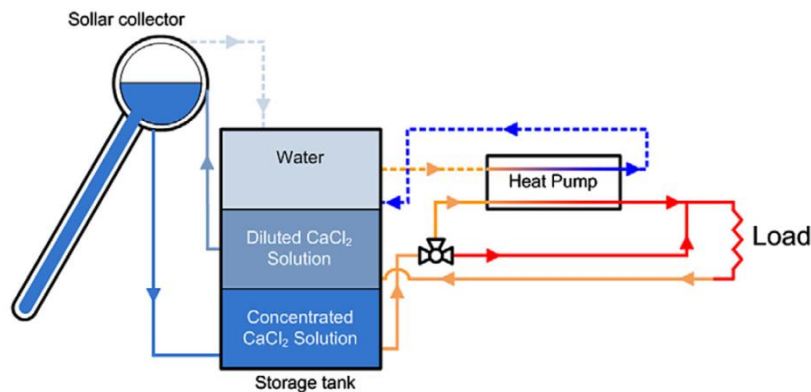


Figure 1.10. Schematic of a closed –cycle absorption heating system with a single tank for storage of water, diluted and concentrated calcium chloride solution (Quinnell and Davidson, 2014)

During the charging period, diluted aqueous CaCl_2 is pumped from the tank and flows to the solar collector where it boils at a temperature between 117-138 °C to produce concentrated aqueous CaCl_2 and water vapor. The concentrated solution returns back to the lower part of the storage tank. The desorbed water vapor condenses either in the solar collector or in the storage tank and is stored on the top of the storage tank.

During the discharging period, concentrated aqueous CaCl_2 and water are pumped from the storage tank and are injected into an absorption heat pump where binding energy and heat of vaporization are transformed into thermal energy to meet space heating and domestic hot water loads. Additionally, when the solar collector temperature is below 117 °C (solution boiling point), the heat released by the solar collector to heat the solution is directly used for space heating needs (once the solution tank temperature is higher than the load temperature) (see Figure 1.10)

As shown in Figure 1.10 and 1.11, the main originality of the sorption system is the use of a single storage tank for the concentrated solution, diluted solution and water in order to increase the system energy density and to reduce costs compared to systems that use separated tanks for solution and water.

Figure 1.11a shows the conceptual design of the single tank. The mixing of stored liquids is minimized by the use of internal devices to control temperature and fluid motion, taking advantage of natural density gradients between the different solutions since the storage fluids are stratified in regions according to their density (which increases with the CaCl_2 mass fraction increase and the temperature decrease). As it is represented in Figure 1.11b, density gradients are formed at the interface between the regions of water, diluted and concentrated solution; where in quiescent conditions mixing by diffusion is not a problem since it is 10000 times slower than thermal conduction. Nevertheless, mixing can be intensified when fluid motion is present in the tank during the charging and discharging periods, reason why low mass flows are preferred in order to preserve the absorption storage.

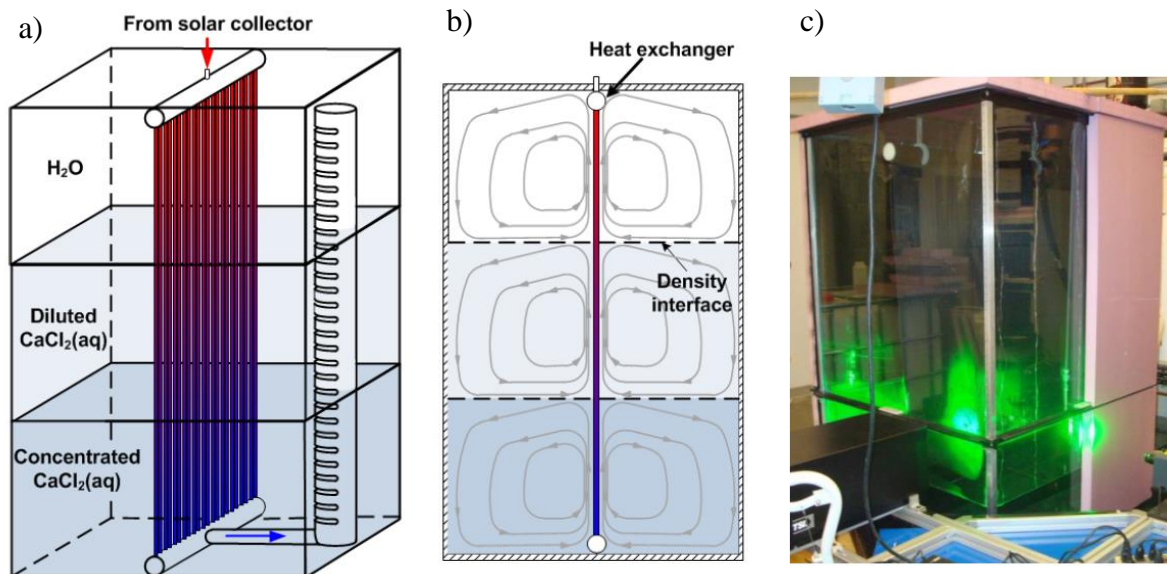


Figure 1.11. Prototype absorption/sensible storage tank. a) Illustration of immersed heat exchanger and stratification manifold; b) convective flow patterns expected during charging period; c) Photograph of prototype liquid CaCl_2 tank including laser sheet and PIV/PLIF imaging cameras (Quinnell and Davidson, 2012¹), (Quinnell and Davidson, 2012²)

An immersed parallel-tube heat exchanger and a stratification manifold (Figure 1.11a) permits to minimize mixing between regions of different CaCl_2 mass fractions, during the charging period hot solution from the solar collector enters through the top of the heat exchanger while heating the tank from top-to-bottom via natural convection; afterwards, the solution enters at the stratification manifold where it rises up to a region of neutral buoyancy and enters into the tank.

Experimental and simulation studies have been carried out to show the viability of the single storage tank (Figure 1.11c), (Quinnell and Davidson, 2012²), (Quinnell and Davidson, 2014). Both studies focused on the effect of natural convection on the overall heat and mass transfer across the interface between layers of different salt mass fractions (solution and water); furthermore, the studies were restricted to sensible heating via the heat exchanger, reason why no fluid was injected or removed from the tank. Results demonstrated that natural convection does not disrupt the stable mass fraction distribution during this mode of operation and thus, that the concept holds promise for long term storage.

1.2.3. Sodium hydroxide ($\text{NaOH-H}_2\text{O}$) – EMPA - Switzerland

As part of the EU funded project COMTES, (Fumey et al., 2015) developed a closed sorption heat storage system based on sodium hydroxide (NaOH) as sorbent and water as sorbate.

The choice of this salt was in accord with propositions made by Liu (Liu et al., 2011), related to aqueous solutions with excellent theoretical storage capacity in absorption systems. Economic reasons also prevailed in the NaOH salt selection since, according to Fumey, its price per ton was 1000 € while those of LiBr and LiCl increased up to 4750 € and 7000 €, respectively.

In order to minimize technological drawbacks, a prototype was constructed operating on a hybrid basis where sensible and sorption heat were stored in water tanks and in the sorption system for diurnal and seasonal storage, respectively.

The prototype was constructed in a 7 m long ship container with an 18 m² solar collector field installed on the top and used as a heat source for operation (Figure 1.12a). For the short-term sensible heat storage; three series connected water tanks (each with a 1 m³ volume) were used, with the first tank dedicated to domestic hot water (higher temperature), while the other 2 tanks were used for space heating purposes (lower temperature). Additional technical characteristics of the heat exchanger are shown in Annex A1.2.

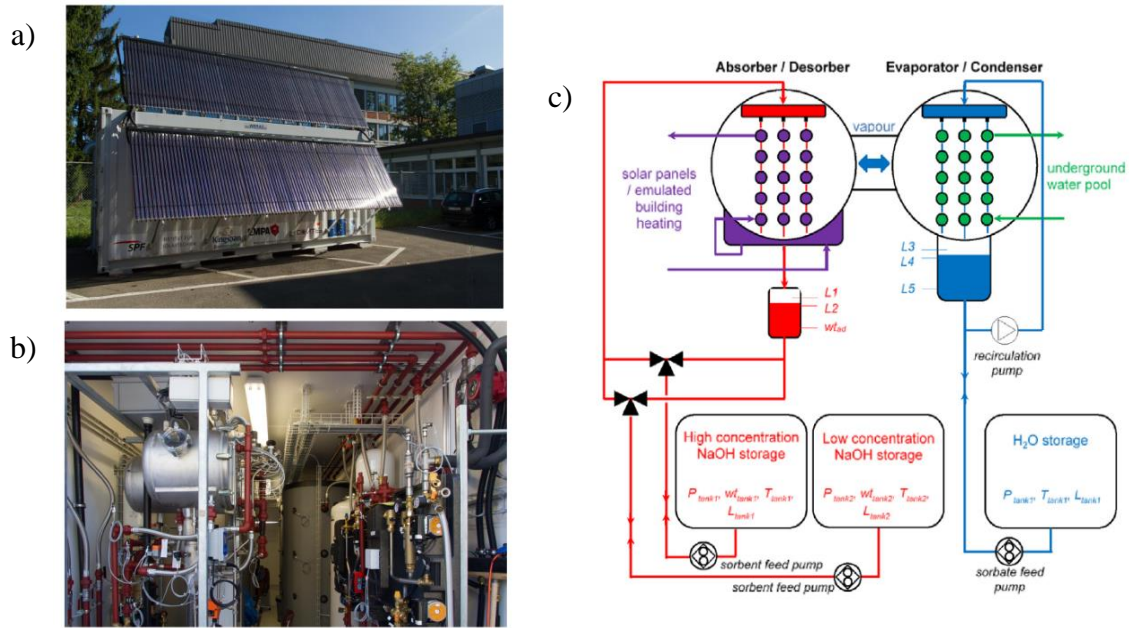


Figure 1.12. a) Picture of the complete prototype from the outside (solar collectors placed on top and side of the ship container); b) Picture of the complete prototype from the inside (Fumey et al., 2015); c) Scheme of the hydraulic concept around the heat and mass exchangers in the sorption system (Daguenet-Frick et al, 2016)

For the long-term sorption heat storage a vacuum container composed of two stainless steel heat and mass exchangers (sorption reaction zone) and three stainless steel tanks were used (Figure 1.12b,c). The tanks, each with a volume of 1.5 m³, permitted the storage of concentrated and diluted aqueous sodium hydroxide (sorbent) and water (sorbate) at ambient temperature. Magnetic gear pumps were used to pump the fluids from the tanks to the heat exchangers (functioning as desorber/condenser or absorber/evaporator) and vice versa. Prior to measurements, a fluid degassing cycle was performed in order to evacuate non-condensable gases.

The working principle of the sorption system is similar to the systems described in previous sections (Daguenet-Frick et al., 2016). Heat and mass exchangers were of the falling film bundle type, as it is shown in Figure 1.13, and were designed to have a thermal power output of up to 8 kW. The active external exchange surfaces associated to the desorber/absorber and condenser/evaporator were of 0.68 m² and 4.2 m², distributed in a 4x18 and 16x2 tubes configuration, respectively (Figure 1.13).

As initial conditions, experimental tests in the sorption system considered a 1000 kg concentrated solution at 50 wt% in a tank and a 700 kg de-ionised water in another tank. PT100 temperature sensors were installed inside the tanks and along both of the heat and mass exchangers in the tubes outside and inside, the latter to measure the falling films and heat transfer fluids temperatures, respectively. In order to avoid possible disturbances, the sodium hydroxide mass concentration was measured using inductive conductivity sensors placed at the solution tanks and at a solution cell located outside of the absorber/desorber unit; nevertheless, due to the low solution mass flows compared to the solution cell volume, instantaneous concentration measurements were not possible.

Difficulties were found in the solution pumping and mass flow measurement at the absorber/desorber heat exchanger due to cavitation phenomena produced by the low pressure operation; limiting the sodium hydroxide mass flow and, consequently, generating an incomplete tube bundle external surface wetting. No surface wetting issues were observed in the condenser/evaporator, in part due to the water recirculation considered in this component (see Figure 1.12c). During the experimental tests, (Daguenet-Frick et al., 2016) the pressure in the desorber (evaporator) was higher than the pressure in the condenser (absorber) since a driving force is required by the vapor to flow between these exchangers, overcoming the sorption process resistance. The estimated pressure gap obtained by Daguenet-Frick et al., considering pressure extrapolations at an Oldham's diagram, was around 20 mbar.



Figure 1.13. Falling film bundle heat and mass exchanger considered in the sorption reaction zone (Daguenet-Frick et al, 2016)

System experimental results in the discharging mode were less than those theoretically calculated. The best measured values were around 1 kW for cases in which a very low temperature difference, around 0 °C, between the absorber and the evaporator were considered (Figure 1.14a). Higher temperature differences reduced the absorber power (200 W for a 14 °C absorber/evaporator temperature difference). Absorption power was also influenced by the sorbent concentration (NaOH wt %): the higher the concentration, the higher the heating rate in the absorber. Another experimental factor influencing the system discharging performance was the wetting of the absorber external tube bundle surface: it was observed that at a solution mass flow of 24 l/h the wetted surface was about 50 – 60%. Higher solution mass flows permitted a better surface wetting and higher exchanged powers. Influence of non-condensable gases on the system performance degradation were also considered by the authors. Figure 1.14b shows one of the initial tests in discharging mode where the reactor is at a pressure 10.3 mbar above the water vapor pressure at the given evaporator temperature, generating a negligible power production in the absorber.

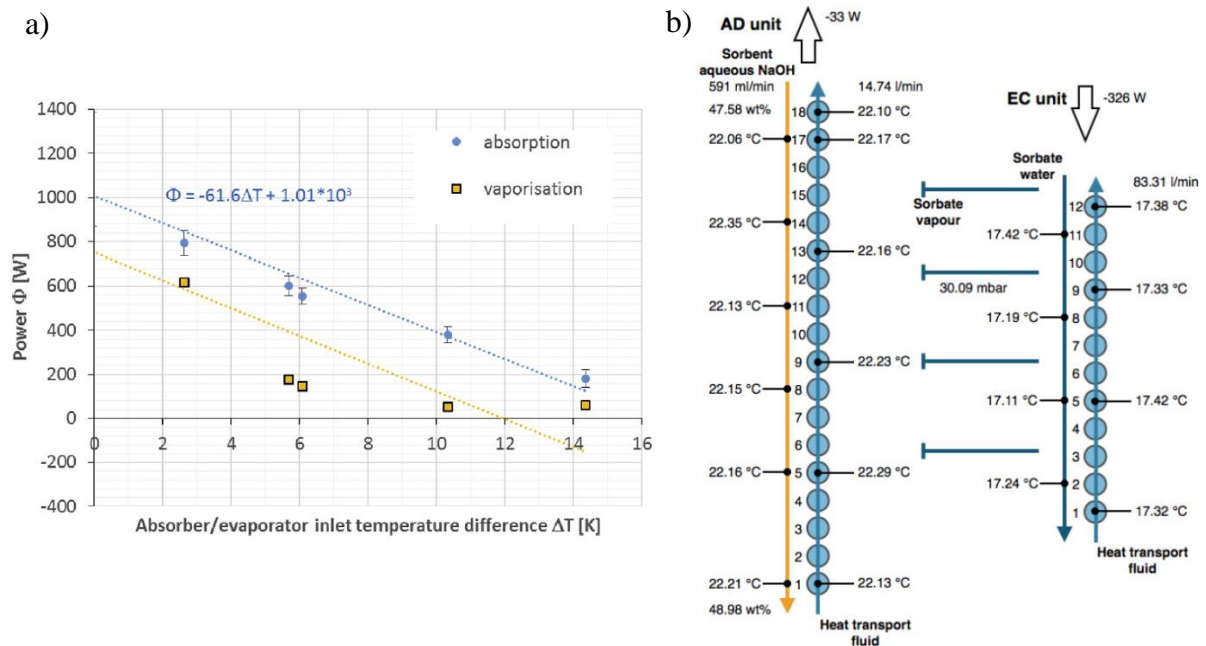


Figure 1.14. a) Power development (Φ) as a function of the temperature difference (ΔT) between absorber and evaporator chamber during discharging process (Daguenet-Frick et al., 2016); b) Illustration of the absorber and evaporator heat and mass exchangers results with approximately 10 mbar pressure resulting from non-condensing gases (Fumey et al., 2015)

Better experimental results were obtained in the charging operating mode due to an adequate wetting of the desorber exchange surface even at low mass flows; this latter being associated to the influence of a high solution temperature on the viscosity and surface tension. The exchanged power increased with the temperature difference between the desorber and condenser. Maximum powers around 9 kW, obtained for a temperature difference of 57 °C, were measured.

An estimate of the system energy storage density equal to 48 kWh/m³ was obtained, considering the volume of the system and the theoretical heat delivered by the sodium hydroxide for a dilution range between 50 to 30 wt%.

1.2.4. Lithium Bromide (LiBr-H₂O) systems

1.2.4.1. LOCIE – University Savoie Mont Blanc - France

(N'Tsoukpoe et al., 2013) constructed a demonstrative prototype at the University Savoie Mont Blanc in France, to test the potential of a long-term absorption heat storage system using the LiBr-H₂O pair.

The main components and the functioning of the proposed storage system are shown in Figure 1.15. The principle is similar as the systems presented before. The charge and discharge phases are not limited to summer and winter. Depending on the solar heat availability and the heating needs of the building, charging and discharging phases occurs throughout the year.

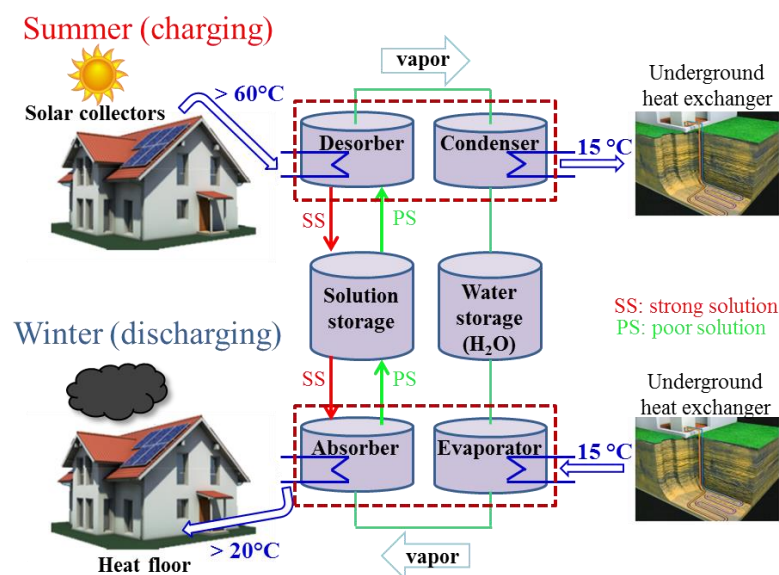


Figure 1.15. Interseasonal absorption storage system principle. Charging mode (top) and discharging mode (bottom).

The prototype was designed to have a heat storage capacity of 8 kWh and a discharging rate of 1 kW (N'Tsoukpoe et al., 2012). Figures 1.16a and 1.16b show a scheme of the sorption heat storage system and the constructed prototype, respectively (N'Tsoukpoe et al., 2013).

Two heat and mass exchangers (absorber/desorber and evaporator/condenser) of shell and tubes type were placed in the reactor. The LiBr solution and water flow on the tube's internal surface while the HTF flows on the tube's external surface (shell side). The tubes are oriented vertically and made of CuZn22Al2 brass type. During the charging/discharging operating mode, vapor produced by the desorption/evaporation process flows through the top or bottom of each tube to the condenser/absorber unit (Figure 1.17a).

Technical characteristics of these heat exchangers are described in Table 1.5. Furthermore, detail of the heat and mass exchangers design is shown in Figure 1.17. In addition, a diagram of the distribution system associated to each heat exchanger is presented in Figure 1.17c.

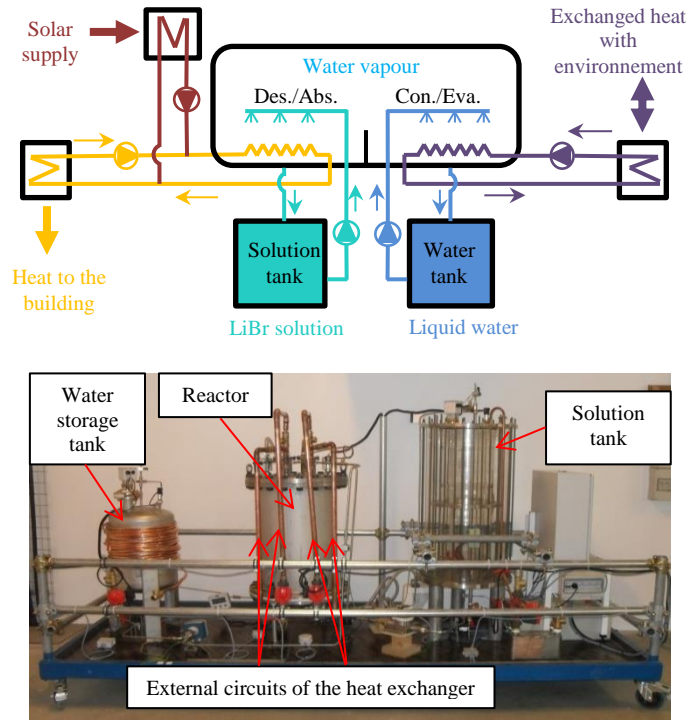


Figure 1.16. a) Schematic of the interseasonal absorption storage system; b) Constructed prototype

Table 1.5. Main features of each heat exchanger (N'Tsoukpoie et al., 2013)

Unit	Value
Tubes material	Brass Aluminum ($\text{CuZn}_{22}\text{Al}_2$)
Length of tube [mm]	620
Inside diameter of tubes [mm]	12
Number of tubes	14
Total internal surface of tubes [m^2]	0.33
Number of orifices per tubes	3
Diameter of each orifice	0.4

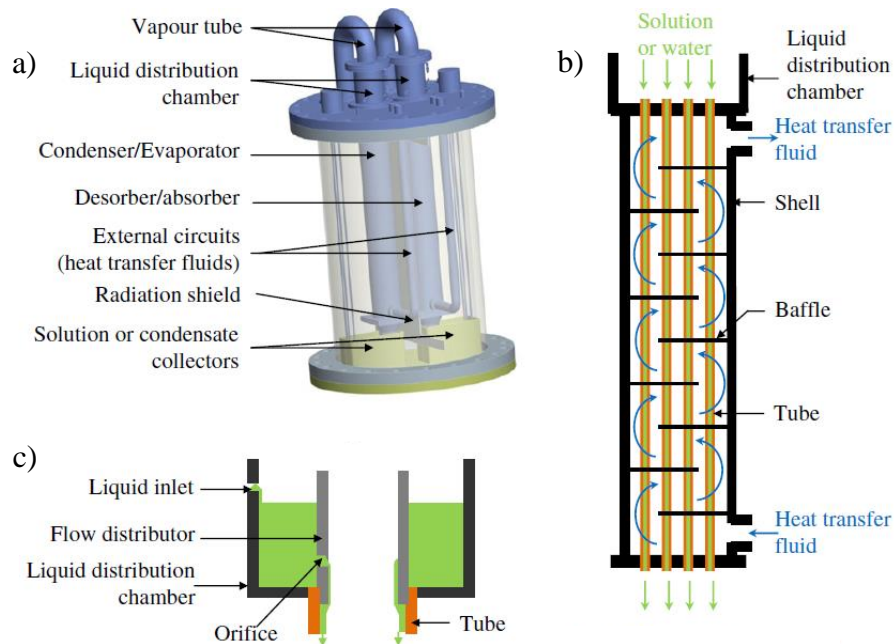


Figure 1.17. Reactor design and operation principle of the heat exchangers. a) Reactor; b) Fluids circulation in the heat exchanger (principle); c) Liquid distribution chamber (principle).

Each heat exchanger was connected to a thermal module that provided controlled flow rate and temperature for the heat transfer fluids. The module connected to the desorber represented the solar collectors during the charging tests and the building during the discharging tests. The module connected to the condenser/evaporator simulated a geothermal heat exchanger. Two additional modules were installed to keep the storage tanks in constant surrounding temperature conditions. Finally, the prototype was instrumented in order to measure temperatures, pressures and mass fractions of the fluids (N'Tsoukpoe et al., 2013).

Several experimental tests in charging and discharging operating mode were carried out and some of the results obtained are summarized in Table 1.6. The tests were run under static conditions and considering a counter-courant flow. In general, the charging mode works in a satisfying manner with an average generation rate around 2 kW, which is acceptable according to the process design (2 - 5 kW). Conversely, the results obtained during the discharging tests showed no significant heat transfer between the absorbing falling film and the HTF (see Table 1.2), even if the absorbing falling film reached a satisfying temperature level . Different reasons were pointed out to explain the prototype low performance in discharging mode: the use of copper alloy (brass aluminum CuZn₂₂Al₂) for the tubes of the absorber/desorber heat exchangers, which did not prove to be corrosion-resistant to the LiBr solution; hydraulic problems associated to a bad distribution of the solution in the tubes top (overflow weirs distribution,); a lack of verticality of the heat exchangers; the presence of non-condensable gases in the reactor; and wettability problems.

Table 1.6. Charging and discharging test results (N'Tsoukpoe et al., 2013)

	Charging process (desorption/condensation)		Discharging process (absorption/evaporation)	
	Test 1	Test 2	Test 9	Test 10
Test duration [minutes]	247	240	150	190
Solution initial concentration [%m_LiBr/m_sol]	52.2	54.8	57.7	57.2
Solution final concentration [%m_LiBr/m_sol]	54.7	56.9	57.1	56.1
Desorber/Absorber inlet HTF temperature [°C]	90	90	26	26.2
Condenser/Evaporator inlet HTF temperature [°C]	20.1	10.1	15	15.1
Desorber/Absorber HTF flow rate [kg/h]	360	720	720	360
Condenser/Evaporator HTF flow rate [kg/h]	360	720	360	360
Solution flow rate [l/h]	38.2	38.2	14.3	43.5
Mass rate of desorbed/absorbed water [kg/h]	1.31	1.02	-0.53	-0.47
Average power of the desorber/absorber [kW]	2.3	2.2	-0.05	0.07
Average power of the condenser/evaporator [kW]	-0.9	-1.1	0.25	0.36

1.2.4.2. Tsinghua university - China

Zhang (Zhang et al., 2014) design and constructed an interseasonal absorption thermal energy storage (ATES) prototype for building space heating purposes.

Figure 1.18 shows a diagram of the prototype proposed by Zhang. The working principle is very similar to the one developed by Climate Well. The system is composed with two tanks, one for the solution and the other for water, connected with a steam pipe. Each tank includes a tube exchanger in its upper part surmounted by a liquid distributor (for solution or water). The heat exchanger is composed of several horizontal tubes distributed in a staggered-arrangement. The HTF flows inside the tubes while the solution or water flows on the external surface. The solution or water are pumped from the bottom barrel and sprayed on the top of the heat exchangers through the liquid distributors (additional technical characteristics of the heat exchanger are shown in Annex A1.3).

The constructed experimental prototype is shown in Figure 1.19 (Zhang et al., 2014). The total space occupied by the system was $3.2 \times 0.62 \times 2 \text{ m}^3$ (length*width*high), with a total inner volume of the solution and water barrels of 0.62 m^3 .

Heat and cooling heating units characterized by heating and cooling rate of 10 kW are connected with the prototype through the HTFs. The total initial LiBr-H₂O solution mass used was 356 kg at a 50% mass concentration, while the total initial water mass used was 34 kg. The system was covered by insulation material to reduce sensible heat losses. The leak rate measured is about $2 \times 10^{-7} \text{ mbar.l/s}$.

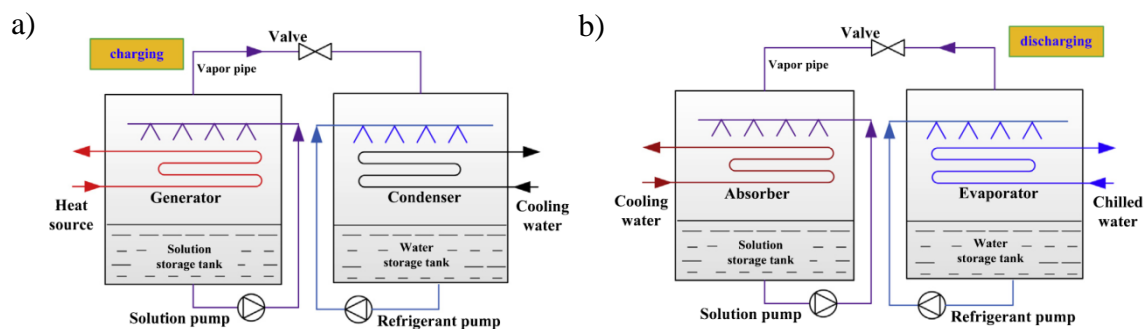


Figure 1.18. Schematic diagram and operational processes of the ATES a) Charging process; b) Discharging process (Zhang et al., 2014)

(Zhang et al., 2014) used the LiBr-H₂O as solution pair for their prototype due to its weaker corrosion (with respect to other solution couples, see Table 1.7), its large temperature running range and its common use in absorption chiller technologies. The solution mass concentrations were measured during experiments using Baume hydrometers.

Table 1.7. Corrosion data of three solution couples for stainless steel 304 (Craig and Anderson, 1995)

Working pair	Concentration	Temperature (°C)	Corrosion (mm/year)
LiBr/H ₂ O	0.5	50	0.008
LiCl/H ₂ O	0.3	116	0.003
NaOH/H ₂ O	0.7	90-143	0.68

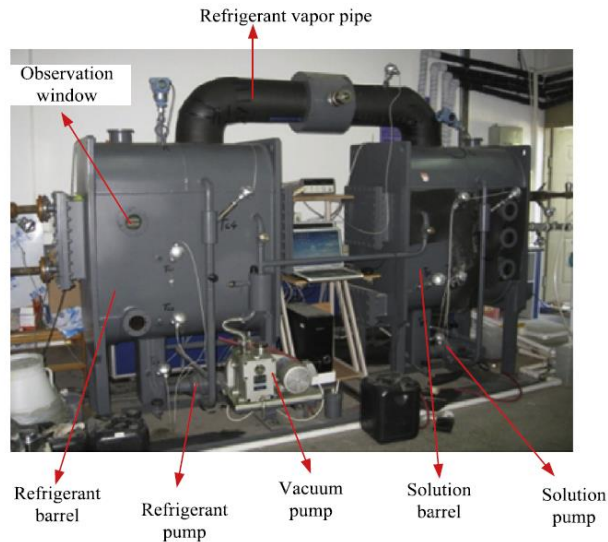


Figure 1.19. Constructed apparatus of the experiment system (Zhang et al., 2014)

Experimental tests in charging mode (desorption/condensation) considered a heat source inlet temperature of 80°C (desorber) and a cooling water inlet temperature of 20 °C (condenser). Tests began with an initial LiBr mass concentration of 56.9% and finished when a value of 61.8% was reached. Experimental results associated to the charging mode gave generating powers between 20 kW and 8 kW; with the higher values shortly observed at the beginning of the tests due to the high temperature difference between the HTF and the solution (the latter at ambient temperature), and the lower values being mainly used to produce vaporization rather than fluids temperature increase.

For the discharging mode (absorption/evaporation), two types of applications were considered: space heating and domestic hot water supply. For the space heating applications, the considered HTF inlet temperatures in the absorber and evaporator were 45 °C and 18 °C, while for the domestic hot water applications the temperatures were 65 °C and 35 °C, respectively. Discharging tests began after the charging tests, once the solution temperature decreased to 45°C (a lower temperature would imply crystals formation and the system blockage at the barrel's bottom). In both cases, the experimental tests ended once the LiBr solution, mass concentration decreased below a value of 56.9%.

Experimental results associated to the discharging mode for space heating applications gave heating rates between 12 kW and 7 kW, with the higher values shortly present at the beginning of the test. The 7 kW heating rate measured was associated not only to the vapor absorption heat but also to the solution temperature; the latter being higher or close to the absorber HTF temperature since these tests began right after the charging tests (once the solution at the barrel bottom decreased to 45°C). Similarly, for the experimental results associated to domestic hot water applications, the heating rate measurements stabilized around 6 kW.

From the previous measurements, the energy storage density of the system, defined as the ratio between the energy output and the maximal volume of weak solution and water, associated to the space heating and domestic hot water applications in discharging mode were 110 kWh/m³ and 88 kWh/m³, respectively. Finally, during the tests, no strong issues related to surface wetting problems in the heat exchangers were reported.

1.2.5. Comparison summary of the study cases

In sections 1.2.1 to 1.2.4, seven interseasonal heat storage prototypes based in sorption processes and aimed for building heating applications were described. Different characteristics, advantages and technical difficulties associated to each case study were presented. Hence, a summary of the main features of these experiences is presented in Table 1.8.

Table 1.8. Main features of the study cases prototypes

Working couple	Case study	Experimental power	ESD	Difficulties
LiCl-H ₂ O	ClimateWell - Sweden	Absorber: 8 kW ⁽¹⁾	85 kWh/m ³ (respect to the prototype volume)	Commercial version of the CW10 TCA mainly aimed for refrigeration applications
	Shangai Jiao Tong University - China	Absorber: 7.3 kW (average)	54.3 kWh/m ³ (respect to the prototype volume)	Risk of solution (or powder) overflowing at the bed units in case of system displacement
CaCl ₂ -H ₂ O	LOCIE – University Savoie Mont Blanc - France	Absorber: very low	Not measured	Non-condensable gases presence and low wettability of the exchange surfaces.
	University of Minnesota - USA	Absorber: --	Not measured	A prototype to test the complete proposed system has yet to be constructed. Possible risk of crystallization and block of solution
NaOH-H ₂ O	EMPA - Switzerland	Absorber: 1 kW (best measured value)	48 kWh/m ³ (respect to the prototype volume) ⁽²⁾	Non-condensable gases presence and low wettability of the exchange surfaces
LiBr-H ₂ O	LOCIE – University Savoie Mont Blanc - France	Absorber: very low	Not measured	Non-condensable gases presence. Corrosion and low wettability of the exchange surfaces
	Tsinghua University - China	Absorber: 7 kW (average measured value)	110 kWh/m ³ (respect to the maximal volume of weak solution and water)	Possible risk of crystallization and block of solution

As shown in Table 1.8, several case studies presented difficulties related mainly to two reasons: low wettability of the exchange surfaces and presence of NCG. Nevertheless, some case studies presented promising Energy Storage Densities (ESD) values considering that the ESD associated to a conventional heat storage water tank (300 liters volume and 30 °C temperature rise) is 35 kWh/m³.

⁽¹⁾ Values associated to a single unit of a CW10 prototype (see Table 1.2).

⁽²⁾ Calculated considering the theoretical heat delivered by the sodium hydroxide for a dilution range between 50 to 30 wt%.

1.3. Conclusions

In this chapter a review of the different technologies able to store heat for building applications using sensible, latent and thermo-chemical means have been made. Emphasis was put on existing absorption heat storage systems and available performances obtained in recent years.

Several weak and strong points are shared by the different systems.

Among the weak points, some of them (LOCIE and EMPA prototypes) presented problems associated to the surface exchange wettability as well as the presence of non-condensable gases which impact the system performance in discharging mode. Possible risks of solution crystallization were also present (Tsinghua University and Minnesota University prototypes) due to a system configuration permitting solution pumping from the bottom of the storage tank.

Among the strong points, several systems presented interesting energy densities for space heating applications, such as the Tsinghua University prototype, the Shanghai Jiao Tong University prototype and the ClimateWell TCA, which registered energy densities of 110 kWh/m³ (respect to the solution and water volume), 54 kWh/m³ (respect to the prototype volume) and 85 kWh/m³ (respect to the prototype volume), respectively; which are around 3 times, 2 times and 2 times higher than that of a conventional heat storage water tank (for a volume of 300 liters and a temperature rise of 30 °C). Furthermore, the ClimateWell TCA was a commercial machine, although mainly oriented to refrigeration applications.

Another identified strong point was that several systems highlighted the importance of the conservation of the sensible heat stored in the solution after the charging process (desorption) in order to use it later during the discharging period (instead of being lost to the ambiance). The latter would permit a complementary contribution to the absorption heat for space heating purposes.

In the following chapters, a study of a new interseasonal absorption heat storage system based on gas/liquid sorption is presented. A system simulation study, a prototype construction and a system simulation projection for real applications along annual periods will be described.

Bibliography

- Ali Memon S.; *Phase change materials integrated in building walls: A state of the art review*. Renew. Sust. Energ. Rev. 31 (2014); p. 870-906.
- ADEME; *Bâtiment, chiffres clés*. <http://www.ademe.fr/sites/default/files/assets/documents/chiffres-cles-batiment-edition-2013-8123.pdf>. Edition 2013 ; p. 42, 86. Last accessed November 2016.
- Bales C.; *Chemical and sorption heat storage*. Proceedings of DANVAK seminar (solar heating systems – Combisystems – heat storage); November 2006.
- Bales C.; *Laboratory Tests of Chemical Reactions and Prototype Sorption Storage Units*. Report of IEA Solar Heating and Cooling programme – Task 32: Advanced storage concepts for solar and low energy buildings, (2008); p. 3–8.
- Bales C., Nordlander S.; *TCA Evaluation – Lab measurements, modelling and system simulation*. Report of the Solar Research Energy Center (SERC), Sweden (2005); p. 2–22.
- C2es; *Outcomes of the U.N. climate change conference in Paris*. <http://www.c2es.org/international/negotiations/cop21-paris/summary>. Last accessed November 2016.
- COP21; *More details about the agreement*. <http://www.cop21.gouv.fr/en/more-details-about-the-agreement/>. Last accessed November 2016.
- Craig B. D., Andeson D. S.; *Handbook of corrosion data*. Metals Park, USA: ASM International; 1995.
- Daguenet-Frick X., Gantenbein P., Müller J., Fumey B., Weber R.; *Seasonal thermochemical energy storage: Comparison of the experimental results with the modelling of the falling film tube bundle heat and mass exchanger unit*. Renew. Energ. (2016); p. 1-12.
- Dutil Y., Rousse D., Lassue S., Zalewski L., Joulin A., Virgone J., Kuznik F., Johannes K., Dumas J. P., Bedecarrats J. P., Castell A., Cabeza L. F.; *Modeling phase change materials behavior in building applications: comments on material characterization and model validation*. Renew. Energ. 61 (2014); p. 132-135.
- EDF; *Le bâtiment, premier poste de consommation d'énergie*. <https://www.edf.fr/media/display/34752>. Last accessed November 2016.

EUROPEAN COMMISSION; *Buildings*. <https://ec.europa.eu/energy/en/topics/energy-efficiency/buildings>. Last accessed November 2016.

EUROPEAN COMMISSION²; *Communication from the Commission to the European Parliament, the Council, the European Economic and Social Committee of the Regions on an EU Strategy for Heating and Cooling*. https://ec.europa.eu/energy/sites/ener/files/documents/1_EN_autre_document_travail_service_part1_v6_0.pdf. Last accessed November 2016.

Fisch M. N., Guigas M., Dalenbäck J. O.; *A review of large scale solar heating systems in Europe*. *Sol. Energy* 63 (1998); p. 355-366.

Fopah Lele A.; *Chapter 2: State of Art of Thermochemical Heat Storage Systems*. A Thermochemical Heat Storage System for Households; Springer Theses; Springer International Publishing Switzerland (2016).

Fumey B., Weber R., Gantenbein P., Daguinet-Frick X., Stoller S., Fricker R., Dorer V.; *Operation results of a closed sorption heat storage prototype*. *Energy Procedia* 73 (2015); p. 324-330.

Hadorn J. C.; *Thermal energy storage for solar and low energy buildings – state of the art*. Servei de Publicacion de la Universitat de Lleida - Spain (2005).

IEA (International Energy Agency); *Key world energy statistics*. <https://www.iea.org/publications/freepublications/publication/KeyWorld2016.pdf>. Last accessed November 2016; p. 6-7.

Lenergieenquestions; *Le bâtiment, premier poste de consommation d'énergie en France*. <https://www.lenergieenquestions.fr/le-batiment-premier-poste-de-consommation-denergie-en-france/>. Last accessed November 2016.

Li G.; *Sensible heat thermal storage energy and exergy performance evaluations*. *Renew. Sust. Energ. Rev.* 53 (2016); p. 897-923.

Liu H.; *Inter-seasonal solar energy storage for buildings by absorption*. PhD thesis at the University of Grenoble, France (2011).

Liu H., N'Tsoukpoe K.E., Le Pierrès N., Luo L.; *Evaluation of a seasonal storage system of solar energy for house heating using different absorption couples*. *Energy Convers. Manag.* 52 (6) (2011); p. 2427-2436.

Lourdudoss S., Stymme H.; *Energy storing absorption heat pump process*. *Int. J. Energ. Res.* 11 (1987); p. 263–274.

N'Tsoukpoe K.E., Liu H., Le Pierrès N., Luo L.; *A review on long-term sorption solar energy storage*. *Renew. Sust. Energ. Rev.* 13 (2009); p. 2385-2396.

N'Tsoukpoe K. E., Le Pierrès N., Luo L.; *Numerical dynamic simulation and analysis of a lithium bromide/water long-term solar heat storage system*. *Energy* 37 (2012); p.346-358.

N'Tsoukpoe K. E., Le Pierrès N., Luo L.; *Experimentation of a LiBr-H₂O absorption process for long-term solar thermal storage: Prototype design and first results*. *Energy* 53 (2013); p.179-198.

N'Tsoukpoe K. E., Rammelberg H. U., Lele A. F., Korhammer K., Watts B. A., Schmidt T., Ruck W. K. L.; *A review on the use of calcium chloride in applied thermal engineering*. *Appl. Therm. Eng.* 75 (2015); p. 513–531.

N'Tsoukpoe K. E., Mazet N., Neveu P.; *The concept of cascade thermochemical storage based on multimaterial system for household applications*. *Energ. Buildings* 129 (2016); p. 138–149.

Neveu P., Tescari S., Aussel D., Mazet N.; *Combined constructural and exergy optimization of thermochemical reactors for high temperature storage*. *Energ. Convers. Manage.* 71 (2013); p. 186–198.

Quinnell J. A., Davidson J. H.¹; *Long-term solar thermal energy storage using aqueous calcium chloride*. In: *Proceedings of the American Solar Energy Society, Washington D.C. (May 2012)*; p. 13–18.

Quinnell J. A., Davidson J. H.²; *Mass transfer during sensible charging of a hybrid absorption/sensible storage tank*. *Energy Procedia* 30 (2012); p. 353–361.

Quinnell J. A., Davidson J. H.; *Heat and mass transfer during heating of a hybrid absorption/sensible storage tank*. *Solar Energy* 104 (2014); p. 19–28.

Rosato A., Sibilio S.; *Preliminary experimental characterization of a three-phase absorption heat pump*. *Int. J. Refrig.* 36 (2013); p. 717–729.

Scapino L., Zondag H. A., Van Bael J., Diriken J., Rindt C. C. M.; *Sorption heat storage for long-term low-temperature applications: A review on the advancements at materials and prototype scale*. *Appl. Energ.* 190 (2017); p. 920–948.

Tittlein P., Gibout S., Franquet E., Johannes K., Zalewsky L., Kuznik F., Dumas J. P., Lassue S., Bedecarrats J. P., David D.; *Simulation of the thermal and energy behaviour of a composite material containing encapsulated-PCM: Influence of the thermodynamical modelling*. *Appl. Energ.* 140 (2015); p. 269-274.

Vandyck T.; Keramidis K.; Saveyin B.; Kitous A.; Vrontisi Z.; *A global stocktake of the Paris pledges: Implications for energy systems and economy*. *Global Environmental Change* 41 (2016); p. 46-63.

Xu J., Wang R. Z., Li Y.; *A review of available technologies for seasonal thermal energy storage*. *Sol. Energy* 103 (2014); p. 610-638.

Yu N., Wang R. Z., Lu Z. S., Wang L. W., Ishugah T.F.; *Evaluation of a three-phase sorption cycle for thermal energy storage*. Energy 67 (2014); p. 468-478.

Yu N., Wang R. Z., Li T. X., Wang W.; *Chapter 28: Progress in Sorption Thermal Energy Storage*. Energy Solutions to Combat Global Warming; Lecture Notes in Energy 33; Springer International Publishing Switzerland (2017).

Zhang X., Li M., Shi W., Wang B., Li X.; *Experimental investigation on charging and discharging performance of absorption thermal energy storage system*. Energy Convers Manage 85 (2014); p. 425-434.

Zhang L., Xu P., Mao J., Tang X., Li Z., Shi J.; *A low cost seasonal solar soil heat storage system for greenhouse heating: Design and pilot study*. Appl. Energ. 156 (2015); p. 213-222.

Zhao Y. J., Wang R. Z., Li T. X., Nomura Y.; *Investigation of a 10 kWh sorption heat storage device for effective utilization of low-grade thermal energy*. Energy 113 (2016); p. 739-747.

Chapter 2. Modelling and simulation of the interseasonal heat storage system

In this project, the chosen system is an absorption storage process, as set before. The working principle of this type of systems has been described in the previous chapter. The objective of this thesis, that follows the ones performed by Liu (2011) and N'Tsoukpoe (2012) in the LOCIE laboratory, is to focus precisely on the heat and mass exchangers, that have proven to be key components of the system, as presented in the previous chapter. A simulation model of the system presented before is thus proposed here, developed and described in the following sub sections. System main components are: the reactor, the LiBr solution tank, the water tank, the solution pipes and the water pipes. A schematic description of this system is shown in Figure 2.1. In the model, special care will be put on the description of the heat and mass exchangers, with the aim to design more efficient exchangers than the ones used in the previous studies. A more detailed study of the tanks will also be used, compared to the previous works, to take into account the convective phenomena happening inside them, as highlighted by N'Tsoukpoe et al. (2013).

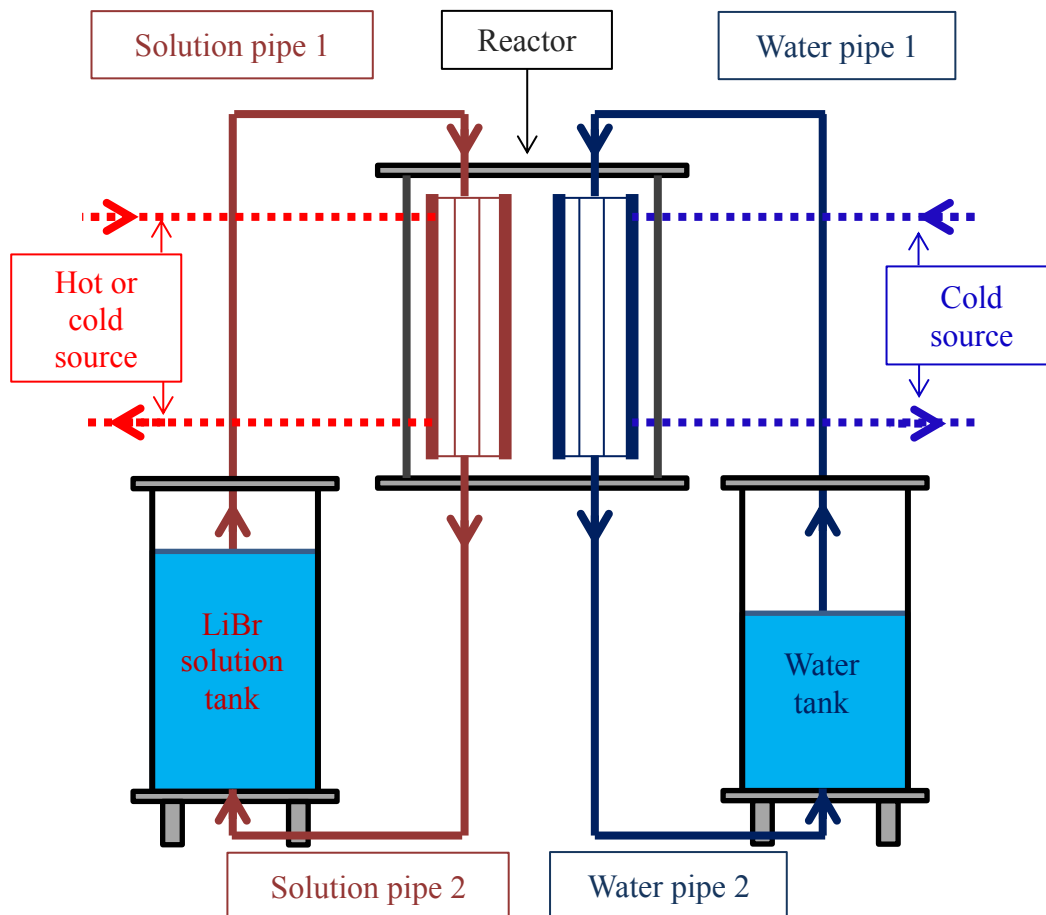


Figure 2.1. Interseasonal sorption heat storage system

2.1. Reactor

As it was mentioned in the previous section, one of the main components of the interseasonal heat storage system is the reactor. Two reversible falling-film exchangers are situated inside this reactor. During the charging period, one heat exchanger operates as a desorber and the other as a condenser meanwhile that during the discharging period one operates as an absorber and the other as an evaporator, respectively. During the process operation, both exchangers are coupled since they interact with the same vapour. In this section a model developed to study the behavior of each heat exchanger inside the reactor is presented.

Flat-plate heat exchangers are considered for the model, where each exchanger includes 2 flat plates. The heat transfer fluid (HTF) flows between the plates whereas the falling films (LiBr solution or water) flow on the outer face of the plates (Figure 2.2, left). Considering the problem symmetry, a 2D model describes heat and mass transfers in half an exchanger. It considers 1 metallic plate, the heat transfer fluid and the falling film

(Figure 2.2, right). The HTF flows in contact with the internal plate's surface and the symmetry plane is considered adiabatic. Heat and mass transfers occur between the reactor's vapor and the falling films while the HTF only exchanges heat with the plate.

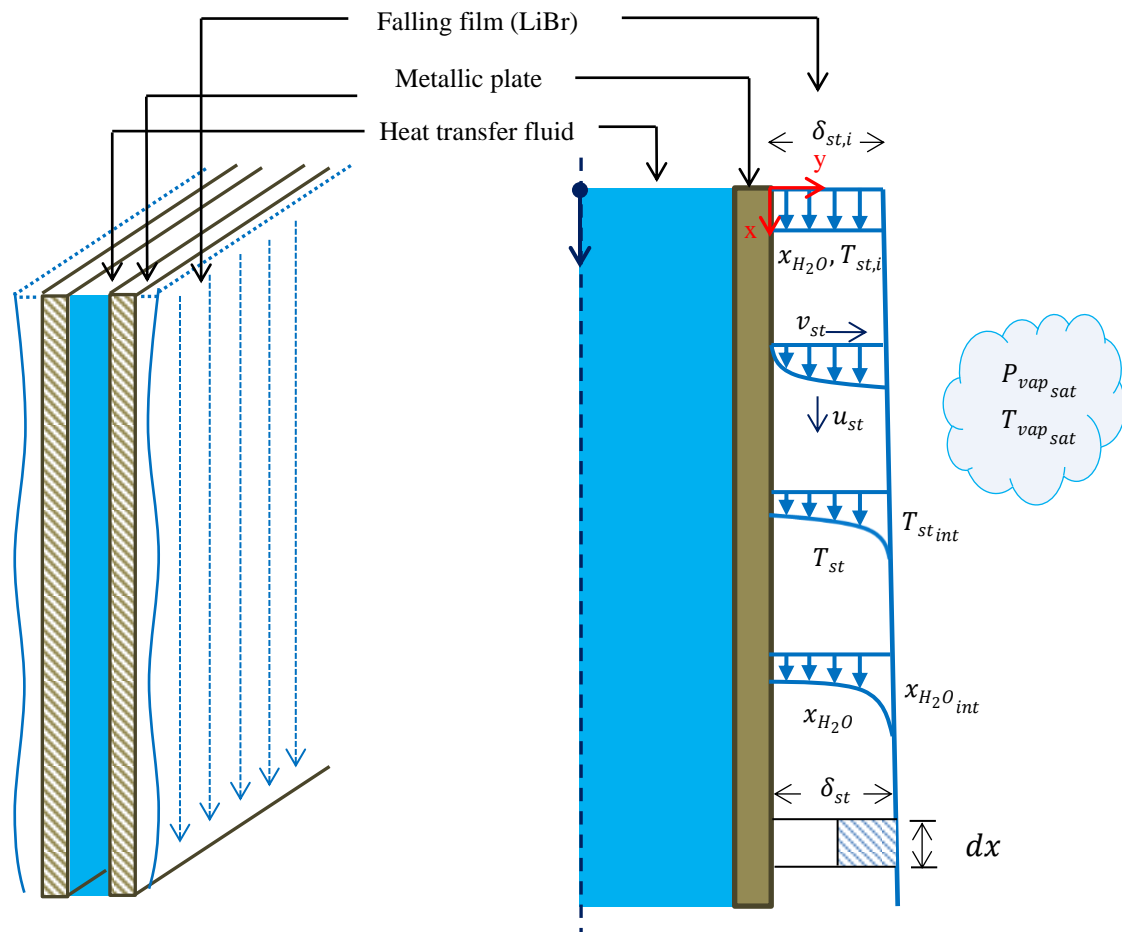


Figure 2.2. Schematic description of the exchanger chosen for the model in the case of the LiBr solution falling film

Different studies describe heat and mass transfers inside falling films (Grossman, 1983), (Killion and Garimella, 2001). In order to describe these mechanisms some hypotheses have been considered, these are:

- Noncondensable gases are not present in the vapor, which permits to neglect the resistance to vapor absorption or condensation at the interface of the falling film.
- Vapor in the reactor is saturated. This hypothesis is true in evaporation/absorption operation; nevertheless, in desorption/condensation operation the produced vapor is overheated (since it is produced in the desorber)⁽¹⁾.
- Convective heat transfer from the liquid phase to the adjacent vapor is neglected.
- The film flow is fully developed and the system is in state conditions (at each time).
- The vapor absorption or desorption rate is small compared to the mass flow rate of the film.
- Vapor is in equilibrium with the film at the liquid free interface.
- No shear forces are exerted on the liquid by the vapor.
- Fluid velocity is zero at the interface between the plate and the film.

⁽¹⁾ For example, at vapor saturated conditions of 15 mbar and 13 °C, the latent heat is 2470 kJ/kg while the specific enthalpy is 2524.7 kJ/kg. At vapor overheating conditions such as 15 mbar and 30 °C, the specific enthalpy is 2556.3 kJ/kg. Hence, the enthalpy difference between overheated vapor and saturated vapor (31.6 kJ/kg) is negligible compared to the latent heat. This permits to model the vapor in saturated conditions during desorption/condensation processes without introducing significant errors.

- Physical properties of the liquid film are considered to be constant.
- No wavelets develop along the film (flat exchangers) (maximum envisaged Reynolds during tests are around 1200).

Considering previous hypothesis, in the following sub-sections the model developed for the absorber/desorber, evaporator and condenser exchangers is described. A comparison of the simulation model against works found in the literature is also shown.

2.1.1. Reactor components simulation models

The models developed for the absorber/desorber and evaporator/condenser in the reactor are described below.

2.1.1.1. Modelling of an absorption/desorption heat exchanger

2.1.1.1.1. Falling film boundary conditions

To describe the heat and mass transfer mechanisms of the solution film in the heat exchanger shown in Figure 2.2, two additional hypotheses are considered (Killion and Garimella, 2001), (Carey, 2008), (Incropera et al., 2011).

- The net pressure force component is very small compared to the body force component.
- The velocity components in the y direction are neglectable.

Considering no shear forces exerted on the interface between the film and the vapor, the film width at each position along the plate can be expressed as (Carey, 2008):

$$\delta = \sqrt[3]{\frac{3\dot{m}_x\mu}{\rho^2 gL}} \quad (2.1)$$

At this interface, the absolute flux of LiBr is zero due to its low volatility; then the mass flux of H₂O absorbed or desorbed per unit surface by the binary mixture of LiBr-H₂O, $\dot{m}''_{H_2O,abs/des}$, can be expressed as (Incropera, 2011):

$$\dot{m}''_{H_2O,abs/des} = \left[\frac{\rho_{st} D_{LiBr-H_2O}}{(1-x_{H_2O})} \left(\frac{\partial x_{H_2O}}{\partial y} \right) \right]_{y=\delta} \quad (2.2)$$

If $\dot{m}''_{H_2O,abs/des}$ is positive vapor absorption happens at the interface. Conversely, if $\dot{m}''_{H_2O,abs/des}$ is negative vapor desorption will be produced at the interface.

In a similar way, the energy balance at this interface is expressed as:

$$\dot{m}''_{H_2O,abs/des} \times [h_{vap_{sat}} - h_{p-H_2O-st}]_{y=\delta} = \left[\lambda_{st} \left(\frac{\partial T_{st}}{\partial y} \right) \right]_{y=\delta} \quad (2.3)$$

Where the left hand side of equation (2.3) expresses the heat of absorption of vapor at the solution interface and h_{p-H_2O-st} is related to partial enthalpy of H₂O in the binary solution.

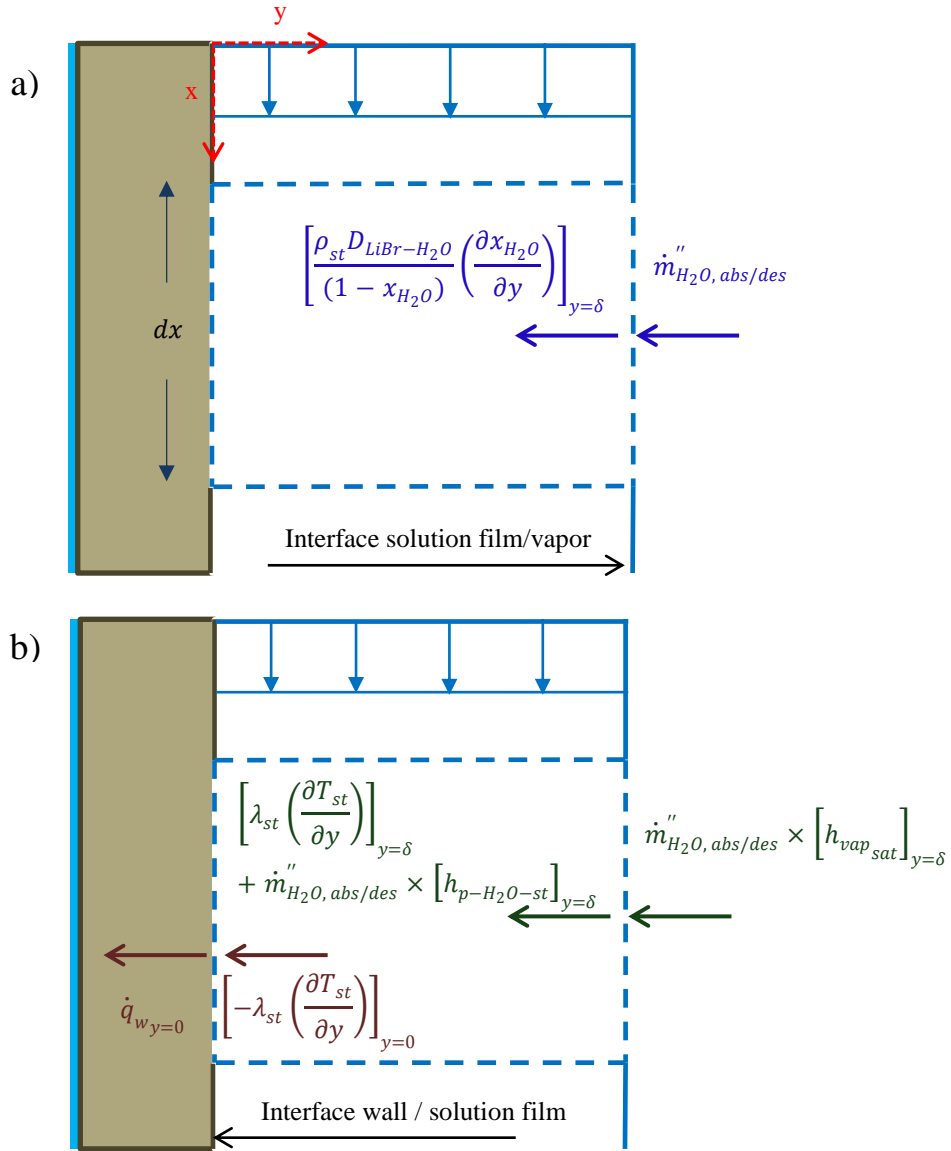


Figure 2.3. Schematic description of the mass and energy fluxes crossing the falling film interfaces. a) Mass fluxes. b) Energy fluxes.

At $y=0$, interface between the plate and the film solution (Figure 2.3), mass transfer is zero whereas energy transfer through this interface, $\dot{q}_{w,y=0}$, is described by:

$$\dot{q}_{w,y=0} = \left[-\lambda_{st} \left(\frac{\partial T_{st}}{\partial y} \right) \right]_{y=0} \quad (2.4)$$

It must be highlighted that equations (2.1), (2.2), (2.3), (2.4) are valid for any position along the falling film interfaces at the heat exchanger.

2.1.1.1.2. Mass and heat transfer convective coefficients of the falling film

Heat and mass transfer convective coefficients at the vapor/film interface and at the wall/film interface at each position along a vertical plate heat exchanger have been determined in previous work by Brauner (Brauner, 1991). These coefficients were obtained solving the film governing equations using an integral formulation and expressing equations in a dimensionless form. Their approach considered concentration and temperature parabolic profiles across the film that could satisfied the boundary conditions at each interface. The development of thermal and species boundary layers was also taken into account.

A computer program was developed by Brauner (Brauner, 1991) using a Runge-Kutta method. Fluxes, and associated convective coefficients, crossing the film interfaces were calculated. These fluxes and coefficients are shown below:

For the mass flux of H₂O absorbed or desorbed per unit surface across the vapor/film interface, $\dot{m}''_{H_2O,abs/des}$; the vapor/film mass convective coefficient, $h_{m_{st,int}}$, is expressed as:

$$h_{m_{st,int}} = \frac{\dot{m}''_{H_2O,abs/des}}{(\rho_{st,int} x_{H_2O,int} - \rho_{st,avg} x_{H_2O,avg})} \quad (2.5)$$

For the heat transfer across the vapor/film interface; the vapor/film heat convective coefficient, $h_{T_{st,int}}$, is expressed as:

$$h_{T_{st,int}} = \frac{\dot{m}''_{H_2O,abs/des} \times [h_{vap_{sat}} - h_{p-H_2O-st}]_{y=\delta}}{(T_{st,int} - T_{st,avg})} \quad (2.6)$$

For the heat transfer across the film/wall interface, $\dot{q}_{w,y=0}$, the film/wall heat convective coefficient, $h_{T_{st,w}}$, is expressed as:

$$h_{T_{st,w}} = \frac{\dot{q}_{w,y}}{(T_{st,avg} - T_{w,st})} \quad (2.7)$$

Brauner (Brauner, 1991) expressed the transfer coefficients using non dimensional numbers, Sherwood and Nusselt numbers, as a function of the downstream distance for the case of isothermal or adiabatic conditions defined as follows.

$$Sh_{int/st} = \frac{h_{m_{st,int}} \delta_i}{D_{LiBr-H_2O}} \quad (2.8)$$

$$Nu_{int/st} = \frac{h_{T_{st,int}} \delta_i}{\lambda_{st}} \quad (2.9)$$

$$Nu_{w/st} = \frac{h_{T_{st,w}} \delta_i}{\lambda_{st}} \quad (2.10)$$

For isothermal cases in which the ratio $(C_{H_2O,i} - C_{H_2O,int,i})/C_i$ (nominal driving force of the absorption/desorption process) is near zero (as is the case in the present system), evaluation of the Nu and Sh numbers with the downstream distance, ξ , are shown in Figure 2.4.

In the following section correlations given by equations (2.5) to (2.10) and by Figure 2.4 will be used to make a mass and energy volume control balance along the heat exchanger.

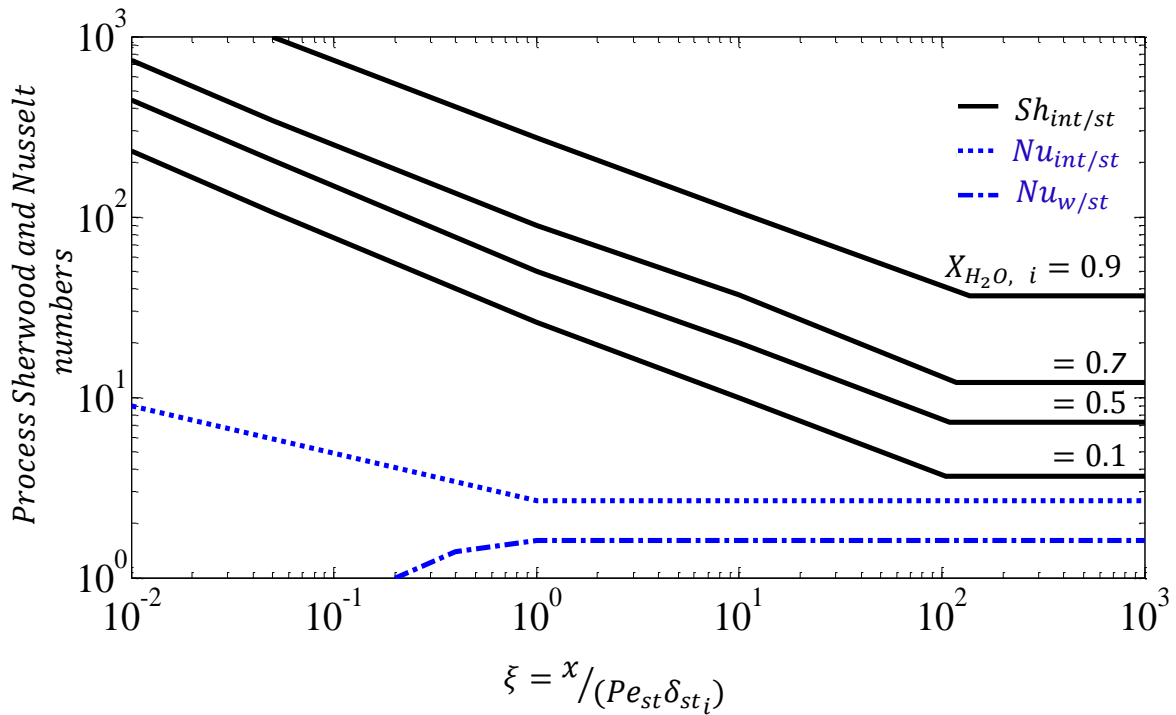


Figure 2.4. Inlet concentration effect on the downstream variation of the local Sherwood and Nusselt number for an isothermal plate⁽¹⁾

The $Nu_{w/st(\xi)}$ correlation in Figure 2.4 indicates that near the plate entrance the $Nu_{w/st(\xi)}$ number is zero; this is correct for the isothermal plate case described by Brauner (Brauner, 1991) where the temperature plate is the same as that of the entrance solution film. Nevertheless, in our simulation model the temperature plate can be different from the entrance solution film temperature since the metallic plate exchanges energy with the HTF and the solution film.

In order to take into account this effect, the wall Nusselt correlation at the entrance zone has been modified as shown in Figure 2.5. This approach is based on the hypothesis that the heat transfer along the film interface and the plate evolves in a similar way.

⁽¹⁾ Definition of the Pe number is shown in the annex B1.1.

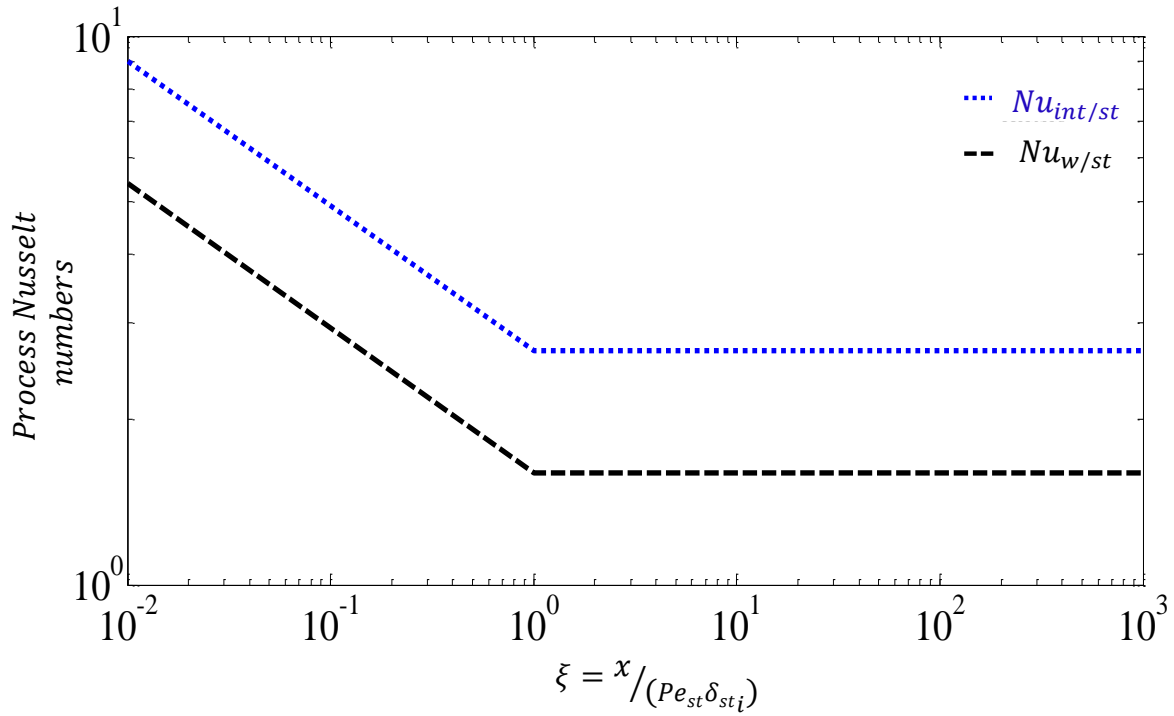


Figure 2.5. Modified Nu correlation

2.1.1.1.3. Nodal discretization and control volume balance

The model considered a nodal division along the absorption/desorption heat exchanger for the falling film, metallic plate and heat transfer fluid as shown in Figure 2.6 This discretization allowed setting mass and energy balances on the control volumes and correlations and hypothesis described in sections above were used in this approach. It must be indicated that, as a first approach, the exchanger was considered in cocurrent configuration.

The corresponding balance equations are shown below.

Energy balance of the LiBr solution film.

$$-\dot{m}_{st, x_o, k} \times h_{st(T_{st_o, k}, x_{H_2O_o, k}, P_{vap_{sat}})} + \dot{m}_{st, x_i, k} \times h_{st(T_{st_i, k}, x_{H_2O_i, k}, P_{vap_{sat}})} + \dot{m}_{H_2O, abs/des_k} \times h_{vap(T_{vap_{sat}}, P_{vap_{sat}})} + \quad (2.11)$$

$$h_{T_{st, w_k}} \times \Delta x \times L \times (T_{w, st_k} - (T_{st_o, k} + T_{st_i, k})/2) = 0$$

Energy balance at the interface between the LiBr solution film and the water vapor.

$$\dot{m}_{H_2O, abs/des_k} \times (h_{vap(T_{vap_{sat}}, P_{vap_{sat}})} - h_{p-H_2O-st(T_{st, int_k}, x_{H_2O, int_k}, P_{vap_{sat}})}) - \quad (2.12)$$

$$h_{T_{st, int_k}} \times \Delta x \times L \times (T_{st, int_k} - (T_{st_o, k} + T_{st_i, k})/2) = 0$$

Mass balance in the LiBr solution film.

$$-\dot{m}_{st, x_o, k} + \dot{m}_{st, x_i, k} + \dot{m}_{H_2O, abs/des_k} = 0 \quad (2.13)$$

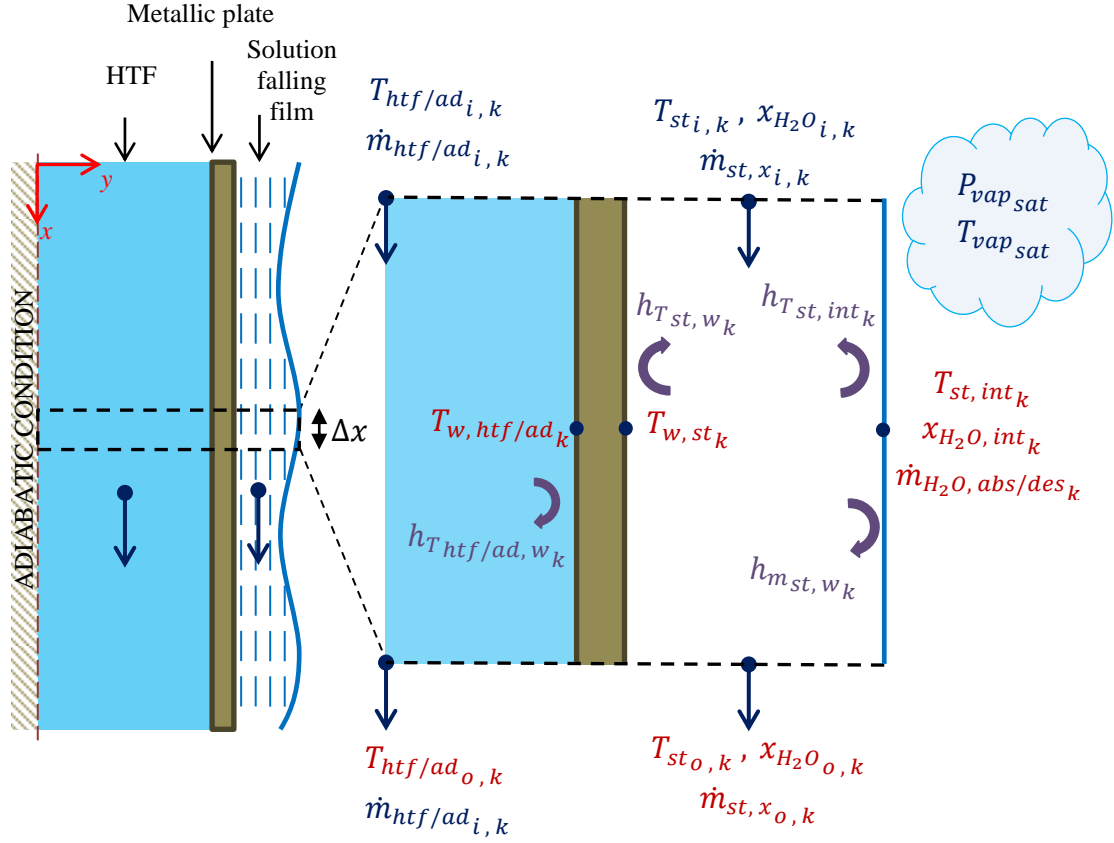


Figure 2.6. Heat exchanger nodal division used for the volume control energy and mass balance in the absorber/desorber

Water mass balance in the LiBr solution film.

$$-\dot{m}_{st,x_o,k} \times x_{H_2O_o,k} + \dot{m}_{st,x_i,k} \times x_{H_2O_i,k} + \dot{m}_{H_2O,abs/des_k} = 0 \quad (2.14)$$

Mass transfer at the interface between the LiBr solution film and the water vapor.

$$\dot{m}_{H_2O,abs/des_k} - h_{m_{st,int_k}} \times \Delta x \times L \times \left[\rho_{st}(T_{st,int_k}, x_{H_2O,int_k}) x_{H_2O,int_k} - \rho_{st}\left(\frac{T_{st_o,k} + T_{st_i,k}}{2}, \frac{x_{H_2O_o,k} + x_{H_2O_i,k}}{2}\right) \left(\frac{x_{H_2O_o,k} + x_{H_2O_i,k}}{2}\right) \right] = 0 \quad (2.15)$$

Equilibrium condition at the interface between the LiBr solution film and the water vapor⁽¹⁾.

$$T_{st,int_k} = f(x_{H_2O,int_k}, P_{vap,sat}) \quad (2.16)$$

Heat transfer between the LiBr solution film and the metallic plate.

$$\left(\frac{\lambda_w}{e_w}\right) \times \Delta x \times L \times (T_{w,st_k} - T_{w,htf/ad_k}) - h_{T_{st,w_k}} \times \Delta x \times L \times \left(\frac{T_{st_o,k} + T_{st_i,k}}{2} - T_{w,st_k}\right) = 0 \quad (2.17)$$

⁽¹⁾ "f" is the equilibrium correlation between the temperature, LiBr mass concentration and vapor pressure at the interface and it is described in the annex B1.2.

Heat transfer between the HTF and the metallic plate.

$$\begin{aligned}
 & h_{T_{htf/ad,w_k}} \times \Delta x \times L \times ((T_{htf/ad_{o,k}} + T_{htf/ad_{i,k}})/2 - T_{w,htf/ad_k}) - \\
 & (\lambda_w/e_w) \times \Delta x \times L \times (T_{w,htf/ad_k} - T_{w,st_k}) = 0
 \end{aligned} \tag{2.18}$$

Energy balance of the HTF⁽¹⁾.

$$\begin{aligned}
 & -\dot{m}_{htf/ad_{i,k}} \times h_{htf(T_{htf/ad_{o,k}})} + \dot{m}_{htf/ad_{i,k}} \times h_{htf(T_{htf/ad_{i,k}})} + \\
 & 2 \times h_{T_{htf/ad,w_k}} \times \Delta x \times L \times (T_{w,htf/ad_k} - (T_{htf/ad_{o,k}} + T_{htf/ad_{i,k}})/2) = 0
 \end{aligned} \tag{2.19}$$

The heat transfer convective coefficient, $h_{T_{htf/ad,w_k}}$, related to the exchange between the inner plate surface and the HTF is given by the Colburn correlation (see Annex B1.3.1).

2.1.1.1.4. Solving procedure

In the absorption/desorption model it is considered that $P_{vap_{sat}}$ and $T_{vap_{sat}}$ ⁽²⁾ are known conditions in the system. Considering that $T_{st_{i,1}}$, $x_{H_2O_{i,1}}$, $\dot{m}_{st,x_{i,k}}$, temperature, mass water concentration and mass flow rate of the inlet solution film are also known as well as $T_{htf/ad_{i,1}}$, $\dot{m}_{htf/ad_{i,1}}$, inlet temperature and mass flow rate of the HTF; then equations (2.11) to (2.19) define a system of 9 equations and 9 unknown variables.

Considering that $h_{m_{st,int_k}}$, $h_{T_{st,int_k}}$, $h_{T_{st,w_k}}$ and $h_{T_{htf/ad,w_k}}$ can be calculated using correlations (2.8), (2.9), (2.10) and correlations in Annex B1.3.1, then the unknown variables associated to the equation system at each control volume will be: $T_{st_{o,k}}$, $x_{H_2O_{o,k}}$, $\dot{m}_{st,x_{o,k}}$, T_{st,int_k} , x_{H_2O,int_k} , $\dot{m}_{H_2O,abs/des_k}$, $T_{htf/ad_{o,k}}$, $T_{w,htf/ad_k}$ and T_{w,st_k} .

Since in the simulation entrance conditions are always known, the equation system for the control volume at “ $k=1$ ” can be solved. Consequently, the found variables $T_{st_{o,1}}$, $x_{H_2O_{o,1}}$, $\dot{m}_{st,x_{o,1}}$ and $T_{htf/ad_{o,1}}$ can be used as entrance conditions for the control volume at “ $k=2$ ” and, afterwards, the system of equation solving process can be repeated for the subsequent control volumes along the heat exchanger. If $\dot{m}_{H_2O,abs/des_k}$ is positive, vapor absorption happens at the interface or, conversely, if $\dot{m}_{H_2O,abs/des_k}$ is negative vapor desorption is produced at the interface.

A code for simulating our described absorption/desorption heat exchanger has been developed in Matlab. Numerical results obtained by our model will be presented and validated in the following sections. Thermo-physical properties correlations for the LiBr solution were obtained from works developed by different authors (Florides et al., 2003), (Saul and Wagner, 1987), (Sorption system consortium), (Yuan and Herold¹, 2005), (Yuan and Herold², 2005), (Hellman and Grossman, 1996). These correlations are described in the Annex B1.2.

⁽¹⁾ The factor 2 multiplying “ $h_{T_{htf/ad,w_k}}$ ” is related to the 2 flat plates composing the canal where the HTF flows in the modeled flat-plate exchanger (see Figure 2.2).

⁽²⁾ In desorption operation the vapor is generally overheated; nevertheless, for simulation simplicity purposes it has been considered that the vapor is in saturated conditions during the desorption process.

2.1.1.2. Modelling of the evaporator

In a similar way to the absorption/desorption heat exchanger, a model has been developed for the evaporation heat exchanger. The same nodal approach and hypothesis indicated in the previous sub-section have been used and are shown in Figure 2.7.

The convective heat transfer coefficients for the evaporator: $h_{T_{wt,w_k}}, h_{T_{wt,int_k}}$ have previously been calculated using the correlations obtained by Brauner (Brauner, 1991).

The corresponding balance for each volume control are shown below.

Energy balance of the water film.

$$\begin{aligned}
 & -\dot{m}_{wt,x_o,k} \times h_{wt(T_{wt_o,k}, P_{vap_{sat}})} + \dot{m}_{wt,x_i,k} \times h_{wt(T_{wt_i,k}, P_{vap_{sat}})} + \\
 & \quad \dot{m}_{H_2O,eva/con_k} \times h_{vap(T_{vap_{sat}}, P_{vap_{sat}})} + \\
 & h_{T_{wt,w_k}} \times \Delta x \times L \times (T_{w,wt_k} - (T_{wt_o,k} + T_{wt_i,k})/2) = 0
 \end{aligned} \tag{2.20}$$

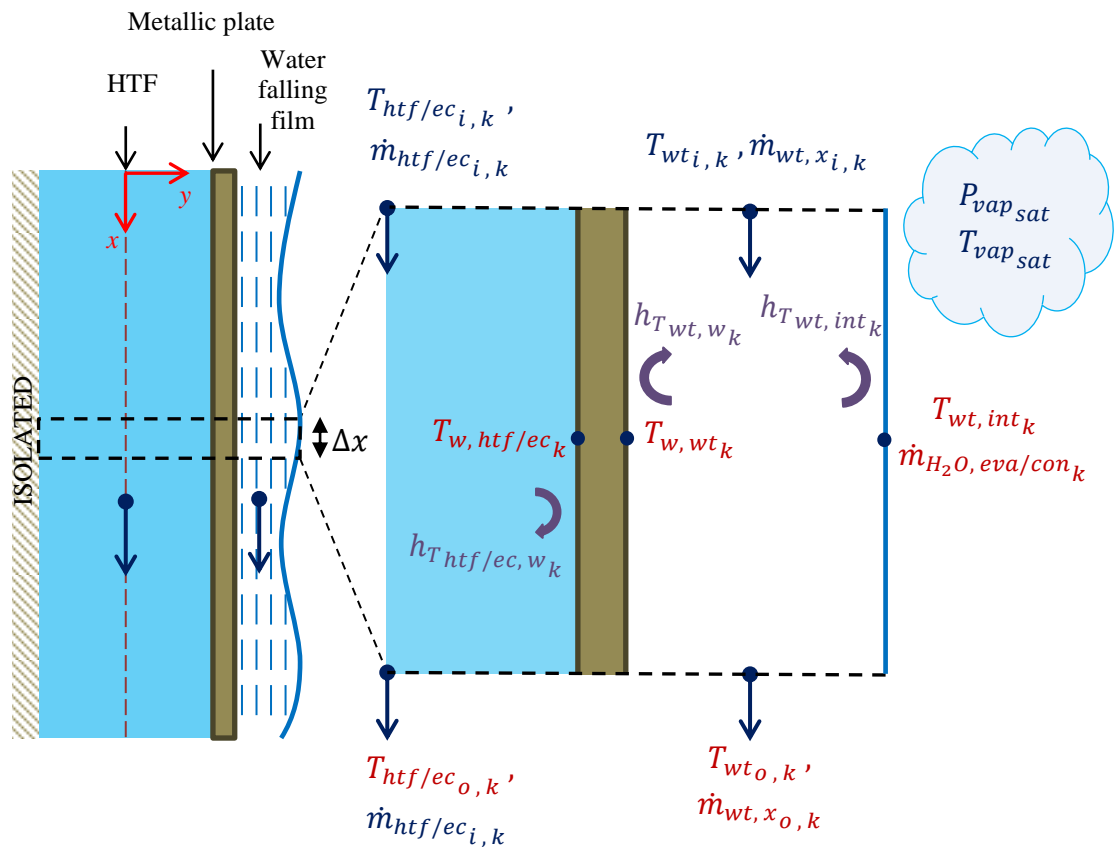


Figure 2.7. Heat exchanger nodal division used for the volume control energy and mass balance in the evaporator

Energy balance at the interface between the water film and the water vapor.

$$\begin{aligned}
 & \dot{m}_{H_2O,eva/con_k} \times (h_{vap(T_{vap_{sat}}, P_{vap_{sat}})} - h_{wt(T_{wt,int_k}, P_{vap_{sat}})}) - \\
 & h_{T_{wt,int_k}} \times \Delta x \times L \times (T_{wt,int_k} - (T_{wt_o,k} + T_{wt_i,k})/2) = 0
 \end{aligned} \tag{2.21}$$

Mass balance in the water film.

$$-\dot{m}_{wt,x_o,k} + \dot{m}_{wt,x_i,k} + \dot{m}_{H_2O,eva/con_k} = 0 \quad (2.22)$$

Equilibrium condition at the interface between the water film and the water vapor.

$$T_{wt,int_k} = f(p_{vap,sat}) \quad (2.23)$$

Heat transfer between the water film and the metallic plate.

$$\begin{aligned} & (\lambda_w/e_w) \times \Delta x \times L \times (T_{w,wt_k} - T_{w,htf/ec_k}) - \\ & h_{T_{wt,w_k}} \times \Delta x \times L \times ((T_{wt_o,k} + T_{wt_i,k})/2 - T_{w,wt_k}) = 0 \end{aligned} \quad (2.24)$$

Heat transfer between the HTF and the metallic plate.

$$\begin{aligned} & h_{T_{htf/ec,w_k}} \times \Delta x \times L \times ((T_{htf/ec_o,k} + T_{htf/ec_i,k})/2 - T_{w,htf/ec_k}) - \\ & (\lambda_w/e_w) \times \Delta x \times L \times (T_{w,htf/ec_k} - T_{w,wt_k}) = 0 \end{aligned} \quad (2.25)$$

Energy balance of the HTF.

$$\begin{aligned} & -\dot{m}_{htf/ec_i,k} \times h_{htf(T_{htf/ec_o,k})} + \dot{m}_{htf/ec_i,k} \times h_{htf(T_{htf/ec_i,k})} + \\ & 2 \times h_{T_{htf/ec,w_k}} \times \Delta x \times L \times (T_{w,htf/ec_k} - (T_{htf/ec_o,k} + T_{htf/ec_i,k})/2) = 0 \end{aligned} \quad (2.26)$$

In a similar way to the absorption/desorption heat exchanger model, it is considered that $P_{vap,sat}$ and $T_{vap,sat}$ are known conditions in the evaporator⁽¹⁾. Considering that $T_{wt_i,1}$, $\dot{m}_{wt,x_i,k}$, temperature and mass flow rate of the inlet water film are known as well as $T_{htf/ec_i,1}$, $\dot{m}_{htf/ec_i,1}$, inlet temperature and mass flow rate of the heat transfer fluid; then equations (2.20) to (2.26) define a system of 7 equations and 7 unknown variables.

Heat and mass transfer along the evaporator are identified through the values obtained for the variable $\dot{m}_{H_2O,eva/con_k}$ at each position. A positive value of $\dot{m}_{H_2O,eva/con_k}$ indicates that water has been condensed from the water liquid film and a negative value indicates that water has been evaporated from the water vapor (this approach also requires having a liquid water film flow at the entrance of the heat exchanger different from zero to avoid inconsistent divisions).

2.1.1.3. Modelling of the condenser

For the case of the condenser heat exchanger, an entrance liquid water film flow equal to zero is considered.

Since condensation of water from the vapor depends on the vapor conditions and the HTF temperature, only two options are possible. In cases where condensation is possible, a Nusselt condensation approach (Carey, 2008) is considered for each volume control (Figure 2.7) and, in cases where condensation is not possible, a zero heat flow is assumed between the vapor and the surface plate since convection and radiation effects are estimated to be negligible.

The corresponding balance equations for each volume control in cases where condensation is possible are shown below.

Falling film thickness of the water film.

⁽¹⁾ In evaporation/absorption operation the vapor is in saturated conditions.

$$\delta_{wt_k} = \sqrt[3]{\frac{3 \times \left(\frac{\dot{m}_{wt,x_{i,k}} + \dot{m}_{wt,x_{o,k}}}{2} \right) \times \mu_{wt} \left(\frac{T_{w,wt_k} + T_{wt,int_k}}{2} \right)}{\left(\rho_{wt} \left(\frac{T_{w,wt_k} + T_{wt,int_k}}{2} \right) \right)^2 gL}} \quad (2.27)$$

Energy balance at the interface between the water film and the water vapor⁽¹⁾.

$$\dot{m}_{H_2O,eva/con_k} \times (h_{vap(T_{vap,sat},P_{vap,sat})} - h_{wt(T_{wt,int_k},P_{vap,sat})}) - \frac{\lambda_{wt} \left(\frac{T_{w,wt_k} + T_{wt,int_k}}{2} \right)}{\delta_{wt_k}} \times \Delta x \times L \times (T_{wt,int_k} - T_{w,wt_k}) = 0 \quad (2.28)$$

Mass balance in the water film.

$$-\dot{m}_{wt,x_{o,k}} + \dot{m}_{wt,x_{i,k}} + \dot{m}_{H_2O,eva/con_k} = 0 \quad (2.29)$$

Equilibrium condition at the interface between the water film and the water vapor.

$$T_{wt,int_k} = f(P_{vap,sat}) \quad (2.30)$$

Heat transfer between the water film and the metallic plate.

$$\left(\frac{\lambda_w}{e_w} \right) \times \Delta x \times L \times (T_{w,wt_k} - T_{w,htf/ec_k}) - \frac{\lambda_{wt} \left(\frac{T_{w,wt_k} + T_{wt,int_k}}{2} \right)}{\delta_{wt_k}} \times \Delta x \times L \times (T_{wt,int_k} - T_{w,wt_k}) = 0 \quad (2.31)$$

Heat transfer between the HTF and the metallic plate.

$$h_{T_{htf/ec,w_k}} \times \Delta x \times L \times ((T_{htf/ec_{o,k}} + T_{htf/ec_{i,k}})/2 - T_{w,htf/ec_k}) - \left(\frac{\lambda_w}{e_w} \right) \times \Delta x \times L \times (T_{w,htf/ec_k} - T_{w,wt_k}) = 0 \quad (2.32)$$

Energy balance of the HTF.

$$-\dot{m}_{htf/ec_{i,k}} \times h_{htf(T_{htf/ec_{o,k}})} + \dot{m}_{htf/ec_{i,k}} \times h_{htf(T_{htf/ec_{i,k}})} + 2 \times h_{T_{htf/ec,w_k}} \times \Delta x \times L \times (T_{w,htf/ec_k} - (T_{htf/ec_{o,k}} + T_{htf/ec_{i,k}})/2) = 0 \quad (2.33)$$

In a similar procedure as in previous sections, equations (2.27) to (2.33) define a system of 7 equations and 7 unknown variables. Heat and mass transfer along the condenser are identified through the value obtained for the variable $\dot{m}_{H_2O,eva/con_k}$ at each position where a positive value of $\dot{m}_{H_2O,eva/con_k}$ indicates that water has been condensed.

⁽¹⁾ In condensation/desorption operation the vapor is generally overheated; nevertheless, for simulation simplicity purposes it has been considered that the vapor is in saturated conditions during the condensation process.

2.1.1.4. Coupling model for the absorption/desorption and evaporation/condensation heat exchangers

A coupling procedure is necessary to describe the evaporation/absorption process and the condensation/desorption process. This approach considers that the vapor generated by the evaporator (desorber) is entirely absorbed (condensed) by the absorber (condenser), the evaporator/absorber (desorber/condenser) working at the same pressure. The water vapor is considered at saturated conditions (Figure 2.8).

All the presented heat exchanger models considered a cocurrent movement for the falling film and the HTF (Figure 2.6 and 2.7). Given the entrance conditions of the LiBr solution film, the HTFs and the liquid water film; the model finds the vapor pressure conditions, $T_{vap\ sat}$ and $P_{vap\ sat}$, that allow to respect the water mass balance in the reactor, as indicated in Equation (2.34).

$$\left(\sum_{k=1}^n \dot{m}_{H_2O, abs/des_k} + \sum_{k=1}^n \dot{m}_{H_2O, eva/con_k} \right)_{(T_{vap\ sat}, P_{vap\ sat})} = 0 \quad (2.34)$$

In addition, entrance conditions are supposed to change very slowly in comparison to the time required for the falling films to reach stationary regimes; therefore, exchangers are supposed to work in quasi steady-state operating mode.

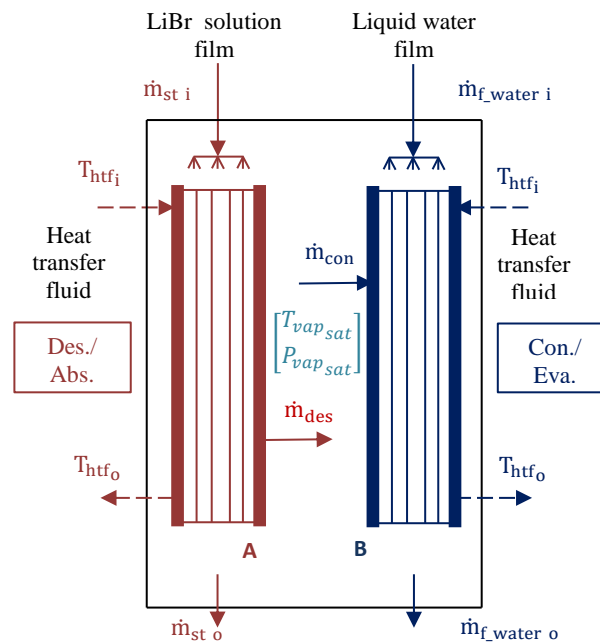


Figure 2.8. Coupling of the evaporator/absorber (desorber/condenser) in the reactor at saturated conditions

Figure 2.9 describes the boundary conditions when the HTF and the solution falling film are in counter-current movement. The same discretization process and balance equations used in co-current configuration are considered in this case. In order to solve the equations system associated to each grid, a shooting method is used. This method consists, given the exchanger boundary conditions, in proposing an initial value for " $T_{htf/ad_o,k}$ " (top of the exchanger) and to solve the grid equations systems from the top to the bottom (similar way as in co-current movement). If at the end of the process, the calculated value " $T_{htf/ad_i,k}$ " (bottom of the exchanger) is equal to the real HTF inlet temperature the process stops; otherwise, another value is proposed for " $T_{htf/ad_o,k}$ " and the process is repeated up to calculate a HTF inlet temperature equal to the real value.

This procedure is similarly applied in the evaporator and condenser when counter-current movement is considered.

For cases in which the absorber and evaporator or the desorber and condenser are coupled, the same method of reactor water mass balance described in Equation (2.34) is used.

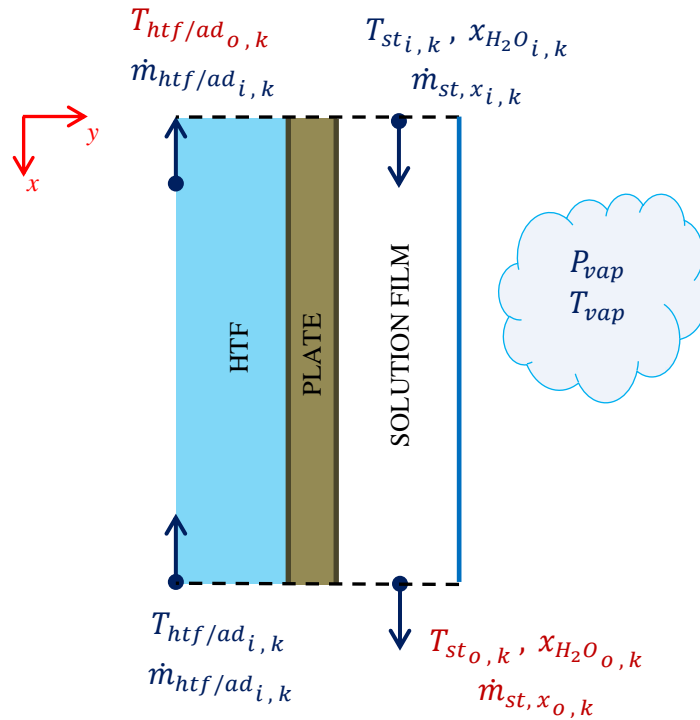


Figure 2.9. Desorber/Absorber boundary conditions in the nodal approach when counter-current movement is considered (bleu: know values, red: unknown values)

2.1.1.5. Modelling of a wetting effect on the metallic plates

For cases in which the transfer surface is not completely wetted (Figure 2.10), two heat transfer modes across the plate heat exchanger are considered in the simulation model: an optimistic and a pessimistic mode denoted as “1F” and “2F” respectively; these transfer modes are also shown in Figure 2.10.

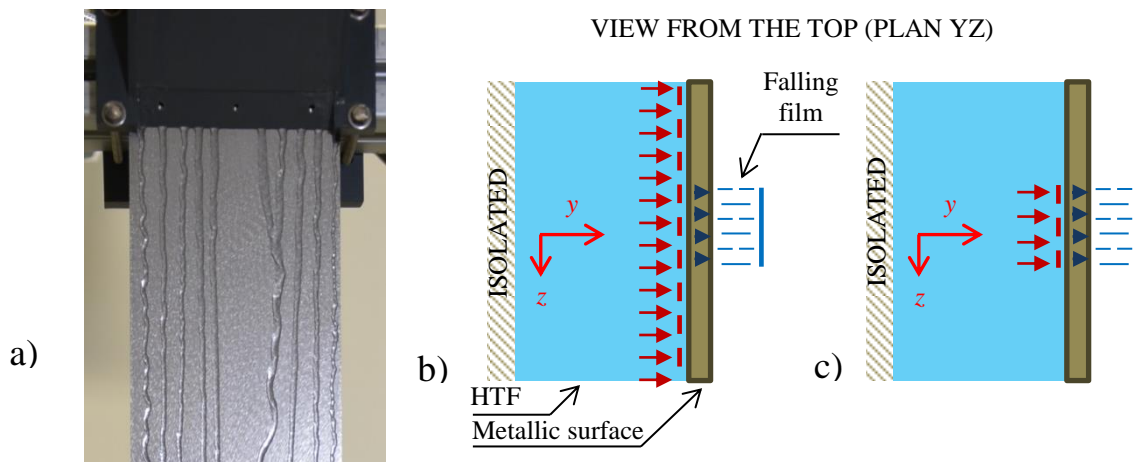


Figure 2.10. Heat transfer across a metallic surface not completely wetted by a falling film. a) Liquid film on stainless steel plate b) Optimistic case transfer mode (1F); c) Pessimistic case transfer mode (2F)

Since the heat transfer surface on the LiBr falling film side is being partially wetted, a fin effect appears. The optimistic case considers a fin efficiency equal to 1, whereas the pessimistic case considers a fin efficiency equal to 0. These transfer modes were modeled by modifying equations (2.11), (2.12), (2.15) and (2.17) to

(2.19) with 2 coefficients: $S_{w,st}$ and $S_{w,htf/ad}$ which are associated to the heat transfer at each side of the wall. The detail of these modifications is described in Annex B1.4⁽¹⁾.

2.1.2. Model validation

In this section the simulation results described in section 2.1.1 are compared against simulation and experimental studies made by other authors; these comparisons are described below.

2.1.2.1. Comparison against a numerical case of water absorption on a LiBr solution film falling along a vertical plate

Karami and Farhanieh (2009) developed a numerical model to describe the absorption of water vapor into a film of aqueous LiBr falling along a vertical plate. This method was based on a 2 axes discretization of the falling film where, at each defined grid, mass, momentum and energy equations were solved using boundary layer conditions and a fully implicit finite difference method. Figure 2.11 shows a comparison between our simulation results and the one developed by Karami and Farhanieh for the case where LiBr solution at saturated conditions enters and flows along a vertical plate heat exchanger such that $P_{vap} = 1000 Pa$, $x_{LiBr_i} = 60\%$, $Re_{sti} = 20.5$ and $T_{htf_i} = 32^\circ C$ ⁽²⁾. The chosen parameters for this comparison were the temperature and the LiBr mass fraction at the interface (vapor/liquid) of the falling film along the plate length.

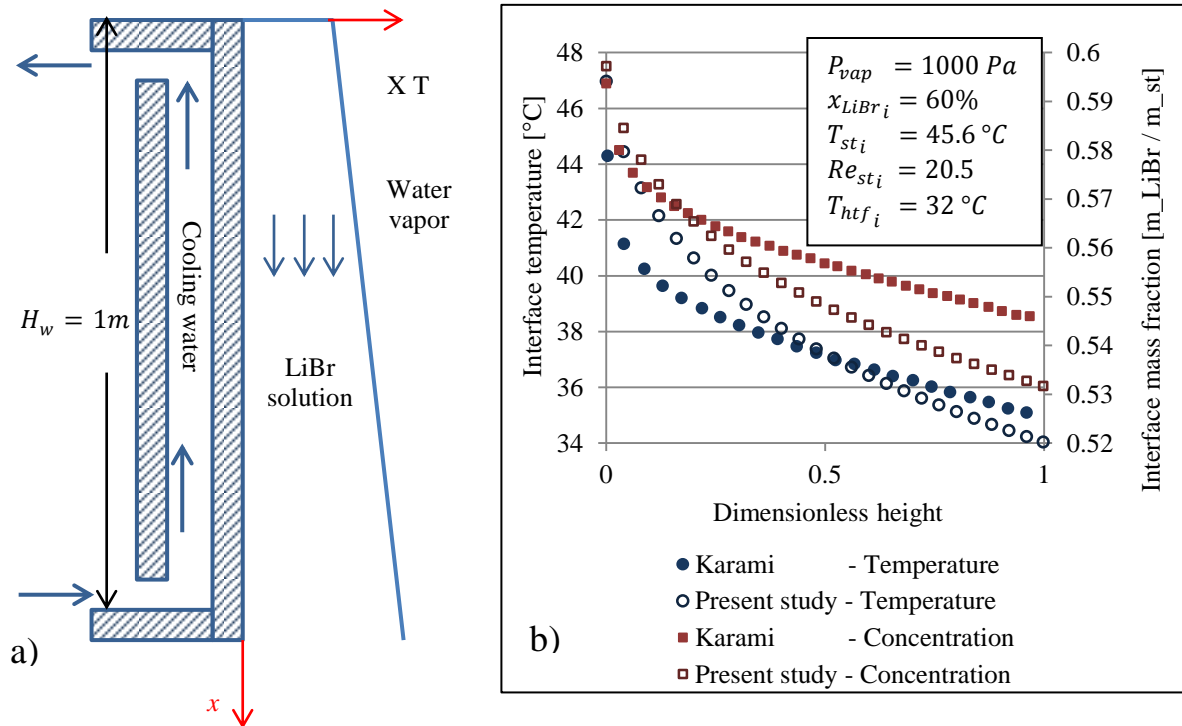


Figure 2.11. Comparison of our simulation model against simulated results obtained by Karami (Karami and Farhanieh, 2009). a) Scheme of the simulated case. b) Comparison of temperature and mass fraction at the film interface.

For our model, Fig 2.11b indicates that at the plate inlet the interface temperature and LiBr concentration are $47^\circ C$ and 59.8% , respectively, and these parameters decrease down to $34^\circ C$ and 53% at the plate outlet, respectively. The interaction between the interface and the vapor (at the indicated pressure) determines the values of the temperature and LiBr concentration at the interface, and these conditions permit the absorption process to happen. Both results (Karami and Farhanieh and our simulation model) share the same magnitude

⁽¹⁾ Additionally, a simulation model for the LiBr solution recirculation between the outlet and inlet of the heat exchanger has been developed and is described in the Annex B1.5.

⁽²⁾ The thermal resistance of the plate wall and the convective resistance between the cooling water (HTF) and the wall were neglected.

order although our model overestimates and underestimates the interface temperature at the top and at the bottom of the vertical plate respectively and, also, mostly underestimates the interface LiBr mass fraction along the plate. These differences are probably related to the different sources used for the equilibrium correlation between the temperature, LiBr mass fraction and vapor pressure at the interface since Karami used correlation given by McNeely (1979) and our simulation model uses correlation given by Hellman and Grossman (1996). Nevertheless, these differences remain relatively small since the maximal values of the ratios between Karami's and our simulation results are 3.8 for the temperature and 0.8 for the LiBr mass fraction⁽¹⁾.

2.1.2.2. Comparison against an experimental case of water absorption on a LiBr solution film falling along a vertical tube

Miller and Keyhani (2001) and Medrano et al. (2002) made experimental tests to study the absorption of water vapor in a LiBr solution film falling on an internal and external stainless steel vertical tube surface respectively (tube length of 1.5 m); in both cases the tubes were refrigerated with cooled water flowing at the external and internal tube's surface respectively.

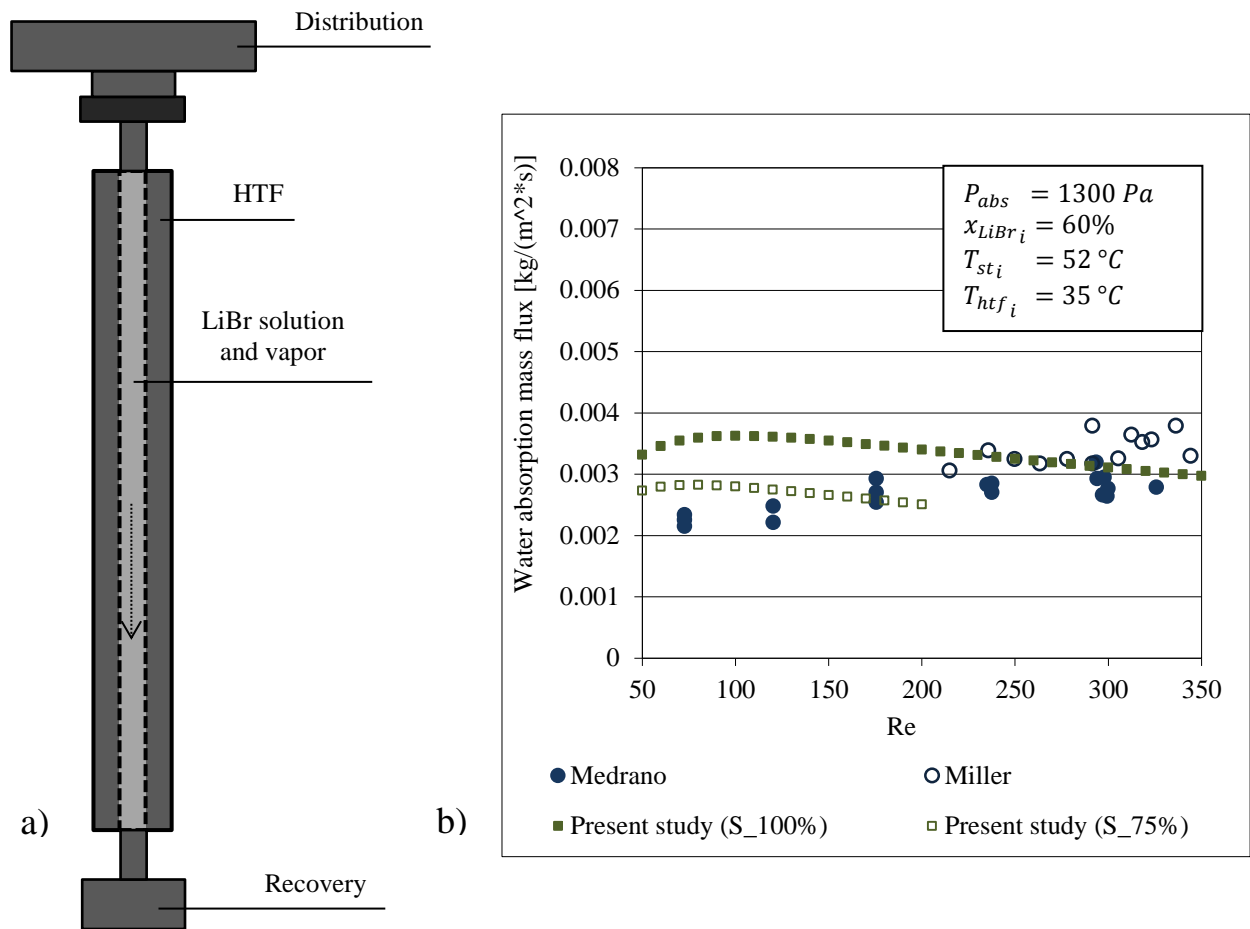


Figure 2.12. Comparison of our simulation model against experimental results obtained by Miller and Keyhani (2001) and Medrano et al. (2002). a) Scheme of the simulated case. b) Comparison of the absorbed mass flux per unit surface for different inlet solution Reynolds numbers.

Figure 2.12 shows the comparison between simulated results obtained with our model (which was previously adapted for a vertical tube geometry considering that $h_{T_{htf}} = 8500 (W/(m^2.K))$ against experimental results

⁽¹⁾ The ratio between the Karami model result and our simulation model result, associated to the interface temperature (vapor/liquid) is defined as: $(T_{st,int}(Karami) - T_{st,i}) / (T_{st,int}(our\ model) - T_{st,i})$. An analogous definition is applied for the interface concentration. The temperature ratio value "3.8" results from the ratio: $(41.1 - 45.6) / (44.4 - 45.6)$.

obtained by Medrano and Miller for a case where LiBr solution at saturated conditions enters and flows along the vertical tubes (inlet conditions described in the figure).

A fairly good agreement between simulation and experimental results is observed for the total absorbed water mass flux at different Reynolds numbers. Best coincidences with the simulation model were obtained for $Re > 250$ when the LiBr solution was considered to completely wet the exchange surface (denoted as S_100%) and at $Re < 250$ when just 75% of the exchange surface (denoted as S_75%) was considered to be wet by the solution (Figure 2.12b); this last hypothesis would be reasonable for the case described by Medrano since the LiBr solution flowed on the inner surface of a tube which had no visual access. Wetting of exchangers surfaces will be further discussed in section 2.1.2.3.

However the experimental absorbed water mass flow rises with the Reynolds number (Medrano data); this behavior would be expected since at higher Reynolds number a waviness can appear at the film interface and can increase the mass transfer coefficient (Chang, 1994)⁽¹⁾.

Nevertheless, Figure 2.12 also shows that our simulated absorbed water mass flow does not have a rising tendency with the rising Reynolds; on the contrary, it seems to there be an optimal maximum at a certain value. This latter behavior would be expected since:

- At very low Reynolds number an increase in the solution mass flow generates a rise in the film interface solution velocity, producing an increase in the absorbed vapor mass; nevertheless, at high Reynolds number the film thickness increases so much up to the point to penalize the heat transfer and, consequently, the mass transfer across the film. This can be verified analyzing Equations 2.8 and 2.9 that define the interface heat and mass convective coefficients, which are inversely proportional to the solution thickness " δ_i " and directly proportional to $Sh_{int/st}$ and $Nu_{int/st}$ numbers, respectively, these latter being also directly proportional to the Reynolds number (see Figure 2.4).
- The simulation model does not consider a wave appearance at the film interface at any Reynolds number⁽²⁾.

⁽¹⁾ According to Chang (Chang, 1994), in vertical falling films: laminar regimes are mainly associated to $Re < 300$, the transition regime is defined by $300 < Re < 1000$ (appearance of long interfacial waves) and the turbulent regime is present for $Re > 1000$ (wavelengths comparable to the film thickness).

⁽²⁾ A wavelets effect component could be introduced in the model in the future, considering adequate correlations.

2.1.2.3. Interpretation of simulation results against an experimental case of desorption/condensation and absorption/evaporation in the reactor of an interseasonal heat storage prototype

N'Tsoukpoe (N'Tsoukpoe, 2012), (N'Tsoukpoe et al., 2013) carried out experimental tests on an interseasonal sorption heat storage system prototype using a LiBr-H₂O aqueous solution as it was described in chapter 1. The experimental results obtained by N'Tsoukpoe in coupled processes of desorption/condensation and absorption/evaporation were used to validate our simulation model as it is shown in the following sections.

2.1.2.3.1. Experimental setup

The prototype setup constructed by N'Tsoukpoe is presented in Figure 2.13a. Inside the prototype reactor, two shell and tubes exchangers are placed. At each heat exchanger LiBr solution or water flows on the tube's internal surface while the HTF flows on the tube's external surface (shell side). The tube is in brass (CuZn₂₂Al₂). Figure 2.13b shows the distribution part for the LiBr solution or water flowing inside the tubes, where at each tube top 3 injections points of 0.4 mm were drilled.

Vapour produced by the desorption/evaporation processes flows through the top or bottom of each tube to the condenser/absorber (Figure 2.13c).

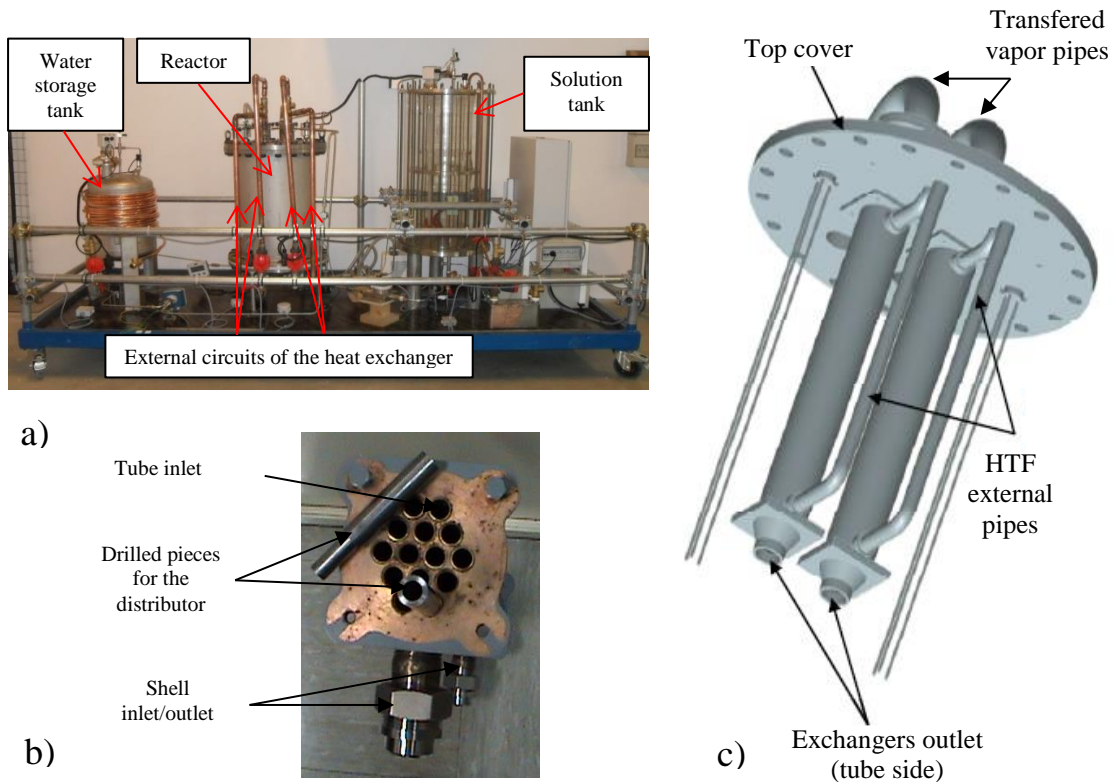


Figure 2.13. a) Constructed prototype of the heat storage system based on sorption process. b) Distribution head for the LiBr solution or water. c) Detail of the shell and tube heat exchangers constructed in the reactor (N'Tsoukpoe et al., 2013)

The prototype is instrumented to measure temperatures, pressures and mass fractions of the fluids. Each heat exchanger is connected to a thermal module that can provide controlled flow rate and temperature for the heat transfer fluids.

2.1.2.3.2. Model's comparison against an experimental case in desorption/condensation operating mode

Experimental results obtained by N'Tsoukpo in desorption/condensation functioning mode (charge) were used to validate our model.

Experimental inlet conditions on the desorber and condenser for the LiBr solution falling film and the HTFs are described in table 2.1. The inlet conditions corresponded to the charge mode (as described in chapter 1). The experimental LiBr mass fraction varied between 54% and 56%; since these fractions were in the system working range which goes from 54% to 60% (higher fractions would have implied crystallization in the desorber).

Table 2.1. Experimental inlet conditions considered for the LiBr solution falling film and HTF on the desorber and condenser (charge mode)

Desorber	\dot{m}_{st_i} [kg/h]	T_{st_i} [°C]	x_{LiBr_i} [m_LiBr/m_st]	\dot{m}_{htf_i} [kg/h] ⁽¹⁾	T_{htf_i} [°C]	Direction movement
	[35 – 40]	[10 – 30]	[0.54 – 0.56]	720	90	Countercurrent
Condenser	$\dot{m}_{f_water_i}$ [kg/h]			\dot{m}_{htf_i} [kg/h]	T_{htf_i} [°C]	Direction movement
	0			360	20	Countercurrent

Experimental inlet conditions mentioned in table 2.1 were also used in the simulation. In both cases, experimentation and simulation, the movement of the HTFs with respect to the falling films was in countercurrent.⁽²⁾

Figure 2.14 shows the comparison between experimental and simulation results for the LiBr solution film and the HTFs leaving the reactor. The compared parameters are the LiBr solution film temperature and mass fraction at the reactor's outlet as well as the HTF outlet temperature at the desorber and condenser.

Values and tendencies of the experimental results shown in Figure 2.14 are explained as follows. At the beginning of the test, the solution tank is filled with homogeneous solution ($x = 54.2\%$, $T_{st} = 10^\circ\text{C}$). The diluted solution is pumped from the top of the tank and concentrated solution is re-injected at the bottom of the tank; the desorption process is active since a concentration difference of about 1% occurs between the inlet and the outlet of the desorber. The tank works in a quasi-plug-flow mode as one can see through Figures 2.14a and 2.14b. After 1h04 an abrupt mass fraction change appears at the inlet of the desorber; corresponding, under these conditions, approximately to the time needed to a particle to shift from the inlet (bottom) to the outlet (top) of the tank, with the high inlet tank solution temperature ($\sim 60^\circ\text{C}$) reinforcing the transport movement. The modifications of the desorber solution inlet temperature and concentration impact the heat transfer with the desorber HTF (Figure 2.14c); although, it seems to have negligible effect on mass transfers within the solution since the heat transfer at the condenser is not affected, underling a constant condensation rate (Figure 2.14d).

⁽¹⁾ The considered HTF for these tests was water.

⁽²⁾ The number of grids considered for the simulation model was 100.

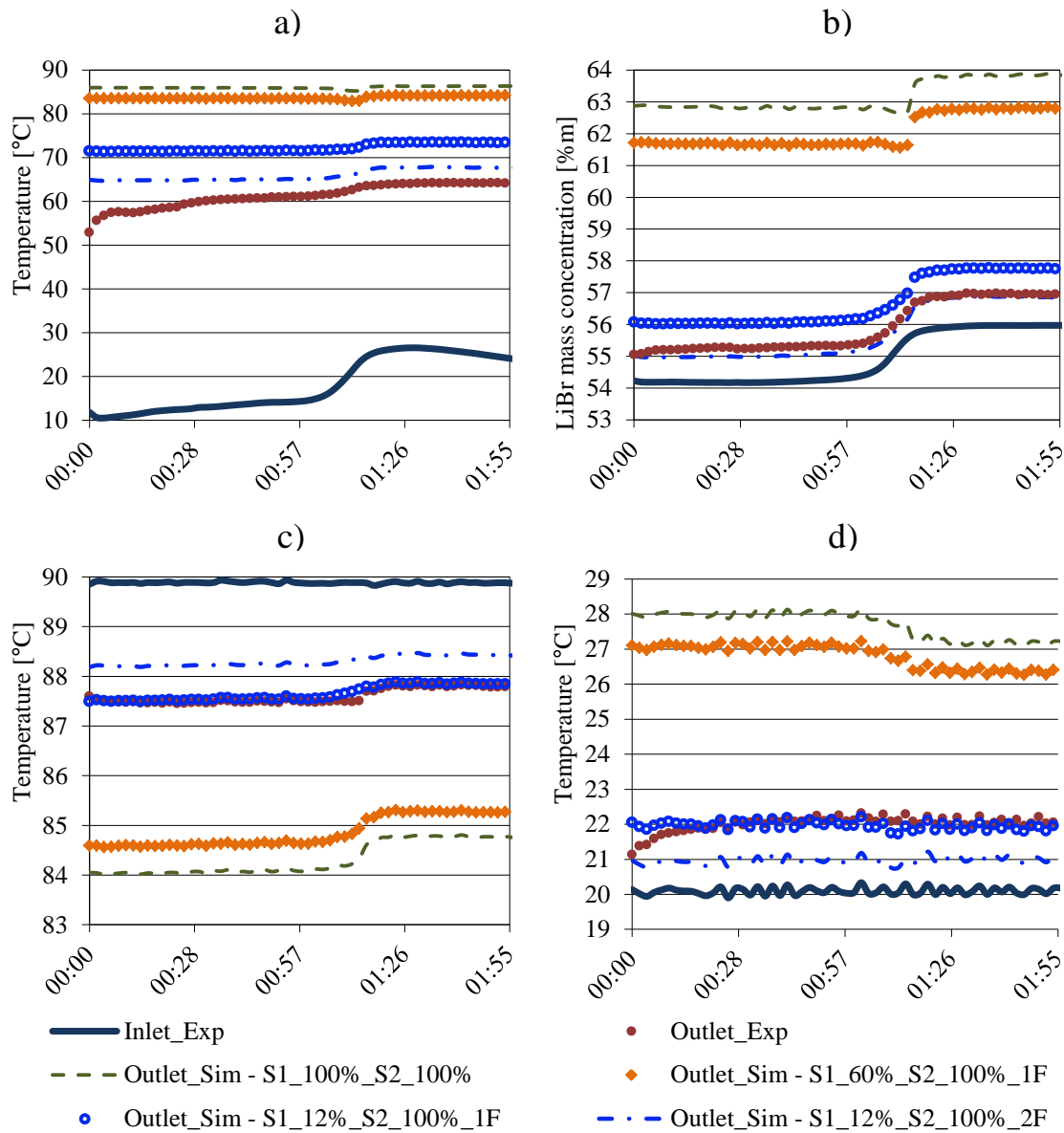


Figure 2.14. Comparison between experimental and simulated results for the desorption/condensation operation mode tests (N'Tsoukpoe et al., 2013). a) LiBr solution temperature; b) LiBr solution mass fraction; c) HTF temperature in the desorber; d) HTF temperature in the condenser.

Numerical simulations considering completely wetted surfaces (S1_100%_S2_100%) have been compared to the experimental results. The qualitative evolutions of the variables are reproduced. However, simulations overestimate the experimental results, with the latter indicating a very low performance of the heat exchangers. A hypothesis to explain this difference consists in considering that the desorber plate surface on the LiBr solution falling film side is not completely wetted by the solution during the tests (for the condenser, since there is no inlet water film flow and the condensation phenomena occurs all over the heat exchange surface, 100% wettability can still be assumed). Consequently, partial wetted surfaces of “S1_60%” and “S1_12%” in the desorber are considered in the simulations (see section 2.1.1.5).

As explained in section 2.1.1.5, two heat transfer modes across the heat exchanger are considered: an optimistic and a pessimistic mode denoted as “1F” and “2F” respectively (see also Figure 2.10).

Figure 2.14 shows a good coincidence between experimental and simulation results for cases in which the desorption transfer surface is considered to be 12% wetted, with better agreements obtained for the LiBr solution mass fraction and the HTF temperatures.

Simulated results indicate that for “S1_12%”, the optimistic case (1F) presents a better heat transfer across the desorber’s metallic exchange surface compared to the pessimistic case (2F). This is observed in figures 2.14a, 2.14b and 2.14c where the outlet-inlet difference temperatures and desorbed masses are bigger in case 1F than in case 2F.⁽¹⁾

It must be remarked that the hypothesis of such low wettability of the LiBr solution on the exchange surface is in agreement with studies made by Drelich (Drelich et al., 2011) which indicate that to have high wettability usually a chemical surface treatment must be done on surfaces.

The considered hypothesis of low wettability of LiBr solution on the heat exchangers metallic surfaces without any treatment was verified through wettability experimental tests made on brass and stainless steel vertical plates. The results of these tests are described in section 2.1.2.3.4.

2.1.2.3.3. Model’s comparison against an experimental case in absorption/evaporation operating mode

In a similar way to the previous section, experimental results obtained by N’Tsoukpoe in absorption/evaporation functioning mode (discharge) were used to validate our simulation model⁽²⁾. The results are shown in Figure 2.15.

Experimental inlet conditions are described in table 2.2. The experimental LiBr mass fraction varied between 55% and 54%.

As in the desorption case, values and tendencies of the experimental results shown in Figure 2.15 are explained as follows. The absorption process is effective since a mass fraction difference around 1% occurs between the inlet and the outlet of the absorber. The concentrated solution is pumped from the top of the tank and the diluted solution is re-injected at the bottom of the tank. Unlike the desorption case, the tank works in a mixed mode as one can see on Figure 2.15b (linear decrease of the mass fraction with time); this is due to the low density of the re-injected solution combined to its medium temperature (~35°C), which both reinforces the solution movement along the tank and permits a uniform variation of physical conditions. Furthermore, the heat losses to the tank surroundings lead to a stabilization of the solution temperature leaving the tank to be injected in the absorber (Figure 2.15a). Heat transfer between the solution and the absorber HTF is limited since the temperature difference between the absorber HTF outlet/inlet is about 0.2 °C whereas it should be higher than 5°C in case of perfect wetting film (Figure 2.15c, the temperature oscillation of the HTF flowing into the absorber enclosed between 26 and 26.5 °C is due to regulation on the prototype and not due to physical phenomenon). Heat transfer between the water and the evaporator HTF seems to be slightly better than the one observed at the absorber HTF but remains substantially smaller compared to what one should have had with perfect wetting film (Figure 2.15d).

⁽¹⁾ An additional case in desorption/condensation functioning mode is described in Annex B1.6.

⁽²⁾ The number of grids considered for the simulation model was 100.

Table 2.2. Experimental inlet conditions considered for the LiBr solution falling film, water film and HTFs on the absorber and evaporator (discharge mode)

Absorber	\dot{m}_{st_i} [kg/h]	T_{st_i} [°C]	x_{LiBr_i} [mLiBr/mSol]	$\dot{m}_{htf_i}^{(1)}$ [kg/h]	T_{htf_i} [°C]	Direction movement
	70	[24 – 26]	[0.55 – 0.54]	360	26	Cocurrent
Evaporator	$\dot{m}_{f_water_i}$ [kg/h]	$T_{f_water_i}$ [°C]		\dot{m}_{htf_i} [kg/h]	T_{htf_i} [°C]	Direction movement
	20	15		720	20	Countercurrent

As for the charging mode, numerical simulations considering completely wetted surfaces (S1_100%_S2_100%) reproduced qualitatively the physical evolution of the phenomenon but overestimated substantially the heat transfer with the HTF. In an analogous procedure as for the desorption/condensation case, best coincidences between experimental and simulated results were obtained for partial wetting of the heat transfer surfaces. Hence, regarding the absorber and evaporator, partially wetted surfaces, “S1_60%_S2_60%” and “S1_20%_S2_20%”, were considered and a particularly good agreement was observed for a wetting percentage equal to 20%⁽²⁾.

It must be commented that although a tendency for a good agreement between experimental and simulation results is obtained in the desorption/condensation and absorption/evaporation tests when the wetted surface percentages are reduced; some simulated parameters, such as the outlet solution temperature (T_{sto}) in Figure 2.14a and the outlet absorber HTF temperature (T_{htfo}) in Figure 2.15c, would not completely match the experimental values even if the surface wetting is further reduced. Hence, this remaining difference could be associated to the influence of others factors not considered by the simulation model, such as the presence of non-condensable gases.

The considered hypothesis of low wettability of LiBr solution and water on the heat exchangers brass metallic surfaces without any treatment was verified through wettability experimental tests made on brass and stainless steel vertical plates. The results of these tests are described in section 2.1.2.3.4.

⁽¹⁾ The considered HTF for these tests was water.

⁽²⁾ An additional case in absorption/evaporation functioning mode is described in Annex B1.6

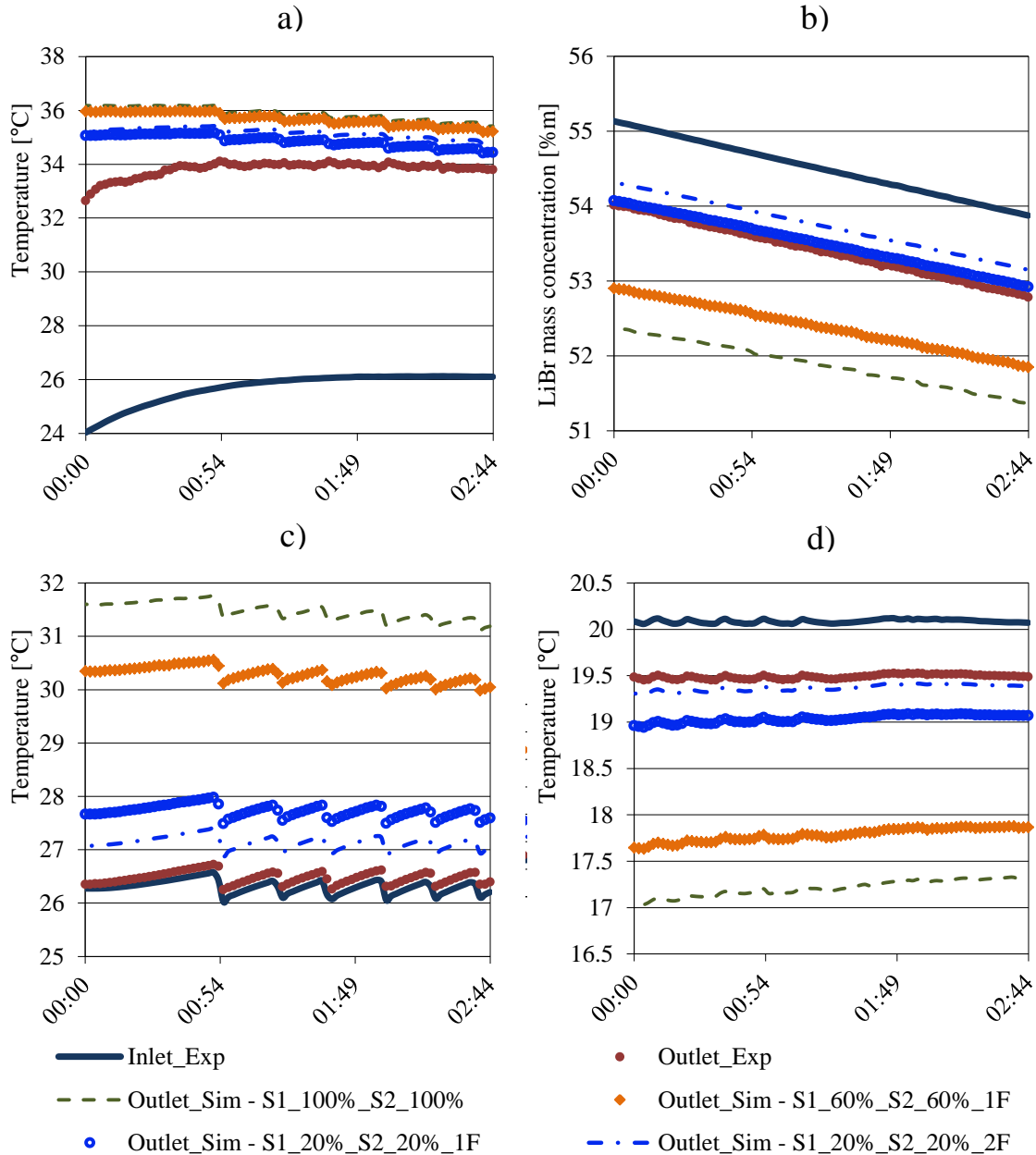


Figure 2.15. Comparison between experimental and simulated results for the absorption/evaporation operation mode (N'Tsoukpoe et al., 2013). a) LiBr solution temperature; b) LiBr mass fraction in the solution; c) HTF temperature in the absorber; d) HTF temperature in the evaporator.

2.1.2.3.4. Wettability tests on brass and stainless steel plates

As mentioned in previous sections, the wettability of metallic surfaces depends on the surface tensions and surface structuration, and it can be improved by chemical methods, Drelich (Drelich et al., 2011). The surface wetted by a falling film depends also on its Reynolds number; the wetting rate increases with the increase of the contact angle between the fluid and the plate's material (Lee et al., 2002).

To investigate the low wettability obtained by our simulation results on falling films with LiBr solution and water, different tests were performed to study the wettability performances of metallic plates with LiBr solution or water falling films. An experimental setup was constructed with this purpose (Figure 2.16). It was composed by a pump, a Coriolis flowmeter, a metallic plate's fixation system, a fluid distributor placed at the top of the metallic plate and a recuperation container placed at the bottom of the metallic plate. All these components

composed a closed loop in which the flow rate was established by the pump and measured by the flowmeter while the LiBr solution or water arrived at the top of the metallic plates through the distributor (placed on only one side of the plates). A camera was installed in front of the plate to register the wetted surface. All tests were made at atmospheric pressure.

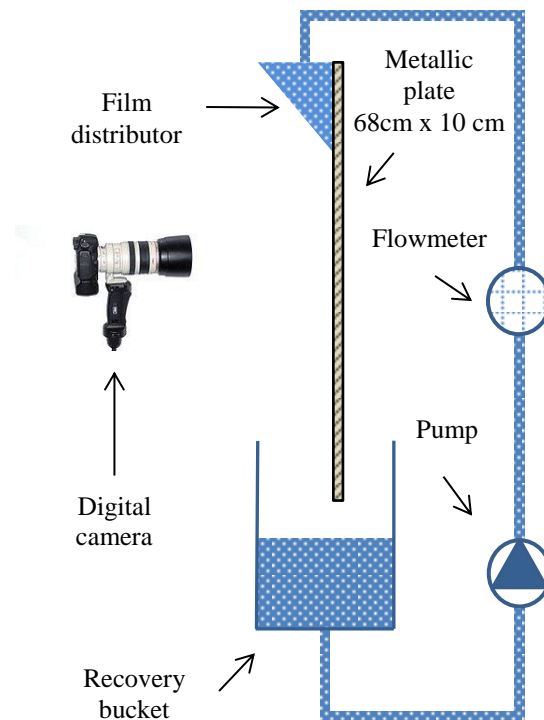


Figure 2.16. Scheme of the experimental setup to test the surface wettability of metallic plates.

Two types of metals were tested: stainless steel (metal used by Miller (Miller and Keyhani, 2001) and Medrano (Medrano et al., 2002), see section 2.1.2.2) and brass CuZn36 (metal used by N'Tsoukpoe (N'Tsoukpoe et al., 2013), see section 2.1.2.3.1). The dimensions of these plates were 68 cm x 10 cm x 1.5 mm. The tests normalized flow rate interval varied between 0 and 2 kg/(h*cm) when LiBr solution was used and between 0 to 7 kg/(h*cm) when water was used (flow rates were normalized over the plate's width). In experimental tests in desorption/condensation and absorption/evaporation modes made by N'Tsoukpoe (detailed in sections 2.1.2.3.2 and 2.1.2.3.3), the maximum normalized flow rates were about 1.5 kg/(h*cm).

All tests began with an increasing flow rate from zero up to the maximal flow rate and, afterwards, with a decreasing flow rate down to zero again. The plate's wetting rate was determined using the image processing software ImageJ (ImageJ, 2015). Images were loaded on the software and a filter was used to determine the boundaries of the falling film defining the wetted surface on the plate. Pictures of the flow along the plates are given in Figure 2.17.

The evolutions of the wetting rates as a function of the flow-rate for both plates are shown in Figure 2.18.

The wetting behavior of the LiBr falling film on stainless steel plates and brass plates was comparable. The wetting rate increases with the flow rate. It reaches a maximum close to 20% for a mass flow rate per unit width of 2 kg/(h*cm). When the flow rate decreases, the wetted plate area remains constant.

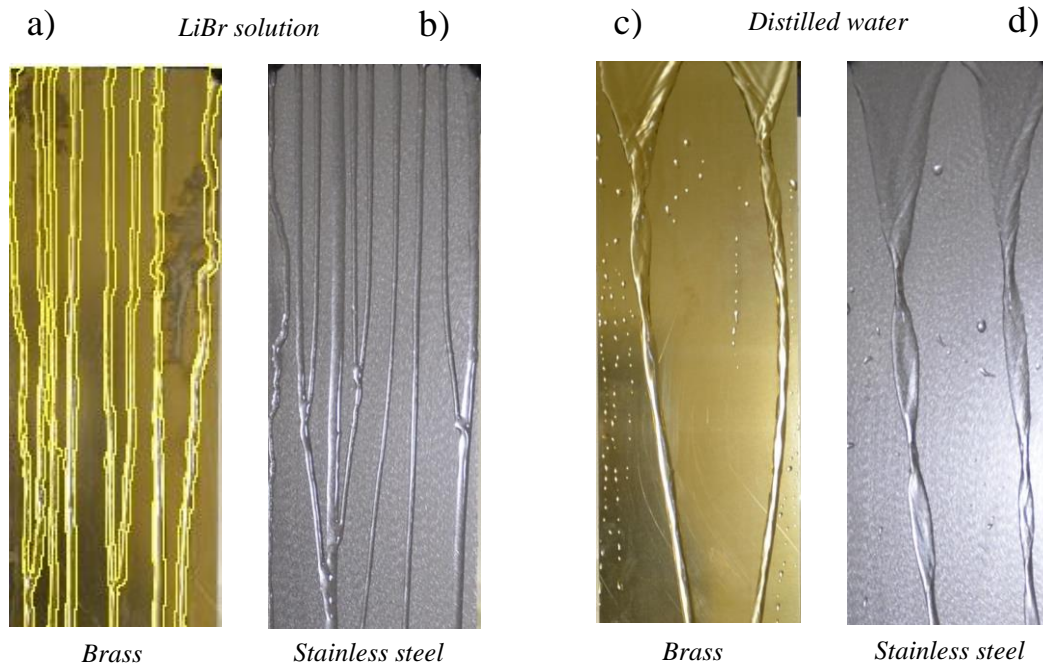


Figure 2.17. Wetted surface at the maximum flow rate. a) Detail of the software treatment for the Brass plate/LiBr solution image; b) LiBr solution wetting the stainless steel surface; c) Distilled water wetting the brass surface before homogenization; d) Distilled water wetting the stainless steel surface before homogenization.

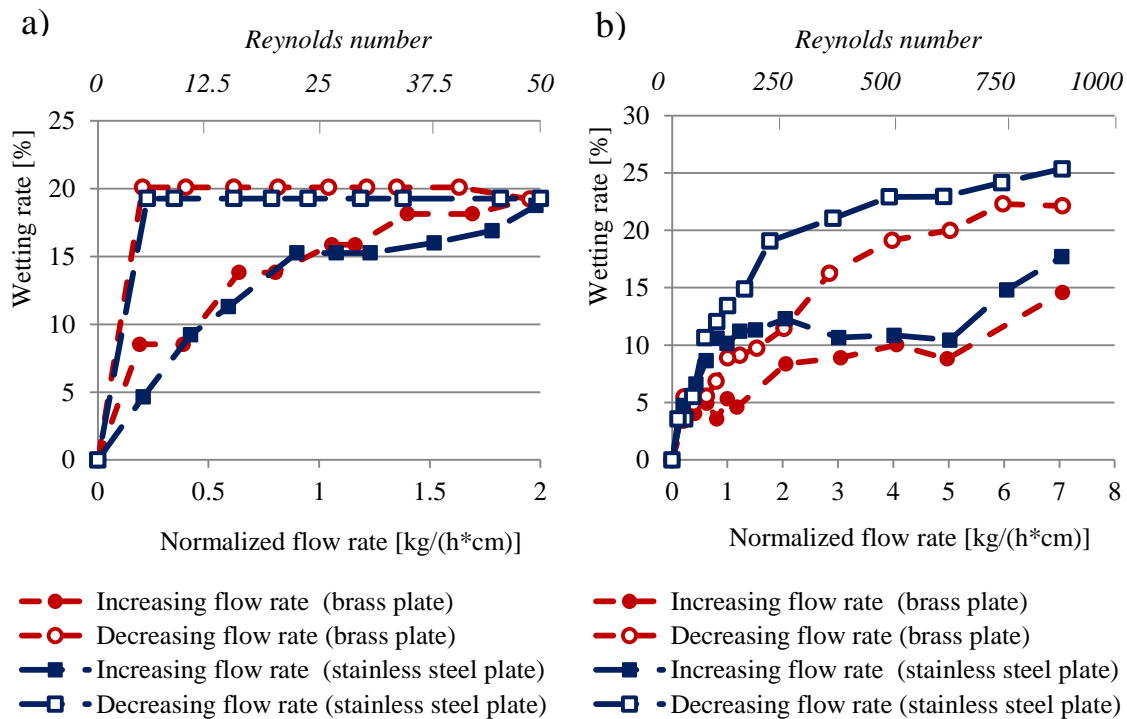


Figure 2.18. Wettability tests made on stainless steel and brass plates at atmospheric pressure. a) With an aqueous LiBr solution (52.5% LiBr concentration). b) With distilled water.

The wetting behavior of the water falling film on stainless steel and brass plates showed that the wetted surface was longer on the stainless steel plate than on the brass plate. It reaches respectively a maximum of about 18% and 15% for a mass flow rate of 7 kg/(h*cm). The hysteresis effect is much more limited with the water falling film compared to the solution falling film, the wetted surface decreasing quasi continuously with the flow rate decrease.

In order to avoid some distribution imperfections present with the water falling film configuration, a distribution homogenization of the water film leaving the distributor was made before starting the tests in the decreasing flow-rate mode, leading to a small increase of the wetting rate between the end of the test in increasing flow-rate mode and the beginning of the test in decreasing flow-rate mode. This homogenization procedure didn't affect significantly the wetting rate, showing the low sensibility of the wetting rate to the distribution homogeneity. No distribution homogenization was done during the LiBr solution tests (see Figure 2.17 and 2.18).

As it was mentioned in sections 2.1.2.3.2 and 2.1.2.3.3, in experimental tests performed by N'Tsoukpoe (N'Tsoukpoe, 2012), (N'Tsoukpoe et al., 2013), shell and tubes heat exchangers were used where aqueous LiBr solution and water flowed on the inner surface of the metallic tubes. The material used for these tubes was brass ($\text{CuZn}_{22}\text{Al}_2$). The film distribution in this system was certainly not optimal since it consisted of only 3 injection points (0.4 mm diameter) located at the top of each brass tube and the maximum normalized flow rate on the inner surfaces was limited to 1.5 kg/(h*cm).

Considering these two limitations and Figures 2.17 and 2.18, it can be affirmed that during the tests described in sections 2.1.2.3.2 and 2.1.2.3.3, the wetted surface percentage on the heat exchangers was probably very low and it could have been in the order of 15-20% for the LiBr solution and 5-10% for water. These results are in good agreement with results obtained in those sections where best fitting between experimental and simulation results were reached when low wetted surface percentages were considered.

Finally, in Figure 2.18 is observed that in increasing flow rate mode the wetted surface percentage increases with the Reynolds number, for both types of plates and both liquid films. This is in agreement with hypothesis of section 2.1.2.2 where it was considered that at low Reynolds number the exchange surface would not be completely wetted (Miller and Keyhani, 2001), (Medrano et al., 2002). Nevertheless, Figure 2.18 also shows that even for high Reynolds (1000) the wetted surface percentage is low (25%), this can be associated with the surface state of the brass and stainless steel plates which were not polished.

2.1.3. Parametrical study and optimal working conditions for a grooved vertical flat plate heat exchanger configuration

In sections 2.1.2.3.2 and 2.1.2.3.3, experimental cases in desorption/condensation and absorption/evaporation coupled processes were used to validate our simulation model (see section 2.1.1.1.3). In those sections it was observed that the system performance was penalized when the LiBr solution or distilled water falling films partially wet the heat transfer surfaces.

In this section a grooved vertical flat plate heat exchanger configuration is proposed in order to ensure a higher surface wetting percentage for the falling films.

In order to study the physical behavior of this new configuration a simulation reference case has been defined and is described in section 2.1.3.1. A simulation parametrical study of the influence of the variation of the heat exchangers inlet working conditions on the system performance is also showed in section 2.1.3.1. Finally, a case with optimal inlet working conditions permitting to obtain a high system performance is showed in section 2.1.3.2.

2.1.3.1. Reference simulation case and inlet working conditions parametrical study

In order to ensure correct process performances a new heat exchanger configuration permitting to improve the surface wetting is proposed as a reference case.

The heat exchanger configuration considered for this study is a grooved vertical flat plate heat exchanger configuration (Figure 2.19), since, as it is mentioned by Do et al. (2008) and Guo et al. (2011), this kind of surface permits a better wetting due to surface tension effects.

The exchangers are composed of 2 grooved plates. LiBr solution or distilled water flows along the grooves external surface while the heat transfer fluid flows in the passage formed between the surface plates. The HTF network considered for each heat exchanger was a flat serpentine passage as it is shown in Figure 2.19.

The geometrical characteristics of the grooved plate exchanger considered for the reference simulation case as well as the hydraulic diameter and passage area of the HTF passage section are showed in Table 2.3.

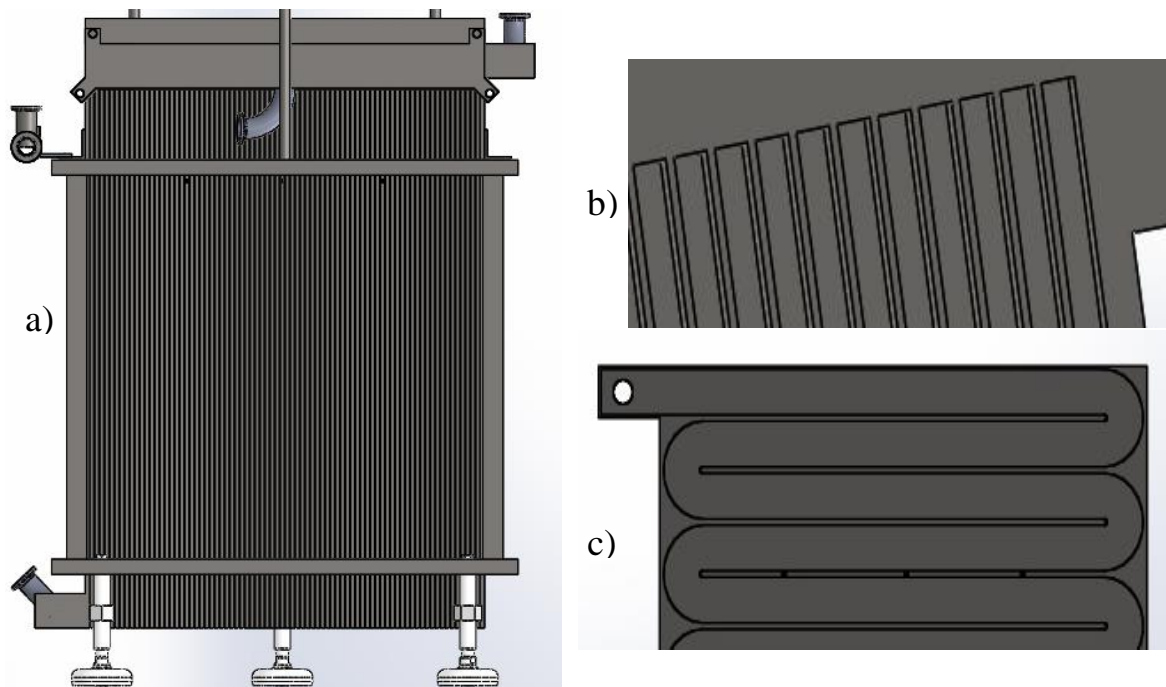


Figure 2.19. Grooved vertical flat plate sandwich configuration. a) front view of the grooved plate; b) Grooves associated to the falling films; c) Flat serpentine network associated to the HTF.

Table 2.3. Grooved vertical flat plate heat exchangers characteristics considered for the reference simulation case

	Plate length [cm]	Plate width [cm] ⁽¹⁾	Plate thickness [cm]	Grooves width [cm]	Number of grooves	HTF: Hydraulic diameter [cm]	HTF: Transversal area [cm ²]
Absorber/Desorber and Evaporator/Condenser heat exchangers	53.3	39.2	0.3	0.4	78	0.375	0.6

⁽¹⁾ Each exchanger has a sandwich configuration, then the total plate width where a falling film flows is: 2 x 39.2 cm = 78.4 cm.

In order to take the proposed grooved vertical plate sandwich configuration into account, an adaptation of the model was carried out through the modification of the control volume balance described in section 2.1.1.1.3 (the heat transfer convective coefficient is detailed in Annex B1.3.1).

2.1.3.1.1. Simulated desorption/condensation process performance

A reference case describing an ideal desorption cycle is proposed. The inlet conditions used for the simulation of this reference case are described in Table 2.4.

Table 2.4. Reference case inlet conditions considered for the LiBr solution falling film and HTF on the desorber and condenser (charge mode)⁽¹⁾

Desorber	\dot{m}_{st_i} [kg/h]	T_{st_i} [°C]	x_{LiBr_i} [m_LiBr/m_st]	\dot{m}_{htf/ad_i} [kg/h] ⁽²⁾	T_{htf/ad_i} [°C]	Direction movement	Wetted surface percentage [%] ⁽³⁾⁽⁴⁾
	60	24	[0.48 – 0.60]	300	70	Counter- current	79.6
Condenser	$\dot{m}_{f_water_i}$ [kg/h]	$T_{f_water_i}$ [°C]		\dot{m}_{htf/ec_i} [kg/h]	T_{htf/ec_i} [°C]	Direction movement	Wetted surface percentage [%]
	0	--		300	15	Counter- current	100

The physical parameters considered for this analysis were: T_{st_o} , x_{LiBr_o} , T_{htf/ad_o} , T_{htf/ec_o} , $\dot{m}_{H_2O, abs/des}$, P_{vap} , which are the system outlet conditions for the LiBr solution, water film and HTF, and also $W_{htf/ad}$ and $W_{htf/ec}$ ⁽⁵⁾, which are the thermal output of the HTF.

Figures 2.20 and 2.21 show the simulated behavior for the considered outlet parameters as a function of the inlet LiBr solution mass fraction, x_{LiBr_i} .

⁽¹⁾ The inlet conditions in Table 2.4 were in the same order of magnitude as those considered in section 2.1.2.3.2.

⁽²⁾ The considered HTF for these simulations was water.

⁽³⁾ The value for the wetted surface percentage was calculated under the hypothesis that the LiBr solution or distilled water falling films completely wet the grooved sections. In the desorber the value is 79.6% since there is a spacing between each groove. In the condenser the value is 100% since it is considered that system conditions permit the vapor to condense uniformly over all the exchange surfaces.

⁽⁴⁾ For cases in which the surfaces are not completely wet, an optimistic heat transfer mode across the plates (1F) was considered (see section 2.1.1.5).

⁽⁵⁾ The energy power given from each HTF to the system for both, the desorber and the condenser, has been calculated with the following correlation: $W_{htf} = \dot{m}_{htf_i} \times c_{p_{htf}} \times (T_{htf_i} - T_{htf_o})$

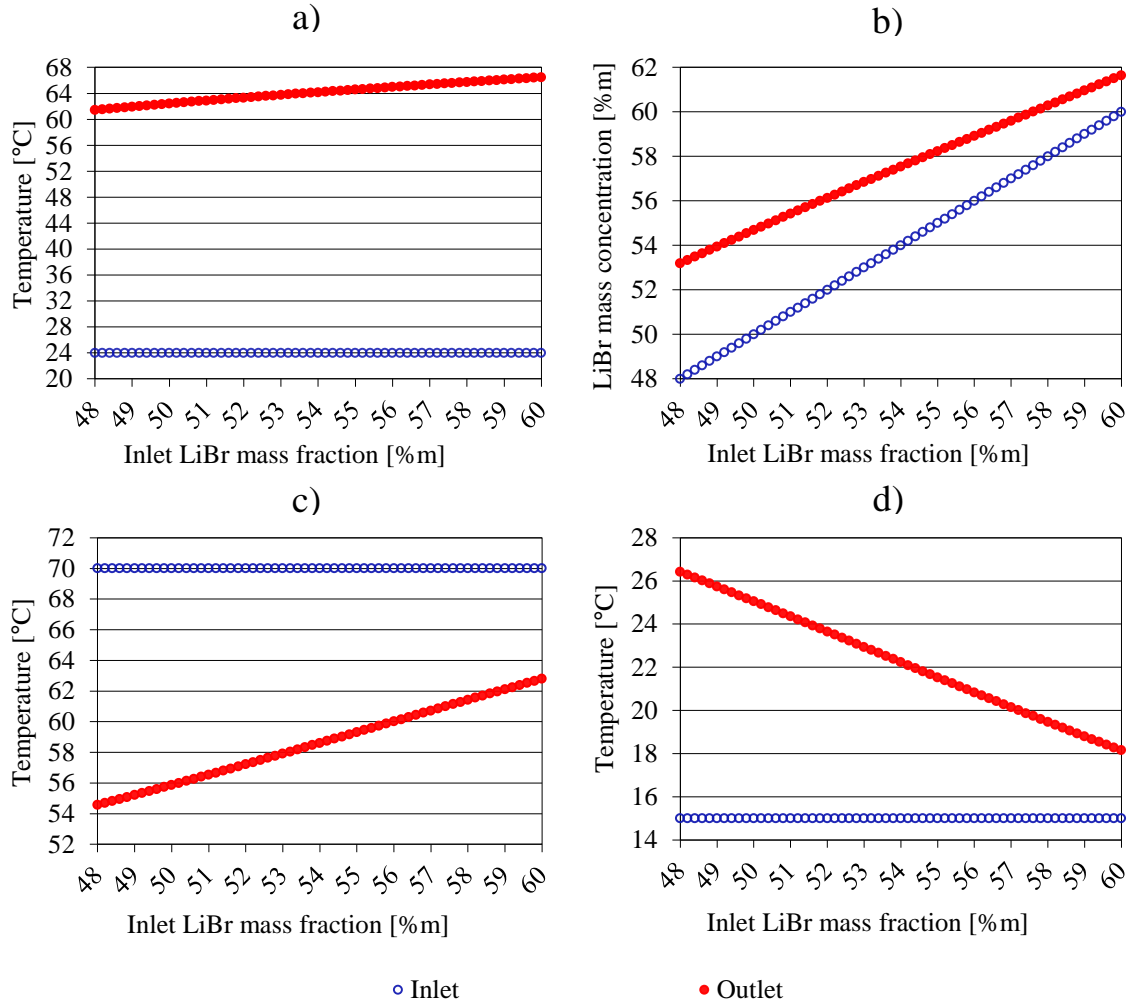


Figure 2.20. Exchangers performance in the desorption/condensation coupled process. a) LiBr solution temperature; b) Solution LiBr mass fraction; c) HTF temperature at the desorber; d) HTF temperature at the condenser.

From Figures 2.20 and 2.21 it can be observed that the inlet/outlet differences associated to x_{LiBr} , $T_{htf/ad}$, $T_{htf/ec}$ and the desorbed water mass flow $-\dot{m}_{H_2O, abs/des}$ decrease with the increase of the inlet LiBr mass fraction x_{LiBr_i} . This physical behavior is due to the inlet solution conditions being different from equilibrium conditions: For a given inlet solution temperature and pressure, the weaker the inlet solution mass fraction, the larger the difference to the equilibrium concentration along the plate is; hence, the bigger the desorption (water mass flow from the bulk to the interface) and inlet/outlet temperature and concentration differences.

A complementary reason associated to the observed behavior is related to the hypothesis that the pressure is constant at all points along the desorber; this latter means that the interface equilibrium mass fraction in the film is only a function of the interface temperature. Considering that the solution bulk and interface mass fractions should not be more than 1% apart (very thin film), in cases in which the inlet solution concentration is low (48% compared to 60%) the interface temperature should be also low, given as a consequence a bigger temperature difference between the desorber HTF and the solution film interface (in desorption processes $T_{htf/ad} > T_{stint}$), reinforcing the heat and mass transfers across the film⁽¹⁾.

⁽¹⁾ The temperature and LiBr mass concentration variations along the film for the desorption/condensation reference case when x_{LiBr_i} is 48% and 60% are shown in Annex B1.7.

In order to study the performance of the system in desorption/condensation coupled processes, an indicator has been selected: the desorbed water mass flow, $-\dot{m}_{H_2O, abs/des}$ (it can give information on the time and energy needed to completely charge an interseasonal heat storage system). A parametrical study of the influence of the variation of the exchangers inlet working conditions on the system performance, considering the indicator described above, is shown below.

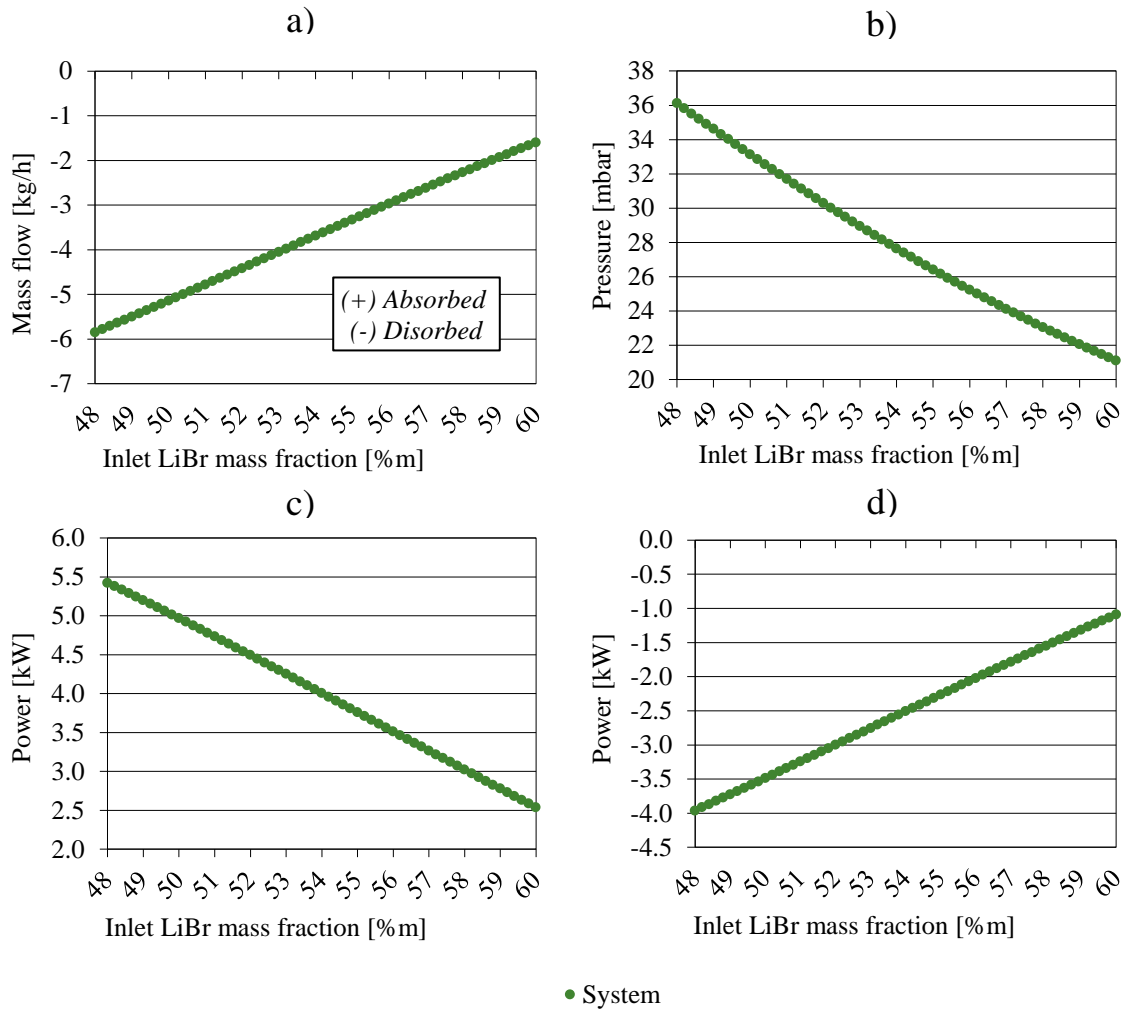


Figure 2.21. Exchangers performance in the desorption/condensation coupled process. a) Water mass flow desorbed from the LiBr solution falling film; b) Pressure of the vapor system; c) Thermal output of the HTF in the desorber; d) Thermal output of the HTF in the condenser.

The considered inlet parameters, and their variations, are described in Table 2.5.

A total of 13 cases, including the reference case, were simulated. Each simulation case considered constant inlet conditions except the LiBr mass inlet fraction which varied from 0.48 to 0.60. The performance of each simulated case respect to the reference case was evaluated through the indicator which is defined in equation (2.35). Performance comparisons between the simulated cases and the reference case (see Table 2.5) are shown in Figure 2.22.

$$\text{Des. water mass flow indicator} = \left(\frac{(-\dot{m}_{H_2O, abs/des_{var\ case}}) - (-\dot{m}_{H_2O, abs/des_{ref\ case}})}{-\dot{m}_{H_2O, abs/des_{ref\ case}}} \right) \times 100 \quad (2.35)$$

Table 2.5. Inlet conditions considered for the study of desorption/condensation process performance.

	Inlet parameters	Reference simulation case ⁽¹⁾	Parameters variation ⁽²⁾				
Desorber	\dot{m}_{st_i} [kg/h]	60	25	50	100	150	250
	\dot{m}_{htf/ad_i} [kg/h]	300	200	400			
	T_{htf/ad_i} [°C]	70	50	60	80		
Condenser	\dot{m}_{htf/ec_i} [kg/h]	300	200	400			
	T_{htf/ec_i} [°C]	15	30				

Figure 2.22a shows that the desorbed water mass flow decreases when the inlet solution mass flow increases (change from 60 kg/h to 100, 150 and 250 kg/h). This is because at higher solution mass flows the film thickness is increased, generating a bigger thermal resistance across the film and, as a result, a reduction in the amount of desorbed water. At an inlet solution mass flow of 50 kg/h the desorbed water lightly increases; nevertheless, at a solution inlet mass flow of 25 kg/h the amount of desorbed water decreases again. This latter behavior indicates that when varying the inlet solution mass flow the simulation model calculates an “optimal” value in which the desorbed water is maximal (in this case around 50 - 60 kg/h). A detailed explanation of this was given in section 2.1.2.2 and is based on the fact that the model does not consider a wave appearance at the vapor/film interface at any Reynolds number, which at high Reynolds numbers would permit to increase the desorbed water flow despite the increase of the thermal resistance.

In Figures 2.22b and 2.22c is observed that the desorbed water is increased when the desorber and condenser HTF inlet mass flows are increased, respectively. This behavior is in agreement with the direct correlation between the convective heat transfer coefficient ($h_{T_{htf,w}}$) in the HTFs and the HTF Reynolds number (see equations 2.21 and 2.38), considering that the HTF canal thickness is constant. Hence, an increase of the HTF mass flow will increase the heat flow across the desorber (condenser), generating a higher desorbed (condensed) water mass flow.

In Figure 2.22d is observed that the desorbed water increases with the HTF inlet temperature in the desorber. This correlation is reasonable since a higher source temperature permits a higher heat flow from the HTF to the solution film, permitting more water to be desorbed. Nevertheless, when the HTF inlet temperature is reduced to 60°C and for a solution at around an inlet solution concentration of 56%, the amount of desorbed water is zero (indicator has a “-100%” value); this latter is explained analyzing more in detail the mass transfer along the desorber. During the desorption/condensation process the solution film, in general, enters the desorber at an under-saturated state, producing at first a vapor absorption in the first centimeters of the desorber and subsequently a vapor desorption along the remaining desorber plate length, giving as a global result a positive desorbed water mass flow (desorbed water > absorbed water). Nevertheless, in the case where $T_{htf/ad_i} = 60^\circ\text{C}$ and $x_{LiBr_i} > 56\%$, the amount of absorbed and desorbed water along the plate are equal, giving as a global result no water being desorbed. Furthermore, since the condenser only works as a “cold plate” (no water film is injected at the top), there cannot be an overall absorbed water mass flow in desorption/condensation operating mode since there is no available water to be evaporated from the condenser⁽³⁾.

⁽¹⁾ Complementary information of the inlet conditions associated to the reference case are showed in Table 2.4.

⁽²⁾ Each value is associated to a simulation case where only the indicated parameter has been modified with respect to the reference case.

⁽³⁾ Further detail on the temperature and LiBr mass concentration variations along the solution film for a desorption/condensation case (reference case) when x_{LiBr_i} is 48% and 60% are shown in Annex B1.7.

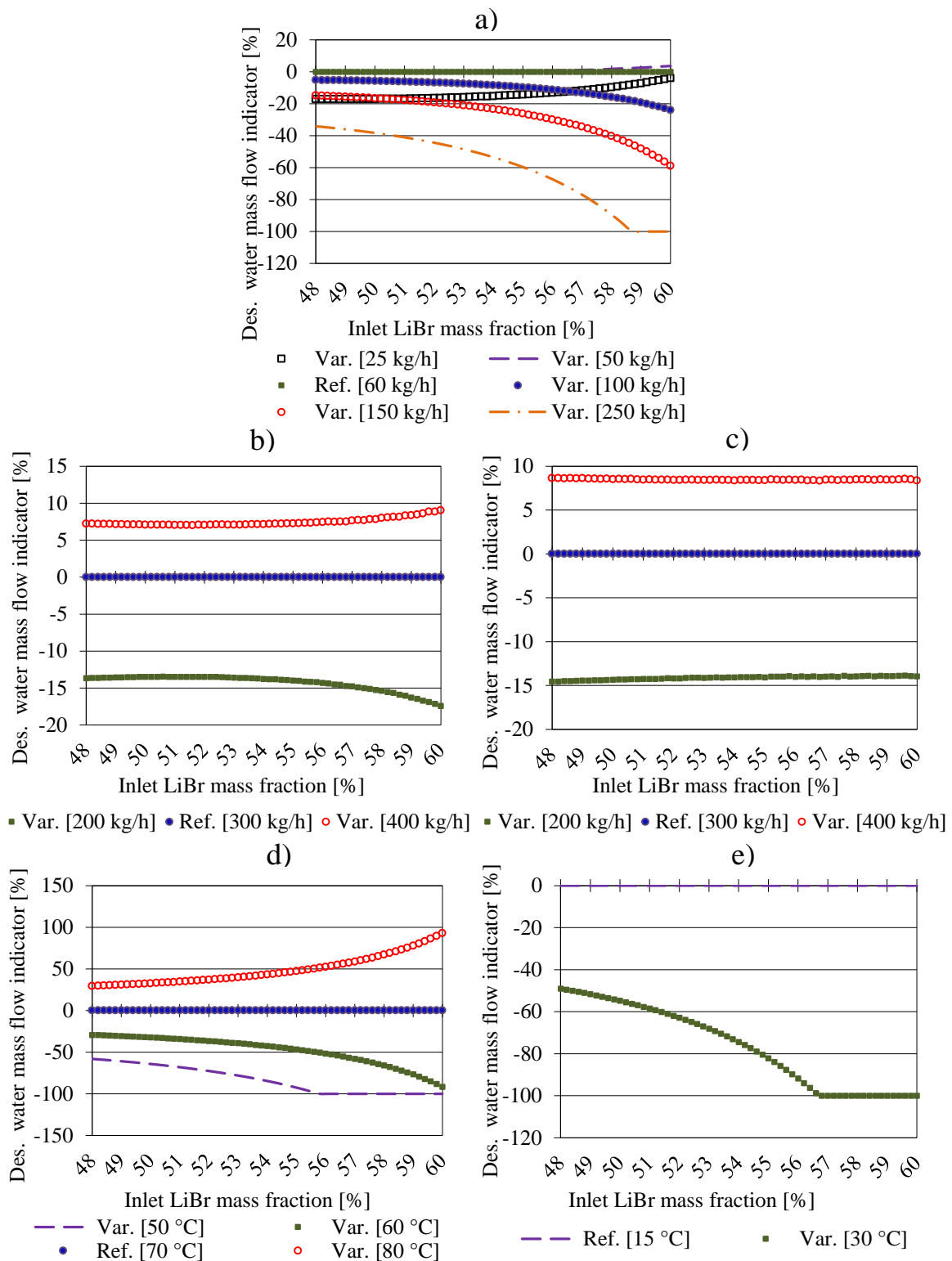


Figure 2.22. Evaluation of the desorbed water mass flow indicator as a function of the inlet LiBr mass concentration for different inlet parameters. a) LiBr solution inlet mass flow; b) Desorber HTF inlet mass flow; c) Condenser HTF inlet mass flow; d) Desorber HTF inlet temperature; e) Condenser HTF inlet temperature.

Figure 2.22e shows that the desorbed water decreases when the HTF inlet temperature in the condenser is increased. This correlation is due to the direct dependence between the HTF condenser temperature and the

vapor pressure in the reactor: since vapor is considered to be in saturated conditions⁽¹⁾, the vapor pressure will be defined by the temperature of the water film formed in the condenser (which is close to the HTF condenser temperature). Hence, at higher HTF condenser temperatures the vapor pressure in the reactor is increased. This affects the performance in the desorber since at high pressures and high solution inlet mass fractions, the temperature of the solution film interface is also increased, reducing the temperature difference between this latter and the desorber HTF; which, at the same time, reduces the heat flow across the desorber.

Average values of the desorbed water mass flow indicator for each simulated case is shown in Figure 2.23; the considered LiBr solution inlet mass flow rang for this average was [0.48-0.60]. One of the parameters that has the highest influence on the system performance in desorption/condensation operating mode is the HTF inlet temperature at the desorber and condenser.

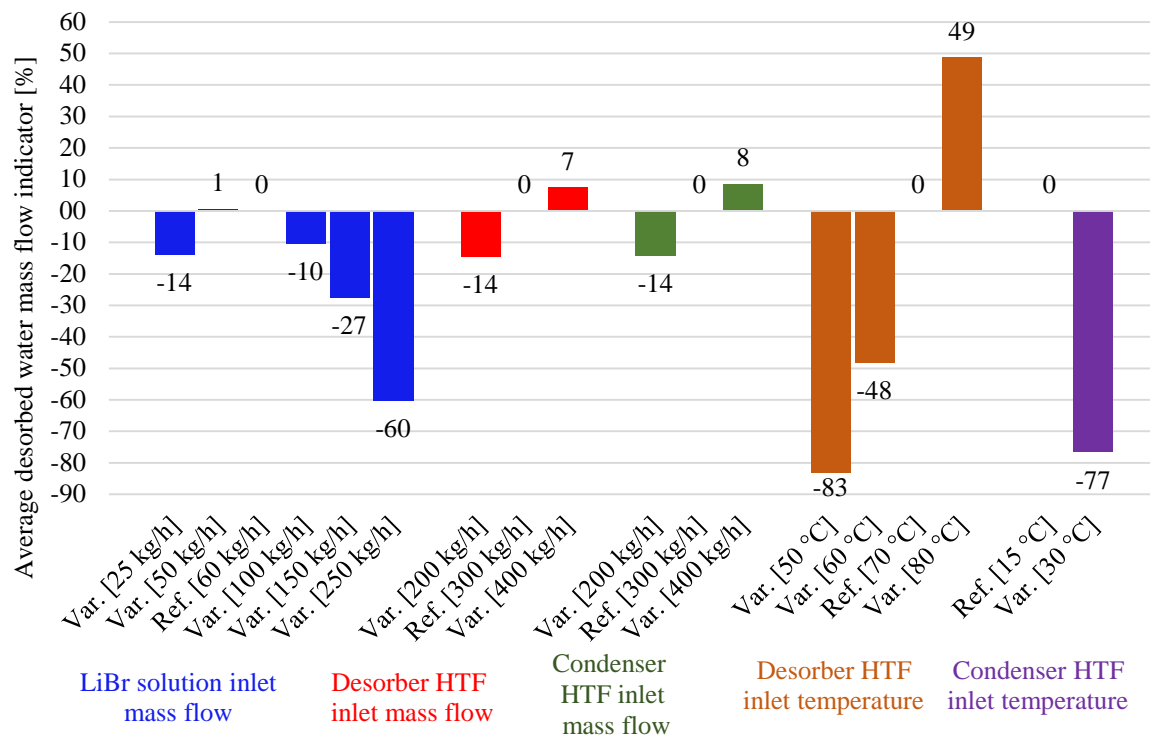


Figure 2.23. Synthesis of the evolution of the average desorbed water mass flow indicator for the different simulated cases.

2.1.3.1.2. Simulated absorption/evaporation process performance

A reference case describing an ideal absorption cycle is proposed in this section. Inlet conditions used for the simulation of this reference case are described in Table 2.6.

The physical parameters considered for this analysis were: T_{st_o} , x_{LiBr_o} , T_{htf/ad_o} , T_{htf/ec_o} , $\dot{m}_{H_2O, abs/des}$, P_{vap} , which are the system outlet conditions for the LiBr solution, water film and HTF, and also $W_{htf/ad}$ and $W_{htf/ec}$ ⁽²⁾, which are the thermal output given from each HTF to the coupled process. Figures 2.24 and 2.25 show the simulated behavior of the considered outlet parameters with respect to the inlet LiBr solution mass fraction, x_{LiBr_i} .

⁽¹⁾ In condensation/desorption operation the vapor is generally overheated; nevertheless, for simulation simplicity purposes it has been considered that the vapor is in saturated conditions during the condensation process.

⁽²⁾ The energy power given from each HTF to the system for both, the absorber and the evaporator, has been calculated with the following correlation: $W_{htf} = \dot{m}_{htf_i} \times c_{p_{htf}} \times (T_{htf_i} - T_{htf_o})$

Table 2.6. Reference case inlet conditions considered for the LiBr solution falling film, water falling film and HTF (discharge mode)⁽¹⁾

Absorber	\dot{m}_{st_i} [kg/h]	T_{st_i} [°C]	x_{LiBr_i} [m_LiBr/m_st]	\dot{m}_{htf/ad_i} [kg/h] ⁽²⁾	T_{htf/ad_i} [°C]	Direction movement	Wetted surface percentage [%] ⁽³⁾⁽⁴⁾
		110	24	[0.48 – 0.60]	300	25	Counter- current
Evaporator	$\dot{m}_{f_water_i}$ [kg/h]	$T_{f_water_i}$ [°C]		\dot{m}_{htf/ec_i} [kg/h]	T_{htf/ec_i} [°C]	Direction movement	Wetted surface percentage [%]
	110	15		300	15	Counter- current	79.6

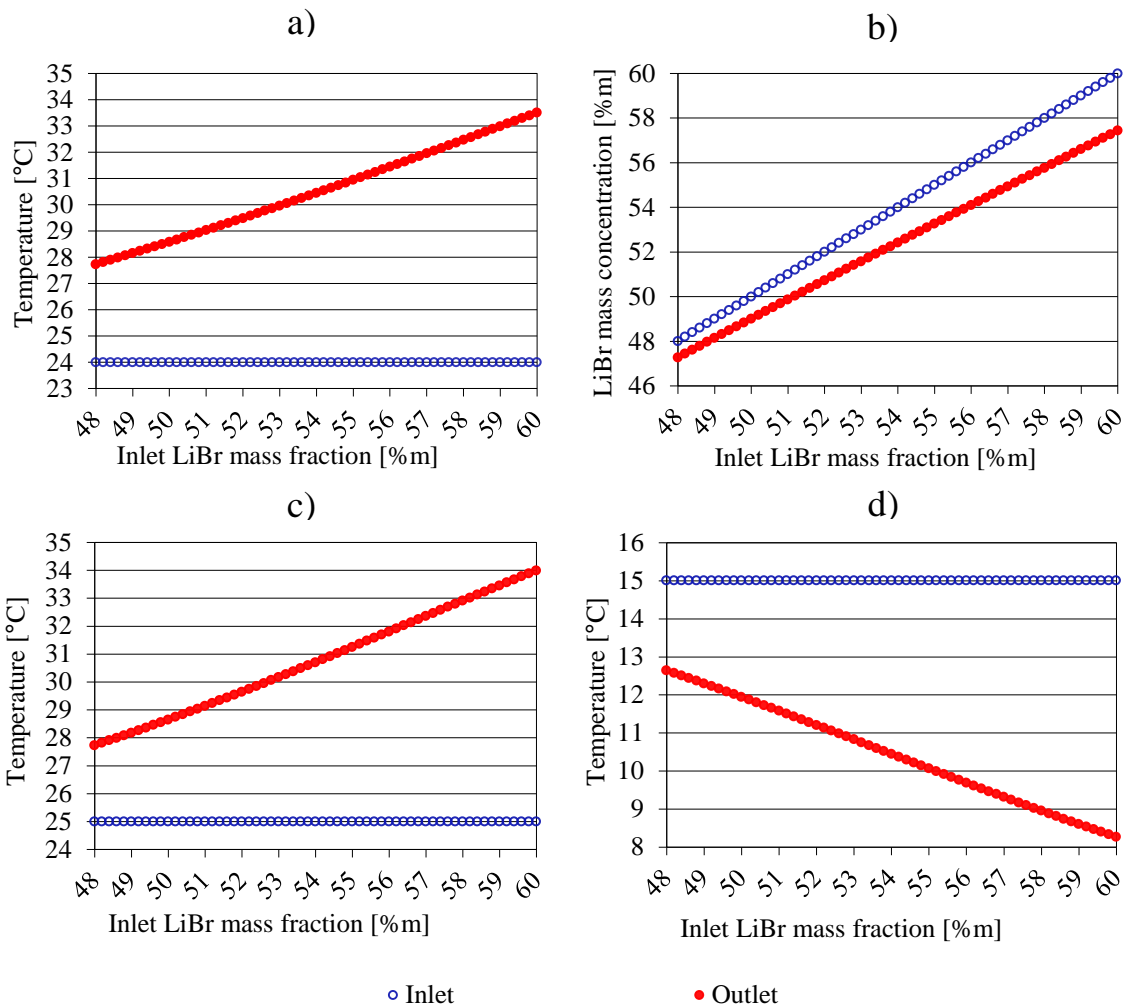


Figure 2.24. Exchangers performance in the absorption/evaporation process. a) LiBr solution temperature; b) LiBr mass fraction in the solution; c) HTF temperature in the absorber; d) HTF temperature in the evaporator.

⁽¹⁾ The inlet conditions in Table 2.6 were in the same order of magnitude as those considered in section 2.1.2.3.3.

⁽²⁾ The considered HTF for these simulations was water.

⁽³⁾ The value for the wetted surface percentage was calculated under the hypothesis that the LiBr solution or distilled water falling films completely wet the grooved sections. In the absorber and evaporator the value is 79.6% since there is a spacing between each groove.

⁽⁴⁾ For cases in which the surfaces are not completely wet, an optimist heat transfer mode across the plates (1F) was considered (see section 2.1.1.5).

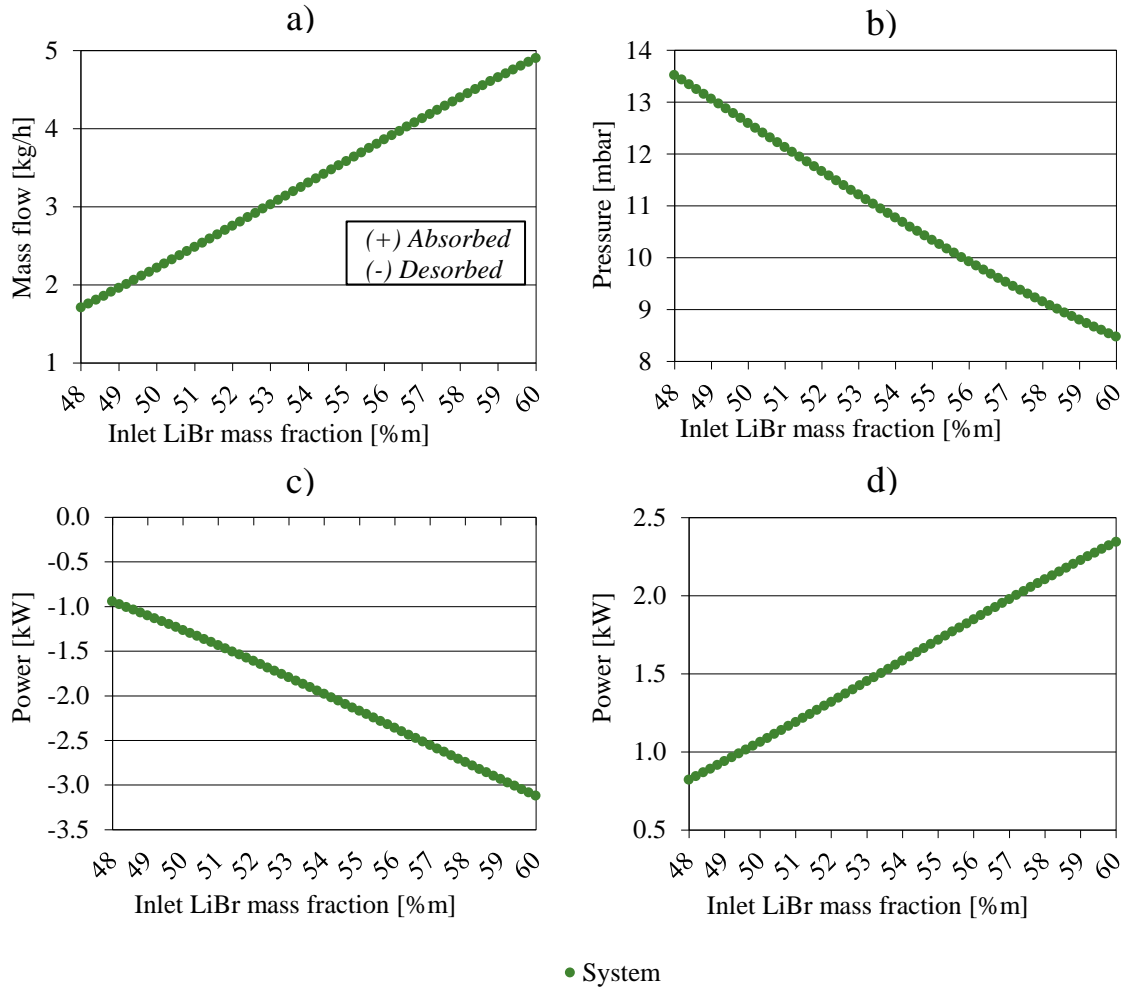


Figure 2.25. Exchangers performance in the absorption/evaporation process. a) Water mass flow absorbed by the LiBr solution; b) Pressure of the vapor; c) Thermal output from the HTF in the absorber; d) Thermal output from the HTF in the evaporator.

From Figures 2.24 and 2.25 it can be observed that the inlet/outlet differences associated to T_{st} , x_{LiBr} , $T_{htf/ad}$, $T_{htf/ec}$ and the absorbed water mass flow $\dot{m}_{H_2O, abs/des}$ increase with the inlet LiBr mass fraction $x_{LiBr,i}$. Similarly, to the desorption/condensation process, this behavior is also due to the inlet solution conditions being different from equilibrium conditions. In addition, for a constant pressure along the absorber, the interface equilibrium mass fraction can be considered a function of the interface temperature. Also, the solution bulk and interface mass fraction differences should not be higher than 1% due to the very thin film thickness⁽¹⁾.

In order to study the performance of the system in absorption/evaporation processes, another indicator has been selected: the absorber HTF outlet temperature, T_{htf/ad_o} (T_{htf/ad_o} can give information of the potential use of the interseasonal heat storage system for building heating applications). A parametrical study of the influence of the heat exchangers inlet working conditions on the system performance, considering this indicator, is shown below. The considered inlet parameters are described in Table 2.7.

⁽¹⁾ The temperature and LiBr mass fraction along the film for the absorption/evaporation reference case when $x_{LiBr,i}$ is 48% and 60% are shown in Annex B1.7.

Table 2.7. Inlet conditions considered for the study of the absorption/evaporation process

	Inlet parameters	Reference simulation case ⁽¹⁾	Parameters variation ⁽²⁾			
			50	80	150	250
Absorber	\dot{m}_{st_i} [kg/h]	110	50	80	150	250
	\dot{m}_{htf/ad_i} [kg/h]	300	100	200	400	
	T_{htf/ad_i} [°C]	25	20	30	40	
Evaporator	$\dot{m}_{f_water_i}$ [kg/h]	110	50	80	150	250
	\dot{m}_{htf/ec_i} [kg/h]	300	100	200	400	
	T_{htf/ec_i} and $T_{f_water_i}$ [°C]	15	5	10	30	

A total of 21 cases, including the reference case, were simulated. Each simulation case considered constant inlet conditions except the LiBr mass inlet concentration which varied from 0.48 to 0.60. The performance of each simulated case with respect to the reference case was evaluated through one indicator, defined in equation (2.36). Performance comparisons between the simulated cases and the reference case are shown in Figure 2.26.

Abs. HTF temperature indicator =

$$\left(\frac{\left(T_{htf/ad_o} - T_{htf/ad_i} \right)_{var\ case} - \left(T_{htf/ad_o} - T_{htf/ad_i} \right)_{ref\ case}}{\left(T_{htf/ad_o} - T_{htf/ad_i} \right)_{ref\ case}} \right) \times 100 \quad (2.36)$$

In general, the influence of the inlet conditions on the system performance was similar to the desorption/condensation cases described in the previous section.

Figure 2.26a shows that the absorber HTF outlet temperature decreases with the solution inlet mass flow increase. This is again due to the increase of the film thermal resistance.

Figure 2.26b shows that the absorber HTF outlet temperature increases with the water film inlet mass flow in the evaporator; nevertheless, at a very high water film flow (>500 kg/h) the absorber HTF outlet temperature should decrease due to the film thickness increase, in a similar behavior to the case shown in Figure 2.22a (desorption/condensation) where an “optimal mass flow value” is found. However, the optimal value in this case is different from the one in the desorption mode since physical properties, such as viscosity, are different.

Figure 2.26c shows that when the absorber HTF inlet mass flow (\dot{m}_{htf/ad_i}) is increased the absorber HTF temperature indicator is reduced. This is associated to the mass energy balance in the absorber HTF. Whenever \dot{m}_{htf/ad_i} increases the absorber thermal output also increases due to a higher convective heat transfer coefficient. Nevertheless, at the same time the absorber HTF inlet/outlet temperature gap ($T_{htf/ad_o} - T_{htf/ad_i}$) is reduced since, despite the higher absorber thermal output, the amount of HTF (\dot{m}_{htf/ad_i}) where this heat must be distributed has also increased⁽³⁾.

In Figure 2.26d is observed that the absorber HTF inlet/outlet temperature difference ($T_{htf/ad_o} - T_{htf/ad_i}$) is increased when the evaporator HTF mass flow is increased. This is due to a higher convective heat transfer coefficient in the evaporator HTF, permitting an increase in the heat flow across the evaporator and, consequently, a higher evaporated water mass flow.

Figure 2.26e shows that when the absorber HTF inlet temperature (T_{htf/ad_i}) is increased the absorber HTF inlet/outlet temperature gap ($T_{htf/ad_o} - T_{htf/ad_i}$) is reduced. In these cases, the vapor pressure proportionally

⁽¹⁾ Complementary information of the inlet conditions associated to the reference case are shown in Table 2.6.

⁽²⁾ Each value is associated to a simulation case where only the indicated parameter has been modified with respect to the reference case.

⁽³⁾ As a result of this analysis, for potential heat storage applications a good agreement between the desired absorber HTF outlet temperature and the absorber HTF thermal output should be found when the absorber HTF mass flow is defined.

increases from around 10 mbar to 15 mbar. Although an increase in the vapor pressure would produce a higher solution film interface temperature (same solution inlet mass fraction in all cases), this temperature increase (from around 32°C to 40°C) happens not to be high enough to heat the absorber HTF.

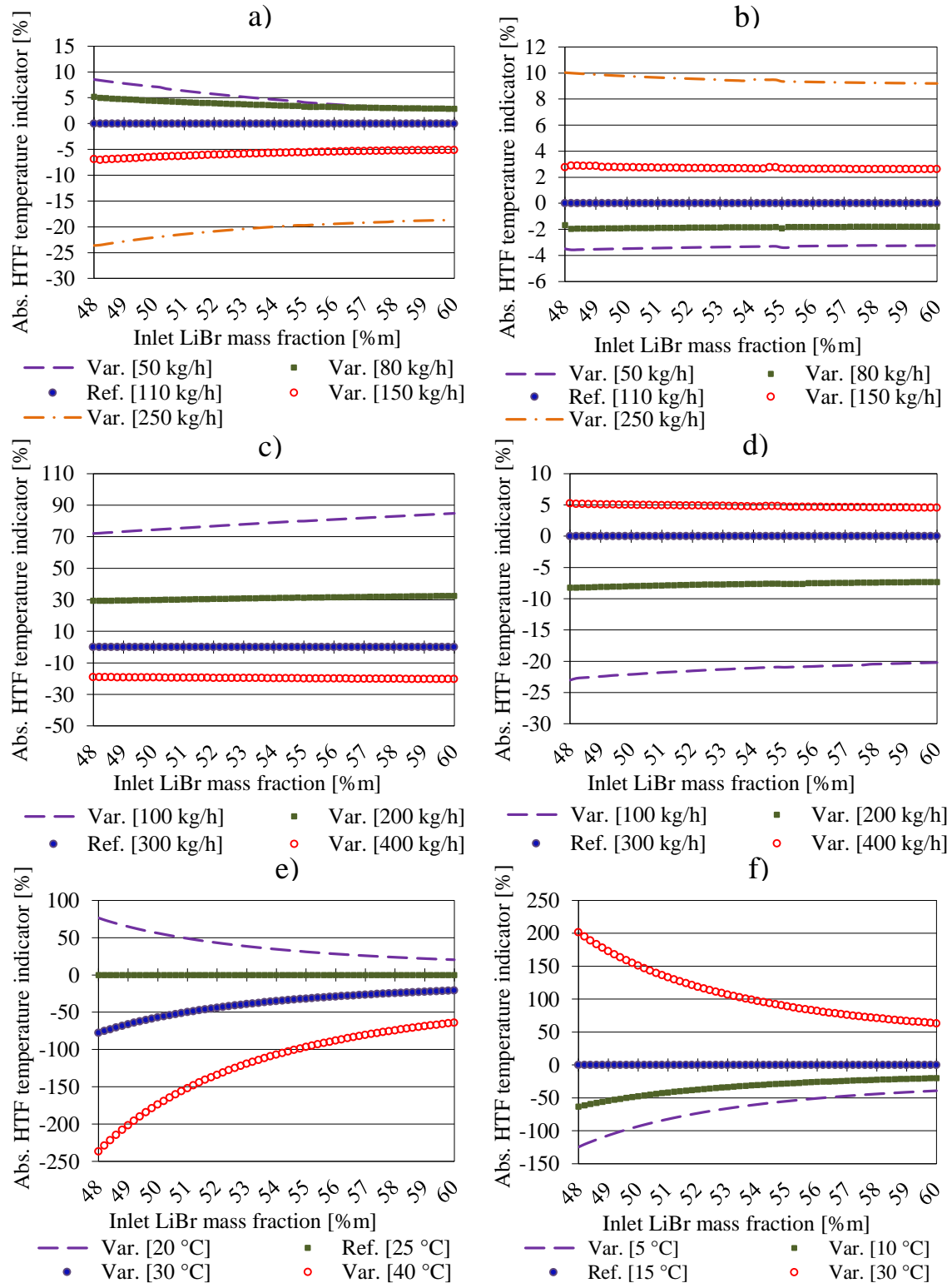


Figure 2.26. Evaluation of the absorber HTF temperature indicator as a function of the inlet LiBr mass fraction for different inlet parameters. a) LiBr solution inlet mass flow; b) Water film inlet mass flow; c) Absorber HTF inlet mass flow; d) Evaporator HTF inlet mass flow; e) Absorber HTF inlet temperature; f) Water film and Evaporator HTF inlet temperatures.

Figure 2.26f shows that the absorber HTF outlet temperature, T_{htf/ad_o} , increases with the water film and evaporator HTF inlet temperatures, $T_{f_water_i}$ and T_{htf/ec_i} . This is associated to the increase of the vapor pressure whenever $T_{f_water_i}$ and T_{htf/ec_i} are increased, permitting a higher solution film interface temperature and, hence, a higher heat transfer across the solution film.

Average values of the absorber HTF temperature indicator for each simulated case are shown in Figure 2.27; the considered LiBr solution inlet mass flow range for this average was [0.48-0.60].

From this study, it can be highlighted that the parameters that have the highest influence on the system performance in absorption/evaporation operating mode are the absorber HTF inlet temperature, the absorber HTF inlet mass flow and the water film and evaporator HTF inlet temperatures.

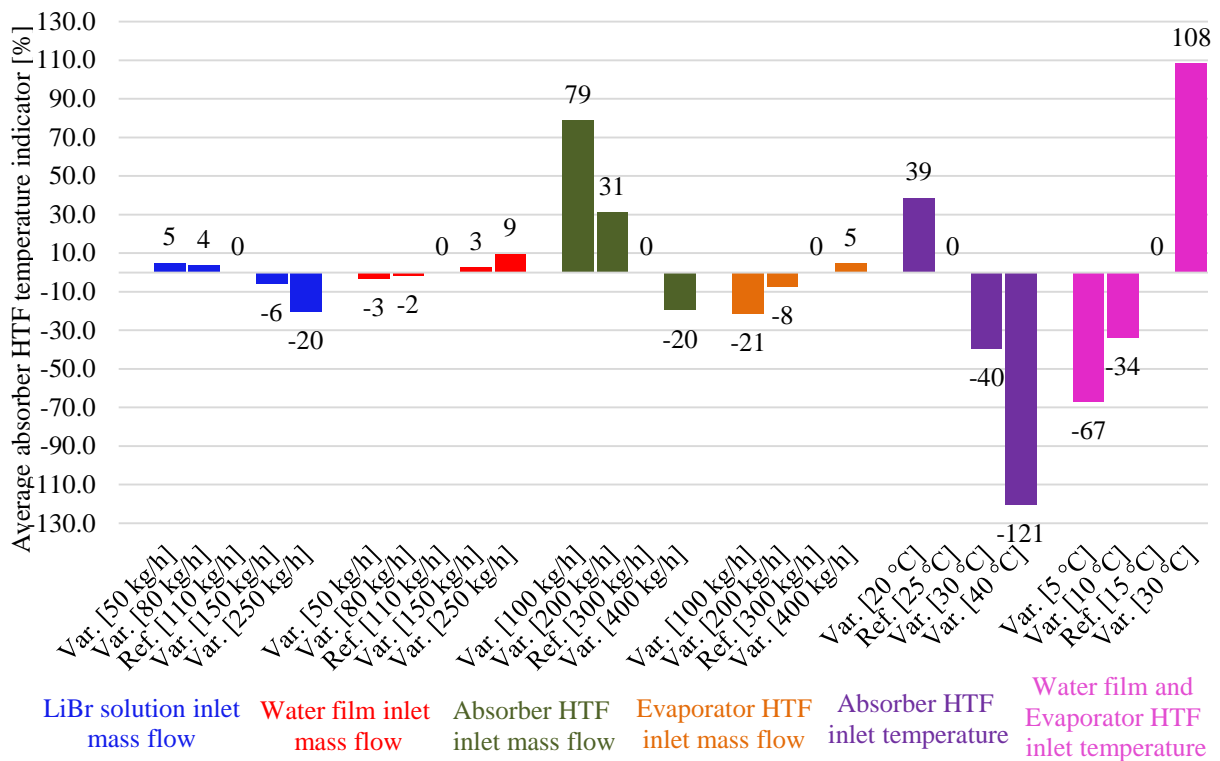


Figure 2.27. Synthesis of the evolution of the average absorber HTF temperature indicator for the different simulated cases.

2.1.3.2. Optimized working conditions

Optimized inlet working conditions to improve the system performance in desorption/condensation and absorption/evaporation operating modes have been selected considering the parametric study carried out in section 2.1.3.1. The system response under these optimized conditions has been simulated and the results are shown in sections below.

2.1.3.2.1. Simulated desorption/condensation process

Inlet working conditions for the optimized cases and the reference case (see section 2.1.3.1.1) are shown in Table 2.8.

Table 2.8. System inlet working conditions considered for the reference and optimized cases in the desorption/condensation operating mode.

	Inlet parameters	Reference simulation case	Optimized simulation case 1	Optimized simulation case 2
Desorber	\dot{m}_{st_i} [kg/h]	60	60	60
	T_{st_i} [°C]	24	24	24
	x_{LiBr_i} [m_LiBr/m_st]	[0.48 – 0.60]	[0.48 – 0.60]	[0.48 – 0.60]
	\dot{m}_{htf/ad_i} [kg/h]	300	400	400
	T_{htf/ad_i} [°C]	70	70	70
	Direction type	Counter-current	Counter-current	Co-current
	Wetted surface percentage [%]	79.6	79.6	79.6
Condenser	$\dot{m}_{f_water_i}$ [kg/h]	0	0	0
	$T_{f_water_i}$ [°C]	--	--	--
	\dot{m}_{htf/ec_i} [kg/h]	300	400	400
	T_{htf/ec_i} [°C]	15	15	15
	Direction type	Counter-current	Counter-current	Co-current
	Wetted surface percentage [%]	100	100	100

As shown in Table 2.8, the parameters modified for optimization purposes were the solution inlet mass flow (\dot{m}_{st_i}), the desorber HTF inlet mass flow (\dot{m}_{htf/ad_i}), the condenser HTF inlet mass flow (\dot{m}_{htf/ec_i}) and the fluids direction type at each exchanger. These parameters have the characteristic of being easy to control by the use of pumps and valves. Conversely, parameters such as the inlet solution temperature (T_{st_i}), inlet desorber HTF temperature (T_{htf/ad_i}) and inlet condenser HTF temperature (T_{htf/ec_i}) are more difficult to control and would imply additional costs in an interseasonal heat storage system⁽¹⁾.

HTF inlet mass flows in the desorber and condenser (\dot{m}_{htf/ad_i} and \dot{m}_{htf/ec_i}) were chosen at 400 kg/h since, as shown in Figures 2.22, an increase of these parameters leads to a rise in the desorbed water mass flow. Even

⁽¹⁾ For example, T_{st_i} can be partially controlled since this solution is pumped from the solution tank, which can be placed underground. If the tank is not insulated, the ground can work as a cooling source; nevertheless, even in this case it is very probable that the solution tank temperature increases after a system charging process. Furthermore, for long term heat storage purposes an insulated solution tank is highly recommended (see studied cases in Chapter 1).

The desorber HTF temperature, T_{htf/ad_i} , required for the desorption/condensation process is usually provided by a solar collector; hence, a precise control of this parameter could imply the use of an additional heat source such as an electrical heater. Although only mass flow parameters have been considered for this optimization, application of the interseasonal heat storage system in dwelling heating cases would also require a dimensioning study of the solar collector surface in order to meet adequate absorber HTF inlet temperature ranges (T_{htf/ad_i}) permitting to completely charge the system.

higher HTF mass flows values could thus have been considered; nevertheless, this would also imply higher-pressure losses and this higher pumping consumption.

Simulated results of the system response in cases described in Table 2.8. are shown in Figure 2.28.

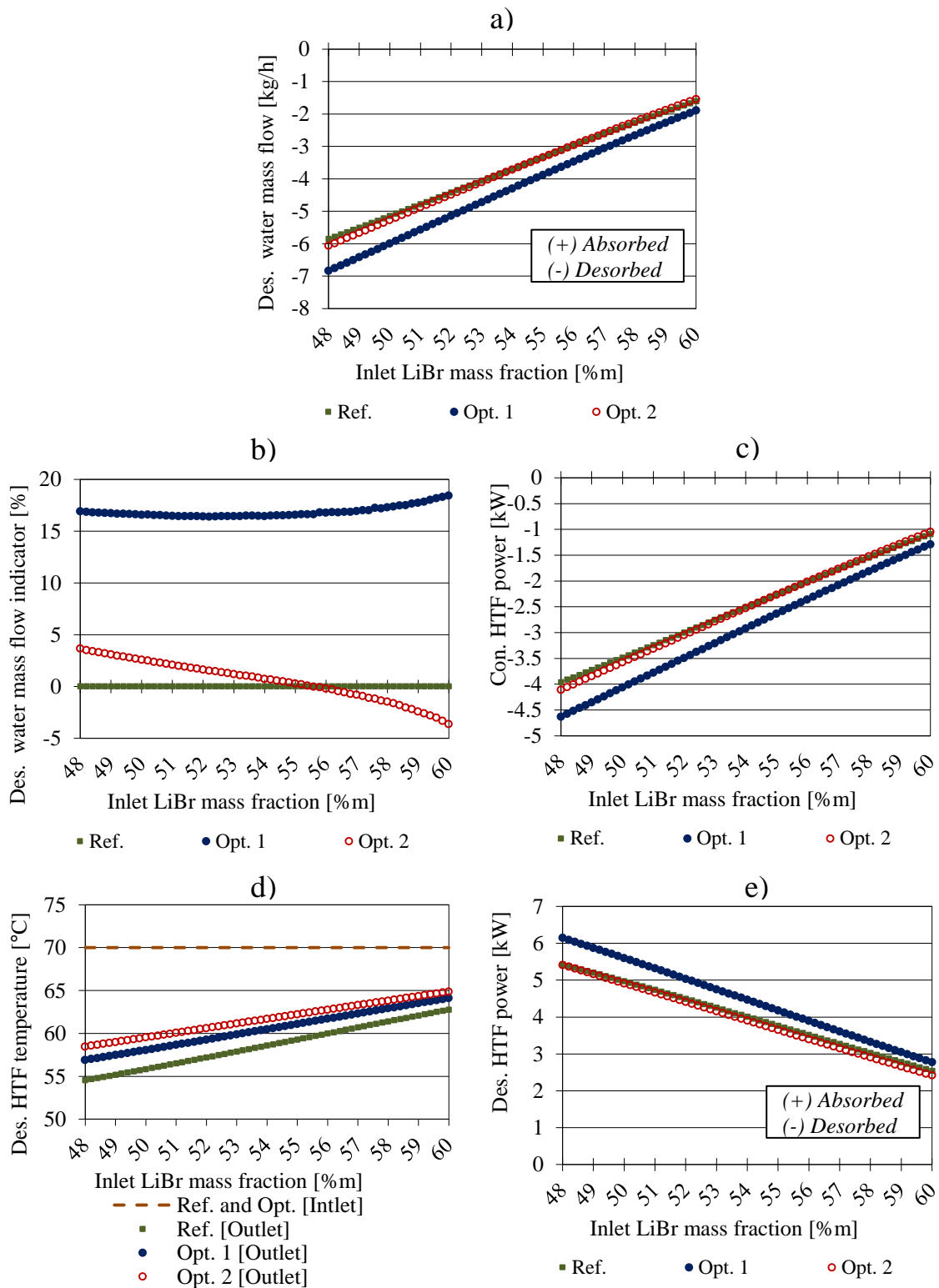


Figure 2.28. Desorption/condensation performance as a function of the inlet LiBr mass fraction for the optimized and reference simulation cases. a) Desorbed water mass flow; b) Desorbed water mass flow indicator; c) Condenser HTF thermal output; d) Desorber HTF temperature; e) Desorber HTF thermal input

In Figure 2.28 is observed that the system performance in the optimized case 1 is better than in the reference case and that the optimized case 2 has a response similar to the reference case. The performance indicators responses (optimized case 1 and reference case) are summarized below:

- For the desorbed water mass flow, $-\dot{m}_{H_2O, abs/des}$: it increased, at $x_{LiBr_i} = 0.48$, from 6 kg/h to 7 kg/h while that, at $x_{LiBr_i} = 0.60$, it increased from 1.6 kg/h to 1.9 kg/h (representing a relative increase of 16% and 19% respectively).
- For the thermal output of the HTF in the condenser, $-W_{htf/ec}$ increased, at $x_{LiBr_i} = 0.48$, from 4 kW to 4.6 kW while, at $x_{LiBr_i} = 0.60$, it increased from 1 kW to 1.3 kW (representing a relative increase of 15% and 30% respectively).
- For the desorber HTF temperature difference, $T_{htf/ad_o} - T_{htf/ad_i}$: a decrease of about 3 K is observed compared to the reference case.
- The thermal HTF input at the desorber increased, at $x_{LiBr_i} = 0.48$, from 5.4 kW to 6.1 kW while that, at $x_{LiBr_i} = 0.60$, it increased from 2.4 kW to 2.8 kW.

In general, in desorption/condensation processes a co-current configuration (Opt. case 2) has a less optimal performance than a counter-current configuration (Opt. case 1).

2.1.3.2.2. Simulated absorption/evaporation process

Considering the results obtained in section 2.1.3.1.2 for the parametrical study of the inlet working conditions influence on the system performance in absorption/evaporation operating mode; two optimized cases permitting to have a higher performance have been selected. It must be remarked that the optimized cases were selected giving more importance to obtain a higher absorber HTF outlet temperature, T_{htf/ad_o} , even at the cost of reducing the absorber HTF power (power given from the system to the HTF in the absorber), $-W_{htf/ad}$.

Inlet conditions for the optimized cases and the reference case (see section 2.1.3.1.2) are shown in Table 2.9. Simulated system response is shown in Figure 2.29.

Similarly to the desorption/condensation cases described in the previous section, the parameters susceptible to be modified for optimization purposes were the solution inlet mass flow (\dot{m}_{st_i}), the water film mass flow ($\dot{m}_{f_water_i}$), the desorber HTF inlet mass flow (\dot{m}_{htf/ad_i}), the condenser HTF inlet mass flow (\dot{m}_{htf/ec_i}) and the fluids direction type at each exchanger.

For example an 80 kg/h mass flow was considered for \dot{m}_{st_i} since it belongs to the values range in which the absorber HTF temperature indicator is maximum (see Figure 2.26a). For $\dot{m}_{f_water_i}$ a value of 150 kg/h was selected which is lightly higher than the reference case value (110 kg/h), permitting an increase of about 3% of the system performance (see Figure 2.26b); higher mass flows could have been considered but this value was chosen for experimental purposes shown in the next chapter. For \dot{m}_{htf/ad_i} and \dot{m}_{htf/ec_i} values, a decrease and an increase with respect to the reference case was chosen, respectively: higher values for the former and lower values for the latter could have been considered but it would have implied a high reduction in the absorber HTF power and a high increase of the pressure losses, respectively.

Table 2.9. System inlet working conditions considered for the reference and optimized cases in the absorption/evaporation operating mode.

	Inlet parameters	Reference simulation case	Optimized simulation case 1	Optimized simulation case 2
Absorber	\dot{m}_{st_i} [kg/h]	110	80	80
	T_{st_i} [°C]	24	24	24
	x_{LiBr_i} [m_LiBr/m_st]	[0.48 – 0.60]	[0.48 – 0.60]	[0.48 – 0.60]
	\dot{m}_{htf/ad_i} [kg/h]	300	200	200
	T_{htf/ad_i} [°C]	25	25	25
	<i>Direction type</i>	Counter-current	Counter- current	Co- current
	<i>Wetted surface percentage</i> [%]	79.6	79.6	79.6
Evaporator	$\dot{m}_{f_water_i}$ [kg/h]	110	150	150
	$T_{f_water_i}$ [°C]	15	15	15
	\dot{m}_{htf/ec_i} [kg/h]	300	400	400
	T_{htf/ec_i} [°C]	15	15	15
	<i>Direction type</i>	Counter- current	Counter- current	Co- current
	<i>Wetted surface percentage</i> [%]	79.6	79.6	79.6

The performance indicators response is summarized below:

- Absorber HTF outlet temperature, T_{htf/ad_o} : increase, at $x_{LiBr_i} = 0.48$, from 27.7 °C to 29 °C while that, at $x_{LiBr_i} = 0.60$, it increased from 34 °C to 38 °C (representing a relative increase of around 45%).
- Thermal absorber HTF output, $-W_{htf/ad}$: decreases about 5% compared to the reference case.
- Absorbed water mass flow, $\dot{m}_{H_2O, abs/des}$: decreases from about 0.2 kg/h.
- The evaporator HTF thermal input, $W_{htf/ec}$: decreases slightly from about 0.2 kW compared to the reference case.

In general, it is observed that in absorption/evaporation processes a co-current configuration has a slightly less optimal performance than a counter-current configuration.

Results obtained in sections 2.1.3.1 and 2.1.3.2 will be used in Chapter 3 to define the tests permitting to study the experimental inlet conditions influence on the system performance. Furthermore, these results complement the annual simulation study of the heat storage system integrated in a dwelling (for covering its heating needs) that will be presented in Chapter 4.

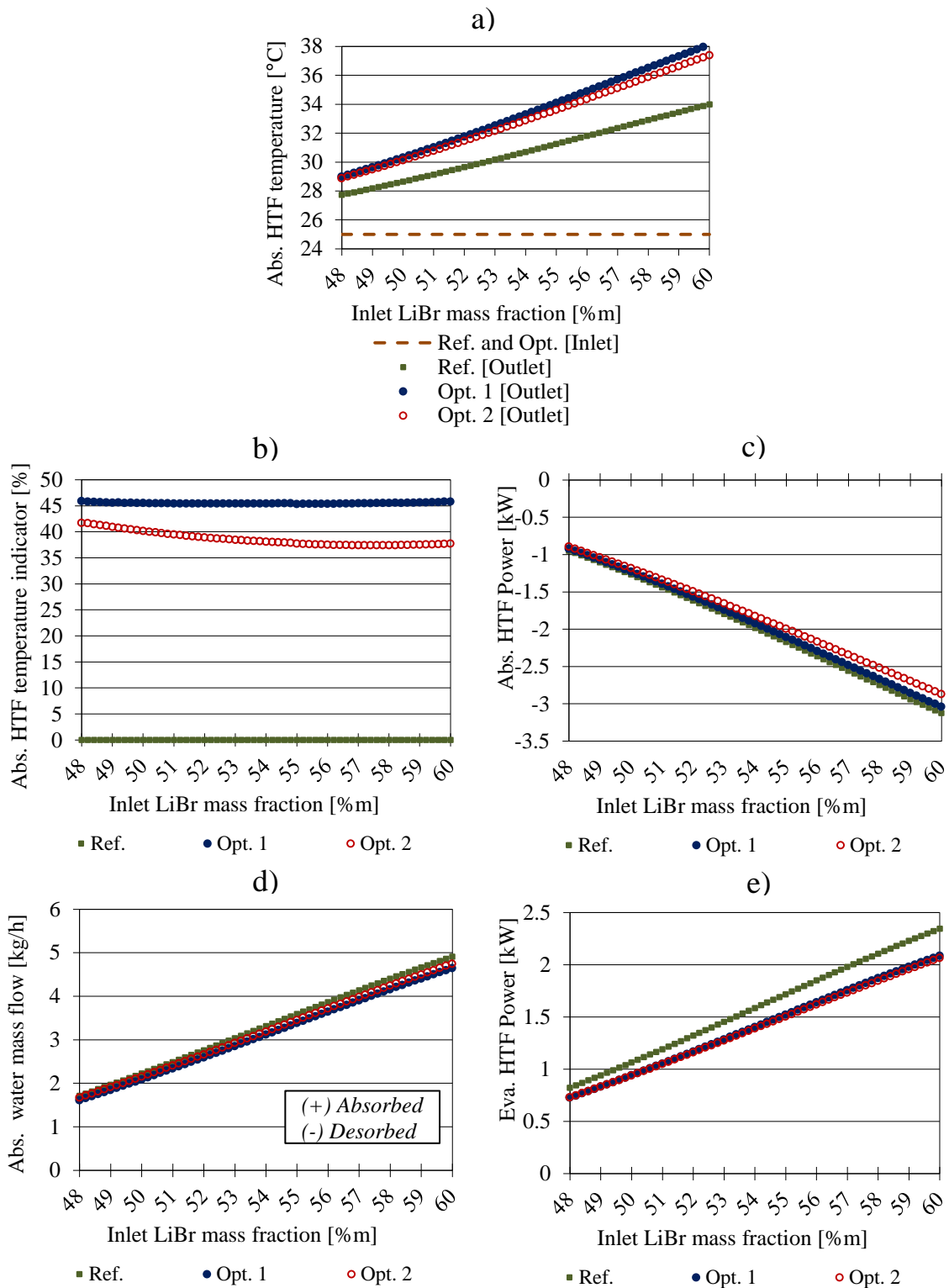


Figure 2.29. Absorption/evaporation performance as a function of the inlet LiBr mass concentration for the optimized and reference simulation cases. a) Absorber HTF temperature; b) Absorber HTF temperature indicator; c) HTF thermal output at the absorber; d) Absorbed water mass flow; e) HTF thermal input at the evaporator

2.1.4. Mesh number and fluids movement direction influence

In this section a study of the influence of the discretization mesh number and the fluid movement type on the system response has been carried out in order to identify the possible differences due to a counter-current or cocurrent operating mode as well as to identify the possibility of reducing the mesh number, and consequently the machine time, needed for each simulation.⁽¹⁾

A reference case for the desorption/condensation and the absorption/evaporation coupled process was selected and the considered inlet conditions were the same as those described in Tables 2.4 and 2.6, respectively.

Eq

All the considered simulation cases for this study are shown below in Table 2.10.

Table 2.10. Simulation cases considered for the mesh number and movement direction sensibility study in desorption/condensation and absorption/evaporation operating modes.

	Cases	Mesh number	Mesh type	Mesh growth rate [%]	Movement direction
Desorption/ Condensation	Reference case	200	Uniform	--	Counter-current
	Variable case 1	100	Uniform	--	Counter-current
	Variable case 2	50	Uniform	--	Counter-current
	Variable case 3	20	Uniform	--	Counter-current
	Variable case 4	100	Uniform	--	Cocurrent
	Variable case 5	5	Proportional	250	Cocurrent
	Variable case 6	5	Proportional	250	Counter-current
Absorption/ Evaporation	Reference case	200	Uniform	--	Counter-current
	Variable case 1	100	Uniform	--	Counter-current
	Variable case 2	50	Uniform	--	Counter-current
	Variable case 3	20	Uniform	--	Counter-current
	Variable case 4	100	Uniform	--	Cocurrent
	Variable case 5	5	Proportional	250	Cocurrent
	Variable case 6	5	Proportional	250	Counter-current

Cases shown in Table 2.10 considered two mesh types: uniform and proportional. For cases in which the mesh type is uniform all the meshes have the same length, whereas for cases in which the mesh type is proportional, one mesh is 250% longer than the previous mesh and consequently up to arriving to the final mesh. The different mesh types considered are shown in Figure 2.30.

In order to compare the different cases described in Table 2.10 with respect to the reference case, some indicators have been defined and are described below.

$$\text{Mesh indicator 1} = \left(\frac{(T_{sto} - T_{sti})_{var\ case} - (T_{sto} - T_{sti})_{ref\ case}}{(T_{sto} - T_{sti})_{var\ case}} \right) \times 100 \quad (2.37)$$

$$\text{Mesh indicator 2} = \left(\frac{(x_{LiBr_o} - x_{LiBr_i})_{var\ case} - (x_{LiBr_o} - x_{LiBr_i})_{ref\ case}}{(x_{LiBr_o} - x_{LiBr_i})_{var\ case}} \right) \times 100 \quad (2.38)$$

⁽¹⁾ In this context, the term “machine time” is defined as the time needed for a computer to simulate a determined case.

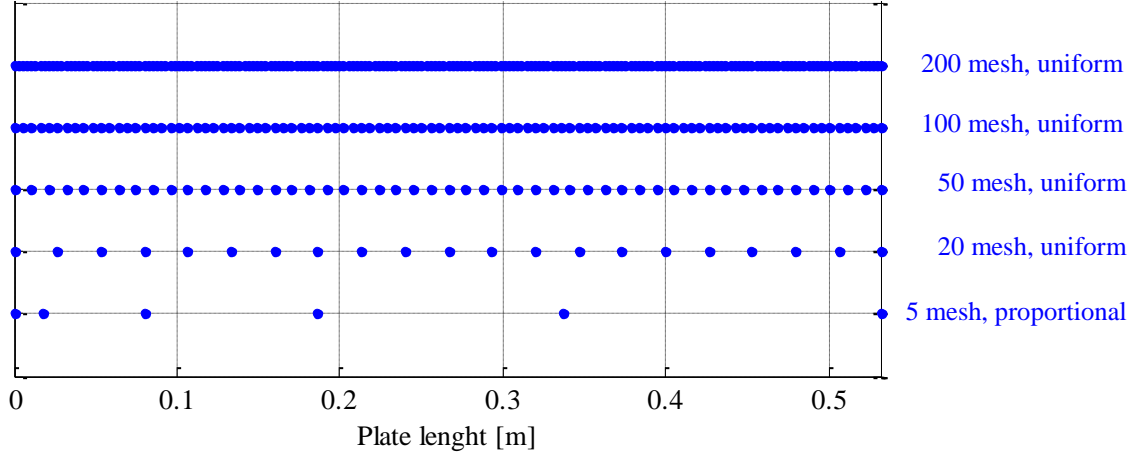


Figure 2.30. Graphical description of the different mesh types considered for the sensibility study.

$$\text{Mesh indicator 3} = \left(\frac{\dot{m}_{\text{H}_2\text{O}, \text{abs/des}_{\text{var case}}} - \dot{m}_{\text{H}_2\text{O}, \text{abs/des}_{\text{ref case}}}}{\dot{m}_{\text{H}_2\text{O}, \text{abs/des}_{\text{ref case}}}} \right) \times 100 \quad (2.39)$$

$$\text{Mesh indicator 4} = \left(\frac{P_{\text{vap}_{\text{var case}}} - P_{\text{vap}_{\text{ref case}}}}{P_{\text{vap}_{\text{ref case}}}} \right) \times 100 \quad (2.40)$$

$$\text{Mesh indicator 5} = \left(\frac{\left(T_{\text{htf/ad}_o} - T_{\text{htf/ad}_i} \right)_{\text{var case}} - \left(T_{\text{htf/ad}_o} - T_{\text{htf/ad}_i} \right)_{\text{ref case}}}{\left(T_{\text{htf/ad}_o} - T_{\text{htf/ad}_i} \right)_{\text{var case}}} \right) \times 100 \quad (2.41)$$

$$\text{Mesh indicator 6} = \left(\frac{\left(T_{\text{htf/ec}_o} - T_{\text{htf/ec}_i} \right)_{\text{var case}} - \left(T_{\text{htf/ec}_o} - T_{\text{htf/ec}_i} \right)_{\text{ref case}}}{\left(T_{\text{htf/ec}_o} - T_{\text{htf/ec}_i} \right)_{\text{var case}}} \right) \times 100 \quad (2.42)$$

Indicators defined from equations (2.41) to (2.46) are related to the LiBr solution temperature, LiBr mass fraction, desorbed/absorbed water mass flow, reactor vapor pressure, absorber/desorber HTF temperature and evaporator/condenser HTF temperature, respectively.

Figure 2.31 shows average values of the mesh indicators, defined above, in the range of x_{LiBr_i} : [0.48-0.60], for each simulation case, in desorption/condensation or absorption/evaporation mode, considered in Table 2.10.

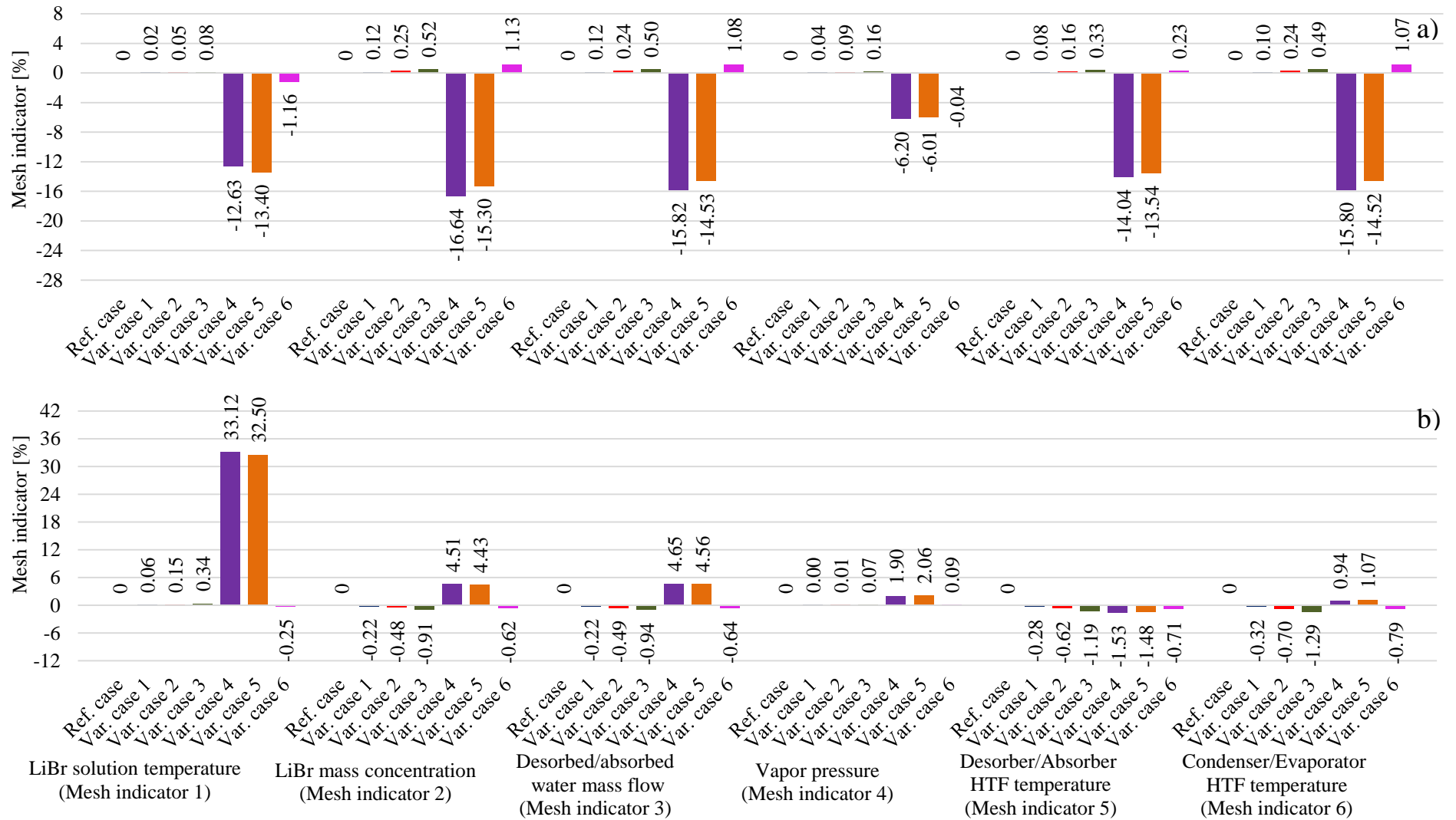


Figure 2.31. Average mesh indicators values for simulation cases with different mesh numbers and fluids movement type; a) Desorption/condensation operating mode; b) Absorption/evaporation operating mode

From Figure 2.31a it can be observed that for the simulated cases in desorption/condensation operating mode:

- The fluids movement type has an influence on the system response when counter-current and cocurrent cases are compared; with a maximum mesh indicator between “Var. case 1” and “Var. case 4” of 16.76% (“Mesh indicator 2/LiBr mass concentration”: 0.12% and -16.64%, respectively).
- According to all the mesh indicators and particularly the “mesh indicator 3” based in the desorbed water mass flow, $\dot{m}_{H_2O, abs/des}$, the performance of the desorber is better in counter-current mode than in co-current mode.
- The mesh number has a negligible influence on the system response for cases in which the fluids movement type is in counter-current; with a maximum mesh indicator difference between “Ref. case” and “Var. case 6” of 1.16% (“Mesh indicator 1/LiBr solution temperature”: 0% and -1.16%, respectively).
- The mesh number has a negligible influence on the system response for cases in which the fluids movement type is in cocurrent; with a maximum mesh indicator percentage gap between the “Var. case 4” and “Var. case 5” of -1.34% (“Mesh indicator 2/LiBr mass concentration”: -16.64% and -15.30%, respectively).

From Figure 2.31b. it can also be observed that for the simulated cases in absorption/evaporation operating mode:

- The fluids movement type has an influence on the system response when counter-current and cocurrent cases are compared mainly on the mesh indicator associated to the LiBr solution temperature; with a maximum mesh indicator difference between “Var. case 4” and “Var. case 6” of 33.37% (“Mesh indicator 1/LiBr solution temperature”: 33.12% and -0.25%, respectively). For the other mesh indicators, the influence is low, with a maximum percentage gap value of 5.29%.
- According to the “Mesh indicator 5” based in the absorber HTF temperature, $T_{htf/ad}$, the performance of the absorber is barely better in counter-current mode than in co-current mode.
- The mesh number has a negligible influence on the system response for cases in which the fluids movement type is in counter-current; with a maximum mesh indicator difference between “Ref. case” and “Var. case 3” of 1.29% (“Mesh indicator 6/Evaporator HTF temperature”: 0% and -1.29%, respectively).
- The mesh number has a negligible influence on the system response for cases in which the fluids movement type is in cocurrent; with a maximum mesh indicator difference between the “Var. case 4” and “Var. case 5” of 0.62% (“Mesh indicator 1/LiBr solution temperature”: 33.12% and 32.50%, respectively).

It can be highlighted that the mesh type has little influence on the simulation results.

Figure 2.32 indicates the “computing time”⁽¹⁾ required by each simulation case described in Table 2.10.

From Figure 2.32 it can be observed that:

- In general, simulation cases in desorption/condensation mode take about 2.4 times more computing time than cases in absorption/evaporation mode when counter-current movement is considered.
- For a mesh number of 100, in desorption/condensation mode the countercurrent movement case takes about 10 times more computing time than the cocurrent movement; nevertheless, in absorption/evaporation mode the magnitude order is about 4 times.

Taking into account the previous results, simulation cases similar to “Variable case 5” can be interesting to model long periods and will be implemented in the system annual simulations presented in Chapter 4.

⁽¹⁾ In this context, the term “computing time” is defined as the time needed for a computer to simulate a determined case.

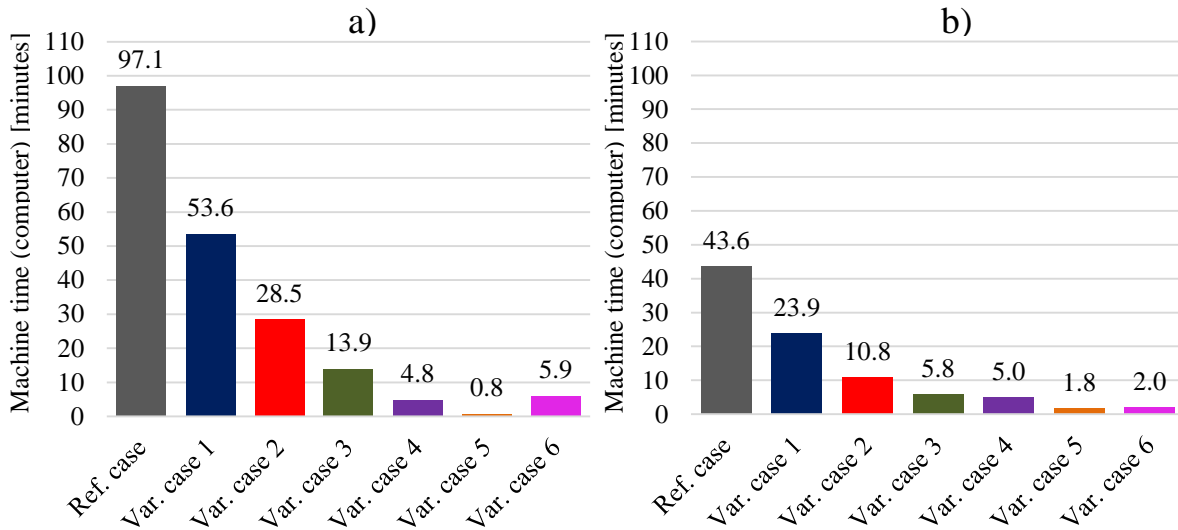


Figure 2.32. Computing time needed for simulation cases with different mesh numbers and fluids direction type; a) Desorption/condensation operating mode; b) Absorption/evaporation operating mode

2.2. Tanks

In this section a model developed to study the behavior of each storage tank (LiBr and water tanks) of the system is presented.

2.2.1. LiBr solution tank model

The model describing a cylindrical tank is 1D. The LiBr solution inlet and outlet are placed at the bottom and at the top of the tank. The tank is considered to be thermally insulated, in stainless steel and its surrounding temperature is considered to be a constant (for example, underground temperature) as it is indicated in Figure 2.33.

Heat and mass transfer are considered along the liquid solution from the bottom to the top of the tank and, simultaneously, convective heat exchanges happen between the bulk solution and the tank wall. Furthermore, under certain circumstances the liquid LiBr solution in the tank can reach very high LiBr mass fractions and crystallize.

In section 2.2.1.1 a discretization and a nodal approach are considered to simulate the behavior of the liquid solution tank. In section 2.2.1.2 a crystallization model is developed to consider the amount of LiBr that can be crystallized during the tank operation. In section 2.2.1.3 some case studies are proposed to show the model response and coherence.

2.2.1.1. Liquid solution tank discretization and nodal approach

A nodal approach has been considered to study the behavior of the liquid solution tank (Figure 2.33), where " k " is related to the node position (subscript) and " l " is related to the time (superscript). A mesh discretization of the tank has been carried out considering 10 meshes. Some additional hypotheses are also considered and are described below (Killion and Garimella, 2001), (Incropera et al., 2011).

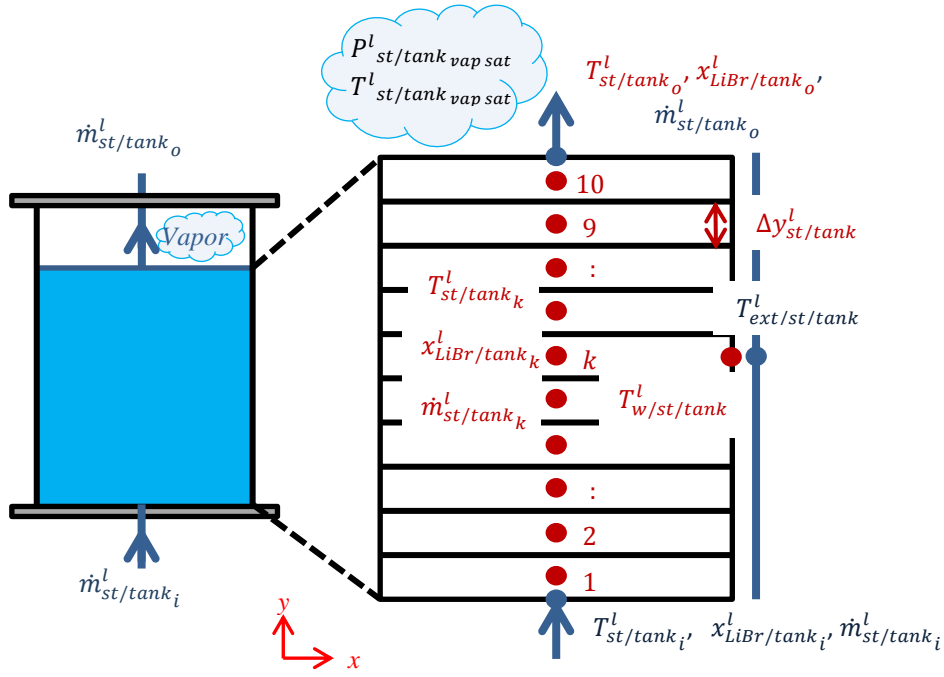


Figure 2.33. Scheme and nodal discretization of the cylindrical LiBr solution tank

- Non condensable gases are not present in the tank vapor
- Vapor in the tank is at equilibrium state with the solution at the liquid/vapor interface.
- Heat transfers from the liquid phase to the adjacent vapor are neglected.
- Mass transfer from the liquid phase to the adjacent vapor is neglected.
- The solution flow in the tank is fully developed and laminar at each time.
- No shear forces are exerted on the liquid solution by the vapor.
- Fluid velocity is zero at the interface between the tank wall and the solution.

Taking into account the scheme Figure 2.33, hypothesis (c) and (d) are expressed below.

For the mass transfer at the liquid/vapor interface:

$$\begin{aligned} \left[\dot{m}''_{H_2O,abs/des} \right]_{y=st/vapor\ tank\ int}^l &= \left[\frac{\rho_{st/tank} D_{LiBr-H_2O}}{(1-x_{H_2O/tank})} \left(\frac{\partial x_{H_2O/tank}}{\partial y} \right) \right]_{y=st/vapor\ tank\ int}^l \approx \\ & \left[\frac{\rho_{st/tank} D_{LiBr-H_2O}}{(1-x_{H_2O/tank})} \right]_{y=st/vapor\ tank\ int} \times \left(\frac{x_{H_2O/tank_o}^l - x_{H_2O/tank_{10}}^l}{(\Delta y/2)} \right) = 0 \end{aligned} \quad (2.43)$$

For the heat transfer at the liquid/vapor interface:

$$\begin{aligned} \left[\dot{m}''_{H_2O,abs/des} \times (h_{st/tank\ vap\ sat} - h_{p-H_2O-st/tank}) \right]_{y=st/vapor\ tank\ int}^l &= \\ \left[\lambda_{st/tank} \left(\frac{\partial T_{st/tank}}{\partial y} \right) \right]_{y=st/vapor\ tank\ int}^l &\approx \\ \left[\lambda_{st/tank} \right]_{y=st/vapor\ tank\ int} \times \left(\frac{T_{st/tank_o}^l - T_{st/tank_{10}}^l}{(\Delta y/2)} \right) &= 0 \end{aligned} \quad (2.44)$$

From Equations 2.47 and 2.48 and considering the hypothesis (c) we obtain that, at any time "l":

$$x_{H_2O/tank_o}^l = x_{H_2O/tank_{10}}^l \text{ or } x_{LiBr/tank_o}^l = x_{LiBr/tank_{10}}^l \quad (2.45)$$

$$T_{st/tank_o}^l = T_{st/tank_{10}}^l \quad (2.46)$$

$$P_{st/tank\ vap\ sat}^l = f(T_{st/tank_o}^l, x_{LiBr/tank_o}^l) \quad (2.47)$$

Some additional hypothesis considered for the simulation model are also indicated below:

- The LiBr solution in the tank is in a transitory state (non steady state).
- Heat and mass differential equations at each grid have been discretized considering an implicit approach.
- Conditions at the time " $l - 1$ " are known (see Figure 2.34).
- The LiBr solution is only in liquid state.
- Nodes 1 to 9 are discretized through a finite difference approach considering temperature, concentration and mass differential equations. Spatial discretization is made using a backward method (non-centered) (for visualization purposes Figures 2.33 and 2.34 show a nodes diagram centered in the volume)
- Node 10 is discretized through a finite volume approach.

From the previous hypothesis, the energy and mass balance equations at each mesh are described below.

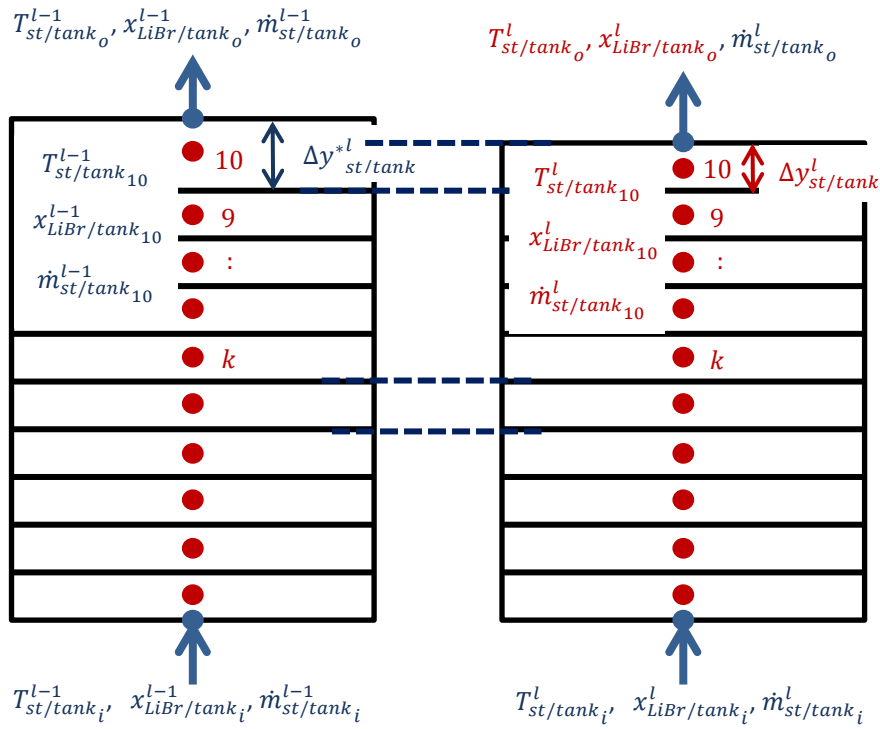


Figure 2.34. Nodal discretization of the LiBr solution tank at the time " $l-1$ " and " l "

For grids from " $k = 2$ " to " $k = 9$ ".

Energy balance

$$\begin{aligned} & \rho_{st/tank_k}^l \left(\frac{h_{st/tank_k}^l - h_{st/tank_k}^{l-1}}{\Delta t} \right) - \left(\frac{4}{D_{h_{st/tank}}} \right) \dot{q}_{w/st/tank_k}^l + \\ & \rho_{st/tank_k}^l \times v_{st/tank_k}^l \left(\frac{h_{st/tank_k}^l - h_{st/tank_{k-1}}^l}{\Delta y_{st/tank}^l} \right) - \\ & \lambda_{st/tank_k}^l \left(\frac{T_{st/tank_{k+1}}^l + T_{st/tank_{k-1}}^l - 2 \times T_{st/tank_k}^l}{(\Delta y_{st/tank}^l)^2} \right) = 0 \end{aligned} \quad (2.48)$$

LiBr mass balance

$$\left(\frac{x_{LiBr/tank_k}^l - x_{LiBr/tank_k}^{l-1}}{\Delta t} \right) + v_{st/tank_k}^l \left(\frac{x_{LiBr/tank_k}^l - x_{LiBr/tank_{k-1}}^l}{\Delta y_{st/tank}^l} \right) - D_{LiBr-H_2O_k}^l \left(\frac{x_{LiBr/tank_{k+1}}^l + x_{LiBr/tank_{k-1}}^l - 2 \times x_{LiBr/tank_k}^l}{(\Delta y_{st/tank}^l)^2} \right) = 0 \quad (2.49)$$

Total mass balance

$$\left(\frac{\rho_{st/tank_k}^l - \rho_{st/tank_k}^{l-1}}{\Delta t} \right) + \left(\frac{\rho_{st/tank_k}^l \times v_{st/tank_k}^l - \rho_{st/tank_{k-1}}^l \times v_{st/tank_k}^l}{\Delta y_{st/tank}^l} \right) = 0 \quad (2.50)$$

For the grid at "k = 1"; when $\dot{m}_{st/tank_i}^l > 0$ the discretized equations are:

Energy balance

$$\rho_{st/tank_1}^l \left(\frac{h_{st/tank_1}^l - h_{st/tank_1}^{l-1}}{\Delta t} \right) - \left(\frac{4}{D_{hst/tank}} \right) \dot{q}_{w/st/tank_1}^l + \rho_{st/tank_1}^l \times v_{st/tank_1}^l \left(\frac{h_{st/tank_1}^l - h_{st/tank_i}^l}{\left(\frac{\Delta y_{st/tank}^l}{2} \right)} \right) - \lambda_{st/tank_1}^l \left(\frac{T_{st/tank_2}^l + 2 \times T_{st/tank_i}^l - 3 \times T_{st/tank_1}^l}{(\Delta y_{st/tank}^l)^2} \right) = 0 \quad (2.51)$$

LiBr mass balance

$$\left(\frac{x_{LiBr/tank_1}^l - x_{LiBr/tank_1}^{l-1}}{\Delta t} \right) + v_{st/tank_1}^l \left(\frac{x_{LiBr/tank_1}^l - x_{LiBr/tank_i}^l}{\left(\frac{\Delta y_{st/tank}^l}{2} \right)} \right) - D_{LiBr-H_2O_1}^l \left(\frac{x_{LiBr/tank_2}^l + 2 \times x_{LiBr/tank_i}^l - 3 \times x_{LiBr/tank_1}^l}{(\Delta y_{st/tank}^l)^2} \right) = 0 \quad (2.52)$$

Total mass balance:

$$\left(\frac{\rho_{st/tank_1}^l - \rho_{st/tank_1}^{l-1}}{\Delta t} \right) + \left(\frac{\rho_{st/tank_1}^l \times v_{st/tank_1}^l - \frac{\dot{m}_{st/tank_i}^l}{\left(\frac{\pi \times (D_{hst/tank})^2}{4} \right)}}{\left(\frac{\Delta y_{st/tank}^l}{2} \right)} \right) = 0 \quad (2.53)$$

It must be remarked that in cases in which $\dot{m}_{st/tank_i}^l = 0$, the tank bottom is considered to be isolated. For those cases, in order to have no heat or mass fluxes coming from the tank bottom, the previous discretized equations for the grid " $k = 1$ " (Equations 2.55 to 2.57) consider that: $T_{st/tank_i}^l = T_{st/tank_1}^l$ and $x_{LiBr/tank_i}^l = x_{LiBr/tank_1}^l$.

For the grid " $k = 10$ ", it must be taken into account that $\dot{m}_{st/tank_i}^l$ can be different from $\dot{m}_{st/tank_o}^l$. To consider this effect a control volume balance has been employed in this grid (Figure 2.33).

For " $k = 10$ ", it is also considered that the size of the grids are different in times " $l - 1$ " an " l ", to take into account the difference in the mass flows entering and leaving the tank (which implies a change in the total solution tank height along time). The heat and mass equations in this grid are shown below.

Energy balance

$$\begin{aligned} & \left(\frac{1}{\pi \times (D_{hst/tank})^2} \right) \times \left(\frac{M_{st/tank_{10}}^l \times h_{st/tank_{10}}^l - M_{st/tank_{10}}^{l-1} \times h_{st/tank_{10}}^{l-1}}{\Delta t} \right) - \\ & \left(\frac{4}{D_{hst/tank}} \right) \times \dot{q}_{w/st/tank_{10}}^l \times \Delta y_{st/tank}^l + (\rho_{st/tank_o}^l \times v_{st/tank_o}^l \times h_{st/tank_o}^l - \\ & \frac{\rho_{st/tank_{10}}^l \times v_{st/tank_{10}}^l \times h_{st/tank_{10}}^l + \rho_{st/tank_9}^l \times v_{st/tank_9}^l \times h_{st/tank_9}^l}{2}) - \\ & \left(\left[\lambda_{st/tank} \left(\frac{\partial T_{st/tank}}{\partial y} \right) \right]_{y=st/vapor\ tank\ int}^l - \frac{\lambda_{st/tank_{10}}^l \times (T_{st/tank_{10}}^l - T_{st/tank_9}^l)}{\Delta y_{st/tank}^l} \right) = 0 \end{aligned} \quad (2.54)$$

LiBr mass balance

$$\begin{aligned} & \left(\frac{1}{\pi \times (D_{hst/tank})^2} \right) \times \left(\frac{M_{LiBr/tank_{10}}^l - M_{LiBr/tank_{10}}^{l-1}}{\Delta t} \right) + (\rho_{st/tank_o}^l \times v_{st/tank_o}^l \times x_{LiBr/tank_o}^l - \\ & \frac{\rho_{st/tank_{10}}^l \times v_{st/tank_{10}}^l \times x_{LiBr/tank_{10}}^l + \rho_{st/tank_9}^l \times v_{st/tank_9}^l \times x_{LiBr/tank_9}^l}{2}) - \\ & \left(\left[\rho_{st/tank} D_{LiBr-H_2O} \left(\frac{\partial x_{LiBr/tank}}{\partial y} \right) \right]_{y=st/vapor\ tank\ int}^l - \frac{\rho_{st/tank_{10}}^l \times D_{LiBr-H_2O_{10}}^l \times (x_{LiBr/tank_{10}}^l - x_{LiBr/tank_9}^l)}{\Delta y_{st/tank}^l} \right) = 0 \end{aligned} \quad (2.55)$$

Total mass balance

$$\left(\frac{1}{\pi \times (D_{h_{st/tank}})^2} \right) \times \left(\frac{M_{st/tank_{10}}^l - M_{st/tank_{10}}^{l-1}}{\Delta t} \right) +$$

$$\left(\rho_{st/tank_o}^l \times v_{st/tank_o}^l - \frac{\rho_{st/tank_{10}}^l \times v_{st/tank_{10}}^l + \rho_{st/tank_9}^l \times v_{st/tank_9}^l}{2} \right) = 0 \quad (2.56)$$

The term $\dot{q}_{w/st/tank_k}^l$, convective heat from the tank wall to the bulk solution at each grid "k", is calculated considering the following hypothesis (Incropera et al., 2011):

- The temperature of the outlet surface of the tank is imposed by the external environment (surroundings)
- Laminar fully developed flow along the solution tank
- Negligible axial conduction heat transfers.
- Forced convection is negligible (plug flow type tank)

Then for each grid "k", $\dot{q}_{w/st/tank_k}^l$ can be expressed as (Incropera et al., 2011)⁽¹⁾:

$$\dot{q}_{w/st/tank_k}^l = \left(\frac{3.66 \times \lambda_{st/tank_k}^l}{D_{h_{st/tank}}} \right) \times (T_{w/st/tank_k}^l - T_{st/tank_k}^l) \quad (2.57)$$

Heat transfer between the external environment and the solution:

$$\dot{q}_{w/st/tank_k}^l \times \pi \times D_{h_{st/tank}} \times \Delta y_{st/tank}^l =$$

$$\left(\frac{\lambda_{w/st/tank}}{e_{w/st/tank}} \right) \times (\pi \times D_{h_{st/tank}} \times \Delta y_{st/tank}^l) \times (T_{ext/st/tank}^l - T_{w/st/tank_k}^l) \quad (2.58)$$

And the mass balance equation for the whole solution tank is expressed as:

$$\sum_{k=1}^{10} (M_{st/tank_k}^{l-1}) + (\dot{m}_{st/tank_i}^l - \dot{m}_{st/tank_o}^l) \times \Delta t =$$

$$\sum_{k=1}^{10} \left(\rho_{st/tank_k}^l \times \left(\frac{\pi \times (D_{h_{st/tank}})^2}{4} \right) \times \Delta y_{st/tank}^l \right) \quad (2.59)$$

Although the tank internal wall temperature, $T_{w/st/tank_k}^l$, should vary with the height; for simplicity purposes it has been considered constant at any position "k".

Equations (2.52) to (2.63) give an equations system of 32 equations and 32 variables, where the unknown variables are: $T_{st/tank_k}^l$, $x_{LiBr/tank_k}^l$, $v_{st/tank_k}^l$, for $k = 1, 2, \dots, 10$, $T_{w/st/tank}^l$ and $\Delta y_{st/tank}^l$.

A code has been developed in Matlab to solve the indicated system. The results of some case studies are shown in the following sections.

⁽¹⁾ In equation 2.62, the term $D_{h_{st/tank}}$ is equivalent to the tank diameter.

2.2.1.1.1. Simulation stability indicators

In order to study the stability convergence of the simulation model, some stability indicators have been considered. These indicators are shown below and are defined at each grid "k" and at each time "l".

The diffusion time, τ_d , and the convection time τ_c are defined as:

$$\tau_{d_k}^l = \frac{(\Delta y_{st/tank}^l)^2}{\alpha_{st/tank_k}^l} \quad (2.60)$$

$$\tau_{c_k}^l = \frac{\Delta y_{st/tank}^l}{v_{st/tank_k}^l} \quad (2.61)$$

The Fourier number, which gives information on the ratio between the time step and the diffusion time in a grid.

$$Fo_{st/tank_k}^l = \frac{\Delta t}{\tau_{d_k}^l} = \frac{\alpha_{st/tank_k}^l \times \Delta t}{(\Delta y_{st/tank}^l)^2} \quad (2.62)$$

The Courant number, which gives information on the ratio between the time step and the convection time in a grid.

$$Co_{st/tank_k}^l = \frac{\Delta t}{\tau_{c_k}^l} = \frac{v_{st/tank_k}^l \times \Delta t}{\Delta y_{st/tank}^l} \quad (2.63)$$

The Peclet number, which gives information of the ratio between the diffusion time and the convection time in a grid.

$$Pe_{st/tank_k}^l = \frac{\tau_{d_k}^l}{2 \times \tau_{c_k}^l} = \frac{v_{st/tank_k}^l \times \Delta y_{st/tank}^l}{2 \times \alpha_{st/tank_k}^l} \quad (2.64)$$

Fourier, Courant and Peclet numbers close to 0 guarantee a stability of the model since they allow to have time steps small enough to ensure the transfer information of diffusion and convection processes; therefore, an adequate simulation step time, Δt , and an adequate grid length, $\Delta y_{st/tank}^l$, have to be selected to ensure the system convergence. It must also be highlighted that for implicit approaches (as the one chosen) the simulation stability is generally guaranteed independently of the values of these indicators⁽¹⁾. Average values of the Fourier, Courant and Peclet numbers ($\overline{Fo}_{st/tank}^l$, $\overline{Co}_{st/tank}^l$, $\overline{Pe}_{st/tank}^l$) along the solution tank have been considered in the stability check, at each time "l", for the case studies presented in section 2.2.1.3 (detail of the Fo , C , and Pe numbers is shown in Annex B2.1).

⁽¹⁾ Nevertheless, as it will be seen in Chapter 4 for the annual system performance simulations, some convergence problems can still appear, requiring to find adequate step time/grid length ratios for each simulated case.

2.2.1.2. LiBr solution crystallization approach

A model has been developed to describe the crystallization of the LiBr solution in the tank.

The crystallization process appears when the liquid LiBr mass fraction, $x_{LiBr/tank_k}^l$, becomes higher than the saturated LiBr mass fraction related to the temperature $T_{st/tank_k}^l$ ⁽¹⁾. Conversely, dissolution develops when salt crystals exist and the liquid LiBr mass fraction, $x_{LiBr/tank_k}^l$, becomes smaller than the saturated LiBr mass fraction.

Hence, the crystallization model will be applied at each grid "k", in the time "l", when one of the following conditions are presented:

- $x_{LiBr/tank_k}^l > f_{cry}(T_{st/tank_k}^l)$ and $M_{cry/st/tank_k}^{l-1} \geq 0$
- $x_{LiBr/tank_k}^l < f_{cry}(T_{st/tank_k}^l)$ and $M_{cry/st/tank_k}^{l-1} > 0$

Where f_{cry} is a function that describes the crystallization curve (saturation curve) of dependence between the solution concentration, $x_{LiBr/tank_k}^l$, and the solution temperature, $T_{LiBr/tank_k}^l$, (Lefebvre et al., 2015) and it is shown in Figure 2.35.

And where $M_{cry/st/tank_k}^{l-1}$ is the amount of crystal mass present in the grid "k" at the time "l - 1".

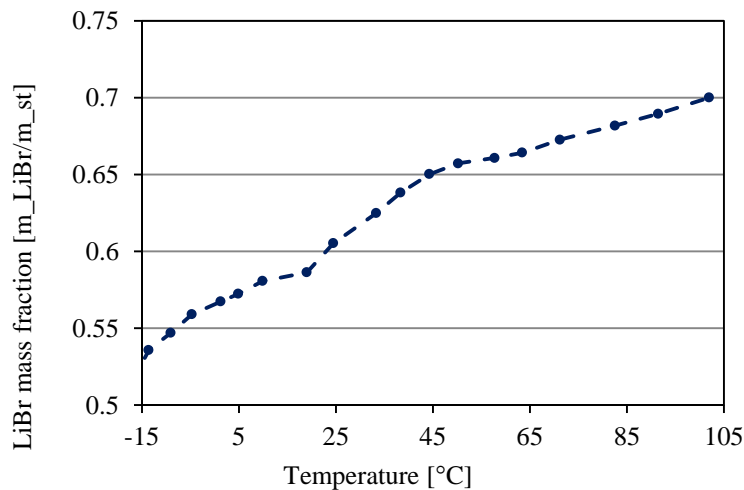


Figure 2.35. LiBr solution crystallization curve (from Lefebvre et al., 2015).

The model initially runs considering only the liquid solution present at the time "l - 1" in order to calculate the temperature, LiBr mass fraction and mass in the liquid solution tank at the time "l". Afterwards, if one of the 2 previous conditions is present in a grid "k", the crystallization model calculates the new amount of crystallized solution, "New($M_{cry/st/tank_k}^l$)", and liquid solution, "New($M_{st/tank_k}^l$)", as well as the new saturated conditions of temperature, "New($T_{st/tank_k}^l$)", and LiBr mass fraction, $f_{cry}(New(T_{st/tank_k}^l))$, at the time "l". For this new calculation, the crystallization model considers the following balance equations at each grid "k":

⁽¹⁾ The correlation between the liquid LiBr solution temperature and the corresponding concentration at which the solution is saturated is called the saturation curve or the crystallization curve.

Energy balance (grid "k"):

$$\begin{aligned}
M_{cry/st/tank_k}^{l-1} \times h_{cry/st/tank_k}^{l-1} + M_{st/tank_k}^l \times h_{st/tank_k}^l(T_{st/tank_k}^l, x_{LiBr/tank_k}^l) = \\
New(M_{cry/st/tank_k}^l) \times h_{cry/st/tank_k}^l(New(T_{st/tank_k}^l), f_{cry}(New(T_{st/tank_k}^l))) + \\
New(M_{st/tank_k}^l) \times h_{st/tank_k}^l(New(T_{st/tank_k}^l), f_{cry}(New(T_{st/tank_k}^l)))
\end{aligned} \tag{2.65}$$

LiBr mass balance (grid "k"):

$$\begin{aligned}
M_{cry/st/tank_k}^{l-1} \times k_{cry/st/tank_k}^{l-1} + M_{st/tank_k}^l \times x_{LiBr/tank_k}^l = \\
New(M_{cry/st/tank_k}^l) \times k_{cry/st/tank_k}^l(New(T_{st/tank_k}^l), f_{cry}(New(T_{st/tank_k}^l))) + \\
New(M_{st/tank_k}^l) \times f_{cry}(New(T_{st/tank_k}^l))
\end{aligned} \tag{2.66}$$

Total mass balance (grid "k"):

$$M_{cry/st/tank_k}^{l-1} + M_{st/tank_k}^l = New(M_{cry/st/tank_k}^l) + New(M_{st/tank_k}^l) \tag{2.67}$$

Equations (2.69), (2.70) and (2.71) permit to solve a system of 3 equations and 3 variables ($New(M_{st/tank_k}^l)$, $New(M_{cry/st/tank_k}^l)$, $New(T_{st/tank_k}^l)$) at each grid "k".

In cases where $New(M_{cry/st/tank_k}^l) < 0$ (complete dissolution of crystals), the following mass and energy balance equations is used to calculate the mass, temperature and LiBr mass fraction of the liquid solution at the grid "k" considering that $New(M_{cry/st/tank_k}^l) = 0$.

Energy balance (grid "k"):

$$\begin{aligned}
M_{cry/st/tank_k}^{l-1} \times h_{cry/st/tank_k}^{l-1} + M_{st/tank_k}^l \times h_{st/tank_k}^l = \\
New(M_{st/tank_k}^l) \times h_{st/tank_k}^l(New(T_{st/tank_k}^l), New(x_{LiBr/tank_k}^l))
\end{aligned} \tag{2.68}$$

LiBr mass balance (grid "k"):

$$M_{cry/st/tank_k}^{l-1} \times k_{cry/st/tank_k}^{l-1} + M_{st/tank_k}^l \times x_{LiBr/tank_k}^l = New(M_{st/tank_k}^l) \times New(x_{LiBr/tank_k}^l) \tag{2.69}$$

Total mass balance (grid "k"):

$$M_{cry/st/tank_k}^{l-1} + M_{st/tank_k}^l = New(M_{st/tank_k}^l) \tag{2.70}$$

Equations (2.72), (2.73) and (2.74) permit to solve, again, a system of 3 equations and 3 variables, where the unknown values are: $New(M_{st/tank_k}^l)$, $New(T_{st/tank_k}^l)$ and $New(x_{LiBr/tank_k}^l)$ at each grid "k".

It must be highlighted that the hypothesis of a fibrous media is considered in the solution tank, preventing the crystals of being dropped at the bottom or of being dragged away.

Additionally, for cases in which crystals are present in the solution tank, the heat balance equations associated to the heat transfers between the bulk liquid solution and the tank wall and between the tank wall and the external environment are modified. Further detail of the approach considered for these cases is described in Annex B2.2.

In the following section, some case studies are presented to check the consistency of this crystallization model.

2.2.1.3. Case studies

Two case studies have been considered: an only liquid solution case and a crystal/liquid solution case.

In both cases the solution tank is considered to have the characteristics and initial conditions shown in Table 2.11.

Table 2.11. Characteristics and initial conditions of the liquid solution tank

$H_{st/tank}^0$ [m]	$D_{h_{st/tank}}$ [m]	$M_{st/tank}^0$ [kg]	$T_{st/tank}^0$ [°C]	$x_{LiBr/tank}^0$	$\lambda_{w/st/tank}$ [W/(m*K)]	$e_{w/st/tank}$ [m]
3.56	1.75	14000	12	0.55	14.9	0.003

The liquid solution and crystal/liquid solution cases are described in the sections below.

2.2.1.3.1. Liquid solution case

When boundary conditions are applied along time, two operating modes have been considered: a charge and a discharge operating mode. Tables 2.12 and 2.13 show the different cases considered for the charge and discharge operating modes, respectively, initial conditions being reported in Table 2.11.

As it is also indicated in Tables 2.12 and 2.13, each simulation case is composed of two periods: the first, in which the boundary conditions (charge or discharge) are applied on the solution tank; and the second, in which the tank is in standby mode and there are no inlet or outlet mass flows. Each of these periods lasts 15 days.

The results of these simulation cases are shown in Figures 2.36 and 2.37.⁽¹⁾

⁽¹⁾ The step time, Δt , considered for all the simulated cases was 30 minutes.

Table 2.12. Liquid solution tank boundary conditions for different cases in charge operating mode

	Period	$\dot{m}_{st/tank_i}^l$ [kg/h]	$\dot{m}_{st/tank_o}^l$ [kg/h]	$T_{st/tank_i}^l$ [°C]	$x_{LiBr/tank_i}^l$	$T_{ext/st/tank_i}^l$ [°C]	Duration [days]
Case 1	Charge	80	80	12	0.58	12	15
	Stop	0	0	--	--	12	15
Case 2	Charge	80	80	40	0.55	12	15
	Stop	0	0	--	--	12	15
Case 3	Charge	75	80	12	0.55	12	15
	Stop	0	0	--	--	12	15
Case 4	Charge	75	80	40	0.58	12	15
	Stop	0	0	--	--	12	15

Table 2.13. Liquid solution tank boundary conditions for different cases in discharge operating mode

	Period	$\dot{m}_{st/tank_i}^l$ [kg/h]	$\dot{m}_{st/tank_o}^l$ [kg/h]	$T_{st/tank_i}^l$ [°C]	$x_{LiBr/tank_i}^l$	$T_{ext/st/tank_i}^l$ [°C]	Duration [days]
Case 5	Discharge	80	80	12	0.52	12	15
	Stop	0	0	--	--	12	15
Case 6	Discharge	85	80	12	0.55	12	15
	Stop	0	0	--	--	12	15
Case 7	Discharge	85	80	12	0.52	12	15
	Stop	0	0	--	--	12	15

As it is shown in Figures 2.36 and 2.37, the liquid solution tank response in charge and discharge operating mode cases seem reasonable.

- In case 1, during the charge mode, the LiBr solution temperatures in the solution tank present some oscillations of the order of 0.2 °C (Figure 2.36a), although the inlet and initial solution temperatures are the same along this period (12°C). These results can be associated to small convergence issues due to the considered step time ($\Delta t = 30 \text{ minutes}$); nevertheless, these oscillations remain low.
- In case 4, during the charge operating mode, it is observed that the contrary effects of introducing a more concentrated solution and, at the same time, emptying the solution tank have an effect on the total amount of LiBr present during this period (Figure 2.36l); where during the first 10 days the LiBr mass is reduced slower than during the next 5 days.
- Analogous effects to those described above are observed during the discharge periods in cases 5 (Figure 2.37a) and 7 (Figure 2.37i).
- During the charge mode, the time constants associated to the mass diffusion and heat diffusion in “case 1” and “case 2” are 9 days 6 hours and 8 days 15 hours respectively (Figures 2.36b and 2.36d). During the discharge mode, the time constant associated to the mass diffusion in “case 5” is 9 days 5 hours (Figure 2.37b).

A study of the stability indicators (see section 2.2.1.1) associated to the case 4 (charge mode) and the case 7 (discharge mode) are described in the Annex B2.1.

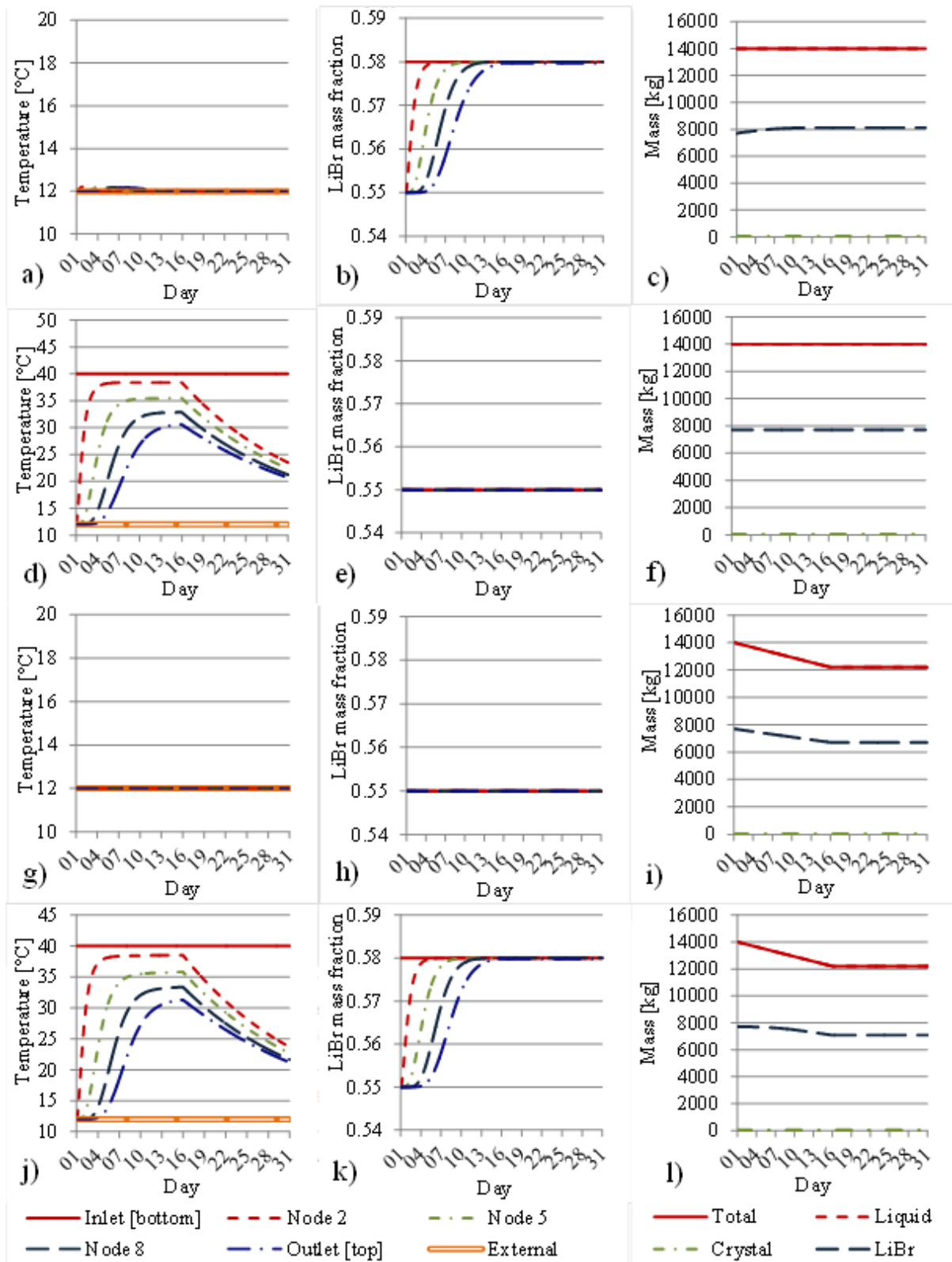


Figure 2.36. Liquid LiBr solution tank. Simulation response of the temperature, LiBr mass fraction and mass parameters for the "charge" mode; a) b) c) Case 1; d) e) f) Case 2; g) h) i) Case 3; j) k) l) Case 4.

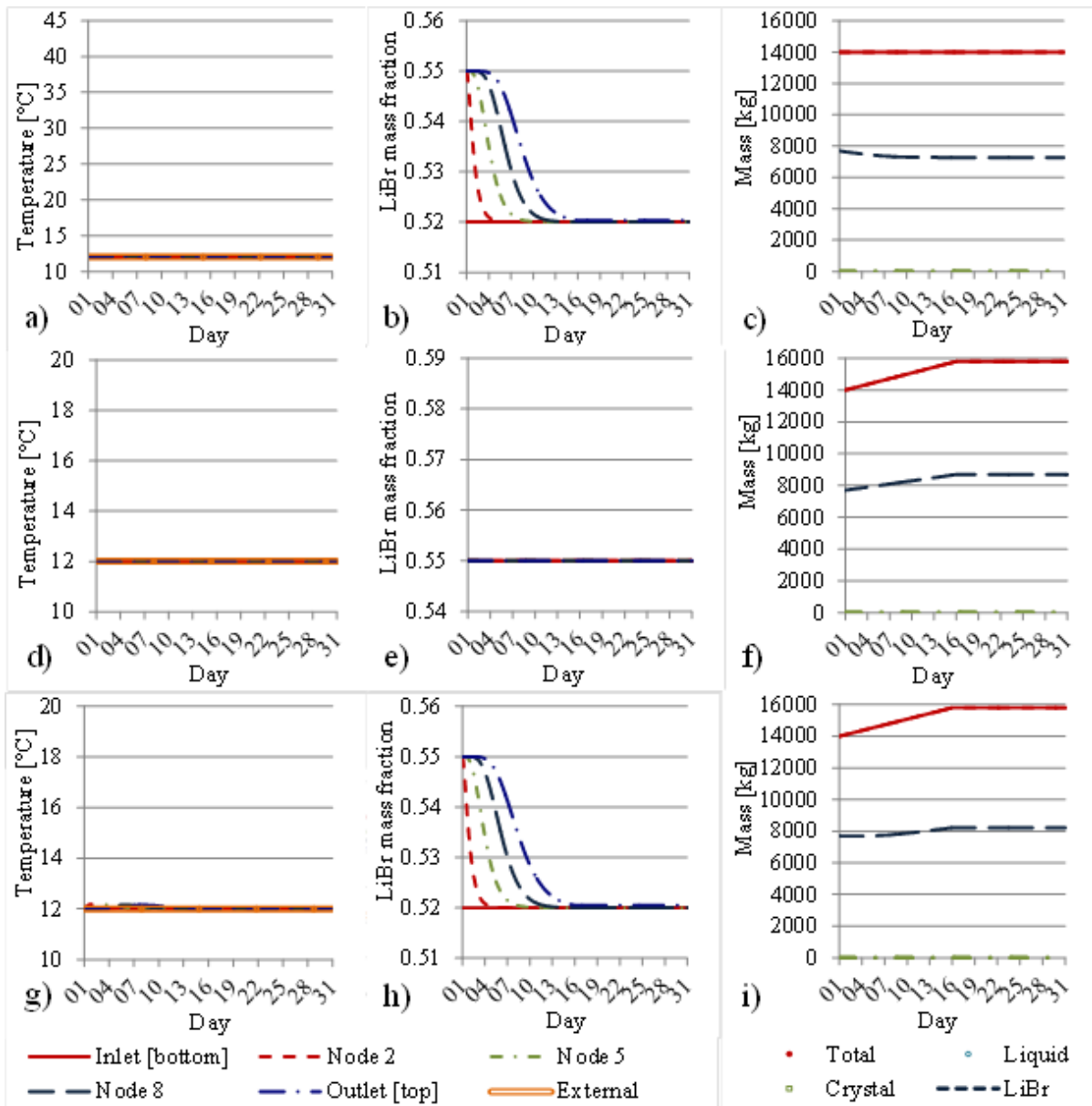


Figure 2.37. Liquid LiBr solution tank. Simulation response of the temperature, LiBr mass fraction and mass parameters for the “discharge” mode; a) b) c) Case 5; d) e) f) Case 6; g) h) i) Case 7.

2.2.1.3.2. Crystal/liquid solution case

A simulation case considering periods of charge and discharge in the solution tank is proposed in order to study the crystallization process. Table 2.14 shows the case (with its corresponding boundary conditions) considered for this study.

The simulation case is composed of three periods: the first period for which charge conditions are applied; the second period for which the tank is in standby mode; and the third period for which discharge conditions are applied. Each of these periods lasts 10 days. The results of this simulation case are shown in Figure 2.38.

Table 2.14. Crystal/liquid solution tank boundary conditions in charge and discharge operating modes

Period	$\dot{m}_{st/tank_i}^l$ [kg/h]	$\dot{m}_{st/tank_o}^l$ [kg/h]	$T_{st/tank_i}^l$ [°C]	$x_{LiBr/tank_i}^l$	$T_{ext/st/tank_i}^l$ [°C]	Duration [days]
Charge	80	80	12	0.59	12	10
Stop	0	0	--	--	12	10
Discharge	80	80	12	0.55	12	10

As it is shown in Figures 2.38, the crystal/liquid solution tank response in charge, standby and discharge mode seems reasonable.

- During the charge period, the crystals start to appear from the second day, as the LiBr mass fraction along the solution tank reaches a value of 0.586, which is associated to the mass fraction of a saturated solution at 12°C. The inlet LiBr mass fraction during the charge period is always 0.59 and the crystal mass increases of about 110 kg per day.
- During the the standby period all the masses remain constant
- During the discharge period, the crystals are diluted very fastly, at a rate of about 1100 kg per day; this can be associated to the inlet LiBr mass fraction during this period which is always 0.55.
- Some small temperature oscillations along the solution tank are observed during all the periods with a maximal value of 0.4°C. These results can be associated to small convergence issues due to the considered step time ($\Delta t = 30 \text{ minutes}$); nevertheless, these oscillations remain low. Another possible factor responsible of these oscillations can be related to the dilution/crystallization enthalpy.
- During the charge period the crystals are mainly formed at the bottom of the tank, with maximal values of 1041 kg and 16 kg in grid 1 and grid 2, respectively.

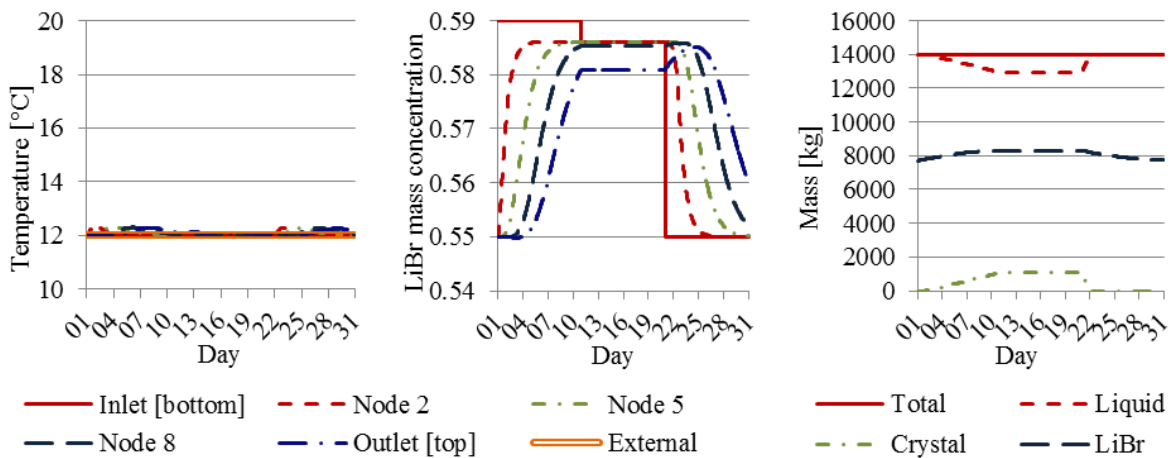


Figure 2.38. Crystal/liquid LiBr solution tank. Simulation response of the temperature, LiBr mass fraction and mass parameters for the charge, standby and discharge modes.

To study the effects of natural convection in the solution tank, two indicators, defined in Equations 2.75 and 2.76, are considered (Incropera et al., 2011).

$$Gr_{st} = \frac{g \times \beta \times (T_{w/st/tank} - T_{st/tank}) \times D_{hst/tank}^3}{\nu_{st}^2} \quad (2.71)$$

$$Ra_{st} = Gr_{st} \times Pr_{st} = Gr_{st} \times \left(\frac{\nu_{st}}{\alpha_{st}} \right) \quad (2.72)$$

Where g is the gravitational acceleration, $T_{w/st/tank}$ is the tank's internal wall temperature, $T_{st/tank}$ is the solution bulk temperature, $D_{hst/tank}$ is the tank hydraulic diameter, ν_{st} solution kinematic viscosity and α_{st} is the solution thermal diffusivity.

β is the expansion coefficient and is approached by Equation 2.77 (Incropera et al., 2011).

$$\beta = -\frac{1}{\rho} \times \left(\frac{\partial \rho}{\partial T} \right) \approx -\frac{1}{\rho_{w/st/tank}} \times \left(\frac{\rho_{st/tank} - \rho_{w/st/tank}}{T_{st/tank} - T_{w/st/tank}} \right) \quad (2.73)$$

Gr_{st} , the Grashof number, is a measure of the ratio of the buoyancy forces to the viscous forces acting on the fluid.

Furthermore, the ratio $\frac{Gr_{st}}{Re_{st}^2}$ provides information on the forced and free convection effects; where for values of $\frac{Gr_{st}}{Re_{st}^2} \gg 1$, forced convection effects may be neglected compared to the free convection effects.

Ra_{st} , the Rayleigh number, is also a measure of the ratio of the buoyancy forces to the viscous forces. For Ra_{st} values less than a critical value (~ 1700), the buoyancy forces cannot overcome the resistance imposed by viscous forces, there is no advection and the heat transfer is produced by conduction. Nevertheless, for Ra_{st} values bigger than the critical value, conditions are thermally unstable and advection is produced in the tank (Incropera et al., 2011).

Figure 2.39 shows average values of $\frac{Gr_{st}}{Re_{st}^2}$ and Ra_{st} for the solution tank, associated to “case 1”, “case 2” and “case 5”.

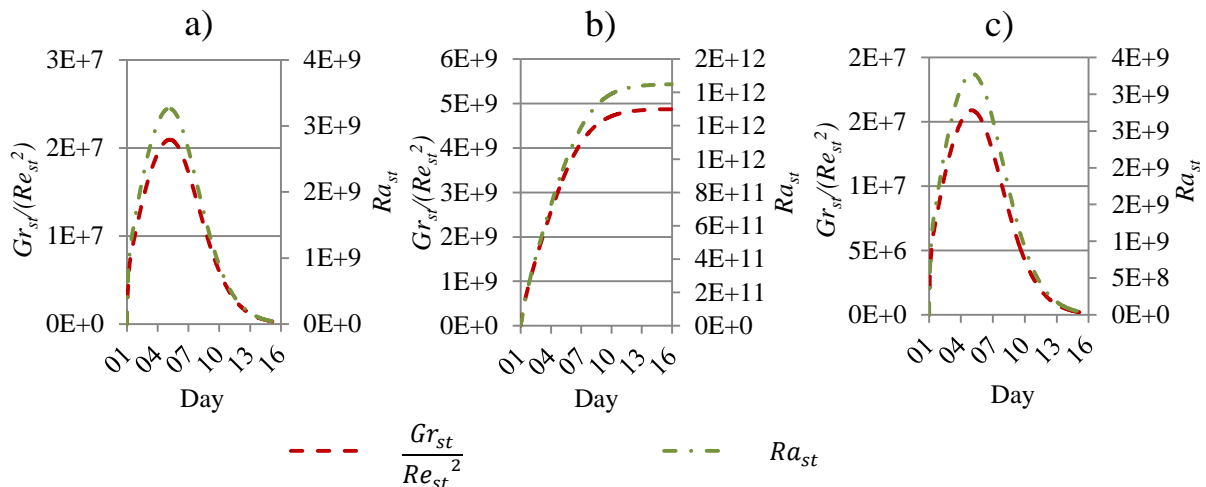


Figure 2.39. Average $\frac{Gr_{st}}{Re_{st}^2}$ and Ra_{st} numbers associated to the solution tank. a) Case 1; b) Case 2; c) Case 5

In Figure 2.39 is observed that in all cases the ratio $\frac{Gr_{st}}{Re_{st}^2}$ and the Rayleigh number, Ra_{st} , are bigger than 1 and 1700 (critical value), respectively. Hence, during the charge and discharge process in the solution tank, the forced convection effects are negligible compared to the free convection effects and that the heat and mass transfers along the tank are produced not only by conduction mechanisms but also by advection mechanisms.

2.2.2. Water tank model

In an analogous way as for the LiBr solution tank model, a model for the cylindrical vertical water tank has been developed.

The model describing the cylindrical tank is 1D. Water inlet and outlet are placed at the bottom and the top of the tank. The tank is considered to be thermally insulated, in stainless steel and its surrounding temperature is considered to be constant (for example, underground temperature) as it is indicated in Figure 2.40.

Heat transfers occur along the liquid water from the bottom to the top of the tank and, simultaneously, convective heat exchanges happen between the bulk water and the tank wall.

A nodal approach has been considered to study the behavior of the water tank (Figure 2.40). A mesh discretization of the tank has been carried out considering 10 meshes. Similar hypothesis as for the solution tank model have been considered. Two of these hypothesis, related to the discretization methods, are shown below.

- Nodes 1 to 9 are discretized through a finite difference approach considering temperature and mass differential equations. Spatial discretization is made using a backward method (non-centered) (for visualization purposes Figure 2.40 shows a nodes diagram centered in the volume).
- Node 10 is discretized through a finite volume approach.

From the previous considerations, energy and mass balance equations at each mesh of the water tank are described below.

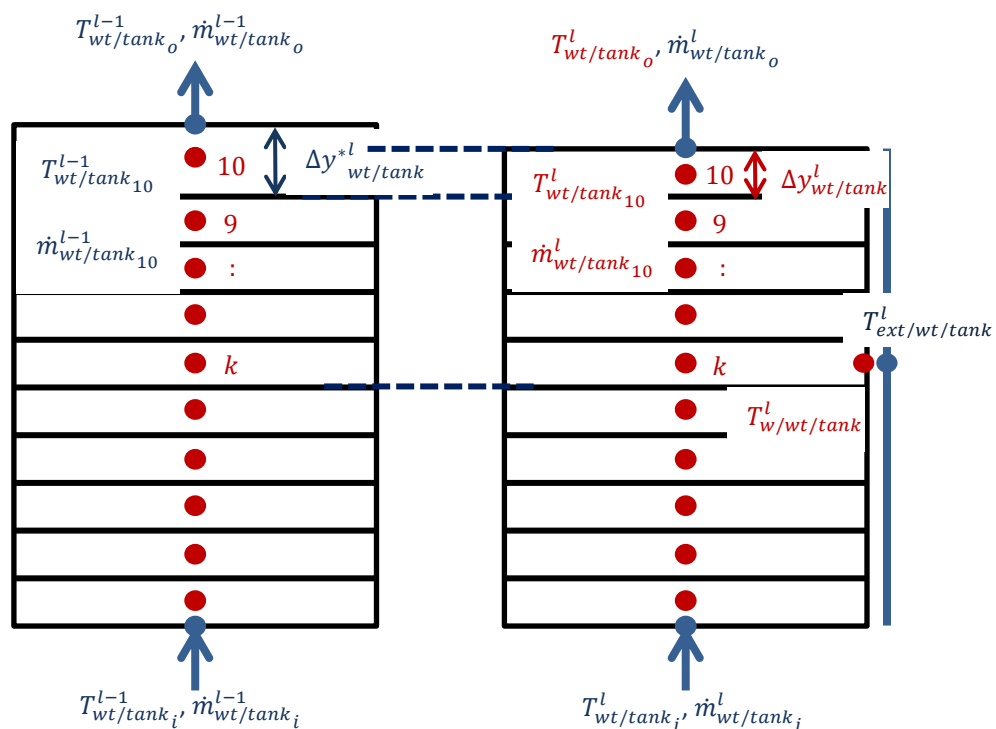


Figure 2.40. Nodal discretization of the water tank at the time "l-1" and "l"

For grids from "k = 2" to "k = 9".

Energy balance

$$\begin{aligned} & \rho_{wt/tank_k}^l \left(\frac{h_{wt/tank_k}^l - h_{wt/tank_k}^{l-1}}{\Delta t} \right) - \left(\frac{4}{D_{h_{wt/tank}}} \right) \dot{q}_{w/wt/tank_k}^l + \\ & \rho_{wt/tank_k}^l \times v_{wt/tank_k}^l \left(\frac{h_{wt/tank_k}^l - h_{wt/tank_{k-1}}^l}{\Delta y_{wt/tank}^l} \right) - \\ & \lambda_{wt/tank_k}^l \left(\frac{T_{wt/tank_{k+1}}^l + T_{wt/tank_{k-1}}^l - 2 \times T_{wt/tank_k}^l}{(\Delta y_{wt/tank}^l)^2} \right) = 0 \end{aligned} \quad (2.74)$$

Total mass balance:

$$\left(\frac{\rho_{wt/tank_k}^l - \rho_{wt/tank_k}^{l-1}}{\Delta t} \right) + \left(\frac{\rho_{wt/tank_k}^l \times v_{wt/tank_k}^l - \rho_{wt/tank_{k-1}}^l \times v_{wt/tank_k}^l}{\Delta y_{wt/tank}^l} \right) = 0 \quad (2.75)$$

For the grid at "k = 1"; when $\dot{m}_{wt/tank_i}^l > 0$ the discretized equations are :

Energy balance

$$\begin{aligned} & \rho_{wt/tank_1}^l \left(\frac{h_{wt/tank_1}^l - h_{wt/tank_1}^{l-1}}{\Delta t} \right) - \left(\frac{4}{D_{h_{wt/tank}}} \right) \dot{q}_{w/wt/tank_1}^l + \\ & \rho_{wt/tank_1}^l \times v_{wt/tank_1}^l \left(\frac{h_{wt/tank_1}^l - h_{wt/tank_i}^l}{\left(\frac{\Delta y_{wt/tank}^l}{2} \right)} \right) - \\ & \lambda_{wt/tank_1}^l \left(\frac{T_{wt/tank_2}^l + 2 \times T_{wt/tank_i}^l - 3 \times T_{wt/tank_1}^l}{(\Delta y_{wt/tank}^l)^2} \right) = 0 \end{aligned} \quad (2.76)$$

Total mass balance

$$\left(\frac{\rho_{wt/tank_1}^l - \rho_{wt/tank_1}^{l-1}}{\Delta t} \right) + \left(\frac{\rho_{wt/tank_1}^l \times v_{wt/tank_1}^l - \frac{\dot{m}_{wt/tank_i}^l}{\left(\frac{\pi \times (D_{h_{wt/tank}})^2}{4} \right)}}{\left(\frac{\Delta y_{wt/tank}^l}{2} \right)} \right) = 0 \quad (2.77)$$

It must be remarked that in cases in which $\dot{m}_{wt/tank_i}^l = 0$, the tank bottom is considered to be isolated. For those cases, in order to have no heat fluxes coming from the tank bottom, the previous discretized equations for the grid "k = 1" (Equations 2.80 and 2.81) consider that: $T_{wt/tank_i}^l = T_{wt/tank_1}^l$.

For the grid "k = 10", it must be taken into account that since $\dot{m}_{wt/tank_i}^l$ can be different from $\dot{m}_{wt/tank_o}^l$, the water tank can be filled or emptied. To consider this effect a control volume balance has been employed in this grid (Figure 2.40).

It must also be highlighted that for " $k = 10$ ", it is considered that the size of the grids are different in times " $l - 1$ " and " l " to take into account the difference in the mass flows entering and leaving the tank (which implies a change in the total water tank height along the time). The energy and mass equations in this grid are showed below.

Energy balance (" $k = 10$ ")

$$\begin{aligned} & \left(\frac{1}{\frac{\pi \times (D_{h_{wt/tank}})^2}{4}} \right) \times \left(\frac{M_{wt/tank_{10}}^l \times h_{wt/tank_{10}}^l - M_{wt/tank_{10}}^{l-1} \times h_{wt/tank_{10}}^{l-1}}{\Delta t} \right) - \\ & \left(\frac{4}{D_{h_{wt/tank}}} \right) \times \dot{q}_{w/wt/tank_{10}}^l \times \Delta y_{wt/tank}^l + (\rho_{wt/tank_o}^l \times v_{wt/tank_o}^l \times h_{wt/tank_o}^l - \\ & \frac{\rho_{wt/tank_{10}}^l \times v_{wt/tank_{10}}^l \times h_{wt/tank_{10}}^l + \rho_{wt/tank_9}^l \times v_{wt/tank_9}^l \times h_{wt/tank_9}^l}{2}) - \\ & \left(\left[\lambda_{wt/tank} \left(\frac{\partial T_{wt/tank}}{\partial y} \right) \right]_{y=wt/vapor\ tank\ int}^l - \frac{\lambda_{wt/tank_{10}}^l \times (T_{wt/tank_{10}}^l - T_{wt/tank_9}^l)}{\Delta y_{wt/tank}^l} \right) = 0 \end{aligned} \quad (2.78)$$

Total mass balance (" $k = 10$ "):

$$\begin{aligned} & \left(\frac{1}{\frac{\pi \times (D_{h_{wt/tank}})^2}{4}} \right) \times \left(\frac{M_{wt/tank_{10}}^l - M_{wt/tank_{10}}^{l-1}}{\Delta t} \right) + \\ & (\rho_{wt/tank_o}^l \times v_{wt/tank_o}^l - \frac{\rho_{wt/tank_{10}}^l \times v_{wt/tank_{10}}^l + \rho_{wt/tank_9}^l \times v_{wt/tank_9}^l}{2}) = 0 \end{aligned} \quad (2.79)$$

The term $\dot{q}_{w/wt/tank_k}^l$, convective heat from the tank wall to the bulk solution at each grid " k ", is calculated considering the following hypothesis (Incropera et al., 2011):

- Uniform temperature of the external surface of the tank
- Laminar fully developed flow along the solution tank
- Negligible axial conduction heat transfers
- Negligible forced convection along the tank wall inside the tank

Then for each grid " k ", $\dot{q}_{w/wt/tank_k}^l$ can be expressed as (Incropera et al., 2011)⁽¹⁾:

$$\dot{q}_{w/wt/tank_k}^l = \left(\frac{3.66 \times \lambda_{wt/tank_k}^l}{D_{h_{wt/tank}}} \right) \times (T_{w/wt/tank_k}^l - T_{wt/tank_k}^l) \quad (2.80)$$

⁽¹⁾ In equation 2.82, the term $D_{h_{wt/tank}}$ is equivalent to the tank diameter.

Total heat transfer across the whole solution tank wall is expressed as:

$$\sum_{k=1}^{10} \left(\dot{q}_{w/wt/tank_k}^l \times \pi \times D_{h_{wt/tank}} \times \Delta y_{wt/tank}^l \right) = \left(\frac{\lambda_{w/wt/tank}}{e_{w/wt/tank}} \right) \times \left(\pi \times D_{h_{wt/tank}} \times \Delta y_{wt/tank}^l \right) \times \sum_{k=1}^{10} \left(T_{ext/wt/tank}^l - T_{w/wt/tank_k}^l \right) \quad (2.81)$$

And the mass balance equation for the whole solution tank is expressed as:

$$\sum_{k=1}^{10} \left(M_{wt/tank_k}^{l-1} \right) + \left(\dot{m}_{wt/tank_i}^l - \dot{m}_{wt/tank_o}^l \right) \times \Delta t = \sum_{k=1}^{10} \left(\rho_{wt/tank_k}^l \times \left(\frac{\pi \times (D_{h_{wt/tank}})^2}{4} \right) \times \Delta y_{wt/tank}^l \right) \quad (2.82)$$

Although the tank internal wall temperature, $T_{w/wt/tank_k}^l$, should vary with the height; for simplicity purposes it has been considered constant at any position "k".

Equations (2.78) to (2.86) lead to a system of 22 equations and 22 variables, where the unknown variables are: $T_{wt/tank_k}^l$, $v_{wt/tank_k}^l$, for $k = 1, 2, \dots, 10$, $T_{w/wt/tank}^l$ and $\Delta y_{wt/tank}^l$.

In an analogous procedure as for the LiBr solution tank, a code has been developed in Matlab to solve the indicated system equation.

In relation to the effects of natural convection in the water tank, for charge and discharge conditions the water kinematic viscosity is around 4 times smaller than the LiBr solution kinematic viscosity (for $T_{wt} = 25^\circ\text{C}$, $\nu_{wt} = 0.9 \times 10^{-6} \text{ m}^2/\text{s}$, while for $T_{st} = 25^\circ\text{C}$, $x_{LiBr} = 0.6$, $\nu_{st} = 4.3 \times 10^{-6} \text{ m}^2/\text{s}$). Hence, numbers such as Gr and Ra are bigger in the water tank than in the solution tank, leading to a similar conclusion as in the solution tank: the forced convection effects are negligible compared to the free convection effects and the heat and mass transfers along the tank are produced not only by conduction mechanisms but also by advection mechanisms.

2.3. Pipes

Additional components of the interseasonal heat storage system are the LiBr solution and water pipes, which connect the solution and water tanks with the reactor. The model describing the cylindrical pipes is 1D. The pipes are in stainless steel covered with an external isolation layer; their external surface is considered to be at a uniform temperature (for example, underground conditions) as it is indicated in Figure 2.41. Heat exchanges develop along the pipes between the bulk solution and the outside.

A nodal approach has been considered to study the physical behavior of the solution pipe (Figure 2.41). A mesh discretization of the pipe has been carried out considering 4 meshes and a laminar and a fully developed solution flow is considered at each time.

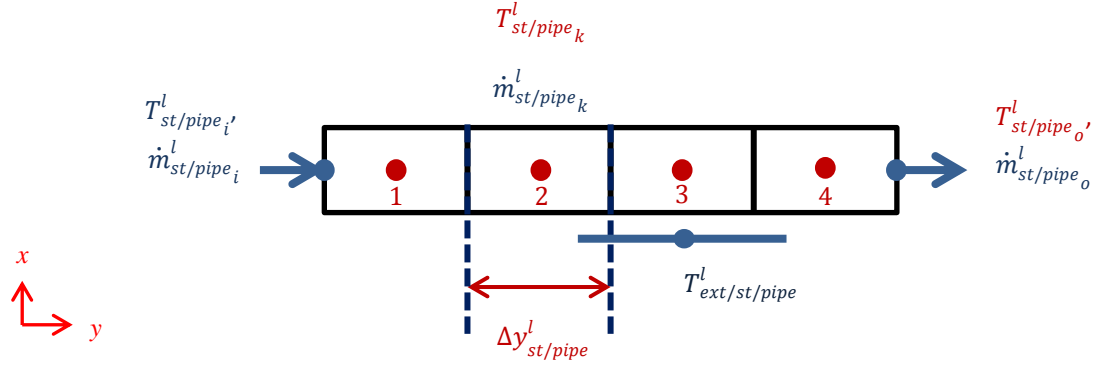


Figure 2.41. Nodal discretization of the LiBr solution cylindrical pipe

The pipes model proposed is in a transitory state (non-steady state). Heat and mass differential equations at each grid have been discretized considering a finite difference and implicit approach. Conditions at the time " $l - 1$ " are known and the spatial discretization is made using a backward method (non-centered).

From the previous indicated hypothesis, the energy balance equations at each grid are described below.

For grids from " $k = 2$ " to " $k = 4$ ".

$$\begin{aligned} \rho_{st/pipe_k}^l \left(\frac{h_{st/pipe_k}^l - h_{st/pipe_k}^{l-1}}{\Delta t} \right) - \left(\frac{4}{D_{h_{st/pipe}}} \right) \dot{q}_{w/st/pipe_k}^l + \\ \rho_{st/pipe_k}^l \times v_{st/pipe_k}^l \left(\frac{h_{st/pipe_k}^l - h_{st/pipe_{k-1}}^l}{\Delta y_{st/pipe}^l} \right) = 0 \end{aligned} \quad (2.83)$$

For grid " $k = 1$ ".

$$\begin{aligned} \rho_{st/pipe_1}^l \left(\frac{h_{st/pipe_1}^l - h_{st/pipe_1}^{l-1}}{\Delta t} \right) - \left(\frac{4}{D_{h_{st/pipe}}} \right) \dot{q}_{w/st/pipe_1}^l + \\ \rho_{st/pipe_1}^l \times v_{st/pipe_1}^l \left(\frac{h_{st/pipe_1}^l - h_{st/pipe_i}^l}{\left(\frac{\Delta y_{st/pipe}^l}{2} \right)} \right) = 0 \end{aligned} \quad (2.84)$$

Where the term $\dot{q}_{w/st/pipe_k}^l$, is related to the heat transfer from the pipe surroundings to the bulk solution at each grid " k ". Then, $\dot{q}_{w/st/pipe_k}^l$ can be expressed as (Incropera et al., 2011):

$$\dot{q}_{w/st/pipe_k}^l = U_{w/st/pipe} \times \left(T_{ext/st/pipe}^l - T_{st/pipe_k}^l \right) \quad (2.85)$$

Where $U_{w/st/pipe}$ is the overall heat transfer coefficient from the external pipe wall to the bulk. It includes the thermal transmittances coefficients related to the bulk/pipe internal wall and pipe internal/external wall.

Equations (2.83) to (2.85) lead to a system of 4 equations and 4 variables, where the unknown variables are: $T_{st/pipe_k}^l$, for $k = 1, 2, \dots, 4$.

2.4. Overall storage system

In order to simulate the whole heat storage system, a compilation procedure of all the system components has been developed and the schematic procedure is described in Figure 2.42.

Equations of the model are expressed in an implicit way except the connection point between the outlet solution tank and the inlet solution pipe 1, at any time “ l ”:

- $T_{st/pipe_1_i}^l = T_{st/tank_o}^{l-1}$
- $x_{LiBr/pipe_1_i}^l = x_{LiBr/tank_o}^{l-1}$

and the connection point between the outlet water tank and the inlet water pipe 1, at any time “ l ”:

- $T_{wt/pipe_1_i}^l = T_{wt/tank_o}^{l-1}$

This implies that 3 outlet conditions calculated in time “ $l-1$ ” are approached as inlet conditions in the time “ l ”.

Since a closed loop is considered between the solution tank, the reactor and the solution pipes, the LiBr mass in the system has to be constant at any time “ l ”. This condition was taken into account in the global model.

For simulation purposes in the tank models; depending on the tank size (height), the simulation time step has to be coherently adapted to the simulation grid length.

The overall system approach presented in this section will be used in Chapter 4 to study the annual interseasonal heat storage system performance when used for dwelling space-heating applications.

Time "l"

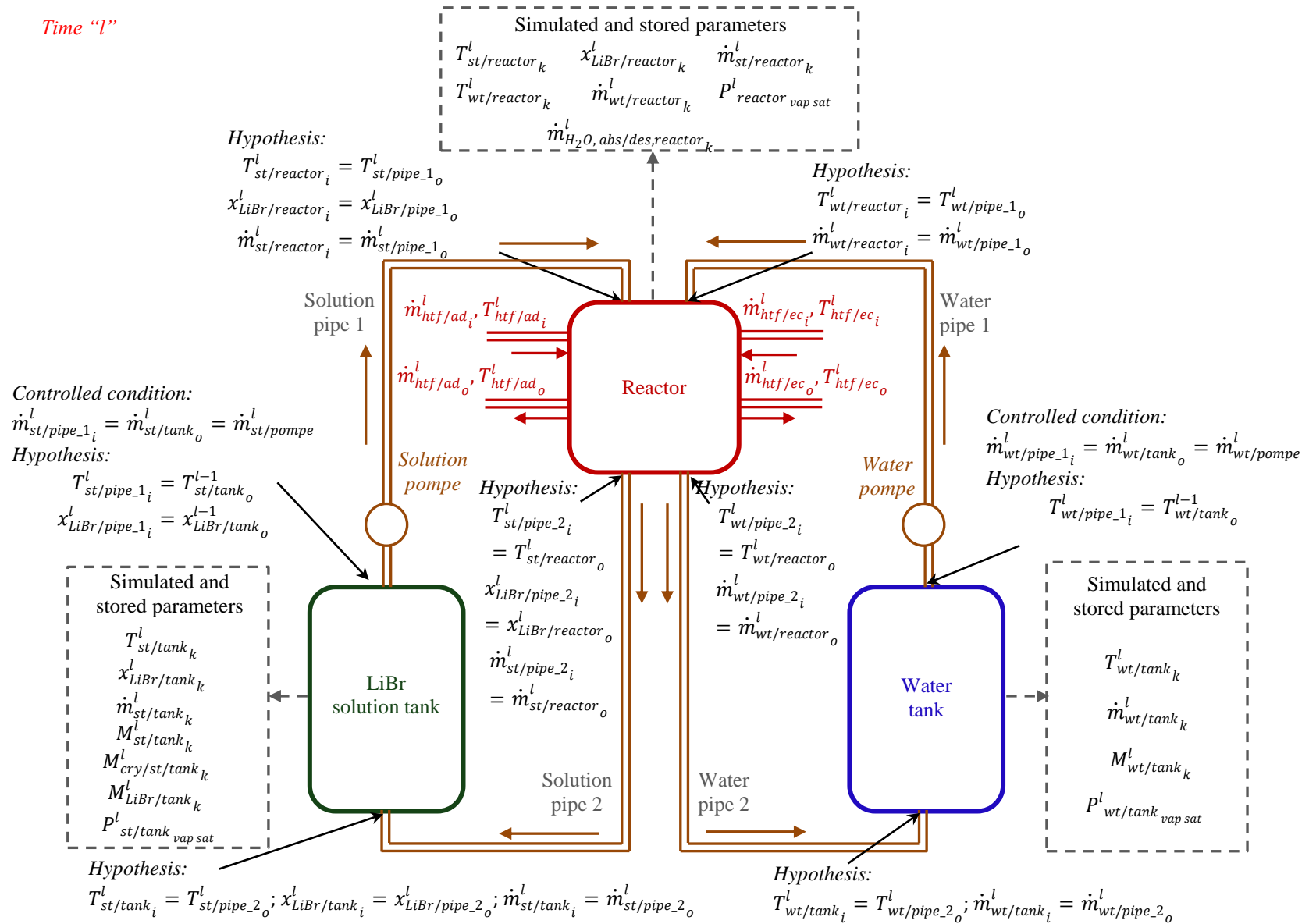


Figure 2.42. Schema of the compilation of the interseasonal heat storage components models

2.5. Conclusions

In this Chapter the components of an interseasonal heat storage system have been modeled.

A model describing the absorption/condensation and desorption/evaporation coupled processes in the system reactor in stationary conditions was developed.

Comparisons of the model against experimental and simulation works of other authors showed a good agreement. Thermo-physical properties correlations used in our model can be different from those used for other simulation works, which could explain the differences between the simulation results.

Experimental results obtained with a prototype of an interseasonal system have been analyzed using our model. Comparisons between simulation and experimental results show a very good coincidence in both absorption and desorption operation modes, when considering reduced wettability values between the LiBr solution or liquid water falling films and the metal surfaces. Best fittings are obtained in both operation modes when considering a wettability of around 20%.

The critical influence of reduction of the falling films wettability on the exchanger surfaces is highlighted; as they can considerably decrease the amount of desorbed water in charge mode or the amount of heat provided to the HTF in discharge mode.

A parametrical study of the influence of heat exchangers inlet conditions on the desorption/condensation and absorption/evaporation coupled process has been performed. Optimum operating conditions have been obtained in charging and discharging operating modes.

An increase of the absorber HTF inlet mass flow increases the absorber HTF power but, at the same time, decreases the absorber HTF outlet temperature, with respect to a reference case; therefore, in space heating applications a good compromise between these 2 parameters must be found.

Optimal inlet working conditions for a proposed grooved vertical plate sandwich heat exchangers configuration are shown. Simulated results indicate that:

- In desorption/condensation mode, the desorbed water mass flow is increased, in average, of 0.6 kg/h, with respect to a reference case.
- In absorption/evaporation operating mode, the absorber HTF outlet temperature is increased of 4 °C, with respect to a reference case, when inlet LiBr solution mass fraction is increased to around 60%.

Considering the fluids direction, the simulated system response for cocurrent and countercurrent movements is different. For these two cases, simulated results indicate that in desorption/condensation operating modes the outlet parameters differ between 6% and 17%; while, in absorption/evaporation operating modes the outlet parameters differ between 1% and 33%. In general, in desorption/condensation and absorption/evaporation modes, a counter-current configuration has a better performance.

Considering the mesh number, the simulated system response does not considerably vary when the mesh number was reasonably reduced. In both operating modes, the outlet parameters differ of less than 2% when a reduction from 200 meshes to 5 meshes was carried out.

A model for the LiBr solution and water tanks are developed considering a 10-meshes discretization and an implicit approach. In the LiBr solution tank a crystallization model was implemented when saturation conditions in the liquid solution are met. Simulation cases to study the model response when inlet conditions are modified were carried out. In all cases, a coherent system response was observed.

Bibliography

- Brauner N.; *Non isothermal vapour absorption into falling film*. Int. J. Heat Mass Tran. Vol. 34, N° 3 (1991); p.767–784.
- Carey V. P.; *Liquid-vapor phase-change phenomena*. Second Edition; Taylor and Francis group, New York (2008); p. 413-475.
- Chang H.-C.; *Wave evolution on a falling film*. Annu. Rev. Fluid Mech. 26 (1994); p.103-136.
- Do K. H.; Kim S. J.; Garimella S. V.; *A mathematical model for analyzing the thermal characteristics of a flat micro heat pipe with a grooved wick*. Int. J. Heat Mass Tran. 51 (2008); p.4637-4650.
- Drelich J., Chibowsky E., Desheng D., Terpilowski K.; *Hydrophilic and superhydrophilic surfaces and materials*. Soft matter 7 (2011); p.9804-9828.
- Florides G. A. Kalogirou S. A., Tassou S. A., Wrobel L. C.; *Design and construction of a LiBr-water absorption machine*. Energ Convers Manage 44 (2003); p.2483-2508
- Grossman G.; *Simultaneous heat and mass transfer in film absorption under laminar flow*. International Journal Heat Mass Transfer Vol. 26, N° 3 (1983); p.357–371.
- Guo L.; Liu Z. C.; Yan Y. Y.; Han Z. W.; *Numerical modeling and analysis of grooved surface applied to film cooling*. J. Bionic Eng. 8 (2011); p.464-473.
- Hellmann H-M., Grossman G.; *Improved property data correlations of absorption fluids for computer simulation of heat pump cycles*. ASHRAE Transactions (1996) 102(1); p. 980-997.
- Image J.; <http://imagej.nih.gov/ij/index.html>. Last accessed 28 December 2015.
- Incropera F., Dewitt D., Bergman T., Lavine A.; *Fundamentals of heat and mass transfer*. Seventh edition; John Wiley & sons (2011); USA; p.675–679.
- Kakaç S., Liu H.; *Heat exchangers – Selection, rating and thermal design*. Second Edition; CRC Press LLC, USA (2002); p. 307-310.
- Karami S., Farhanieh B.; *A numerical study on the absorption of water vapor into a film of aqueous LiBr falling along a vertical plate*. Heat Mass Transfer 46 (2009); p.197–207.
- Killion J., Garimella S.; *A critical review of models of coupled heat and mass transfer in falling film absorption*. International Journal of Refrigeration 24 (2001); p.755–797.
- Lee K. B., Chun B. H., Lee J. C., Hyun J. C. Kim S. H.; *Comparison of heat and mass transfer in falling film and bubble absorbers of ammonia-water*. Exp Heat Transfer 15 (2002); p.191-205.
- Lefebvre E., Fan L., Gagnière E., Benicci S., Auroux A., Magnin D.; *Lithium bromide crystallization in water applied to an interseasonal heat storage process*. Chem. Eng. Sci. 13 (2015); p.2-8.
- Liu H.; *Inter-seasonal solar energy storage for buildings by absorption*. PhD thesis at the University of Grenoble, France (2011).
- McNeely L.A.; *Thermodynamic properties of aqueous solutions of lithium bromide*. ASHRAE Trans (1979); P. 85-413.
- Medrano M., Bourouis M., Coronas A.; *Absorption of water vapour in the falling film of water-lithium bromide inside a vertical tube at air-cooling thermal conditions*. International Journal of Thermal Sciences 41 (2002); p. 891–898.
- Miller W.A., Keyhani M.; *The correlation of simultaneous heat and mass transfer experimental data for aqueous lithium bromide vertical falling film absorption*. J. Solar Energy Engrg. Trans. ASME 123 (1) (2001); p. 30–42.
- N'Tsoukpoe K.E.; *Étude du stockage à long terme de l'énergie solaire thermique par procédé d'absorption LiBr–H₂O pour le chauffage de l'habitat*. Doctoral thesis defended the 19th Mars 2012. University of Savoie, France.
- N'Tsoukpoe K.E., Le Pierrès N., Luo L.; *Experimentation of a LiBr-H₂O absorption process for long-term solar thermal storage: Prototype design and first results*. Energy 53 (2013); p.179-198.
- Saul A, Wagner W.; *International equations for the saturation properties of ordinary water substance*. Journal of physical and chemical reference data 1987; 16(4): p. 893-901.
- Sorption System Consortium; *Mid-Year Report Addendum – Examination and Reconciliation of LiBr/H₂O Property Data*. Carrier Corp. Syracuse, New York (online, last accessed December 2015).
- Yuan Z., Herold K. E¹.; *Specific heat measurements on Aqueous Lithium Bromide*. HVAC&R Res Vol. 11 N° 3 (2005); p.361-375
- Yuan Z., Herold K. E².; *Thermodynamic properties of Aqueous Lithium Bromide using a multiproperty free energy correlation*. HVAC&R Res Vol. 11 N° 3 (2005); p.377-393

Chapter 3. Experimental prototype of the interseasonal heat storage system

Based on the results obtained and analyzed in the previous chapters, an experimental prototype of the interseasonal heat storage system was constructed.

In this chapter the experimental performance of the constructed prototype is presented. In section 3.1 the conception and construction are described. In section 3.2 the system gas leakage rate and the results of the experimental tests in charge and discharge operating modes are shown. In section 3.3 a comparison of the system experimental behavior against simulated results is presented in order to validate the simulation model described in Chapter 2. Finally, in section 3.4 the conclusions of this chapter are indicated.

3.1. Prototype conception and construction

The conception and construction of the prototype are described in this section.

3.1.1. Prototype conception

In recent years Liu (Liu, 2010) and N'Tsoukpoe (N'Tsoukpoe, 2013) constructed experimental prototypes based on the interseasonal heat storage working principle described before. Liu constructed a prototype based on an aqueous solution couple of $\text{CaCl}_2\text{-H}_2\text{O}$ while N'Tsoukpoe constructed a similar prototype based on the $\text{LiBr-H}_2\text{O}$ couple. In both cases their experimental prototypes were composed of a reactor, where two heat exchangers were coupled working as a desorber/condenser (charge) and as an absorber/evaporator (discharge), a solution tank and a water tank. Regarding the disposition of these elements, they were all placed at the same height.

In the present thesis, the prototype was constructed based on the same prototype configurations; nevertheless, major modifications were considered, such as a 2-stage elements disposition, where the reactor is placed above the tanks. Another difference with respect to the previous studies is the heat exchanger technology considered for this prototype. In Figure 3.1, a scheme of the prototype is shown. The technical characteristics of the system components as well as of the sensors, the connecting elements and the thermal modules are described below⁽¹⁾.

3.1.1.1. Reactor container and heat exchangers

As it was mentioned in the previous chapters, the system reactor is composed of two heat and mass exchangers. At each heat exchanger an energy transfer happens between a HTF (heat transfer fluid) and a falling film (LiBr solution or water). The two heat exchangers are coupled and work as a desorber/condenser and as an absorber/evaporator in the charge and discharge operating modes, respectively.

The technical characteristics proposed for the reactor container and the heat exchangers are shown in Figure 3.2.

For the reactor container (Figure 3.2a) a cylindrical configuration was proposed, with 2 windows placed in the lateral side in order to observe the films falling on the exchange surfaces. Airtightness characteristics were considered in the container design and the required material was stainless steel 304L in order to minimize possible corrosion process due to the use of the $\text{LiBr-H}_2\text{O}$ solution⁽²⁾.

As shown in Figure 3.1, a draining line is required at the bottom of the reactor in order to evacuate, in cases where it is needed, liquid solution or liquid water that leaves the heat exchangers' exchange surfaces.

⁽¹⁾ Additional technical description of the prototype components is presented in Annex C1.1.

⁽²⁾ As it will be described in section 3.2, no corrosion was present during the experimental tests since, in addition to the materials selection, the reactor worked at pressures around 10 mbar with, in principle, no air presence.

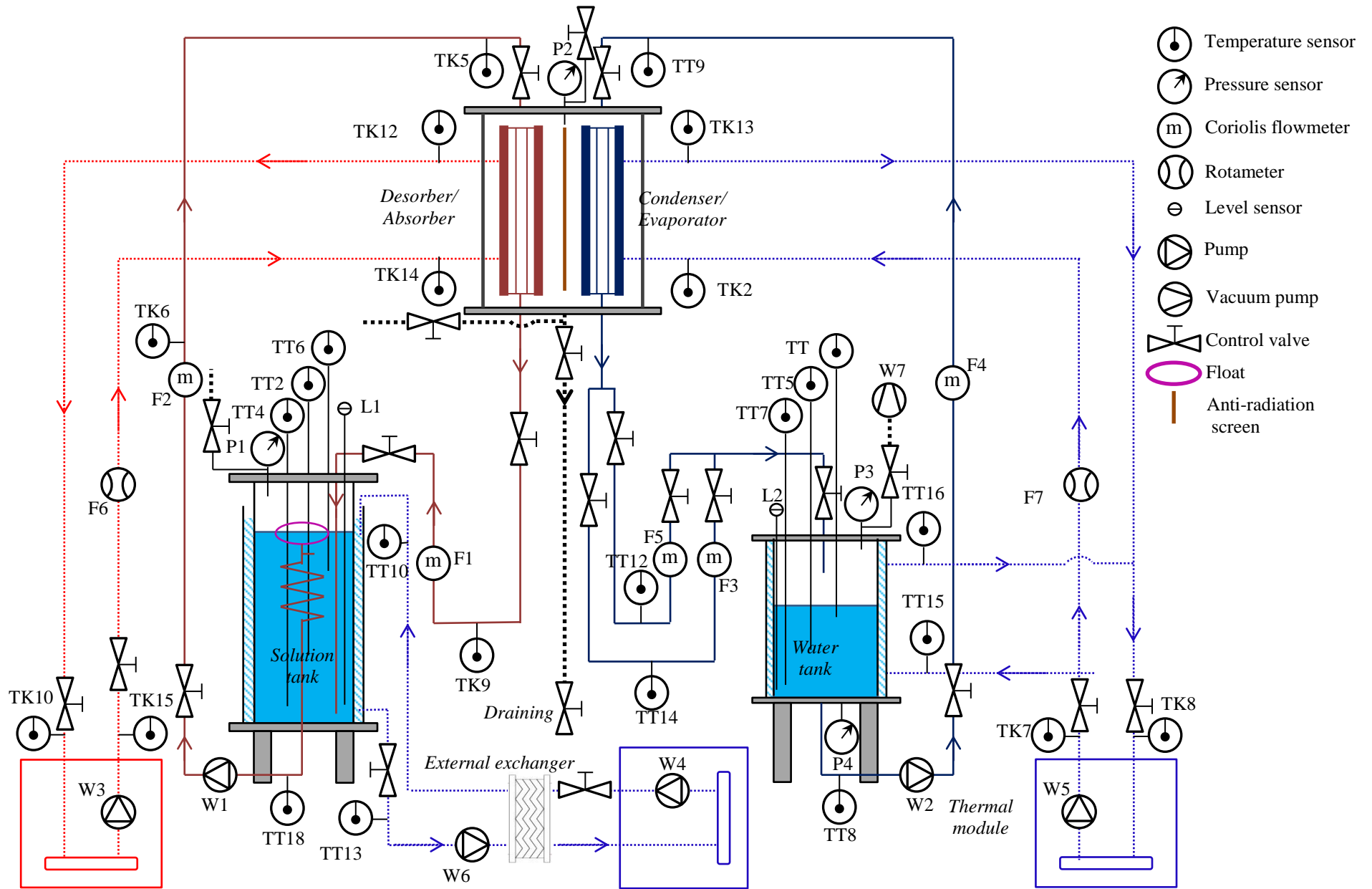


Figure 3.1. Interseasonal heat storage system prototype schema

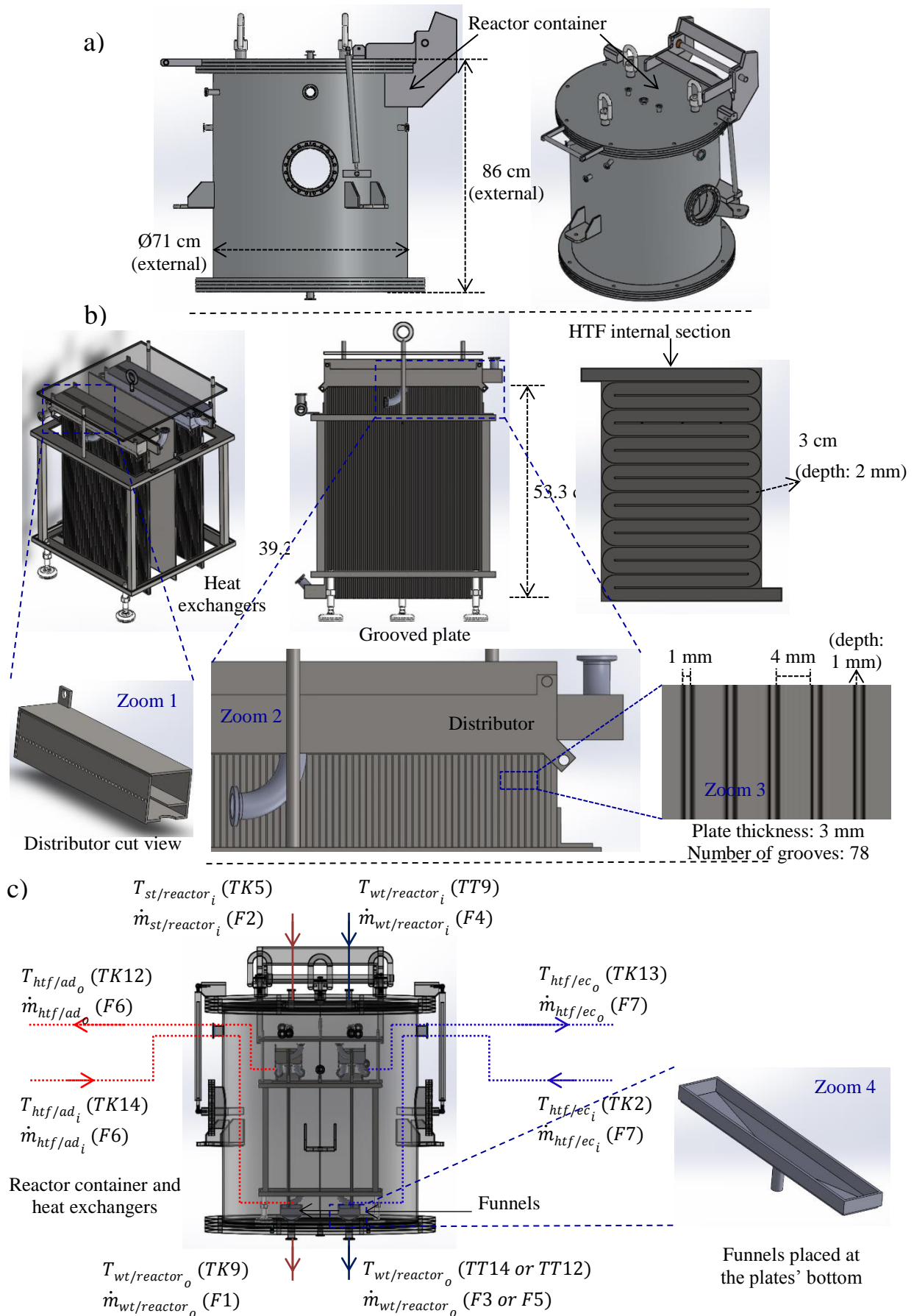


Figure 3.2. a) Reactor container design; b) sandwich grooved vertical flat plate heat exchangers design; c) Container and heat exchangers assembling

For the heat exchanger design (Figure 3.2b) a sandwich grooved vertical plate configuration, similar to the configuration studied in section 2.1.3 (Table 2.3), was considered. The solution arriving at the top of the heat exchanger is distributed to flow at both sides of the exchanger's plate. A similar configuration is considered for the water film. As it is mentioned by Do et al. (Do et al., 2008) and Guo et al. (Guo et al., 2011) a grooved surface allows a better wetting of the falling films flowing along and within the grooves, which can ensure a uniform distribution and wetting all over the exchange surfaces. Also, an internal baffle serpentine passage was conceived for the HTF. In Figure 3.2c, the assembling of the reactor container and the two heat exchangers is shown.

The dimensioning criteria and simulated performance of the proposed heat exchangers was described in section 2.1.3. Nevertheless, two additional criteria were taken into account: to maximize the energy storage density of the system (which would imply to rise the produced heating power, and, consequently, to maximize the exchange plate surface size respect to the reactor container) and to be capable to observe the behavior of the falling films flowing along the grooved surfaces (which would be easier by considering only one plate for each heat exchanger).

3.1.1.2. LiBr solution tank

The technical characteristics considered for the LiBr solution tank are given in Figure 3.3.

A double envelope configuration has been considered for the solution tank, where the internal cylinder (in glass) contains the LiBr solution and the space between the internal and external cylinder (in acrylic glass) contains a HTF to control the solution tank temperature. The space corresponding to the HTF is not a closed space, reason why an external exchanger is used between the HTF space and the associated thermal module, as it is indicated in Figure 3.1. Airtightness characteristics were considered for the internal cylinder design and most components materials were in glass and stainless steel.

As it is indicated in Figure 3.3 (red arrows), in the solution tank the solution is pumped out from the top interface by the use of a float and it is re-introduced in the tank at the bottom by a tube. This configuration was proposed in order to avoid to pump out solution from places where crystals could possibly accumulate and block the tubes (the formed crystals have a higher density than the liquid solution and have a tendency to deposit at the tank bottom).

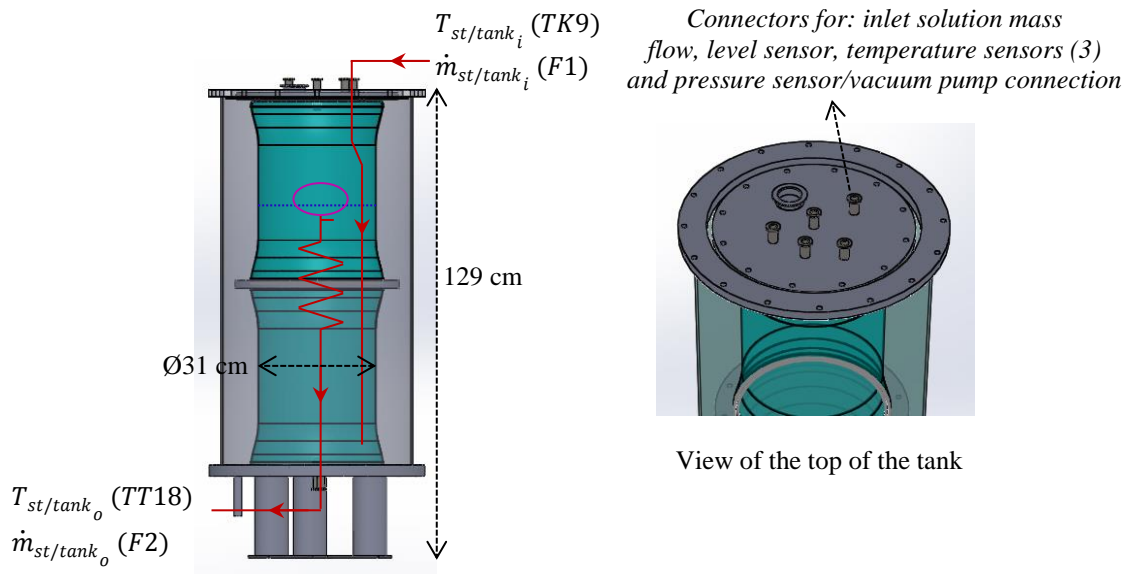


Figure 3.3. LiBr solution tank design

3.1.1.3. Water tank

The technical characteristics of the water tank are indicated in Figure 3.4.

A double envelope configuration has also been considered for the water tank. The internal cylinder contains distilled water and a narrow closed space between the internal and external cylinder contains a HTF aimed to control the water tank temperature. Airtightness characteristics were considered for the internal cylinder design and all components are in stainless steel.

In this tank the water is pumped out from the bottom and is re-introduced at the top.

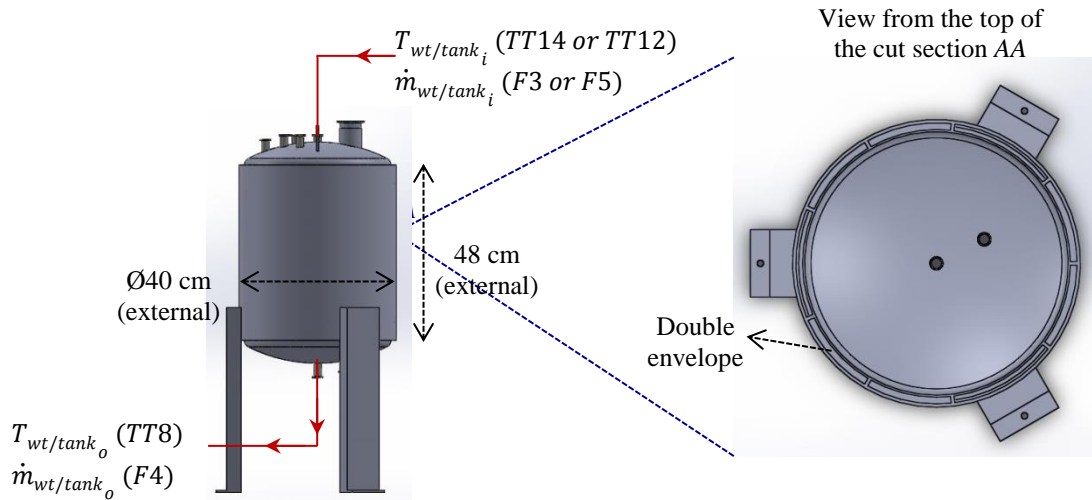


Figure 3.4. Water tank design

3.1.1.4. Connection pipes

Since in the system the reactor, the LiBr solution tank and the water tank are at low pressures (around 10 mbar), special tubes capable to maintain vacuum conditions and manufactured by Fullvac have been used. The tubes diameter used was 16 mm. On the other hand, tubes capable to resist higher pressures (around 2 bar) have been used for the connection pipes associated to the HTF. For the HTF, conventional plumbing material was used.

3.1.1.5. Thermal modules and pumps

Three thermal modules are needed by the prototype. They control the solution tank temperature, the absorber/desorber HTF temperature and the water tank and the evaporator/condenser HTF temperatures, respectively. From the simulation study results obtained in section 2.1.3, the heating power associated to the desorber HTF can be up to 5 kW; while the cooling power associated to the condenser/evaporator HTF can be up to 4 kW.

Two pumps, W1 and W2, are required to pump the solution and the distilled water from the tanks to the reactor. Three main characteristics are needed for these pumps: resist a possible corrosion produced by the LiBr solution, maintain vacuum conditions and pump at very low flows (around 60 kg/h). A vacuum pump is also used (W7) to put the reactor container, solution tank and water tank in vacuum conditions before the experimental tests beginning.

3.1.1.6. Flowmeters

As indicated in Figure 3.1: 7 flowmeters are required in the prototype, including 5 associated to the internal circuit.

Between the evaporator/condenser and the water tank, 3 flowmeters are required: F3, F4 and F5. F3 and F4 are used when the heat exchanger works as an evaporator, and F5 is used when the associated heat exchanger works as a condenser. Two different flowmeters, F3 and F5, are required at the evaporator/condenser outlet since the associated mass flow in evaporation and condensation processes are very different (as indicated in section 2.1.3).

Associated to the absorber/desorber, 2 flowmeters are required: F1 and F2. In addition, these flowmeters have to measure the solution density in order to calculate the LiBr mass fraction. The correlation used to calculate the LiBr mass fraction as a function of the solution density and temperature was proposed by Hellman and Grossman (Hellmann and Grossman, 1996).

As indicated in Figures 3.1 and 3.5, the flowmeters F1, F3 and F5, at the heat exchangers outlets, are placed in the final section of a necessary “U” shaped tube; thus, a 65 cm minimal distance between the tanks top and the reactor bottom is necessary.

The configuration defined by the two previous characteristics allows to flow the solution or water leaving the reactor through the flowmeters, by gravity forces.

Indeed, since the reactor and the tanks have close vapor pressures, the solution or water leaving the reactor is “pushed” by the liquid column formed in the 65 cm height between the reactor bottom and the tank’s top. Hence, F1, F3 and F5 also have to guarantee very low pressure losses (Figure 3.5).

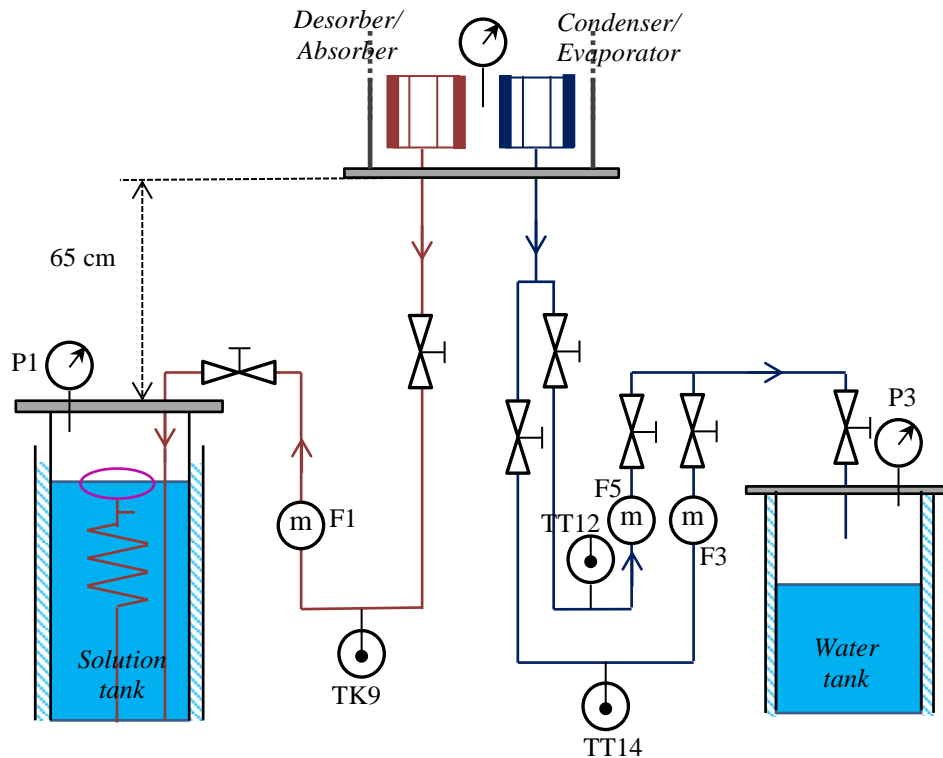


Figure 3.5. Flowmeters positioning associated to the solution and water leaving the reactor.

3.1.1.7. Temperature, pressure and level sensors

As shown in Figure 3.1, four pressure sensors, two level sensors and several temperature sensors are required by the prototype.

Most of the sensors are placed in the internal circuit. All these sensors must maintain vacuum conditions.

As shown in Figure 3.1, two pressure sensors are placed at the bottom and at the top of the water tank; since this configuration allows measuring the liquid water level inside this tank.

3.1.2. Prototype construction

Considering the technical characteristics indicated before, the interseasonal heat storage prototype was constructed. Table 3.1 shows the technical characteristics of the system sensors and elements, and some images of the final prototype are shown in Figure 3.6.

Table 3.1. System elements technical characteristics

Prototype component	Reference ⁽¹⁾	Purpose	Unit	Characteristics
Pumps	W1, W2	Pump the LiBr solution and the distilled water	-	Iwaki MDGR15K, volumetric pump with magnetic driving force
Connecting pipes and valves		Connect the solution tank and the water tank to the reactor	-	Polyvinyl chloride (PVC) and stainless steel tubes and connectors ISO KF. Valves in stainless steel 316L, maximal leakage rate $< 9.10^{-9}$ mbar.l/s of He.
Thermal modules		Control the solution tank, water tank and HTFs temperatures	-	Unichiller HUBER 055TH (connected to the solution tank): Heating power, 2 kW; Cooling power at 15°C, 5.5 kW; Operating temperature range, -10 to 100°C; delivery at 2 bar, 43.5 l/min 055TH4 (connected to the desorber/absorber): Heating power, 4 kW; Cooling power at 15°C, 5.5 kW; Operating temperature range, -10 to 100°C; delivery at 2 bar, 43.5 l/min 060TH (connected to the water tank and the condenser/evaporator): Heating power, 2 kW; Cooling power at 15°C, 6 kW; Operating temperature range, -20 to 100°C; delivery at 2 bar, 61 l/min

⁽¹⁾ Respect to Figure 3.1.

Table 3.2. System sensors technical characteristics

Prototype component	Reference ⁽¹⁾	Purpose	Unit	Characteristics
Coriolis flowmeters	F1, F2, F3, F4, F5	<p>Measure the mass flows and the density associated to LiBr solution and distilled water.</p> <p>Measure the desorbed and absorbed water mass flow in the reactor (F1, F2).</p> <p>Measure the condensed and evaporated water mass flow in the reactor (F3, F4, F5).</p>	kg/h, kg/m ³	<p><u>For F1, F2:</u> Krohne Optimass 6400 S15 Nominal flow rate: 3800 kg/h Density scale: 100 – 3000 kg/m³ Uncertainty: <i>Mass flow:</i> If mass flow \geq 190 kg/h, 0.1% of the measured value. If mass flow < 190 kg/h, 0.19 kg/h. <i>Density:</i> 1 kg/m³.</p> <p><u>For F3:</u> Krohne Optimass 1000 S15 Maximal flow rate: 6500 kg/h Zero stability: 0.65 kg/h Density scale: 400 – 2500 kg/m³ Uncertainty: <i>Mass flow:</i> 0.15% of the measured value + zero stability <i>Density:</i> 2 kg/m³.</p> <p><u>For F4, F5:</u> Yokogawa Rotamass RCCS31 Nominal flow rate: 170 kg/h Maximal flow rate: 300 kg/h Zero stability: 0.0085 kg/h Density scale: 900 – 1100 kg/m³ Uncertainty: <i>Mass flow:</i> 0.1% of the measured value + zero stability <i>Density:</i> 1 kg/m³.</p>
Rotameters	F6, F7	Measure the mass flows associated to the HTFs	kg/h	<p><u>For F6:</u> Krohne 63-650 kg/h Uncertainty: 1% of the measured value</p> <p><u>For F7:</u> Kobold 50 - 500 kg/h (0.22 - 2.2 GPM) KSK Maximal mass flow: 500 kg/h Uncertainty: 4% of full scale</p>
Temperature sensors	TK, TT	Measure the temperature of the LiBr, solution, distilled water and HTFs	°C	Thermocouples T and K. Uncertainty: 0.2 °C ⁽²⁾
Pressure sensors	P1, P2, P3 and P4	Measure the pressure in the tanks and in the reactor (in water tank: vapor pressure and water level)	mbar	<p>P1: Kobold, scale 0 - 250 mbar; uncertainty 0.25 mbar.</p> <p>P2: Pfeiffer BROOKS, scale 0 - 133.3 mbar; uncertainty 0.5% of reading.</p> <p>P3, P4: Keller, scale 0 - 300 mbar; uncertainty 0.3 mbar, capable to be in contact with water.</p>
Level sensors	L1, L2	Measure the liquid solution and water levels in the tanks	cm	Capacitive level meter for liquids KOBOLD NMC Uncertainty: 1.5% of probe length

⁽¹⁾ With respect to Figure 3.1.

⁽²⁾ A calibration process was realized for all the thermocouples taking as reference sensor a PT100 specially aimed for calibration purposes. The process is described in Annex C1.2.

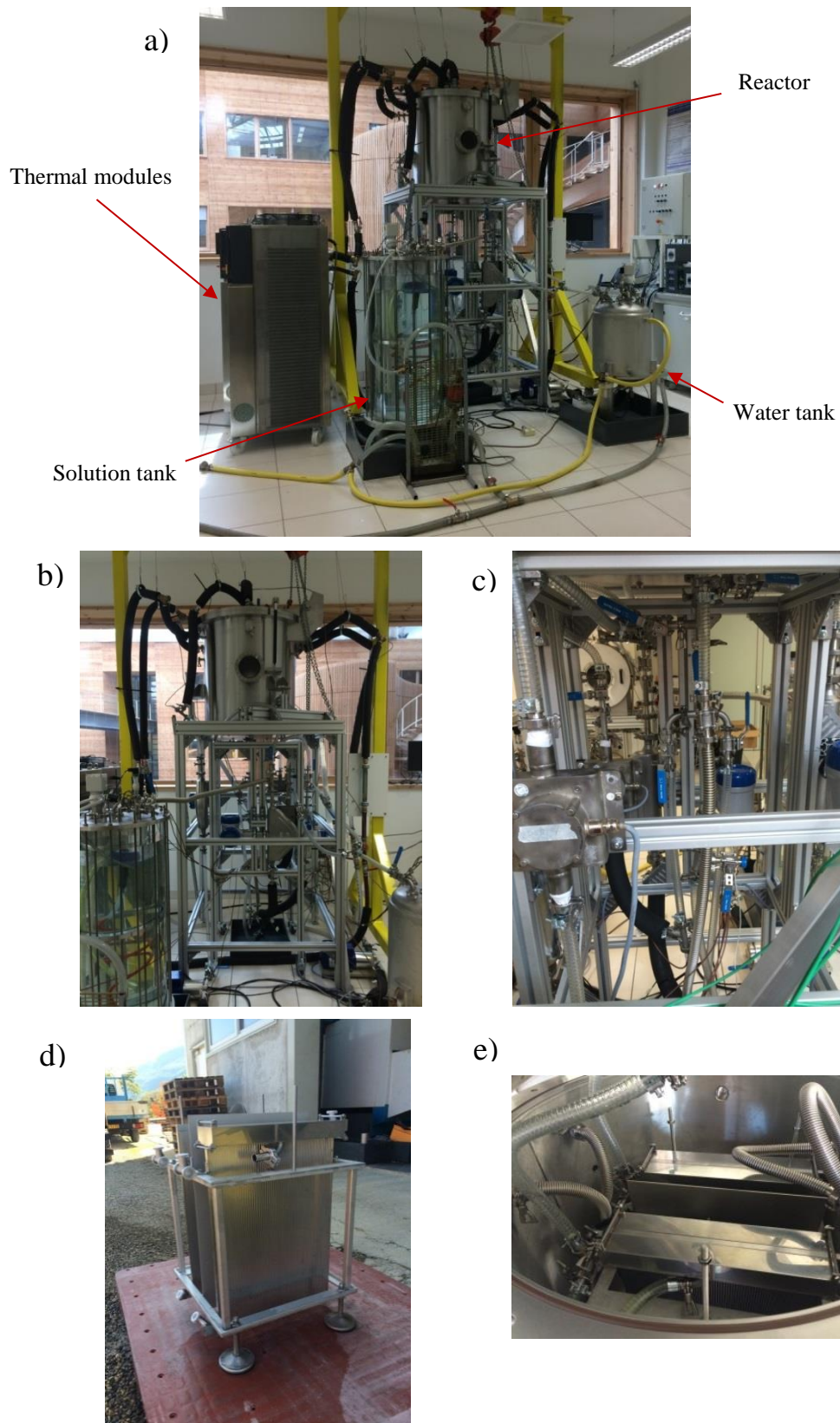


Figure 3.6. Constructed interseasonal heat storage prototype. a) b) Views of the global assembled system; c) Detail of the Coriolis flowmeters and the connecting tubes at the reactors outlet; d) Grooved flat plate heat exchangers; e) Detail of the heat exchangers positioning in the reactor container

3.2. Experimental tests

In this section, the experimental tests performed to evaluate the performance of the interseasonal heat storage system are shown.

In section 3.2.1 different tests carried out to evaluate the gas leakage rate of the main prototype components are shown. In section 3.2.2 the experimental plan for tests in desorption/condensation and absorption/evaporation operating modes are shown. In section 3.2.3 the experimental tests results made in charge and discharge operating modes are presented. Finally, section 3.2.4 describes the system physical behavior when crystallization conditions in the solution tank are reached.

3.2.1. Gas leakage rate

The capability of 3 components of the prototype to keep vacuum conditions was tested and is presented in this section. The selected components were the reactor container, the solution tank and the water tank.

Three periods were chosen to carry out the gas leakage rate tests:

- Before the prototype assembly, which implied to test the components separately and in dry conditions (only air inside).
- After the prototype assembly and before the experimental tests, which implied to make the tests when LiBr solution, water and heat exchangers were inside the solution tank, water tank and reactor, respectively. The components were separated by the valves.
- After the prototype assembly and after the experimental tests (LiBr solution, water and exchangers inside the solution tank, water tank and reactor, respectively).

The results of these tests are shown in Table 3.3.

Table 3.3. Gas leakage rate associated to the prototype main components⁽¹⁾

Component	Gas leakage rate (before assembly) [(mbar.l)/s]	Gas leakage rate (after assembly/before tests) [(mbar.l)/s]	Gas leakage rate (after tests) [(mbar.l)/s]
Reactor	$2.33 \cdot 10^{-5}$	No apparent leak	$2.67 \cdot 10^{-4}$
Solution tank	$4.33 \cdot 10^{-4}$	$2.72 \cdot 10^{-4}$	$2.94 \cdot 10^{-5}$
Water tank	$3.65 \cdot 10^{-4}$	No apparent leak	$5.96 \cdot 10^{-5}$

In general, very low gas leakage rates are obtained in the system components (Umrath et al., 2007) (Medrano et al., 2002). For tests made after assembly, in some elements the leakage rate was not possible to measure since the associated final vapor pressure did not increase with respect to the initial pressure during the measurement, considering the uncertainty of the pressure sensors (Tables 3.1).

⁽¹⁾ The gas leakage rate calculation depends of the component volume and the pressure variation of this element in a determined time interval. The calculation method is described in Annex C1.3 as well as the graphical variation of pressure of each component.

3.2.2. General experimental plan

From simulation results obtained in section 2.1.3 for a grooved vertical plate heat exchanger configuration, a plan for the desorption/condensation and the absorption/evaporation tests of the prototype is proposed. The components working conditions associated to each case are shown in Tables 3.3 and 3.4.

As shown in Table 3.4, for the desorption/condensation operating mode the influence of 3 parameters is studied: the solution mass flow in the reactor (\dot{m}_{st_i}), the HTF desorber temperature (T_{htf/ad_i}) and the HTF desorber and condenser mass flows (\dot{m}_{htf/ad_i} , \dot{m}_{htf/ec_i}). These parameters were chosen since, as it is mentioned in section 2.1.3.1.1, their modification can have an impact on the system performance; where: a \dot{m}_{st_i} increasing, a T_{htf/ad_i} increasing and a \dot{m}_{htf/ad_i} and \dot{m}_{htf/ec_i} increasing can reduce, increase and increase the desorbed water mass flow, respectively.

Similarly, as it is shown in Table 3.5, for the absorption/evaporation operating mode the influence of 4 parameters is studied: the solution mass flow in the reactor (\dot{m}_{st_i}), the HTF absorber temperature (T_{htf/ad_i}), the HTF absorber mass flow (\dot{m}_{htf/ad_i}) and the HTF evaporator mass flow (\dot{m}_{htf/ec_i}). These parameters were chosen since, as it is mentioned in section 2.1.3.1.2, a \dot{m}_{st_i} increasing, a T_{htf/ad_i} increasing, a \dot{m}_{htf/ad_i} increasing and a \dot{m}_{htf/ec_i} increasing can reduce, reduce, increase and increase the power given from the reactor to the absorber HTF, respectively. In cases in which \dot{m}_{htf/ad_i} is increased, although the absorber power increases, the difference between the absorber HTF outlet and inlet temperatures decreases.

Table 3.4. Experimental plan for desorption/condensation operating mode tests; components working conditions

Components	Parameters	Reference case	Additional cases (modified parameters with respect to the reference case)					
			80	100	--	--	--	--
Desorber	\dot{m}_{st_i} [kg/h]	60	80	100	--	--	--	--
	x_{LiBr_i} [m_LiBr/m_st]	[0.52 – 0.60]	--	--	--	--	--	--
	\dot{m}_{htf/ad_i} [kg/h] ⁽¹⁾	300	--	--	--	--	200	400
	T_{htf/ad_i} [°C]	70	--	--	60	80	--	--
	Type	Counter-courant	--	--	--	--	--	--
	Maximum wetted surface percentage [%] ⁽²⁾	79.6	--	--	--	--	--	--
LiBr solution tank	$T_{st/tank_{envp}}$ [°C]	19	--	--	--	--	--	--
Condenser	$\dot{m}_{f_water_i}$ [kg/h]	0	--	--	--	--	--	--
	\dot{m}_{htf/ec_i} [kg/h]	300	--	--	--	--	200	400
	T_{htf/ec_i} [°C]	15	--	--	--	--	--	--
	Type	Counter-courant	--	--	--	--	--	--
	Maximum wetted surface percentage [%]	100	--	--	--	--	--	--
Water tank	$T_{wt/tank_{envp}}$ [°C]	15	--	--	--	--	--	--

⁽¹⁾ The considered HTF was water.

⁽²⁾ The value for the wetted surface percentage was calculated under the hypothesis that the LiBr solution or distilled water falling films completely wet the grooved sections. In the desorber the value is 79.6% since there is a spacing between each groove. In the condenser the value is 100% since the water film inlet mass flow is zero and it is considered that the system conditions permit the vapor to condense uniformly over all the exchange surfaces (grooves and space between them).

Table 3.5. Experimental plan for absorption/evaporation operating mode tests; components working conditions

Components	Parameters	Reference case	Additional cases (modified parameters with respect to the reference case)					
			80	60	--	--	--	--
Absorber	\dot{m}_{st_i} [kg/h]	110	--	--	--	--	--	--
	x_{LiBr_i} [m_LiBr/m_st]	[0.52 – 0.60]	--	--	--	--	--	--
	\dot{m}_{htf/ad_i} [kg/h]	300	--	--	--	200	--	200
	T_{htf/ad_i} [°C]	30	--	--	25	--	--	--
	Type	Counter-courant	--	--	--	--	--	--
	Maximum wetted surface percentage [%] ⁽¹⁾	79.6	--	--	--	--	--	--
LiBr solution tank	$T_{st/tank_{envp}}$ [°C]	19	--	--	--	--	--	--
Evaporator	$\dot{m}_{f_water_i}$ [kg/h]	110	--	--	--	--	--	--
	\dot{m}_{htf/ec_i} [kg/h]	300	--	--	--	--	400	400
	T_{htf/ec_i} [°C]	15	--	--	--	--	--	--
	Type	Counter-courant	--	--	--	--	--	--
	Maximum wetted surface percentage [%]	79.6	--	--	--	--	--	--
Water tank	$T_{wt/tank_{envp}}$ [°C]	15	--	--	--	--	--	--

The working conditions shown in Tables 3.3 and 3.4 are based on ideal conditions that were considered in the simulations cases in section 2.1.3.2. However, as it will be observed in the following section, the working conditions in the experiments did vary along time in the tests and, in some cases, were not possible to stabilize due to experimental limitations.

Tests consider absorber HTF inlet temperatures of 25°C and 30°C, since these conditions can be coherently associated to a determined dwelling in order to cover its heating needs during the discharge periods.

⁽¹⁾ In the absorber and evaporator the value of the wetted surface percentage is 79.6% since there is a spacing between each groove.

3.2.3. Tests

Based on the general plan described above, six experimental tests in desorption/condensation and four in absorption/evaporation operating modes were performed and are presented below.

3.2.3.1. Desorption/condensation: typical results

Six experimental tests in desorption/condensation operating mode were carried out; the working conditions of 2 of these tests are shown in Table 3.6. The main difference between the two selected configurations was the desorber HTF inlet temperature, T_{htf/ad_i} , which increased from 70°C to 80°C⁽¹⁾.

The system physical behavior for Test 1 is shown in Figures 3.7 to 3.9.

Table 3.6. Working conditions for the experimental tests in desorption/condensation operating mode

		13/10/2015	14/10/2015
Components	Parameters	Test 1	Test 2
Desorber	\dot{m}_{st_i} [kg/h]	~60	~30
	x_{LiBr_i} [m_LiBr/m_st]	[0.56 - 0.60]	[0.54]
	\dot{m}_{htf/ad_i} [kg/h]	300	300
	T_{htf/ad_i} [°C]	68	75
	Observed wetted surface percentage [%] ⁽²⁾	~28% (~35%)	~16% (~20%)
LiBr solution tank	$T_{st/tank_{envp}}$ [°C]	19	19
	\dot{m}_{htf/ec_i} [kg/h]	300	300
	T_{htf/ec_i} [°C]	15	15
	Observed wetted surface percentage [%]	100%	100%
Water tank	$T_{wt/tank_{envp}}$ [°C]	15	15

As it is observed in Figure 3.7a and 3.9b, although the solution tank envelope was maintained at 19°C, the solution inside the tank increased its temperature along the time; which, as it is indicated in Figure 3.7c, produced an increase of the mass flow of the pumped solution due to a reduction of its viscosity. Hence, a manual control of the associated pump was needed in order to maintain the solution average mass flow around 58 kg/h.

In Figure 3.7b the solution LiBr mass fraction entering and leaving the reactor is shown⁽³⁾. The gap between these mass fractions decreases along the time and, in average, is around 1.2%; the solution inlet mass fraction increases along the time in a stair shape, which is associated to the time required by the solution to diffuse from the bottom to the top of the solution tank (plug flow).

⁽¹⁾ The results of the remaining cases are shown in Annex C2.1.

⁽²⁾ In the term “~28% (~35%)” for example, the term “(~35%)” refers to the observed wetting respect to the grooved surface, while the term “~28%” refers to the observed wetting respect to the total surface, which is calculated as: 79.6%*(35%) (see Table 3.4).

⁽³⁾ The LiBr mass concentration measurement was done using a correlation found in literature (see Annex C2.2), which depends of the solution density and temperature (measured with the associated Coriolis flowmeters and thermocouples shown in Figure 3.1).

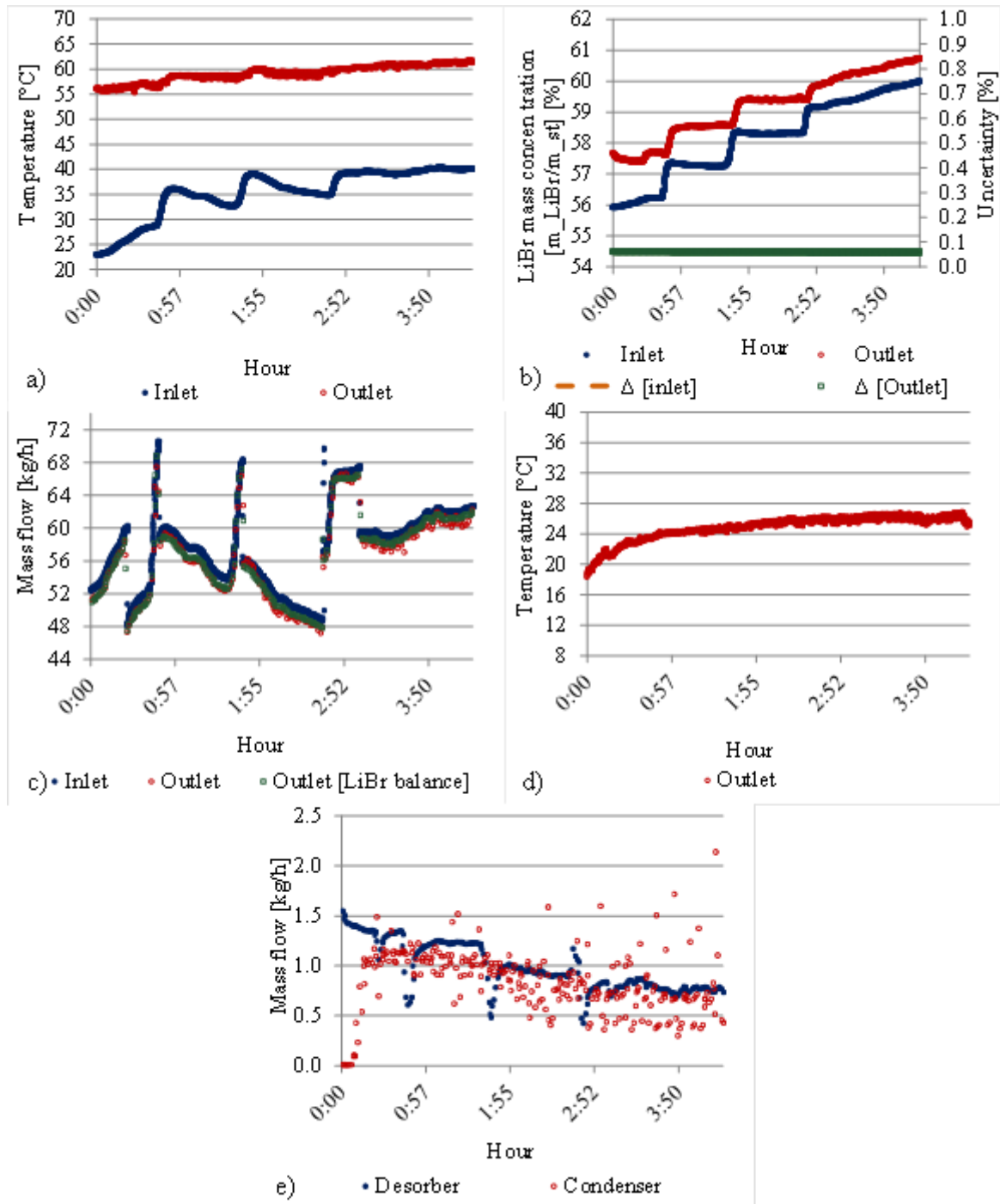


Figure 3.7. Experimental results obtained in desorption/condensation operating mode for the Test 1. a) LiBr solution temperature (desorber); b) LiBr mass concentration (desorber); c) LiBr solution mass flow (desorber); d) Water film temperature (condenser); e) Desorbed/condensed water (reactor)

In Figure 3.7c, the solution mass flows entering and leaving the reactor are shown⁽¹⁾. As it is observed, the inlet mass flow varied along the test between 48 and 72 kg/h.

⁽¹⁾ Two methods were used to measure the solution outlet mass flow: one considering the reading given by the Coriolis flowmeter F1, and the other through a LiBr mass balance between the solution inlet and outlet mass flows. Both methods give similar results. The latter method was considered for further calculations in this Chapter and it is described in Annex C2.3.

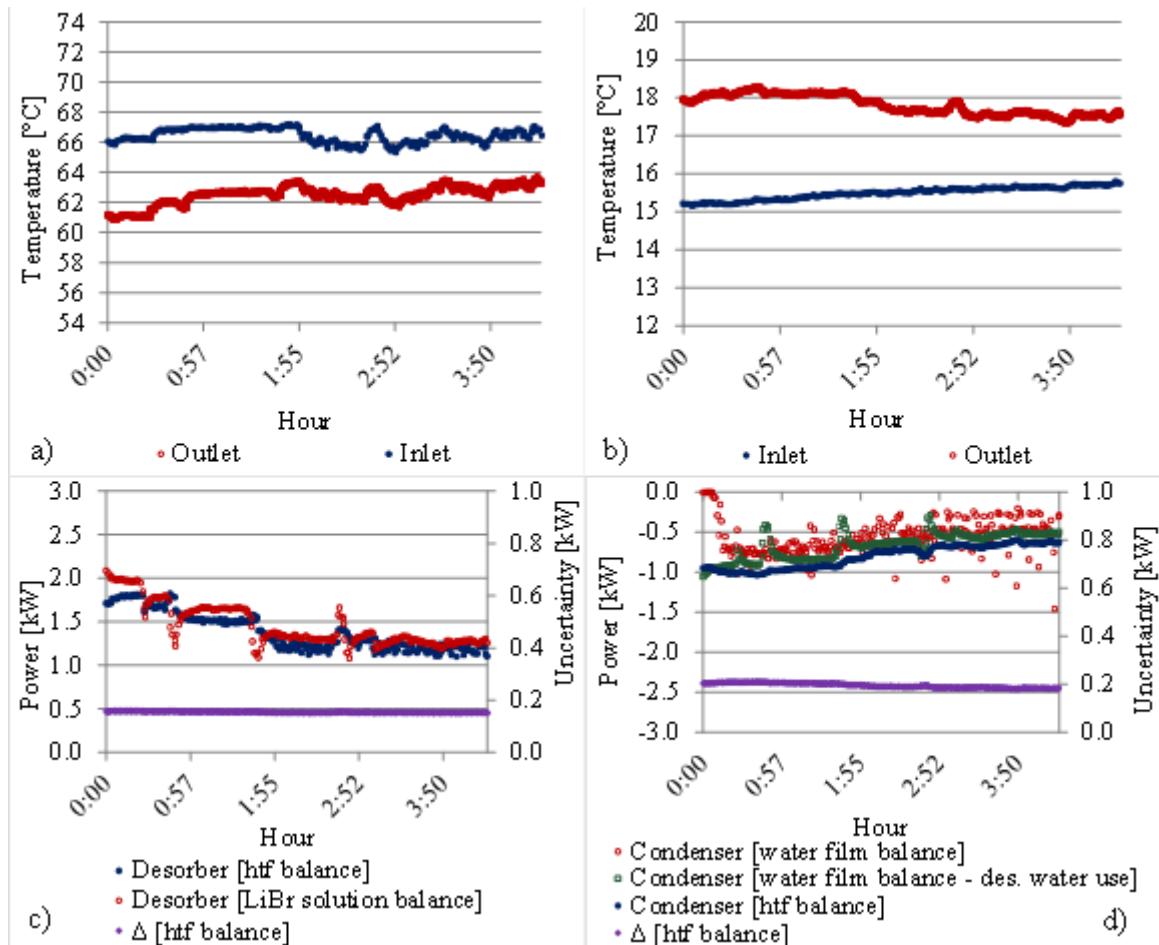


Figure 3.8. Experimental results obtained in desorption/condensation operating mode for the Test 1. a) HTF temperature (desorber); b) HTF temperature (condenser); c) Power given from the HTF to the system (desorber); d) Power given from the HTF to the system (condenser)

Figure 3.7d shows that the temperature of the condensed water film leaving the reactor increases along the time even with the reactor's vapor pressure remaining constant (Figure 3.9a). This temperature rise is associated to the influence of the ambient temperature on the U shape pipe where the condensed water is received (Figure 3.5), considering its very low mass flow respect to the LiBr solution (1 to 60 kg/h).

In Figure 3.7e the mass flow of the desorbed and condensed water inside the reactor is shown. These values were calculated by the difference between the outlet and inlet mass flows for the solution (Figure 3.7c) and for the water film (F5). Both mass flows show similar values and they vary from 1.5 kg/h to 0.75 kg/h. In addition, the mass flows decrease along the time, which is associated to the LiBr mass fraction increase of the solution entering the desorber.

In Figures 3.8a,b the desorber and condenser HTF temperatures are shown; associated to these curves in Figures 3.8c and 3.8d, the desorber power (power given from the HTF to the desorber) and the condenser power (power given from the HTF to the condenser), respectively, are presented.

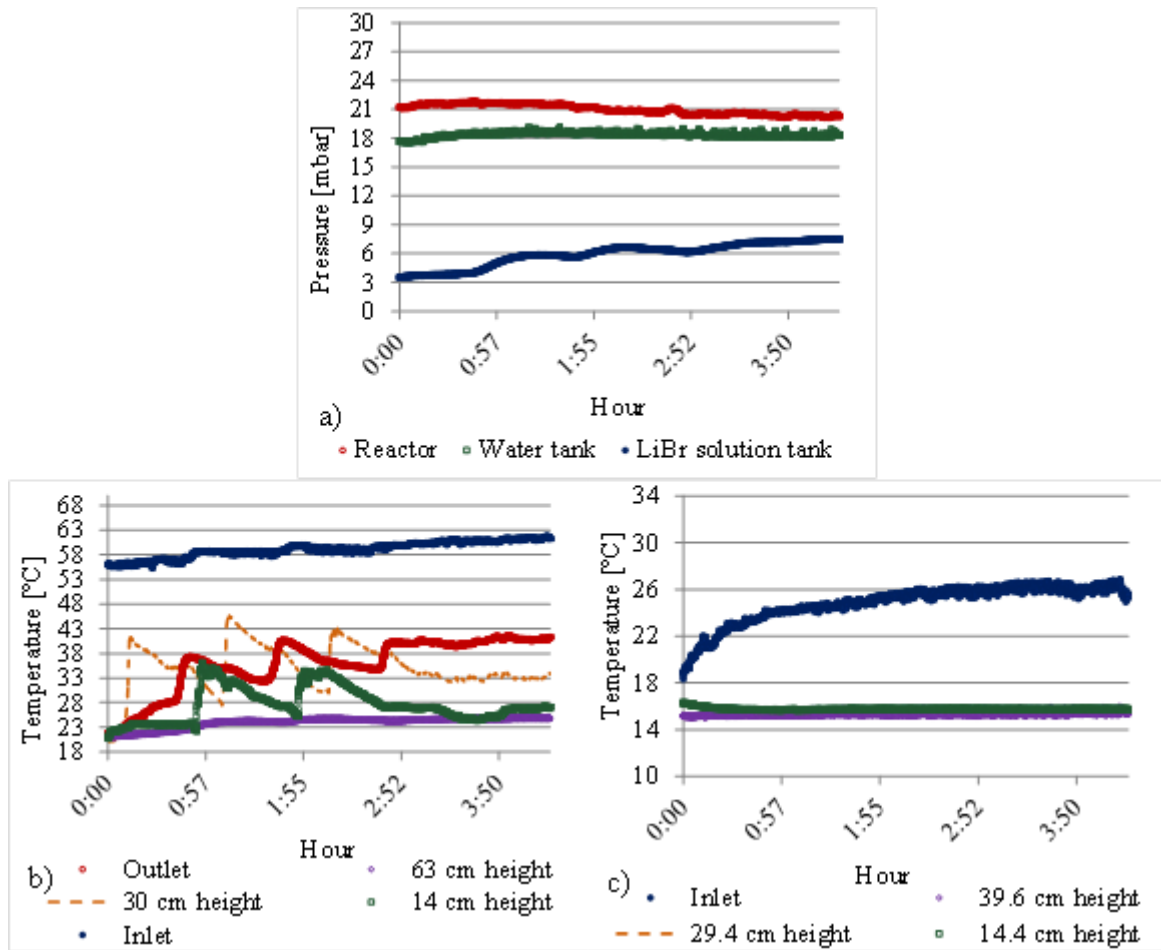


Figure 3.9. Experimental results obtained in desorption/condensation operating mode for the Test 1. a) Vapor pressure; b) LiBr solution temperature (solution tank); c) Water temperature (water tank)

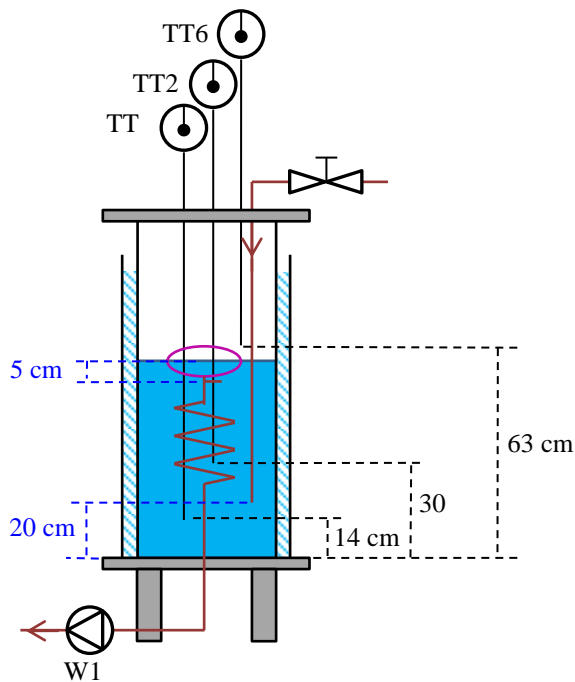


Figure 3.10. Inlet, outlet and thermocouples positioning at the solution tank

Two methods have been employed to calculate the powers: considering an energy balance on the HTF and considering an energy balance on the falling film; as shown in Equations 3.1 and 3.2, respectively, for the desorber HTF.

Analogous equations are applied to calculate the condenser power.

$$\text{Power given from the desorber HTF to the system} = \dot{m}_{htf_i} \times c_{p_{htf}} \times (T_{htf_i} - T_{htf_o}) \quad (3.1)$$

$$\begin{aligned} \text{Power given from the desorber HTF to the system} = \dot{m}_{st_o} \times h_{st_o} - \\ \dot{m}_{st_i} \times h_{st_i} + |\dot{m}_{H_2O, abs/des}| \times h_{vap}(T_{vap_{sat}}, P_{vap_{sat}}) \end{aligned} \quad (3.2)$$

In addition, in Figure 3.8d, the condenser power labeled “water film balance – des. water use” refers to the power calculated by an energy balance on the falling film but considering the desorbed water mass flow instead of the condensed water mass flow.

As shown in Figure 3.8c and 3.8d, a good coincidence is observed between the desorber HTF power and the condenser HTF power calculated using Equations (3.1) and (3.2). In Figure 3.8c it is observed that the desorber HTF power varies from 1.8 kW to 1 kW while in Figure 3.8d the condenser HTF power varies from -1kW to -0.5 kW. This difference is mainly due to 2 reasons: the reaction enthalpy for the desorption and condensation phenomena are different (see Annex B1.2) and the variation of the sensible heat in the solution film and in the water film, is also different (see Figures 3.7a and 3.7d). Furthermore, in both cases the power decreases with time because the solution LiBr mass fraction entering the reactor increases.

The approaches employed in this section to calculate the powers associated to the HTFs will be analogously used in the next section for the absorption/evaporation operating mode tests.

In Figure 3.9a it is observed that the vapor pressure in the reactor and in the water tank are higher than in the LiBr solution tank. This is because, in general, the solution film temperature in the reactor is higher than the solution tank temperature, which implies a higher vapor pressure. For the case of the pressure in the water tank, in general it is higher than in the solution tank since, for a same temperature, the saturation vapor pressure is higher at low LiBr mass fractions. A Dühring diagram indicating the working conditions of the solution tank, water tank and reactor is shown in Annex C2.4.

In Figure 3.9b the temperatures inside the solution tank are shown. The solution average temperature increases along the time even if the tank envelope temperature remains controlled at 19°C. Since the solution inlet and outlet points are not exactly placed at the tank’s bottom and top interface, respectively; some measured points in the tank are not strongly influenced by the hot inlet solution (see Figure 3.10). This is the case of the point at “14 cm height” (closer to the bottom) which should have a temperature higher than the point at “30 cm height”, but it is not the case since the real solution inlet position is at a position a little higher than 14 cm. At the “63 cm height” point the temperature does not strongly vary along the time since the thermocouple measures the solution tank vapor temperature (the solution level in the tank is below 60 cm during this test)⁽¹⁾.

⁽¹⁾ Similar temperature profiles were observed in the remaining tests at the “63 cm height” point.

In Figures 3.11 and 3.12, the prototype behavior during Test 2 are shown. As it was mentioned before, the main difference between Test 1 and Test 2 was the desorber HTF inlet temperature which increased from 68 °C to 75 °C.

In Figure 3.11b it is observed that the LiBr mass fraction of the solution leaving the reactor varies between 57% and 59% and the LiBr mass fraction difference between the solution inlet and outlet in the reactor varies between 3 and 5%. At ~20 minutes an abrupt increase in the outlet LiBr mass fraction is observed, this is associated to the reduction of the inlet solution mass flow to values below 25 kg/h (Figure 3.11c). The inlet LiBr mass fraction is approximately constant during this test, as it is shorter than Test 1, and that the stair shape observed during the previous test is still not observable.

In Figure 3.11c it is observed that the solution mass flow varies between 40 and 20 kg/h, these relative low values were due to experimental limitations when the desorber HTF inlet temperature was increased. A more detailed explanation of this phenomenon is indicated at the end of this section.

In Figure 3.11d the desorbed and condensed water mass flows in the reactor are indicated: both mass flows have a good coincidence with an almost constant value around 2 kg/h, which is between 0.5 and 1.3 kg/h higher than the values obtained in Test 1. It must be highlighted that these values are a bit lower than the desorbed water mass flows obtained in section 2.1.3.1.1 for a simulation case with inlet conditions close to those of Test 1 and Test 2; where, for an inlet solution LiBr mass concentration variation from 0.54 to 0.60, the desorbed water mass flow varies from 3.7 to 1.6 kg/h, respectively (see Figure 2.21a).

The difference between the experimental and the simulated results⁽¹⁾ is related to the wetted surface percentage in the desorber (see Table 3.6), which is around 25% experimentally, a third part of the maximal possible wetting, 79.6% (see Table 2.4). This experimental low wetted surface penalizes the desorption process performance.

A description of the experimental limitations responsible for the low surface wettings is presented later in this section. Furthermore, a more detailed comparison between the experimental and simulated results is shown in section 3.3.

In Figure 3.11e it is observed that the reactor vapor pressure in Test 2 is around 24 mbar, which is 2 mbar higher than in Test 1. Again, these values are lower than the pressures obtained in section 2.1.3.1.1 for a simulation case; where, for the same inlet solution LiBr mass fraction variation, the pressure varies from 28 to 21 mbar (see Figure 2.21b). This can be associated to the low wetting of the desorber, which penalizes the solution interface temperature increase and, consequently, the vapor pressure in the reactor (see Annex C2.4).

In Figures 3.12a and 3.12b the desorber and condenser HTFs temperatures are indicated and, associated to these parameters, in Figures 3.12c and 3.12d the desorber and condenser powers are shown.

In Figure 3.12c it is observed that the 2 power calculation methods give similar values with powers varying between 2 and 1.7 kW; where these powers are in average higher by 0.5 kW to the corresponding power measured in Test 1. Similarly, in Figure 3.12d the condenser power is also calculated by 3 different methods obtaining similar values around -1.3 kW; which, in average, are -0.5 kW higher than in Test 1.

Nevertheless, the values mentioned above are lower than the desorber and the condenser powers obtained in section 2.1.3.1.1 for a simulation case; where, for the same inlet solution LiBr mass concentration variation, the desorber and condenser powers vary from 4 to 2.5 kW and from -2.5 to -1.1 kW, respectively (see Figures 2.21c and 2.21d). This will be discussed in section 3.3.

Finally, in average the system prototype performance is better in Test 2 than in Test 1 due to the increase of the desorber HTF inlet temperature.

⁽¹⁾ Test 1: for $x_{LiBr_i} = [0.56-0.60]$, the experimental and simulated desorbed water mass flows vary between 1.5 to 0.7 kg/h and 3 to 1.6 kg/h, respectively. Test 2: for $x_{LiBr_i} = 0.543$, the experimental and simulated desorbed water mass flows are about 2 kg/h and 3.61 kg/h, respectively.

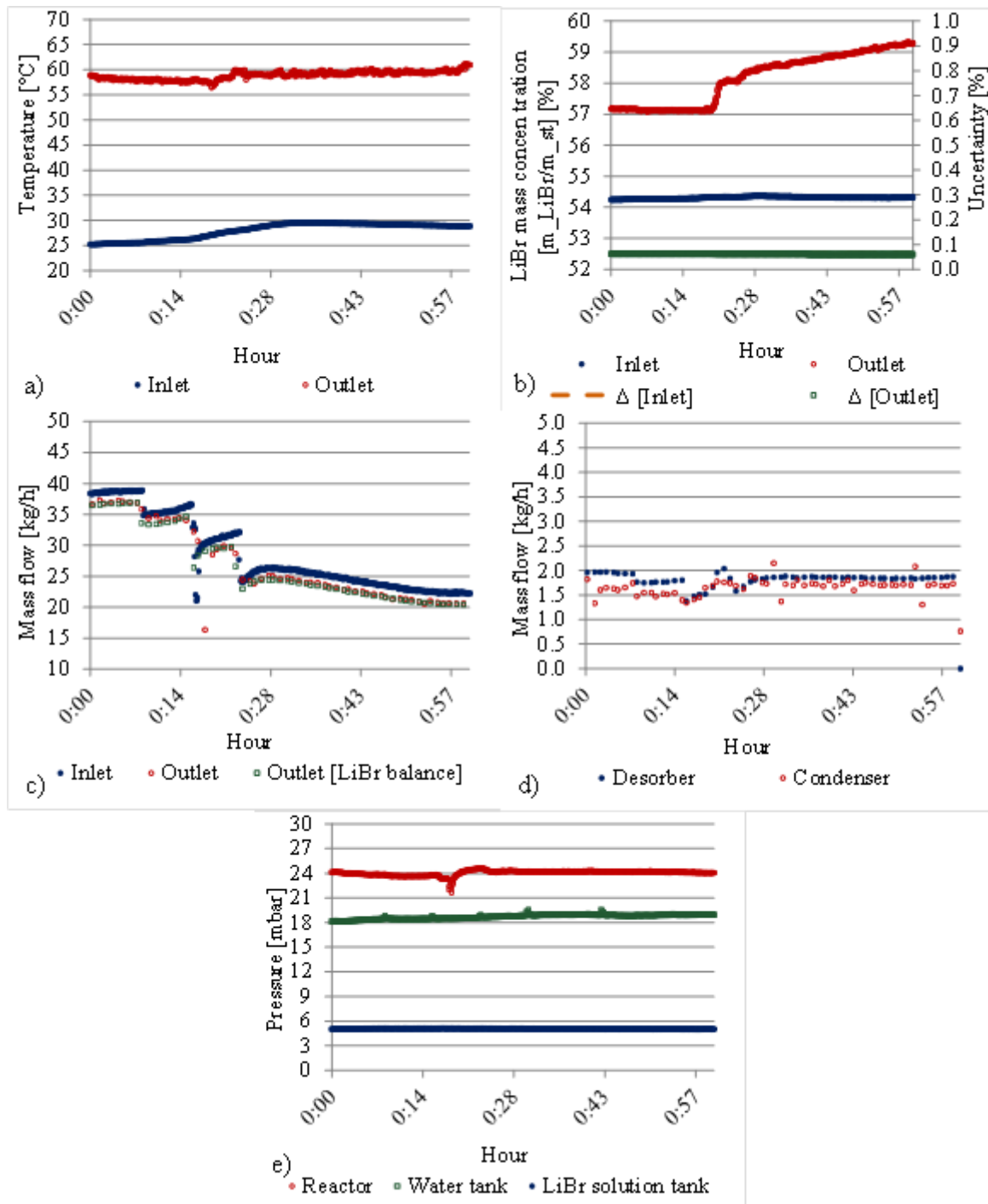


Figure 3.11. Experimental results obtained in desorption/condensation operating mode for the Test 2. a) LiBr solution temperature (desorber); b) LiBr mass concentration (desorber); c) LiBr solution mass flow (desorber); d) Desorbed/condensed water (reactor); e) Vapor pressure of the system main components

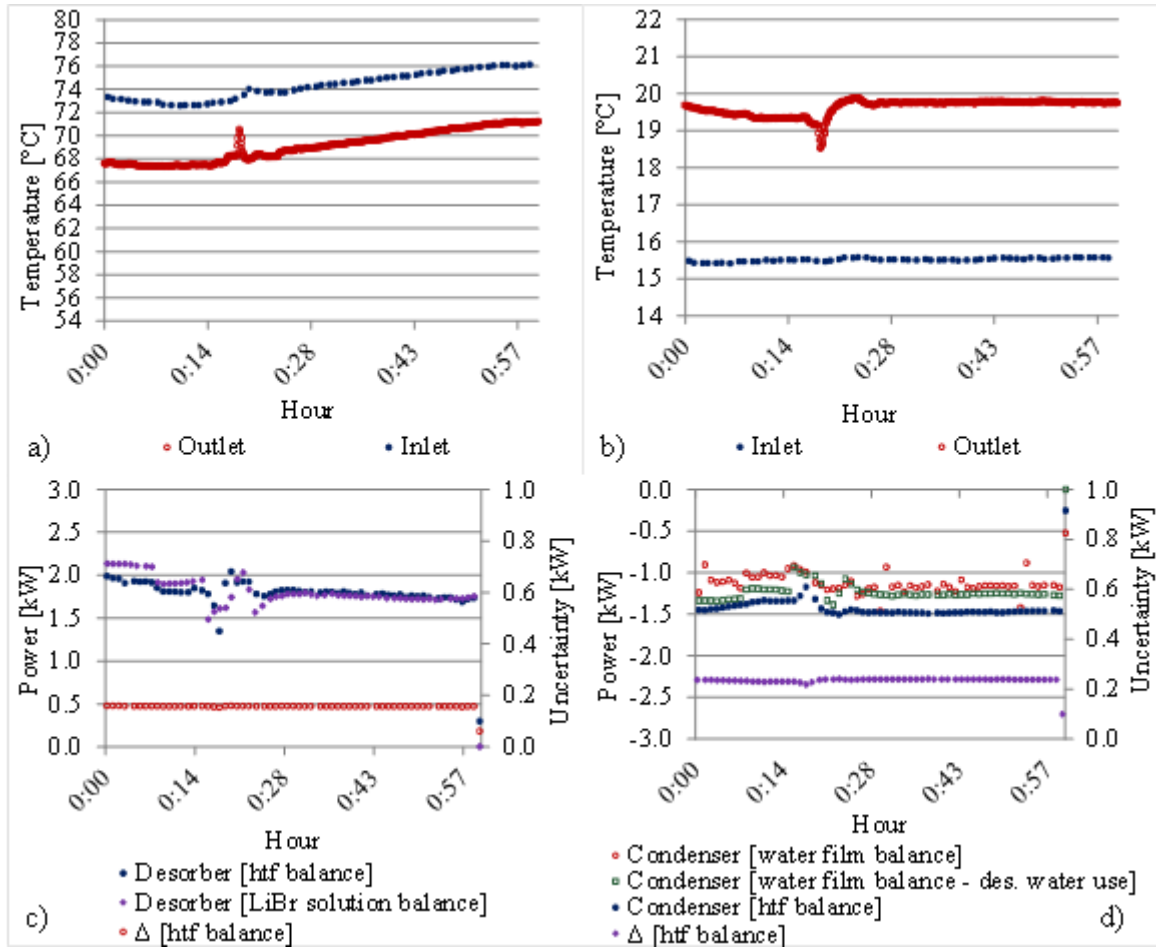


Figure 3.12. Experimental results obtained in desorption/condensation operating mode for the Test 2. a) HTF temperature (desorber); b) HTF temperature (condenser); c) Power given from the HTF to the system (desorber); d) Power given from the HTF to the system (condenser)

3.2.3.2. Desorption/condensation: summary of the results

The working conditions and experimental results associated to all the tests made in desorption/condensation operating mode are summarized in Table 3.7. The physical behavior of each system component during Tests 3 to 6 are described in detail in Annex C2.1.1.

Table 3.7. Components working conditions and system performance of all the experimental tests in desorption/condensation operating mode

		13/10/15	14/10/15	14/10/15	21/10/15	26/10/15	26/10/15
Components	Parameters	Test 1	Test 2	Test 3	Test 4	Test 5	Test 6
Desorber	Duration [min]	260	60	158	250	163	140
	\dot{m}_{st_i} [kg/h]	~50-70	~40-20	~50-75	~40-85	~53-75	~53-71
	x_{LiBr_i} [m_LiBr/m_st]	[0.56 - 0.60]	[0.54]	[0.54-0.59]	[0.54-0.595]	[0.548-0.565]	[0.568-0.592]
	<i>Reynolds</i> [inlet]	88-145	87-138	98-157	85-185	94-155	116-159
	\dot{m}_{htf/ad_i} [kg/h]	300	300	300	400	300	295
	T_{htf/ad_i} [°C]	66-67	72-76	66	64-68	58	59-77
	Observed wetted surface percentage ⁽¹⁾ [%]	~28% (~35%)	~16% (~20%)	~28% (~35%)	~28% (~35%)	~28% (~35%)	~28% (~35%)
LiBr solution tank	$T_{st/tank_{envp}}$ [°C]	19	19	19	19	19	19
	<i>Reynolds</i> [outlet]	0.3-7	2.5-7	0.5-8	1.4-7.2	0.1-8.2	1.1-9.4
	\dot{m}_{htf/ec_i} [kg/h]	300	300	300	400	300	300
	T_{htf/ec_i} [°C]	15.5	15.5	15.5	15.5	15.5	15.5
	Observed wetted surface percentage [%]	100%	100%	100%	100%	100%	100%
Water tank	$T_{wt/tank_{envp}}$ [°C]	15	15	15	15	15	15
System	Power given from the desorber HTF to the system	2 to 1 kW	2 to 1.72 kW	1.85 to 1.2 kW	2 to 1.5 kW	1.5 to 0.9 kW	0.9 to 2 kW
	Power given from the condenser HTF to the system	-1 to -0.5 kW	-1.5 kW	-1.2 to -0.6 kW	-1.2 to -0.7 kW	-0.6 to -0.4 kW	-0.5 to -1.2 kW

Test 3 was made in order to check the results repeatability. In Test 3, the inlet working conditions are almost the same as those considered for Test 1. In Test 3, the desorber HTF power varies between 1.85 and 1.2 kW and the

⁽¹⁾ In the term “~28% (~35%)” for example, the term “(~35%)” refers to the observed wetting respect to the grooved surface, while the term “~28%” refers to the observed wetting respect to the total surface, which is calculated as: $79.6\% \cdot (35\%)$ (see Table 3.4).

condenser power varies between -1.2 to -0.6 kW, which are similar to the powers obtained in Test 1. The small differences between these powers can be associated to the way the inlet solution mass flow was regulated along the tests (see Figure 3.7 and Annex C2.1.1).

In Test 4, the HTFs mass flows were increased from 300 kg/h to 400 kg/h, with respect to the Test 1. As a result, the desorber and condenser powers varied from 2 to 1.5 kW and from -1.2 to -0.7 kW, respectively; which are a little higher than those obtained in Test 1. The small increase of these powers with the HTFs mass flow increase is in agreement with the simulation parametrical study results obtained in section 2.1.3.1.1.

In Test 5, the desorber HTF inlet temperature is reduced from 66-67°C to 58°C, with respect to Test 1. As a result, the desorber and condenser powers varied from 1.5 to 0.9 kW and from -0.6 to -0.4 kW, respectively; which are lower than those obtained in Test 1. Once more, this is in agreement with the simulation parametrical study results (see section 2.1.3.1.1).

In Test 6, the desorber HTF inlet temperature varies from 59 to 77°C, keeping the remaining inlet conditions similar as those in Test 1. Along the test, the desorber and condenser powers increase from 0.9 to 2 kW and from -0.5 to -1.2 kW, respectively. Although the inlet LiBr mass concentration increases along the time, which should generate a power decrease, the desorber and condenser powers increase due to a stronger influence of the desorber temperature.

A common characteristic of all the tests is that the observed wetting in the desorber was low. One of the reasons of this low wettability is related to the exchangers metallic surface characteristics, which limited the uniform falling films wetting, as will be detailed below.

Another common characteristic of the tests where most of the inlet conditions were constant, is that the desorber and condenser powers decreased along the time with the increase of the inlet solution LiBr mass fraction; which is in agreement with the simulation parametrical study results obtained in section 2.1.3.1.1. Moreover, in a real system, during the summer period, it would be possible to balance the effect of the solution enrichment by an increase of the temperature of the HTF coming from the solar collectors.

Along the desorption/condensation tests, some experimental limitations appeared and, in some cases, prevented to perform some planned tests (see Table 3.4). Two main experimental limitations were present:

- Low wettability of the heat exchangers surfaces.
- LiBr solution overheating in the desorber.

Figure 3.13 shows pictures of the LiBr solution falling film and the condensed vapor on the desorber and condenser surfaces, respectively. As indicated in Tables 3.5 and 3.6, the wetting of the LiBr solution film was low (around 30%). This limitation was not expected during the tests, since the heat exchanger configuration (grooved flat plate) should improve the distribution of the solution in all the grooves. Nevertheless, the solution presented a tendency to flow in the grooves corners. To solve this problem, one can suggest to treat the exchange surfaces by chemical methods in order to improve their wettability (Drelich et al., 2011).

Low wettability experimental limitations were also observed during the absorption/evaporation operating mode tests described in the following section.

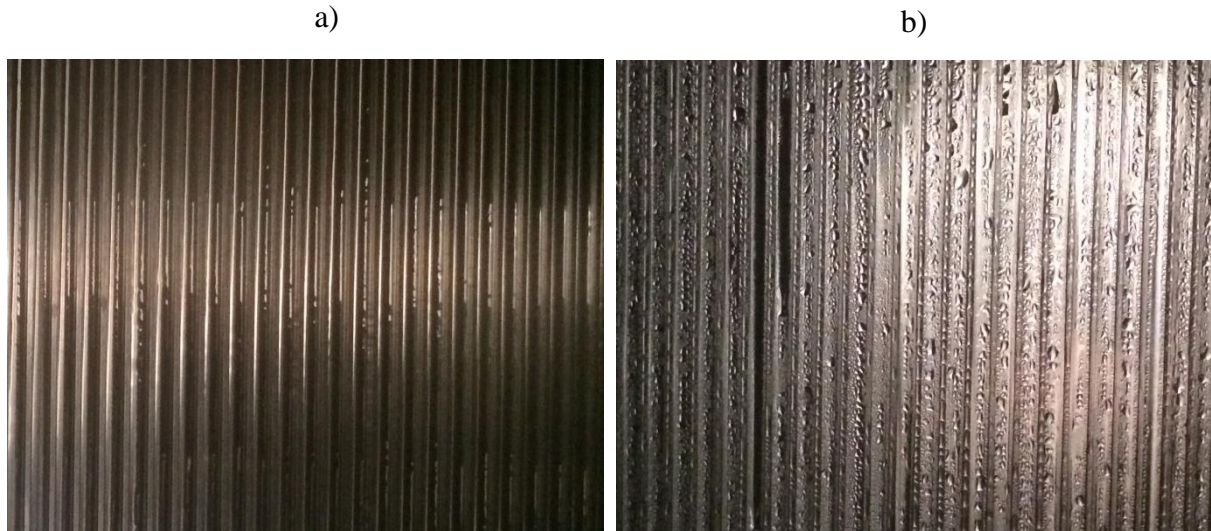


Figure 3.13. Experimental limitations in the desorption/condensation tests due to low wettability in the heat exchangers grooved surfaces. a) LiBr solution falling film flowing along the desorber; b) Condensed water along the condenser

The second experimental limitation was related to the LiBr solution overheating in the desorber when the desorber HTF temperature was 80 °C or higher. Indeed, when the desorber HTF was at high temperatures, little projections of LiBr solution droplets leaving the desorber exchange surface were observed, requiring the use of the draining system at the bottom of the reactor container (Figure 3.1). It was also observed in these cases that the solution projections were intensified when the solution mass flow increased.

From the analysis of the experimental solution temperatures and vapor pressure in the reactor, and after verification that no overflowing was happening in the funnel placed at the desorber's bottom, it was concluded that the cause of the appearance of LiBr solution projections was due to solution ebullition.

An example of the solution film ebullition appearance is associated to the working conditions at the end of Test 2 (see Figure 3.11 and Figure 3.12). In those conditions the solution film leaving the reactor is at a temperature of 61°C and at a LiBr mass concentration of 59.3%, while the reactor is at a vapor pressure of 24 mbar. Considering the LiBr solution Dühring diagram shown in Annex C2.4, under the same described conditions of LiBr mass fraction and vapor pressure, the solution saturation temperature is around 61°C. The HTF entering into the desorber is at a temperature of 76°C leading to a wall superheat at the entrance close to 15 °C. This value appears to be the onset of boiling superheat of lithium bromide solution in such situation. This value is comparable to the values obtained by Fujikawa et al. (2015) in their study on pool boiling heat transfer if aqueous lithium bromide solution is at low pressure.

In order to avoid further solution projections leaving the desorber, Test 2 was stopped after 1 hour time.

3.2.3.3. Absorption/evaporation: typical results

Four experimental tests in absorption/evaporation operating mode were carried out; the working conditions of 2 of these tests are shown in Table 3.8. The main differences between the two selected configurations are the absorber HTF inlet temperature, T_{htf/ad_i} , and the evaporator HTF inlet mass flow, \dot{m}_{htf/ec_i} , which increased from 25 °C to 30 °C and from 300 kg/h to 400 kg/h, respectively.

The system behavior associated to Test 7 is shown from Figures 3.14 to 3.16.

Table 3.8. Working conditions for two tests in absorption/evaporation operating mode

		14/10/2015	15/10/2015
Components	Parameters	Test 7	Test 8
Absorber	\dot{m}_{st_i} [kg/h]	~110	~110
	x_{LiBr_i} [m_LiBr/m_st]	[0.59 - 0.54]	[0.59 - 0.54]
	\dot{m}_{htf/ad_i} [kg/h]	300	300
	T_{htf/ad_i} [°C]	25	30
	Observed wetted surface percentage [%] ⁽¹⁾	~72% (~90%)	~60% (~75%)
LiBr solution tank	$T_{st/tank_{envp}}$ [°C]	19	19
Evaporator	$\dot{m}_{f_water_i}$ [kg/h]	110	110
	\dot{m}_{htf/ec_i} [kg/h]	300	400
	T_{htf/ec_i} [°C]	15	15
	Observed wetted surface percentage [%] ⁽²⁾	~24% (~30%)	~24% (~30%)
Water Tank	$T_{wt/tank_{envp}}$ [°C]	15	15

As it is observed in Figures 3.14a and 3.16b, since the solution leaving the reactor was below 29°C and the solution tank envelope was maintained at 19°C, the solution inside the tank lightly increased its temperature along time. In Figure 3.14c, it is observed that the mass flow of the pumped solution decreased along time; this behavior was probably related to the pump internal functioning since the solution temperature and LiBr mass concentration curves shown in Figures 3.14a and 3.14b would indicate an opposite effect. A manual control of the associated pump was needed at ~50 minute in order to maintain the solution average mass flow around 110 kg/h.

In Figure 3.14b the solution LiBr mass fraction entering and leaving the reactor is shown. During this absorption process the “step-like” variation presented during the desorption phase is not observed, which can be associated to the solution density distribution along the solution tank. In desorption processes, strong solution is pumped back at the tank’s bottom (higher density) and weak solution is pumped out from tank’s top (lower density); hence the tank configuration facilitates stratification. In absorption processes, weak solution is pumped into the tank’s bottom and strong solution is pumped out from the tank’s top; hence, the strong solution at the top presents a tendency to go to the bottom (and vice versa), facilitating a solution mixing along the tank and avoiding to observe an “step-like” variation.

The gap between the inlet and outlet LiBr mass fractions in the reactor is slowly reduced along time and, in average, is around 1%. The solution inlet mass fraction decreases along time (Figure 3.14b). The temperature of the solution is above 28 °C (Figure 3.14a), allowing heating-up a building with a low-temperature heating floor.

⁽¹⁾ In term “~72% (~90%)”, the term “(~90%)” refers to the observed wetting respect to the grooved surface, while the term “~72%” refers to the observed wetting respect to the total surface, which is calculated as: 79.6%*(90%) (see Table 3.5).

⁽²⁾ In term “~24% (~30%)”, the term “(~30%)” refers to the observed wetting respect to the grooved surface, while the term “~24%” refers to the observed wetting respect to the total surface, which is calculated as: 79.6%*(30%) (see Table 3.5).

In Figures 3.14d and 3.14e, the temperatures and mass flows of the water film entering and leaving the reactor are shown, respectively. In Figure 3.14d it is observed that the water film temperature at the outlet is lower than at the inlet, which is in agreement with the energy losses along the film due to the evaporation process.

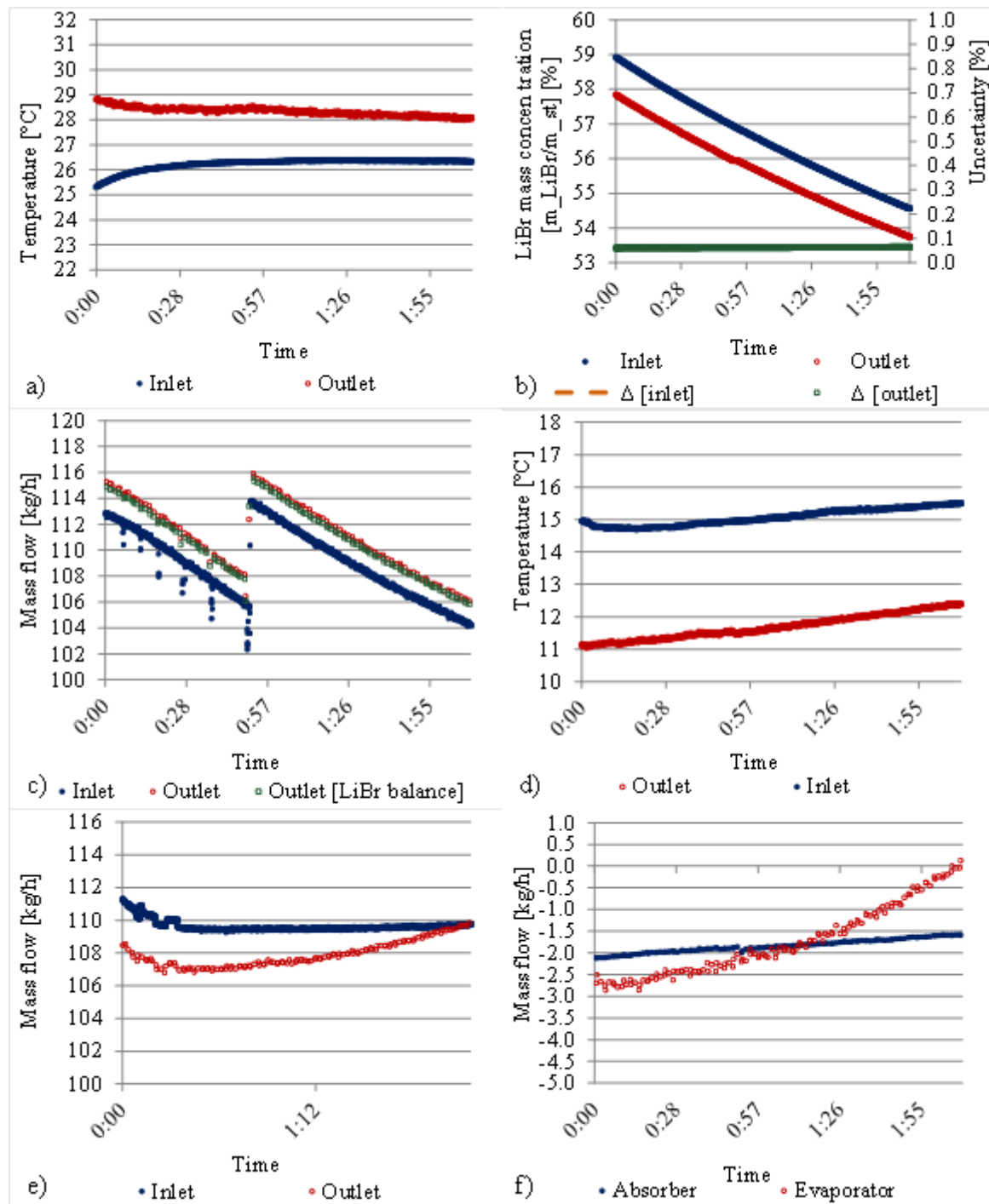


Figure 3.14. Experimental results obtained in absorption/evaporation operating mode for Test 7. a) LiBr solution temperature (absorber); b) LiBr fraction (absorber); c) LiBr solution mass flow (absorber); d) Water film temperature (evaporator); e) Water film mass flow (evaporator); f) Absorbed/evaporated water (reactor)

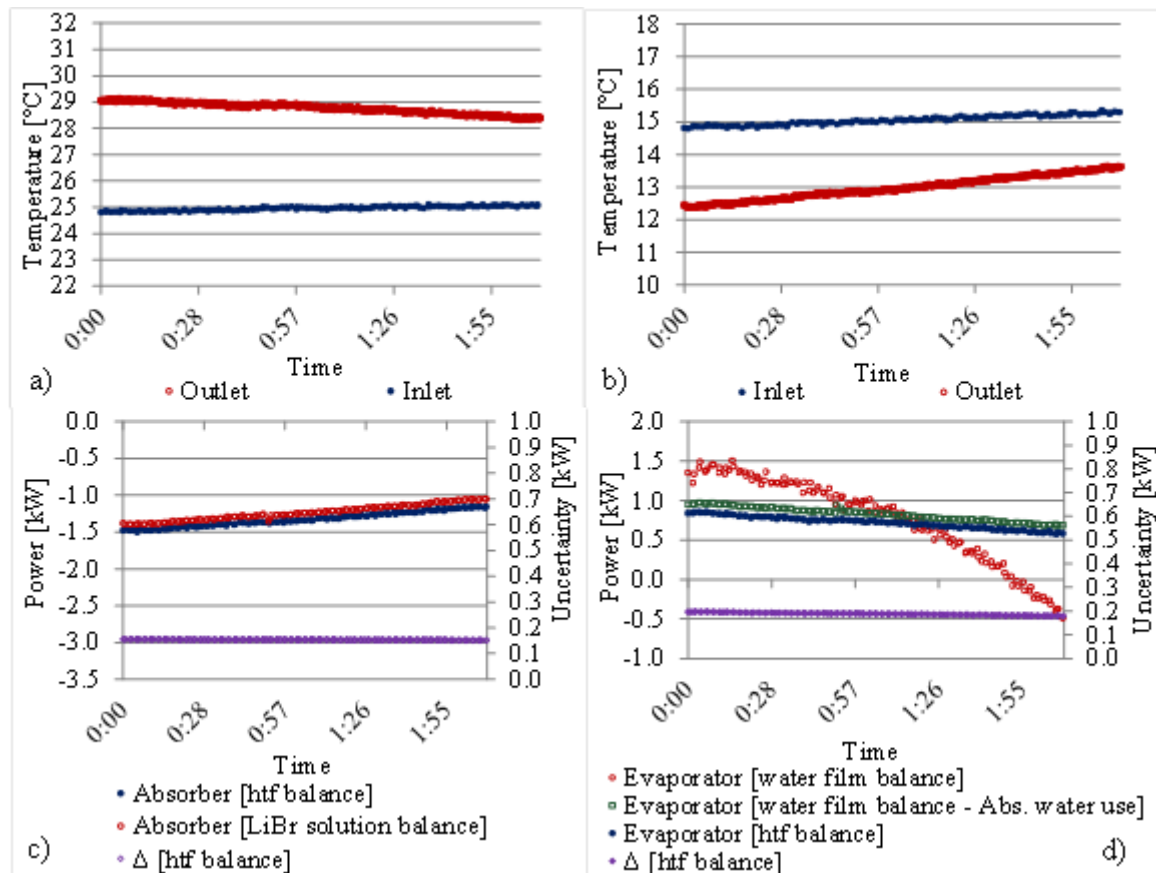


Figure 3.15. Experimental results obtained in absorption/evaporation operating mode for the Test 7. a) HTF temperature (absorber); b) HTF temperature (evaporator); c) Power given from the HTF to the system (absorber); d) Power given from the HTF to the system (evaporator)

In Figure 3.14e, it is observed that the water film mass flow at the outlet is lower than at the inlet, which is in agreement with the evaporation process. Nevertheless, after ~20 minutes the outlet mass flow starts to increase and to approach the inlet mass flow, reducing the measured evaporated water mass flow. A similar behavior was observed in Tests 8 to 10 and, in some cases, water mass flows higher at the outlet than at the inlet were present. Considering the latter observation and comparing it against other system measured parameters, such as the water film and evaporator HTF temperatures, it was concluded that the measurement of the water film mass flow leaving the reactor was not accurate due to a problem in the associated Coriolis flowmeter “F3”. Hence, calculations of mass and energy balance along absorption tests used only the measurements of flowmeters F1 and F2.

In Figure 3.14f the mass flow of the absorbed and evaporated water inside the reactor is shown. Both mass flows show approximately similar values, with the absorbed water mass flow varying from -2 kg/h to -1.5 kg/h; also, the mass flow is reduced along time, which is associated to the LiBr mass fraction decrease of the solution entering the absorber.

In Figures 3.15a,b the HTF absorber and HTF evaporator temperatures are shown; associated to these curves in Figures 3.15c and 3.15d, the absorber power (power given from the HTF to the absorber) and the evaporator power (power given from the HTF to the evaporator), respectively, are presented.

In Figure 3.15a it is observed that the absorber HTF outlet temperature is increased between 4 °C and 3 °C with respect to its inlet temperature. The temperature difference reduction along time is associated to the reduction of the LiBr mass fraction entering the reactor. In Figure 3.15b it is observed that the evaporator HTF outlet temperature is reduced between 2.5 °C and 1.5 °C with respect to its inlet temperature, which is due to the heat given to the water film to produce the evaporation. The HTF temperature increase and decrease in the absorber

and evaporator, respectively, are comparable to the solution temperature increase and water film temperature decrease, which are in average 2 °C (Figure 3.14a) and 3.5 °C (Figure 3.14d), respectively.

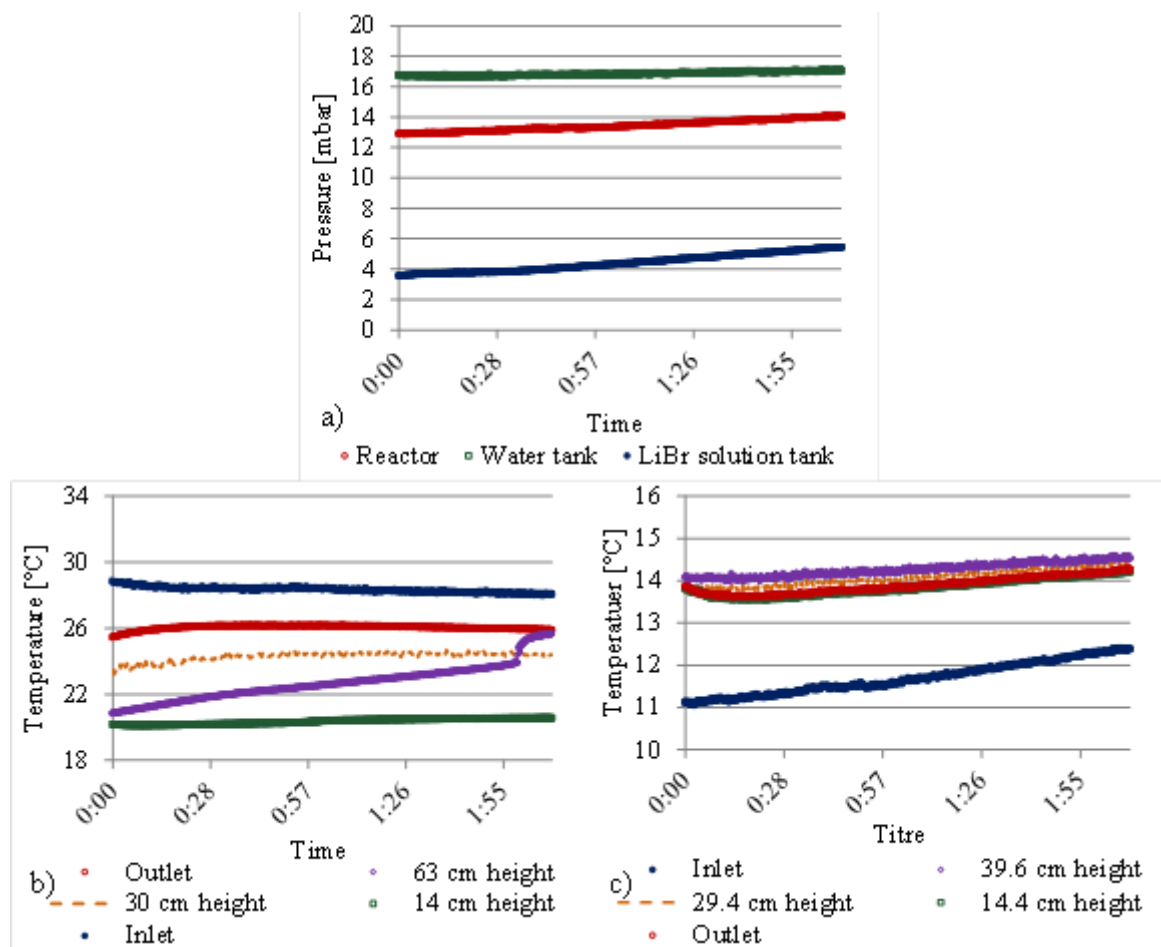


Figure 3.16. Experimental results obtained in desorption/condensation operating mode for the Test 7. a) Vapor pressure; b) LiBr solution temperature (solution tank); c) Water temperature (water tank)

As it is shown in Figures 3.15c and 3.15d, a good coincidence is observed between the absorber power and the condenser power calculated by analogous approaches as described in Equations (3.1) and (3.2). The absorber power varies from -1.5 kW to -1 kW while the evaporator power varies from 1 kW to 0.6 kW; in both cases the power decreases with time because the solution LiBr mass fraction entering the reactor also decreases.

In Figure 3.15d, the evaporator power labeled “water film balance – abs. water use” refers to the power calculated by an energy balance in the falling film but considering the absorbed water mass flow instead of the evaporated water mass flow; this last approach presents better coincidences with the “htf balance” approach and will be used in further analysis.

In Figure 3.16a it is observed that the vapor pressure in the reactor is around 13 mbar which is at least 8 mbar lower than the reactor pressure measured in the desorption/condensation tests. A vapor pressure in desorption/condensation higher than in absorption/evaporation is in agreement with the behavior presented in the Dühring diagram (see Annex C2.4) and with the simulation results obtained previously for similar conditions. Indeed, in the absorption/evaporation reference case described in section 2.1.3.1.2, for a solution inlet LiBr mass fraction variation from 0.59 to 0.54, the reactor vapor pressure varies from 8.8 to 10.8 mbar. Additionally, the experimental wetting in the absorber and evaporator (see Table 3.8) is around 72% and 24%, respectively, which is lower than the simulated wetted surface percentages (79.6%, see Table 2.6).

Since the vapor in the reactor is considered in saturated conditions, the vapor pressure will be strongly influenced by the water falling film interface temperature in the evaporator⁽¹⁾. Considering that the experimental wetting in the evaporator is strongly penalized (~24%, Table 3.8), the heat and mass transfer from the falling film to the vapor is reduced (due to the smaller exchange surface). This latter implies to have higher water film interface temperatures than in cases with well wetted surfaces (a lower heat transfer across the film implies a lower temperature difference between the HTF and the water film), which, consequently, generates higher vapor pressures in the reactor.

In Figures 3.16b,c the temperatures inside the tanks are shown; the average temperatures inside these components do not vary strongly along the time. In the solution tank the internal temperature goes from 20 to 24 °C, which is lower than the temperatures measured in Test 1 (desorption/condensation mode). This is due to the temperature of the solution returning to the tank; which during Test 7 is around 28°C (Figure 3.16b), while in Test 1 is around 60°C (see Figure 3.9b).

In Figures 3.17 and 3.18, the prototype performance during Test 8 is shown. As it was mentioned before, the main differences between working conditions in Test 7 and Test 8 were the absorber HTF inlet temperature, T_{htf/ad_i} , and the evaporator HTF mass flow, \dot{m}_{htf/ec_i} , which increased from 25 °C to 30 °C and from 300 kg/h to 400 kg/h, respectively.

In Figure 3.17b it is observed that the LiBr mass fraction of the solution leaving the reactor varied between 58% and 54% and the LiBr mass fraction difference between the inlet and outlet solution in the reactor was around 0.9%.

In Figure 3.17d the absorbed water mass flow in the reactor is indicated; the mass flow varied from 1.5 kg/h to 1 kg/h which was around 0.5 kg/h lower than the values obtained in Test 7. This result agrees with the parametrical study made in section 2.1.3.1.2; where for a simulation case with similar conditions as for Test 7, an increase in the absorber HTF inlet temperature from 25 °C to 30 °C represented a performance reduction of ~40 % and an increase in the evaporator HTF mass flow from 300 kg/h to 400 kg/h represented a performance increase of ~5%.

In Figure 3.17e it is observed that the reactor vapor pressure in Test 8 is around 15 mbar, which is 3 mbar higher than in Test 7. This fits with the solution film temperature increase (see Figures 3.17a and 3.14a).

In Figures 3.18a and 3.18b the absorber and evaporator HTFs temperatures are indicated and, associated to these parameters, the absorber and evaporator powers are shown in Figures 3.18c and 3.18d.

In Figure 3.18a it is observed that the absorber HTF outlet temperature is increased between 2.5 °C and 2 °C with respect to its inlet temperature; where the temperature difference reduction along time is associated to the reduction of the LiBr mass fraction entering the reactor. In Figure 3.18b it is observed that the evaporator HTF outlet temperature is reduced between 1 °C and 0.5 °C with respect to the evaporator HTF inlet temperature.

In Figure 3.18c it is observed that the 2 considered calculation methods (htf balance and LiBr solution balance) give similar values with powers varying between -0.9 and -0.6 kW; where these powers are in average lower by 0.6 kW than the corresponding powers measured in Test 7. This reduction is in agreement with the simulated results obtained in the parametrical study (section 2.1.3.1.2), where when the absorber HTF inlet temperature is increased, the absorber power would decrease, since the temperature difference between the solution film and the HTF is reduced.

⁽¹⁾ Vapor and interface have also the same temperature, since the interface is at a thermodynamic equilibrium.

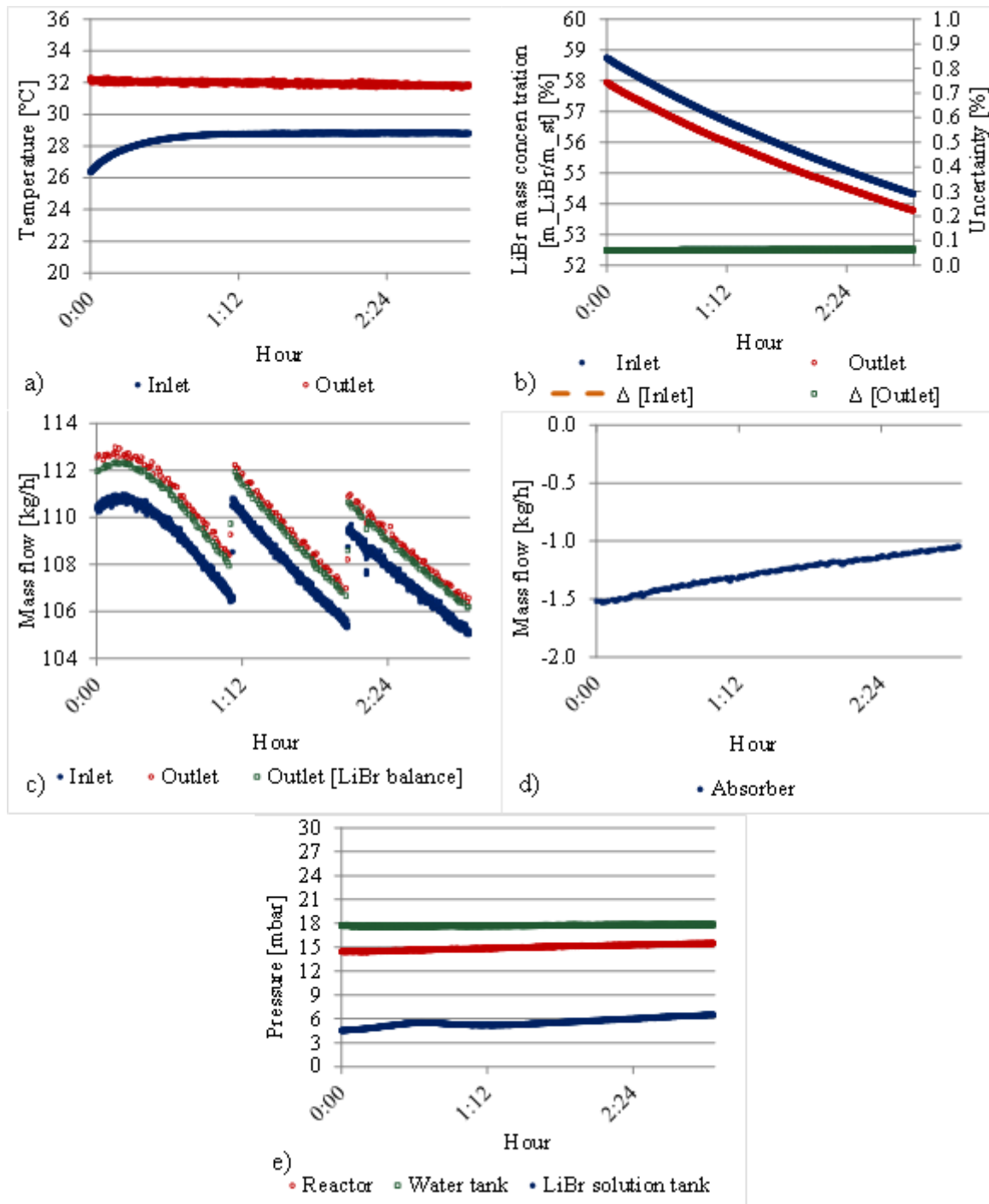


Figure 3.17. Experimental results obtained in absorption/evaporation operating mode for the Test 8. a) LiBr solution temperature (absorber); b) LiBr mass concentration (absorber); c) LiBr solution mass flow (absorber); d) Absorbed water (reactor); e) Vapor pressure of the system main components

Similarly, in Figure 3.18d the condenser power is also calculated by 2 different methods obtaining similar values and that covered a range from 0.5 to 0.1 kW; these values were in average 0.4 kW lower than in Test 7. Again, this reduction is in agreement with the simulated results (section 2.1.3.1.2).

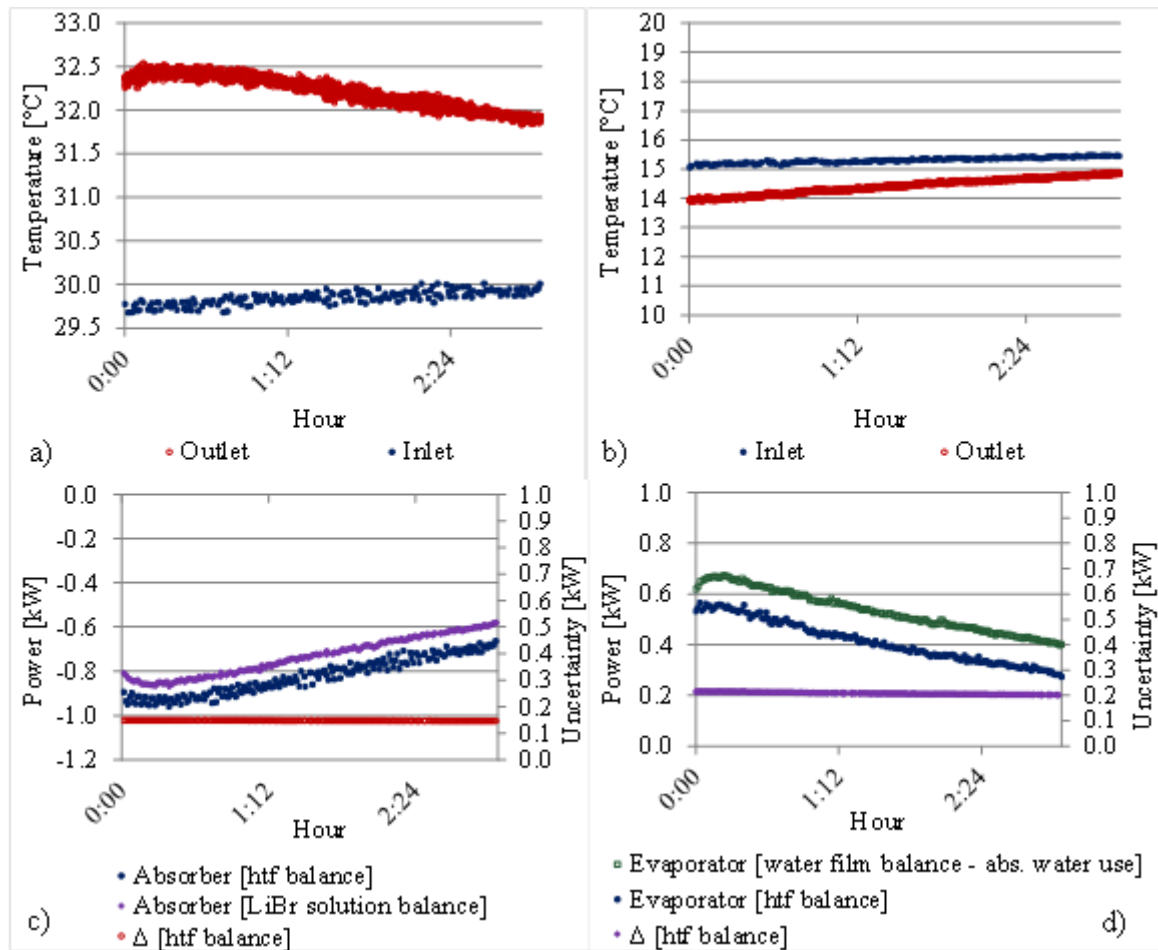


Figure 3.18. Experimental results obtained in absorption/evaporation operating mode for the Test 8. a) HTF temperature (absorber); b) HTF temperature (evaporator); c) Power given from the HTF to the system (absorber); d) Power given from the HTF to the system (evaporator)

Concerning the absorber and evaporator powers; although an increase in the evaporator HTF mass flow was tested in Test 8 to increase these powers; the absorber HTF inlet temperature increase had, at the end, a bigger influence by reducing them.

3.2.3.4. Absorption/evaporation: summary of the results

The working conditions and experimental results associated to all the absorption/evaporation tests are summarized in Table 3.9. The physical behavior of the system during Tests 9 to 10 are described in detail in Annex C2.1.2.

A common characteristic of all the tests is that, again, the observed wetted surface percentage in the absorber and the evaporator was low, as it was explained in section 3.2.3.2 (experimental limitations).

Another characteristic is that the absorber and evaporator HTF powers decreased along time with the decrease of the inlet solution LiBr mass concentration; which is in agreement with the simulation study (section 2.1.3.1.2).

In Test 9 the inlet solution mass flow in the reactor was reduced from ~110 kg/h to ~70 kg/h, with respect to the inlet conditions in Test 8. As a result, the absorber and evaporator powers varied from -0.7 to -0.45 kW and from 0.45 to 0.1 kW, respectively; which were a little lower than those obtained in Test 8. According to the simulations, a reduction in the inlet solution mass flow should increase these powers; nevertheless, a reduction

is observed. This latter behavior is explained by the wetting in the absorber, which is strongly reduced from ~60%, in Test 8, to ~24% in Test 9, when the inlet solution mass flow is reduced; generating, therefore, a reduction in the system performance.

Table 3.9. Working conditions and system performance of all the experimental tests in absorption/evaporation operating mode

		14/10/2015	15/10/2015	22/10/2015	27/10/2015
Components	Parameters	Test 7	Test 8	Test 9	Test 10
Absorber	Duration [min]	129	183	203	298
	\dot{m}_{st_i} [kg/h]	~114-106	~111-105	~65-73	~116-103
	x_{LiBr_i} [m_LiBr/m_st]	[0.59 - 0.545]	[0.587 - 0.543]	[0.589-0.55]	[0.59-0.55]
	Reynolds [inlet]	78-84	97-109	148-169	133-140
	\dot{m}_{htf/ad_i} [kg/h]	300	300	300	200
	T_{htf/ad_i} [°C]	25	29.8-30	29.6-30	29.3-29.9
	Observed wetted surface percentage [%] ⁽¹⁾	~72% (~90%)	~60% (~75%)	~24% (~30%)	~40% (~50%)
LiBr solution tank	$T_{st/tank_{envp}}$ [°C]	19	19	19	19
Evaporator	$\dot{m}_{f_water_i}$ [kg/h]	110	112-109	106-110	114-110
	Reynolds [inlet]	1235-1246	1250-1283	1247-1305	1297-1365
	\dot{m}_{htf/ec_i} [kg/h]	300	400	400	400
	T_{htf/ec_i} [°C]	15	15.2	15.2	15-15.6
	Observed wetted surface percentage [%] ⁽²⁾	~24% (~30%)	~24% (~30%)	~24% (~30%)	~24% (~30%)
Water tank	$T_{wt/tank_{envp}}$ [°C]	15	15	15	15
System	Power given from the absorber HTF to the system	-1.5 to -1 kW	-0.9 to -0.6 kW	-0.7 to -0.45 kW	-0.5 to -0.3 kW
	Power given from the evaporator HTF to the system	1.0 to 0.6 kW	0.6 to 0.3 kW	0.45 to 0.1 kW	0.25 to 0.05 kW

In Test 10 the absorber HTF mass flow was reduced from 300 kg/h to 200 kg/h, with respect to the inlet conditions in Test 8. As a result, the absorber and evaporator HTF powers varied from -0.5 to -0.3 kW and from 0.25 to 0.05 kW, respectively; which were lower than those obtained in Test 8. According to the simulations, a reduction in the absorber HTF mass flow should reduce these powers, which actually happens. Nevertheless, a reduction in the absorber HTF mass flow should also increase the temperature difference between the absorber HTF outlet and inlet temperatures, which does not happen since this temperature gap remains almost the same in both tests, around 2.5 °C. This latter behavior is explained by the wetting of the absorber, which is reduced from ~60%, in Test 8, to ~40% in Test 10.

⁽¹⁾ In term “~72% (~90%)”, the term “(~90%)” refers to the observed wetting respect to the grooved surface, while the term “~72%” refers to the observed wetting respect to the total surface, which is calculated as: 79.6%*(90%) (see Table 3.5).

⁽²⁾ In term “~24% (~30%)”, the term “(~30%)” refers to the observed wetting respect to the grooved surface, while the term “~24%” refers to the observed wetting respect to the total surface, which is calculated as: 79.6%*(30%) (see Table 3.5).

Finally, in a similar way as in the desorption/condensation tests, a low wettability on the heat exchangers surfaces was observed in both, the absorber and the evaporator. However, since the working temperatures in these tests were around 30 °C, no liquid solution projections and overflowing were observed.

3.2.4. Crystallization

Additional tests to those indicated in sections 3.2.3.1 and 3.2.3.3 were carried on in order to study the system performance when crystallization conditions are reached in the solution tank. The physical behavior of these tests in desorption/condensation and absorption/evaporation operating modes are described in the sections below.

3.2.4.1. Desorption/condensation functioning

Three tests in desorption/condensation operating mode were carried out in different days (days 1, 3 and 4) to enable the crystals formation.

Each of these tests progressively increased the amount of crystal formed at the end of the day, with the test in “day 4” producing an excessive amount of crystals in the solution tank, as it is shown in Figure 3.19. In “day 4” the crystals were rapidly formed, finishing with almost all the solution tank crystalized (Figure 3.19d).

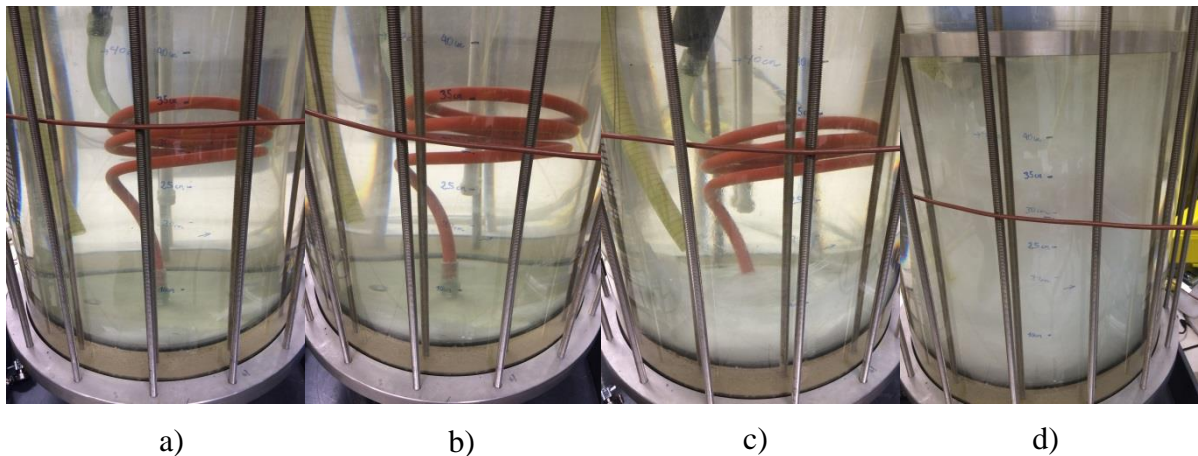


Figure 3.19. LiBr solution crystals formation during the desorption/condensation tests. a) End of day 1; b) End of day 3; c) During the day 4; d) End of day 4.

The solution temperature and LiBr mass fraction permitting to form the crystals during the “day 4” test are described in Figure 3.20. It is observed that although crystals were formed all along the test (Figure 3.19c), the solution in the tank did not stay at constant saturated conditions⁽¹⁾; but, conversely, behaved as if no crystals were present. This can be explained due to the LiBr fraction gradient along the tank height and due to the crystals tendency to sink to the tank bottom because of their higher density; both aspects could prevent the liquid solution to reach the saturated conditions during the test. An equilibrium state between the solid and liquid solution eventually could be reached along time, once the desorption process was stopped.

⁽¹⁾ The LiBr solution crystallization curve (saturation curve) is described in section 2.2.1.2 (Figure 2.35).

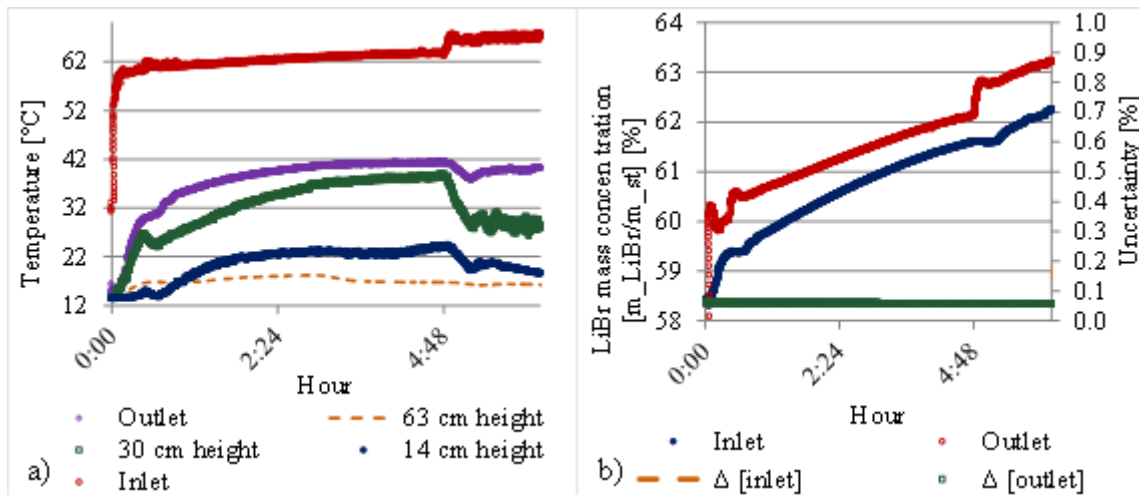


Figure 3.20. LiBr solution along the crystals formation in “day 4” test (desorption/condensation). a) LiBr solution temperature (solution tank)⁽¹⁾; b) LiBr mass fraction (desorber)

During these 3 desorption/condensation tests, a solution mal distribution appeared at the top of the desorber, generating that several grooves had no solution flowing along them. This behavior could be associated to a possible crystal formation inside the reactor distribution system, which can prevent the solution from passing through the corresponding distribution holes (see Annex C1.1).

A method to ensure a good surface wetting is to increase the solution mass flow up to a value where all the grooves are completely wet and, afterwards, reduce the mass flow down to the system working conditions. Nevertheless, since an increase in the solution mass flow could generate some solution projections outside the desorber (see section 3.2.3.2, experimental limitations), this method was not used.

Another experimental limitation in these 3 tests appeared at the end of “day 4” when almost all the solution inside the tank crystallized; this latter generated a solution solidification inside the coil pipe, preventing the liquid solution from being pumped out of the tank. Hence, a better management of the position where the crystals are formed should be considered in further experiences.

3.2.4.2. Absorption/evaporation functioning

Two tests in absorption/evaporation operating mode were carried out in two different days (days 2 and 5) to evaluate the system performance when crystals are present in the solution tank.

The absorption/evaporation test in “day 5” was carried out after “day 4” desorption/condensation test described in section 3.2.4.1. In order to reduce the amount of formed crystals, the solution tank envelope temperature was increased from 16 °C to 21 °C⁽²⁾. The tank state during the “day 5” absorption/evaporation test is shown in Figure 3.21.

⁽¹⁾ During and after the “day 4” desorption/condensation test, the solution tank envelope was maintained at a temperature around 16 °C.

⁽²⁾ A solution temperature around 21 °C implies a saturated LiBr mass fraction around 0.59, while a 16 °C temperature corresponds to a 0.58 mass fraction (see Figure 2.35, crystallization curve). Hence, a higher temperature (21 °C) can avoid crystals formation at mass fractions below 0.59.

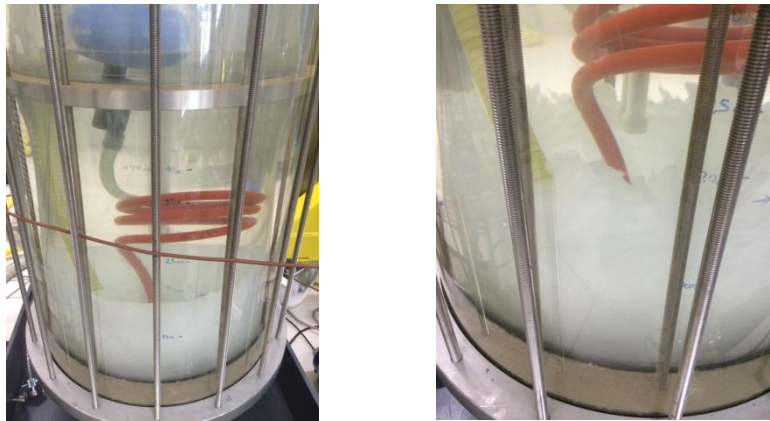


Figure 3.21. LiBr solution crystals formed in the solution tank during the “day 5” absorption/evaporation test.

The solution temperature and solution LiBr mass fraction during the “day 5” are described in Figure 3.22. Again, although crystals were present all along the test (Figure 3.21), the solution in the tank did not stay at constant saturated conditions; but, conversely, behaved as if no crystals were present (see Figure 3.22b).

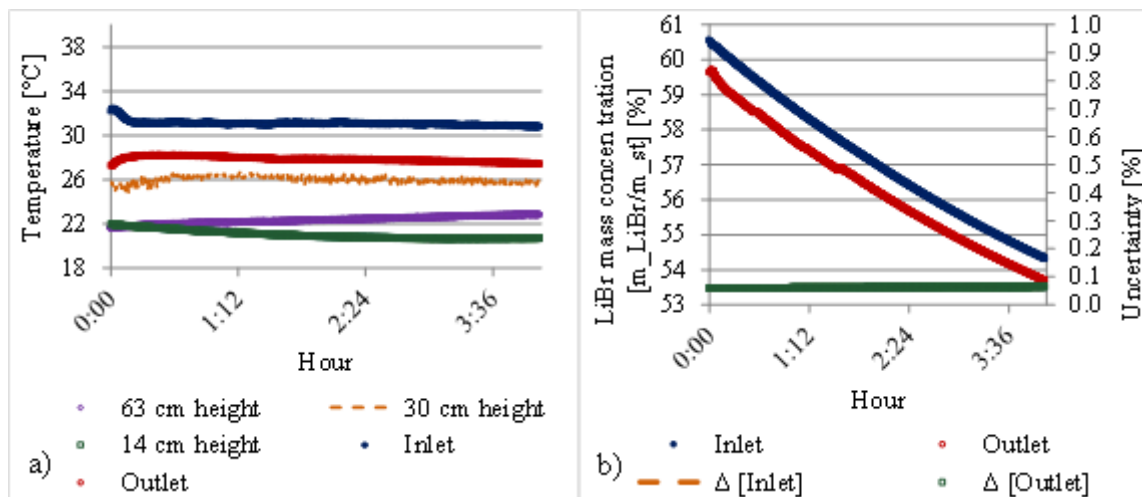


Figure 3.22. LiBr solution conditions along the crystals dilution “day 5” test (absorption/evaporation). a) LiBr solution temperature (solution tank)⁽¹⁾; b) LiBr mass concentration (absorber)

Finally, during these 2 tests no distribution problem was observed on the absorber, since a good wetting was possible by increasing the solution mass flow up to a value (~250 kg/h) where all the grooves were completely wet and, afterwards, reducing the mass flow down to the system working conditions.

⁽¹⁾ During and after the “day 5” absorption/evaporation test, the solution tank envelope was maintained at a temperature around 21°C.

3.2.5. Energy storage density

In Chapter 1 several interseasonal heat storage system prototypes constructed in recent years were described. A useful indicator permitting to compare these different systems was suggested: the energy storage density (ESD) of the system.

The $ESD_{V-system}$ is defined as the ratio between the absorber energy output (energy given to the absorber HTF during the discharging period) and the volume occupied by the system, as it is described in Equation (3.3).

$$ESD_{V-system} = \frac{\text{Absorber energy output}}{\text{System volume}} = \frac{\int_{t=\text{beginning of test}}^{t=\text{end of test}} \left(\dot{m}_{htf/absorber_i} \times c_{p_{htf/absorber}} \times (T_{htf/absorber_o} - T_{htf/absorber_i}) \right) \times dt}{\text{System volume}} \quad (3.3)$$

A variation of the ESD in Equation (3.3) considers the maximum volume of diluted solution and water instead of the system volume. This definition, denoted as $ESD_{V-st-wt}$, is presented in Equation (3.4).

$$ESD_{V-st-wt} = \frac{\text{Absorber energy output}}{\text{Diluted LiBr solution and water volume}} \quad (3.4)$$

A third definition of the energy storage density, ESD_m , considers the solution mass instead of the system volume, as it is defined in Equation (3.5).

$$ESD_m = \frac{\text{Absorber energy output}}{\text{LiBr solution mass of the system}} \quad (3.5)$$

Considering the indicators defined in Equations (3.3), (3.4) and (3.5), in Table 3.10 are shown the energy storage densities obtained during Test 7 and 8 (discharge operating mode), described in section 3.2.3.4.

Table 3.10. Prototype ESD during Tests 7 and 8 (discharge operating mode) – ($x_{LiBr_i} \approx [0.59 - 0.54]$)

	Prototype volume ⁽¹⁾ [m ³]	Maximal diluted solution and water volume [m ³]	Prototype initial LiBr solution mass [kg]	$ESD_{V-system}$ [kWh/m ³]	$ESD_{V-st-wt}$ [kWh/m ³]	ESD_m [kWh/kg]
Test 7	0.465	0.0854	92 (at $T_{st} = 25$ °C, $x_{LiBr} = 48.96$ %)	6.2	33.7	0.031
Test 8				5.4	29.6	0.027

From results obtained in Table 3.10, it is observed that the ESD in Test 7 is higher than in Test 8, even if the former had a shorter duration (~ 2 hours) than the latter (~ 3 hours). This is due to the higher absorber output power presented in Test 7 (-1.5 kW to -1 kW) compared to Test 8 (-0.9 kW to -0.6 kW). It must be highlighted that in both tests, the inlet LiBr mass fraction varied from ~0.59 to ~0.54.

⁽¹⁾ Volume associated to the solution tank, water tank and the reactor container (see Annex C1.3).

The ESDs shown in Table 3.10 are relatively low compared to other projects, such as the seasonal heat storage system prototype proposed by Zhang (Zhang et al., 2014)⁽¹⁾ (see Chapter 1), which presented a $ESD_{V-st-wt} \approx 110 \text{ kWh/m}^3$, when associated to space heating applications.

Moreover, the main difference here is that the maximum mass fraction difference between the beginning and the end of the phase was not reached. Considering a mass fraction variation between 0.66 and 0.52⁽²⁾ would increase significantly the ESD values.

It must be noted that our ESD values did not consider a possible sensible heat contribution from the solution stored in the solution tank. Indeed, at the end of each test (charge or discharge) the solution tank was cooled down to temperatures around 20 °C, producing a loss of the sensible heat gained by the liquid solution during the desorption/condensation process (solution arriving at temperatures above 50 °C).

Finally, an insulation of the solution tank and an improvement of the heat exchangers surfaces wettability would considerably increase the system ESD values presented in Table 3.10.

3.3. Comparison of the experimental results against simulation

The model described in section 2.1 was thus used to simulate the prototype functioning under the same inlet conditions as two experimental tests in desorption/condensation and absorption/evaporation operating modes, presented in section 3.2.

Each simulated case considered the same heat exchangers configuration (type, size and material) and the same inlet working conditions as the experimental tests: water film and solution inlet temperatures, inlet LiBr mass fractions, HTF inlet temperatures and mass flows and the same observed wetted surface percentages.

The simulated outlet conditions are compared against the experimental ones. For comparison purposes, two indicators are defined as follows.

$$Indicator\ 1 = \left| \left(\frac{(Param_o - Param_i)_{sim} - (Param_o - Param_i)_{exp}}{(Param_o - Param_i)_{exp}} \right) \times 100 \right| \quad (3.6)$$

$$Indicator\ 2 = \left| \left(\frac{Param_{sim} - Param_{exp}}{Param_{exp}} \right) \times 100 \right| \quad (3.7)$$

These indicators describe the relative gap between experimental and simulation results.

The parameters associated to “Indicator 1” are the ones that vary during the fluids flow through the reactor: the solution temperature, the solution LiBr mass fraction, the desorber/absorber HTF temperature and the condenser/evaporator HTF temperature, denoted as T_{st} , x_{LiBr} , $T_{htf/ad}$ and $T_{htf/ec}$ respectively.

The parameters associated to “Indicator 2” are the reactor pressure, the absorbed/desorbed water mass flow, the water film temperature⁽³⁾, the desorber/absorber power and the condenser/evaporator power, denoted as $P_{reactor}$, $\dot{m}_{H_2O, abs/des}$, T_{f_water} , $W_{htf/ad}$ and $W_{htf/ec}$ respectively.

The details of the comparison at each operating mode are shown in the following sections.

⁽¹⁾ Prototype based in sorption processes using also a LiBr-H₂O aqueous solution.

⁽²⁾ This mass fraction working range is more adequate for dwelling heating application as it will be studied in Chapter 4.

⁽³⁾ In absorption/evaporation functioning mode the water film temperature is associated to “Indicator 1”.

3.3.1. Desorption/condensation

Two experimental tests were chosen for comparison against the simulation results in desorption/condensation operating mode. In Figures 3.23 and 3.24 are presented the experimental and simulated prototype performance associated to different parameters for Test 1. The same information is presented for Test 2 in Annex C3.1.1 (Figures C22, C23).

In Table 3.11 is presented the average values of Indicators 1 and 2, defined in Equations (3.6) and (3.7), associated to the two tests.

Table 3.11. Comparison between experimental and simulation results associated to Test 1 and Test 2 in the prototype desorption/condensation operating mode

	Parameter	Test 1 ⁽¹⁾	Test 2 ⁽²⁾
Indicator 1 [%] (Average value)	T_{st}	10.1	21.3
	x_{LiBr}	15.9	9.0
	$T_{htf/ad}$	7.4	5.2
	$T_{htf/ec}$	25.0	13.1
Indicator 2 [%] (Average value)	$P_{reactor}$	5.4	6.7
	$\dot{m}_{H_2O, abs/des}$	15.7	8.4
	T_{f_water}	30.2	23.7
	$W_{htf/ad}$	7.8	5.9
	$W_{htf/ec}$	25.5	13.6

For Test 1, in Table 3.11 and in Figures 3.23 and 3.24 it is observed that a good agreement is present between the experimental test and the simulation model results. In Table 3.11 is shown that the parameter with smallest agreement is the water film temperature, T_{f_water} , with an average value associated to the “Indicator 2” of 30%. This latter result can be associated to the temperature sensor position (see Figure 3.1) and to the low outlet water film mass flow, which is around 1 kg/h; although the outlet water film can be at a temperature around 17°C (shown by the simulation), it does not have an influence on the water temperature where the sensor is placed due to its low mass flow and to the heat transfer from the prototype to its surroundings (no isolation was present at this point of the prototype). The increase in the experimental water temperature (Figure 3.23e) can be associated to the ambient temperature increase during the test due to the thermal modules functioning in the test room.

For Test 2, in Table 3.11 it is shown that a good agreement is present between the experimental test and the simulation model results. The parameter with smallest agreement is again the water film temperature, T_{f_water} , with an average value, associated to the “Indicator 2”, of 23.7%.

The results obtained by the model in both tests are optimistic and higher than the experimental values. It must be highlighted that the observed wetted surface percentage has a strong influence on the simulation results.

Finally, the previous results show that the simulation model is capable to adequately describe the system performance in the charge mode (desorption/condensation).

⁽¹⁾ Experimental inlet conditions in Test 1 were considered for the simulation model, particularly the observed wetting surface percentage in the desorber and condenser, which had values of “~28% (~35%)” and “100%”, respectively (see Table 3.7).

⁽²⁾ Experimental inlet conditions in Test 2 were considered for the simulation model, particularly the observed wetting surface percentage in the desorber and condenser, which had values of “~16% (~20%)” and “100%”, respectively (see Table 3.7).

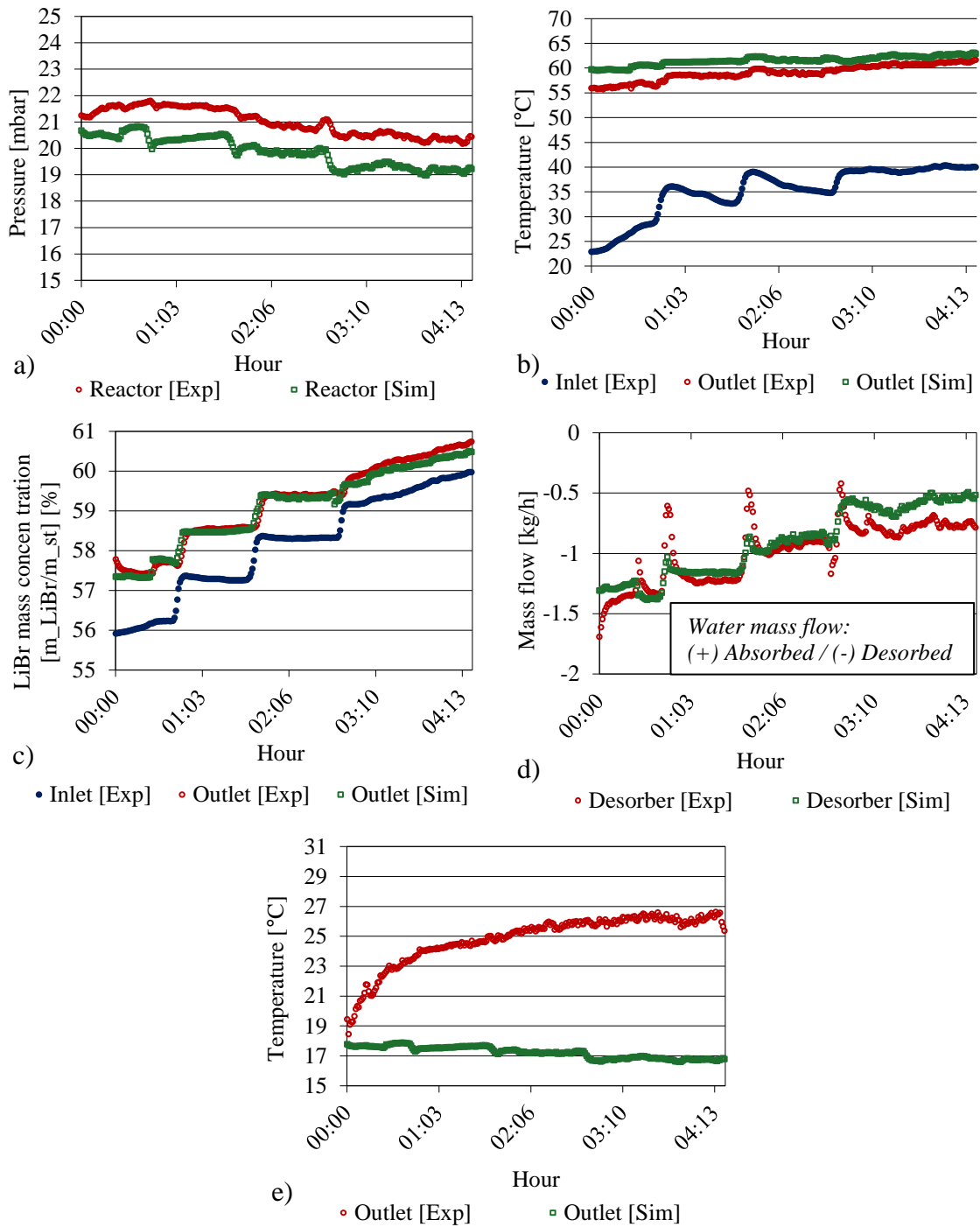


Figure 3.23. Comparison between experimental and simulated results obtained in desorption/condensation operating mode for the Test 1. a) Pressure in the reactor b) LiBr solution temperature (desorber); c) LiBr mass concentration (desorber); d) Desorbed/condensed water mass flow (reactor); e) Water film temperature (condenser)

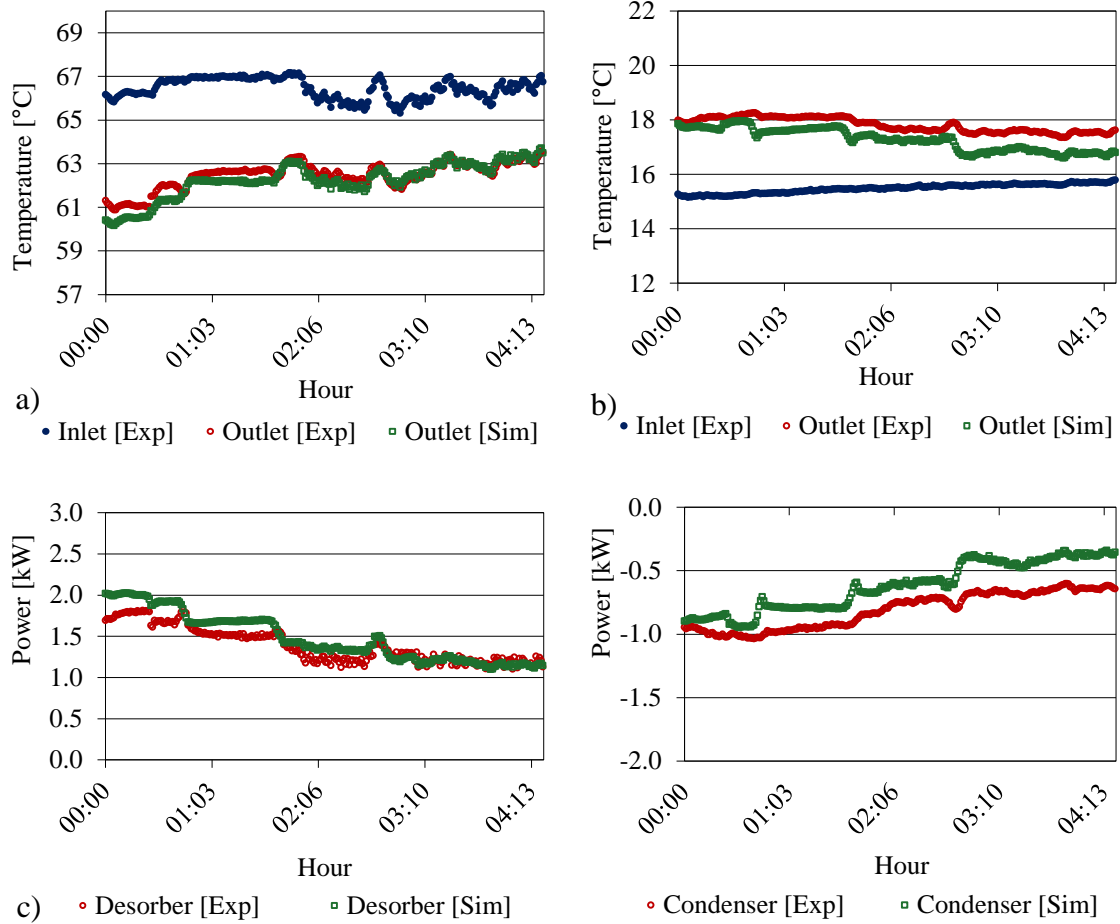


Figure 3.24. Comparison between experimental and simulated results obtained in desorption/condensation operating mode for the Test 1. a) HTF temperature (desorber); b) HTF temperature (condenser); c) Power given from the HTF to the system (desorber); d) Power given from the HTF to the system (condenser)

3.3.2. Absorption/evaporation

Two tests were chosen for comparison against the simulation results in absorption/evaporation operating mode. In Figures 3.25 and 3.26 are presented the experimental and simulated prototype performance associated to different parameters for Test 7. The same information is presented for Test 8 in Annex C3.1.2.

In Table 3.12 is presented the average values of Indicators 1 and 2 during the two tests.

Table 3.12. Comparison between experimental and simulation results associated to Test 7 and Test 8 in the prototype absorption/evaporation operating mode

	Parameter	Test 7 ⁽¹⁾	Test 7 [$\Delta P = 4$ mbar]	Test 8 ⁽²⁾	Test 8 [$\Delta P = 5$ mbar]
Indicator 1 [%] (Average value)	T_{st}	95.2	15.8	71.9	16.0
	x_{LiBr}	55.9	6.5	83.6	9.0
	T_{f_water}	128.7	53.2	140.6	47.3
	$T_{htf/ad}$	41.5	2.7	66.9	5.8
	$T_{htf/ec}$	39.8	4.5	98.3	11.0
Indicator 2 [%] (Average value)	$P_{reactor}$	40.4	22.7 ⁽³⁾	33.9	15.1 ⁽⁴⁾
	$\dot{m}_{H_2O, abs/des}$	57.4	6.6	85.4	9.1
	$W_{htf/ad}$	41.4	2.8	66.8	6.0
	$W_{htf/ec}$	39.2	4.9	98.1	11.0

For Test 7 and Test 8, in Table 3.12 is observed a very poor coincidence between simulation and experimental results, with “Indicator 2” minimal average values associated to $W_{htf/ec}$ in Test 7 and to $P_{reactor}$ in Test 8, of 39.2% and 33.9% respectively. In relation to the absorbed water mass flow, $\dot{m}_{H_2O, abs/des}$, it is observed that the “Indicator 2” average values are 57.4% and 85.4% respectively.

In order to explain this difference between experiments and simulation, the hypothesis of a non-condensable gas presence in the reactor is proposed. Indeed, although the gas leakage rate of the system components was qualified as acceptable (see Table 3.3 and Annex C1.3), a very weak amount of non-condensable gases has a non-negligible impact on the system performance, as will be developed below.

A possible source of non-condensable gases (NCG) could be associated to a degazation process of components inside the reactor, such as the PVC tubes. Another possible source of NCG could be present inside the liquid solution in the solution tank or inside the liquid water in the water tank (the NCG being transported from the tanks to the reactor during the system operation), since neither the tanks nor the reactor dispose of a non-condensable gas purge equipment⁽⁵⁾⁽⁶⁾.

Sabir et al. (1999) mention that the presence of NCG in film absorbers are detrimental since even a low value of 2% air can reduce the performance by more than six times; this latter is due to the additional resistance to absorption produced by a layer of non-condensable gas around the solution interface.

⁽¹⁾ Experimental inlet conditions in Test 7 were considered for the simulation model, particularly the observed wetting surface percentage in the absorber and evaporator, which had values of “~72% (~90%)” and “~24% (~30%)”, respectively (see Table 3.9).

⁽²⁾ Experimental inlet conditions in Test 8 were considered for the simulation model, particularly the observed wetting surface percentage in the absorber and evaporator, which had values of “~60% (~75%)” and “~24% (~30%)”, respectively (see Table 3.9).

⁽³⁾ With respect to the simulated water vapor partial pressure in the evaporator.

⁽⁴⁾ With respect to the simulated water vapor partial pressure in the evaporator.

⁽⁵⁾ Such as 45° inclined tube-shaped condenser, usually placed at the container’s top and operated in periods where the system is stopped.

⁽⁶⁾ Vacuum conditions in the tanks were obtained by using a vacuum pump after the solution and water were inside the tanks. A further and complementary evacuation of non-condensable gases would be possible by the use of the purge equipment.

As shown in Figure 3.27a, Sabir et al. (1999) also indicate that this non-condensable layer in the absorber produces a partial vapor pressure around the solution interface lower than the partial vapor pressure in the reactor.

Hence, a more adequate configuration, shown in Figure 3.27b, is proposed for the model, to take into account the NCG influence in the reactor. This new configuration proposes that the partial vapor pressures in the absorber and in the evaporator are different, with the water vapor partial pressure at the water film interface (evaporator) being higher than the water vapor partial pressure at the solution film interface (absorber). This model improvement was implemented and results are presented in Table 3.12 and Figures 3.25 and 3.26.

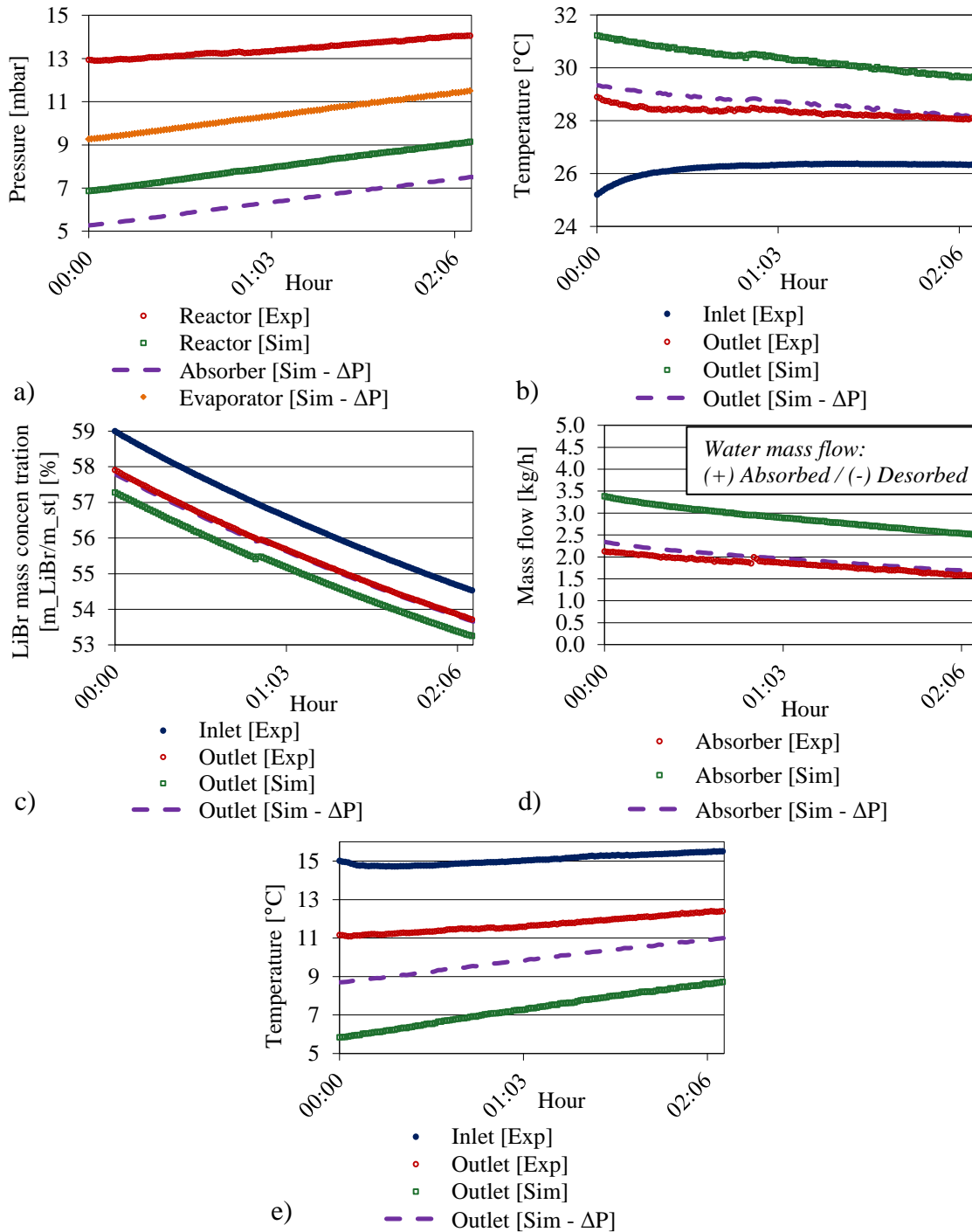


Figure 3.25. Comparison between experimental and simulated results obtained in absorption/evaporation operating mode for the Test 7 - (with $\Delta P = 4$ mbar). a) Pressure in the reactor; b) LiBr solution temperature (absorber); c) LiBr mass concentration (absorber); d) Absorbed/evaporated water mass flow (reactor); e) Water film temperature (evaporator)

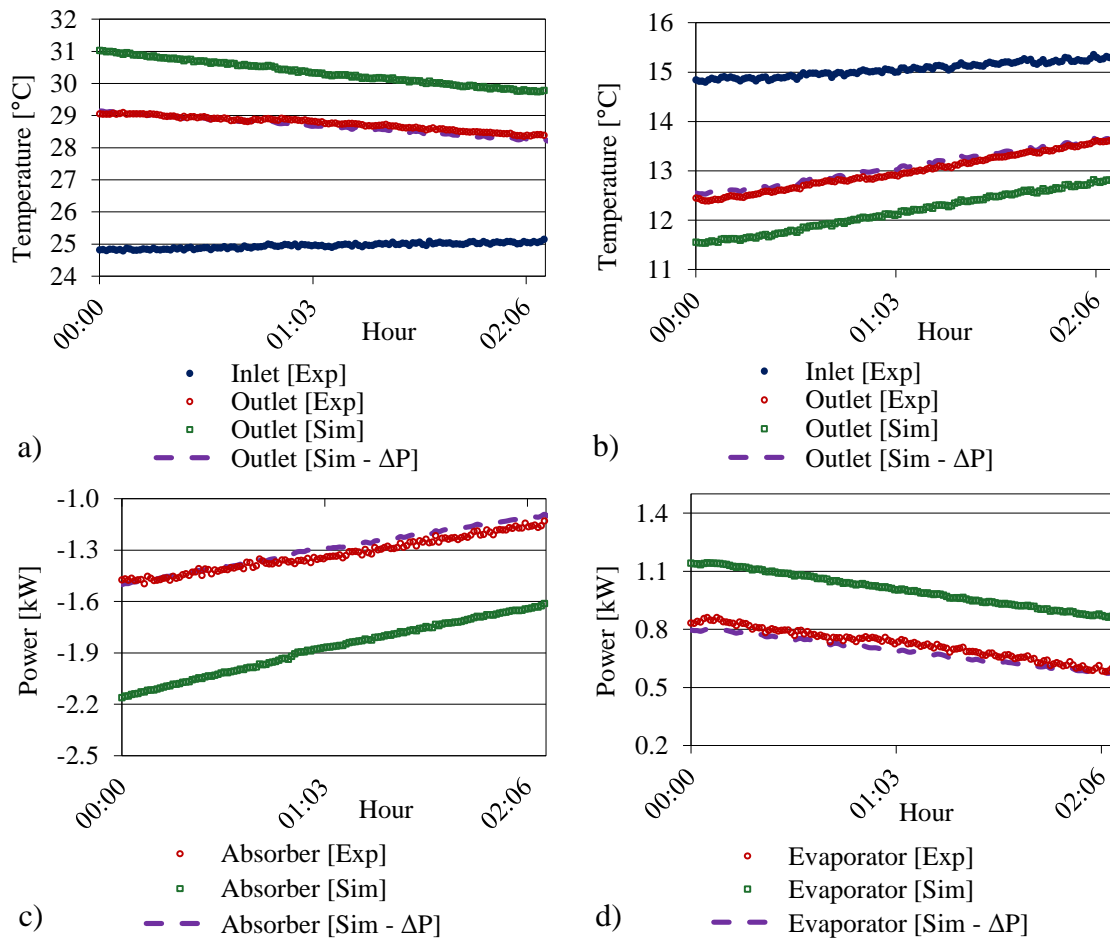


Figure 3.26. Comparison between experimental and simulated results obtained in absorption/evaporation operating mode for the Test 7 - (with $\Delta P = 4$ mbar). a) HTF temperature (absorber); b) HTF temperature (evaporator); c) Power given from the HTF to the system (absorber); d) Power given from the HTF to the system (evaporator)

For Test 7 and Test 8; in Table 3.12 is observed that in general a good agreement is present between the test and the simulation results when a NCG presence is considered. The partial water vapor pressure in the absorber, $P_{vap-pp_{absorber}}$, is lower in “ ΔP ” than the partial water vapor pressure in the evaporator, $P_{vap-pp_{evaporator}}$. The “ ΔP ” value is selected through an “optimization process” in which a “ ΔP ” permitting to obtain best fittings between the simulated and experimental absorbed/evaporated water mass flows is chosen. From Figure 3.27b it must also be understood that the “real” total pressure in the reactor, $P_{reactor}$, is composed of the partial water vapor pressure in the evaporator, $P_{vap-pp_{evaporator}}$, and the partial pressure associated to the NCG, $P_{noncondensable\ gas-pp}$. Indeed, the partial water vapor pressure along the absorber, $P_{vap-pp_{absorber}}$, is a local pressure generated by the presence of the NCG.

In Figure 3.25a, in Test 7, when a NCG presence is considered, the simulated partial vapor pressure in the evaporator is higher than in the absorber by a “ $\Delta P = 4$ mbar”; a similar behavior is observed for Test 8 considering a “ $\Delta P = 5$ mbar”. For both tests, the average $P_{reactor}$ “Indicator 2” value⁽¹⁾ shows good agreement of 22.7% and 15.1% respectively.

⁽¹⁾ This indicator is calculated with respect to the simulated partial vapor pressure in the evaporator.

For Test 7, Figure 3.25a also shows that the pressure difference between the experimental total reactor pressure and the simulated evaporator water vapor partial pressure is 3.5 mbar; with this remaining gap pressure possibly belonging to the NCG ($P_{noncondensable\ gas-pp}$).

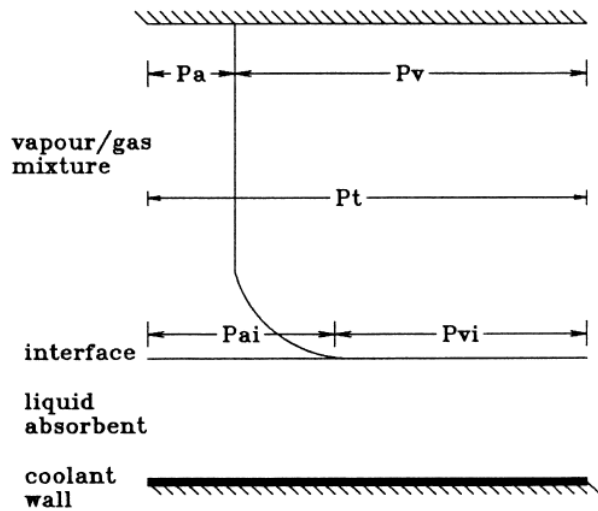
For Test 7, in Table 3.12, the parameter with less agreement is the water film temperature, T_{f_water} , with an average value, associated to the “Indicator 1”, of 53.2%. Although this latter seems a high value, it can be observed in Figure 3.25e that it represents a temperature difference between experimental and simulation of 2°C in average; the reason of an experimental outlet water film temperature higher than in the simulation could be associated, once again, to the influence of the ambiance temperature. A similar behavior is observed for Test 8.

P_a : partial pressure of NCG in the bulk of the vapor/NCG mixture

P_v : partial pressure of vapor in the bulk of the vapor/NCG mixture

P_{ai} : partial pressure of NCG at the interface

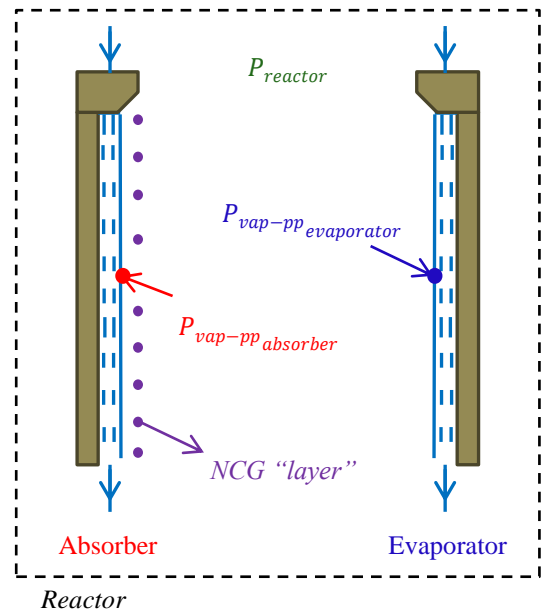
P_{vi} : partial pressure of vapor at the interface



a)

$$P_{reactor} = P_{vap-pp_{evaporator}} + P_{noncondensable\ gas-pp}$$

$$P_{vap-pp_{evaporator}} = P_{vap-pp_{absorber}} + \Delta P$$



b)

Figure 3.27. Non-condensable gas presence during the absorption/evaporation process. a) Pressure gradient in the absorbing film (Sabir et al., 1999); b) Scheme of the evaporator/absorber pressure gap considered in the model

Although in the absorption/evaporation processes the hypothesis of NCG is proposed, during the desorption/condensation processes these gases could also be present. Indeed, as shown in Figure 3.23a and C22a, the average pressure difference between experimental and simulation are 1 mbar and 1.5 mbar for Test 1 and 2, respectively.

Nevertheless, as shown in Table 3.11, a good agreement between simulation and experimental results was obtained in the desorption/condensation tests without considering a non-condensable gases presence. This latter would be due to 2 reasons:

- The first reason, as it is mentioned by Huang et al. (2015), is that in cases of dropwise condensation (DWC), which was our case (see Figure 3.13), the heat transfer coefficient is up to 10 times higher than in cases of film wise condensation (FWC).
- The second reason, as it is shown in Table 3.7 and Figure 3.13, is that the observed wetted surface percentage in the condenser was 100%, which was considerably higher than the observed wetted surface percentages in the absorber (see Table 3.9). Since the NCG layer is locally formed along the condenser and the absorber, a bigger heat transfer surface in the former would permit to reduce the negative effect produced by the NCG.

From these 2 previous physical behaviors, it could be considered that, although NCG would have been present in the desorption/condensation processes, the NCG did not have a significant influence on the system performance during the charging tests.

It must also be indicated that, as it is shown in Table 3.11, the Reynolds numbers associated to the water film in the evaporator were around 1200; although these values are in the laminar transition regime, $Re < 1800$ (Incropera et al., 2011), (Chang, 1994)⁽¹⁾, they were 10 times higher than the Reynolds associated to the solution film in the absorber. Although the evaporator model presented in Chapter 2 is proposed for laminar regimes, water films with Reynolds number close to the turbulent region can have a tendency to present important waves, which would increase the mass transfers at the interface.

The previous results show that the model is capable to adequately describe the system performance in discharge mode (absorption/evaporation functioning), in particular when a non-condensable gas presence is considered in the reactor. However, one limitation is that a parameter, “ ΔP ”, has to be adapted at each experience; furthermore, further experiences and applications should aim to reduce this “ ΔP ” in order to improve the system performances.

Although the simulation and experimental results have a good agreement in the desorption/condensation and absorption/evaporation processes; it must be remarked that the observed wetted surface percentages considered in the experimental tests (Tables 3.6 and 3.8) were visually estimated since it was not technically possible to measure them during the tests. Hence, further tests should ensure the complete wetting of the grooves through a surface chemical treatment (Drelich et al., 2011).

Finally, an extrapolation of the experimental results obtained in Test 7 and 8 for the absorber HTF power (Figures 3.15c and 3.18c) was carried out to determine the prototype ESD when a wider solution mass fraction variation is considered. In Table 3.10 the experimental prototype ESD was calculated for a mass fraction variation between 0.59 and 0.54; in Table 3.13 an extrapolated prototype ESD is presented by considering a mass concentration range between 0.66 and 0.52⁽²⁾. As a result, it is observed that the extrapolated ESD increase in 3.5 times respect to the initially measured ESD, and becomes comparable to the ESD of the seasonal heat storage prototype proposed by Zhang (Zhang et al., 2014)⁽³⁾ ($ESD_{V-st-wt} \approx 110 \text{ kWh/m}^3$, see Chapter 1).

Table 3.13. Extrapolated prototype ESD for Tests 7 and 8 (discharge operating mode) –
($x_{LiBr_i} \approx [0.66 - 0.52]$)

	$ESD_{V-system}$ [kWh/m ³]	$ESD_{V-st-wt}$ [kWh/m ³]	ESD_m [kWh/kg]
Test 7	21.9	119.6	0.111
Test 8	20.0	109.0	0.101

⁽¹⁾ According to Chang (Chang, 1994), in vertical falling films: laminar regimes are mainly associated to $Re < 300$, the transition regime is defined by $300 < Re < 1000$ (appearance of long interfacial waves) and the turbulent regime is present for $Re > 1000$ (wavelengths comparable to the film thickness).

⁽²⁾ This mass fraction working range is more adequate for dwelling heating application as it will be studied in Chapter 4.

⁽³⁾ Prototype based in sorption processes using also a LiBr-H₂O aqueous solution.

3.4. Conclusions

In this Chapter, the conception and construction stages of the prototype of an interseasonal heat storage system by sorption process have been presented. The heat exchangers configuration selected for this prototype was a grooved vertical flat plate heat exchanger configuration.

Several experimental tests in desorption/condensation operating mode (charge) and absorption /evaporation operating mode (discharge) were carried out.

For the desorption/condensation operating mode:

- In average, a desorbed/condensed water mass flow between 0.5 kg/h and 2 kg/h was obtained and the powers associated to the desorber HTF and the condenser HTF were between 1 kW and 2 kW and between -0.5 kW and -1.5 kW, respectively.
- The solution temperature in the solution tank increased along the tests up to 50°C at certain points, even with the tank envelope always maintained at 19° C.
- The vapor pressure in the reactor was between 21 and 24 mbar.
- A reduction of the process performance appeared when the LiBr mass fraction entering the reactor increased.
- An increase of the process performance was obtained when the desorber HTF temperature was increased.
- Overflowing and solution projections appeared when the solution falling film temperature was increased up to points where ebullition was possible. During the tests, this happened when the desorber HTF temperature was around 75°C.

For the absorption/evaporation operating mode:

- In average, an absorbed/evaporated water mass flow between 1 kg/h and 2 kg/h was obtained and the powers associated to the absorber HTF and the evaporator HTF were between -0.6 kW and -1.5 kW and between 0.3 kW and 1.0 kW, respectively.
- The solution temperature in the solution tank increased up to 26°C.
- The vapor pressure in the reactor was between 12 and 15 mbar.
- A reduction of the process performance appeared when the LiBr mass fraction entering the reactor decreased.
- A reduction in the absorber power and in the temperature difference between the absorber HTF inlet and outlet is produced, when the absorber HTF inlet temperature was increased.

In both operating modes, charge and discharge, a low wettability on the heat exchangers surfaces can appear if a chemical treatment on the exchanger grooved surfaces is not previously applied.

In both operating modes, the system can work under normal conditions even if crystals are present in the solution tank; nevertheless, an inadequate management of the position where the crystals are formed can produce LiBr crystallization in the tubes, preventing the liquid solution to be pumped. Moreover, a good design of the solution film distributor (at the top of the absorber/desorber) must be done in order to avoid solution accumulation and crystallization in periods where the system is in standby. Additionally, regarding the reactor container design, a fixation system should be considered for the funnels as well as to ensure the tightness between the funnel's outlet and the reactor's outlet tube.

In general, in absorption/evaporation operating mode, better system performances can be obtained if the system works with LiBr mass fractions higher than 0.60.

The reactor model was used to simulate the prototype functioning of experimental tests. In general, a good agreement was obtained between simulation and experimental results. This comparison, nevertheless, suggests the presence of non-condensable gases in the reactor during these processes, with an important influence in the absorption/evaporation operating mode manifested by a 4 to 5 mbar partial water vapor pressure gap between the evaporator and the absorber.

A first experimental calculation of the system energy storage density (ESD) during the discharging processes gave values between 29.6 and 33.7 kWh/m³ (for a mass fraction variation between 0.59 and 0.54). Better ESD values would be possible through an insulation of the solution tank and an improvement of the wetted surface in the heat exchangers. Furthermore, an extrapolation of the experimental results to determine the experimental prototype ESD, when a mass fraction variation between 0.66 and 0.52 is considered, was carried on giving values between 109 and 119.6 kWh/m³.

Finally, an extrapolation of the prototype experimental results indicates that in absorption/evaporation mode, at LiBr mass fractions around 65%, the system can increase the temperature of a HTF⁽¹⁾ from 25°C to 31°C or from 30°C to 34°C. Simulated results of a system with similar working conditions, perfect wetting and no non-condensable gases (see section 2.1.3.1.2) indicates that at a LiBr mass fraction around 65% the HTF can be heated from 25°C to 37°C. Considering that building/dwelling space heating applications require HTF temperatures around 35°C (EREKA, 2016), (ADEME, 2016), the interseasonal heat storage system can partially cover the heating required by this application⁽²⁾. Furthermore, since a solar collector is coupled to the heat storage system to ensure the charging period (desorption/condensation); during the discharging period the same solar collector can be used for space heating.

To guarantee a good performance, an adequate dimensioning of the system components and solar collector is required. A parametrical study of the performance of the interseasonal heat storage system coupled to a dwelling is presented in Chapter 4.

Bibliography

- ADEME; *Les chauffe-eau thermodynamiques individuels (CETI) – Fiches techniques de l'ADEME*. <http://www.ademe.fr/sites/default/files/assets/documents/fiche-technique-ademe-sur-chauffe-eau-thermodynamiques-individuels-ceti-2013.pdf>. Last accessed October 2016.
- ASHRAE; *ASHRAE handbook: Fundamental*. ASHRAE, Atlanta, 2005.
- Chang H.-C.; *Wave evolution on a falling film*. Annu. Rev. Fluid Mech. 26 (1994); p.103-136.
- Do K. H.; Kim S. J.; Garimella S. V.; *A mathematical model for analyzing the thermal characteristics of a flat micro heat pipe with a grooved wick*. Int. J. Heat Mass Tran. 51 (2008); p.4637-4650.
- Drelich J., Chibowsky E., Desheng D., Terpilowski K.; *Hydrophilic and superhydrophilic surfaces and materials*. Soft matter 7 (2011); p.9804-9828.
- Fujikawa Y., Mori K., Takaoka D., Wakabayashi T., Kawakami R., *Pool Boiling Heat Transfer Characteristics of Aqueous Lithium Bromide Solution*. JSEM, 15 (2015); p. 37-42
- Guo L.; Liu Z. C.; Yan Y. Y.; Han Z. W.; *Numerical modeling and analysis of grooved surface applied to film cooling*. J. Bionic Eng. 8 (2011); p.464-473.
- Hellman H-M, Grossman G.; *Improved property data correlations of absorption fluids for computer simulation of heat pump cycles*. ASHRAE Transactions 102 (1), (1996); p. 980–997.
- Huang J., Zhang J., Wang L.; *Review of vapor condensation heat and mass transfer in the presence of non-condensable gas*. Applied Thermal Engineering 89 (2015); p. 469–484.
- Incropera F., Dewitt D., Bergman T., Lavine A.; *Fundamentals of heat and mass transfer*. Seventh edition; John Wiley & sons (2011); USA; p.389–390.
- Liu H.; *Stockage inter-saisonnier d'énergie solaire pour l'habitat par absorption*. Doctoral thesis defended the 17th December Mars 2010. University of Savoie, France.
- Medrano M., Bourouis M., Coronas A.; *Absorption of water vapour in the falling film of water-lithium bromide inside a vertical tube at air-cooling thermal conditions*. International Journal of Thermal Sciences 41 (2002); p. 891–898.

⁽¹⁾ Water at a mass flow around 300 kg/h.

⁽²⁾ It must be highlighted that in discharging mode (space heating), the system can work at night periods.

N'Tsoukpoe K.E.; *Étude du stockage à long terme de l'énergie solaire thermique par procédé d'absorption LiBr-H₂O pour le chauffage de l'habitat*. Doctoral thesis defended the 19th Mars 2012. University of Savoie, France.

EREKA; *Le guide du plancher chauffant*. <https://plancher-chauffant.ooreka.fr/>. Last accessed October 2016.

Sabir H. M., Eames I. W., Suen K. O.; *The effect of non-condensable gases on the performance of film absorbers in vapour absorption systems*. Applied Thermal Engineering 19 (1999); p. 531–541.

Umrath W., Adam H., Bolz A., Boy H., Dohmen H., Gogol K., Jorisch W., Mönning W., Munding H., Otten H., Scheer W., Seiger H., Schwarz W., Stepputat K., Urban D., Wirtzfeld H., Zenker H.; *Fundamentals of Vacuum Technology*. Erlikon Leybold Vacuum (2007); p.14, 110.

Zhang X., Li M., Shi W., Wang B., Li X.; *Experimental investigation on charging and discharging performance of absorption thermal energy storage system*. Energ Convers Manage 85 (2014); p. 425–434.

Chapter 4. Interseasonal heat storage system annual performance

In this Chapter a global simulation model of the interseasonal heat storage system coupled to a dwelling is developed to study its annual performance when dwelling heating needs (DHN) are required to be partially or completely covered. Figure 4.1 shows a scheme of the components of the global model during each system operating mode: charge (summer) and discharge (winter).

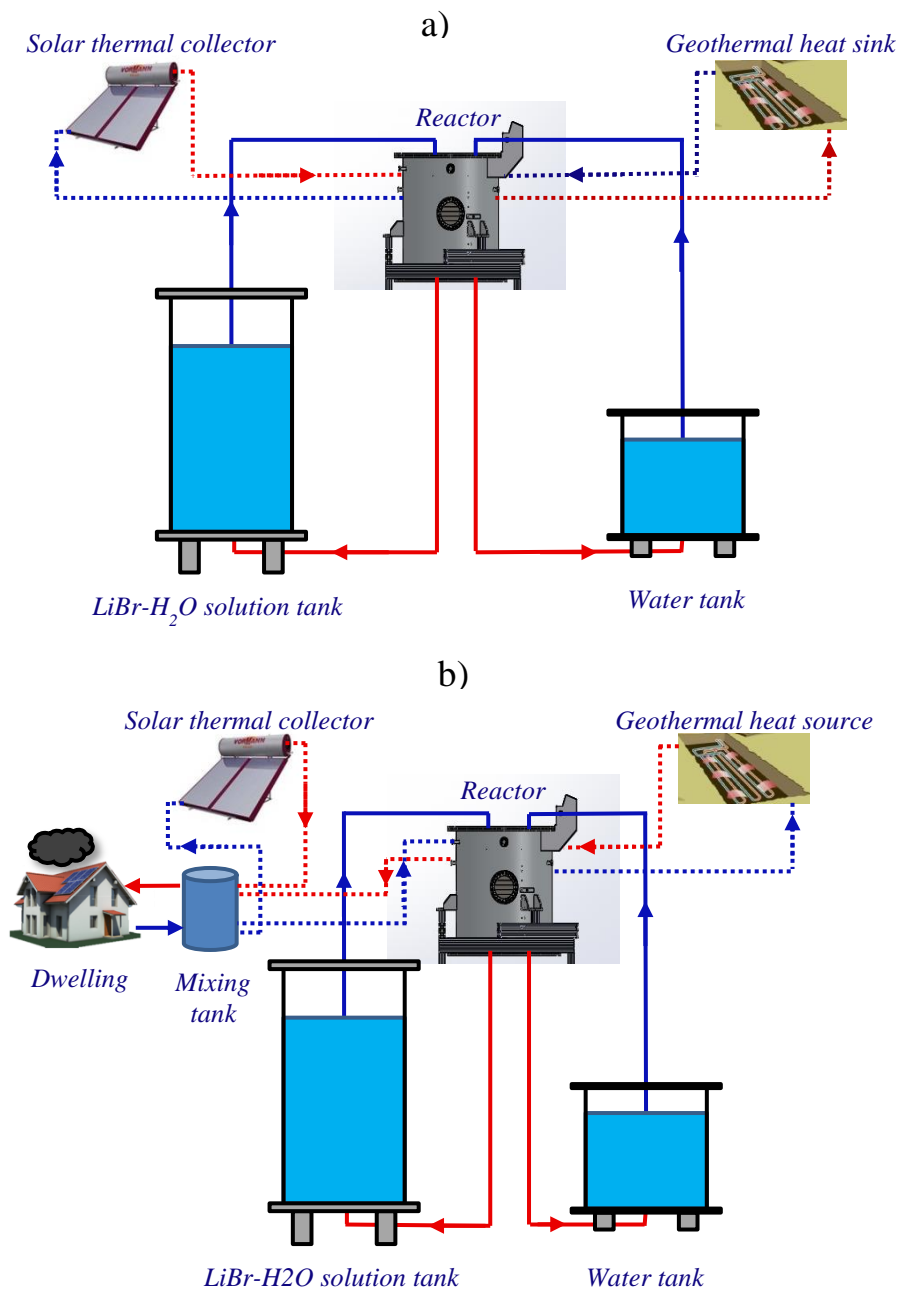


Figure 4.1. Scheme of the components of the interseasonal heat storage system by absorption. a) In charging period (summer); b) In discharging period (winter)

As it is observed in Figure 4.1, during the charging period (summer) a solar thermal collector is used to heat the HTF associated to the desorber, permitting the desorption of vapor from the LiBr solution falling film and, at the same time, a heat sink is used to cool down the HTF associated to the condenser, permitting the condensation of the vapor produced in the reactor.

During the discharging period (winter) a mixing tank is considered as an intermediary element between the dwelling and the solar thermal collector/system reactor. A solar thermal collector is used to heat a HTF. When the HTF outlet temperature is high enough to contribute to cover the dwelling heating needs, the associated HTF

is pumped to the mixing tank. Similarly, the interseasonal heat storage system is used to heat a HTF. When the temperature of the HTF leaving the absorber is high enough to contribute to cover the dwelling heating needs, it is pumped to the mixing tank. At the same time a geothermal heat source is used to heat the HTF of the system evaporator. Although the HTFs associated to the solar collector and the absorber are in a parallel configuration, they both share the same inlet temperature, corresponding to the mixing tank temperature. This last hypothesis considers that the mixing tank temperature is constant and equal to the temperature of the HTF leaving the dwelling and arriving at the mixing tank. This simplification was assumed to avoid having to simulate precisely the building's behavior.

In section 4.1 the global simulation model developed for the interseasonal heat storage system coupled to a dwelling is presented. In section 4.2 a simulation reference configuration for a low energy consumption (LEC) dwelling is considered to study the storage system annual performance. In section 4.3 a simulation parametrical study of the influence of some components size on the system performance is carried out and an optimal configuration is proposed. Finally, in section 4.4 a simulation study of the system behavior for a reference configuration is shown when the LiBr-H₂O solution is replaced by a KCOOH-H₂O solution.

4.1. Interseasonal heat storage system/dwelling simulation model

In this section a global simulation model permitting to couple the interseasonal heat storage system simulation model developed in Chapter 2 with a LEC dwelling is developed.

As it is indicated in Figure 4.1, three additional components are considered with respect to the system compilation shown in section 2.4; these elements are: a solar thermal collector, a heat source/sink and a mixing tank. The new components models and their coupling conditions with the heat storage system are given in the sections below.

4.1.1. Solar thermal collector

A model for the solar thermal collector is presented in this section. As it was indicated above, a solar thermal collector is present in both the charging and discharging system operating modes.

In order to simplify the global model and reduce the machine time⁽¹⁾ needed for annual simulations, this component is considered to be in steady conditions.

Figure 4.2 shows an scheme of the solar thermal collector and Equations 4.1 and 4.2 describe the energy balance considered to calculate the associated HTF outlet temperature.

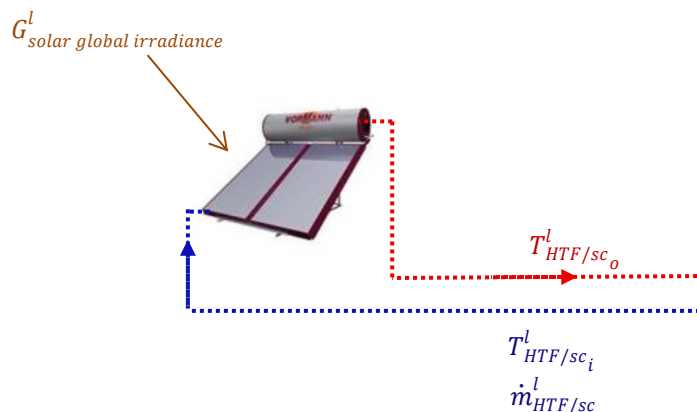


Figure 4.2. Scheme of the solar thermal collector

⁽¹⁾ In this context, the term “machine time” is defined as the time needed for a computer to simulate a determined case.

$$\begin{aligned} \dot{m}_{HTF/sc}^l \times c_{p_{HTF/sc}} \times (T_{HTF/sc_o}^l - T_{HTF/sc_i}^l) = \\ a_0 \times A_{sc} \times G_{solar\ global\ irradiance}^l - a_1 \times A_{sc} \times (T_{HTF/sc_{avg}}^l - T_{ext.amb.}^l) - \\ a_2 \times A_{sc} \times (T_{HTF/sc_{avg}}^l - T_{ext.amb.}^l)^2 \end{aligned} \quad (4.1)$$

$$T_{HTF/sc_{avg}}^l = \frac{T_{HTF/sc_o}^l + T_{HTF/sc_i}^l}{2} \quad (4.2)$$

Where a_0 is the solar collector optical efficiency and a_1, a_2 are the solar collector thermal loss coefficients. The term "l" is related to the time, for discretization purposes.

For cases in which $G_{solar\ global\ irradiance}^l = 0$ (night period) the HTF mass flow is zero and it is considered that $T_{HTF/sc_i}^l = T_{HTF/sc_o}^l = T_{ext.amb.}^l$.

During the charging period (summer), in order to connect the thermal solar collector with the system reactor, the HTF solar collector outlet temperature must be higher than an established threshold temperature.

$$T_{HTF/sc/ch.\ op.\ mode_o}^l > T_{HTF/sc/ch.\ op.\ mode_{min.threshold}}^l \quad (4.3)$$

Similarly, during the discharging period (winter), in order to connect the thermal solar collector with the mixing tank, the HTF solar collector outlet temperature must be higher than an established threshold temperature.

$$T_{HTF/sc/disch.\ op.\ mode_o}^l > T_{HTF/sc/disch.\ op.\ mode_{min.threshold}}^l \quad (4.4)$$

4.1.2. Heat source/sink

A model for the heat source/sink is presented in this section. As it was indicated above, it is present in both the charging and discharging operating modes.

The heat source/sink is considered to be the ground. Figure 4.3 shows a scheme of this component. Also, for both operating modes, charging and discharging, it is considered as a simplification assumption that at any time the heat source/sink HTF outlet temperature is equal to the ground temperature, as it is indicated in Equation 4.5, as the aim of this project was not to simulate precisely a geothermal pipe behavior.

$$T_{HTF/hs_o}^l = T_{ground}^l \quad (4.5)$$

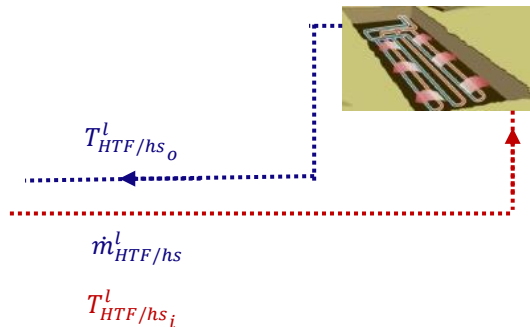


Figure 4.3. Scheme of the heat sink

4.1.3. Mixing tank

A model for the mixing tank is presented in this section. As it was indicated above, the mixing tank is considered to be an intermediary element between the dwelling and the solar thermal collector/system reactor and is present only during the discharging operating mode.

Figure 4.4 shows a scheme of the mixing tank and the components associated to this element. The energy contributions coming in parallel from the solar collector and the system reactor to cover the dwelling heating needs are made through the mixing tank.

For cases in which the dwelling heating needs (DHN) cannot be completely covered by the solar collector and/or the system reactor, an electrical heat source directly connected to the mixing tank is considered to be used.

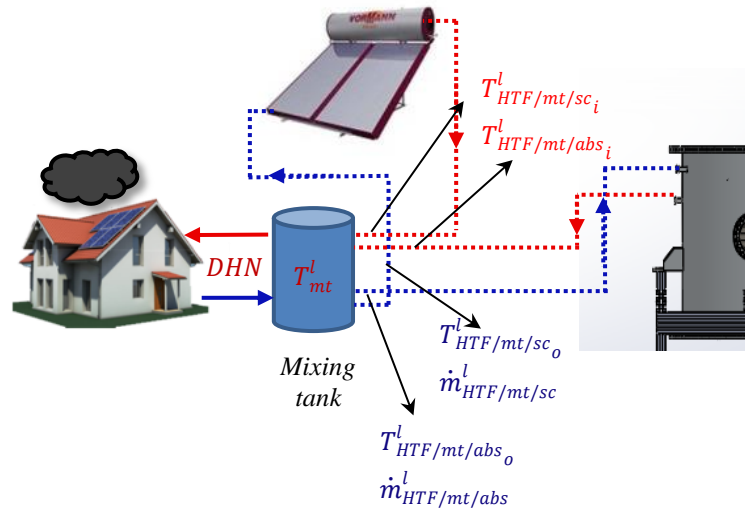


Figure 4.4. Scheme of the mixing tank and its associated components

As it was previously indicated, the mixing tank component is considered to operate in the discharging operating mode, which is equivalent to say that it operates when the dwelling heating needs (DHN) are higher than zero.

If at certain time “*l*”, the DHN are higher than zero, then the energy balance at the mixing tank is described by Equation 4.6, shown below.

$$\begin{aligned}
 W_{DHN} \times \Delta t_{DHN}^l &= \dot{m}_{HTF/mt/abs}^l \times c_{p_{HTF/mt/abs}} \times \left(T_{HTF/mt/abs_i}^l - T_{HTF/mt/abs_o}^l \right) \times \Delta t_{HTF/mt/abs}^l + \\
 &\quad \dot{m}_{HTF/mt/sc}^l \times c_{p_{HTF/mt/sc}} \times \left(T_{HTF/mt/sc_i}^l - T_{HTF/mt/sc_o}^l \right) \times \Delta t_{HTF/mt/sc}^l + W_{electrical\ source} \\
 &\quad \times \Delta t_{DHN}^l
 \end{aligned} \tag{4.6}$$

Where Δt_{DHN}^l is the time interval, associated to the time “*l*”, in which the dwelling needs space heating. The terms $\Delta t_{HTF/mt/sc}^l$ and $\Delta t_{HTF/mt/abs}^l$ are associated to time intervals in which the solar collector and the system reactor operate, respectively. Of course, $\Delta t_{HTF/mt/sc}^l \leq \Delta t_{DHN}^l$ and $\Delta t_{HTF/mt/abs}^l \leq \Delta t_{DHN}^l$ for each time step.

During night periods, since the solar collector cannot operate then $\Delta t_{HTF/mt/sc}^l = 0$, nevertheless, since in this same period the system reactor can operate then $\Delta t_{DHN}^l \geq \Delta t_{HTF/mt/abs}^l$. A $\Delta t_{HTF/mt/abs}^l$ lower than Δt_{DHN}^l is associated to a case in which the heating power produced in the reactor is higher than the power required in the dwelling.

During day periods; as the system reactor and the solar collectors can work simultaneously, a preference is given to the solar collector to operate during a time interval $\Delta t_{DHN}^l = \Delta t_{HTF/mt/sc}^l$. A strong simplification was considered for cases in which the heat produced by the solar collector during a whole time interval Δt_{DHN}^l is higher than the heating needs, $W_{DHN} \times \Delta t_{DHN}^l$, as the surplus energy is assumed to be used in the next time interval associated to the time “ $l+1$ ”.

In cases in which the solar collector and the system reactor cannot completely cover the heating needs; an electrical source is considered to operate at an adaptable power $W_{electrical\ source}$ during the whole time interval Δt_{DHN}^l .

As it was mentioned before, a hypothesis considering the mixing tank temperature constant and equal to the temperature of the HTF leaving the dwelling was established for simplification purposes. Then the HTFs leaving the tank follow conditions described in Equations 4.7 and 4.8.

$$T_{HTF/mt/sc_o}^l = T_{mt}^l \quad (4.7)$$

$$T_{HTF/mt/abs_o}^l = T_{mt}^l \quad (4.8)$$

4.1.4. Global compilation

As it was mentioned before, each of the components described in section 4.1.1, 4.1.2 and 4.1.3 were coupled to the interseasonal heat storage described in section 2.4.

Figures 4.5 and 4.6 show the schematic procedure considered to couple all the described components (in charging and discharging operating mode, respectively) in order to simulate the annual performance of the interseasonal heat storage system, when it is associated to a solar dwelling.

Finally, it has been considered that during the periods in which the DHN are zero, the system works in charging mode, even during the winter days.

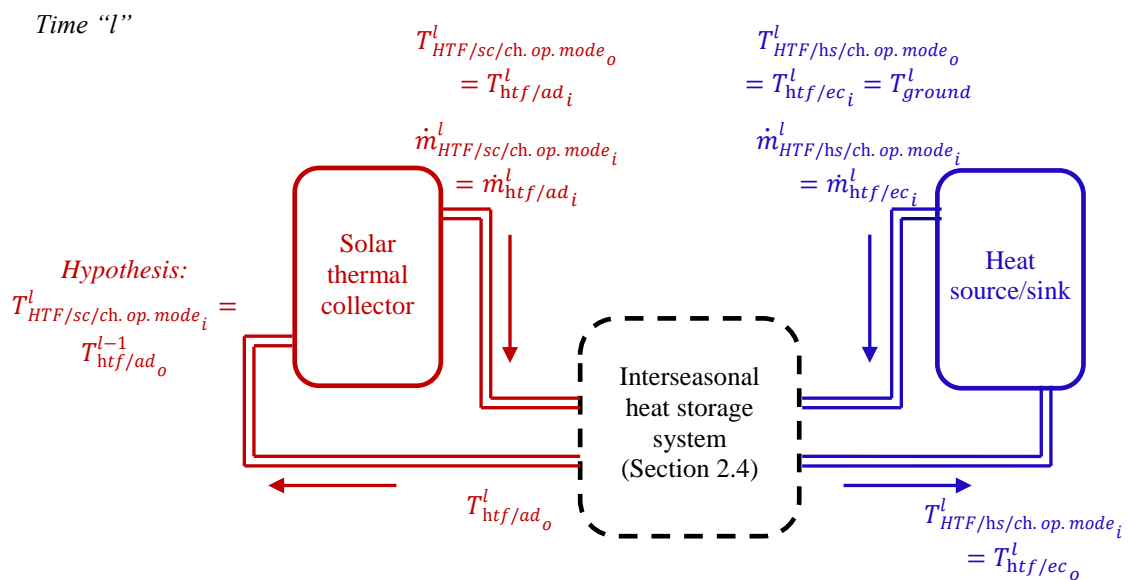


Figure 4.5. Scheme of the coupling of the components of the interseasonal heat storage system when it is associated to a dwelling. Charging operating mode.

Time “l”

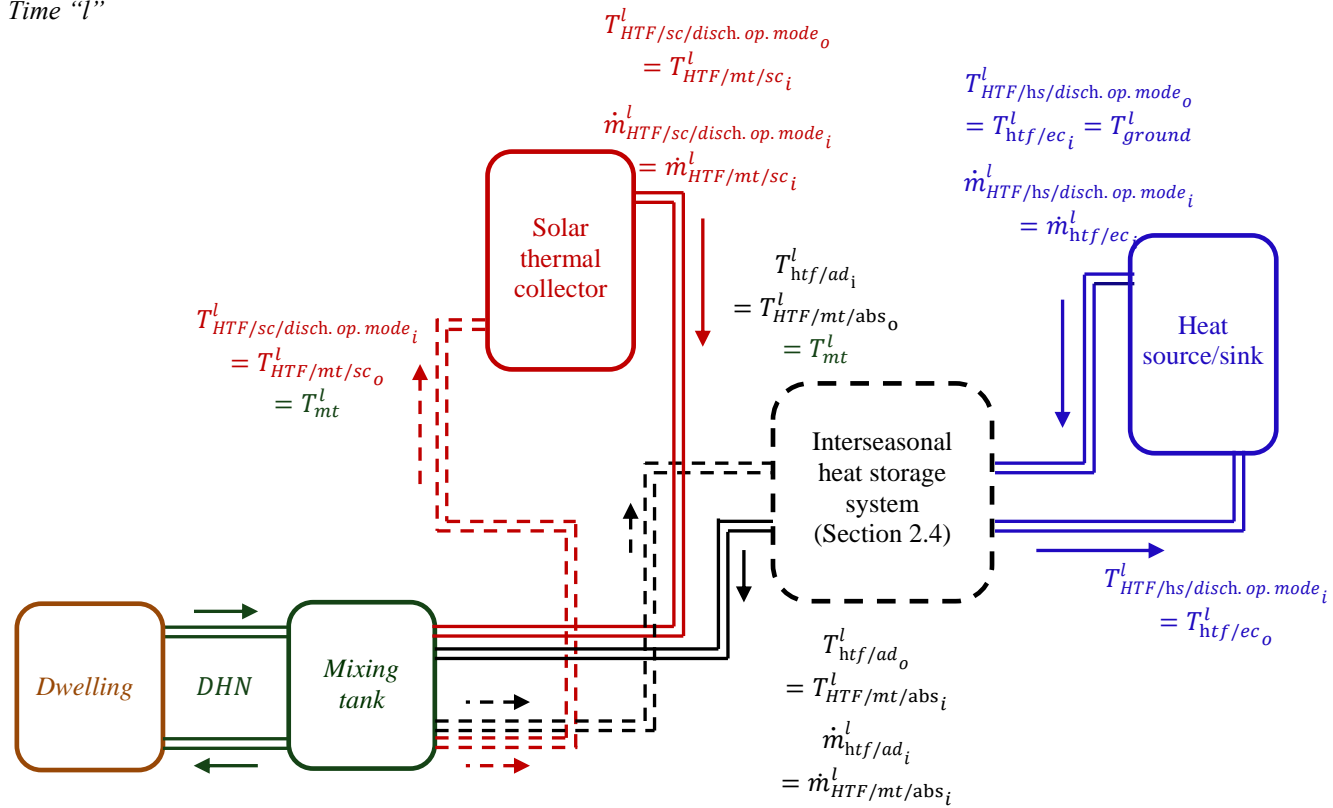


Figure 4.6. Scheme of the coupling of the components of the interseasonal heat storage system when it is associated to a dwelling. Discharging operating mode.

4.2. Simulation reference configuration

In this section a reference configuration case of the interseasonal heat storage system coupled to a dwelling is proposed in order to simulate the annual system performance when covering the dwelling heating needs.

The technical characteristics considered for the dwelling, solar collector, heat source/sink, mixing tank and the heat storage system (described in section 2.4) in the simulation reference case are presented in section 4.2.1, while its simulated annual performance is presented in section 4.2.2.

4.2.1. Technical characteristics

In this section, the technical characteristics considered for the heat storage system and the dwelling were similar to the case proposed by N'Tsoukpoe (N'Tsoukpoe, 2012) to simulate the annual performance of an interseasonal heat storage system based on a LiBr-H₂O solution.

4.2.1.1. Dwelling

The considered dwelling is a passive dwelling located in the city of Chambéry, France. The dwelling characteristics and the annual heating power required to heat the inner ambiances are shown in Table 4.1 and Figure 4.7, respectively (Dangel, 2010).

The solar irradiance and the atmospheric temperature were obtained from measurements made in Chambéry in 2005 (Valentin et al., 2006). As it is also indicated in Table 4.1, the ground temperature is considered to be constant at 12°C (Moch et al., 2014).

The heating power shown in Figure 4.7 has to be provided by a HTF entering the dwelling at a temperature above 25°C; since the model considers that this HTF leaves the dwelling, in direction to the mixing tank, always at a temperature of 25°C (see section 4.1.3).

Table 4.1. Dwelling technical characteristics

Dwelling type	Standard passive
Surface [m ²]	120
Location	Chambéry, France
Annual heating needs [kWh]	2189
Ground temperature, T_{ground}^l [°C]	12

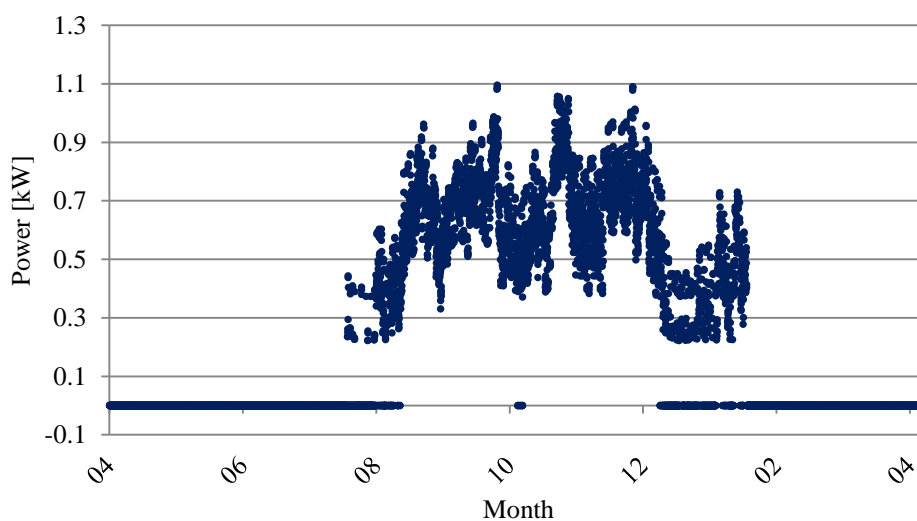


Figure 4.7. Annual heating power required by the passive dwelling (Dangel, 2010)

4.2.1.2. Heat storage system

In section 2.4, it was indicated that the heat storage system is composed of the system reactor, the LiBr solution tank, the water tank and the pipes connecting each element. The system reactor is composed of two coupled heat exchangers working as desorber/condenser or absorber/evaporator in the charging and discharging period, respectively.

The heat exchangers dimensioning considered in this study (Table 4.2) is the same dimensioning considered in section 2.1.3 for a grooved vertical flat plate heat exchanger configuration, since the latter presented a simulated power in the absorber between 1.0 and 3.1 kW (Figure 2.25c), which can meet the heating power demand required by the dwelling along the year (Figure 4.7).

The dimensioning associated to the initial value of the solution tank and the water tank is based in the following simple approach: From Figure 4.7 it can be considered that the average heating power required along the discharging period (6 months) is 0.6 kW. From Figure 2.25 (power in the absorber of the grooved vertical plate exchanger configuration) it can be deducted that to generate a power around 0.6 kW an absorbed water mass flow around 1 kg/h is needed. Then, during the discharging period, the total amount of water absorbed in the reactor would be around 2678 kg. If we consider that the LiBr mass fraction along this period changes from 0.6 to 0.5; then the required mass at the beginning (end) of the charging (discharging) period should be around 16000 kg.

Tables 4.3, 4.4 and 4.5 describe the technical characteristics associated to the LiBr solution tank, water tank and pipes, respectively, used for this reference simulation case.

It must be remarked that the system annual simulations results shown in sections 4.2.2 and 4.3 start in May, which is the beginning (end) of the charging (discharging) period; consequently, the tanks mass initial values shown in Tables 4.3 and 4.4 correspond to this departing point.

The initial water tank mass considered is 6315 kg, which corresponds to the beginning of the charging period and could increase above 8000 kg at the end of the charging period. This important initial mass in the water tank was to ensure a good simulation convergence of the water tank model described in section 2.2.2. An analogous criterion was considered for the LiBr solution tank model (see section 2.2.1).

Table 4.2. Reactor and heat exchangers characteristics

Number of heat exchangers	2
Material	Stainless steel
Heat exchangers type	Grooved vertical sandwich flat plate
Plate height [cm]	53.3
Plate width [cm] ⁽¹⁾	39.2
Plate thickness [cm]	0.3
Number of grooves per heat exchanger side	78
Grooves width [cm]	0.4
Wetted surface percentage [%] ⁽²⁾	79.6
Direction movement	Cocurrent
Number of grids in the model	5

⁽¹⁾ Each heat exchanger has a sandwich configuration (2 plates assembled), then the total plate width where a falling film flows is: 2×39.2 cm = 78.4 cm.

⁽²⁾ The value for the wetted surface percentage was calculated under the hypothesis that the LiBr solution or distilled water falling films completely wet the grooved sections. In the desorber, absorber and evaporator the value is 79.6% since there is a spacing between each groove. In the condenser the value is 100% since it is considered that system conditions permit the vapor to condense uniformly over all the exchange (plate) surfaces (grooves and the space between them).

In Table 4.3 an initial mass of 14132 kg was considered for the LiBr solution tank. The influence of this initial mass on the system performance will be studied in section 4.3.

Table 4.3. LiBr solution tank characteristics

Initial liquid solution mass [kg]	14132
Initial solution temperature [°C]	12
Initial LiBr mass concentration	0.544
Solution tank outlet mass flow, $\dot{m}_{st/tank_o}^l$ [kg/h]	80
Initial solution height [m]	3.61
Tank diameter [m]	1.75
Wall thickness [mm]	3
Wall material	Stainless steel
Wall insulation thickness [cm]	0
External temperature [°C]	12
Number of grids	10

Table 4.4. Water tank characteristics

Initial water mass [kg]	6315
Initial water temperature [°C]	12
Water tank outlet mass flow, $\dot{m}_{wt/tank_o}^l$ [kg/h]	80
Initial water height [m]	2.5
Tank diameter [m]	1.75
Wall thickness [mm]	3
Wall material	Stainless steel
Wall insulation thickness [cm]	0
External temperature [°C]	12
Number of grids	10

Table 4.5. Pipes characteristics

	LiBr solution and water
Pipe material	Stainless steel
Length [m]	6
Diameter [mm]	25
Pipe thickness [mm]	1.5
Insulation thickness [cm]	1
Thermal conductivity of insulation [W/(m.K)]	0.037
External temperature [°C]	12
Number of grids	4

A simulation period of 2 years was considered for this reference case, the time step associated to each component is indicated in Table 4.6. Different time steps were considered for the reactor, solution tank, water tank and pipes.

Since the model associated to the reactor considers stationary conditions, an hourly time step was chosen in order to reduce the time required to simulate the annual system performance. Nevertheless, since the solution tank, water tank and pipes models consider no stationary conditions; then, an adequate ratio between the grid size and the step time must be chosen in order to avoid simulation divergences (see section 2.2.1.1.1). The tanks models consider a higher number of grids than the pipes models (10 against 4), then a bigger step time was considered for the tanks in order to avoid very long simulation machine times⁽¹⁾.

Table 4.6. Simulation time step associated to each system component

	Step time [minutes]
Reactor	60
Solution tank	30
Water tank	30
LiBr solution pipes	15
Water pipes	15

4.2.1.3. Mixing tank

The mixing tank characteristics are described in Table 4.7. A 25 °C mixing tank temperature is considered since, as it is described in section 4.2.1.1, the model considers that the HTF responsible for providing the dwelling heating power leaves the dwelling, in direction to the mixing tank, at a constant temperature of 25 °C. Then, in order to ensure an energy contribution for the dwelling heating, the HTFs arriving at the mixing tank and coming from the reactor and the solar collector during the discharging period must have temperatures above 25 °C.

Table 4.7. Mixing tank characteristics

Mixing tank temperature, (discharge mode), T_{mt} [°C]	25
--	----

4.2.1.4. Solar collector

The solar thermal collector characteristics are similar to those used in Task 32 of the IEA-SHC (Heimrath and Haller, 2007) and are described in Table 4.8.

The HTF mass flow considered for the solar collector was of the same magnitude as the HTF mass flow considered for the grooved flat plate desorber, as it is described in section 2.1.3, since these elements are connected in the charging period (see section 4.1.4). The same HTF mass flow value was proposed in the discharging period.

Solar collector HTF minimal outlet temperatures of 25 °C and 50 °C were proposed for the discharging and charging periods, respectively. The value considered for the discharging period corresponds to the dwelling heating power hypothesis (see section 4.2.1.1). The value considered for the charging period is an initial value that can be high enough to ensure the desorption processes to happen in the reactor; nevertheless, the influence of the variation of this parameter on the system performance will be studied in section 4.3.

Finally, it must be indicated that the solar collectors were considered to work in “low flow” mode in order to optimize their performance⁽²⁾.

⁽¹⁾ A simulation machine time is considered as the time required by a computer to simulate the system performance.

⁽²⁾ In solar collector applications, a ratio between the HTF and the collector surface of 50 l/(h.m²) is normally used; nevertheless, in our simulated reference case the ratio is around 16.7 l/(h.m²) (see Table 4.8).

Table 4.8. Solar thermal collector characteristics

Surface, A_{sc} [m ²]	12
a_0 [-]	0.8
a_1 [W/(m ² .K)]	3.5
a_2 [W/(m ² .K ²)]	0.015
Ethylene glycol percentage (antifreeze) [%]	30
HTF minimal outlet temperature (charging mode), $T_{HTF/sc/ch.op.mode_{min.threshold}}$ [°C]	50
HTF minimal outlet temperature (discharging mode), $T_{HTF/sc/disch.op.mode_{min.threshold}}$ [°C]	25
HTF mass flow (discharging and charging mode), \dot{m}_{HTF/sc_i} [kg/h]	200

4.2.1.5 Heat source/sink

The heat source/sink characteristics are described in Table 4.9. The heat sink HTF outlet temperature is considered to be constant and equal to 12°C, which is the same value considered for the ground temperature (see Table 4.1).

The HTF mass flow associated to the heat source/sink is the same value as the HTF mass flow considered for the grooved flat plate evaporator and condenser (see section 2.1.3), since these elements are connected in the discharging and charging period, respectively.

Table 4.9. Heat sink characteristics

HTF outlet temperature (discharging and charging mode), T_{HTF/hs_o} [°C]	12
HTF mass flow (discharge and charge mode), \dot{m}_{HTF/hs_i} [kg/h]	200

The simulated system annual performance associated to the described reference configuration case is shown in section 4.2.2.

4.2.2. Simulated annual performance

The results of the reference configuration case are shown below in Figures 4.8 to 4.11.

A two years period was considered to simulate the heat storage system performance. The first year was used as an initialization period where the system interacts with the surroundings. The simulation results shown in the following figures correspond to the second year period, which has a considerable lower influence to the initial conditions than the first year.

In Figure 4.8a and 4.8b the inlet/outlet HTFs temperatures in the desorber/absorber and condenser/evaporator heat exchangers are shown. In Figure 4.8a for example, it is observed that during the charging period the desorber HTF inlet temperature is higher than 50°C, which corresponds to the minimal threshold temperature imposed, while during the discharging period the absorber HTF inlet temperature is 25°C, which corresponds to the temperature of the mixing tank. In Figure 4.8b it is observed that the condenser/evaporator HTF inlet temperature is always 12°C, which corresponds to the ground temperature and its outlet temperature.

In Figures 4.8a and 4.8b it is observed that during the discharging period the system can also operate in charging mode when the DHN are zero; as it was mentioned in section 4.1.4.

In Figures 4.8c and 4.8d the power given from or consumed for⁽¹⁾ the HTF in each heat exchanger is shown. In Figure 4.8c for example it is shown that during the charging period the power given by the HTF to start the desorption process can increase up to 6 kW, while during the discharging period the power consumed by the HTF, and which then is used to cover the DHN, goes from 1 to 2 kW.

A similar shape power behavior is observed in Figure 4.8d in relation to the condenser/evaporator HTF in the charging/discharging period, nevertheless at given moments during the charging period (summer), the HTF in the condenser is cooled instead of being heated (positive power instead of negative power) which implies that an absorption/evaporation process is happening in the reactor instead of a desorption/condensation process. This latter observation is confirmed in Figure 4.8e where the desorbed/absorbed water mass flow in the reactor is shown. The reason of this physical behavior is related to the desorber HTF inlet temperature: inlet temperatures barely higher than 50°C cannot guarantee a desorption process since the available energy is used to barely increase the LiBr solution falling film temperature but not to start a vapor liberation, permitting, conversely, an absorption process to happen. In order to avoid this latter behavior to happen, higher desorber HTF inlet temperatures must be imposed in the reactor; the influence of this parameter on the system performance is studied in section 4.3.3 through the variation of the solar collector HTF outlet temperature threshold during the charging periods.

In Figure 4.8f the vapor pressure associated to the system reactor, LiBr solution tank and water tank is shown. In general, it is observed that the pressure in the reactor is higher during the charging periods and the pressure in the LiBr solution tank is lower than in the other components and varies between 2 to 5 mbar. This also shows that the flowing of the solution between the reactor and its tank could be performed without pumping, as was done in the prototype (section 3.1.1.6).

⁽¹⁾ The power given from each HTF to the system for both, the desorber/absorber and the condenser/evaporator, has been calculated with the following correlation: $W_{htf} = \dot{m}_{htf_i} \times c_{p_{htf}} \times (T_{htf_i} - T_{htf_o})$

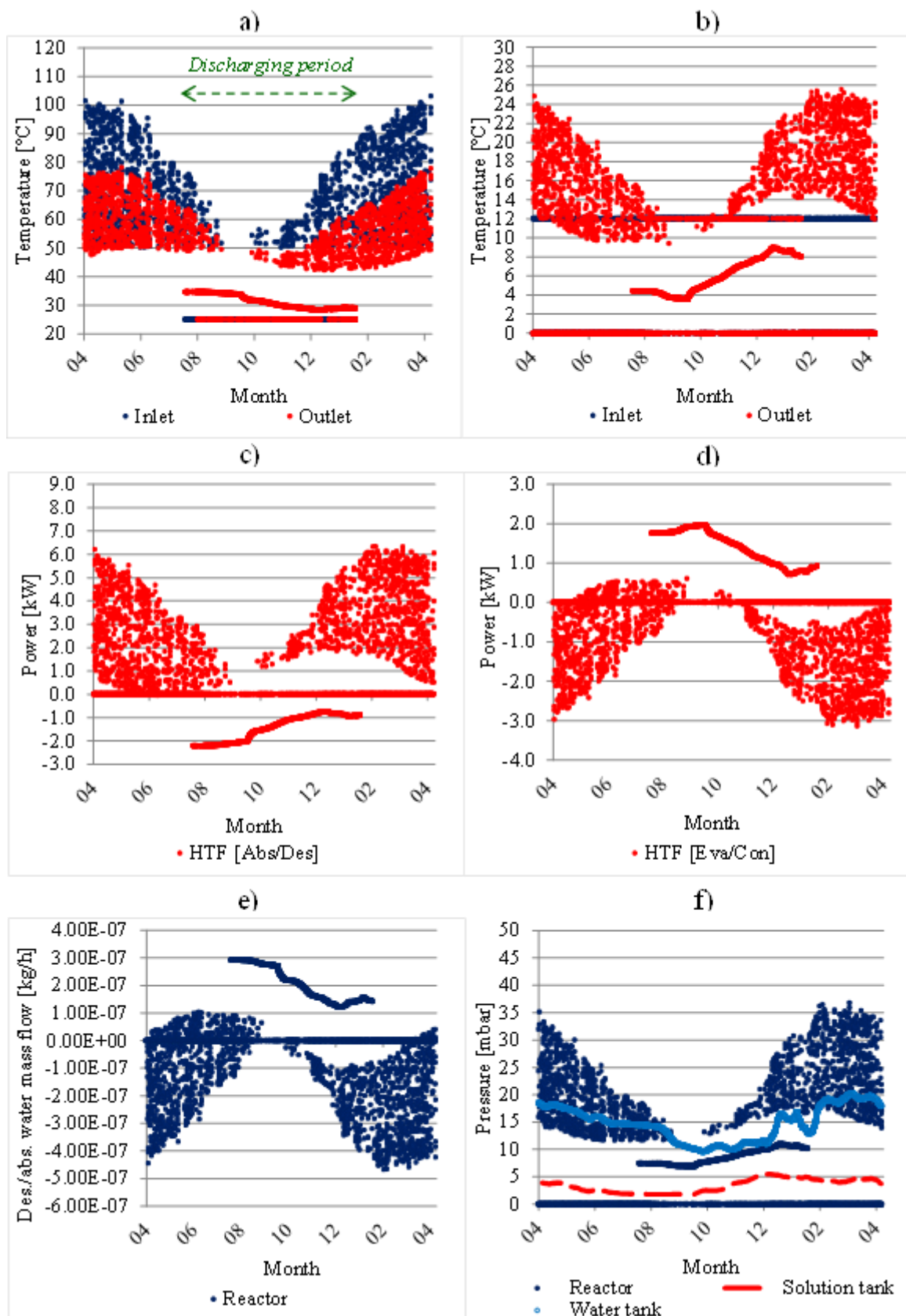


Figure 4.8. System reactor annual physical behavior (second year). a) HTF desorber/absorber temperature; b) HTF condenser/evaporator temperature; c) HTF desorber/absorber power; d) HTF condenser/evaporator power; e) Desorbed (-)/Absorbed (+) water mass flow; f) System components pressure

In Figure 4.9 and 4.10 the LiBr solution tank and water tank physical behaviors are observed. In both tanks, the inlet is considered to be at the bottom while the nodes⁽¹⁾ 2, 5 and 8 goes from bottom to top.

In Figure 4.9a the LiBr solution temperature in the tank is shown. During the charging period the solution inlet temperature goes from 40 to 70°C while during the discharging period the inlet temperature is between 25 and 35°C. In general the solution temperature is higher than the surrounding temperature (12 °C, “External wall”), and the lower nodes have a higher temperature than the higher nodes, since they are closer to the tank inlet.

Several consequences can be derived from the tank’s inlet and outlet positioning. During the charging period, solution at a higher temperature and LiBr mass fraction is pumped in at the tank bottom while solution at a lower temperature and LiBr mass fraction is pumped out from the tank top; producing, as a main effect⁽²⁾, a denser solution presence at the bottom, which favors a solution tank stratification. Hence, temperature and LiBr mass concentration values at the solution tank outlet (top) are likely to present a stair-shape behaviour. Conversely, during the discharging period, solution at a lower LiBr mass fraction is pumped in at the tank bottom while solution at a higher LiBr mass fraction is pumped out from the tank top (temperatures along the tank are similar, Figure 4.9), promoting a no-stratification of the solution tank. Hence, a linear-shape behaviour could be expected for temperature and LiBr mass fraction values at the tank outlet (top).

Additionally, since the solution tank is in general at higher temperatures than the surroundings, the tank heat losses will be determined by the tank insulation. For cases in which insulation is considered, a better conservation of the solution sensible heat is possible but, at the same time, higher LiBr mass fractions would be required for crystals to appear. Conversely, for cases in which no-insulation is present an important amount of the solution sensible heat is lost, facilitating the formation of crystals. The effect of the solution tank insulation thickness on the system performance will be studied in section 4.3.1.

In Figure 4.9a is also observed that several points associated to “Inlet [bottom]” show a temperature below 20 °C. Those values belong to periods where no solution mass flow enters or leaves the solution tank and correspond to the solution temperature at the pipe’s outlet connected to the solution tank inlet⁽³⁾ (the solution in the pipe being more influenced by the external ambient temperature due to its small mass). It must be also highlighted that in periods where the solution tank inlet mass flow equals to zero, the inlet solution temperature and LiBr mass fraction values do not influence on the solution tank model (see section 2.2.1.1).

In Figure 4.9b the LiBr mass fraction in the tank is shown. During the charging periods the inlet concentration is higher than the outlet concentration due to a more concentrated solution coming from the reactor, where the maximum gap observed between inlet/outlet is around 0.035. Contrarily, during the discharging periods the inlet concentration is lower than the outlet concentration, where the maximum gap observed between outlet/inlet is around 0.026. It is also observed that at the beginning of this second year simulation, the solution tank average concentration is about 0.573, which is higher than the tank initial concentration, 0.544; while at the end of this second year simulation the solution tank average concentration is about 0.587. The solution tank then tends to reach an annual periodical behavior that could be attained along the years if the meteorological conditions were also periodical.

Figures 4.9c and 4.9d show the mass and height of the liquid solution, the crystal solution, the LiBr (liquid and crystal form) and the total solution present in the LiBr solution tank. A formation of crystals is observed between the months 6 and 10, with a maximum crystal fraction of 18%. The influence of the crystals formation is observed in Figure 4.9b in the higher nodes (node 8 and outlet) where their shape is different from lower nodes. Indeed, even though during the charging process the solution LiBr mass fraction and temperature are higher near the tank’s bottom (inlet), the solution crystallization starts near the tank’s top; this is because a solution temperature rise also increases the LiBr mass fraction value required for crystals to appear (and viceversa, see section 2.2.1.2 and Figure 2.35). Hence, in periods where the solution tank is in standby and starts to lose heat to the surroundings, the cooler solution near the top is more likely to be the first to reach saturation conditions.

⁽¹⁾ For discretization purposes, a node is considered to be at the center of a grid (see Tables 4.2, 4.3, 4.4 and 4.5)

⁽²⁾ A secondary effect can be associated to the temperature difference between the bottom and top of the solution tank (around 15 to 40 °C, see Figure 4.9a), which does not favor a solution tank stratification.

⁽³⁾ See Figure 4.1.

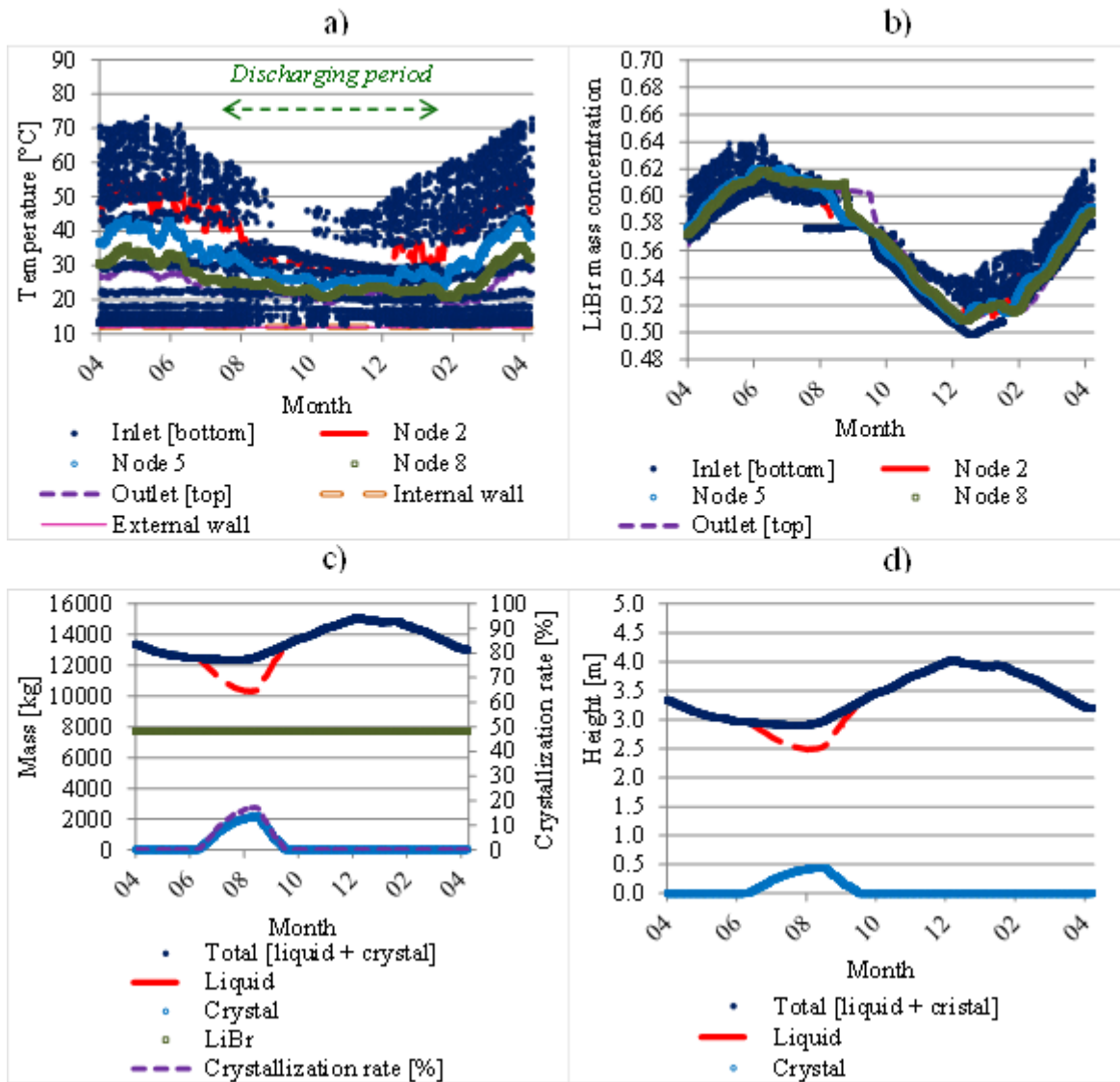


Figure 4.9. LiBr solution tank annual physical behavior (second year). a) Temperature; b) LiBr mass fraction; c) Masses; d) Heights

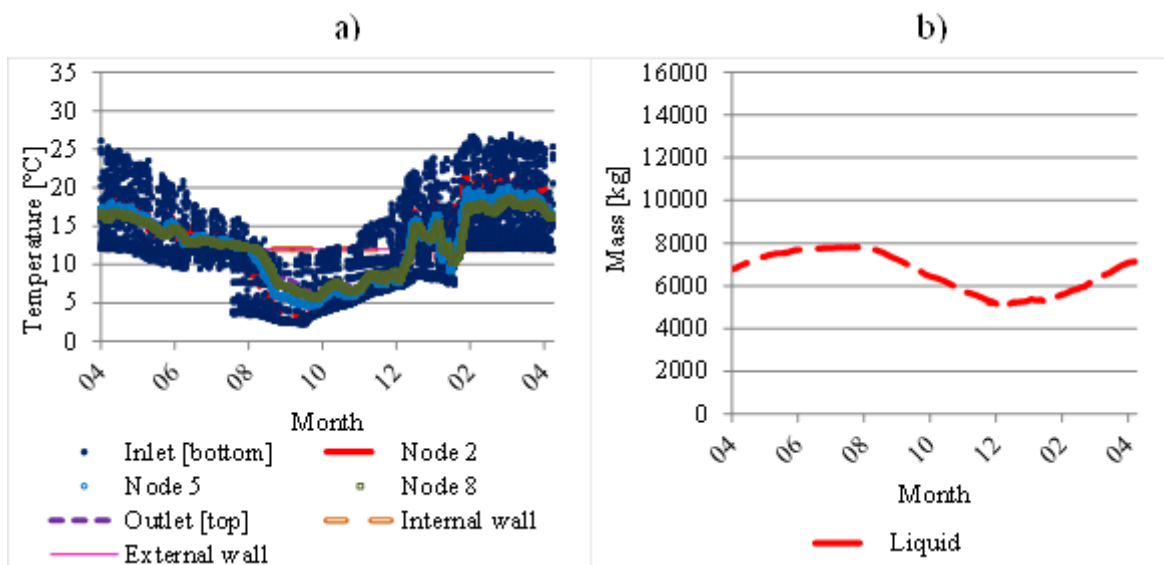


Figure 4.10. Water tank annual physical behavior. a) Temperature; b) Mass

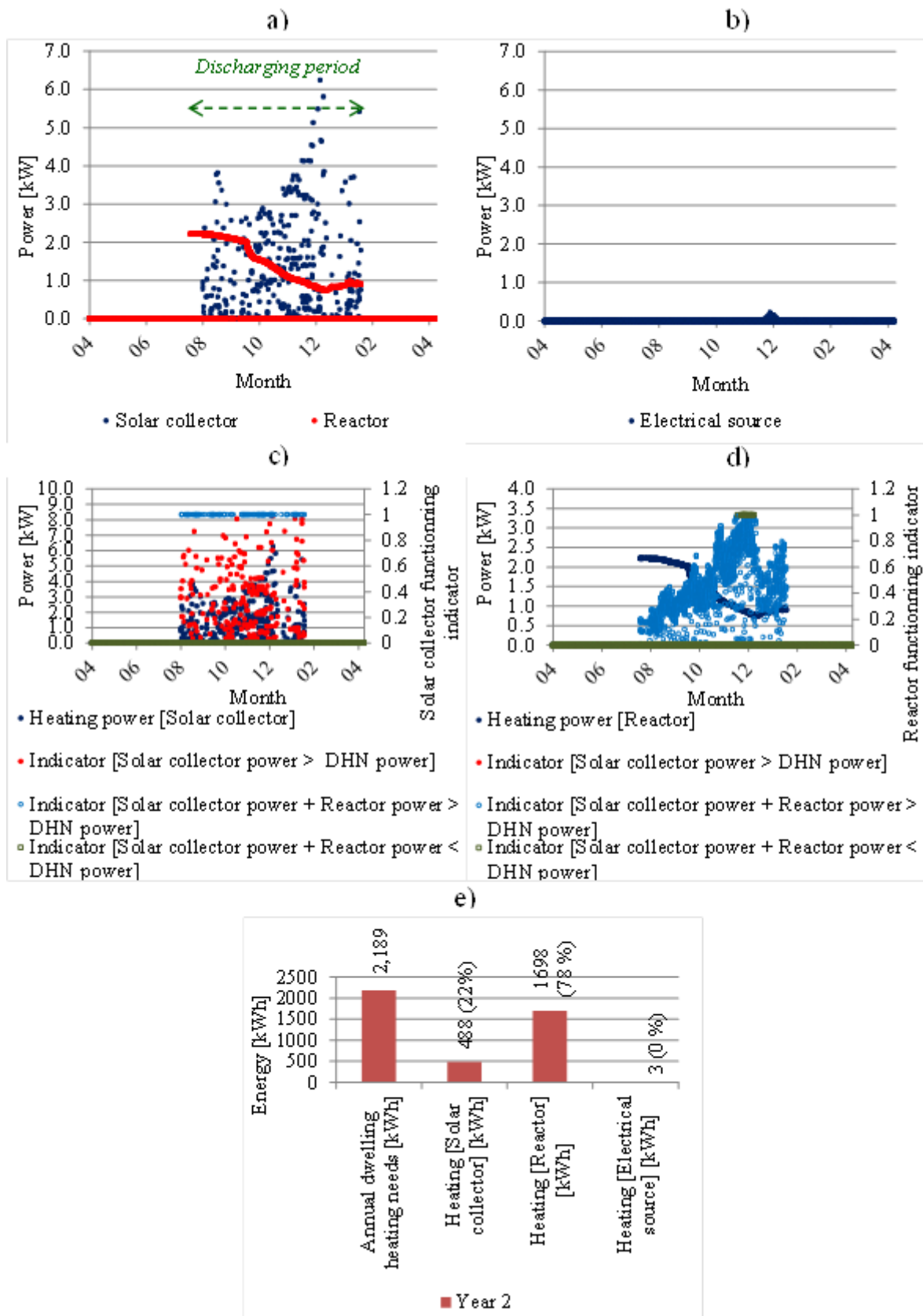


Figure 4.11. System annual performance (second year). a) Heating power provided by the reactor and the solar collector; b) Heating power provided by the electrical source; c) Reactor working period in discharge mode; d) Solar collector working period in discharge mode; e) Dwelling heating needs coverage provided by different sources

In Figure 4.10a the water temperature in the tank is shown. A maximal temperature around 25 °C is reached during the charging period while a minimal temperature around 5°C is reached during the discharging period; this behavior is associated to the water falling film in the reactor (water is pumped from the tank to the reactor and then reintroduced to the tank): in charging periods the water falling film gains energy from the condensation process while in discharging periods it loses energy due to the evaporation process. In Figure 4.10b the water mass in the tank is observed. In both, Figures 4.10a and 4.10b, it is observed that conditions at the beginning and at the end of this second year are different from the initial conditions, showing a system tendency to reach a periodical behavior.

Figure 4.11 shows the system performance for covering the DHN during the second year simulation. In Figures 4.11a and 4.11b the heating power generated by the solar collector, the reactor and the electrical source during the discharging period are observed. The available heating power generated by the solar collector can have values as high as 6 kW, which correspond to the day periods where the irradiance is maximal (the power provided by the solar collector to the reactor during the charging period is not presented here). The system reactor can generate heating powers from about 0.8 to 2 kW, with higher values at the beginning of the discharging period due to the solution higher LiBr mass concentrations entering the reactor (see section 2.1.3.1.2). The electrical source is needed during a small period of this second year (maximal value around 0.3 kW) at the end of the discharging period.

In Figures 4.11c and 4.11d the time functioning (functioning indicator) associated to the solar collector and the system reactor in the discharging period is observed. As shown in Figures 4.7 and 4.11a, the available power generated by the solar collector and the reactor is in general higher than the heating power needed by the dwelling; and also, as it was indicated in section 4.1.3, both solar collector and reactor, can work together and individually, with a preference to use the power generated by the solar collector.

In Figure 4.11c and 4.11d, it is observed that in time intervals (hourly intervals) where the solar collector heating power is higher than the DHN power (red curve), the solar collector can cover the DHN in a fraction of the time interval⁽¹⁾ (values between 0 and 1) while the reactor does not work (values of 0). In periods in which the solar collector heating power is not high enough to cover by itself the DHN power; and the solar collector heating power plus the reactor heating power is higher than the DHN power (blue curve), a working priority is given to the solar collector to work during the whole time interval (values equal to 1, Figure 4.11c), while the reactor works a fraction of the time interval (values between 0 and 1, Figure 4.11d). In periods in which the solar collector heating power plus the reactor heating power is lower than the DHN power (green curve), the reactor functioning indicator is equal to 1 (Figure 4.11d), while the solar collector functioning indicator can be 1 or 0 (day and night, respectively, Figure 4.11c). An electrical source is needed during this latter period since the solar collector and the reactor cannot completely cover the DHN power (see Figure 4.11b).

In Figure 4.11e, the annual dwelling heating needs coverage provided by the solar collector, the system reactor and the electrical source are shown.

Although the solar collector generated power can be, in certain periods, higher than the reactor generated power, it is the latter which has a more consistent contribution to cover the dwelling heating needs with a coverage percentage of about 78%. Contrarily, the electrical source has an almost negligible coverage percentage.

This implies that the current system dimensioning is capable to cover the DHN without the use of an electrical source. Furthermore, since during the discharging period a working priority is given to the solar collector, its contribution to the DHN (22%) should not vary if the solar collector dimensioning is not modified; then, the reactor contribution to the DHN could vary depending on how much the system dimensioning is modified.

In the following section 4.3, a study of different system configurations is shown in order to find a more interesting configuration which could increase the system performance and/or reduce the system costs.

⁽¹⁾ As it was commented in section 4.1.3, the solar collector is in fact considered to work during the whole time interval. Nevertheless, in cases in which the heat produced by the solar collector during this interval is higher than the heating needs, the surplus energy is assumed to be used in the next time interval.

4.3. Parametrical study and improved configuration

In this section, a study of the influence of the modification of certain parameters on the system performance is carried out. Four parameters are considered: the solution tank insulation thickness, the initial solution tank mass, the solar collector surface and the solar collector HTF minimal threshold outlet temperature during charging mode, $T_{HTF/sc/ch.op.mode}^{l,min.treshold}$. The other system characteristics are the same as those described section 4.2.1 for the reference configuration. The annual simulated results for the considered cases are described below in sections 4.3.1, 4.3.2 and 4.3.3.

4.3.1. Solution tank insulation thickness

In this section a study of the influence of the solution tank insulation thickness on the annual system performance is performed. In Table 4.10 a description of the considered cases is indicated.

In Figures 4.12 and 4.13, the annual simulated results for the solution tank temperature, the tank LiBr mass fraction, the tank mass and the heating power generated by the solar collector and the reactor are shown. In Figure 4.14 the annual dwelling heating needs coverage provided by the solar collector, the system reactor and the electrical source are shown.

Table 4.10. Simulation cases considered to study the solution tank insulation thickness influence on the system capability to cover the dwelling heating needs

	Wall insulation thickness [cm]	Wall insulation thermal conductivity [W/(m.K)]
Case 1 (Reference case)	0	0.037
Case 2	10	
Case 3	20	
Case 4	30	

As it was mentioned before, the remaining system characteristics of each case are the same as those considered for the reference configuration case described in section 4.2.1 and the “Case 1”, where no isolation is present, corresponds exactly to the reference configuration.

In Figures 4.12a, 4.12b, 4.12c and 4.12d the LiBr solution tank temperature along the second year simulation is shown for cases 1, 2, 3 and 4, respectively. An important increase of the solution average temperature is observed when an insulation is present, passing from a minimal temperature in “node 5” of around 25 °C, when no isolation is considered, to a minimal temperature of around 32 °C, 35 °C and 37 °C, when a 10, 20 and 30 cm insulation thickness is considered, respectively. Similarly, an increase of the solution inlet temperature is observed, passing from maximal inlet temperatures around 70°C to maximal inlet temperatures above 80°C.

In Figures 4.12e, 4.12f, 4.12g and 4.12h the LiBr mass fraction in the solution tank along the year is shown for cases 1, 2, 3 and 4, respectively. An increase of the average LiBr mass fraction for cases with an insulation is observed. For example, during the second year simulation the minimal LiBr mass fraction in “node 5” goes from about 0.51, when no insulation is present, to about 0.56, 0.57 and 0.58, when a 10, 20 and 30 cm isolation is present, respectively. The maximal LiBr mass fraction of the solution inlet is increased, passing from a value of 0.64 to values above 0.70. The increase in the solution LiBr mass fraction is related to the increase of the solution tank temperature: since the solution pumped to the reactor during the charging period is at a higher temperature, a bigger portion of the energy given by the HTF is used for the water desorption (instead of only increasing the solution temperature), which consequently permits to obtain higher mass fractions in the solution leaving the reactor and going back to the tank. A solution tank with high mass fractions can favor the crystal presence; and also, as it was indicated in section 2.1.3.1.2, a solution with high mass fractions can generate a higher power in the absorber during the discharging period.

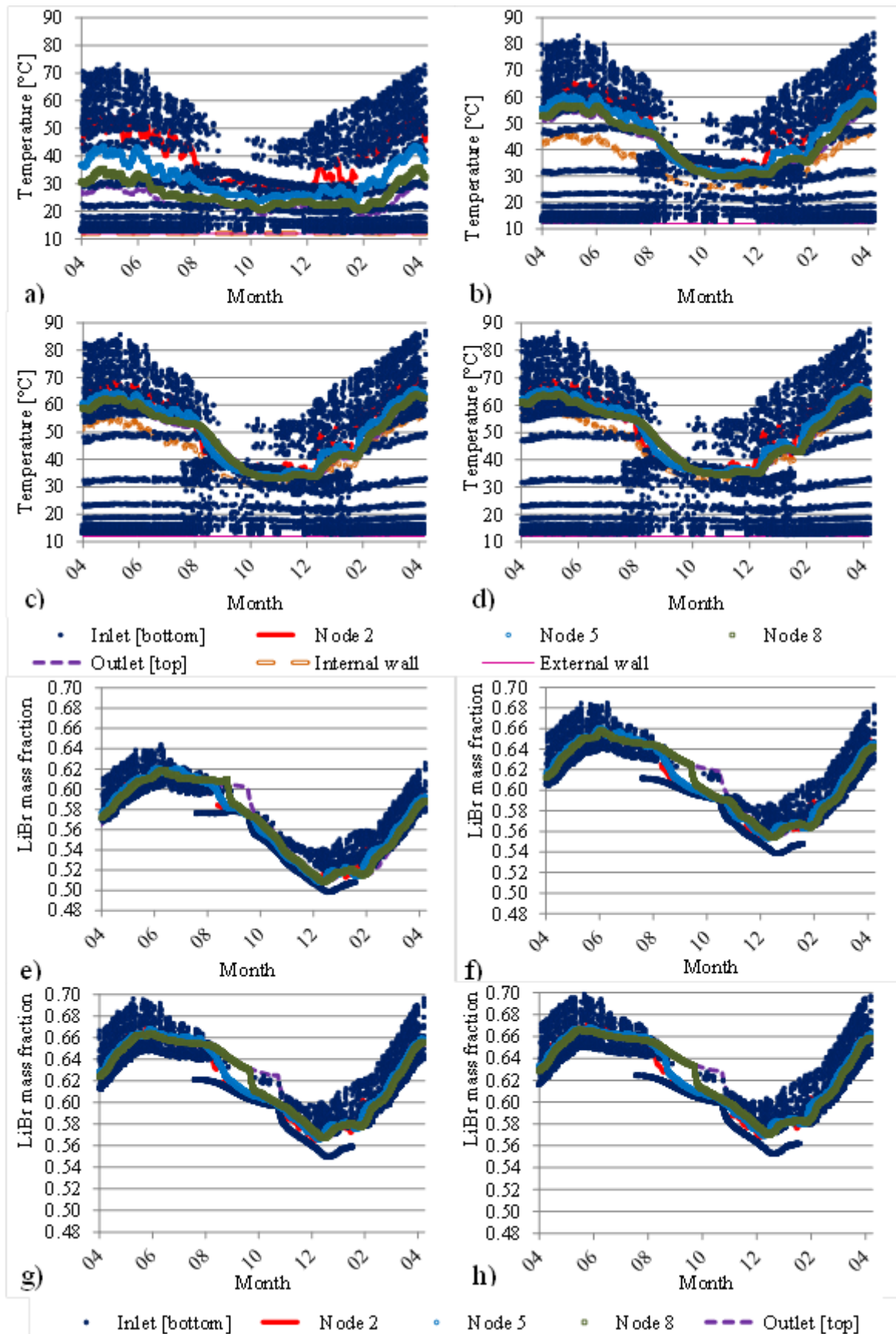


Figure 4.12. Solution tank temperature (a), b), c), d)) and LiBr mass concentration (e), f), g), h)) annual physical behavior for cases in Table 4.10 (second year). a) e) No insulation (reference case); b) f) 10 cm wall thickness insulation; c) g) 20 cm wall thickness insulation; d) h) 30 cm wall thickness insulation

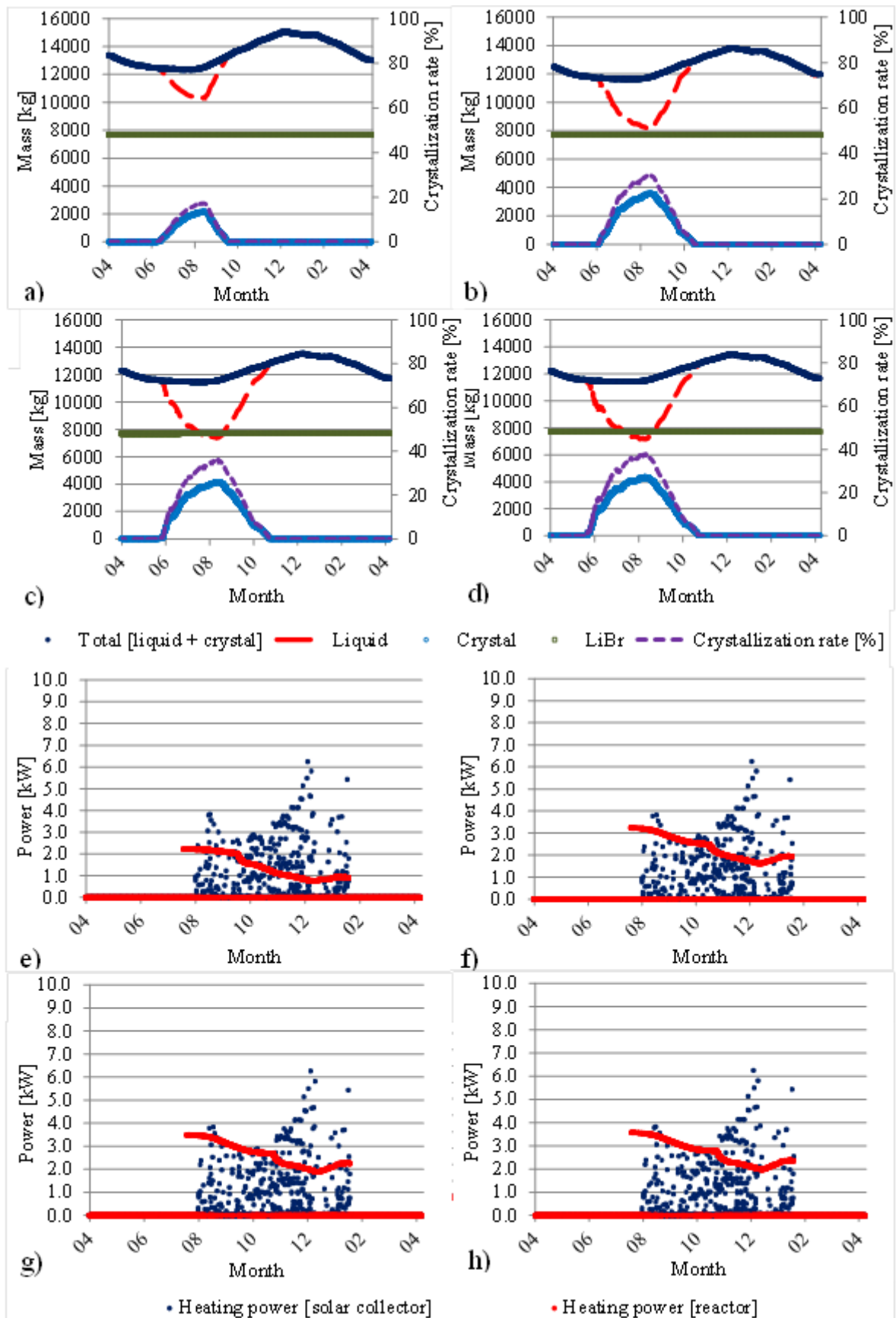


Figure 4.13. Solution tank mass physical behavior (a), b), c), d)) and solar collector and system reactor generated heating power (e), f), g), h)) for cases in Table 4.10. a) e) No insulation (reference case); b) f) 10 cm wall thickness insulation; c) g) 20 cm wall thickness insulation; d) h) 30 cm wall thickness insulation

In Figures 4.13a, 4.13b, 4.13c and 4.13d the mass in the solution tank during the year is shown for cases 1, 2, 3 and 4, respectively (all cases begin with the same initial mass at year 1). A more important presence of crystal is observed in cases where the wall insulation is thicker; passing, for the second year simulation, from a maximal crystallization rate of 16%, when no insulation is present, to maximal crystallization rates of 29%, 34% and 36%, when a 10, 20 and 30 cm insulation thickness is present, respectively. As it was mentioned before, this behavior is due to a higher mass fraction in the solution tank, which permits to reach saturation conditions that increase the presence of crystals⁽¹⁾. From a technical point of view, a higher amount of crystals in the tank implies a better management of the remaining liquid solution, since the pumping of this latter must not be affected by the presence of crystals. However the maximal crystallization rate is around 40%, which can be acceptable in actual tanks.

In Figures 4.13e, 4.13f, 4.13g and 4.13h the solar collector and the system reactor heating powers during the year are shown for cases 1, 2, 3 and 4, respectively. The generated solar collector heating power does not change its shape and values when a tank isolation is present since the solar collector dimensioning is not modified; nevertheless, the generated reactor heating power is strongly influenced. During the second year simulation the maximal heating power generated by the reactor increases from 2.22 kW, when no isolation is present, to 3.2 kW, 3.5 kW and 3.6 kW, when a 10, 20 and 30 cm isolation thickness is present, respectively. As it was mentioned above, since the LiBr mass fraction in the tank is increased and, consequently, the solution arriving at the reactor during the discharging period is more concentrated, an increase in the absorber HTF power is produced (see section 2.1.3.1.2).

Finally, in Figures 4.14a, 4.14b, 4.14c and 4.14d the dwelling heating needs coverage provided by the solar collector, the system reactor and the electrical source are shown for cases 1, 2, 3 and 4, respectively. For all cases it is observed that the electrical source contribution is negligible; and also, during the second year simulation it is observed that the heating energy provided by the system reactor almost does not change from 1698 kWh (78%), when no isolation is present, to 1701 kWh (78%), 1701 kWh (78%) and 1701 kWh (78%), when a 10, 20 and 30 cm isolation thickness is present, respectively. This latter behavior can be understood since the generated solar collector heating power (which has a priority to be consumed) does not depend of the configuration of the remaining system components and, at the same time, the dimensioning of the remaining system components permits to ensure coverage of the DHN without the use of an electrical source (even in the case of a 0 cm isolation which presented the lower generated reactor heating power).

From the previous analysis, “case 3” (20 cm wall isolation thickness) was selected as a new reference case, denoted as “Reference case B”, to study the influence of the variation of the LiBr solution tank initial mass on the yearly system performance to cover the dwelling heating needs. The results of this study are shown in section 4.3.2.

⁽¹⁾ The increase of the crystallization rate occurs even when a rise of the solution temperature is present (this latter implying to reach higher LiBr mass fractions for crystals to appear, see section 2.2.1.2). Indeed, the increase of the solution inlet LiBr mass fraction “compensates” the opposite effect generated by the increase of the solution temperature.

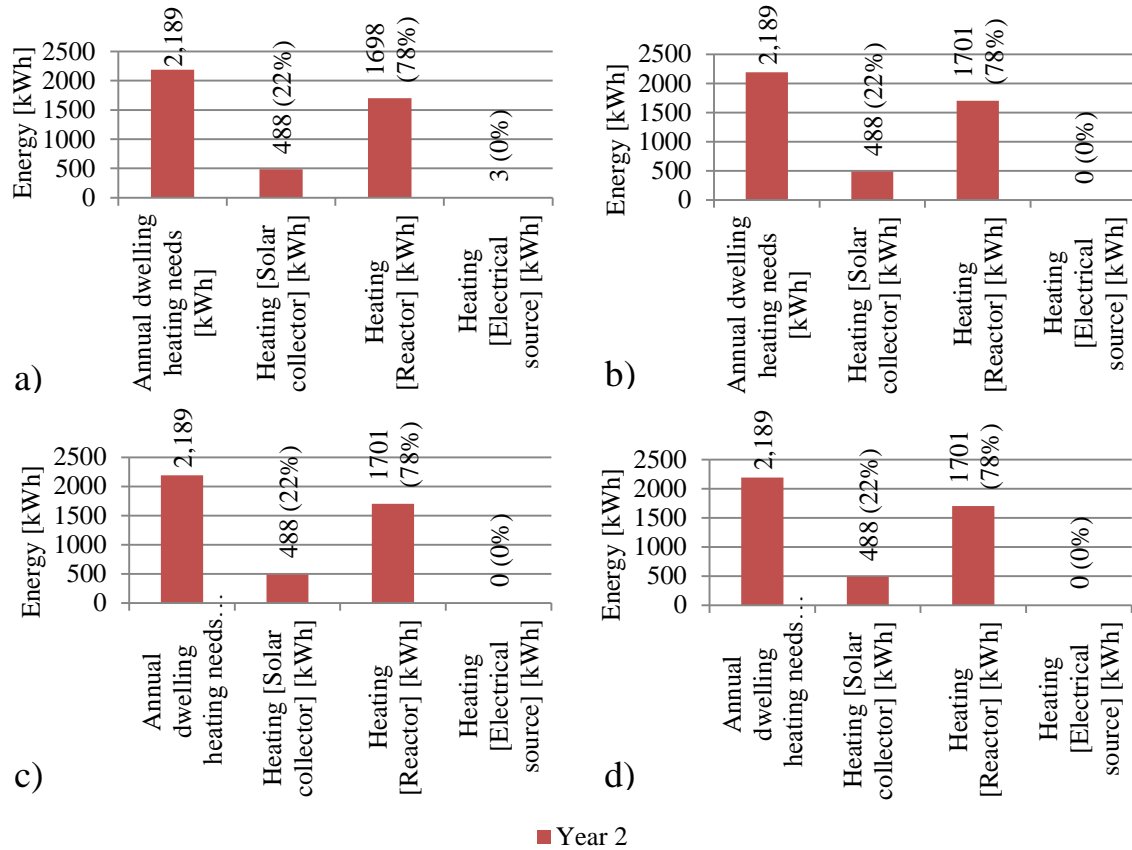


Figure 4.14. System annual performance: dwelling heating needs coverage provided by different sources for cases in Table 4.10. a) No insulation (reference case); b) 10 cm wall thickness insulation; c) 20 cm wall thickness insulation; d) 30 cm wall thickness insulation.

4.3.2. Initial solution tank mass

In this section a study of the influence of the solution mass on the annual system performance is studied. “Reference case B” (case 3) described in the previous section is used as a base case in this section.

In Table 4.11 a description of the considered cases is indicated. Four simulation cases are considered, covering an initial solution tank mass from 14000 to 8000 kg.

In Figures 4.15 and 4.16, the annual simulated results for the solution tank temperature, the LiBr tank mass fraction, the solution tank mass and the heating power generated by the solar collector and the reactor are shown. In Figure 4.17 the annual dwelling heating needs coverage provided by the solar collector, the system reactor and the electrical source are shown.

Table 4.11. Simulation cases considered to study the solution mass influence on the system capability to cover the dwelling heating needs

	Initial solution tank mass [kg]
Case 3 (“Reference case B”)	14132
Case 5	12000
Case 6	10000
Case 7	8000

It must be remarked that the remaining technical system characteristics of the “reference case B” (case 3) and the cases 5, 6 and 7 are the same as those considered for the reference configuration described in section 4.3.1. In Figures 4.15a, 4.15b, 4.15c and 4.15d the LiBr solution tank temperature along the year is shown for the “reference case B” (case 3) and the cases 5, 6 and 7, respectively. Similar solution temperature profiles and average temperatures are observed when the initial solution tank mass is reduced. During the second year simulation for example, the maximal and minimal temperatures in “node 5” are around 70°C and 35°C, respectively, when the solution tank initial mass is 14132 kg, 12000 kg, 10000 kg and 8000 kg. These similar temperature profiles are related to the crystallization and de-crystallization processes during the end and beginning of the charging and discharging period, respectively. Indeed, during several months the crystals presence ensures the conservation of saturation conditions which limits a strong variation in the solution temperature conditions: hence, a lower initial solution tank mass implies a more important presence of crystals and, therefore, a maintain of saturation conditions a longer time.

Additionally, in Figures 4.15a, 4.15b, 4.15c and 4.15d it is observed that whenever the initial solution tank mass is reduced, the internal wall temperature values are drastically reduced and become closer to the external temperature values. This is associated to the approach considered in the crystallization model, described in section 2.2.1.2, for the heat transfer across the solution tank wall when crystals are present in the tank. Further detail of the considered approach can be found in Annex B2.2.

In Figures 4.15e, 4.15f, 4.15g and 4.15h the LiBr mass fraction in the solution tank along the year is shown for the “reference case B” (case 3) and the cases 5, 6 and 7, respectively. In a similar behavior as for the solution tank temperature, similar LiBr mass concentration profiles are observed when the initial solution tank mass is reduced. At the end of second year simulation for example, the mass concentration in “node 5” is around 0.66, when the solution tank initial mass is 14132 kg, 12000 kg, 10000 kg and 8000 kg, respectively. Also, around the months 8 to 11, an important mass concentration gap between the “node 5” and the “node 8” is observed; this gap is associated to the crystallization process which is stronger in the higher nodes⁽¹⁾. Analogously as for the solution temperature, the similar LiBr mass concentration profiles are related to the crystals presence which maintains the solution in saturated conditions during several months and limits a strong variation in the concentration. A maintain of the solution in saturated conditions with high values of LiBr mass fraction implies to generate a higher absorber heating power during the first months of the discharging period.

⁽¹⁾ As it was commented in section 4.2.2, during the charging months in periods where the solution tank is in standby and starts to lose heat to the surroundings (for example at night), the solution near the top is more likely to be the first to reach saturated conditions since it is at a cooler temperature, respect to the tank bottom, and the LiBr mass fraction required for crystals to appear is lower.

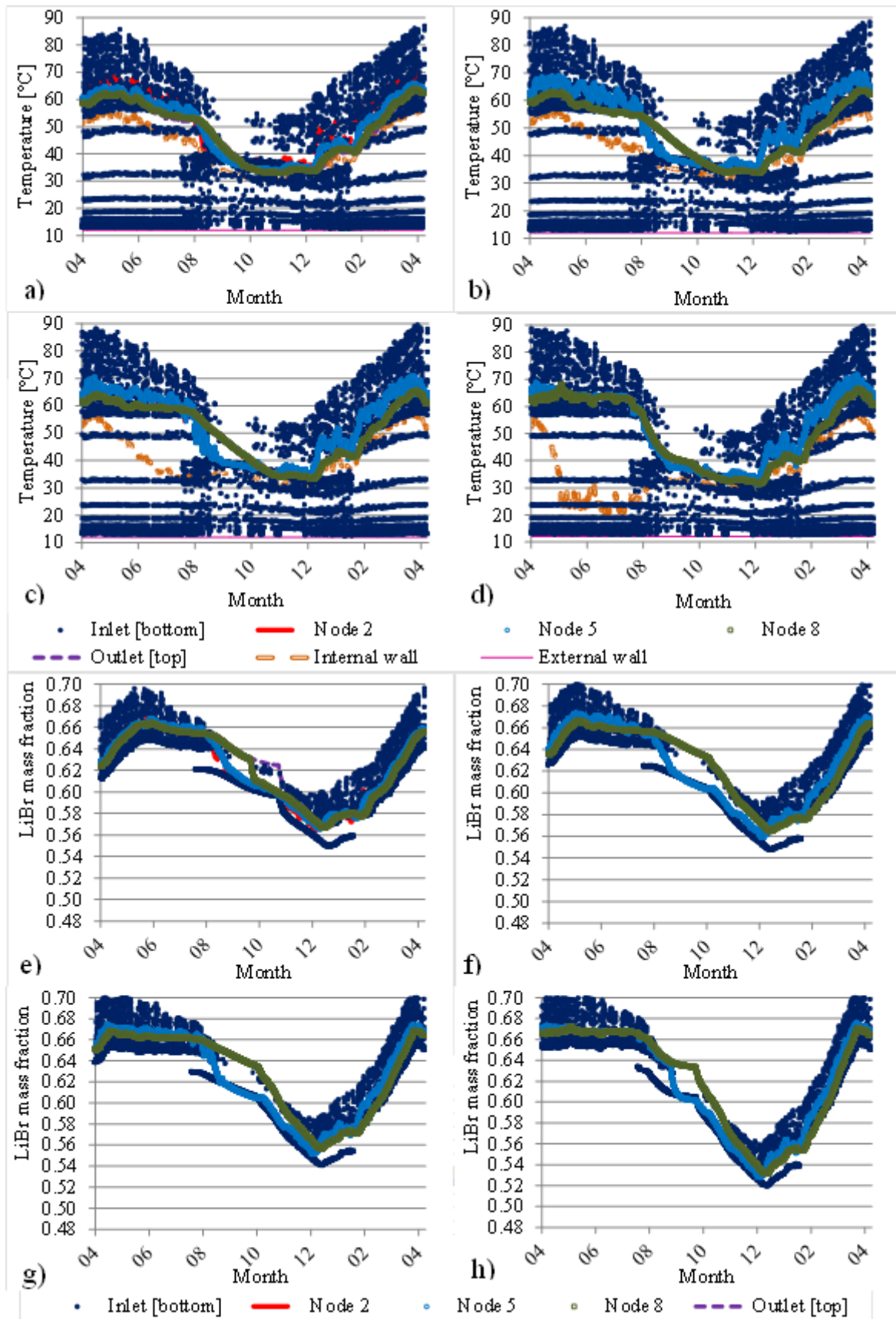


Figure 4.15. Solution tank temperature (a), b), c), d)) and LiBr mass concentration (e), f), g), h)) annual physical behavior for cases in Table 4.11 (second year). a) e) 14132 kg initial solution tank mass (reference case B); b) f) 12000 kg initial solution tank mass; c) g) 10000 kg initial solution tank mass; d) h) 8000 kg initial solution tank mass.

In Figures 4.16a, 4.16b, 4.16c and 4.16d the mass in the solution tank during the year is shown for the “reference case B” (case 3) and the cases 5, 6 and 7, respectively. A more important presence of crystal is observed in cases where the initial solution tank mass is lower; passing, for the second year simulation, from a maximal crystallization rate of 35%, when the solution tank initial mass is 14132 kg, to 54%, 83% and 95% ⁽¹⁾, for solution tank initial masses of 12000 kg, 10000 kg and 8000 kg, respectively.

In Figures 4.16e, 4.16f, 4.16g and 4.16h the solar collector and the system reactor heating powers during the year are shown for the “reference case B” (case 3) and the cases 5, 6 and 7, respectively. The generated solar collector heating power does not change its shape and values when the initial solution tank mass is reduced. The generated reactor heating power is also barely influenced. During the second year simulation it is observed that the maximal and the minimal heating power generated by the reactor is around 3.5 kW and 2 kW, when the solution tank initial mass goes from 14132 kg to 8000 kg. Although cases with a lower initial solution tank mass presented a higher crystallization rate; in all cases the crystals saturation LiBr mass fraction was similar, generating also similar heating powers in the reactor.

Finally, in Figures 4.17a, 4.17b, 4.17c and 4.17d the dwelling heating needs coverage provided by the solar collector, the system reactor and the electrical source are shown for the “reference case B” (case 3) and the cases 5, 6 and 7, respectively. For all cases the electrical source contribution is negligible; and also, the heating provided by the system reactor barely change and is around 1701 kWh for all the simulated cases. This behavior is associated to the fact that the generated solar collector heating power (which has a priority to be consumed) barely depends of the configuration of the remaining system components and, on the other hand; although the solution tank initial mass is reduced, the storage system has still the capability to partially cover the dwelling heating needs without the use of an electrical source.

It must be indicated that a further reduction of the initial solution tank mass is not possible since as it is observed in Figure 4.16d, the crystallization rate reaches values higher than 90% for the case of an 8000 kg initial solution mass.

From the previous analysis, the “case 7” (20 cm wall isolation thickness and 8000 kg initial solution tank mass) is selected as a new reference case, denoted as “Reference case C”, to study the influence of the variation of the solar collector surface on the annual system performance. The results of this study are shown in section 4.3.3.

⁽¹⁾ To avoid convergence difficulties in certain simulation cases, a modification of the LiBr solution tank model was made to consider 2 meshes instead of 10 meshes (see section 2.2.1) and smaller simulation time steps.

⁽²⁾ For case 7 (8000 kg), in Figure 4.16d is observed that the solution tank reaches a constant 95% crystallization rate value during months 6 to 8. Normally, under those conditions the whole solution tank should be crystallized; nevertheless, since the model cannot simulate the tank behavior without liquid solution, the observed particular shape of the crystallization rate curve is obtained.

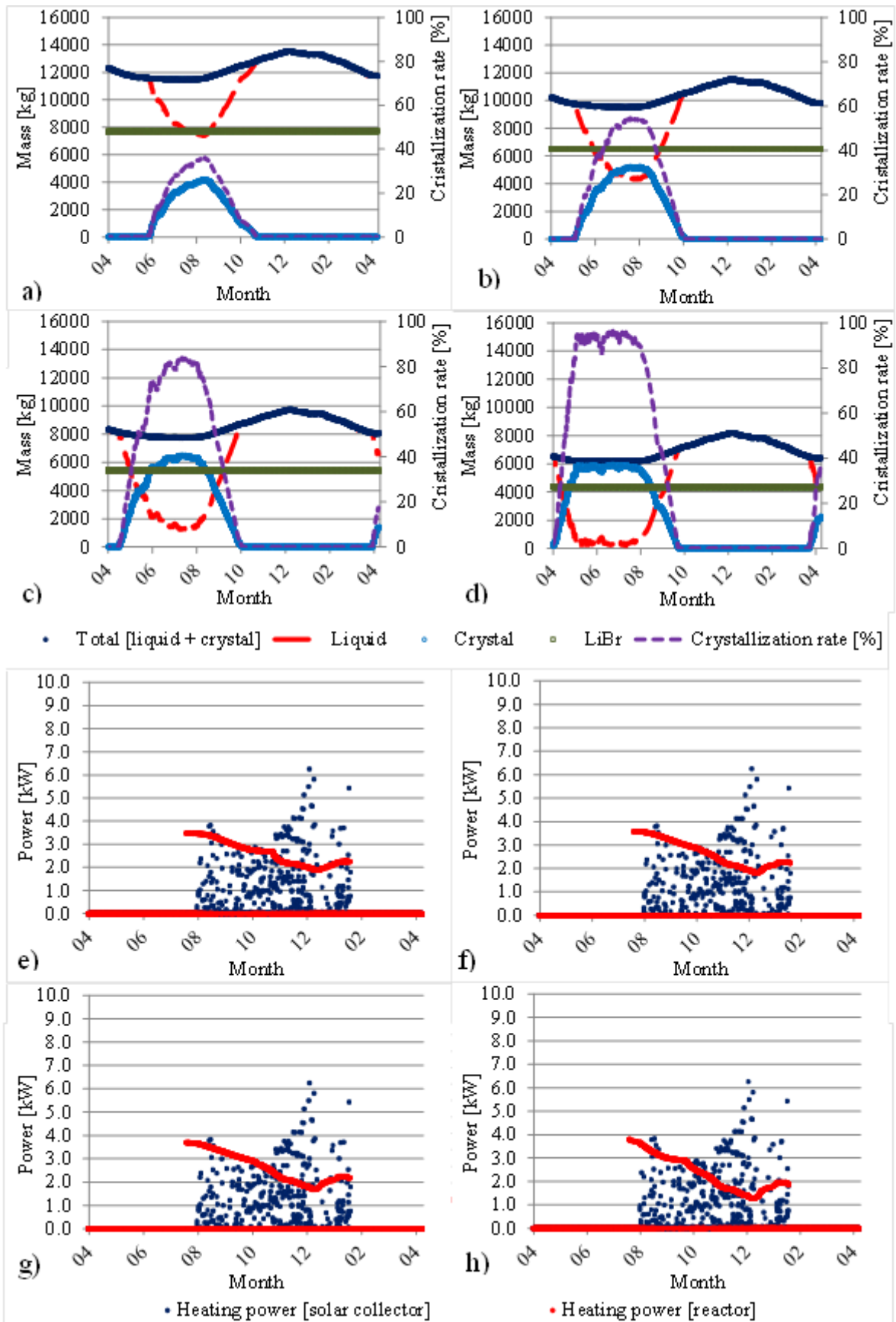


Figure 4.16. Solution tank mass physical behavior (a), b), c), d)) and solar collector and system reactor generated heating power (e), f), g), h)) for cases in Table 4.11 (second year). a) e) 14132 kg initial solution tank mass (reference case B); b) f) 12000 kg initial solution tank mass; c) g) 10000 kg initial solution tank mass; d) h) 8000 kg initial solution tank mass

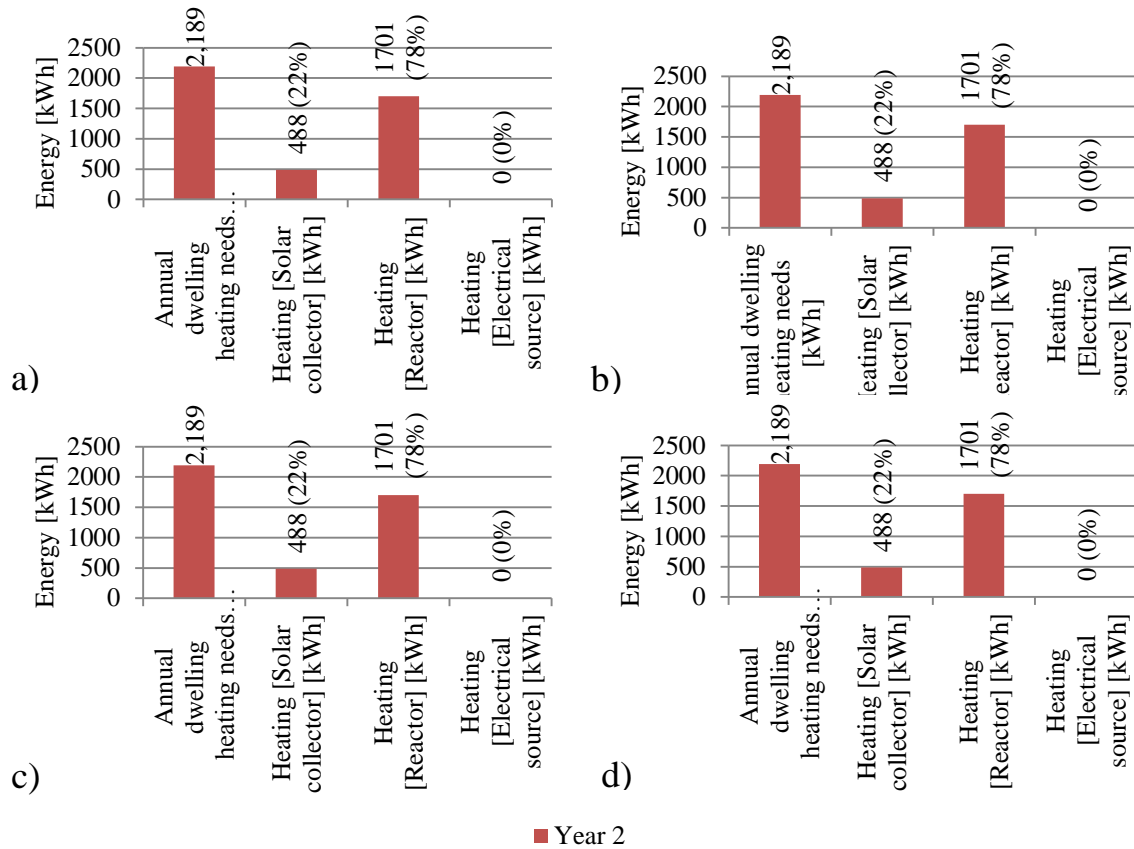


Figure 4.17. System energy annual performance: dwelling heating needs coverage provided by different sources for cases in Table 4.11 (second year). a) 14132 kg initial solution tank mass (reference case B); b) 12000 kg initial solution tank mass; c) 10000 kg initial solution tank mass; d) 8000 kg initial solution tank mass.

4.3.3. Solar collector surface and solar collector HTF outlet temperature

In this section a study of the influence of the solar collector surface and the solar collector HTF minimal threshold outlet temperature (in charging mode), $T_{HTF/sc/ch.op.mode}^{l,min.treshold}$, on the annual system performance is studied. “Reference case C” (case 7) described in the previous section is used as a base case in this section.

In Table 4.12 a description of the cases associated to the solar collector surface variation is indicated. Three simulation cases are considered covering a solar collector surface variation from 12 to 8 m².

In Figures 4.18 and 4.19, the annual simulated results for the solution tank temperature, the tank LiBr mass concentration, the tank mass and the heating power generated by the solar collector and the reactor are shown. In Figure 4.20 the annual dwelling heating needs coverage provided by the solar collector, the system reactor and the electrical source are shown.

Table 4.12. Simulation cases considered to study the solar collector surface influence on the system capability to cover the dwelling heating needs

	Solar collector surface [m ²]
Case 7 (“Reference case C”)	12
Case 8	10
Case 9	8

It must be remarked that the remaining technical system characteristics of the “reference case C” (case 7) and the cases 8 and 9 are the same as those considered for the reference configuration described in section 4.3.2.

In Figures 4.18a, 4.18b and 4.18c the LiBr solution tank temperature along the second year simulation is shown for the “reference case C” (case 7) and the cases 8 and 9, respectively. A decrease of the solution average temperature is observed when the solar collector surface is reduced. For example, the maximal temperature in “node 5” reduces from 72°C, when the solar collector surface is 12 m², to 68 °C and 61 °C, for solar collector surfaces of 10 m² and 8 m², respectively. In a similar behavior, the maximal inlet solution temperature reduces from 90°C to 70°C. It is observed that during the charging period (in certain moments) when the solar collector surface is high, the inlet solution temperature is also high; nevertheless, during the discharging period the inlet solution temperature mainly oscillates between 30 to 40 °C for all the simulated cases, which are temperatures capable to cover the dwelling heating needs as it is described further bellow. It must also be indicated that in Figures 4.18a and 4.18b an important difference in values and shape is observed for the “inner wall temperature”; this behavior is associated to the considered simulation model for cases where crystals are formed in the solution tank, which was explained in detail for a similar case in section 4.3.2.

In Figures 4.18e, 4.18f and 4.18g the LiBr mass fraction in the solution tank along the year is shown for the “reference case C” (case 7) and the cases 8 and 9, respectively. In a similar behavior as for the solution tank temperature, a decrease of the average LiBr mass concentration is observed when the solar collector surface is reduced. During the second year simulation for example, the maximal mass concentration in “node 5” decreases from 0.68, when the solar collector surface is 12 m², to 0.66 and 0.64, for solar collector surfaces of 10 m² and 8 m², respectively. This latter is due to a smaller solar collector surface, which penalize the energy given to the reactor for the desorption processes to happen. Also, during the months 8 to 11 in the second year, the mass concentration gap between the “node 5” and the “node 8” decreases, which implies a weaker crystallization process. Indeed, when the desorption process is stronger more crystals are produced in certain places of the solution tank; hence, during the discharging period when the crystals are diluted, the solution mass fraction in those places stays a longer time at saturated conditions, in comparison to the solution tank places where no crystals were formed.

In Figures 4.19a, 4.19b and 4.19c the mass in the solution tank along the year is shown for the “reference case C” (case 7) and the cases 8 and 9, respectively. A less important presence of crystals is observed in cases when the solar collector surface is reduced; passing from a maximal crystallization rate of around 95%, when the solar collector surface is 12 m², to 18% and 0%, for solar collector surfaces of 10 m² and 8 m², respectively. Again, this latter behavior is related to the reduction of the energy provided to the desorption processes, due to the reduction of the solar collector surface.

In Figures 4.19e, 4.19f and 4.19g the solar collector and the system reactor heating powers along the year are shown for the “reference case C” (case 7) and the cases 8 and 9, respectively. The generated solar collector heating power decreases when the solar collector surface is reduced; for all the studied cases, the HTF mass flow associated to the solar collector is considered to be constant (200 kg/h) in order to avoid an influence of the heat convective coefficient associated to the HTF bulk and the solar collector inner tubes surfaces. The generated reactor heating power is lightly reduced. The minimal heating power generated by the reactor decreases from 1.3 kW, when the solar collector surface is 12 m², to 0.9 kW and 0.6 kW for solar collector surfaces of 10 m² and 8 m², respectively. This latter behavior is associated to the decrease in the LiBr mass concentration in the solution tank; which, as it was mentioned before, is related to the reduction of the energy permitting the desorption processes, due to the reduction of the solar collector surface.

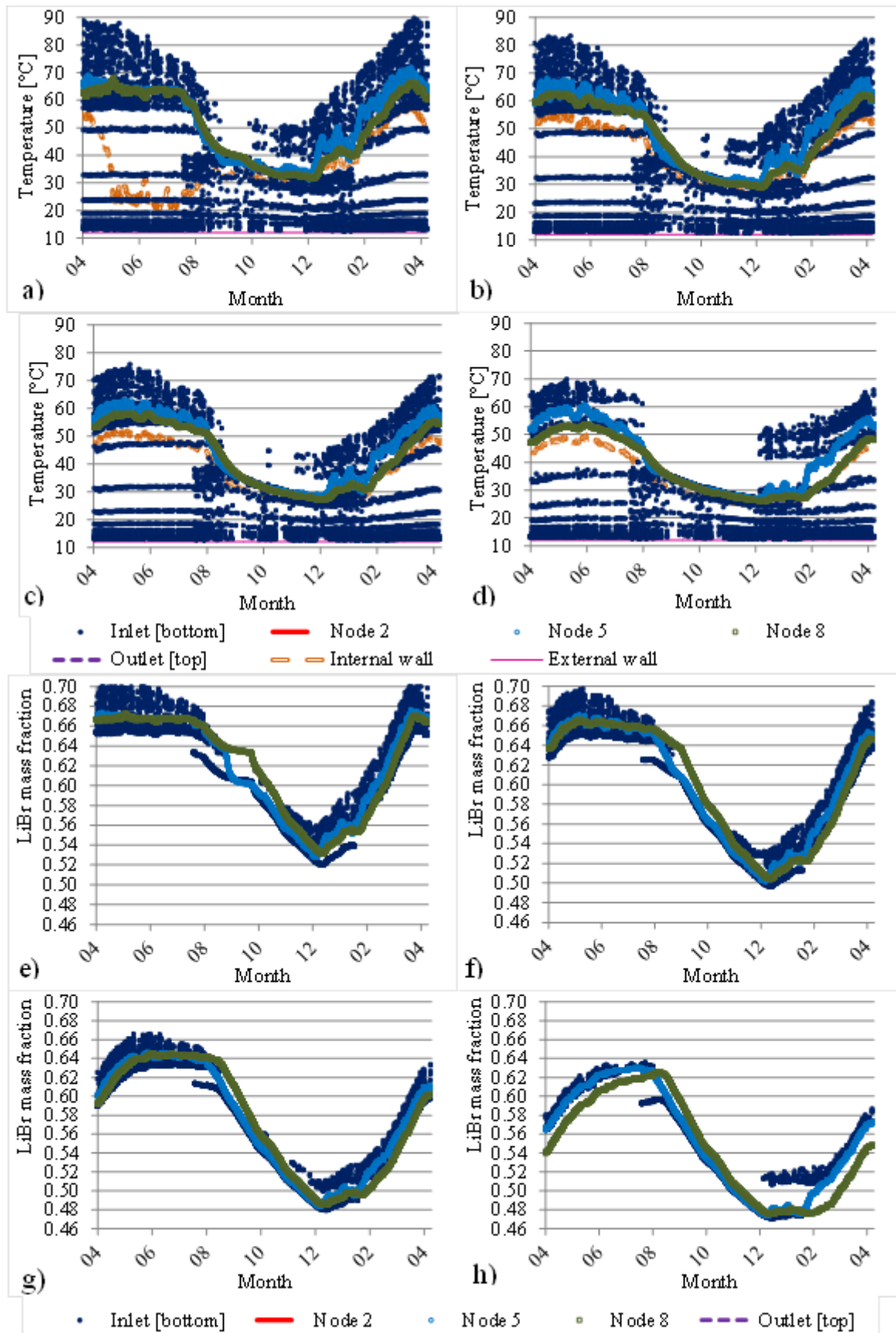


Figure 4.18. Solution tank temperature (a), b), c), d)) and LiBr mass fraction (e), f), g), h)) annual physical behavior for cases in Tables 4.12 and 4.13 (second year). a) e) 12 m² solar collector surface (reference case "C"); b) f) 10 m² solar collector surface; c) g) 8 m² solar collector surface (reference case "D"); d) h) 70 °C solar collector HTF minimal threshold outlet temperature (charging mode)

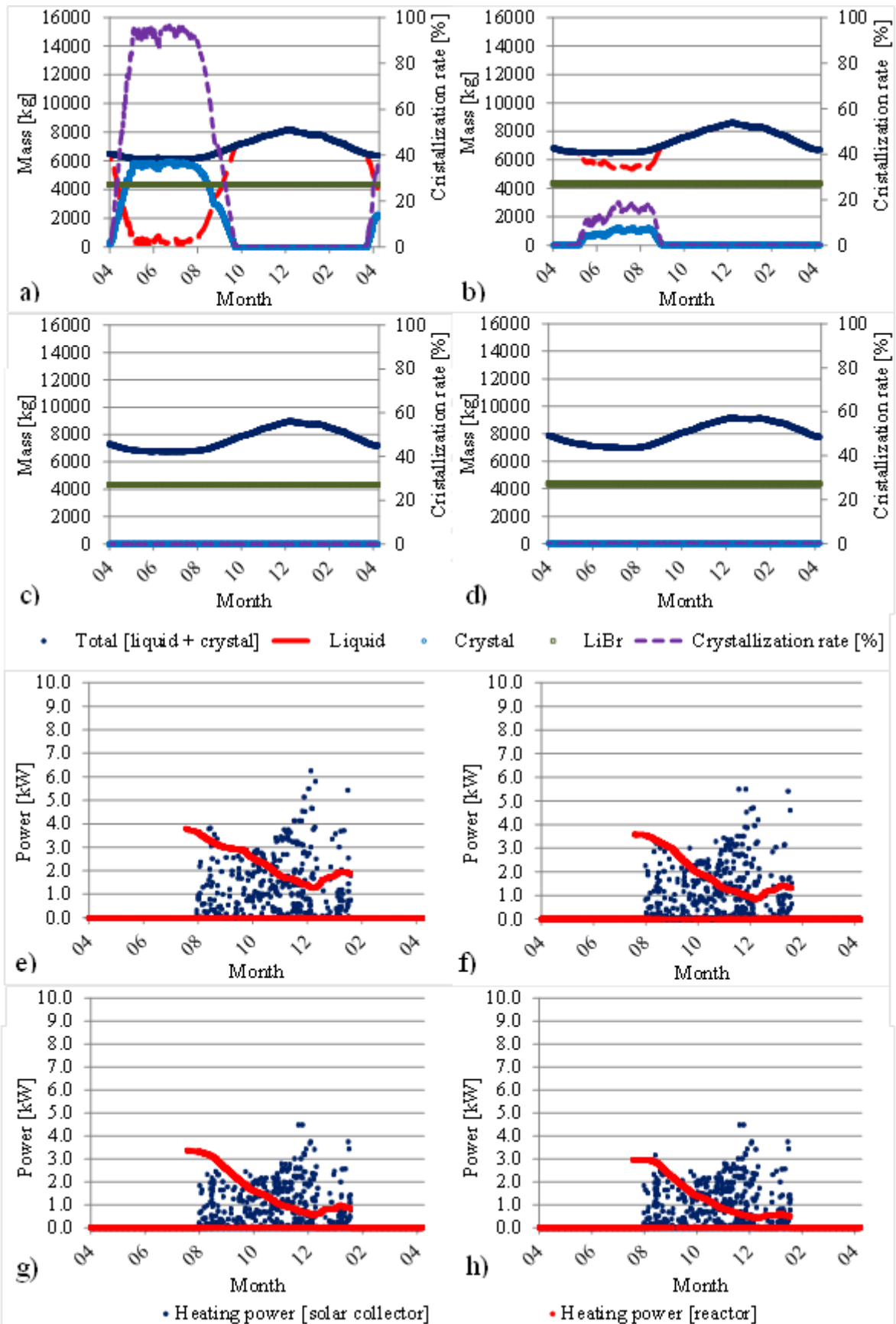


Figure 4.19. Solution tank mass physical behavior (a), b), c), d)) and solar collector and system reactor generated heating power (e), f), g), h)) for cases in Tables 4.12 and 4.13 (second year). a) e) 12 m² solar collector surface (reference case "C"); b) f) 10 m² solar collector surface; c) g) 8 m² solar collector surface (reference case "D"); d) h) 70 °C solar collector HTF minimal threshold outlet temperature (charging mode)

Finally, in Figures 4.20a, 4.20b and 4.20c the dwelling heating needs coverage provided by the solar collector, the system reactor and the electrical source are shown for the “reference case C” (case 7) and the cases 8 and 9, respectively. For all cases it is observed that the heating generated by the solar collector is reduced when the solar collector surface is reduced; with values, for the second year, of 488 kWh, 474 kWh and 436 kWh for surfaces of 12 m², 10 m² and 8 m², respectively. It is also observed that in all the cases the heat generated by the electrical source always remains low; with a maximal 31 kWh value in the second year for the 8 m² surface case.

Thus, although the heat generated by the solar collector is reduced due to a solar collector surface reduction, the interseasonal heat storage system is capable to cover this reduction while keeping the energy generated by the electrical source very low⁽¹⁾.

From the previous analysis, the “case 9” (20 cm wall isolation thickness, 8000 kg initial solution tank mass and 8 m² solar collector surface) was selected as a new reference case, denoted as “Reference case D”, to study the influence of the variation of the solar collector HTF minimal threshold outlet temperature (in charging mode), $T_{HTF/sc/ch.op.mode}^{l,min.treshold}$, on the annual system performance to cover the dwelling heating needs. The results of this study are shown in the following.

This study is carried out in order to find system working conditions permitting to avoid absorption processes to happen during the charging period, as it was highlighted in section 4.2.2 and in Figure 4.8e.

In Table 4.13 a description of the cases associated to the HTF minimal threshold outlet temperature variation is indicated.

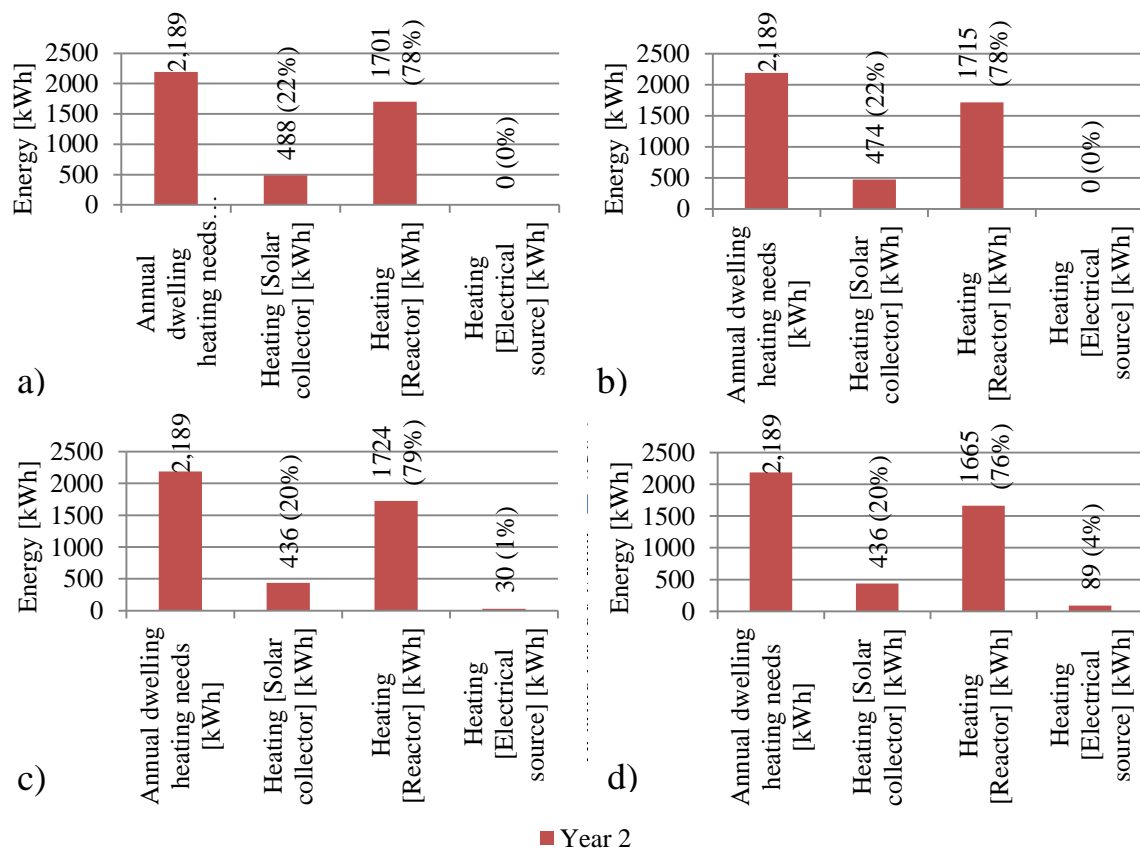


Figure 4.20. System energy annual performance: dwelling heating needs coverage provided by different sources for cases in Tables 4.12 and 4.13 (second year). a) 12 m² solar collector surface (reference case “C”); b) 10 m² solar collector surface; c) 8 m² solar collector surface (reference case “D”); d) 70 °C solar collector HTF minimal threshold outlet temperature (charge mode)

⁽¹⁾ Furthermore, by considering the “case 9” (8 m² solar collector surface), a further reduction of the solution tank initial mass (8000 kg) would be possible in order to reduce the system costs.

Table 4.13. Simulation cases to study the solar collector HTF minimal threshold outlet temperature (charging mode) influence on the system capability to cover the dwelling heating needs.

	Solar collector HTF minimal threshold outlet temperature (charge operation mode), $T_{HTF/sc/ch. op. mode}^{l, min. threshold}$ [°C]
Case 9 (“Reference case D”)	50
Case 10	70

The remaining technical system characteristics of the “reference case D” (case 9) and the case 10 are the same as those previously considered for the reference configuration described in section 4.3.3.

Figures 4.18d, 4.18h, 4.19d, 4.19h and 4.20d show the “Case 10” annual simulated results for the solution tank temperature, the solution tank LiBr mass fraction, the tank mass, the heating power generated by the solar collector/reactor and the annual dwelling heating needs coverage provided by the solar collector, the system reactor and the electrical source respectively.

The main differences between the “reference case D” and the case 10 are described below:

- The solution tank temperature for the “Case 10” ($T_{HTF/sc/ch. op. mode}^{l, min. threshold} = 70^{\circ}C$) is slightly lower than for the “reference case D” ($T_{HTF/sc/ch. op. mode}^{l, min. threshold} = 50^{\circ}C$). This is because, since the solar collector surface remains the same for both cases, the number of hours in which the desorption process is possible is reduced in “Case 10” (since a higher solar collector HTF outlet temperature, 70 °C, is demanded) and; consequently, the amount of hours in which hot solution is reintroduced to the tank is also reduced.
- The solution tank LiBr mass concentration for the “Case 10” ($T_{HTF/sc/ch. op. mode}^{l, min. threshold} = 70^{\circ}C$) is slightly lower than for the “reference case D” ($T_{HTF/sc/ch. op. mode}^{l, min. threshold} = 50^{\circ}C$). The “node 5” mass concentration for example, at the end of the year is reduced from 0.61 to 0.57, in an analogous way as for the solution tank temperature; this is because “Case 10” presents a reduction in the number of hours in which the desorption process happens. Furthermore, for “Case 10” a more important LiBr mass concentration gap is observed between the “node 8” and the “inlet solution” during months 12 to 2, compared to the “Reference case D” (see Figures 4.18h and 4.18g, respectively). This is because a higher $T_{HTF/sc/ch. op. mode}^{l, min. threshold}$ (70 °C) is used in “Case 10” during the charging process, ensuring to have only high concentrated solution leaving the reactor and entering the solution tank, respect to “Reference case D” (conversely, the total number of desorption hours is lower in the former case than in the latter case).
- Both cases, “Case 10” ($T_{HTF/sc/ch. op. mode}^{l, min. threshold} = 70^{\circ}C$) and “reference case D” ($T_{HTF/sc/ch. op. mode}^{l, min. threshold} = 50^{\circ}C$) do not present crystals along the second year simulations; nevertheless the solution mass in the former is lightly higher than in the later. This behavior is also related to the reduction in “Case 10” of the number of hours in which desorption processes are possible. Since at the end of the second year in “case10” the LiBr mass concentration in the solution tank is lower than in “reference case D”; then the amount of total mass in the former is higher than in the latter case.
- The heating power generated by the solar collector in “Case 10” ($T_{HTF/sc/ch. op. mode}^{l, min. threshold} = 70^{\circ}C$) is the same than for the “reference case D” ($T_{HTF/sc/ch. op. mode}^{l, min. threshold} = 50^{\circ}C$), since the solar collector surface is the same for both cases. Nevertheless, the heating power generated by the system reactor in “Case 10” is slightly lower than in “reference case D”, since the LiBr mass fraction in the solution tank for the former case is lower than for the latter case.

- The annual dwelling heating needs coverage provided by the system reactor for the “Case 10” ($T_{HTF/sc/ch.op.mode_{min.threshold}}^l = 70^\circ C$), 1665 kWh, is lower than for the “reference case D” ($T_{HTF/sc/ch.op.mode_{min.threshold}}^l = 50^\circ C$), 1724 kWh. An increase in the heating provided by an electrical source is also observed in “Case 10”. Both behaviors are related to the reduction of the heating power generated by the system reactor in “case 10”.

Although a more strict condition to permit the desorption process to happen is imposed in “Case 10” through a $70^\circ C$ solar collector HTF minimal threshold outlet temperature ($T_{HTF/sc/ch.op.mode_{min.threshold}}^l$), the system reactor ends having a lower energy coverage than in the “reference case D”, as it was mentioned before.

A more detailed explanation of this physical behavior can be obtained from Figure 4.21 where the desorbed/absorbed water mass flows in the reactor for the “reference case D” and the “Case 10” are shown.

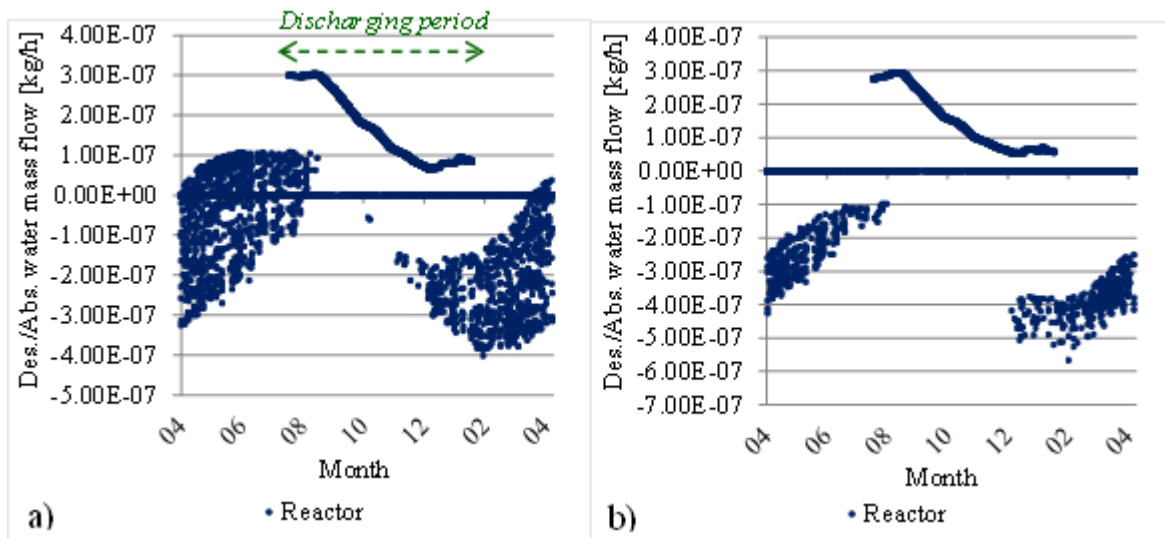


Figure 4.21. Annual desorbed (-)/absorbed (+) water mass flow in the reactor (second year). a) “Reference case D” ($T_{HTF/sc/ch.op.mode_{min.threshold}}^l = 50^\circ C$); b) Case 10 ($T_{HTF/sc/ch.op.mode_{min.threshold}}^l = 70^\circ C$)

In Figure 4.21a, related to the “reference case D” (where $T_{HTF/sc/ch.op.mode_{min.threshold}}^l = 50^\circ C$), during the system charging period in certain moments the reactor can work in an undesirable absorption/evaporation operating mode. This behavior was observed and discussed in section 4.2.2 (see Figure 4.8e) where solar collector HTF outlet temperatures barely higher than $T_{HTF/sc/ch.op.mode_{min.threshold}}^l = 50^\circ C$, cannot guarantee a desorption process, since the available energy is used to barely increase the LiBr solution falling film temperature but not to start a vapor desorption, permitting, conversely, an absorption process to happen.

Moreover, it is observed in Figure 4.21b that a very high threshold temperature limits the occurrence of desorption/condensation processes. This latter limitation is the reason why the annual dwelling heating needs coverage provided by the system reactor in “Case 10” was lower than in the “reference case 10”. A $T_{HTF/sc/ch.op.mode_{min.threshold}}^l$ between $70^\circ C$ and $50^\circ C$ would be considered as a more ideal threshold condition.

As it was defined in section 3.2.5, an indicator capable to evaluate the global performance of the interseasonal heat storage system is the *energy storage density* indicator (ESD). Three types of ESD were considered:

- $ESD_{V-system}$, defined as the ratio between the absorber energy output (energy given to the absorber HTF during the discharging period) and the volume occupied by the system.
- $ESD_{V-st-wt}$, defined as the ratio between the absorber energy output and the maximal volume of diluted solution and water.
- ESD_m , defined as the ratio between the absorber energy output and the system LiBr solution mass.

In Table 4.14, the values associated to the ESD during the discharging period ($DHN > 0$) for the Case 9 (“Reference case D”) are shown.

Table 4.14. System ESD for Case 9 during the second year simulation (discharging period)

	Annual heating power (Reactor) [kWh]	System volume ⁽¹⁾ [m ³]	Maximal diluted solution and water volume [m ³]	System initial LiBr solution mass [kg]	$ESD_{V-system}$ [kWh/m ³]	$ESD_{V-st-wt}$ [kWh/m ³]	ESD_m [kWh/kg]
Case 9 (“Reference case D”)	1723.6	15.2	10.9	8000	113.2	157.7	0.216

In Table 4.14 it can be observed that the simulated values obtained for the system annual ESD are very optimistic and at least five times higher than the experimental ESD obtained for the interseasonal heat storage prototype described in section 3.2.5. This can be associated to the simulation hypothesis of perfect wetting of the heat exchangers surfaces as well as the absence of non-condensable gases. Another reason can be related to the LiBr solution mass fraction values entering the reactor during the discharging period, which for the simulated system covers a range from 0.66 to 0.56, quite higher than the prototype working range described in Table 3.10 (section 3.2.5), which goes from 0.59 to 0.54.

Another indicator capable to evaluate the global performance of the interseasonal heat storage system is the *system efficiency coefficient* (COP) which is defined as the annual heating power generated by the reactor divided by the annual electrical consumption generated by the internal components of the system. In this context, the only system internal components permitted to consume electricity are the solution tank and water tank pumps responsible to pump the liquids from the tanks to the reactor. The value associated to the *system annual efficiency coefficient* is shown in Table 4.15.

Table 4.15. System annual efficiency coefficient for Case 9 during the second year simulation

	Annual heating power (Reactor) [kWh]	Annual working hours of the solution tank pump [h]	Annual working hours of the water tank pump [h]	Pumps power ⁽²⁾ [kW]	COP
Case 9 (“Reference case D”)	1723.6	2977	1359	0.18	2.2

The system annual efficiency coefficient observed in Table 4.15 is comparable to those of standard refrigeration machines (3 to 6) (Cap et al., 2013). It must also be indicated that a complementary evaluation parameter along the system efficiency coefficient could be the system cost, in order to choose an optimal interseasonal system configuration.

In general, in this section although the solution tank and the solar collector characteristics were modified, the heat storage system was always capable to cover the dwelling heating needs employing a very negligible amount of energy generated by an electrical source. Therefore, an improved system configuration requiring lower material costs, compared to the reference case for the range of dimensioning tests, can be found. A possible interesting configuration would imply a 20 cm solution tank isolation thickness, 8000 kg of solution, 8 m² solar collector surface and about 60°C solar collector HTF minimal threshold outlet temperature in charging

⁽¹⁾ Detail of volume associated in “Case 9” for: the solution tank (1.75 m diameter and 3 m height), water tank (1.75 m diameter and 3.2 m height) and the reactor container (0.316 m³) (this latter with same volume as the reactor described in Annex C1.3).

⁽²⁾ The pumps power correspond to the power of the same pump used for the interseasonal heat storage prototype described in Chapter 3 (see Table 3.1), since the experimental solution and water mass flows are comparable to those of the present simulated annual system (see Table 4.3 and 4.4).

mode. However as this parameter study was not intended to be an optimization procedure, other more interesting configurations, considering different values combination, can be found.

4.4. Heat storage system annual performance with a KCOOH- H₂O solution

During previous years, two projects have been carried out to study the performance of a system permitting to store the solar energy for long periods by sorption processes; these projects were PROSSIS 1 (Procédé de Stockage Solaire Inter-Saisonnier) and PROSSIS 2, which were developed between 2008 to 2012 and 2012 to 2016, respectively (Agence National de la Recherche, 2007), (Agence National de la Recherche, 2011).

As part of the research made during the project PROSSIS 2, the thermo-physical performance of different aqueous solutions, couple salt + water, were evaluated in order to study the performance of the interseasonal heat storage system when these solutions were used instead of the standard couple LiBr-H₂O, employed during the project PROSSIS 1 (Lefebvre, 2015). As a result of this study, an aqueous solution composed by the couple KCOOH-H₂O was proposed as an alternative option capable to accomplish the energy system requirements and, at the same time, reduce the material costs.

In this section a simulation study of the interseasonal heat storage system performance to cover an annual dwelling heating need when an KCOOH-H₂O aqueous solution is used has been carried out.

A modification of the simulation model developed in Chapter 2 was carried out by considering thermophysical properties of a KCOOH-H₂O solution found in the literature (Balarew et al., 2001), (Lefebvre, 2015), (Longo and Gasparella, 2015), (Longo and Gasparella, 2016). Properties correlations are shown in Annex D.

Technical system characteristics considered for this simulation case were the same as those used in section 4.2.1 for the reference case with exception of 2 parameters: the initial solution mass and salt concentration, which were modified and are indicated in Table 4.16. The initial solution mass was increased of 4000 kg in order to ensure the simulation model convergence (and avoid very shorts time steps)⁽¹⁾, while the initial salt mass fraction was increased to permit the apparition of crystals along the simulated period, since the saturation curve associated to the KCOOH-H₂O is higher than the saturation curve associated to the LiBr-H₂O (see Annex D and section 2.2.1.2).

Table 4.16. Simulation case characteristics considered to study the system capability to cover the dwelling heating need when a KCOOH-H₂O solution is used.

	Initial solution tank mass [kg]	Initial solution tank mass concentration [-]
Case 11	18000	0.676

A similar approach as for the simulated cases with LiBr solution, described in the previous section, was used. The simulated system physical behavior is shown in Figure 4.22.

In Figure 4.22a, the annual solution tank temperature profiles are shown. During the desorption period, the inlet solution tank temperature is about 10°C lower in “Case 11” than in the “reference case” with LiBr-H₂O (see section 4.3.1). This temperature difference is associated to the difference in the thermophysical properties of both aqueous solutions (see Annexes B1 and D1), which has an influence in the heat transfer to the solution film in the reactor. However, the KCOOH-H₂O solution temperature profile along the nodes is similar to the reference case profile with LiBr-H₂O, since in both cases the tank is not isolated.

In Figure 4.22b, the annual solution tank mass fraction profiles are shown. During the second year simulation, the mass concentration in “node 5” varies between 0.73 and 0.82. In general, from the beginning of the second year the KCOOH mass concentration profile has a tendency to reach a periodical behavior, similarly as for the reference case profile with LiBr, with a second year final KCOOH concentration around 0.81.

⁽¹⁾ To avoid convergence difficulties in the simulation of the KCOOH-H₂O solution tank, a 2 meshes approach was considered. Hence, in results shown in Figures 4.22a and 4.22b, the values associated to “node 2” and “node 5” are the same, while the values associated to “node 8” and “Outlet [top]” are also similar.

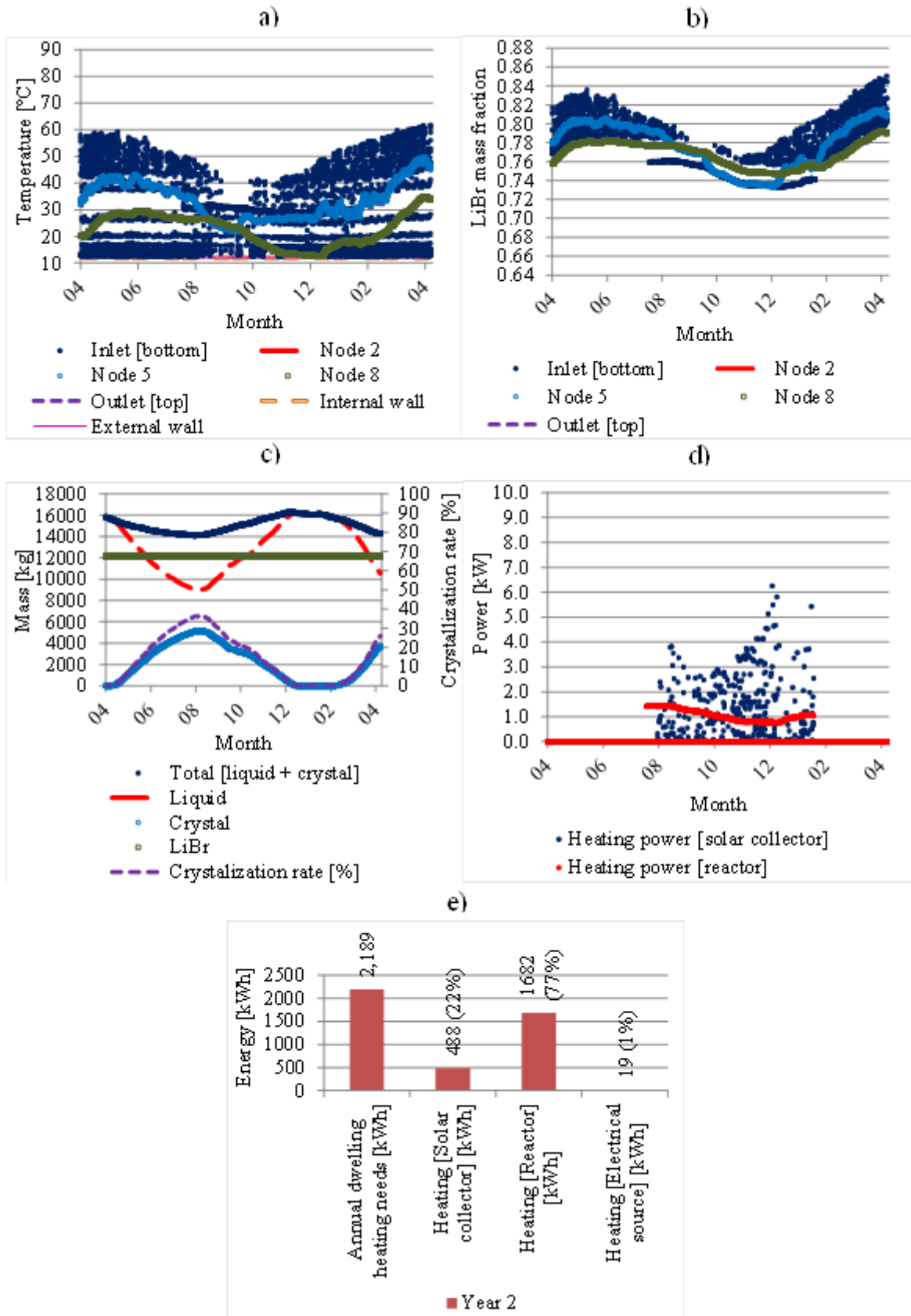


Figure 4.22. System annual physical behavior (second year). a) Solution tank temperature; b) Solution tank KCOOH mass fraction; c) Solution tank mass; d) Heating power provided by the solar collector and the reactor; e) Dwelling annual heating needs coverage provided by different sources

In Figure 4.22c, the annual solution tank mass profiles are shown. A crystal formation is observed during the second year simulation with a maximal crystal ratio of 38%. A larger crystal presence time period is observed with respect to the reference case with LiBr; with a 7 months' time compared to a 3 month's time, respectively. This is because the KCOOH solution in the tank reaches saturation conditions very fast at the beginning of the desorption period, as it can be observed in Figures 4.22a (solution temperature) and 4.22b (KCOOH mass fraction), for nodes 5 and 8, and in Figure D1 (KCOOH solubility crystallization curve) shown in Annex D1.1.5. Furthermore, this latter behavior is also influenced by the considered initial solution tank mass concentration (0.676), which is likely close to saturated conditions.

In Figure 4.22d the solar collector and the system reactor heating powers along the second year simulation are shown. The generated reactor heating power during the second year simulation varies between 0.8 kW and 1.4 kW; which is in general lower than with LiBr, that varies between 0.8 and 2.2 kW.

Finally, in Figures 4.22e the heating needs coverage provided by the solar collector, the system reactor and the electrical source are shown. The dwelling heating needs generated by the reactor during the second year simulation is 1682 kWh, which corresponds to a 77% energy coverage which is very similar to the value calculated with LiBr; in both cases, the dwelling heating generated by the electrical source is negligible. The reason why the heating needs coverage provided by the reactor in both cases is the same can be understood analyzing Figure 4.23.

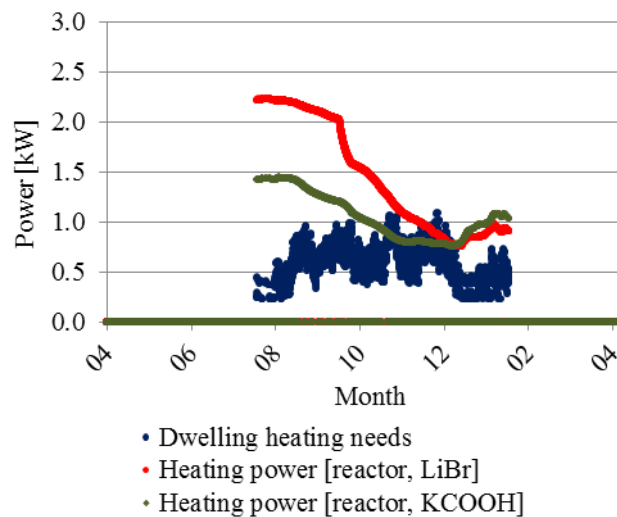


Figure 4.23. System annual physical behavior (second year). Dwelling heating needs and heating power provided by the reactor in “case 11” (KCOOH) and in “reference case” (LiBr)

In Figure 4.23 the heating power provided by the reactor in “Case 11” (KCOOH-H₂O) and “reference case” (LiBr-H₂O), as well as the dwelling heating needs along the second year simulation are shown. Although the reactor heating power is lower in the “Case 11” than in the case with LiBr, both powers are in general higher than the heating needs, which explains why there is little need of an electrical source.

All the previous studied cases presented in section 4.3 also did not require an electrical heating source because of the reactor heating power being higher than the dwelling heating needs. A parametrical study of the heat exchangers dimensions could be interesting in order to avoid a reactor over-dimensioning and to reduce costs.

In general, the use of a KCOOH-H₂O aqueous solution in the interseasonal heat storage system can have a similar coverage rate of the annual dwelling heating needs as for the case where LiBr-H₂O solution is used. Nevertheless, a special attention has to be paid to the system dimensioning (reactor, solution tank, solar collectors surface, etc.) in order to always ensure that the heating needs coverage provided by the solar collector, the reactor and the electrical source correspond to the desired values.

A parametrical study could also be carried out to find several optimal conditions in which the system performance, using a KCOOH-H₂O solution, is improved. Nevertheless, present limitations could be associated to this study such as the limited information of some KCOOH-H₂O thermo-physical properties (mass diffusivity, partial enthalpy, etc.) (see Annex D).

Another limitation to the simulation study shown in this section, which can be applied to the previous cases with LiBr in section 4.3, is that two optimistic conditions were considered: a complete wetting of the heat exchangers exchange surface by the falling films and the absence of incondensable gases; nevertheless, as it was studied in chapter 3, both of these limitations could appear in constructed systems. Therefore, further parametrical studies could also consider these two pessimistic scenarios.

Finally, as part of the researches programmed in project PROSSIS 2 (Agence National de la Recherche, 2011), current experimental tests on an interseasonal heat storage system prototype using a KCOOH-H₂O solution are carried out and the results of the system performance should be published in the near future.

4.5. Conclusions and outlooks

In this Chapter a model of an interseasonal heat storage system by sorption process coupled to a LEC dwelling is developed and some case studies are proposed to analyze the system annual performance.

In section 4.1 an overall system configuration required to couple the interseasonal heat storage system to a dwelling in order to cover its heating needs with solar energy is proposed. Associated elements required for this coupling were introduced; these elements were: a solar thermal collector, a heat source/sink and a mixing tank. Simulation models and working conditions hypothesis associated to the solar collector, heat source/sink and mixing tank were presented. A coupling model aimed to describe the annual physical interactions between the interseasonal heat storage system and the dwelling was presented.

In section 4.2 a system reference configuration was defined and studied. The system technical characteristics were described and the simulated annual performance of the reference configuration were shown.

The interseasonal heat storage system is capable to partially cover the annual heating needs of a 120 m² LEC dwelling, with a heat provided by the system reactor of 1698 kWh (equivalent to a 78% coverage). A parametrical study of the influence of certain parameters on the system performance was carried out. The modified parameters were the solution tank isolation thickness, the solution mass, the solar collector surface and the solar collector minimal threshold outlet temperature in charging mode.

The main influences of these changes on the system physical behavior, with respect to the reference configuration defined in section 4.2.1, are indicated below.

- In general, when the solution tank isolation thickness is increased, the average temperature and LiBr mass concentration in the solution tank increases, as well as the crystallization rate and the heating power generated by the reactor.
- When the solution mass is reduced, the average temperature and LiBr mass fraction in the solution tank and the heating power generated by the reactor are lightly affected; nevertheless the crystallization rate is strongly increased.
- When the solar collector surface is reduced, the average temperature and LiBr mass fraction in the solution tank decreases as well as the crystal ratio and the heating power generated by the solar collector and the reactor. Although a reduction in the component heating power, the storage system does not require an important increase of electricity consumption.
- When the solar collector HTF minimal threshold outlet temperature in charging mode is increased, a positive or negative influence on the system performance is produced depending on how much this temperature has been increased. A very low value permits undesirable absorption/evaporation processes to happen in the reactor during the charging period, which represents a penalization of the system performance; on the other hand, a very high value can avoid certain desorption/condensation processes to happen in the reactor during the charging period, which can also represent a penalization of the system performance.
- In relation to “Case 9” (“Reference case D”), the energy storage density and the system efficiency coefficient were calculated for the second year simulation; the obtained values were 157.7 kWh/m³ ($ESD_{V-st-wt}$) and 2.2, respectively, which indicates a good system performance.

- In general, although modifications of some technical characteristics of the system components, the interseasonal heat storage system was capable to cover the annual dwelling heating needs with a negligible use of an electrical source. At the same time, all the proposed changes could permit to reduce the global system cost.
- In general, several possible system configurations exist and their performance will depend on the dwelling heating demand, as well as the components interaction.

Finally, in section 4.4 a case study of the interseasonal heat storage system performance to cover annual dwelling heating needs when a KCOOH-H₂O aqueous solution is used was carried out. In general, this system shows a 7 months crystal presence period and is capable to cover the annual dwelling heating needs with a negligible use of an electrical source.

Some outlooks in relation to the annual performance study of the interseasonal heat storage system presented in this chapter can be:

- A parametrical study of the influence of the components that were not studied in this chapter; such as, for example, the solar collector technical characteristics (permitting to study different technologies), the mixing tank temperature (which could be related to the comfort temperature desired inside the dwelling) and the heat exchangers size (which has an influence on the system generated heating power).
- A study to determine the heat storage system Coefficient of Performance (COP); considering for this calculation, for example, the heating energy provided by the reactor during the discharging period against the electrical energy consumed by the system pumps along the simulated year. Complementary, a system Life Cycle Analysis (LCA) would be worth considering.
- A coupling of the global interseasonal heat storage system model with another commercial simulation tools, such as TRNSyS or EnergyPlus for example, in order to simulate scenarios in which the system interacts with more complex and realistic dwelling/building components.
- A technical-economic study to compare the system performance, under different dimensioning cases, when a LiBr-H₂O couple and a KCOOH-H₂O couple are used.
- A comparison study between the system simulated performance when a KCOOH-H₂O couple is used, against experimental tests that are currently being carried out using this couple in the system prototype.

Among the possible limits that could appear in further studies, it is worth mentioning the following:

- Simulation convergence difficulties in the model could appear in cases where the crystal fraction in the solution tank is very high. In order to avoid these convergence issues, a reduction in the number of meshes in the tank is recommended as well as a reduction in the simulation time step.
- An impact of the limited information of some KCOOH-H₂O thermo-physical properties can be expected on the system simulated performance for cases in which this couple is used.

Bibliography

- Agence Nationale de la Recherche; *Stockages innovants de l'énergie (Stock-E) – Projet PROSSIS (2007)*. <http://www.agence-nationale-recherche.fr/?Projet=ANR-07-STKE-0008>; last access, August 2016.
- Agence Nationale de la Recherche; *Systèmes Energétiques Efficaces Décarbonés (SEED) – Projet PROSSIS- (2011)*. <http://www.agence-nationale-recherche.fr/?Project=ANR-11-SEED-0011>; last access, August 2016.
- Balarew C.; Dirkse T. P.; Golubchikov O. A.; Salomon M.; Trendafilova S.; Ageyeva T.; Baldini P.; D'Andrea G.; *IUPAC-NIST Solubility Data Series 73. Metal and Amonium Formate Systems*. J. Phys. Chem. Ref. Data 30 (2001); p. 1-163.
- Cap J. F., Laga S., Flores C., Stutz B.; *Modélisation d'un absorbeur eau/bromure de lithium à film ruisselant*. Société Française Thermique (SFT), 2013, p. 1-8.
- Dangel U.; *Sustainable Architecture in Vorarlberg - Energy Concepts and Construction System*. 1st ed: Birkhäuser Basel, 2010.
- Heimrath R, Haller M.; *The Reference Heating System, the Template Solar System of Task 32*. IEA Solar Heating and Cooling programme “Advanced storage concepts for solar and low energy buildings”, 2007.
- Lefebvre E.; *Procédé par absorption avec stockage d'énergie solaire intersaisonnier intensifié par la cristallisation de l'absorbant: Recherche & caractérisation thermodynamique de nouveaux couples; Conception de la cuve de stockage*. Doctoral thesis defended in October 2015. University of Lyon 1-Claude Bernard; Lyon, France.
- Longo A. G., Gasparella A.; *Three years experimental comparative analysis of a desiccant based air conditioning system for a flower greenhouse: Assessment of different desiccants*. Appl. Therm. Eng. 78 (2015); p. 584-590.
- Longo A. G., Gasparella A.; *Experimental measurement of thermophysical properties of H₂O/KCOOH (potassium formate) desiccant*. Int. J. Refrig. 62 (2016); p. 106-113.
- Moch X., Palomares M., Claudon F., Stutz B.; *Geothermal helical heat exchangers: Comparison and use of two-dimensional axisymmetric models*. Appl. Therm. Eng. 73 (2014); p.689-696.
- N'Tsoukpoe K.E.; *Étude du stockage à long terme de l'énergie solaire thermique par procédé d'absorption LiBr–H₂O pour le chauffage de l'habitat*. Doctoral thesis defended the 19th Mars 2012. University of Savoie, France.
- N'Tsoukpoe K.E., Le Pierrès N., Luo L.; *Experimentation of a LiBr-H₂O absorption process for long-term solar thermal storage: Prototype design and first results*. Energy 53 (2013); p.179-198.
- Valentin T. B.; *Intégration énergétique dans les bâtiments par l'utilisation combinée de l'énergie solaire et de la géothermie basse température*. Doctoral thesis defended in 2006. University of Savoie, France.

General conclusions and outlooks

General conclusions

The present thesis encompasses the study of an interseasonal sorption heat storage system based on a LiBr-H₂O couple and aimed to cover the annual heating needs of a simple family house building with solar heat. In order to demonstrate the feasibility of this process, several stages were covered: a state of the art of different sorption experimental prototypes constructed during the last 5 years and applied for building heating, the development of a model permitting to simulate the proposed heat storage system, the construction of a prototype to evaluate the system performance and, finally, an annual simulation study of the system operation when coupled to a dwelling.

A review of different technologies capable to store heat for building applications was carried out. An emphasis was made on existing absorption heat storage prototypes constructed in recent years; from this latter, seven case studies cases were analyzed. Some weak points found from this systems review were: some prototypes presented exchange surface wettability problems and non-condensable gases presence in the reactor, having a negative impact on their performance; furthermore, some solution crystallization risks were identified due to a system configuration permitting a solution pumping from the tank's bottom. Systems strengths were also identified: interesting energy storage densities (ESD) for space heating applications were identified in some cases, such as for the Tsinghua university prototype (LiBr-H₂O), the Shanghai Jiao Tong university prototype (LiCl-H₂O) and the ClimateWell thermo-chemical accumulator (LiCl-H₂O), which respectively presented ESD of 110 kWh/m³ (with respect to the solution and water volume), 54 kWh/m³ (with respect to the prototype volume) and 85 kWh/m³ (with respect to the prototype volume), respectively. Furthermore, another identified key feature was related to the conservation of the sensible heat stored in the solution after the charging processes, since it could be used later during the discharging period in order to improve the systems efficiencies. In general, the key importance of a good reactor design, in order to obtain the envisaged heat and mass transfer processes, is showed; consequently, the importance of a simulation model capable to predict the reactor functioning (in particular) is also highlighted. In the work following this review, a detailed and original simulation model for the reactor is proposed, and is particularly emphasized since it considers a fine analysis of the physical processes happening all along the heat and mass exchangers, in comparison to traditional models that considers global heat and mass transfer coefficients or imposed equilibrium stage between the reactor outlet conditions and the vapor pressure.

A simulation model of the components of the heat storage system was developed. A LiBr-H₂O solution was considered for the system since correlations for its physical properties have been widely obtained among the years. The modeled components were: the reactor (composed of two heat exchangers working as a desorber/absorber and condenser/evaporator during the charging/discharging periods, respectively), the solution tank, the water tank and the pipes. Furthermore, a model permitting to simulate the crystals formation in the solution tank was also proposed. A comparison of the absorber model against other models found in the literature gave a good agreement. In addition, a comparison of the reactor model against experimental results associated to a sorption system prototype constructed by N'Tsoutkpoe (N'Tsoutkpoe et al., 2013) was carried out; again, a good coincidence was found and the critical influence of the wetting of the heat exchangers surfaces in the system performance was put in evidence (a wetting percentage around 20% was concluded to be responsible for the low absorption powers). In addition, a heat exchanger configuration based on a flat grooved surface and aimed to improve the surface wetting was proposed; simulated absorption powers between 1 and 3 kW were obtained for a LiBr mass fraction operation between 0.48 and 0.60, respectively. A parametrical study of this heat exchanger was carried out and the influence of inlet conditions (such as temperatures and mass flows) on the system performance for the charge and discharge operating modes was presented; permitting, consequently, to obtain an optimized system functioning. Finally, in general the simulated performance of the heat exchanger is higher in counter-current mode than in co-current mode.

The constructions of an interseasonal heat storage prototype based on a LiBr-H₂O solution was described. Based on the study made in the previous chapter, a grooved flat plate heat exchanger with the same dimensions was considered for the system; also, a 92 kg initial solution mass was considered for the solution tank. Gas leakage

rate tests were carried for the reactor and tanks giving values, in general, lower than 10^{-4} (mbar.l)/s. In order to study the inlet conditions influence on the prototype performance, an experimental plan was proposed for the charging and discharging tests. For the desorption/condensation tests a better performance was found at lower LiBr mass fractions and when the desorber HTF temperature was increased; nevertheless, for this latter some little solution projections appeared at HTF temperatures around 75 °C due to an ebullition phenomenon on the solution film. In general, for the charging tests the desorbed/condensed water mass flow varied between 0.5 and 2 kg/h and the desorber and condenser powers were between 1 and 2 kW and -0.5 and -1.5 kW, respectively. For the absorption/evaporation tests a higher performance was found at higher LiBr mass fractions. Furthermore, a reduction of the absorber power and of the temperature difference between the absorber HTF inlet and outlet is observed, when the absorber HTF inlet temperature was increased. In general, the absorbed/evaporated water mass flow varied between 1 and 2 kg/h and the absorber and evaporator powers were between -0.6 and -1.5 kW and 0.3 and 1.0 kW, respectively. The crystallization phenomenon in the solution tank was also studied and absorption/desorption tests were carried out when crystals were present in the tank; in both tests the system behaved as if no crystals were present and the LiBr mass fraction presented a slope variation. Although grooved heat exchangers were used in the prototype, in several tests a low wettability was observed in the exchange surfaces, varying between 30 and 90% in the absorber. A comparison between experimental and simulated results obtained with our prototype and our model, respectively, was carried out. A good agreement was found in the desorption/condensation tests. In absorption/evaporation tests a weaker agreement was initially found. The hypothesis of the presence of non-condensable gases in the reactor was proposed since, as it is indicated by different authors, its effect can be very detrimental to the absorption/evaporation process; nevertheless, a lower impact on the desorption/condensation process could be expected due to a higher wetted surface in the condenser. By considering this latter hypothesis, a good agreement was found between simulation and experiences for most of the parameters (difference lower than 16%) in the discharging tests and a vapor partial pressure difference around 4 mbar between the evaporator and absorber was highlighted. Finally, an experimental $ESD_{V-st-wt}$ around 30 kWh/m³ was found for a LiBr mass fraction range between 0.59-0.54; an extrapolation of these results to a 0.52-0.66 range allowed to obtain an $ESD_{V-st-wt}$ around 110 kWh/m³.

A study of the annual performance of the interseasonal heat storage system coupled to a low energy consumption (LEC) dwelling was performed. In addition to the system components, a solar collector, a geothermal heat source/sink and a mixing tank were modelled. The solar collector was modeled to work during the charging period as a heat source for the desorption process and during the discharging period as a heat source for the dwelling heating needs (working in parallel with the reactor). The mixing tank was modeled to be the medium permitting to transfer the heat contributions from the solar collector and reactor to the dwelling during the discharging period. The dwelling considered was a 120 m² LEC building located in Chambéry, France, with an annual heating need of 2189 kWh. A reference case was proposed; the initial solution and water tank masses were 14132 kg (LiBr mass fraction 0.544) and 6315 kg, respectively; the tanks were considered to be kept underground (12 °C ground temperature) and the solar collector surface and mixing tank temperature were 12 m² and 25 °C, respectively. A two years' operation was simulated, with the first year used as an initialization period where the system interacts with the surroundings. Results on the reference case indicated that the storage system is capable to cover 78% of the annual dwelling heating needs (DHN) with the remaining 22% being covered directly by the solar collector; additionally, a presence of crystals was observed with a maximum crystallization rate of 16% and the heating power generated by the reactor varied between 0.75 and 2.2 kW. A parametrical study of the influence of the tank insulation thickness, solution tank initial mass and solar collector surface on the system performance was carried out. It was concluded that: an increase of the solution tank thickness increases the solution tank temperature, LiBr mass fraction, crystallization rate and reactor heating power; a reduction of the initial solution tank mass mainly generates a strong increase of the crystallization rate; a reduction of the solar collector surface generates a reduction of the solution tank temperature, LiBr mass fraction, crystallization rate and the solar collector/reactor heating powers. A calculation of the system $ESD_{V-st-wt}$ and the COP was made for the simulated second year giving values of 157 kWh/m³ and 2.2, respectively. Finally, a study of the system performance when a KCOOH-H₂O aqueous solution is used was carried out; it was observed that the system is capable to cover the annual DHN with a negligible use of an electrical source and that, in a period of one year, crystals are present during 7 months in the solution tank.

Outlooks

Several stages were covered in this thesis; nevertheless, along these stages new questions and different limitations were identified and were not possible to cover and solve during the thesis. These aspects are summarized in the following as perspectives possible to address through a further research in the future.

In relation to the simulation model developed for the reactor (absorber/desorber and evaporator/condenser), a further comparison against other simulation and experimental results found in the literature can be carried out; furthermore, the presence of wavelets at the interface between the falling film (solution or water) and the vapor in transitory regimes could be also modeled. Another phenomenon that could be modeled is related to the presence of non-condensable gases in the reactor and its effect on the sorption processes; indeed, in Chapter 3, it was observed that better coincidences between simulation and experiences were obtained in the discharging tests when considering a vapor partial pressure difference between the evaporator and the absorber. A possible path to model the NCG could be to simulate a “resistance term” permitting to calculate the partial vapor pressure difference between absorber/evaporator (or desorber/condenser) and to predict the amount of NCG in the reactor.

In relation to the solution tank model, in the study cases presented in Chapter 2 some temperature oscillations lower than 0.4°C were observed although inlet/outlet and initial conditions had the same temperature (in one case these oscillations could be due to the crystals dissolution enthalpy). In order avoid this effect, lower grid lengths and step times could be considered; in addition, a discretization through a finite volume approach could be used for the internal nodes instead of a finite difference approach. Another research topic could be related to the crystallization model; a model improvement could be made in order to simulate the crystals movement along the tank due to buoyancy forces. In addition, a comparison of the solution tank model against other simulation tools (TRNSyS, Comsol, etc.) can be done for some cases since, at present, no models capable to simulate a liquid height variation along time were found.

In relation to the experimental prototype, a characterization of the surface wetting with respect to the solution/water film mass flows could be made at ambience pressure. Improvements in the distributor design could be also looked for to ensure a uniform wetting of all the grooves. A system permitting to collect possible solution projections due to a film ebullition during desorption processes should be envisaged. An improvement of the surface wetting of the grooved heat exchangers could be obtained through a chemical surface treatment. In relation to the solution tank, a mechanism permitting to introduce an external solution in periods where the prototype is in standby should be envisaged; it could be useful in cases in which solution is drained out of the system (for example due to projections generated by solution ebullition). An improvement of the control of the solution and water pumping could be done in order to maintain a constant mass flow even if temperature and density variations appear along time. A purge equipment aimed to evacuate the NCG in the reactor and tanks should be also considered. Experimental tests considering other interesting sorption couples such as the $\text{KCOOH-H}_2\text{O}$ solution could be also made in a future research; furthermore, this would permit a comparison against simulated results obtained with our model.

In relation to the annual performance of the interseasonal heat storage system coupled to a LEC dwelling, a further study of the influence on the system performance of other parameter such as the solar collector technical characteristics, the mixing tank temperature or the heat exchangers size can be carried out. A comparison of the system COP against the economic cost could be used as a more general performance parameter; in addition, a Life Cycle Analysis could be also considered. A coupling of the heat storage system model with another simulation tool such as TRNSyS or EnergyPlus would be interesting since it could permit to model scenarios where the system interacts with more complex and realistic dwelling/building components. Finally, an improvement in the model code permitting to recognize scenarios in which the simulation does not converge would be interesting in order to avoid long machine times.

ANNEX A

Annex A1

In this section more detailed technical characteristics of some of the different heat and mass exchangers technologies associated to the interseasonal heat storage systems presented in section 1.2 are shown.

A1.1. Closed heat storage system based on water absorption/desorption in aqueous lithium chloride (LiCl-H₂O) – Shanghai Jiao Tong university - China

In section 1.2.1.2 a seasonal closed heat storage prototype based on water sorption processes using an aqueous lithium chloride solution was presented. In this section additional technical characteristics of the heat and mass exchangers associated to the indicated prototype are shown.

As it was previously commented, the heat and mass exchanger in the absorber/desorber was based in a modular copper coil-tray heat exchanger where the tray was capable to hold the LiCl solution and avoid leakage. Technical characteristics of the absorber/desorber heat and mass exchanger are shown in Table A1. In this exchanger the bed units are connected by manifold tubes in parallel and the coils are soldered to the trays using tin solder. The composite material was filled into each bed using a shovel and uniformly covered the top of the coil. In order to avoid sorbent powder from spilling, a copper mesh screen was placed above the sorbent.

Table A1. Technical characteristics of the heat and mass exchanger considered for the prototype reactor (Zhao et al., 2016)

Number of sorption bed units	25
Total mass of LiCl [kg]	11.75
LiCl mass per bed unit [kg]	0.47
Space gap between trays [mm]	5
Tray diameter [cm]	38
Tray thickness [mm]	17
Coil diameter [mm]	5
Coil thickness [mm]	0.5
Coil length [m]	8.8

A1.2. Closed heat storage system based on water absorption/desorption in aqueous sodium hydroxide (NaOH-H₂O) – EMPA - Switzerland

As it was mentioned in section 1.2.3, the heat and mass exchangers used in the system were of the falling film bundle type and were constructed in stainless. As it is shown in Figure A1, each heat exchanger, including its manifold, was designed to fit in a 40 cm stainless steel vacuum tube container.

The absorber/desorber exchanger design is based in a 4 x 18 tubes configuration, with a tube's outer and inner diameters of 12 mm and 10 mm, respectively, an active tube length of 30 cm and a total active external area of 0.68 m². The evaporator/condenser exchanger design is based in a 16 x 12 tubes configuration, with a tube's outer and inner diameters of 12 mm and 10 mm, respectively, an active tube length of 70 cm and a total active external area of 4.2 m². A nickel plate bended metal sheet was installed in the feedthrough (Figure A1a) in order to avoid liquid splashes from one container to the other and to work as a thermal infrared isolation.

Each heat exchanger is furnished with a manifold consisting of an array of dripping nozzles whereby the solution and water are uniformly distributed on the tubes (Figure A1b). In Figure A1c is observed the formation of solution droplets during the system operation (mainly in absorption/evaporation mode).

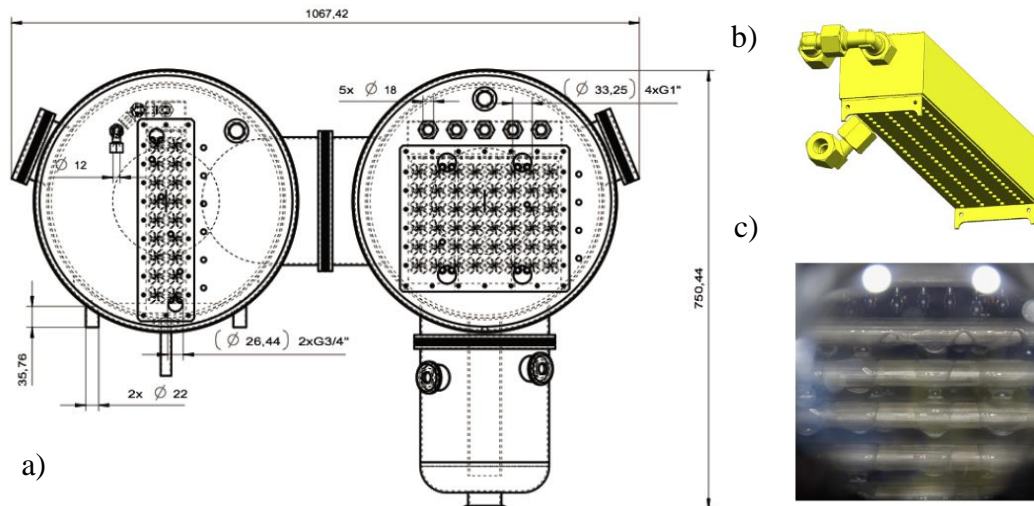


Figure A1. a) CAD drawing of the heat and mass exchangers: AD on the left and EC on the right (mm scale); b) AD manifold assembly; c) Flow of solution over the tubes in the AD tube bundle: fine droplets group reducing the wetted surface on the tubes. (Fumey et al., 2015), (Daguenet-Frick et al, Article in Press)

A1.3. Closed heat storage system based on water absorption/desorption in aqueous lithium bromide (LiBr-H₂O) – Tsinghua university - China

In section 1.2.4.2 it was mentioned that Zhang (Zhang et al., 2014) constructed a prototype of an interseasonal heat storage system for building space heating based in sorption processes using a LiBr-H₂O solution. The heat and mass exchangers considered a staggered-arrangement composed of several horizontal tubes; where a HTF flowed in the internal tubes, while solution or water flowed, in a cross direction (from top to bottom), on the external tubes surface. A liquid distributor composed of five nozzles was installed on top of each heat exchanger to permit the spraying of solution or water; additionally, baffles were installed on the distributor sides to avoid outside fluid splashing. Figure A2 shows the detail of the heat and mass exchanger and distributor design, as well as images of the solution and water flowing over the tubes surface. Design parameters associated to the heat exchanger are shown in Table A2.

Table A2. Design parameters of the heat and mass exchangers (Zhang et al., 2014)

	Evaporator	Condenser	Absorber	Desorber
Tube inner diameter [mm]	16	16	16	16
Tube thickness [mm]	0.8	0.8	0.8	0.8
Tube length [m]	0.944	0.944	0.944	0.944
Number of tubes	78	78	52	52
Area of tubes [m ²]	3.70	3.70	2.47	2.47
KF [kW/K]	7.77	12.95	2.96	3.21
Material	304 Stainless-steel	304 Stainless-steel	304 Stainless-steel	304 Stainless-steel

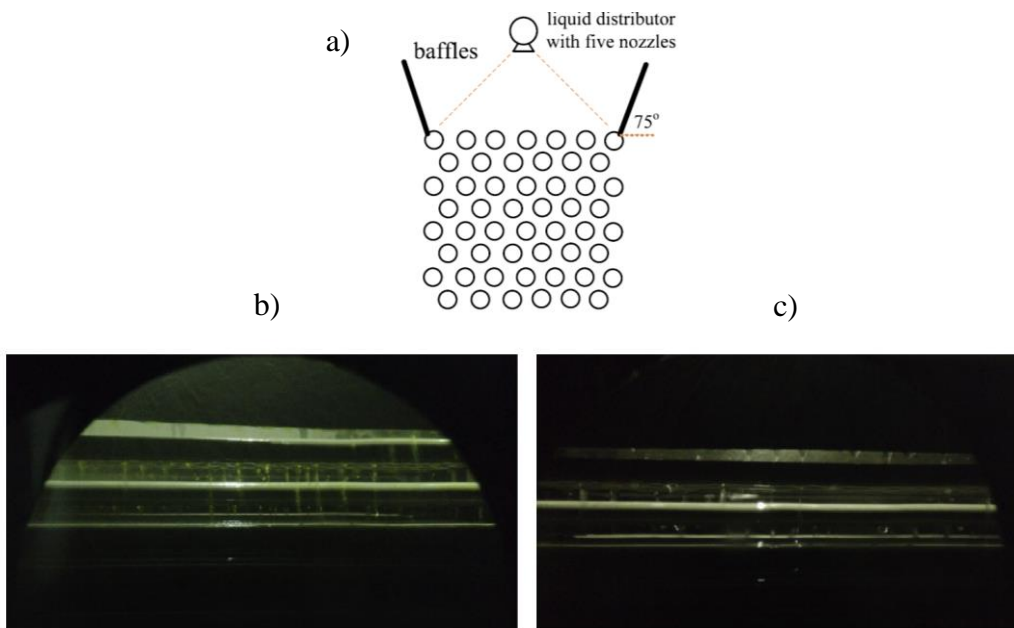


Figure A2. a) Side view of heat exchanger and liquid distributor; b) Distribution of LiBr-H₂O solution; c) Distribution of water

ANNEX B

Annex B1

B1.1. Physical numbers

Different physical numbers used for the model are shown below:

Pe_{st} , the local number of Peclet for the falling film solution, is defined as:

$$Pe_{st} = \frac{1}{4} \times Re_{st} \times Pr_{st} \quad (B1.1)$$

Re_{st} the local numbers of Reynolds, is defined as:

$$Re_{st} = \frac{D_{h_{st}} \times u_{st}}{\nu_{st}} \quad (B1.2)$$

Where $D_{h_{st}}$, the hydraulic diameter of the falling film, is defined as:

$$D_{h_{st}} = \frac{4 \times A_{tr,st}}{Per_{tr,st}} = 4 \times e_{st} \quad (B1.3)$$

Pr_{st} the hydraulic diameter of the falling film is of Prandtl, is defined as:

$$Pr_{st} = \frac{\nu_{st}}{\alpha_{st}} \quad (B1.4)$$

B1.2. Physical correlations for the LiBr solution

Physical correlations obtained from the literature and used for the model are indicated below:

The **LiBr solution density correlation** obtained by (Florides et al., 2003) is indicated below:

$$\rho_{st} = 1145.36 + 470.84 \times x_{LiBr} + 1374.79 \times (x_{LiBr})^2 - (0.333393 + 0.571749 \times x_{LiBr}) \times (T + 273.15) \quad [kg/m^3] \quad (B1.5)$$

Where: $0.2 < x_{LiBr} < 0.6$ and $0^\circ C < T < 200^\circ C$

The **LiBr solution absolute viscosity correlation** obtained by (Sorption System Consortium, 2015) is indicated below:

$$\mu_{st} = \frac{\exp\left(A_0 + A_1 \times (x_{LiBr})^2 + \frac{B_0}{TK} + \frac{B_1}{TK} \times (x_{LiBr})^2 + \frac{C_0}{(TK)^2} + \frac{C_1}{(TK)^2} \times (x_{LiBr})^2\right)}{1000} \quad \left[\frac{kg}{(m \times s)}\right] \quad (B1.6)$$

Where:

$A_0 = -2.3212641667148$	$A_1 = 3.190587778753$
$B_0 = -609.44957160372$	$B_1 = 963.16370163469$
$C_0 = 372994.85578423$	$C_1 = -35211.99698739$
$TK = T + 273.15$	

And: $0.35 < x_{LiBr} < 0.7$ and $20^\circ C < T < 300^\circ C$

The **LiBr solution thermal conductivity correlation** obtained by (Sorption System Consortium, 2015) is indicated below:

$$\lambda_{st} = A_0 + A_1 \times x_{LiBr} + B_0 \times TK + B_1 \times TK \times x_{LiBr} + C_0 \times (TK)^2 + C_1 \times (TK)^2 \times x_{LiBr} + D_0 \times (TK)^3 + D_1 \times (TK)^3 \times x_{LiBr} \quad \left[\frac{W}{(m \times K)} \right] \quad (B1.7)$$

Where:

$A_0 = -0.880453887702949$	$A_1 = 0.883985046484968$
$B_0 = 0.00898659269884302$	$B_1 = -0.007666522227789178$
$C_0 = -1.55427759660091E - 05$	$C_1 = 1.38873506415764E - 05$
$D_0 = 7.3203107999836E - 09$	$D_1 = -6.31953452062666E - 09$
$TK = T + 273.15$	

And: $0.3 < x_{LiBr} < 0.6$ and $20^\circ C < T < 100^\circ C$

The **LiBr solution specific heat correlation** obtained by (Florides et al., 2003) is indicated below:

$$c_{p_{st}} = 0.0976 \times (100 \times x_{LiBr})^2 - 37.512 \times (100 \times x_{LiBr}) + 3825.4 \quad \left[\frac{J}{(kg \times K)} \right] \quad (B1.8)$$

Where: $0 < x_{LiBr} < 1$.

The **LiBr solution binary mass diffusion coefficient correlation** obtained by (AUTHOR) is indicated below:

$$D_{LiBr-H_2O} = D_{LiBr-H_2O_{ref}} \times \frac{\mu_{st}(T_{ref}-273.15, x_{LiBr})}{\mu_{st}(T_{ref}, x_{LiBr})} \times \frac{TK}{T_{ref}} \quad \left[\frac{m^2}{s} \right] \quad (B1.9)$$

Where:

$D_{LiBr-H_2O_{ref}} = (10^{-9}) \times (1.231 + 189.319 \times b_0 - 17275.827 \times (b_0)^2 + 327172 \times (b_0)^3)$
$b_0 = \left(\frac{1}{86.845} \right) \times \left(\frac{x_{LiBr}}{1 - x_{LiBr}} \right)$
$TK = T + 273.15 [K]$
$T_{ref} = 298.15 [K]$

Where: $0 < x_{LiBr} < 1$ and $T [^\circ C]$

The **LiBr solution enthalpy correlation** obtained by (Yuan and Herold², 2005) is indicated below:

$$\begin{aligned} h_{st} = & A_0 + A_1 X + A_2 X^2 + A_3 X^3 + A_4 X^{1.1} \\ & - (TK)^2 \times (C_0 + C_1 X + C_2 X^2 + C_3 X^3 + C_4 X^{1.1}) \\ & - 2 \times (TK)^3 \times (D_0 + D_1 X + D_2 X^2 + D_4 X^{1.1}) - 3 \times (TK)^4 \times (E_0 + E_1 X) \\ & + (F_0 + F_1 X) \times \left(\frac{1}{TK - T_{ref}} + \frac{TK}{(TK - T_{ref})^2} \right) \\ & + p \times (V_0 + V_1 X + V_2 X^2 - V_6 TK^2 - V_7 X(TK^2)) \\ & + (\ln(TK) - 1) \times (L_0 + L_1 X + L_2 X^2 + L_3 X^3 + L_4 X^{1.1}) \\ & - TK \times (M_0 + M_1 X + M_2 X^2 + M_3 X^3 + M_4 X^{1.1}) \end{aligned} \quad \left[\frac{kJ}{(kg)} \right] \quad (B1.10)$$

Where:

$A_0 = 5.506219979E3$	$A_1 = 5.213228937E2$	$A_2 = 7.774930356$
$A_3 = -4.575233382E - 2$	$A_4 = -5.792935726E2$	
$B_0 = 1.452749674E2$	$B_1 = -4.984840771E - 1$	$B_2 = 8.836919180E - 2$
$B_3 = -4.870995781E - 4$	$B_4 = -2.905161205$	
$C_0 = 2.648364473E - 2$	$C_1 = -2.311041091E - 3$	$C_2 = 7.559736620E - 6$
$C_3 = -3.763934193E - 8$	$C_4 = 1.176240649E - 3$	
$D_0 = -8.526516950E - 6$	$D_1 = 1.320154794E - 6$	$D_2 = 2.791995438E - 11$
$D_4 = -8.511514931E - 7$		
$E_0 = -3.840447174E - 11$	$E_1 = 2.6254693387E - 11$	
$F_0 = -5.159906276E1$	$F_1 = 1.114573398$	
$L_0 = -2.183429482E3$	$L_1 = -1.266985094E2$	$L_2 = -2.364551372$
$L_3 = 1.389414858E - 2$	$L_4 = 1.583405426E2$	
$M_0 = -2.267095847E1$	$M_1 = 2.983764494E - 1$	$M_2 = -1.259393234E - 2$
$M_3 = 6.849632068E - 5$	$M_4 = 2.767986853E - 1$	
$V_0 = 1.176741611E - 3$	$V_1 = -1.002511661E - 5$	$V_2 = -1.695735875E - 8$
$V_3 = -1.497186905E - 6$	$V_4 = 2.538176345E - 8$	$V_5 = 5.815811591E - 11$
$V_6 = 3.057997846E - 9$	$V_7 = -5.129589007E - 11$	
$TK = T + 273.15 [K]$		
$X = 100 \times x_{LiBr}$		
$p = \frac{P}{1000} [kPa]$		
$T_{ref} = 220 [K]$		

Where: $0 < x_{LiBr} < 1$, $T [^{\circ}C]$ and $P [Pa]$

The correlation for the water partial enthalpy in the solution obtained by (Yuan and Herold², 2005) is indicated below:

$$\begin{aligned}
h_{p-H_2O-st} = & A_0 - A_2X^2 - 2 \times A_3X^3 - 0.1 \times A_4X^{1.1} \\
& - (TK)^2 \times (C_0 - C_2X^2 - 2 \times C_3X^3 - 0.1 \times C_4X^{1.1}) \\
& - 2 \times (TK)^3 \times (D_0 - D_2X^2 - 0.1 \times D_4X^{1.1}) - 3 \times (TK)^4 \times (E_0) \\
& + (F_0) \times \left(\frac{1}{TK - T_{ref}} + \frac{TK}{(TK - T_{ref})^2} \right) \quad \left[\frac{kJ}{(kg)} \right] \quad (B1.11) \\
& + p \times (V_0 + V_2X^2 - V_6TK^2) \\
& + (\ln(TK) - 1) \times (L_0 - L_2X^2 - 2 \times L_3X^3 - 0.1 \times L_4X^{1.1}) \\
& - TK \times (M_0 - M_2X^2 - 2 \times M_3X^3 - 0.1 \times M_4X^{1.1})
\end{aligned}$$

Where:

$A_0 = 5.506219979E3$	$A_1 = 5.213228937E2$	$A_2 = 7.774930356$
$A_3 = -4.575233382E - 2$	$A_4 = -5.792935726E2$	
$B_0 = 1.452749674E2$	$B_1 = -4.984840771E - 1$	$B_2 = 8.836919180E - 2$
$B_3 = -4.870995781E - 4$	$B_4 = -2.905161205$	
$C_0 = 2.648364473E - 2$	$C_1 = -2.311041091E - 3$	$C_2 = 7.559736620E - 6$
$C_3 = -3.763934193E - 8$	$C_4 = 1.176240649E - 3$	
$D_0 = -8.526516950E - 6$	$D_1 = 1.320154794E - 6$	$D_2 = 2.791995438E - 11$
$D_4 = -8.511514931E - 7$		
$E_0 = -3.840447174E - 11$	$E_1 = 2.6254693387E - 11$	
$F_0 = -5.159906276E1$	$F_1 = 1.114573398$	
$L_0 = -2.183429482E3$	$L_1 = -1.266985094E2$	$L_2 = -2.364551372$
$L_3 = 1.389414858E - 2$	$L_4 = 1.583405426E2$	
$M_0 = -2.267095847E1$	$M_1 = 2.983764494E - 1$	$M_2 = -1.259393234E - 2$
$M_3 = 6.849632068E - 5$	$M_4 = 2.767986853E - 1$	
$V_0 = 1.176741611E - 3$	$V_1 = -1.002511661E - 5$	$V_2 = -1.695735875E - 8$
$V_3 = -1.497186905E - 6$	$V_4 = 2.538176345E - 8$	$V_5 = 5.815811591E - 11$
$V_6 = 3.057997846E - 9$	$V_7 = -5.129589007E - 11$	
$TK = T + 273.15 [K]$		
$X = 100 \times x_{LiBr}$		
$p = \frac{P}{1000} [kPa]$		
$T_{ref} = 220 [K]$		

Where: $0 < x_{LiBr} < 1$, $T [^{\circ}C]$ and $P [Pa]$

The *correlation for the equilibrium (saturated) condition at the interface between the water film and the water vapor* obtained by (Saul and Wagner, 1987) is indicated below:

$$\begin{aligned}
 T_{H_2O_{sat}} = & (3.37595948586144E - 05) \times \left(\ln \left(\frac{P}{22064000} \right) \right)^6 \\
 & + (2.12003737295472E - 03) \times \left(\ln \left(\frac{P}{22064000} \right) \right)^5 \\
 & + (5.91993855043397E - 02) \times \left(\ln \left(\frac{P}{22064000} \right) \right)^4 \\
 & + (0.976561958843236) \times \left(\ln \left(\frac{P}{22064000} \right) \right)^3 \\
 & + (10.767649771597) \times \left(\ln \left(\frac{P}{22064000} \right) \right)^2 \\
 & + (88.0085016175992) \times \left(\ln \left(\frac{P}{22064000} \right) \right) + 373.128542324967
 \end{aligned} \quad [^{\circ}C] \quad (B1.12)$$

Where: P [Pa] is the saturated pressure associated to $T_{H_2O_{sat}}$

The *correlation for the equilibrium condition at the interface between the LiBr solution film and the vapor* obtained by (Hellman and Grossman, 1996) is indicated below:

$$T_{LiBr_{equ}} = A \times \tau_c + B \quad [^{\circ}C] \quad (B1.13)$$

Where:

$A = 1 + \sum_{i=1}^{10} AA_i \times (100 \times x_{LiBr})^i$
$B = 0 + \sum_{i=1}^{10} BB_i \times (100 \times x_{LiBr})^i$
$\tau_c = T_{H_2O_{sat}(P)}$

and

$AA_1 = -0.00068242821$	$BB_1 = 0.16634856$
$AA_2 = 0.0005873619$	$BB_2 = -0.055338169$
$AA_3 = -0.00010278186$	$BB_3 = 0.011228336$
$AA_4 = 0.0000093032374$	$BB_4 = -0.001102839$
$AA_5 = -0.0000004822394$	$BB_5 = 0.000062109464$
$AA_6 = 0.000000015189038$	$BB_6 = -0.0000021112567$
$AA_7 = -2.9412863E - 10$	$BB_7 = 0.000000043851901$
$AA_8 = 3.4100528E - 12$	$BB_8 = -5.4098115E - 10$
$AA_9 = -2.167148E - 14$	$BB_9 = 3.6266742E - 12$
$AA_{10} = 5.7995604E - 17$	$BB_{10} = -1.0153059E - 14$

Where: $0 < x_{LiBr} < 1$ and P [Pa] are the associated equilibrium conditions to $T_{LiBr_{equ}}$ at the LiBr solution film interface.

The **water superheat steam enthalpy correlation** obtained by (Florides et al, 2003) is indicated below:

$$h_{vap_superheat\ steam} = \left(\frac{HSH_2 - HSH_1}{100} \right) \times (T - T_{H_2O\ sat(P)}) + HSH_1 \quad \left[\frac{kJ}{kg} \right] \quad (B1.14)$$

Where:

$HSH_1 = 32.508 \times \ln\left(\frac{P}{1000}\right) + 2513.2$
$HSH_2 = 0.00001 \times \left(\frac{P}{1000}\right)^2 - 0.1193 \times \left(\frac{P}{1000}\right) + 2689$

Where: P [Pa] and T [°C]

The **saturated water-vapor enthalpy correlation** obtained by (Florides et al, 2003) is indicated below:

$$h_{vap_sat} = -0.00125397 \times T^2 + 1.88060937 \times T + 2500.559 \quad \left[\frac{kJ}{kg} \right] \quad (B1.15)$$

Where T [°C]

The **water density correlation** obtained by (Florides et al, 2003) is indicated below:

$$\rho_{H_2O} = 0.000015451 \times T^3 - 0.0059003 \times T^2 - 0.019075 \times T + 1002.3052 \quad \left[\frac{kg}{m^3} \right] \quad (B1.16)$$

Where T [°C]

The **water specific heat correlation** obtained by (Florides et al, 2003) is indicated below:

$$c_{p_{H_2O}} = 0.000003216145833 \times T^4 - 0.000798668982 \times T^3 + 0.0780295139 \times T^2 - 3.0481614 \times T + 4217.737 \quad \left[\frac{J}{kg \times K} \right] \quad (B1.17)$$

Where T [°C]

The **water thermal conductivity correlation** obtained by (Florides et al, 2003) is indicated below:

$$\lambda_{H_2O} = -6.5104167E - 10 \times T^4 + 0.00000018923611 \times T^3 - 2.671875E - 5 \times T^2 + 0.0027103175 \times T + 0.5520119 \quad \left[\frac{W}{m \times K} \right] \quad (B1.18)$$

Where T [°C]

The **water absolute viscosity correlation** obtained by (Florides et al, 2003) is indicated below:

$$\mu_{H_2O} = (10^{-6}) \times (0.000031538716146 \times T^4 - 8.913055428199999E - 3 \times T^3 + 0.9795876934 \times T^2 - 55.4567974 \times T + 1791.74424) \quad \left[\frac{kg}{(m \times s)} \right] \quad (B1.19)$$

Where T [°C]

B1.3. Simulation model adaptation to a heat exchanger configuration

B1.3.1. Flat plate configuration

Considering the flat plate heat exchanger configuration described in Figure 2.6; the heat transfer convective coefficient, $h_{T_{htf/ad}, w_k}$, related to the exchange between the inner plate surface and the HTF is given by the Colburn correlation⁽¹⁾.

Hence, $h_{T_{htf/ad}, w_k}$, can be calculated using the following correlations (Incropera et al., 2011):

$$h_{T_{htf/ad}, w_k} = \frac{Nu_{htf_k} \times \lambda_{htf}(T_{htf/ad_i, k})}{D_{h_{htf}}} \quad (B1.20)$$

$$Nu_{htf_k} = 0.023 \times Re_{htf_k}^{4/5} \times Pr_{htf_k}^{1/3} \quad (B1.21)$$

Where $D_{h_{htf}}$, Re_{htf_k} , Pr_{htf_k} and Nu_{htf_k} are the hydraulic diameter and the local Reynolds, Prandtl and Nusselt numbers, which are related to the heat exchanger geometry and configuration.

B1.3.2. Shell and tube configuration

Since the model described in section 2.1.1 corresponds to a 2D flat plate heat exchanger configuration, an adaptation to a shell and tubes heat exchanger configuration has been done. This adaptation consisted mainly on a geometrical equivalence since curvature effects are negligible considering the thickness of the falling film. The physical hypothesis considered for this model's adaptation were:

- The curvature of the cylindrical tube has no influence on the falling film mass and energy balance equations described in section 2.1.1 since the film thickness is very small compared to the diameter tube.
- The energy losses on the external surface of the shell are negligible (overall convection heat transfers since vapor pressure was very low in the reactor).
- The convection heat transfer coefficient between the exchange surface and the heat transfer fluid corresponds to that of a shell and tubes heat exchanger configuration.
- The cylindrical geometry is taken into account for the conduction transfer.

Table B1 describes the geometrical characteristics of the shell and tube heat exchanger configuration that were considered for the model's adaptation.

Table B1. Shell and tubes exchanger characteristics

Shell and tubes heat exchanger configuration	Tubes height [m]	Tube contact perimeter [m]	Number of tubes	Tube thickness [m]	Shell hydraulic diameter [m]	Tube thermal conductivity [W/(m*K)]
	0.62	0.0367	14	0.001	0.0157	100

The convection heat transfer coefficient between the tube external surface and the heat transfer fluid was calculated considering correlations given by Kakaç and Liu (Kakaç and Liu, 2002); one of these correlations, adapted to the grid "k" in the heat exchanger discretization described in section 2.1.1, is showed below.

⁽¹⁾ The HTF is considered to flow in a flat canal at turbulent regimes.

$$Nu_{w/htf,k} = 0,36 \times Re_{htf/i,k}^{0,55} \times Pr_{htf/i,k}^{1/3} \times \left(\mu_{H_2O}(T_{htf,i,k}) / \mu_{H_2O}(T_{w,htf,k}) \right)^{0,14} \quad (B1.22)$$

Where the Reynolds number $Re_{htf/i,k}$ depends on the shell and tube heat exchanger geometry, such as the baffles cut percentage.

B1.4. Modelling of a wetting effect on the metallic plates

As it was described in section 2.1.1.5, equations (2.11), (2.12), (2.15) and (2.17) to (2.19) were modified with 2 coefficients: $S_{w,st}$ and $S_{w,htf/ad}$, to model the heat transfer on a metallic surface partially wetted (Figure 2.9). Two transfer modes were considered: an optimistic and a pessimistic mode denoted as “1F” and “2F” where the optimistic case considers a fin efficiency equal to 1, whereas the pessimistic case considers a fin efficiency equal to 0. The modified equations are shown below.

Energy balance of the LiBr solution film.

$$\begin{aligned} -\dot{m}_{st,x_o,k} \times h_{st(T_{st_o,k}, x_{H_2O_o,k}, P_{vap_{sat}})} + \dot{m}_{st,x_i,k} \times h_{st(T_{st_i,k}, x_{H_2O_i,k}, P_{vap_{sat}})} + \\ \dot{m}_{H_2O,abs/des_k} \times h_{vap(T_{vap_{sat}}, P_{vap_{sat}})} + \\ h_{T_{st,w_k}} \times \Delta x \times L \times S_{w,st} \times (T_{w,st_k} - (T_{st_o,k} + T_{st_i,k})/2) = 0 \end{aligned} \quad (B1.23)$$

Energy balance at the interface between the LiBr solution film and the water vapor.

$$\begin{aligned} \dot{m}_{H_2O,abs/des_k} \times (h_{vap(T_{vap_{sat}}, P_{vap_{sat}})} - h_{p-H_2O-st}(T_{st,int_k}, x_{H_2O,int_k}, P_{vap_{sat}})) - \\ h_{T_{st,int_k}} \times \Delta x \times L \times S_{w,st} \times (T_{st,int_k} - (T_{st_o,k} + T_{st_i,k})/2) = 0 \end{aligned} \quad (B1.24)$$

Mass transfer at the interface between the LiBr solution film and the water vapor.

$$\begin{aligned} \dot{m}_{H_2O,abs/des_k} - h_{m_{st,int_k}} \times \Delta x \times L \times S_{w,st} \times [\rho_{st}(T_{st,int_k}, x_{H_2O,int_k})^{x_{H_2O,int_k}} - \\ \rho_{st}((T_{st_o,k} + T_{st_i,k})/2, (x_{H_2O_o,k} + x_{H_2O_i,k})/2) \left(\frac{x_{H_2O_o,k} + x_{H_2O_i,k}}{2} \right)] = 0 \end{aligned} \quad (B1.25)$$

Heat transfer between the LiBr solution film and the metallic plate.

$$\begin{aligned} \left(\lambda_w / e_w \right) \times \Delta x \times L \times S_{w,htf/ad} \times (T_{w,st_k} - T_{w,htf/ad_k}) - \\ h_{T_{st,w_k}} \times \Delta x \times L \times S_{w,st} \times ((T_{st_o,k} + T_{st_i,k})/2 - T_{w,st_k}) = 0 \end{aligned} \quad (B1.26)$$

Heat transfer between the heat transfer fluid and the metallic plate.

$$\begin{aligned} h_{T_{htf/ad,w_k}} \times \Delta x \times L \times S_{w,htf/ad} \times ((T_{htf/ad_o,k} + T_{htf/ad_i,k})/2 - T_{w,htf/ad_k}) - \\ \left(\lambda_w / e_w \right) \times \Delta x \times L \times S_{w,htf/ad} \times (T_{w,htf/ad_k} - T_{w,st_k}) = 0 \end{aligned} \quad (B1.27)$$

Energy balance of the heat transfer fluid⁽¹⁾.

$$\begin{aligned}
 & -\dot{m}_{htf/ad,i,k} \times h_{htf(T_{htf/ad,o,k})} + \dot{m}_{htf/ad,i,k} \times h_{htf(T_{htf/ad,i,k})} + \\
 & 2 \times h_{T_{htf/ad,w_k}} \times \Delta x \times L \times S_{w,htf/ad} \times (T_{w,htf/ad,k} - (T_{htf/ad,o,k} + T_{htf/ad,i,k})/2) = 0
 \end{aligned} \tag{B1.28}$$

- Where in the optimistic case “1F”: $S_{w,htf/ad} = 100\%$ and $0 < S_{w,st} < 100\%$.
- Where in the pessimistic case “2F”: $0 < S_{w,htf/ad} = S_{w,st} < 100\%$.

B1.5. Modelling of recirculation

A recirculation system between the LiBr solution outlet and inlet in the heat exchanger has been simulated. It considers that a certain percentage of the falling film mass flow leaving the reactor (bottom) can be reintroduced in the heat exchanger distribution box (top) as it is shown in Figure B1. This kind of system is used to facilitate an energy exchange between the solution outlet, which can be at a high temperature (40°C), and the solution inlet, which can be at a low temperature (20°C), obtaining a higher efficiency. A recirculation system also allows to increase the actual solution mass flow entering the heat exchanger.

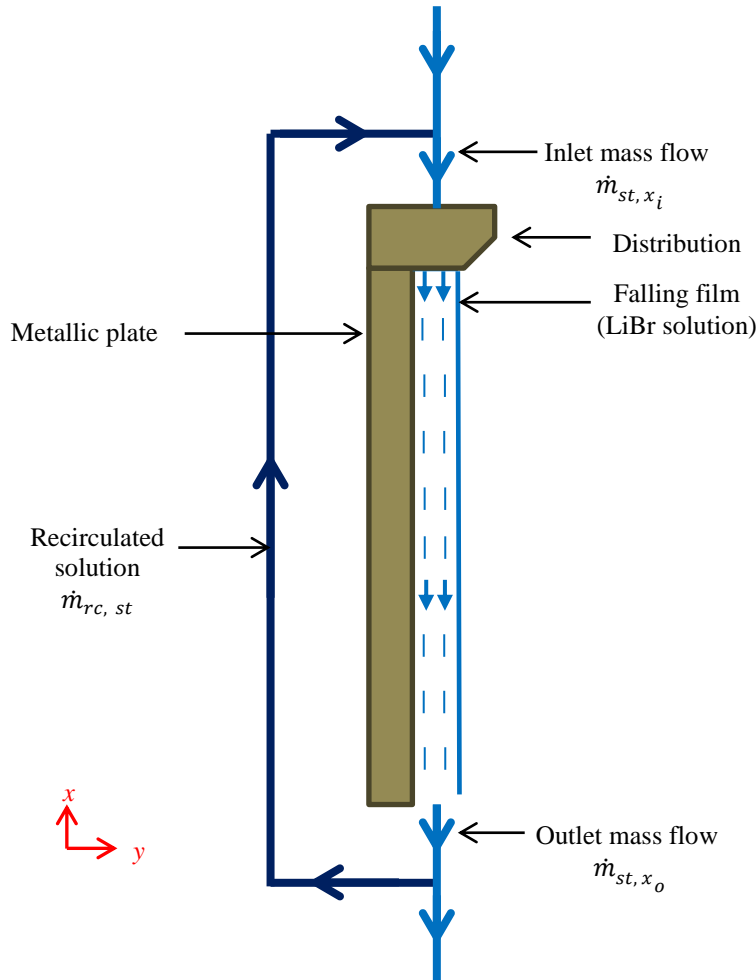


Figure B1. Scheme of a recirculation system in a heat exchanger for a LiBr solution falling film.

⁽¹⁾ The factor 2 multiplying “ $h_{T_{htf/ad,w_k}}$ ” is related to the 2 flat plates composing the canal where the HTF flows in the modeled flat-plate exchanger (see Figure 2.2).

The recirculation percentage, RC , is defined as the ratio between the recirculating solution mass flow, $\dot{m}_{rc, st}$, and the outlet solution mass flow, \dot{m}_{st, x_o} , as it is defined by Equation (B1.29).

$$RC = \frac{\dot{m}_{rc, st}}{\dot{m}_{st, x_o}} \quad (\text{B1.29})$$

A system flow chart of the simulated recirculation system described is shown in Figure B2.

The inlet solution mass flow in the heat exchanger is defined by the value \dot{m}_{st, x_i} . In cases where recirculation is possible, \dot{m}_{st, x_i} is adapted in order to maintain the same amount of introduced solution at the top of the heat exchanger (see Figure B2).

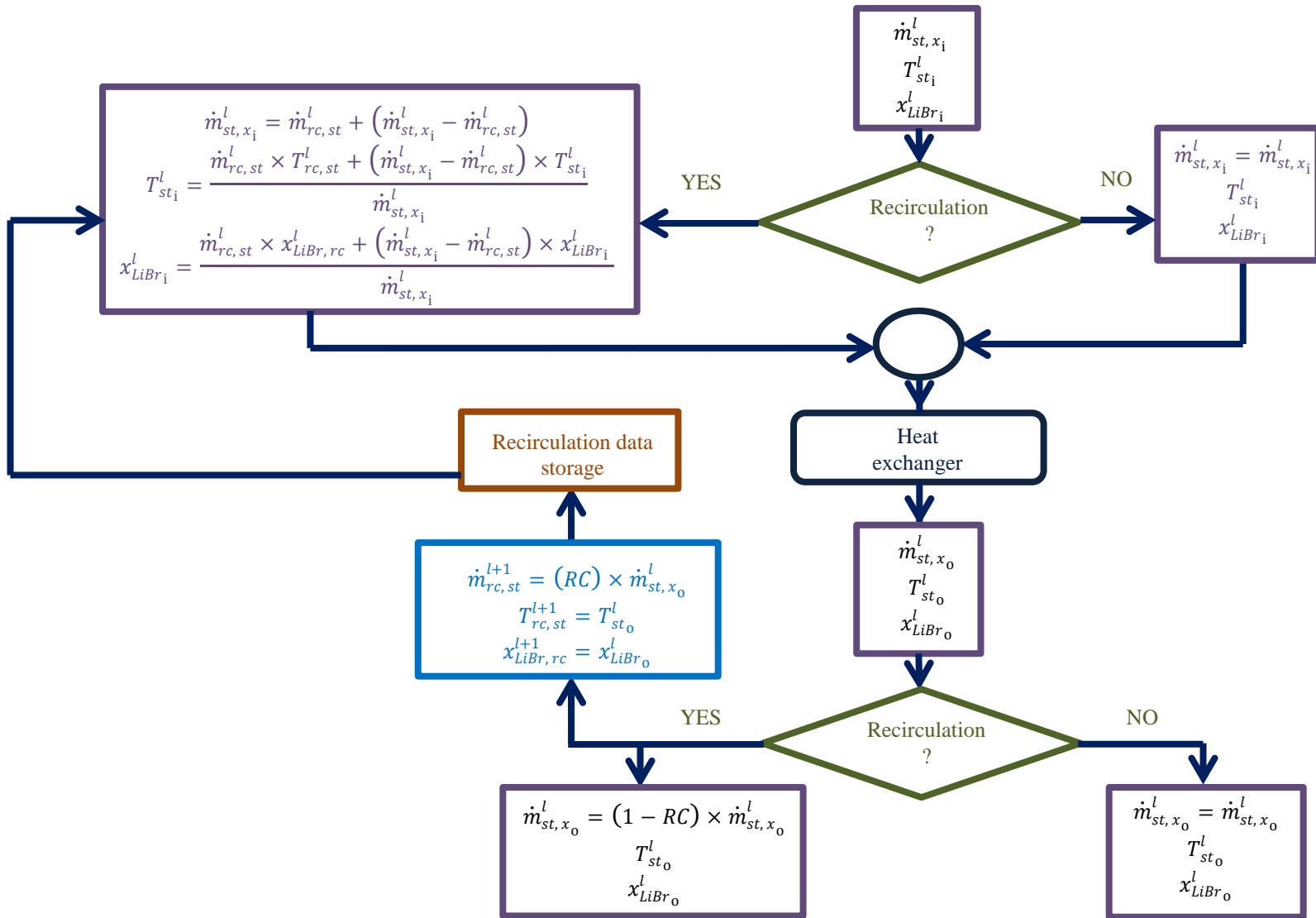


Figure B2. System flow chart for a recirculation system in a heat exchanger for a LiBr solution falling film at a time "l".

B1.6. Comparison against an experimental case of desorption/condensation and absorption/evaporation in the reactor of an interseasonal heat storage prototype: additional cases

In sections 2.1.2.3.2 and 2.1.2.3.3, two additional experimental tests carried out by N'Tsoukpoe (2012), (N'Tsoukpoe et al., 2013) in desorption/condensation and absorption/evaporation mode have been compared to our simulations. Comparisons between experimental and simulation results are described in the following sections.

B1.6.1. Simulation model validation for a desorption/condensation operating mode

Experimental inlet conditions on the desorber and condenser for the LiBr solution falling film and the HTF are described in table B2.

Table B2. Experimental inlet conditions considered for the LiBr falling film and heat exchangers on the desorber and condenser (charge mode)

Desorber	\dot{m}_{st_i} [kg/h]	T_{st_i} [°C]	x_{LiBr_i} [m_LiBr/m_st]	\dot{m}_{htf_i} [kg/h]	T_{htf_i} [°C]	<i>Direction movement</i>
		[63 – 66]	[27 – 34]	[0.56 – 0.60]	720	90
Condenser	$\dot{m}_{f_water_i}$ [kg/h]			\dot{m}_{htf_i} [kg/h]	T_{htf_i} [°C]	<i>Direction movement</i>
	0			720	10	Countercurrent

Experimental inlet conditions mentioned in table B2 were used as inlet conditions in the simulation. Figure B3 shows the comparison between experimental and simulation results for the LiBr solution film and the HTF leaving the reactor.

In a similar way to the case described in section 2.1.2.3.2, Figure B3 shows a good coincidence between experimental and simulation results for cases in which the desorption transfer surface is considered to be 18% wetted, with better agreements obtained for the LiBr solution mass fraction and the HTF temperatures.

B1.6.2. Simulation model validation for an absorption/evaporation operating mode

Experimental inlet conditions on the absorber and evaporator for the LiBr solution falling film, water film and the heat transfer fluids are described in table B3.

Table B3. Experimental inlet conditions considered for the LiBr falling film, water film and heat exchangers on the absorber and evaporator (discharge mode)

Absorber	\dot{m}_{st_i} [kg/h]	T_{st_i} [°C]	x_{LiBr_i} [mLiBr/mSol]	\dot{m}_{htf_i} [kg/h]	T_{htf_i} [°C]	<i>Direction movement</i>
		36	[15 – 17]	[0.53 – 0.52]	360	22
Evaporator	$\dot{m}_{f_water_i}$ [kg/h]	$T_{f_water_i}$ [°C]		\dot{m}_{htf_i} [kg/h]	T_{htf_i} [°C]	<i>Direction movement</i>
	43	[13 – 14]		720	15	Countercurrent

Experimental inlet conditions mentioned in table B3 were used as inlet conditions in the simulation model. Figure B4 shows the comparison between experimental and simulation results for the LiBr solution film, water film and the HTF leaving the reactor.

Again, Figure B4 shows a good coincidence between experimental and simulation results for cases in which the absorption and evaporation transfer surfaces are considered to be 16% wetted.

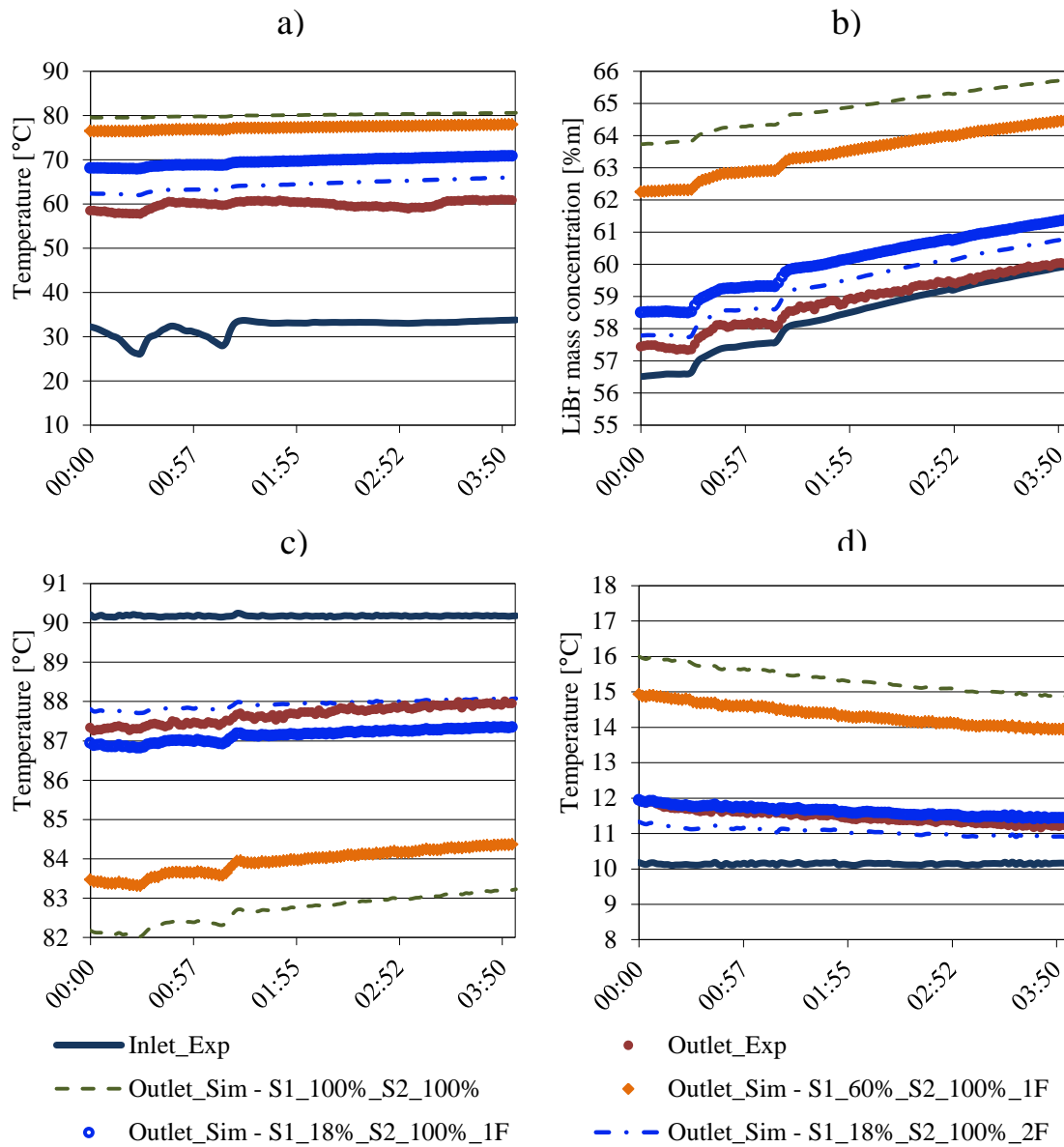


Figure B3. Comparison between experimental and simulated results for desorption/condensation tests made by N'Tsoukpoe et al. (2013). a) LiBr solution temperature; b) LiBr solution mass fraction; c) HTF temperature in the desorber; d) HTF temperature in the condenser.

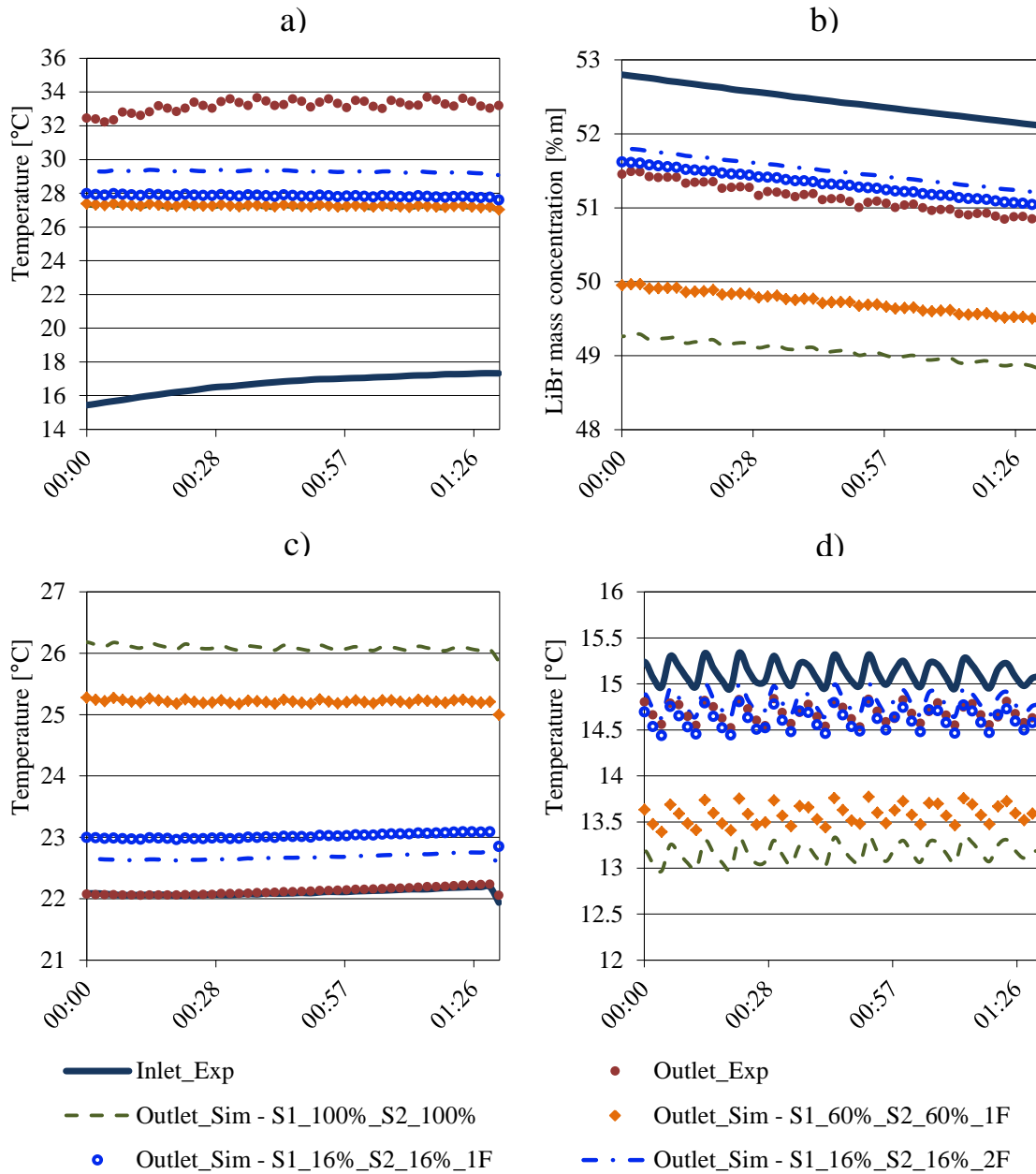


Figure B4. Comparison between experimental and simulated results for absorption/evaporation tests made by N'Tsoukpoe et al. (2013). a) LiBr solution temperature; b) LiBr mass fraction in the solution; c) HTF temperature in the absorber; d) heat transfer fluid temperature in the evaporator.

B1.7. Simulated desorption/condensation and absorption/evaporation process performance

In this section, the temperature and LiBr mass fraction variations along the solution film for the desorption/condensation and absorption/evaporation reference cases described in Tables 2.4 and 2.6, respectively, are described. At each operating mode (Figures B5 and B6), two cases are described with the solution inlet LiBr mass concentration, x_{LiBr_i} , at 48% and 60%.

These results permit an easier analyze of temperature and mass fraction differences across the solution film, as well as its dependence and interaction with x_{LiBr_i} and the HTF, respectively.

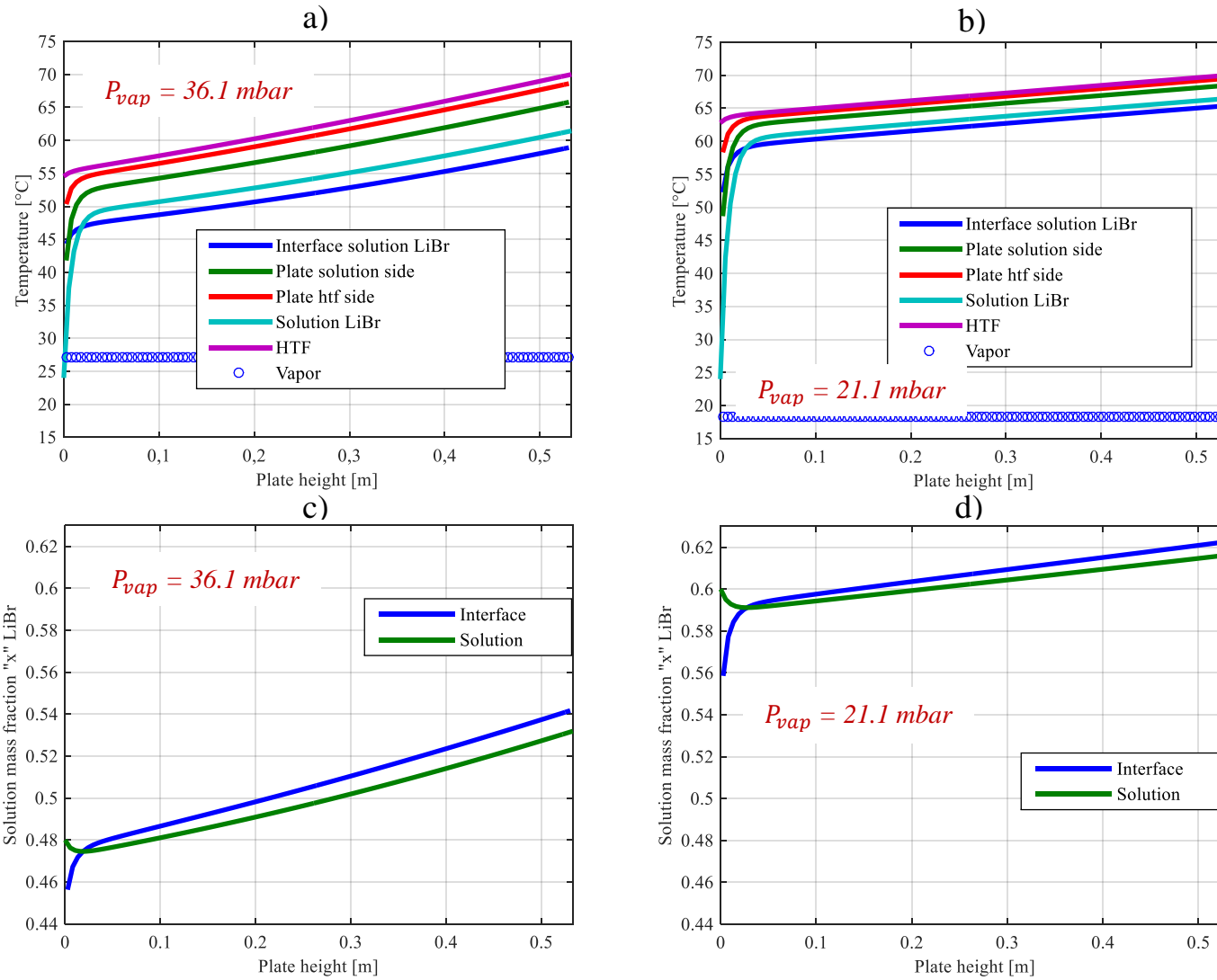


Figure B5. Temperature and LiBr mass fraction profiles along the solution film in desorption/condensation mode (reference case, countercurrent). a) Temperature ($x_{LiBr_i}=48\%$); b) Temperature ($x_{LiBr_i}=60\%$); c) LiBr mass fraction ($x_{LiBr_i}=48\%$); d) LiBr mass fraction ($x_{LiBr_i}=60\%$)

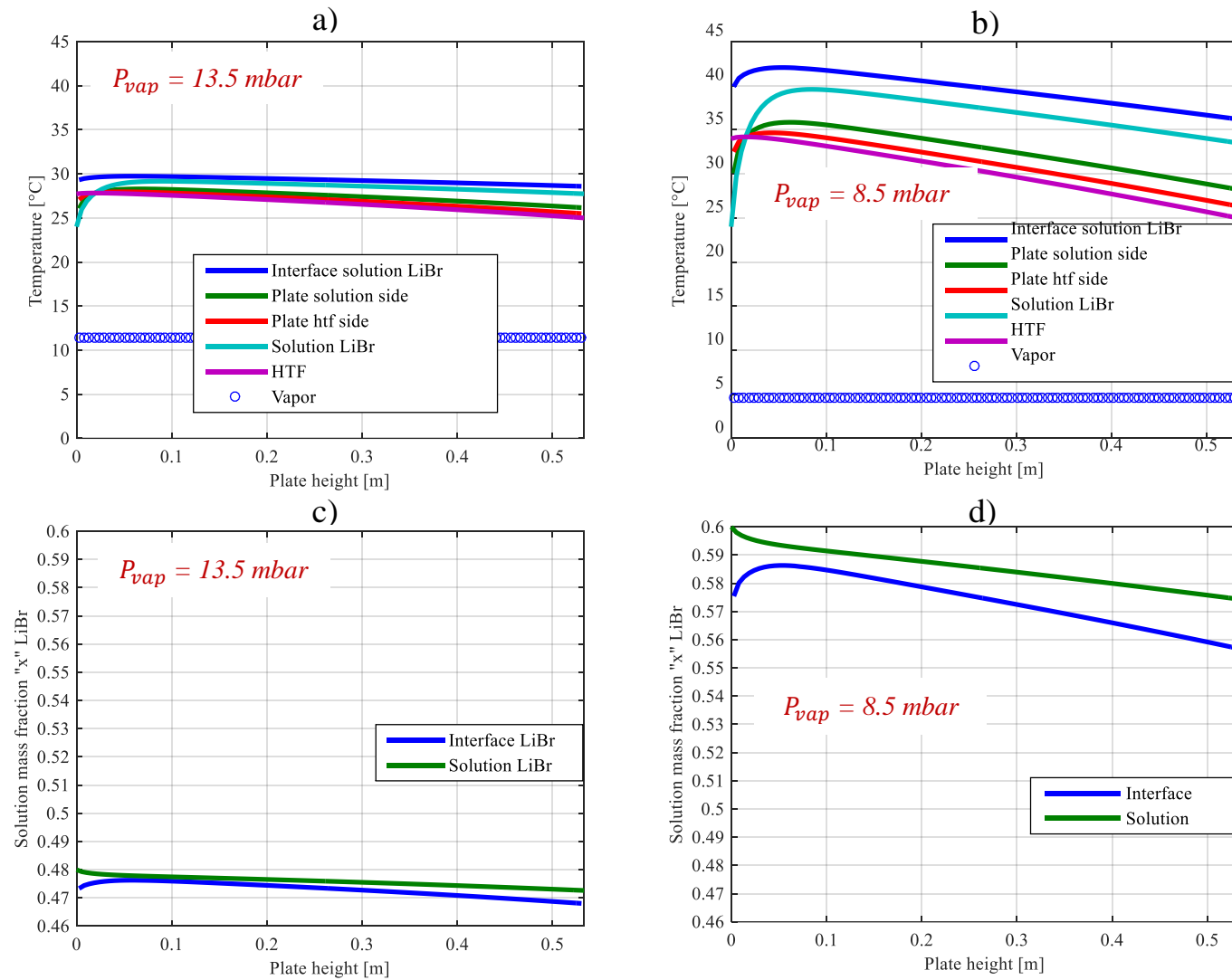


Figure B6. Temperature and LiBr mass fraction profiles along the solution film in absorption/evaporation mode (reference case, countercurrent). a) Temperature ($x_{LiBr_i}=48\%$); b) Temperature ($x_{LiBr_i}=60\%$); c) LiBr mass fraction ($x_{LiBr_i}=48\%$); d) LiBr mass fraction ($x_{LiBr_i}=60\%$)

Annex B2

B2.1. Liquid solution tank simulation model stability indicators

As it was indicated in section 2.2.1.1, some stability indicators were considered to study the stability convergence of the simulation model developed for the liquid LiBr solution tank; these indicators were the Fourier number, the Courant number and the Peclet number.

Considering the simulation cases defined in section 2.2.1.3.1, a charge and a discharge case were selected to study their stability convergence through the average values of the defined indicators. The stability behavior of these cases are shown below in Figure B7.

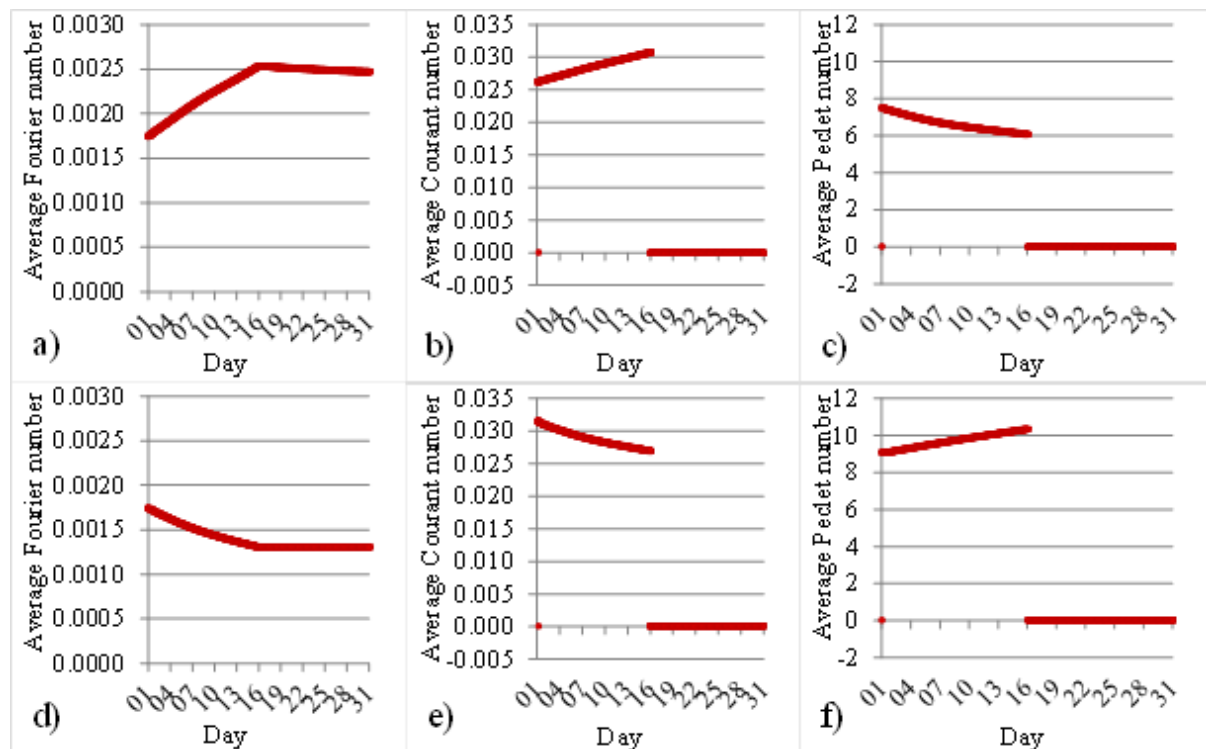


Figure B7. Simulation stability indicators for the liquid LiBr solution tank. Average values for the Fourier, Courant and Peclet numbers; a) b) c) Charge mode (case 4); d) e) f) Discharge mode (case 7).

From these results it can be established that in order to ensure a convergence in the solution tank model, the selected time step (" Δt ") and grid size (" Δy ") values must permit to obtain Fourier numbers, Courant numbers and Peclet numbers below 0.025, 0.03 and 8, respectively, as it is observed in Figure B7.

B2.2. Heat transfer across the solution tank wall in crystals presence

For cases in which crystals are present in the solution tank, the heat balance equations associated to the heat transfers between the bulk liquid solution and the tank wall and between the tank wall and the external environment are modified. Hence, the energy balance on the liquid solution and the heat losses to the surroundings are approached by Equation (B1.30) shown below⁽¹⁾:

⁽¹⁾ This equation is an adaptation of Equation (2.58) for cases where crystallization happens.

$$\pi \times D_{h_{st/tank}} \times \sum_{k=1}^{10} \left(\dot{q}_{w/st/tank_k}^l \times \Delta y_{st/tank}^l \right) =$$

$$\left(\frac{\lambda_{w/st/tank}}{e_{w/st/tank}} \times \pi \times D_{h_{st/tank}} \right) \times \sum_{k=1}^{10} \left(\left(\Delta y_{st/tank}^l + \Delta y_{st/cry/tank_k}^l \right) \times \left(T_{ext/st/tank}^l - T_{w/st/tank_k}^l \right) \right) \quad (\text{B1.30})$$

Where $\Delta y_{st/cry/tank_k}^l$ and $\Delta y_{st/tank}^l$ are the height of formed crystals and the height of liquid solution, respectively, at a certain grid “k”. It must be remarked that whenever the presence of crystals increase (cases with low initial solution tank mass), “ $\Delta y_{st/tank}^l + \Delta y_{st/cry/tank_k}^l > \Delta y_{st/tank}^l$ ”, and consequently, the temperature difference between the external and internal wall will be smaller than the temperature gap between the internal wall and the bulk solution.

Again, it must be highlighted that the model firstly considers an energy, species and mass balance only taking into account the liquid solution (inlet/outlet solution mass flows and the surrounding heat losses⁽¹⁾ are comprised in this balance). Afterwards, if saturation conditions are reached, a new energy, species and mass balance is made in order to determine the amount of formed crystals.

⁽¹⁾ The surrounding heat losses are approached by equation 2.58 or equation B1.30, depending if there is a crystal presence at the initial conditions of the step time “l”.

ANNEX C

Annex C1

C1.1. Prototype components technical description

In this section, the dimensions of the reactor container, solution tank, water tank and heat exchangers are shown. Additional pictures of the prototype are also presented.

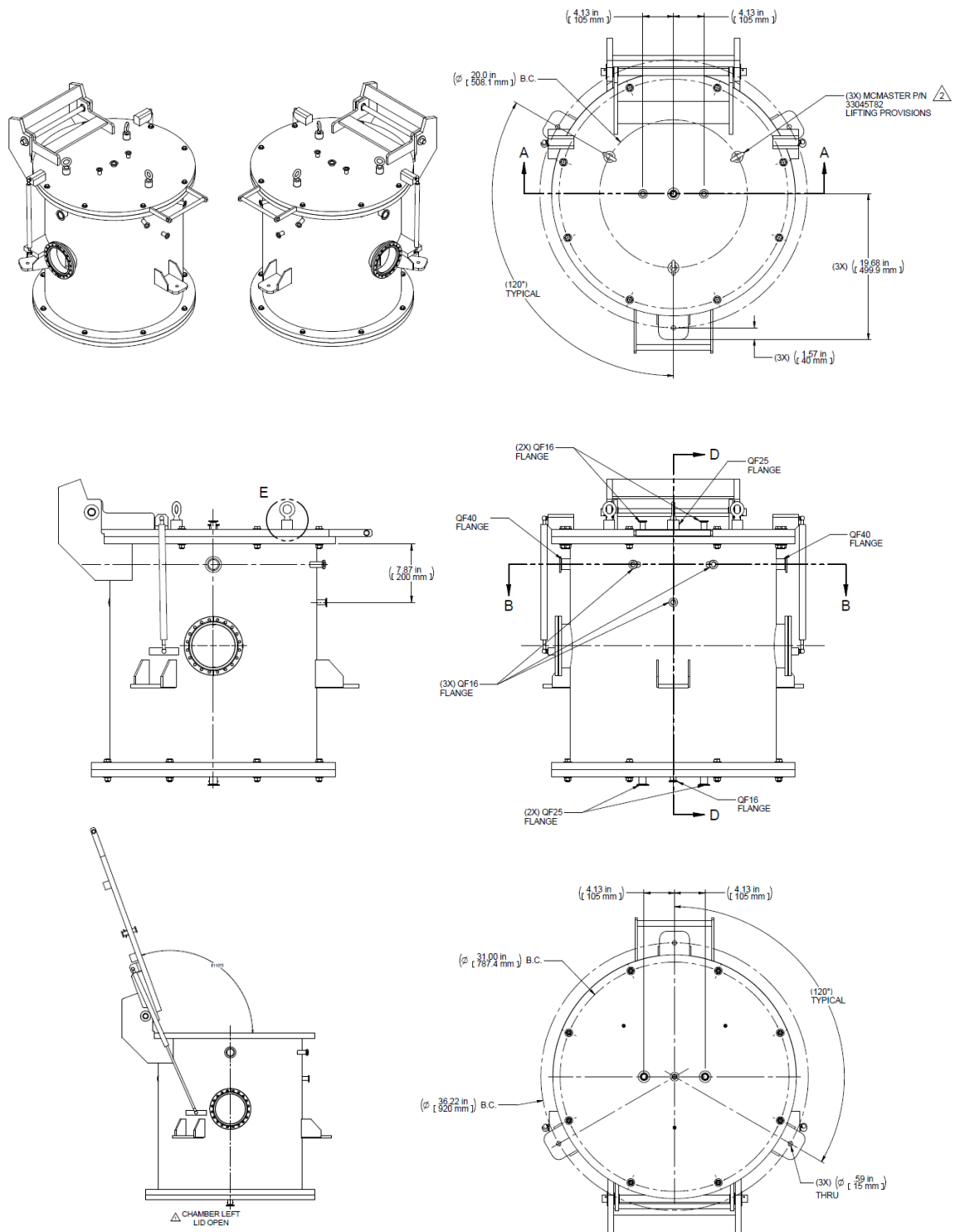


Figure C1. Reactor container design dimensions

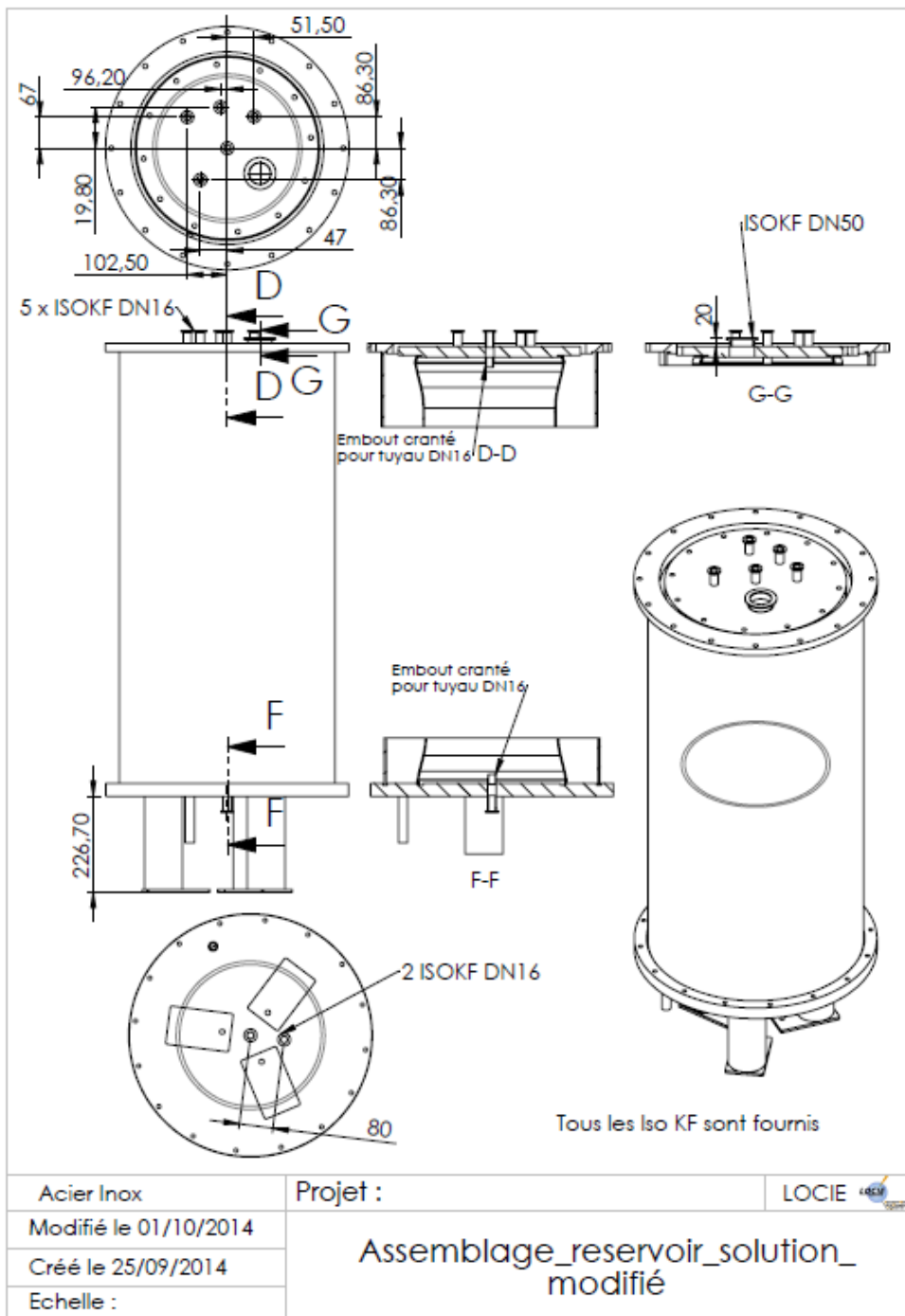


Figure C2. Solution tank design dimensions

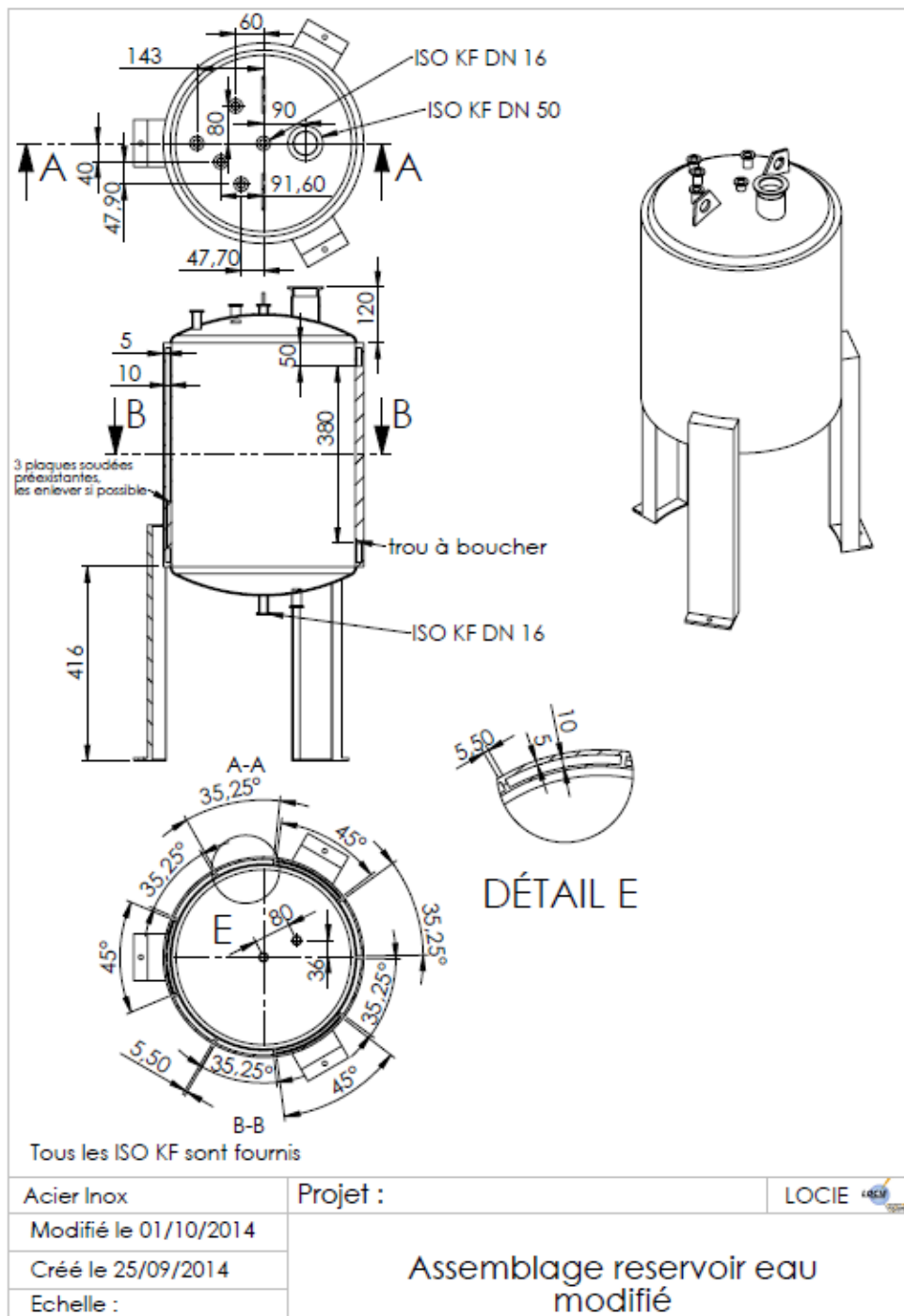


Figure C3. Water tank design dimensions

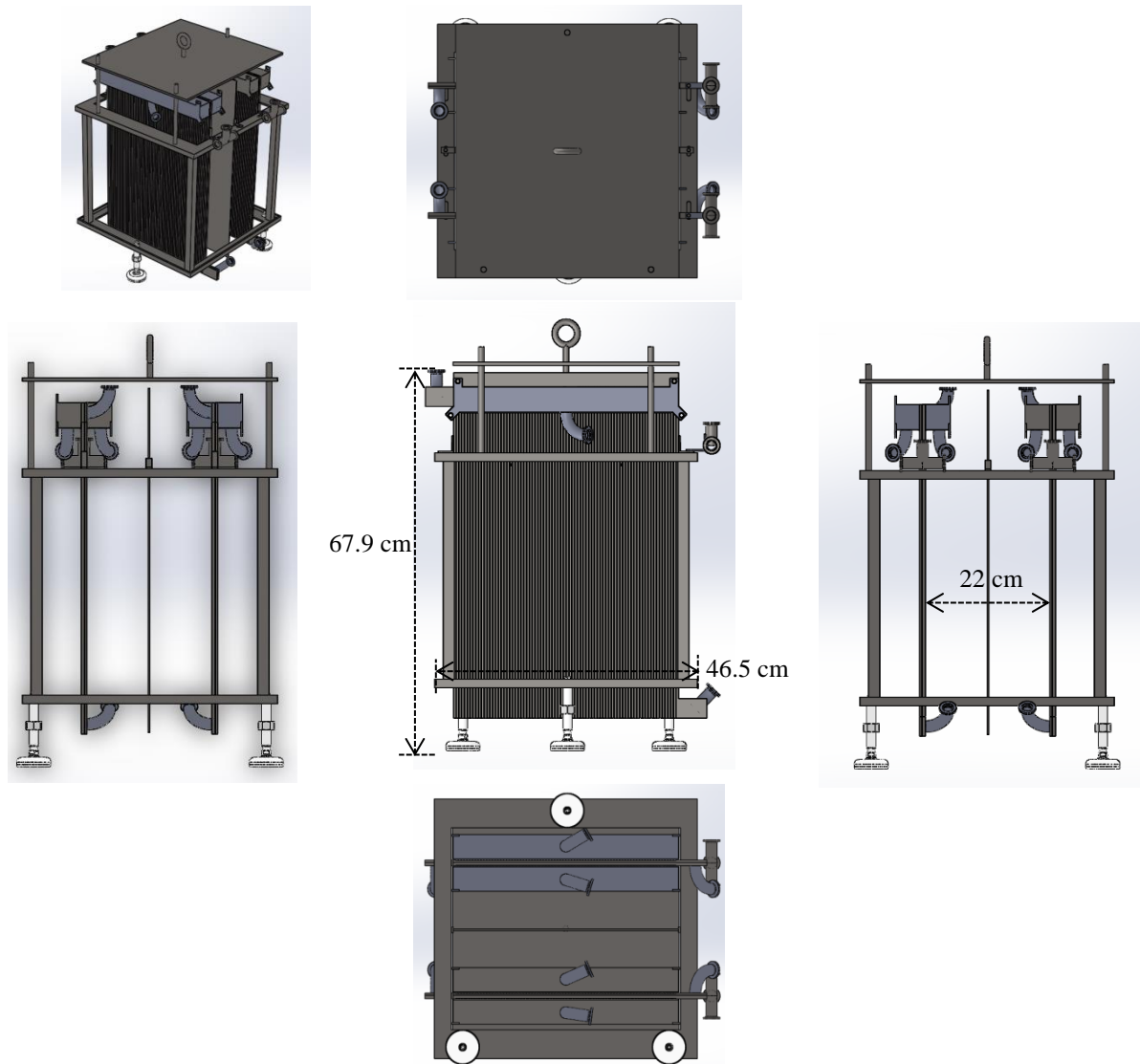


Figure C4. Heat exchangers dimensions

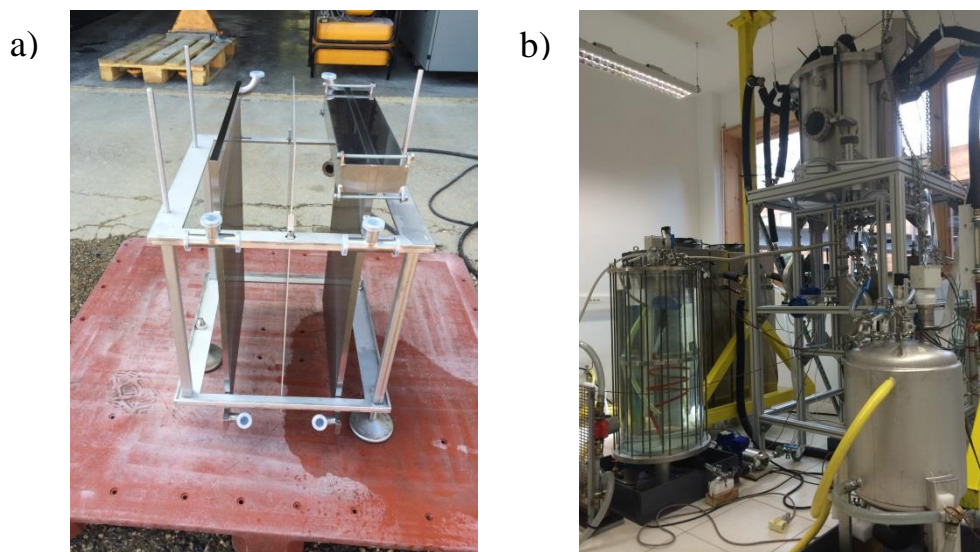


Figure C5. Constructed interseasonal heat storage prototype. a) Heat exchangers partially assembled; b) Global system

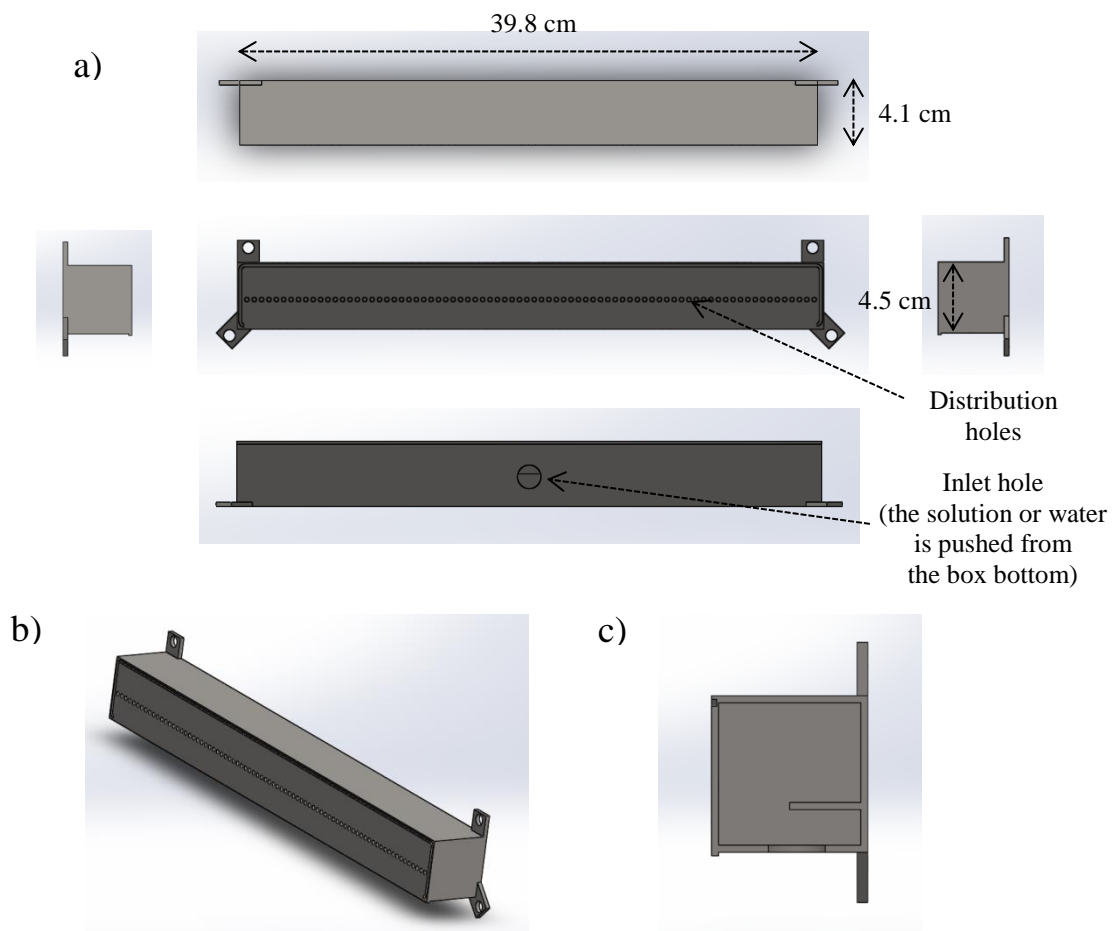


Figure C6. Heat exchangers distribution system (distribution box). a) Side views; b) Perspective view; c) Detail of the box interior

C1.2. Temperature sensors calibration

A calibration process for the temperature sensors was made in order to reduce the uncertainty measure. As it was mentioned in section 3.1.2, the sensors were thermocouples of types T and K. A platinum resistant thermometer (PT100) was used as a reference sensor.

The calibration setup was composed of a small copper cylinder (5 cm diameter x 5 cm height) where some little orifices were made to fix the temperature sensors. All these elements were placed inside a thermal module (chiller) filled with water where the temperature was controlled.

Stable temperature conditions in the range of 0 to 100°C⁽¹⁾ were used as reference points to compare the thermocouples and PT100 measures and to calculate a polynomial calibration curve associated to the former. Figure C7 shows the measures gap between some thermocouples⁽²⁾ and the PT100 for different temperatures.

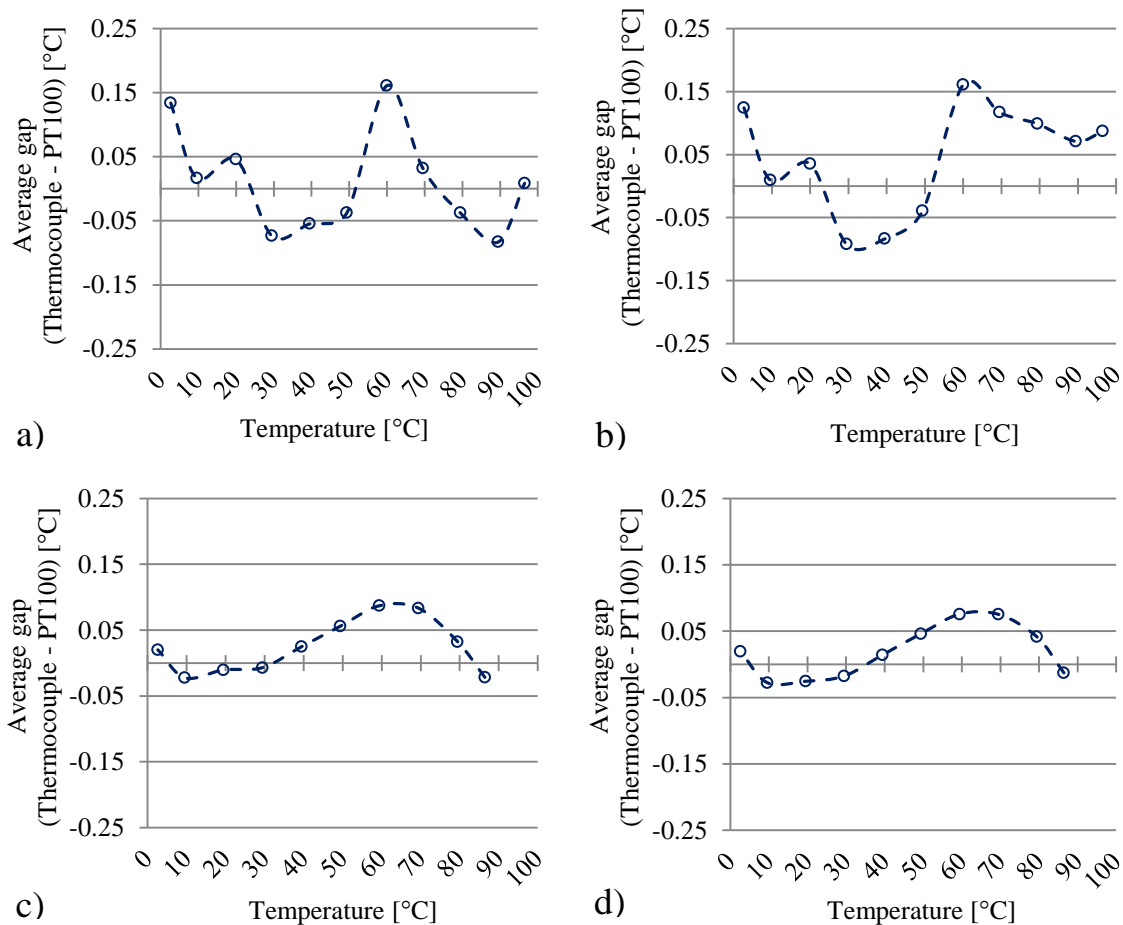


Figure C7. Average gap in the measure between thermocouples and PT100 at different temperatures. a) Thermocouple TK2 (type K); b) Thermocouple TK3 (type K); c) Thermocouple TT2 (type T); d) Thermocouple TT3 (type T)

⁽¹⁾ The water presented a percentage of glycol to avoid freezing at temperatures close to 0 °C.

⁽²⁾ The thermocouples measures were made using the calibration curve calculated in the previous stage.

C1.3. System gas leakage rate calculation method

In section 3.2.1 the measured gas leakage rate associated to the solution tank, water tank and reactor container was shown.

Since no vacuum system can ever be absolutely vacuum-tight, a parameter capable to describe the “leak rate” is defined and denoted as “ Q_L ”, with its corresponding units in mbar.l/s. Hence, if at an enclosed and evacuated vessel of 1 liter, the pressure varies of 1 mbar per second, it can be expressed that the system presents a leak rate of $Q_L = 1$ mbar.l/s. Positive values of Q_L are associated to conditions in which the vessel pressure is lower than its surroundings, while negative values indicate that the vessel pressure is higher than its surroundings.

This definition of leak rate is also associated to the mass flow leaving or entering the container, as it is shown in Equation C1, considering the ideal gas equation and the corresponding gas temperature and gas molar mass.

$$Q_L = \frac{\Delta(p \cdot V)}{\Delta t} = \frac{R \cdot T}{M} \cdot \frac{\Delta m}{\Delta t} \quad (C1)$$

Where p is the gas pressure in mbar, V is the container volume in liters, Δt is the time interval in seconds, R is the ideal gas constant which is 83.14 mbar.l/(mol.K), T is the temperature in K, M is the gas molar mass in g/mol and Δm is the mass variation in grams.

Umrath (Umrath et al., 2007) considers that since no system is completely “hermetically sealed”, the measured leak rate must be low enough for the operating pressure, gas balance and physical process in the vacuum container not be influenced. To determine the vacuum requirements of a system, the following values of working pressures and leak rates proposed by Umrath (Umrath et al., 2007) are shown below:

Working pressures; ultra-high vacuum conditions: $10^{-14} \text{ mbar} < p < 10^{-7} \text{ mbar}$, high vacuum conditions: $10^{-7} \text{ mbar} < p < 10^{-3} \text{ mbar}$, medium vacuum conditions: $10^{-3} \text{ mbar} < p < 1 \text{ mbar}$, rough vacuum conditions⁽¹⁾: $1 \text{ mbar} < p < 1000 \text{ mbar}$.

Leak rates; very tight systems: $Q_L < 10^{-6} \text{ mbar.l/s}$, sufficiently tight systems: $Q_L \approx 10^{-5} \text{ mbar.l/s}$, leaky system $Q_L > 10^{-4} \text{ mbar.l/s}$.

Furthermore, Medrano (Medrano et al., 2002) propose that acceptable leak conditions in absorption processes are around $2 \cdot 10^{-4} \text{ mbar.l/s}$.

As it was indicated in section 3.2.1 (Table 3.3), the different components of our system shows leak rates values below $4.5 \cdot 10^{-4} \text{ mbar.l/s}$, which are almost in the “sufficiently tight” category. Hence, it can be considered that our system presents acceptable leak conditions.

Pressure measurements of the system components were carried out in three periods: Before assembly, after assembly/before tests and after assembly/after tests, as it is described in Table 3.3. Results of these gas leakage rate tests are shown in Figure C8.

Table C1. Volume associated to the prototype main components

Component	Volume [l]
Reactor	316.7
Solution tank	73.1
Water tank	75.4

⁽¹⁾ Different propositions are found in the literature for the vacuum conditions classification; some of them consider, for example, medium and low vacuum intervals, $10^{-3} \text{ mbar} < p < 33 \text{ mbar}$ and $33 \text{ mbar} < p < 1000 \text{ mbar}$, respectively.

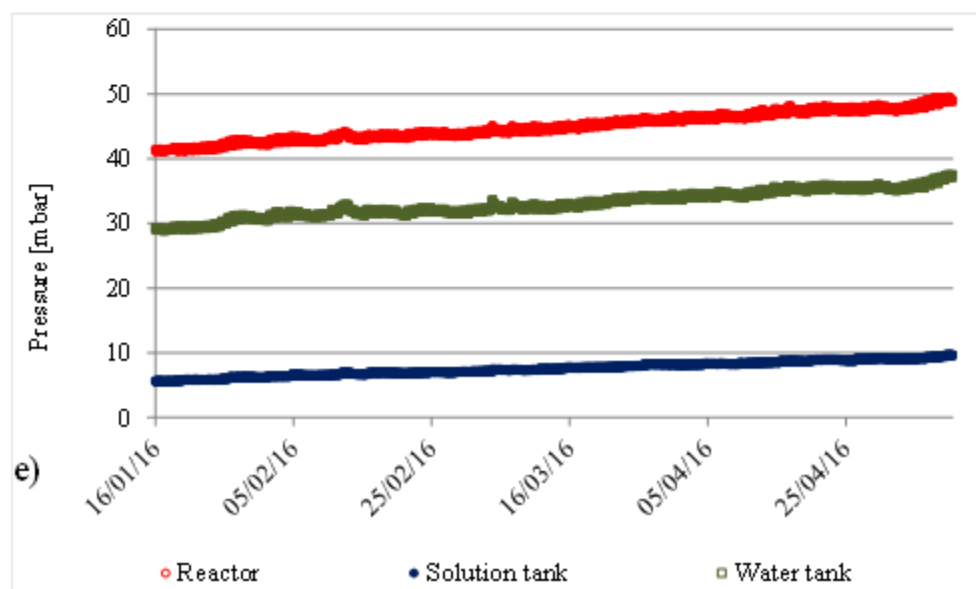
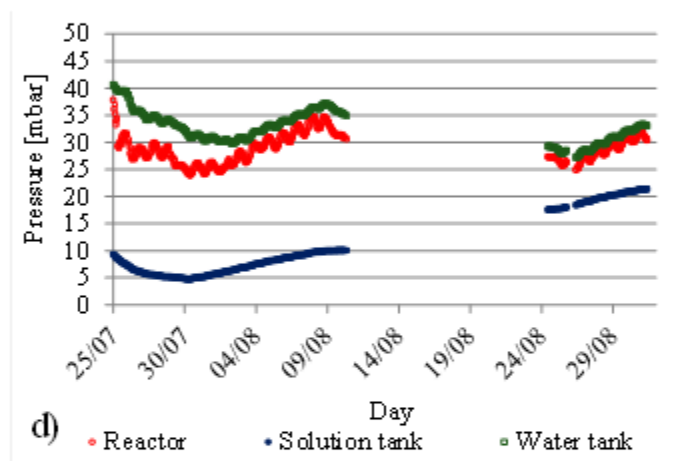
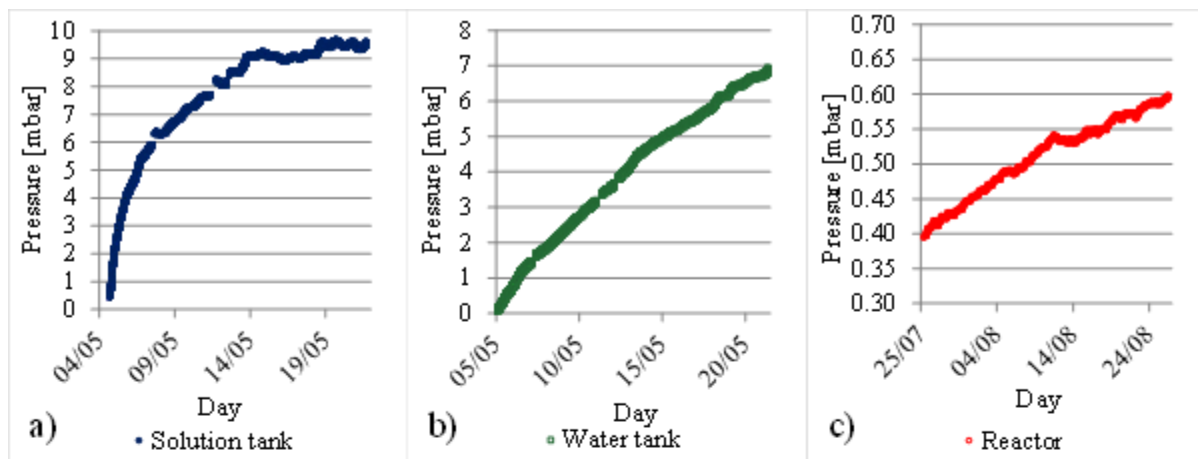


Figure C8. Interseasonal heat storage prototype gas leakage rate tests. a) b) c) Before assembly; d) After assembly/before experimental tests; e) After assembly/after experimental tests

Measurements shown in Figure C8e were carried out for 5 months; nevertheless, the period used for the leak rate calculation covered about 4 months, from January to Mai 2016. Figure C8e shows that although the reactor increased its leakage rate compared to previous tests (Figure C8c,d) ⁽¹⁾; this could be related to the increase in the reactor pressure at the end of the year 2015, which would imply the opening of a valve connecting the reactor to another pipe.

Annex C2

C2.1. Experimental tests in desorption/condensation and absorption/evaporation operating mode

In section 3.2.3 the experimental tests in desorption/condensation and absorption/evaporation modes made in the prototype were described. The physical behavior observed during these tests are described in the sections bellow.

⁽¹⁾ See Table 3.3.

C2.1.1. Desorption/Condensation experimental tests

The experimental results obtained for the Tests 3 to 6, described in Table 3.7, are shown in the figures below.

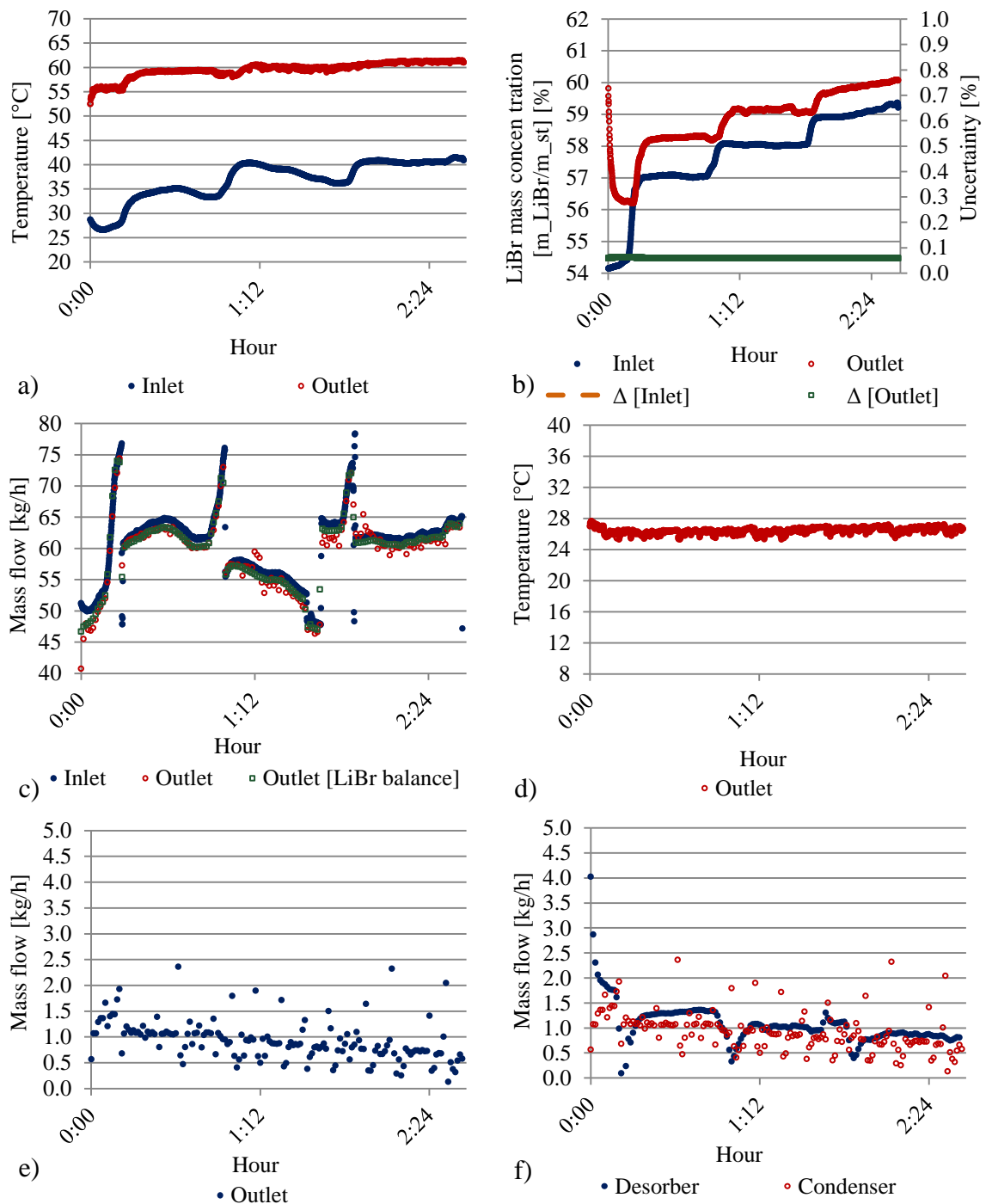


Figure C9. Experimental results obtained in desorption/condensation operating mode for the Test 3. a) LiBr solution temperature (desorber); b) LiBr mass concentration (desorber); c) LiBr solution mass flow (desorber); d) Water film temperature (condenser); e) Water film mass flow (condenser); f) Desorbed/condensed water mass flow (reactor)

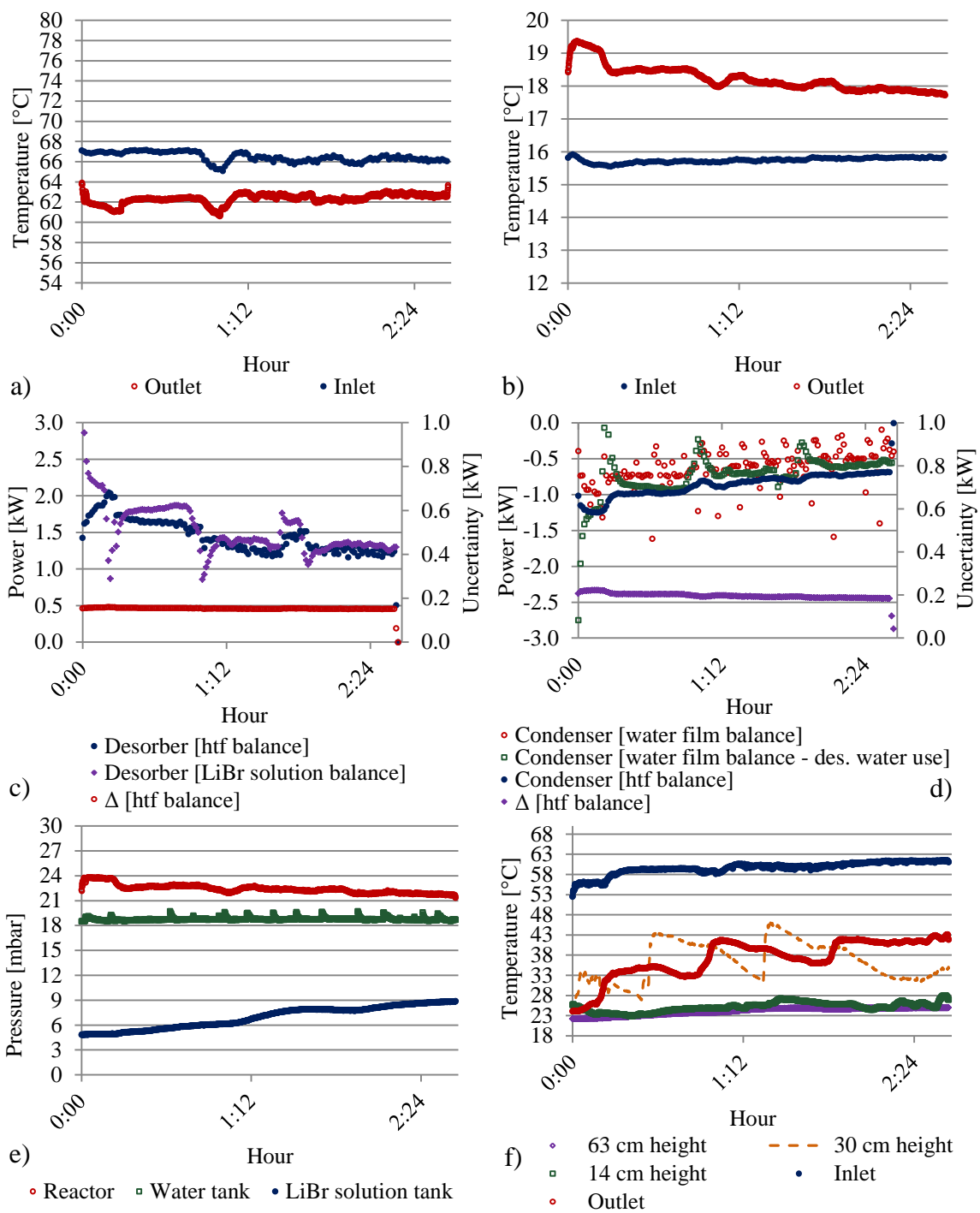


Figure C10. Experimental results obtained in desorption/condensation operating mode for the Test 3. a) HTF temperature (desorber); b) HTF temperature (condenser); c) Power given from the HTF to the system (desorber); d) Power given from the HTF to the system (condenser); e) Vapor pressure; f) LiBr solution temperature (solution tank)

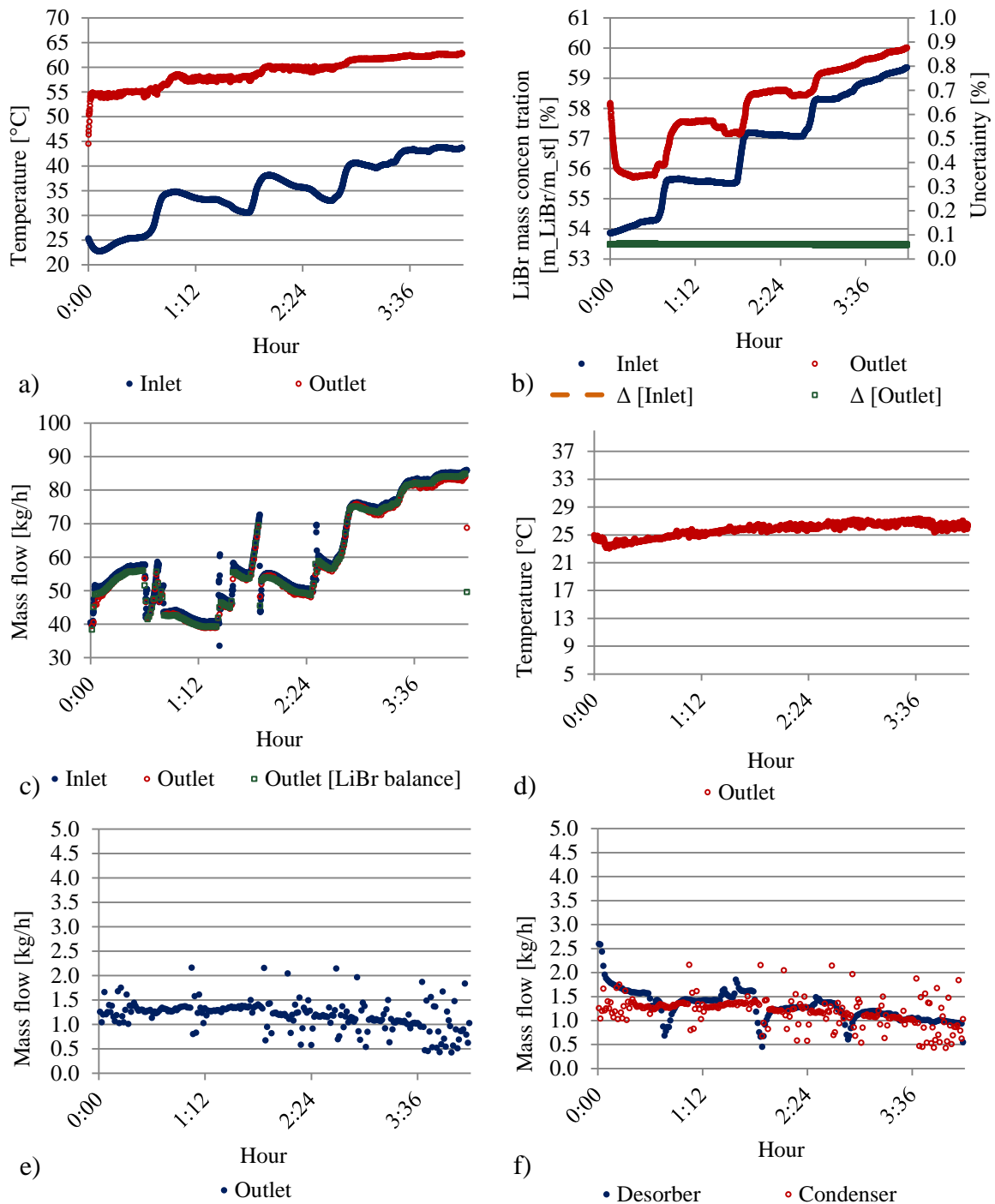


Figure C11. Experimental results obtained in desorption/condensation operating mode for the Test 4. a) LiBr solution temperature (desorber); b) LiBr mass concentration (desorber); c) LiBr solution mass flow (desorber); d) Water film temperature (condenser); e) Water film mass flow (condenser); f) Desorbed/condensed water mass flow (reactor)

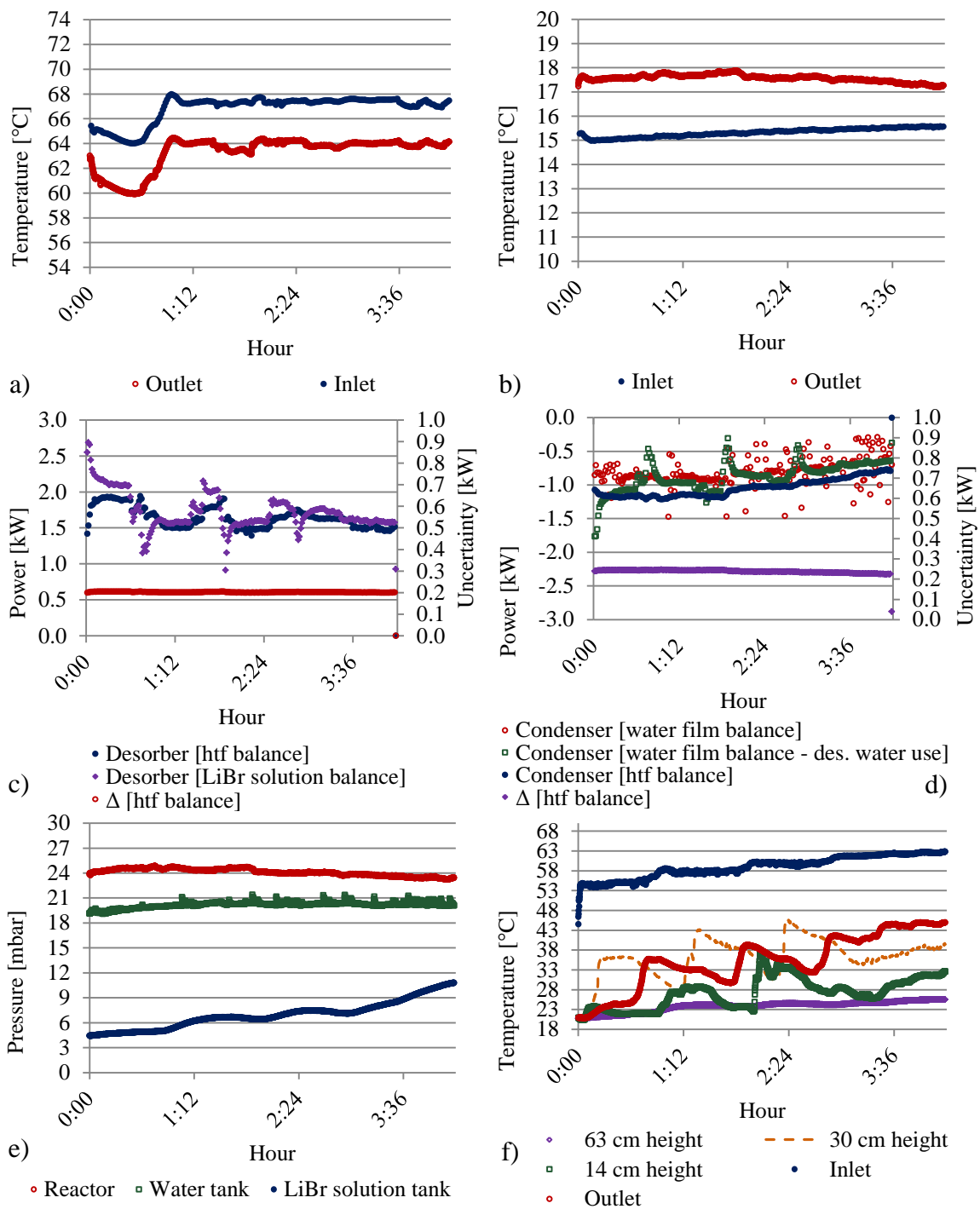


Figure C12. Experimental results obtained in desorption/condensation operating mode for the Test 4. a) HTF temperature (desorber); b) HTF temperature (condenser); c) Power given from the HTF to the system (desorber); d) Power given from the HTF to the system (condenser); e) Vapor pressure; f) LiBr solution temperature (solution tank)

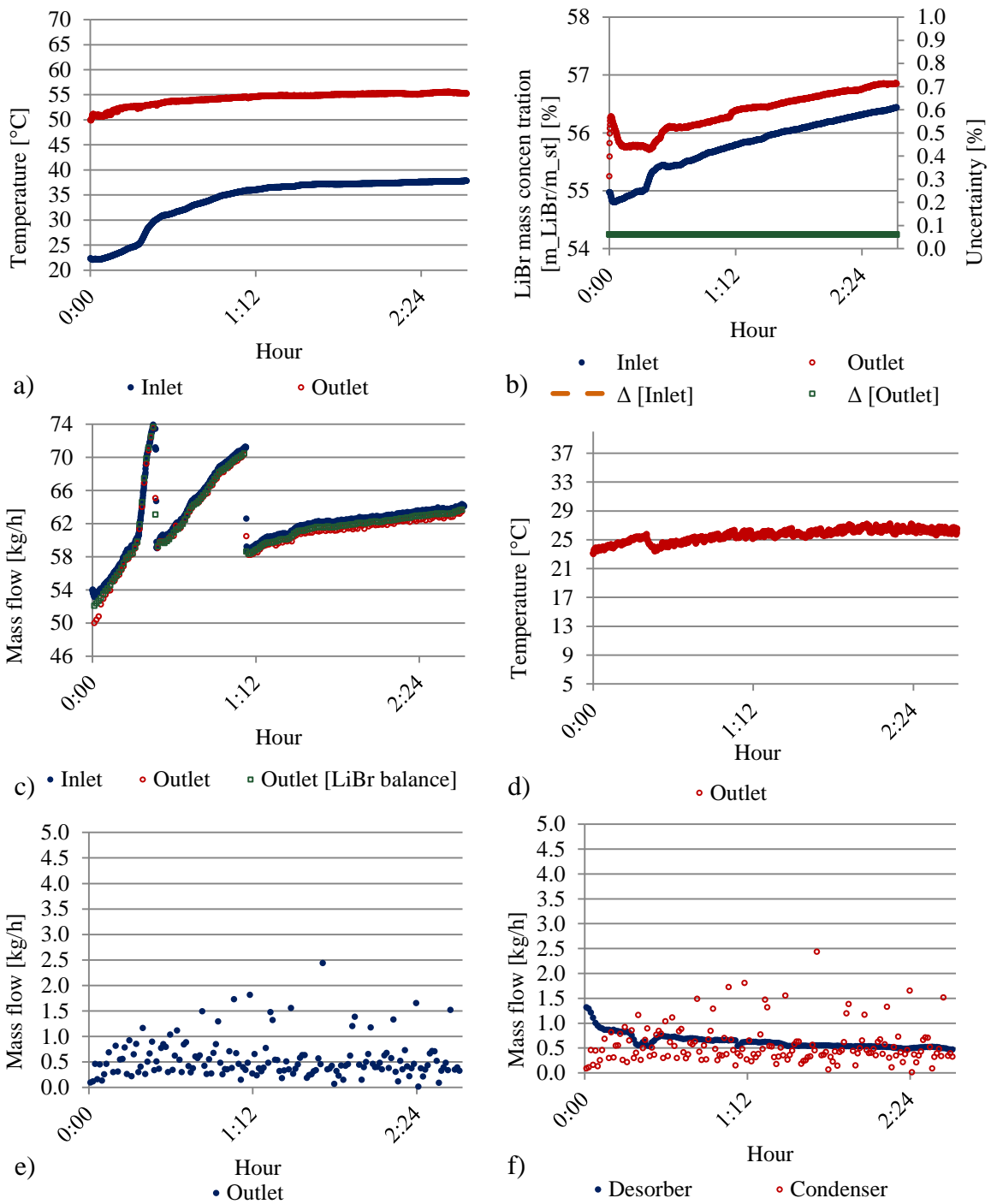


Figure C13. Experimental results obtained in desorption/condensation operating mode for the Test 5. a) LiBr solution temperature (desorber); b) LiBr mass concentration (desorber); c) LiBr solution mass flow (desorber); d) Water film temperature (condenser); e) Water film mass flow (condenser); f) Desorbed/condensed water mass flow (reactor)

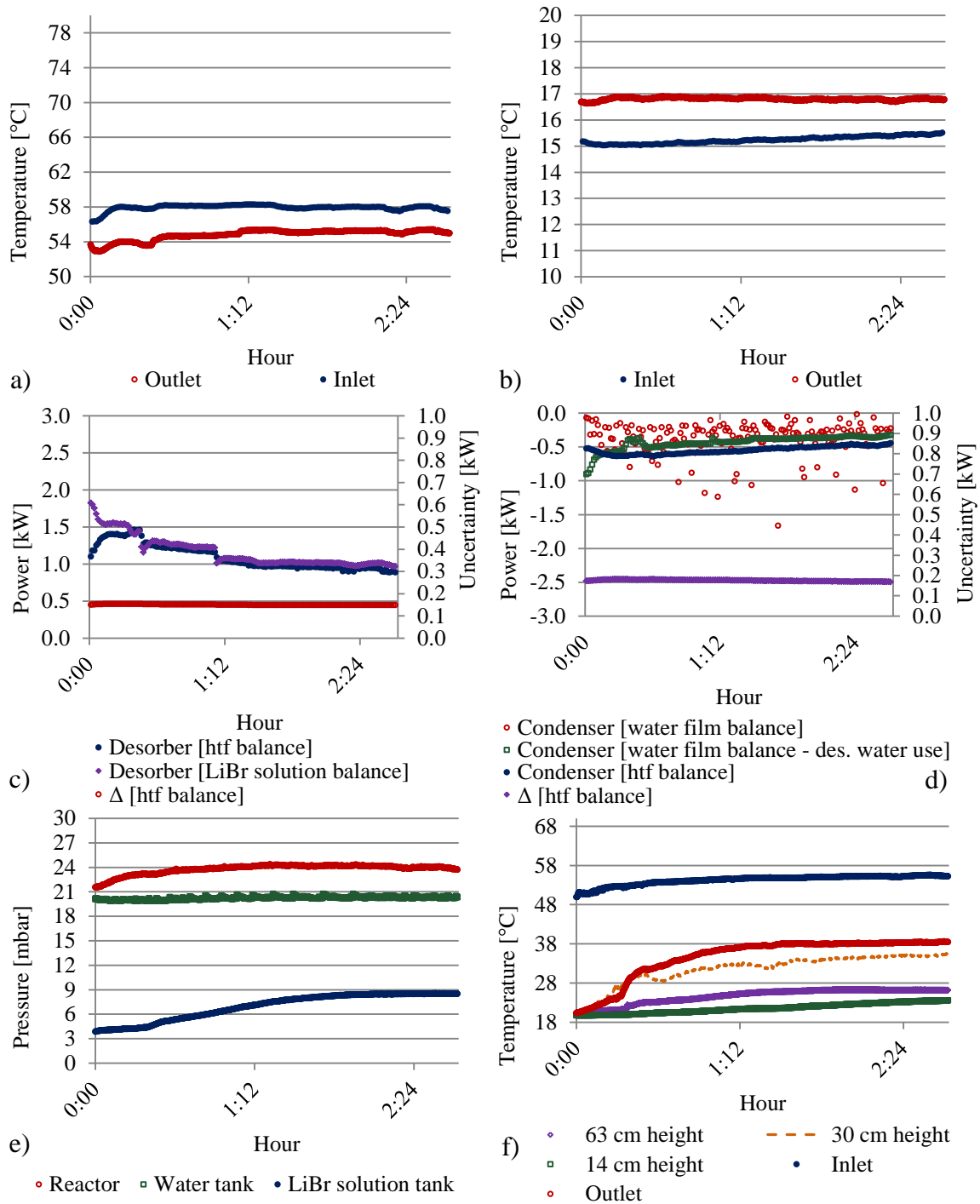


Figure C14. Experimental results obtained in desorption/condensation operating mode for the Test 5. a) HTF temperature (desorber); b) HTF temperature (condenser); c) Power given from the HTF to the system (desorber); d) Power given from the HTF to the system (condenser); e) Vapor pressure; f) LiBr solution temperature (solution tank)

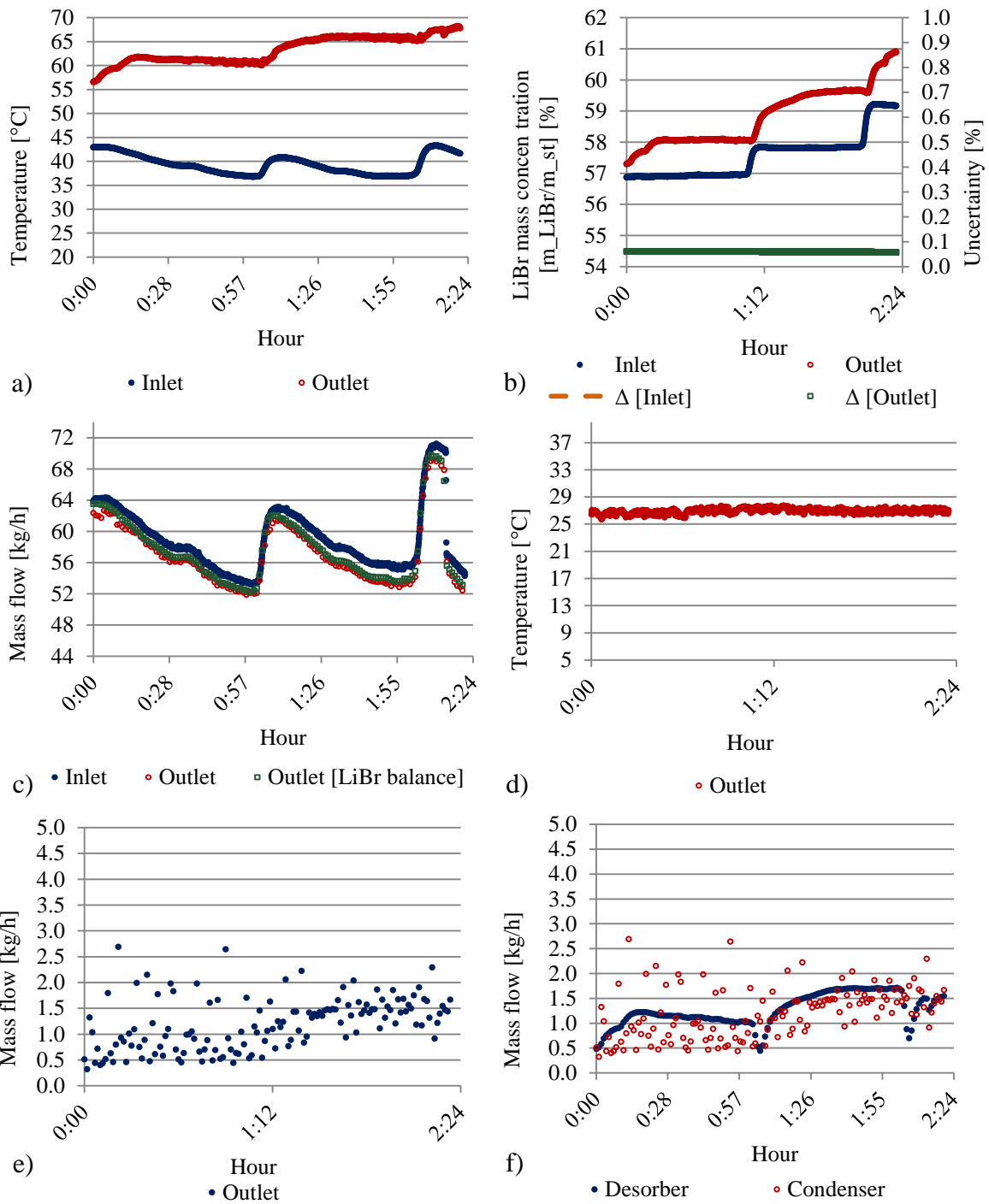


Figure C15. Experimental results obtained in desorption/condensation operating mode for the Test 6. a) LiBr solution temperature (desorber); b) LiBr mass concentration (desorber); c) LiBr solution mass flow (desorber); d) Water film temperature (condenser); e) Water film mass flow (condenser); f) Desorbed/condensed water mass flow (reactor)

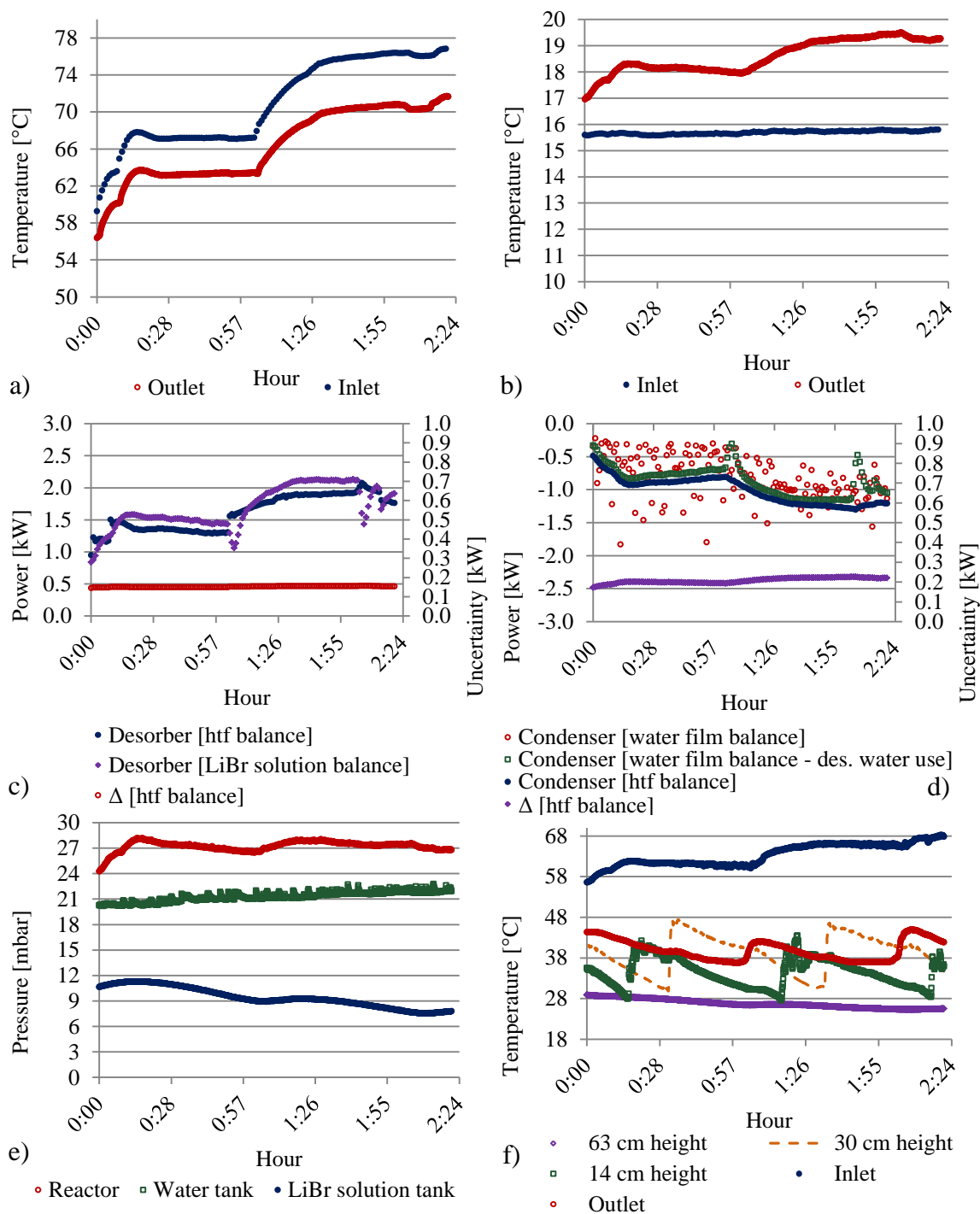


Figure C16. Experimental results obtained in desorption/condensation operating mode for the Test 6. a) HTF temperature (desorber); b) HTF temperature (condenser); c) Power given from the HTF to the system (desorber); d) Power given from the HTF to the system (condenser); e) Vapor pressure; f) LiBr solution temperature (solution tank)

C2.1.2. Absorption/Evaporation experimental tests

The experimental results obtained for the Tests 7 to 10, described in Table 3.9, are shown in the figures bellow.

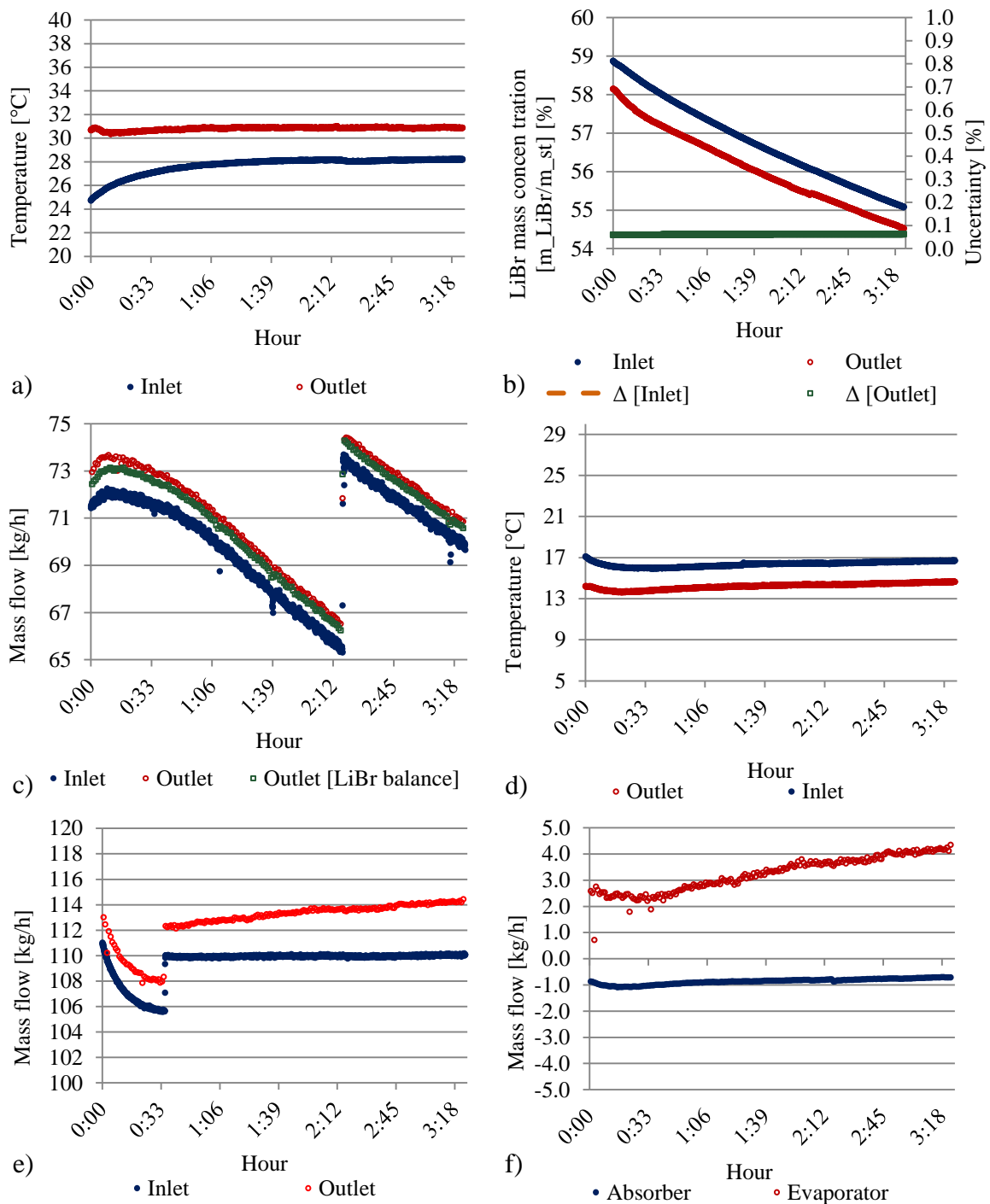


Figure C17. Experimental results obtained in absorption/evaporation operating mode for the Test 9. a) LiBr solution temperature (absorber); b) LiBr mass concentration (absorber); c) LiBr solution mass flow (absorber); d) Water film temperature (evaporator); e) Water film mass flow (evaporator); f) Absorbed/evaporated water mass flow (reactor)

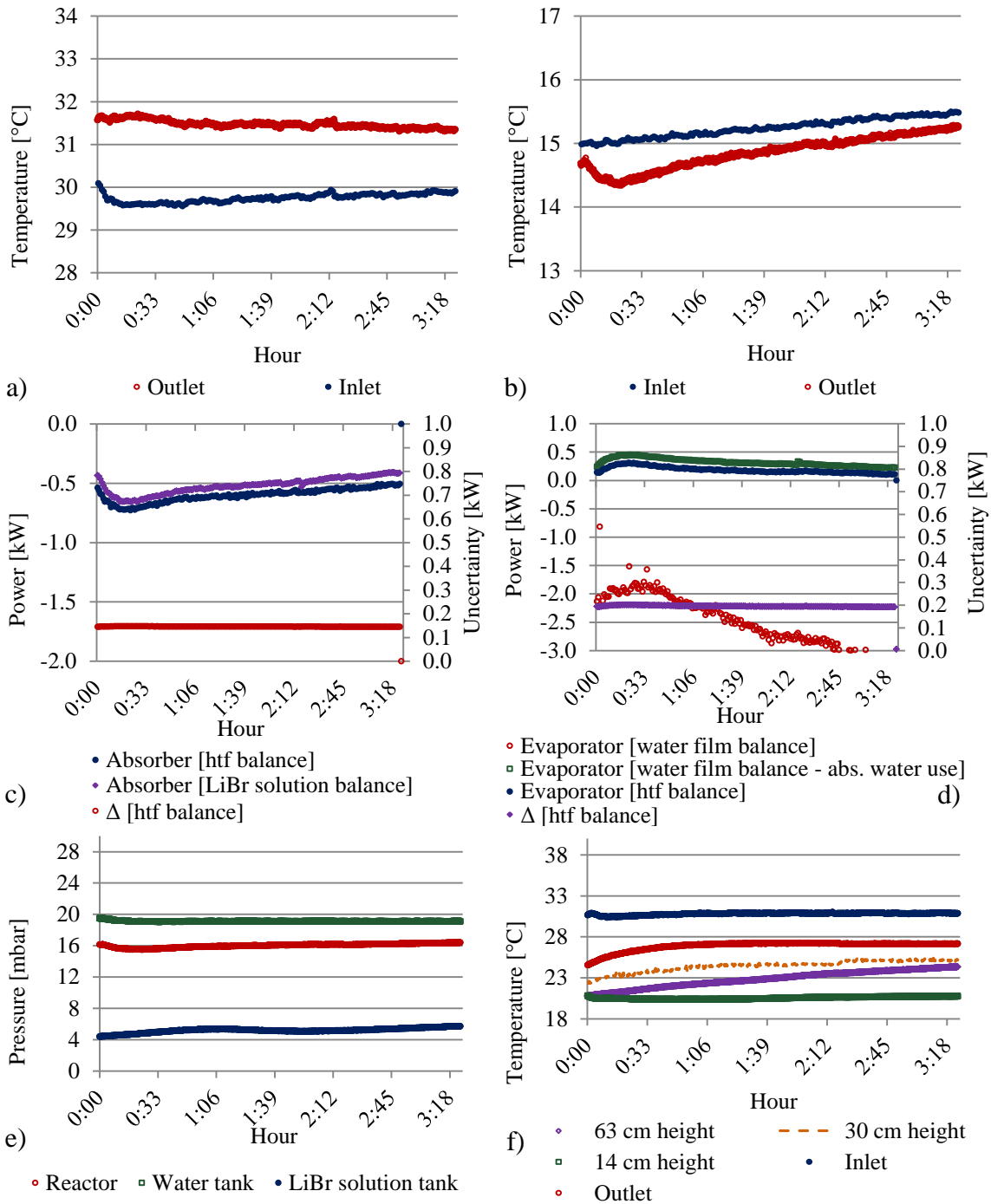


Figure C18. Experimental results obtained in absorption/evaporation operating mode for the Test 9. a) HTF temperature (absorber); b) HTF temperature (evaporator); c) Power given from the HTF to the system (absorber); d) Power given from the HTF to the system (evaporator); e) Vapor pressure; f) LiBr solution temperature (solution tank)

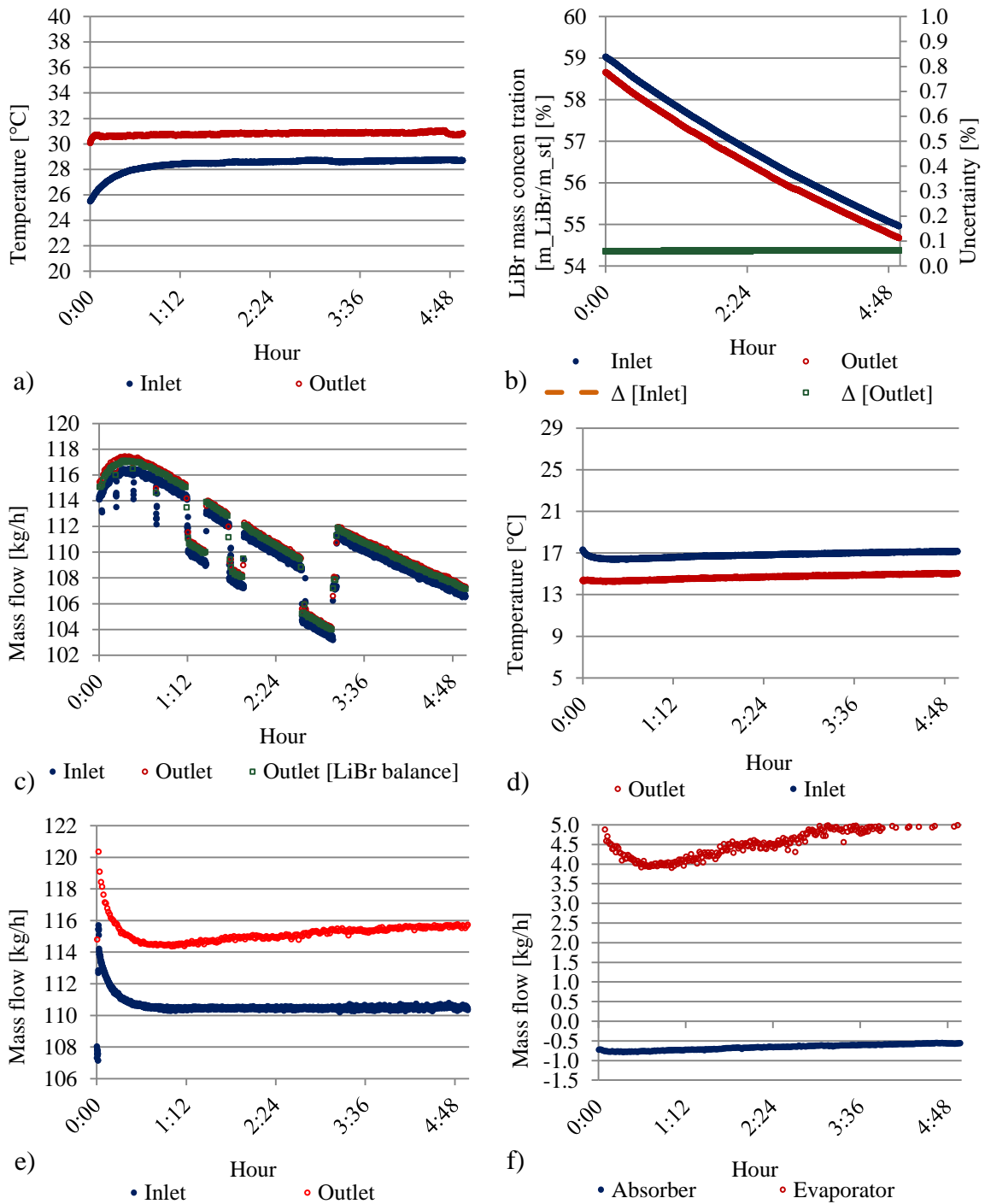


Figure C19. Experimental results obtained in absorption/evaporation operating mode for the Test 10. a) LiBr solution temperature (absorber); b) LiBr mass concentration (absorber); c) LiBr solution mass flow (absorber); d) Water film temperature (evaporator); e) Water film mass flow (evaporator); f) Absorbed/evaporated water mass flow (reactor)

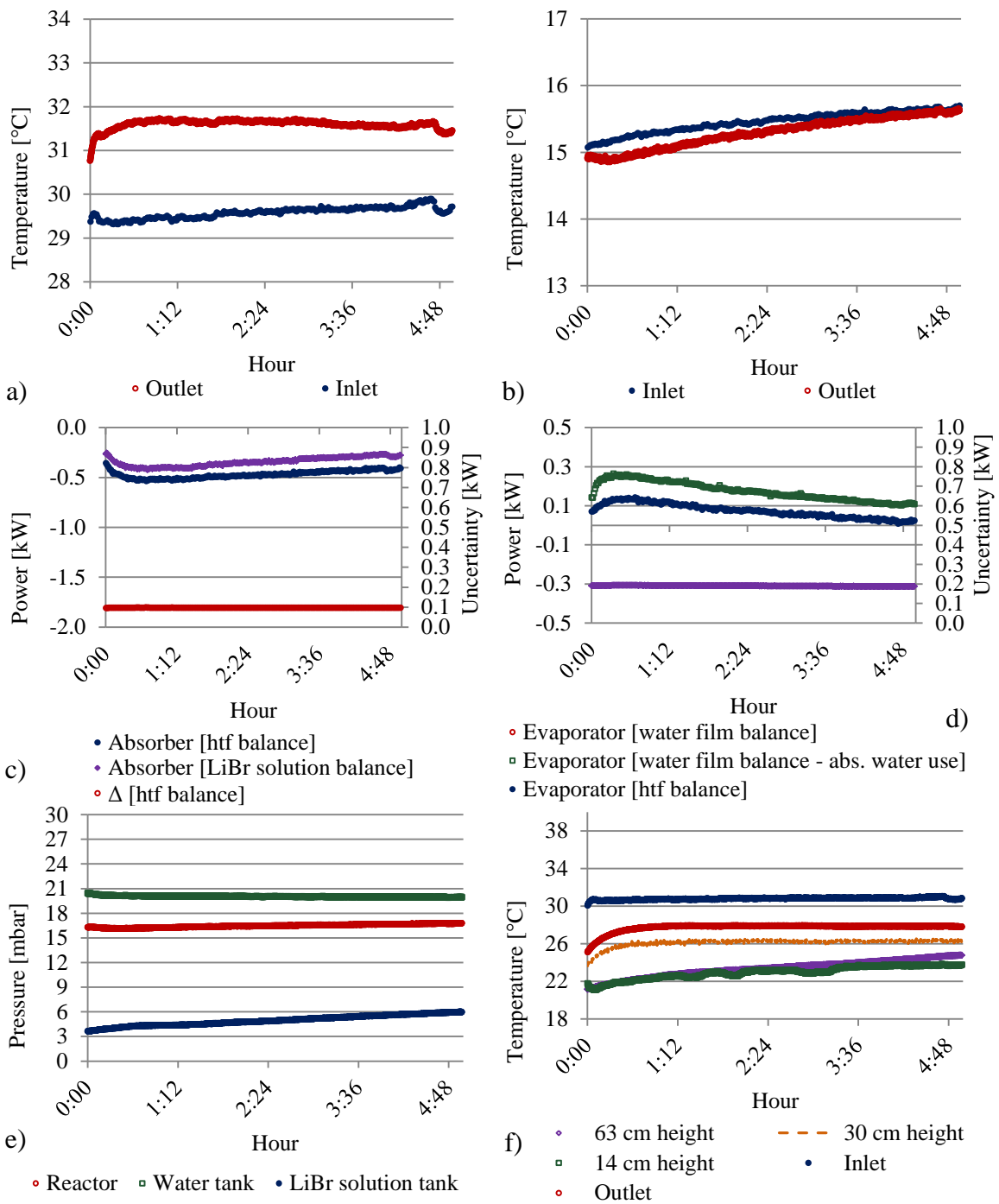


Figure C20. Experimental results obtained in absorption/evaporation operating mode for the Test 10. a) HTF temperature (absorber); b) HTF temperature (evaporator); c) Power given from the HTF to the system (absorber); d) Power given from the HTF to the system (evaporator); e) Vapor pressure; f) LiBr solution temperature (solution tank)

C2.2. Solution LiBr mass concentration correlation

To calculate the LiBr mass concentration in the solution a correlation proposed by Hellmann (Hellmann and Grossman, 1996) and relating the solution density with the solution temperature and solution LiBr mass concentration is used. This correlation is shown in Equation C2.

$$\rho_{st} = \frac{1145.36 + 470.84 * x_{LiBr} + 1374.79 * (x_{LiBr}^2)}{1000} - (33.3393 + 57.1749 * x_{LiBr}) * \frac{(T + 273.15)}{100000} \quad (C2)$$

Where: ρ_{st} is the solution density (in g/cm³), x_{LiBr} is the solution LiBr mass concentration (values from [0-1]) and T is the solution temperature (in °C).

C2.3. LiBr mass balance in the reactor

To calculate the solution outlet mass flow in the reactor, an approach considering the solution LiBr mass balance can be used.

During the desorption or absorption process, the solution losses or gains water, respectively. Hence, in steady conditions, the amount of LiBr present in the solution entering and leaving the reactor remains constant. Then, the solution outlet mass flow can be calculated using Equation C3, described below.

$$\dot{m}_{LiBr} = \dot{m}_{st_i} * x_{LiBr_i} = \dot{m}_{st_o} * x_{LiBr_o} \quad (C3)$$

Where, \dot{m}_{LiBr} is the LiBr mass flow which remains constant, \dot{m}_{st_i} is the solution inlet mass flow, \dot{m}_{st_o} is the solution outlet mass flow, x_{LiBr_i} is the inlet solution LiBr mass concentration and x_{LiBr_o} is the outlet solution LiBr mass concentration.

Since, the solution LiBr mass concentrations can be calculated using a correlation proposed by Hellmann (Hellmann and Grossman, 1996) (see Annex C2.2) and the solution inlet mass flow can be measured by the Coriolis flowmeter F2; then, the solution outlet mass flow can be calculated using Equation C3.

C2.4. Dühring diagram associated to the system components

In order to identify the pressure working conditions associated to the solution tank, water tank and reactor, a Dühring diagram is shown in Figure C21.

Considering as working hypothesis that: the LiBr mass fraction in the reactor and in the solution tank are the same (50%) and the water tank, solution tank and reactor solution film temperatures are 20°C, 20°C and 40°C, respectively; then, the saturation vapor pressure associated to these elements during the desorption processes can be estimated in Figure C21.

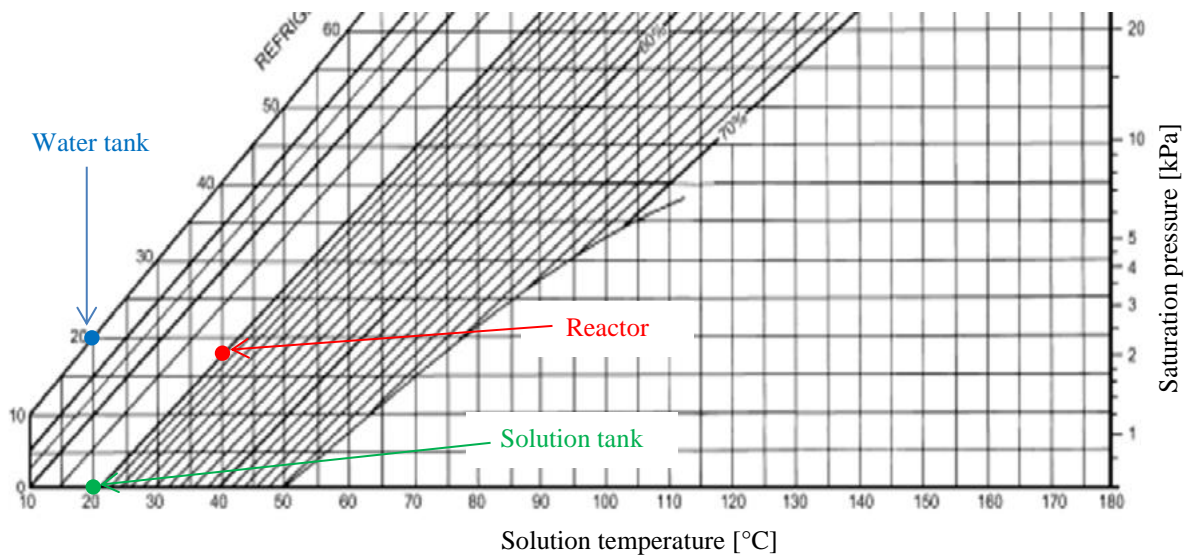


Figure C21. Equilibrium chart for aqueous Lithium Bromide solutions (ASHRAE, 2005). Working vapor pressures of the system components.

A similar behavior can be expected during the absorption processes, which implies that the vapor pressures in the water tank and in the reactor are, in general, higher than in the solution tank.

Annex C3

C3.1. Comparison against simulation

As it was mentioned in section 3.3, the model described in section 2.1 was used to simulate the prototype functioning under the same inlet conditions of two experimental tests in desorption/condensation and absorption/evaporation operating modes, presented in section 3.2.

In this section, a comparison between the experimental and simulated results associated to one test in desorption/condensation mode (charge) and on test in absorption/evaporation mode (discharge) are presented.

C3.1.1. Desorption/condensation

As it was mentioned in section 3.3.1, the experimental Test 2 was chosen to compare against the simulation model in desorption/condensation operating mode. In Figures C22 and C23 are presented the experimental and simulated prototype performance associated to different parameters for Test 2.

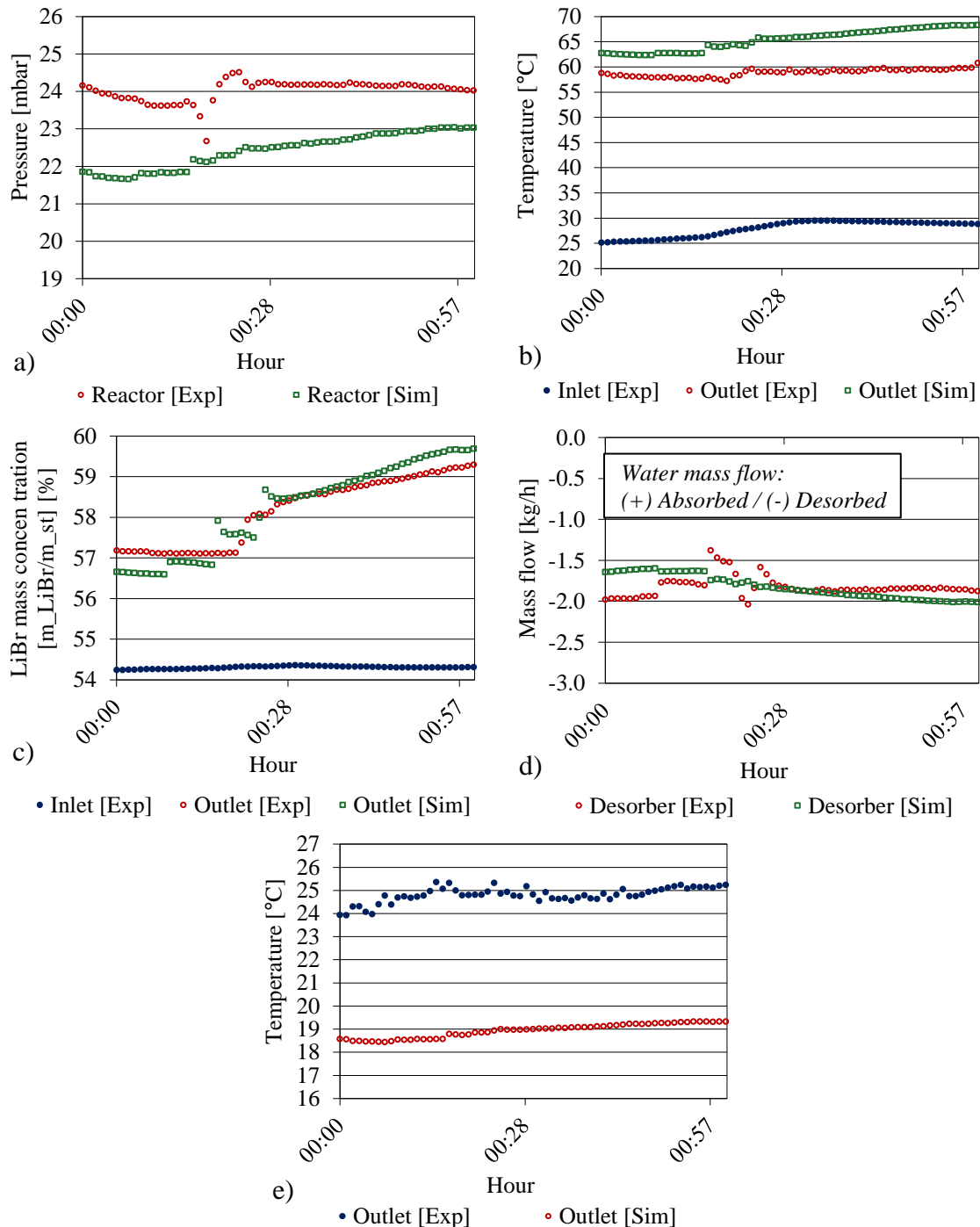


Figure C22. Comparison between experimental and simulated results obtained in desorption/condensation operating mode for the Test 2. a) Pressure in the reactor b) LiBr solution temperature (desorber); c) LiBr mass concentration (desorber); d) Desorbed/condensed water mass flow (reactor); e) Water film temperature (condenser)

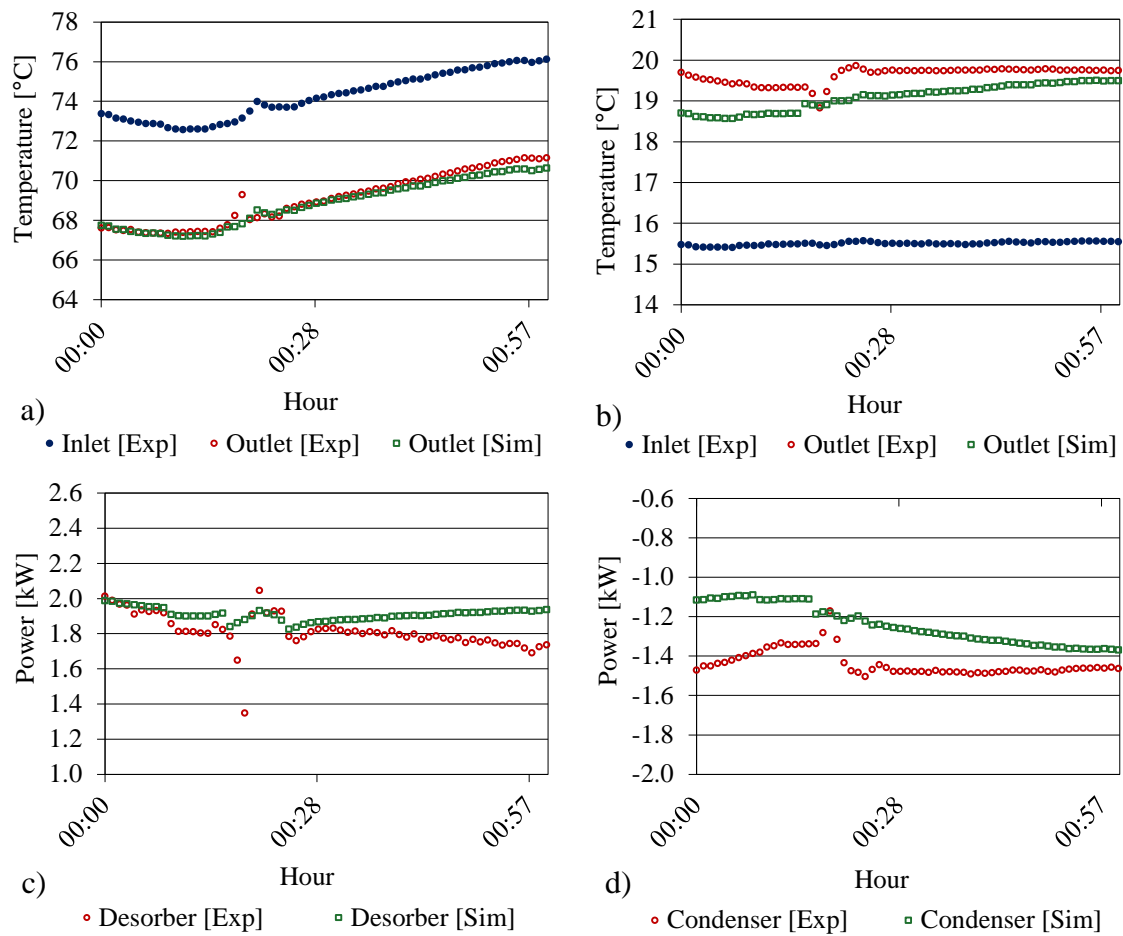


Figure C23. Comparison between experimental and simulated results obtained in desorption/condensation operating mode for the Test 2. a) HTF temperature (desorber); b) HTF temperature (condenser); c) Power given from the HTF to the system (desorber); d) Power given from the HTF to the system (condenser);

C3.1.2. Absorption/evaporation

As it was mentioned in section 3.3.2, the experimental Test 8 was chosen to compare against the simulation model in absorption/evaporation operating mode. In Figures C24 and C25 are presented the experimental and simulated prototype performance associated to different parameters for Test 8.

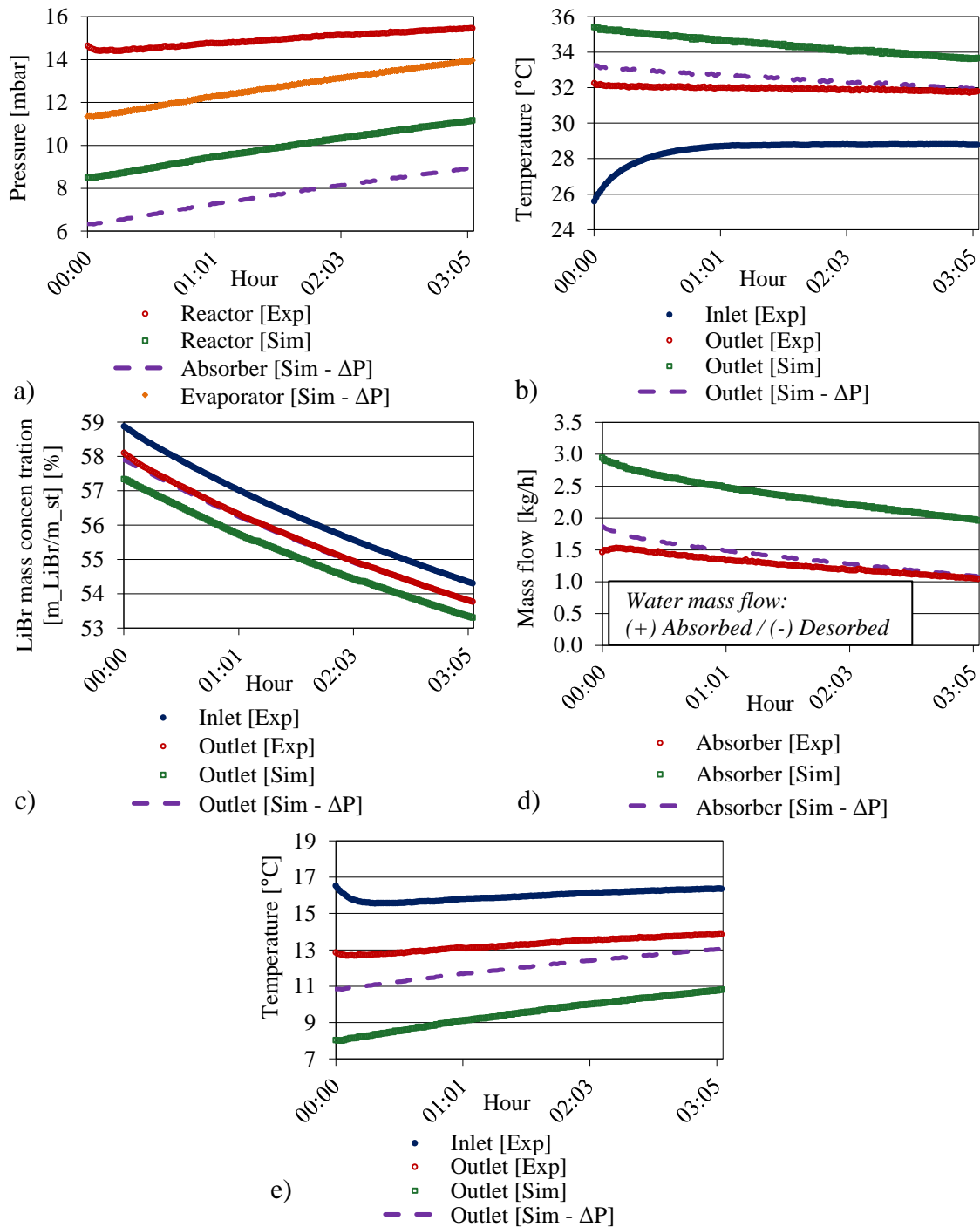


Figure C24. Comparison between experimental and simulated results obtained in absorption/evaporation operating mode for the Test 8. a) Pressure in the reactor b) LiBr solution temperature (absorber); c) LiBr mass concentration (absorber); d) Absorbed/evaporated water mass flow (reactor); e) Water film temperature (evaporator)

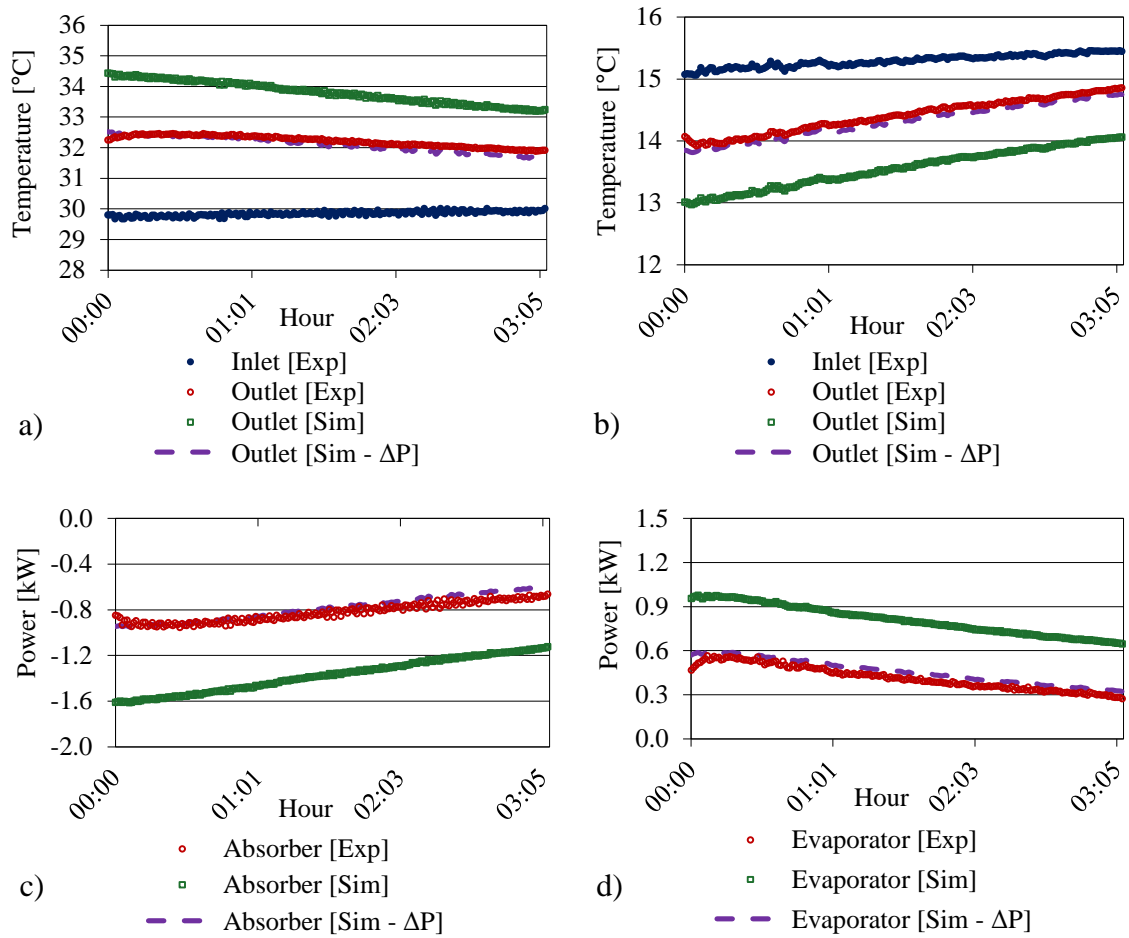


Figure C25. Comparison between experimental and simulated results obtained in absorption/evaporation operating mode for the Test 8. a) HTF temperature (absorber); b) HTF temperature (evaporator); c) Power given from the HTF to the system (absorber); d) Power given from the HTF to the system (evaporator)

ANNEX D

Annex D1

D1.1. Physical properties correlations for the KCOOH-H₂O solution

In this section the physical properties correlations found in the literature for the KCOOH-H₂O solution are described; these properties were: the density, the thermal conductivity, the absolute viscosity, the specific heat, the solution crystallization curve and the correlation for the equilibrium condition at the interface between the KCOOH-H₂O solution film and the vapor.

All these physical properties were used in the simulation model developed in Chapter 2 in order to study the interseasonal heat storage annual performance when a KCOOH-H₂O solution is used instead of a LiBr-H₂O solution.

KCOOH-H₂O properties not found in the literature were considered to be the same as those of LiBr-H₂O (binary mass diffusion, solution enthalpy and water partial enthalpy in the solution).

D1.1.1. Density

The KCOOH-H₂O solution density correlation obtained by (Lefebvre, 2015) is indicated below:

$$\rho_{KCOOH-H_2O} = \alpha T + \beta \quad [kg/m^3] \quad (D1.1)$$

Where:

$\alpha = A_1 \times (100 \times x_{KCOOH})^2 + A_2 \times (100 \times x_{KCOOH}) + A_3$	
$\beta = B_1 \times (100 \times x_{KCOOH}) + B_2$	
$A_1 = 5.2056E - 05$	$B_1 = 6.9766E00$
$A_2 = -7.1330E - 03$	$B_2 = 9.8993E02$
$A_3 = -1.6900E - 01$	

Where: $0.1 < x_{KCOOH} < 0.75$ and $0^\circ C < T < 60^\circ C$

D1.1.2. Specific heat

The KCOOH-H₂O solution specific heat correlation obtained by (Lefebvre, 2015) is indicated below:

$$c_{p_{KCOOH-H_2O}} = aT + b \quad \left[\frac{J}{(kg \times K)} \right] \quad (D1.2)$$

Where:

$a = \alpha \ln(100 \times x_{KCOOH}) + \beta$	
$b = \alpha' \exp(\beta' \times 100 \times x_{KCOOH})$	
$\alpha = 0.98384$	$\alpha' = 4.1694E03$
$\beta = -1.8266$	$\beta' = -9.5842E - 03$

Where: $0.05 < x_{KCOOH} < 0.50$ and $-30^\circ C < T < 50^\circ C$

D1.1.3. Thermal conductivity

The $KCOOH-H_2O$ thermal conductivity correlation obtained by (Longo and Gasparella, 2015) , (Longo and Gasparella, 2016) is indicated below:

$$\begin{aligned} \lambda_{KCOOH-H_2O} = & (0.563 + 2.02 \times 10^{-3} \times T - 8.31 \times 10^{-6} \times T^2) + \\ & (-0.116 - 3.78 \times 10^{-3} \times T + 2.84 \times 10^{-5} \times T^2) \times x_{KCOOH} + \\ & (-0.14 + 3.87 \times 10^{-3} \times T - 3.48 \times 10^{-5} \times T^2) \times (x_{KCOOH})^2 \end{aligned} \quad \left[\frac{W}{(m \times K)} \right] \quad (D1.3)$$

Where: T [$^{\circ}C$] and x_{KCOOH} [salt mass fraction]

D1.1.4. Absolute viscosity

The $KCOOH-H_2O$ absolute viscosity correlation obtained by (Longo and Gasparella, 2015), (Longo and Gasparella, 2016) is indicated below:

$$\begin{aligned} \mu_{KCOOH-H_2O} = \mu_{H_2O} \times \exp \left[\left(1.119 - \frac{3.615 \times 10^2}{TK} - \frac{10.23}{(TK)^2} + \frac{0.984}{(TK)^3} \right) + \right. \\ \left. \left(3.737 - \frac{95.37}{TK} - \frac{8.764}{(TK)^2} + \frac{1.064}{(TK)^3} \right) \times x_{KCOOH} + \right. \\ \left. \left(-7.673 - \frac{62.7}{TK} + \frac{15.92}{(TK)^2} + \frac{1.101}{(TK)^3} \right) \times (x_{KCOOH})^2 + \right. \\ \left. \left(3.46 + \frac{2.168 \times 10^3}{TK} + \frac{17.74}{(TK)^2} + \frac{1.095}{(TK)^3} \right) \times (x_{KCOOH})^3 \right] \end{aligned} \quad \left[\frac{kg}{(m \times s)} \right] \quad (D1.4)$$

Where $\mu_{H_2O} \left[\frac{kg}{(m \times s)} \right]$ is the absolute viscosity of pure water (a function of temperature) and it is described in the Annex B1.2.

Where:

$$TK = T + 273.15$$

Where: T [$^{\circ}C$] and x_{KCOOH} [salt mass fraction].

D1.1.5. Solubility crystallization curve

Solubility curves associated to the KCOOH-H₂O solution have been measured by (Lefebvre, 2015) and (Balarew et al., 2001). Figure D1 shows the experimental curve measured by these authors.

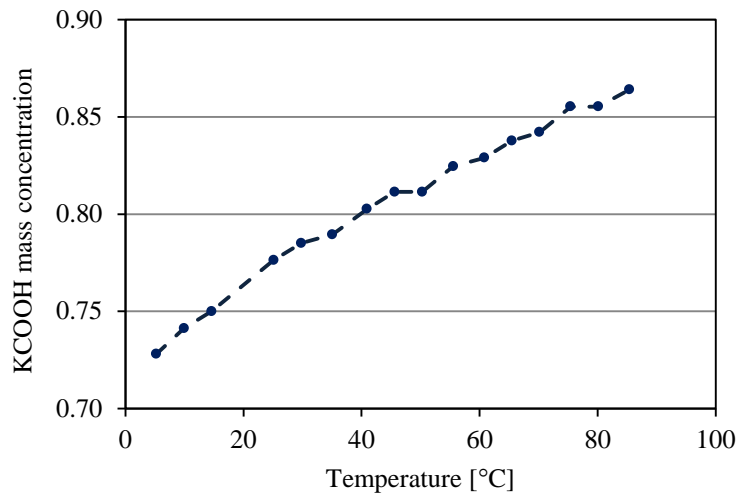


Figure D1. KCOOH-H₂O solution solubility curve (Lefebvre, 2015)

From the experimental data shown in Figure D1, a polynomial function is proposed to describe the correlation between the temperature and the mass concentration in the KCOOH-H₂O solubility curve. The proposed correlation is described below in Equation D1.5.

$$f_{cry}(T) = x_{KCOOH_{sat}} = 1.2887 \times 10^{-7} \times T^3 - 2.5025 \times 10^{-5} \times T^2 + 0.0029722 \times T + 0.71332 \quad [-] \quad (D1.5)$$

Where: $0.7 < x_{KCOOH} < 0.9$ and $0^\circ\text{C} < T < 100^\circ\text{C}$.

D1.1.6. Vapor pressure of the KCOOH-H₂O solution

A graphical correlation for the equilibrium condition at the interface between the KCOOH-H₂O solution and the vapor was obtained by (Lefebvre, 2015) and is shown in Figure D2.

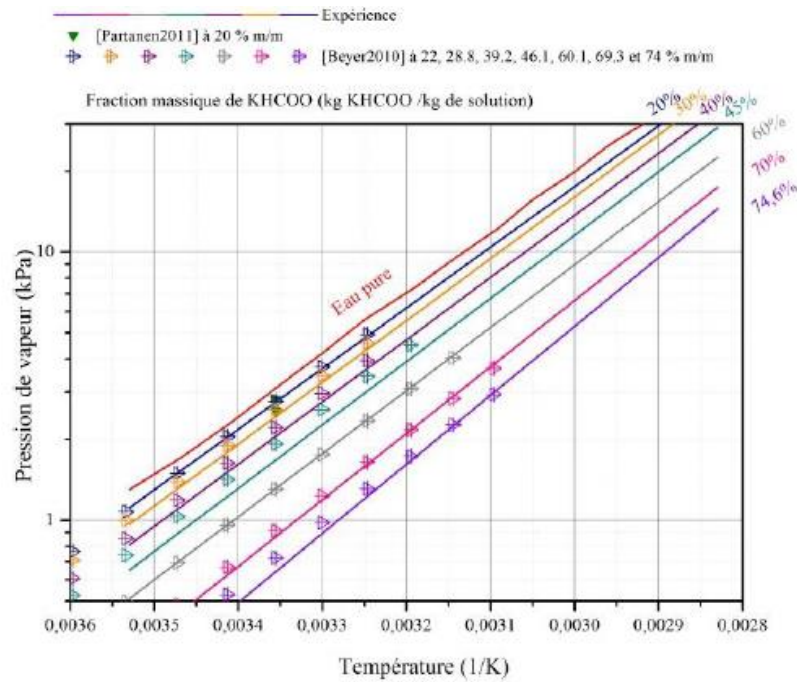


Figure D2. Vapor pressure curves for the KCOOH-H₂O solution (Lefebvre, 2015)

From experimental data shown in Figure D2, a correlation function between the vapor pressure, the KCOOH mass concentration and the temperature was developed considering several straight-lines interpolations.

$$T_{KCOOH_{equ}} = \text{fonction}(P, x_{KCOOH}) \quad [^{\circ}\text{C}] \quad (\text{D1.6})$$

Where:

If $x_{KCOOH} \geq 0.7$

$$Inv_T_min = -0.000405042065704 \times \log_{10} \left(\frac{P}{1000} \right) + 0.003330252103407$$

$$Inv_T_max = -0.000391870026180 \times \log_{10} \left(\frac{P}{1000} \right) + 0.003282113832506$$

$$T_{KCOOH_{equ}} = \left(\left(\frac{Inv_T_max - Inv_T_min}{0.746 - 0.7} \right) \times (x_{KCOOH} - 0.7) + Inv_T_min \right)^{-1} - 273.15 \quad [^{\circ}\text{C}]$$

If $0.6 \leq x_{KCOOH} < 0.7$

$$Inv_T_min = -0.000426548617119 \times \log_{10} \left(\frac{P}{1000} \right) + 0.003406194621180$$

$$Inv_T_max = -0.000405042065704 \times \log_{10} \left(\frac{P}{1000} \right) + 0.003330252103407$$

$$T_{KCOOH_{equ}} = \left(\left(\frac{Inv_T_max - Inv_T_min}{0.7 - 0.6} \right) \times (x_{KCOOH} - 0.6) + Inv_T_min \right)^{-1} - 273.15 \quad [^{\circ}\text{C}]$$

If $x_{KCOOH} < 0.6$

$$Inv_T_min = -0.000424669638553 \times \log_{10} \left(\frac{P}{1000} \right) + 0.003449779708358$$

$$Inv_T_max = -0.000426548617119 \times \log_{10} \left(\frac{P}{1000} \right) + 0.003406194621180$$

$$T_{KCOOH_{equ}} = \left(\left(\frac{Inv_T_max - Inv_T_min}{0.6 - 0.45} \right) \times (x_{KCOOH} - 0.45) + Inv_T_min \right)^{-1} - 273.15 \text{ [}^\circ\text{C]}$$

Where: $0 < x_{KCOOH} < 1$ and P [Pa] are the associated equilibrium conditions to $T_{KCOOH_{equ}}$ at the KCOOH solution film interface.